City University London

NUMERICAL SIMULATION OF NONLINEAR RESPONSE OF MOORED FLOATING STRUCTURES TO STEEP WAVES

By

Shiqiang Yan

Msc, B.Eng.

Supervisor

Dr. Qingwei Ma

A thesis submitted to

City University

in fulfilment of requirement of degree of

Doctor of Philosophy

School of Engineering and Mathematical Sciences

City University, London

December, 2006

CONTENTS

LIST OF FIGURES

LIST OF TABLES

ACKNOWLEDGEMENTS

This study is sponsored through the project 'Nonlinear Response of Moored Floating Structures to Steep Waves 'funded by the UK Engineering and Physical Sciences Research Council (EPSRC, GR/R78701) , for which the author is most grateful.

I would like to give my sincere gratitude to my supervisor Dr. Q.W. Ma for the guidance, inspiration, assistance and supervision he has shown in helping me complete this work. The patience and encouragement when various problems occurred are much appreciated. I would also like to thank him for his comments on the draft of this thesis.

I am indebted to Mr. S. Chidavaenzi and Miss M. Careddu in our research group, who read the manuscript in detail. Their valuable suggestions and discussions lead to a significant improvement of this thesis. I would also offer my thanks to my colleagues in the school, for their suggestions and discussion on my work.

Finally I also thank my wife, Yang Zhang for her unconditional support and endless patience. I also give my deep appreciation to my mother. Without them, this work would not have been completed.

DECLARATION

No portion of the work referred to in the thesis has been submitted in support of an application for other degree or qualification of this or any other university or other institute of learning.

I grant powers of discretion to the City University Library to allow this thesis to be copied in whole or in part without any reference to me. This permission covers only single copies made for study purpose subject to normal condition of acknowledgement.

ABSTRACT

This thesis presents a newly developed Quasi Arbitrary Lagrangian-Eulerian Finite Element Method (QALE-FEM) for numerically simulating wave-body interaction problems based on the fully nonlinear potential theory. The boundary value problem in this model is solved by a finite element method (FEM). The main difference between this method and the conventional FEM is that the complex mesh is generated only once at the beginning of the calculation and is moved at all other time steps in order to conform to the motion of the free surface and structures. This feature allows one to use an unstructured mesh with any degree of complexity without the need of regenerating it every time step, which is generally inevitable and very costly. Due to this feature, the QALE-FEM has high computational efficiency when applied to problems associated with the complex interaction between large steep waves and structures since the use of an unstructured mesh in such a case is likely to be necessary. In order to achieve overall high efficiency, some numerical techniques, including the method to move interior nodes, the technique to redistribute the nodes on the free surface, the scheme to calculate velocities, are developed. To overcome the difficulty associated with the force and acceleration of free-response floating bodies, an ISITIMFB (Iterative Semi-Implicit Time Integration Method for Floating Bodies) iterative procedure is developed.

The developed QALE-FEM method is applied to simulate the waves generated by a wavemaker and their interaction with sandbars on the seabed, waves generated by a floating body in forced motion, the response of a 2D or 3D freely floating body to a steep wave. Some of the results have been validated by analytical solutions, experimental data and numerical results from other methods. Satisfactory agreements are achieved. The convergence properties of this model in cases with or without floating bodies are all investigated. The nonlinearities associated with different cases are investigated. The mesh quality is also investigated using either qualitative or quantitative methods. The results show the mesh quality during long-period simulation is retained. The efficiency of the QALE-FEM method is finally discussed and compared with other methods. It is concluded that the QALE-FEM method is 10 times faster than the conventional FEM method in case with unstructured mesh and at least 7 times faster than the fast BEM methods for the fully nonlinear waves.

LIST OF SYMBOLS

a	amplitude of the motion of the wavemaker
a_b	sandbar amplitude; amplitude of the motion of a floating body
c	phase velocity of wave
d	water depth
$d_{c\max}$	maximum distance from the gravitational centre to the wetted body surface
e	element
$\vec{e}_x, \vec{e}_y, \vec{e}_z$	unit vectors in the x-,y- and z-directions
$\vec{f}_h$, $\vec{N}_h$	hydrodynamic force and moment
$\vec{f}_m$, $\vec{N}_m$	force and moment due to the mooring line
g	gravitational acceleration
k	wave number, spring stiffness in the spring analogy method
k_b	wave number of sandbar patch
k_m	stiffness of a mooring line
k^{linear}	linear spring stiffness
l	distance of two spatial points, model of $\vec{l}$
$\vec{l}$	spatial vector
m	rank of the MLS formulation
$\vec{n}, \vec{\tau}_x, \vec{\tau}_y$	normal and tangential vectors
$\vec{n}_b$	direction perpendicular to the normal vector of the body surface
$\vec{n}_r$	replacer of $\vec{n}$ for calculating velocity at nodes near crest
p	water pressure
q	element quality
$\vec{r}_b$	position vector relative to the gravitational centre
$\vec{r}_m$	position vector of the mooring point relative to the gravitational centre
$s_{\max}$	radius of influence area
t, τ	dimensional time and nondimensionlised time
$\vec{u}$	velocity vector of the flow
u, v, w	x-,y- and z-directional velocity components of fluids
x,y,z	spatial coordinates in a Cartesian coordinate system

$\vec{x}$	spatial coordinate
γ_b , γ_f	coefficients in the definition of the spring stiffness
θ^{ijk}	facing angle in an element *i-j-k*
$\vec{\theta}(\alpha,\beta,\gamma)$	Euler angles
κ	weight coefficient for semi-spring stiffness; curvature of the curve
λ	wave length
λ_b	wave length of sandbar patch
ν_0	magnitude of the damping coefficient
ξ	curvilinear coordinates
ρ	density of the fluid
$\vec{\tau}_b$	orthogonal vector of $\vec{n}_b$
τ_w	tangential vector of the waterlines
ψ , φ	initial position of and velocity potential on the free surface
ω	wave frequency
ω_b	circular frequency of the motion of a floating body
ϕ	velocity potential
$\hat{w}$, ϖ	weight function
A	wave amplitude
A,B	coefficient matrices of MLS formulation
B	width of the tank
B_b	Breadth of the floating body
C_g	group velocity of the water wave
C^{ijk}	torsional stiffness in an element *i-j-k*
D_r	initial draft of the floating body
E_r ,*err*	relative error
$\vec{F}$, $\vec{N}$	force and moment acting on the floating body
$\vec{F}_s$	resultant spring force
$F^{ijk}_{torsional}$	force generated by the torsional springs
H	wave height
J	objective function of MLS method; node number
K_r	reflection coefficient
L	length of the tank

L_b	Length of the floating body
L_{bp1} , L_{bp2}	distances from the point to the front and lee sides of the bar patch
L_m	length of the damping zone
$L_{\max}$, $L_{\min}$	maximum and minimum wave lengths
L_s	length of the curved waterline
L_w	distance between the wavemaker and the floating body
L_{wp}	distance from the wavemaker to the point considered
M^{ijk}	moment due to the torsional springs
N, E	node number and element number
$N_J(x, y, z)$	shape function of the FEM
P	basis functions in MLS method
Q_s	mesh quality
R^{ijk}	matrix for converting rotational angle to nodal displacement
R_i, R_c	inradius and circumradius of an element
$\vec{S}$	translational displacement of the floating body
S_b	wetted body surface
S_n	Numann boundary
S_P	Dirichlet boundary
S_w	waterlines
$S_w, U_w, \dot{U}_w$	displacement, velocity and acceleration of the wavemaker
T	wave period
T_f	cut-off time of the ramp function
$\vec{U}$	velocity of the body surface
$\vec{\dot{U}}_c, \vec{\dot{\Omega}}, \vec{U}_c, \vec{\Omega}$	acceleration ,angular acceleration, velocity and angular velocity of body
Δijk	triangle *i-j-k*
$\Delta\vec{r}$	nodal displacement
Δt	time step
$\Delta x, \Delta y$	x- and y-directional mesh sizes on the free surface
Δs	arc-segment length
ΔS_n	triangular surface of element
Φ	acceleration potential

Ψ^{fs}, Ψ^{bs}	correction coefficients of the spring stiffness due to free surfaces and body surfaces, respectively
$\forall$	fluid domain; volume of an element
$[A]$,$[B]$	coefficient matrices of the FEM formulaiton
$[B]$	matrix formed by Euler angles
$[E_{ij}]$	matrix based on the Euler angle of spring *i-j*
$[M]$, $[I]$	mass and inertia matrices
∇	gradient operator
∇^2	Laplace equation operator
$\frac{\partial}{\partial t}$	Partial time derivative in the Cartesian coordinate system
$\frac{\partial \varsigma}{\partial x}$, $\frac{\partial \varsigma}{\partial y}$	local slopes of the free surface
$\frac{D}{Dt}$	substantial derivative defined as $\frac{D}{Dt} = \frac{\partial}{\partial t} + \nabla\phi \cdot \nabla$
$\frac{\delta\phi}{\delta t}$	rate of change of velocity potential obtained by following a point on the body surface

1. INTRODUCTION

1.1. Background

Use of moored floating structures, such as SPARs and FPSOs, as production and storage systems is now an ever-increasing practice in offshore oil and gas industry, particularly with the operations moving to deeper sea. Operating in such environments, the structures are more likely to be exposed to very harsh seas and therefore may not avoid undergoing large loading and motions, which will result in many undesired consequences. While the environmental conditions are affected by tide, wind, current and waves, the effect of waves is of most concern.

Fig.1.1.1 Freak waves and ships (http://www.tvnz.tx.co.nz)

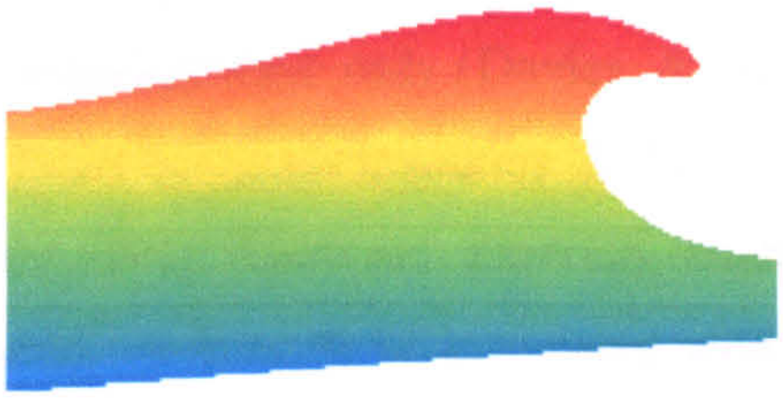

Fig.1.1.2. Overturning wave

The responses of floating structures to waves are very complicated, particularly in cases involving steep waves. There are two typical effects of waves which may inflict significant damage to the structures. The first one is the destructive energy released by steep waves, such as freak waves (Fig 1.1.1) and overturning waves (Fig 1.1.2). This effect may result in huge instantaneous huge loads on the floating structure causing it to capsize. The second one is the so called resonance problem. This phenomenon not only makes the structures undergo relatively huge motion, but also creates large forces which may also cause capsizing of ships or damage to the structures. This may result in high risk in the operation of the structures and lead to seasickness of people who work and live on these vessels. Furthermore, the large motion of these moored floating vessels may cause additional large tension in mooring lines that may already be critically loaded. Due to this fact, the responses of the floating structures to steep waves need to be carefully investigated in order to optimise the design/operation and avoid the latent risk from the waves.

On the other hand, the floating structures and their response to the waves also affect the waves themselves. Generally, the surface of the structure reflects and scatters the incident waves. This makes the waves around the structure become much steeper and/or more complex. This

interaction between the waves and the floating structures complicates the problem rendering it nonlinear. Its accurate prediction lies in the vigorous analysis of the interaction between the structures and the waves.

Many researchers have studied this complex wave-structure interaction problem by using various analytical methods based on linear or higher order scattering analyse either in time domain or in frequency domain, e.g. linear models in the frequency domain (Newman, 1977; Mei, 1989), linear models in the time domain (Bratland, Korsmeyer & Newman, 1997), higher order methods in frequency domain (perturbation theory by Davies, & Heathershaw,1984; Faltinsen, Newman.& Vinje., 1995, Malenica & Molin,1995, multiple scale analysis by Mei,1985, mild-slope approach by Chamberlain & Porter,1995) and higher order methods in time domain (Sclavounos & Kim, 1995, Skourup, Buchmann & Bingham,1997). Although these studies are useful for calculating wave loads and radiation damping on a body, most of the works have been simplified and applied to cases with small to moderate wave steepness. They have until recently been limited to the problems involving wave only (Davies, & Heathershaw, 1984; Mei, 1985; Chamberlain & Port, 1995), fixed body (Sclavounos & Kim, 1995) and forced-motion body (Eatock Taylor, Wang & Wu,1994). They are generally unable to give satisfactory results for cases with strong nonlinearity, such as those associated with extremely steep waves and their interaction with the floating bodies. As indicated by Koo & Kim (2004), third order or higher order contributions of the force on a freely floating body in their test cases are very obvious. This means a fully nonlinear analysis is necessary to deal with these problems, particularly when the waves are very steep or overturning as shown in Fig.1.1.1 and Fig.1.1.2.

In order to consider full nonlinearity associated with wave-structure interaction problems, all terms with different order should be taken into account in the expansions. Therefore, the expansions are difficult or impossible to solve analytically. Although an experimental investigation can be carried out, it is expensive and the results might only be applicable to some special cases. This generates more interest in numerically simulating nonlinear water waves and their interaction with structures.

To numerically simulate these problems, there are mainly two classes of theoretical models for cases with finite water depth. One is based on the general flow theory and the other is based on the potential theory. In the first class of models, the Navier-Stokes and continuity equations together with proper boundary conditions are solved, while in the second class, the Laplace's equation with fully nonlinear boundary conditions is dealt with. For brevity, the first class models will be called NS models and the second called FNPT (fully nonlinear potential theory) models in this work. Various numerical methods, such as finite element, finite volume and finite difference methods have been used to solve the Navier-Stokes and continuity equations in investigating nonlinear water waves and their interaction with fixed structures. Whatever method is used, solving NS equations is always a time consuming task.

In the FNPT models, the flow is commonly described using potential theory in which the viscosity of fluid, the surface tension and compressibility are all neglected. Based on the potential flow assumption, the flow can be governed by a Laplace's equation about the velocity potential. The Laplace's equation is linear, but the problem is made nonlinear by the boundary conditions on the free surface. The numerical results obtained by many researchers (Longuet-Higgins,& Cokelet,1976; Wu & Eatock Taylor ,1995 ; Ma, Wu & Eatock Taylor ,2001b and Grilli, Guyenne & Dias, 2001) have proved that this model leads to satisfactory results even in cases with overturning waves. The number of unknowns in the FNPT models is smaller than that in NS models. In addition, the complexity of the Laplace's equation is also undoubtedly lower than the Navier-Stokes and continuity equations. Therefore, FNPT has high CPU advantage of FNPT models instead of NS models.

In these models, the key task is to solve the boundary value problem about the velocity potential. To do so, boundary element methods (BEMs) have been used in many publications, such as Cao, Schultz & Beck (1991), Celebi, Kim& Beck (1998), Clauss & Steinhagen (1999), Grilli, Guyenne&Dias (2001), Fochesato & Dias (2006), and so on, and have produced many impressive and useful results. Finite element methods (FEMs) have also been developed and used for two and three dimensional problems (Cai & Langtangen, 1998; Westhuis & Andonowati , 1998; Ma, Wu & Eatock Taylor ,2001; Wu & Hu, 2004). Though both methods have proved to be quite efficient, the FEMs need less memory and so are computationally more efficient, as indicated by Wu & Eatock Taylor (1995) , Ma (1998) and Ma, Wu & Eatock Taylor (2001a,2001b). A drawback of the FEMs, however, is that an unstructured mesh is generally required for complex interaction between water waves and structures (e.g. the mesh around the complex-shape floating bodies or overturning waves) and may need to be remeshed at every time step to follow the motion of waves and/or structures. Repeatedly regenerating such a mesh can make the required CPU time prohibitive in a simulation of several thousands steps on a normal workstation. How to reduce the computational expense in dealing with mesh has become a bottleneck of FEM for numerical simulation of nonlinear interaction between steep waves and freely floating bodies.

1.2. Objectives of the study

This study will develop a new finite element scheme based on a fully nonlinear potential theory to simulate the interaction between steep waves and three-dimensional freely floating bodies. In this method, the computational mesh is moved, in place of regenerating it, to conform to the motion of the boundary. All the simulations will be carried out in a numerical wave tank. The main tasks are,

1. Develop a robust method to move the unstructured mesh in order to conform to the motion of the boundary;

2. Develop a velocity calculation method to evaluate the velocity at the nodes on the free surface and the body surface based on the velocity potential suitable for the arbitrary and moving the mesh;
3. Develop a method to calculate the motion of the free-response floating structures;
4. Apply these methods to simulate the steep waves and their interaction with sandbars on the sea bed;
5. Apply these methods to simulate two-dimensional and three-dimensional interaction between waves and free-response floating bodies.

1.3. Outline of the thesis

A literature review and a discussion of previous work are presented in Chapter 2. The mathematical formulation and numerical models are described and discussed in Chapter 3. A scheme to move the computational mesh and the method to calculate the velocity follows in Chapter 4 and 5. In Chapter 6, an iterative procedure to calculate the acceleration of and force acting on the floating body is presented. Chapter 7 presents the application of this method in the modelling the steep waves in a numerical tank and its interaction with sandbars on the seabed. The interaction between steep waves and two-dimension floating bodies are presented in Chapter8, while Chapter 9 gives the validation and discussion for 3D response of the floating body to steep waves. The thesis ends with the conclusion and recommendations for the future work in the Chapter 10.

2. LITERATURE REIVEW AND DISCUSSION OF PREVIOUS WORKS

This chapter reviews previous studies associated with modelling the interaction between steep waves and floating bodies. There are various methodical models such as linear model in the frequency domain, linear model in the time domain, high order model in the frequency domain, high order model in the time domain based on the assumption for potential flow. Detailed review of these models has been given by Ma (1998). The present thesis focuses on the modelling of fully nonlinear water waves and their interaction with floating bodies.

2.1. Mathematical models

To numerically simulate the fully nonlinear water wave problem, two types of mathematical models are commonly employed. As described in Chapter 1, one is based on the general flow theory (NS models) and the other is based on the potential theory (FNPT models).

2.1.1 NS models and different formulations

In the community of researchers who use NS models, the Navier-Stokes and continuity equations together with proper boundary conditions are solved. Because viscosity is taken into account in the Navier-Stokes equations, the NS models are more widely used in cases where the viscosity plays an important role, e.g. viscous dynamic free surface (Hirt & Nichols ,1981; Huerta, Liu,1988; Navti, Lewis & Taylor,1998; Spivak, Vanden-Broeck & Miloh,2002; Yue, Lin & Patel ,2003; Greaves,2004 and Wu, Eatock Taylor.& Greaves,2004), boundary layer near the moving boundary (Zhang & Chwans, 1996, 1999), shallow water waves and/or breaking waves (Chen, 2003; Hieu, Katsutoshi & Ca,2004; Devrard D., Marcer, Grilli & Fraunie .etc., 2005; Layton, Christara & Jackson, 2006) , wave-current-body interaction (Park,Kim& Miyta 2001). In the above applications, the common character of the computational domain is that the boundary of the domain, i.e. the free surface and the body surface, is moving during the whole calculation. According to this character, three different formulations have been suggested in order to treat the deformation of the fluid domain. They are Eulerian, Lagrangian and arbitrary Lagrangian-Eulerian (ALE) formulations.

In the Eulerian formulation, a fixed computational mesh is employed. The fluid moves relative to the mesh. Use of this formulation can handle, with relative ease, large distortions of interfaces between two different materials by employing proper interface capturing techniques (such as volume of fluids and level set). For example, Hirt & Nichols (1981) modeled the dynamics of free surface boundaries, Navti, Lewis & Taylor (1998), Yue, Lin & Patel (2003) and Greaves (2004) followed. Though they got acceptable results, a larger domain than necessary was employed in their application. This is because the domain must cover the area

where the fluid may reach. Furthermore, an extra governing equation should be solved which may smear the interfaces and the flow details near the air-fluid boundary. In addition, it seems have difficulty in handling cases with interfaces of three different materials, such as those with floating bodies in waves.

In the Lagrangian formulation, all nodes follow their corresponding fluid particles. In the other words, the velocity of the mesh nodes is equal to the velocity of the particles. As a result, the formulation allows a sharp tracking of interfaces between different materials. For instance, Donea , Fasoli-Stella & Giuliani (1976) simulated the transient fluid-structure problems by using FEM. However, if large distortions of the fluid domain occur, some nodes may become too close to or too far from others, leading to a breakdown of the computing process if remeshing is not performed.

The arbitrary Lagrangian Eulerian (ALE) formulation is a hybrid approach, in which the computational mesh does not need to adhere to fluid particles or to be fixed in space but can be moved arbitrarily. Based on this description, both the Eulerian and Lagrangian methods are special cases of the ALE method. This provides a capability to keep the character of the computational mesh and avoid any mesh collapsing or frequent remeshing. Therefore, the ALE formulation can make use of the merits of both the Lagrangian and Eulerian formulations and alleviate many of their drawbacks. Specifically, the interface can be precisely tracked without necessarily remeshing. Of course, the nodes have to be moved in order to conform to the deformation or distortion of interfaces or boundaries and the governing equations are made a bit more complex to account for the moving velocities of the mesh. The ALE formulation has been discussed and used in many publications. Huerta & Liu (1988), Henning & Peter (2000), Teng, Zhao & Bai (2001), Souli & Zolesio (2001) and Fabián, Raúl & Srinivasan (2004), .et al. are some recent applications of this method in the free surface problems.

Finite element, finite volume and finite difference methods are commonly used to solve the NS models in one of the above formulations/descriptions. However, there are three unknowns in 2-dimensional and four in 3-dimensional NS equation. Solving such an equation is always a time consuming task.

2.1.2. FNPT models

However, the velocity potential, in place of velocities is solved as unknown in the FNPT model. The governing equation is therefore simplified as a Laplace's equation for velocity potential. After the velocity potential is solved, the velocity can be obtained by calculating the spatial derivative of the velocity potential. The pressure can be estimated by using Bernoulli's equations. So they need much less computational resources to solve than the NS model. The FNPT model has high superiority in effective simulation of water waves. The linear Laplace's equation is made nonlinear by the boundary conditions on the free surface and the body surface.

A fully nonlinear boundary condition makes the simulation closer to the physical problem and so more suitable for some cases than second-order or higher order nonlinear boundaries which are usually used in analytical solutions.

In this model, the viscosity is ignored. Nevertheless, Comparison with experimental data, such as Clauss & Steinhagen (1999), Ma, Wu & Eatock Taylor (2001b) , has shown that the results obtained by this model are accurate enough in many cases. Grilli, Guyenne, &, Dias (2001) also gave accurate enough results even for cases with overturning waves and shoaling over a sea bed with complex geometry. Therefore, the FNPT model instead of the NS model should be employed if a case considered does not involve wave breaking and/or with small structures. The FNPT model has thus been adopted in many publications for problems associated with the nonlinear water waves and their interactions with structures.

The Laplace's equation is independent of time, but the boundary condition is time-dependent. These models are usually solved by a time marching procedure suggested by Longuet-Higgins & Cokelet (1976). Once the wave profile and the position of the structure are known in a time step, a mixed Dirichlet and Newman boundary value problem is formed which can be solved by a numerical method such as the finite element, boundary element method or other numerical methods. The velocities obtained at the nodes on the free surface will give a new free surface profile. The Bernoulli equation is applied to find the force acting on the structure, Newton's law will provide the new acceleration, velocity of the structure and therefore gives the new position of the structure. All of these will enable the problem to be solved at the next time step. The procedure can be repeated in principle for any desired period of time. Although Longuet-Higgins & Cokelet (1976) only focused their attention on two-dimensional wave problems, the results they obtained showed a high potential for their approach to be used for more complex problems. Their work created a foundation for the development of this model. Soon afterwards, Vinje & Brevig (1981) included two-dimensional submerged bodies in a fluid domain. Lin, Newman & Yue (1984) investigated the motion of the floating body.

Since then, many researchers worked on FNPT models and published many valuable papers. Most of them studied nonlinear waves propagating in a tank or its interaction with the seabed or submerged bodies. For example, Grilli, Skourup & Svendsen (1989), Grilli & Svendsen (1990), Ferrant (1994), Wu & Eatock Taylor (1994, 1995), Grilli, & Subramanya (1996), Grilli & Horrillo (1997) covered two dimensional cases. Cao, Schultz. & Beck (1991), Celebi Kim & Beck (1998), Grilli, Guyenne & Dias (2000) , Grilli, Guyenne & Dias (2001), Fochesato, Dias& Grilli (2003), Biausser, Grilli &. Fraunié (2003), Fochesato Dias & Grilli (2005) and Grilli, Fochesato & Dias (2005) simulated three dimensional cases.

In those applications, there are no surface piercing structures and therefore no intersecting lines (waterlines) between the structures and the free surface. Once a piercing structure, e.g. cylinder, is involved, the singularity problem and other problems associated with the waterlines

should be treated. Lin, Newman & Yue (1984), Wang, Yao & Tulin (1995), Grilli & Svendsen (1990), Grill & Subramanya (1994), Rainey (1997) discussed this problem and suggested different methods to deal with different singularity problems. A detailed review can be found in Ma (1998). Based on their suggestions, many investigations on the interaction between the waves and fixed or forced-motion structures have been made by various researchers. For example, Xue & Yue (1995), Ferrant (1995), Ma (1998) , Kim, Celebi & Kim (1998), Ma, Wu & Eatock Taylor (2001), Ferrant, Touze & Pelletier (2003), Markiewicz, Ben-Nasr, & Mahrenholtz (2003) simulated the wave scattered by fixed cylinders. Kashiwagi (1996) simulated the waves generated by a heaving floating body. Hu, Wu & Ma (2002) investigated the interaction between the waves and the forced-motion cylinders while Wang (2005) simulated the ship waves.

However, the publications about the interaction between fully nonlinear waves and free-response bodies are still very limited. One reason is the difficulty of evaluating the force on and acceleration of the floating body. This problem will be discussed in Section 2.5. Using the techniques for solving such a problem, several researchers have investigated 2D cases. Wu & Eatock Taylor (1996,2003) simulated the transient motion of a floating body in steep water waves. Beck (1994, 1999), Cao, Beck & Schultz (1994) made nonlinear computation of wave loads on and motions of a free-response rectangular barge in incident waves. Tanizawa (1995) ,Tanizawa & Minami (1998) , Tanizawa Minami & Naito (1999) , Koo (2003) and Koo & Kim (2004) simulated 2-dimensional barge-type freely floating body. Kashiwagi & Momoda (1998), Kashiwagi (2000) and Contento (2000) investigated wave-induced motions of 2-dimensional floating body with complicated shapes, Wang & Wu (2006) simulate the response of a 2D non-wall-sided body to nonlinear water waves. Compared to 2-dimensional problem, the three-dimensional problem is relatively more difficult to simulate not only because of more computing resource requirements but also because of many numerical difficulties, such as fitting the body surface, tracing the wave profiles and resolving the singularity problem on the waterlines. To author's knowledge, very few researchers presented numerical results for 3D cases. Only Wu & Hu (2004) have recently modelled the fully nonlinear interaction between waves and a three-dimensional cylindrical FPSO-like structure. Though, they presented interesting and encouraging results, the body geometry was relatively simple. The cases they simulated are symmetrical along the y-axis. This means that only 3 degrees of freedom is considered in their application. The nonlinear three-dimensional model also forms the basis of this study.

It should be pointed out that Boussinesq type models are also commonly used to simulate highly nonlinear water waves. (Madsen, Murray & Sorensen,1991,1992; Nwogu 1993; Wei, Kirby & Grilli .et al. 1995; Gobbi & Kirby, 1999; Madsen, Bingham & Liu,2002 ; Walkley & Berzins, 2002; Madsen, Bingham & Schaffer,2003; Fuhrman & Bingham,2004; Fuhrman,

Bingham & Madsen,2005 ; Koutandos, Karambas & Koutitas,2004). However, Boussinesq equations are obtained by integrating Laplace's equation in the vertical direction (the classic derivation can be found in Peregrine, 1967), it is therefore impossible to solve the problem involving free-response floating bodies because the fluid might be separated from the floating body in vertical direction. Hence, Boussinesq type models are not suitable in cases involving freely floating bodies.

2.2. Numerical methods

Both in the NS model and the FNPT model, the governing equation together with the corresponding boundary condition are impossible to be solved analytically. A numerical technique is therefore necessary to solve the above models. In order to achieve high computational efficiency the FNPT model is chosen in this work because it requires much less computing resources than the NS model. In order to solve the FNPT model, one key task is to solve the boundary value problem (BVP) for velocity potential. For this purpose, different numerical methods, such as finite difference methods (FDMs), finite volume methods (FVMs), boundary element methods (BEMs) and finite element methods (FEMs) have been used.

FDMs and FVMs are commonly used to solve NS or Boussinesq type models to investigate the nonlinear water waves and their interaction with fixed structures. Only few publications presented their applications to FNPT models. For example, Telste (1985), Yueng & Wu (1989) and Yeung & Vaidhanathan (1990) proposed a FD procedure to simulate nonlinear fluid motion in a tank, Mayer, Garapon & Sorensen (1997), Hu, Greaves & Wu(2002) applied finite volume method to simulate the wave flow and got well agreement with experimental data. The boundary fitting problems associated with the FDMs make it difficult to be adopted in wave-structure interaction problem. Except in the simulation of overturning wave problems, FVMs are also not commonly used.

Apart from the above mesh based methods, meshless methods such as Smoothed Particle Hydrodynamics method (see, for example, Monaghan, 1988, 1994; Shao & Lo, 2003), Moving-particle Semi-implicit method (see, for instance, Ataie-Ashtiani & Farhadi, 2006) and Meshless local Petrov-Galerkin method (see, for example, Ma, 2005) are also used by many researchers. Nevertheless, the mesh based methods are mainly considered here.

2.2.1. Boundary element method

In the BEMs, a Green function together with integrating the source on the boundaries of the fluid domain is used to solve the BVP. For the linear problem, a Green function which satisfies both the Laplace's equation in the fluid domain and the boundary condition on the free surface can be found (Wehausen & Laitone, 1960), only the sources distributed on the body surface are needed. Accordingly, the BEM is more efficient than any other methods. However, the

advantage is lost when dealing with nonlinear problems because the source over the free surface is also needed. In order to overcome this problem, a perturbation expansion was applied on the free surface. This allows a boundary condition to be imposed on a fixed boundary. Based on this feature, the Green function is calculated only once in the beginning. Therefore, the efficiency is still high. By using this approach, Zhang& Willams (1996) simulated a second order problem in a time domain associated with wave diffraction and radiation, Skourup, Buchmann & Bingham (1997) modelled wave runup on vertical cylinder.

Obviously, for the fully nonlinear problem, the free surface as well as the body surface is changing during the whole calculation. On the other hand, a second-order approximation of the perturbation expansions is not accurate enough. Both the Green function and the integration of the source on both free surfaces and body surfaces have to be calculated at every time step. These repeated calculations undoubtedly increase the computational cost of BEMs. Nevertheless, since Longuet-Higgins & Cokelet (1976) used BEM to simulate a 2D fully nonlinear wave-structure problem, many researchers have applied BEMs based on FNPT and produced useful results, such as Vinje & Brevig (1981), Lin, Newman & Yue (1984) , Grilli, Skourup & Svendsen (1989), Grilli & Svendsen (1990), Cao, Schultz & Beck (1991),Beck (1994), Wang, Yao & Tulin (1995), Tanizawa (1995),Kashiwagi (1996), Grilli & Horrillo (1997), Celebi, Kim & Beck (1998), Kim, Celebi & Kim (1998) ,Tanizawa & Minami (1998), Tanizawa Minami & Naito (1999) ,Grilli, Guyenne & Dias (2000), Grilli, Guyenne & Dias (2001), Fochesato, Dias& Grilli (2003), Biausser, Grilli &. Fraunié (2003),Koo& Kim (2004), Fochesato Dias & Grilli (2005) and Grilli, Fochesato & Dias (2005), etc.

However, two common problems are involved in the BEMs. The first one is the well-known singularities problem associated with the source distribution on the real surface of the fluid boundary. The integration around the singularities should be specially treated which always results in costly calculation. As discussed by Grilli & Svendsen (1990), near the intersections of boundary (e.g. between the free surface and lateral boundaries) or in other regions of the free surface near the overturning breaker jets, the singular problem exists. Grilli & Svendsen (1990) and Grilli & Subramanya (1994) developed different schemes to treat the weakly singular and quasi-singular problem. These methods have been widely used. Some examples can be found in Grilli, Guyenne & Dias (2000), Grilli, Guyenne & Dias (2001), Fochesato, Dias& Grilli (2003), Biausser, Grilli &. Fraunié (2003), Fochesato Dias & Grilli (2005) and Grilli, Fochesato & Dias (2005). But the loss of the accuracy for such method may be several orders of magnitudes when the distance to the collocation node becomes very small. An alternative method, developed by Cao, Schultz& Beck (1991) and Beck, Cao, Scorpio& Schultz (1994) is the desingularised boundary integral method. In the desingularised method the sources are distributed on an artificial surface outside the fluid domain. In order to simulate the actual problem, the resultant source from the artificial surface should satisfy the boundary condition. This method can avoid

the singularity problem existing on the boundary surface. Recent applications can be found in Lalli (1998), Longuet-Higgins (2001), Schoberg & Chaplin (2003) and Schoberg & Rainey (2003). All the above applications demonstrated that the desingularised method is efficient.

The second problem with BEMs comes from the coefficient matrices of algebraic equations in the BEMs. The coefficient matrices are fully populated because every node in the BEM is affected by all the other nodes. To store these coefficient matrices, massive memory is required. For the purpose of saving the memory required, some researchers used higher-order BEMs (Xü & Yue,1992; Grilli, Guyenne & Dias,2000,2001). However, solving such fully-populated algebraic equations is still a time consuming process. Though Fochesato & Dias (2006) presented a fast BEM method which introduced the fast multipole algorithm to reduce the computing complexity from $O(N^2)$ to nearly $O(N)$ where N is the number of the nodes on the boundary. Compared to the conventional BEM by Grilli, Guyenne & Dias (2000, 2001), the fast BEM improves the efficiency dramatically. Even so, the CPU time required is still very high. For example, in a case with 6,022 nodes on the boundary, 329s per time step is needed for the fast BEM method, but 1,852s for conventional BEM (Fochesato & Dias, 2006).

2.2.2. Finite element method

Beside the BEMs, FEMs are also efficient for solving such BVP problems. In this method, an equivalent weak formulation, instead of the original governing equation, is used. The whole fluid domain is discretised into a computational mesh. The unknown at each node can be expressed in terms of a shape function. Using the Galerkin method, the weak formulation of the Laplace equation and the boundary conditions can be described as algebraic equations. The BVP problem is therefore solved. The application of FEM in the water wave problems can be traced back to Nakayama & Washizu (1980) who studied the liquid motion in a container subjected to a forced pitching oscillation. Lee& Leonard (1988) followed.

Wu & Eatock Taylor (1994,1995) and Eatock Taylor (1996) extended FEM to FNPT models and simulated different types of nonlinear waves, including the waves generated by a piston wave maker, standing waves in a container and forced oscillation of a cylinder. Since then, many researchers have applied the FEM to treat different wave-body interaction problems. For example, Broderick & Leonard (1995) simulated nonlinear response of membranes to ocean waves, Sannasiraj & Sundaravadivelu (1995) investigated the hydrodynamic behaviour of long floating structures in directional seas, Ma (1998) and Ma, Wu & Eatock Taylor (2001) extended FEM into 3D applications, i.e. waves generated by a piston wave maker, sloshing waves in a container, the nonlinear interaction between waves and fixed cylinders. Cai, Langtangen & Nielsen .et al. (1998) simulated 3D water waves in a wave tank with an obstacle submerged under water or a surface piercing obstacle. Kanoria & Mandal (2002) investigated water waves scattered by a submerged circular-arc-shaped plate. Further applications can be found in

Sannasiraj, Sundar & Sundarravadivelu (1998) , Sannasiraj, Sundaravadivelu, Sundar (2000), Westhuis & Andonowati (1998), Cho, Jeong & Woo (2004), Wu & Hu (2004), Zheng, Shen & You .et al. (2004), Bai, Choo & Chung .et al (2005), Kyoung, Hong & Kim .et al. (2005), Sriram, Sannasirai & Sundar (2005)and Wang & Khoo (2005).

Unlike the BEMs, the FEMs require the whole fluid domain to be discretised. Therefore, the number of nodes or unknowns in FEM is much larger than in BEM. Nevertheless, nonzero elements in the matrix for the FEM may be less than in that of for the BEM since any node in the FEMs only those connected with the node. Ma (1998) has analyzed the number (P_e) of non-zero elements in the coefficient matrix for FEM and the number (P_b) for BEM by considering a rectangular-box fluid domain as an example. He concluded that

$$\frac{P_b}{P_e} \propto \frac{4}{9}\max(M_1, M_2, N) \tag{2.2.1}$$

where M_1, M_2 and N are the number of planes along the length, width and depth respectively. It is clear that as the number of nodes increases, the FEM needs much less memory than that for BEM. Wu & Eatock Taylor (1995) compared the FEM with the BEM for 2D cases and suggested that the FEM was actually more efficient in terms of storage requirement and solution time than the equivalent boundary element method. Similar conclusions were reached by Westhuis & Andonowati (1998), Cai, Langtangen & Nielsen et al. (1998) using the results of similar comparison.

As is known, the fluid domain is being deformed at different instances during the calculation because of the motion of the free surface and the floating body. Therefore, the computational mesh in the FEM or the grid in the BEM should follow the deformation of the fluid domain. In the applications where BEMs are used, only the grid on the boundaries is required. The nodes on the boundaries usually follow the fluid particles determined by the physical boundary conditions on those boundaries in the time marching procedure of the FNPT models. In this situation, the nodes tend to group themselves in regions of high curvature and also may lead to distort the grid. This phenomenon leaves regions of lower curvature poorly defined. Therefore, the grid required usually should be regenerated in the applications using BEM (Heister, 1997).

In applications where FEMs are used, the whole mesh including the surface mesh needs to be updated at every time step to follow the motion of waves and structures. Undoubtedly, generating the whole mesh is more difficult and hence more expensive than generating the surface mesh. On this point, FEMs seem less efficient than BEMs, particularly in cases where an unstructured mesh is required.

Conventionally, a simple structured mesh has been used in applications where the FEM is employed, such as Wu & Eatock Taylor (1994, 1995), Ma (1998) and Ma, Wu & Eatock Taylor (2001a,b). That is because a structured mesh is easy to generate and therefore requires less CPU

time to regenerate at every time step. For the same purpose, Wu & Hu (2004) have recently employed a hybrid mesh. In their approach, a 2D mesh in a horizontal plane (say, the free surface at t=0) is first generated and then vertical lines are drawn to construct a 3D mesh. The 2D mesh is formed by combining an unstructured mesh in a region near structures with a simple structured mesh (similar to Heinze, 2003) in other regions. This is a sensible approach but restricted to cylindrical structures without roll and pitch motions. Once the floating bodies are in roll/pitch motion, the above approach is not applicable and so an unstructured mesh is necessary in order to discretise the area around the floating body. For example, Wang & Wu (2006) used an unstructured mesh based FEM to simulate 2D interaction between the nonlinear waves and non-wall floating bodies. In their cases, the CPU time required for regenerating the 2D unstructured mesh may be much more than that required for all the other numerical processes, such as solving BVPs and calculating velocities on the boundaries. Obviously, it takes much more time to generate a 3D unstructured mesh than a 2D mesh. Repeatedly regenerating such a mesh can make the required CPU time prohibitive in a simulation of several thousands steps on a normal workstation.

In order to reduce the CPU time spent on regenerating the required mesh at every time step, Turnbull, Borthwick & Eatock Taylor (2003) developed a coupled structured-unstructured mesh based FEM for simulating the wave-structure interaction. In their applications, the fluid domain was separated into several sub-domains, those near the structures and the rest. The mesh is unstructured in the sub-domains near the structures but structured in others. This method reduced the CPU time spent on regenerating the mesh required through reducing the area where the unstructured mesh would cover. Actually, the problem associated with regenerating a mesh repeatedly was not fully solved. An unstructured mesh in a sub-domain still needs to be regenerated at every time step. Alternatively, Wu, Eatock Taylor & Greaves (2004) developed a coupled finite element and boundary element method. In this coupled method, FEM is used away from the body while the BEM is used in the region near the body. The combination is based on the consideration of the efficiency of the FEM and the BEM in computation and mesh generation, respectively. As has been mentioned above, only the boundary mesh is required for the BEM. One only needs to regenerate the surface mesh, in place of regenerating a complex unstructured mesh, in the area around the floating bodies. Because different methods are used in different sub-domains, an iterative method is needed to make the velocity potential continuous in the intersecting area between the sub-domains where the FEM is applied and the one where the BEM is applied.

Apart from the above approaches, Cai, Langtangen & Nielsen et al (1998) developed a finite element formulation based on a time-dependent fluid domain mapping technique. A fixed reference domain, which is mapped from the actual fluid domain time to time, is employed for the finite element solver. But this method may not give results as good as those obtained by Wu

& Eatock Taylor (1994,1995) in which remeshing is carried out repeatedly, as indicated by Westhuis & Andonowati (1998).

It is concluded that the problem associated with the computational mesh has further limited the development of the FEMs in the wave-body interaction problems. In order to overcome this problem, a robust method needs to be developed herein.

2.3. Existing methods for the calculation of velocities

As mentioned in Section 2.1.2, the velocities on the boundaries provide a possibility to update the free surface and the position of the bodies in the time marching process of FNPT models. The error in the velocity calculation in the current time step may be brought to the next time step through the procedure of updating the position of the free surface and the body surface. That means the error may be accumulated in the calculation. Accurate estimation of the velocity on the boundary is one of the most important procedures in the time marching process. Because an FEM method is used in this thesis, only the velocity calculation schemes in the applications where FEMs are employed are discussed in this section.

A directed approach is to solve the velocity in a similar way to that for the velocity potential. To do so, a mixed element method and a formulation based on the Galerkin method were developed by Wu & Eatock Taylor (1994) and were found to lead to satisfactory results. This approach was recently followed by Wang & Wu (2006). In this approach, the velocity components as well as velocity potential are treated as unknowns. Therefore, more memory and CPU time is required than solving velocity potential only. On the other hand, the velocity at every node in the fluid domains is solved in this approach. But only the velocities on the free surface and the body surface are required in most of the cases, unless one wants to investigate the velocity field of the fluid domain. In this aspect, this approach is not effect.

Alternatively, the velocities can be alternatively estimated by calculating the spatial derivatives of velocity potential. Wu & Eatock Taylor (1995) suggested a FD scheme to calculate the velocity once the velocity potential was available. In this scheme, the velocity at a node is estimated by using the velocity potentials at this node and the nodes connected to it. Their results indicated that this method could achieve similar accuracy and require far less CPU time than the other methods. However, the neighbours of a node on the free surface are distributed either on or below the surface, the normal (or nearly vertical) component of the velocity estimated by the approach generally possesses relatively low accuracy, which is understandable from the fact that backward or forward FD schemes approximating a derivative have a lower order of accuracy than a central scheme. In order to enhance the overall accuracy, a technique was developed and applied by Ma (1998) and Ma, Wu & Eatock Taylor (2001a,b) for simulating 3D wave-structure interaction. A mixed FD formulation was developed and employed in their applications. Fig.2.3.1 shows a node *I* on the free surface and its neighbours,

i.e. nodes I+1, I +2. I +3 and I +4 on the free surface, nodes I +5, I +6 in the fluid domain below node I. A vertical line starts from node I will pass through nodes I+5 and I+6 at spacing h_1 and h_2.

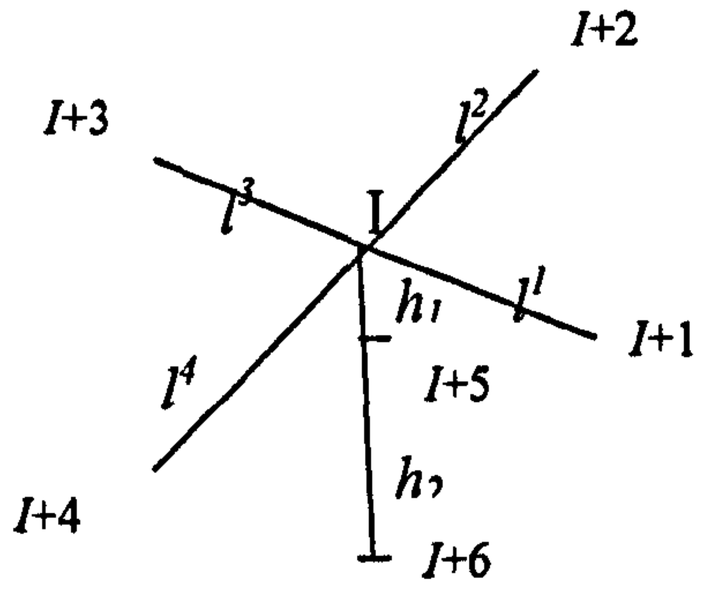

Fig.2.3.1 Node and its neighbours

First of all, the vertical velocity component w is calculated using a combination of a two-point and a three-point numerical difference formula as follows,

$$w = \frac{2}{3h_1}\left(\frac{2h_1 + h_2}{h_1 + h_2} + \frac{1}{2}\right)\phi_I - \left(\frac{2}{3h_2} + \frac{1}{h_1}\right)\phi_{I+5} + \frac{2}{3h_2}\left(\frac{h_1}{h_1 + h_2}\right)\phi_{I+6} \qquad (2.3.1)$$

where ϕ is the velocity potential, the subscript I, I+5, I+6 represent the velocity potential at nodes I ,I+5 and I+6. In this equation, the weights for the two-point and three-point numerical difference formula are taken as 1/3 and 2/3, respectively.

Once the vertical velocity component w is obtained, the horizontal components u and v can be found by using the principle of directional derivative, i.e.,

$$\frac{\partial \phi}{\partial l} = \frac{\partial \phi}{\partial x}\frac{\partial x}{\partial l} + \frac{\partial \phi}{\partial y}\frac{\partial y}{\partial l} + \frac{\partial \phi}{\partial z}\frac{\partial z}{\partial l} = u\frac{\partial x}{\partial l} + v\frac{\partial y}{\partial l} + w\frac{\partial z}{\partial l} \qquad (2.3.2)$$

in which l is a vector starting from node I to the node connected with it. All the partial derivative terms can be approximated by a two-point difference scheme. For every node k on the free surface connected to node I, Eq. (2.3.2) can be rewritten as

$$u_i l_x^k + v_i l_y^k = \frac{\partial \phi}{\partial l^k} - w l_z^k \qquad (2.3.3)$$

in which l_x^k, l_y^k, l_z^k are the components of the vector l^k in the x-,y- and z-directions. In Ma (1998) and Ma,Wu & Eatock Taylor (2001a,b), only the nodes on x- and y-directions are considered (which are I+1,I+2,I+3 and I+4 in Fig.2.3.1). The vectors l start from I to each node, i.e. l1,l2.l3 and l4, are divided into four groups: (l^1, l^2), (l^2, l^3), (l^3, l^4) and (l^4, l^1). For each group, u_i and v_i are estimated by using Eq. (2.3.3). The averages of u_i and v_i are taken as the horizontal velocities at the node I. For brevity, this method is called traditional 3-point method in this thesis.

This approach has been proved to be efficient and accurate by Ma (1998) and Ma, Wu & Eatock Taylor (2001b). However, it is only applicable in cases involving structured mesh with special structure, i.e., there are at least two nodes coinciding in the vertical direction of node *I* and four nodes on the free surface crossing the *x*- or *y*-direction. Once an unstructured mesh is used, it is impossible to satisfy the requirement of the above approach. Therefore, this approach does not work in cases where unstructured meshes are used. In order to remove this limitation, a velocity calculation scheme based on the mixed FD scheme will be developed in this thesis.

2.4. Smoothing and recovery technique

As is known, all the numerical methods can only give an approximate result. In the FEM method, the continuous fluid domain is described by a series of discrete nodes. The velocity potential in the fluid domain is therefore approximated by those at a number of nodes by using a shape function. In order to decrease the error between the finite element solution and the exact solution, one may increase the number of the nodes. However, the computational cost increases as well.

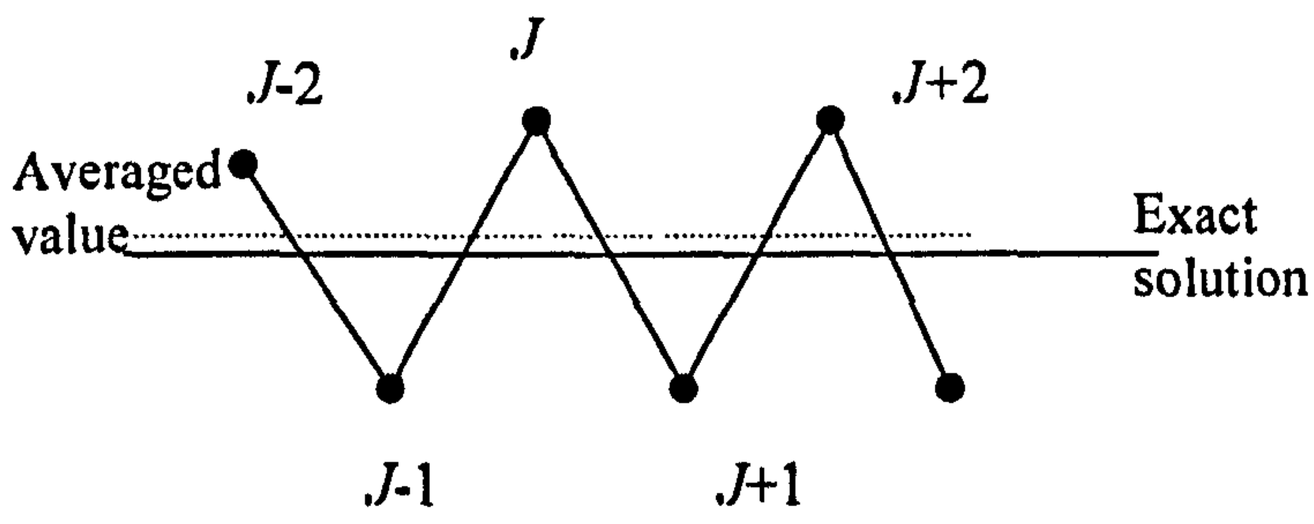

Fig.2.4.1 Sketch of the saw-tooth problem

In fact, the finite element solution, particularly in cases using a linear shape function, oscillates near the exact solution as sketched in Fig. 2.4.1. This non-physical phenomenon is the well-known saw-tooth problem. Such a oscillation can be removed by using post-processing techniques, such as the smoothing or the patch recovery techniques. The effectiveness of these techniques have been validated and suggested by Ma (1998), Ma, Wu & Eatock Taylor (2001a,b) , Koo & Kim (2004), Wu & Hu (2004),Wang & Wu (2006) and so on.

2.4.1. Smoothing technique

Longuet-Higgins and Cokelet (1976) first introduced the evenly spaced 5-point smoothing scheme as

$$\overline{w}_J = \frac{1}{16}(-w_{J-2} + 4w_{J-1} + 10w_J + 4w_{j+1} - w_{j+2}) \tag{2.4.1}$$

where w is the physical quantity(such as the velocity components) to be smoothed and $\overline{w}$ is the smoothed value. Subscripts in Eq. (2.4.1) indicate node numbers. *J-2,J-1,J+1,J+2* are located at both side of the node J as shown in Fig.2.4.1. This scheme is efficient in avoiding the non-physical saw-tooth instability problem during the time marching process. Ma (1998) and Ma, Wu & Eatock Taylor (2001a,b) used this scheme to smooth the velocity on the free surface in 2D cases. They compared the results obtained by using different meshes. It was found that the saw-tooth problem exists even if a very fine mesh is used but the smoothed result in cases with coarse meshes does not contain specious oscillations. This implies that the smoothing technique is more efficient at improving the accuracy of the finite element solution than using mesh refinement.

However, Eq (2.4.1) is only applicable to nodes with equal spacing. In cases with an unstructured mesh, the distribution of the nodes is irregular. In order to overcome this problem, Koo (2003) and Koo & Kim (2004) modified and extended Eq (2.4.1) to variable-node-space cases and got satisfactory results. In their modified equation, the x-directional distance between two successive nodes on the curve is taken into account as a weight. For the same reason, Wang & Wu (2006) applied an energy method for smoothing. In their method, an objective equation is formed in order to minimize the difference between the original value and the smoothed value at all the nodes on the curve which should be smoothed. Therefore, additional equations should be solved. The efficiency is relatively lower than the above approach.

2.4.2. Recovery technique

As mentioned above, the smoothing technique may only be applicable to smooth the physical quantities along a curve. If a 3D unstructured mesh is used, this type of technique may not work. As an alternative, a patch recovery technique is usually applied in order to avoid the saw-tooth problem. The main idea behind this method is that the velocity at a node i is assumed to be fitted by a polynomial over a patch on the surface (see Fig.2.4.2), e.g. the free surface and the body surface. To achieve this, many methods were developed and applied in the past decade, a detailed review can be found in Maisano, Micheletti & Perotto .et al. (2006). One of the most widely used methods in practice is the superconvergent point method developed by Zienkiewicz & Zhu,1987,1992). Ma (1998) and Ma, Wu & Eatock Taylor (2001a) extended this method to recover the velocity on the free surface in a 3D case. In their application, the velocity on the patch (Fig.2.4.2) is assumed to satisfy the following linear function of horizontal coordinates x and y,

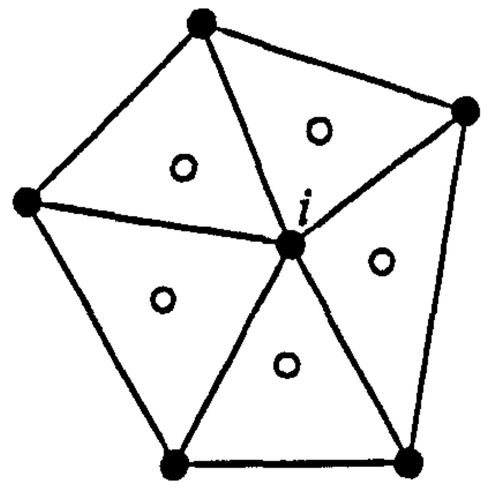

Fig.2.4.2 Sketch of a triangular patch

$$w_i^* = a + bx + cy \tag{2.4.2}$$

where w_i^* is the fitted velocity at node i on the free surface. In this case, the patch is obtained by projecting the free surface elements into *oxy* plane (see Fig.2.4.3).

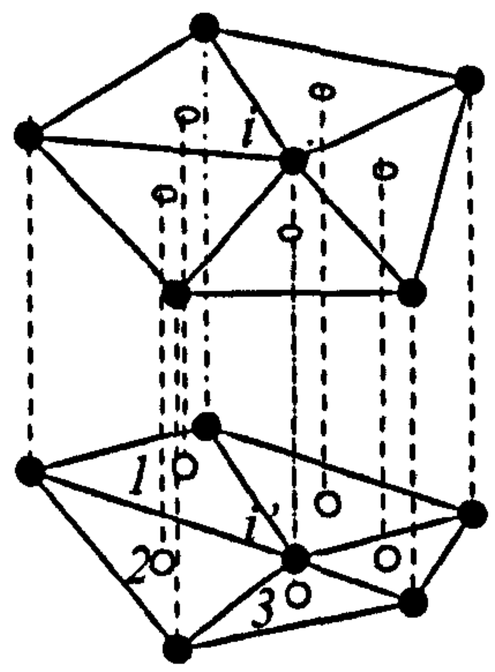

Fig.2.4.3 Elements and their projection on the oxy plane

The least squares method is then employed to fit the polynomial by the sampling points (the hollow circles in Fig.2.4.2) in the patch. The sampling points are the central points of the triangles which are so called the superconvergent points where the finite element solution is more accurate than that in other area (Zienkiewicz & Zhu, 1992). In order to estimate the velocity at the superconvergent point J ($J=1,2,3,...M$), the interpolating formulation based on the shape function is used.

$$w_J^s = a^s + b^s x_J + c^s y_J = \sum_{J=1} N_J w_J \tag{2.4.3}$$

where w_J^s is the velocity at J^{th} superconvergent point. x_J, y_J is the horizontal coordinates of J^{th} superconvergent point. N_J is the shape function. The coefficient a^s, b^s, c^s is calculated,

$$\begin{bmatrix} a^s \\ b^s \\ c^s \end{bmatrix} = \begin{bmatrix} \alpha_1 & \beta_1 & \gamma_1 \\ \alpha_2 & \beta_2 & \gamma_2 \\ \alpha_3 & \beta_3 & \gamma_3 \end{bmatrix} \begin{Bmatrix} w_1 \\ w_2 \\ w_3 \end{Bmatrix} \tag{2.4.4}$$

in a triangle element where the node number is in the turn *l*-*m*-*n* ($l, m, n = 1,2,3$),

$$\alpha_l = \frac{1}{2\Delta}(x_m y_n - y_m x_n) \tag{2.4.5}$$

$$\beta_l = \frac{1}{2\Delta}(y_m - y_n) \tag{2.4.6}$$

$$\gamma_l = -\frac{1}{2\Delta}(x_m - x_n) \tag{2.4.7}$$

in which Δ is the area of this element.

A special treatment should be applied for the nodes on the boundary. Different methods were suggested by Ma (1998) to treat the nodes on the boundaries, i.e. using smoothing technique mentioned above to treat plane-type boundary (Fig.2.4.4 a and b) and replacing value at point A in Fig.2.4.4 c) by the recovered value at point B.

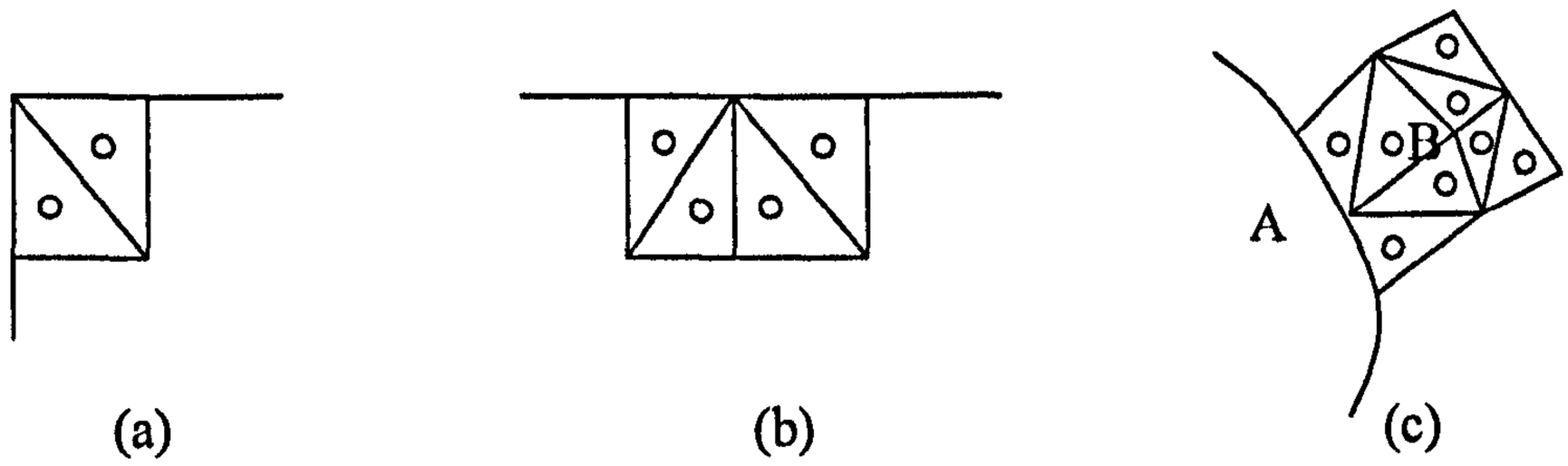

Fig.2.4.4 Patch around the boundary nodes

This method has been proved efficient by Ma (1998) and has been widely used in 3D wave-structure interaction problems where the FEM is used (for example, Hu, Wu & Ma, Q.W.,2003; Wu & Hu,2004). However, this approach is not applicable to the case where the velocity in the patch is not a single-value function of (x,y), e.g. the body surfaces and the free surface with overturning jets.

2.5. Existing methods for calculation of force

In the FNPT model, the position and the velocity of the floating bodies should be given before solving the boundary value problem for velocity potential. For a free-response floating body, Newton's law is used to calculate the acceleration and velocity of the free-response floating body. The force, which is necessary for Newton's law, can be obtained by integrating the pressures along the body surface (Ma, 1998). The pressure p can be evaluated by using Bernoulli's equation

$$p = -\rho\left(\frac{\partial\phi}{\partial t} + \frac{1}{2}|\nabla\phi|^2 + gz + c\right) \tag{2.5.1}$$

where ρ is the density of the fluid, g is the gravitational acceleration and c is an arbitrary function of time independent of spatial variable which is usually be omitted by redefining velocity potential appropriately.

It can be seen that the time derivative of the velocity potential ($\partial\phi/\partial t$) is required for force calculation. The simplest way to calculate $\partial\phi/\partial t$ is to use a backward FD scheme:

$$\left(\frac{\partial\phi}{\partial t}\right)^n = \frac{\phi^n - \phi^{n-1}}{\Delta t} \tag{2.5.2}$$

where Δt is the time step and the superscript n denotes the n^{th} time step. However, the nodes or collocation points on the body surface move from one time step to another. As a result, a direct calculation of this term may be impossible unless an approximated interpolating method is used. Because of this, Lin, Newman & Yue (1984) developed a FD scheme based on the total time derivative $\frac{D\phi}{Dt}$ obtained by following a fluid particle,

$$\frac{\partial\phi}{\partial t} = \frac{D\phi}{Dt} - \nabla\phi\cdot\nabla\phi \tag{2.5.3}$$

They used this method to investigate body-induced wave problems. For the same reason, Sen (1993) developed a similar scheme to calculate the pressure on a 2D moving body, employing a slightly different expression for $\partial\phi/\partial t$,

$$\frac{\partial\phi}{\partial t} = \frac{\delta\phi}{\delta t} - \vec{U}\cdot\nabla\phi \tag{2.5.4}$$

in which $\vec{U}$ is the velocity of the body surface; $\frac{\delta\phi}{\delta t}$ represents the rate of change of velocity potential obtained by following a point on the body surface. However, the scheme may suffer from a problem of the saw-tooth instabilities, as pointed out by Sen (1993) and Tanizawa (1995), when it is applied to deal with the problems with free-response floating bodies. Ma (1998) had also derived a force calculation formulation where $\partial\phi/\partial t$ is absent from the formula. This was referred as a integrated force method. However, it is restricted to cases where the vertical surfaces are fixed. Once a floating body with rotational motion is involved, this method is not applicable.

An alternative is to solve the boundary value problem for the term. The boundary value problem for $\partial\phi/\partial t$ is similar to the one for the velocity potential itself. This approach has been widely applied (see, for example, Ma, Wu & Eatock Taylor, 2001a,b; Ma,1998;

Kashiwagi,1996,2000; Wu & Eatock Taylor,2003; Wu & Hu,2004) in which the term $\partial\phi/\partial t$ satisfies the Laplace equation in the fluid domain

$$\nabla^2\left(\frac{\partial\phi}{\partial t}\right)=0 \tag{2.5.5}$$

The boundary condition on free surface can be written as

$$\frac{\partial\phi}{\partial t}=-g\zeta-\frac{1}{2}|\nabla\phi|^2 \tag{2.5.6}$$

where ζ is the elevation of the free surface. On the boundary of floating bodies, particularly on an accelerating boundary, the condition becomes complicated. Wu& Eatock Taylor (1996) and Ma (1998) has derived the equation,

$$\frac{\partial}{n}\frac{\partial\phi}{\partial t}=[\vec{\dot{U}}_c+\vec{\dot{\Omega}}\times\vec{r}_b]\cdot\vec{n}-\vec{U}_c\cdot\frac{\partial\nabla\phi}{\partial n}+\vec{\Omega}\cdot\frac{\partial}{\partial n}[\vec{r}_b\times(\vec{U}_c-\nabla\phi)] \tag{2.5.7}$$

in which $\vec{\dot{U}}_c,\vec{\dot{\Omega}},\vec{U}_c,\vec{\Omega}$ are acceleration ,angular acceleration, velocity and angular velocity of body, $\vec{r}_b$ is the position vector.

Apart from this, Tanizawa (1995) introduced a concept of acceleration potential. Similar to the velocity potential, the acceleration of the fluid particle can be determined from the gradient of acceleration potential Φ which satisfies

$$\Phi=\frac{\partial\phi}{\partial t}+\frac{1}{2}|\nabla\phi|^2 \tag{2.5.8}$$

The governing equation and the boundary condition on free surface is the same as Eq. (2.5.5) and (2.5.6), respectively. The boundary condition on the body surface satisfies

$$\frac{\partial\Phi}{\partial n}=\vec{n}\cdot(\vec{\dot{U}}_c+\vec{\dot{\Omega}}\times\vec{r}_b)+q \tag{2.5.9}$$

and

$$q=\vec{n}\cdot\vec{\Omega}\times(\vec{\Omega}\times\vec{r}_b)-k_n(\nabla\phi-\vec{U}_c-\vec{\Omega}\times\vec{r}_b)^2+n\cdot2\vec{\Omega}\times(\nabla\phi-\vec{U}_c-\vec{\Omega}\times\vec{r}_b) \tag{2.5.10}$$

where k_n is normal curvature of the body surface along the path of fluid. Substitute Eq. (2.5.8) into (2.5.9)

$$\frac{\partial}{n}\frac{\partial\phi}{\partial t}=[\vec{\dot{U}}_c+\vec{\dot{\Omega}}\times\vec{r}_b]\cdot\vec{n}+q-\frac{\partial}{\partial n}(\frac{1}{2}|\nabla\phi|^2) \tag{2.5.11}$$

Koo (2003) and Koo & Kim (2004) applied this approach to simulate a 2D case with freely floating bodies using the BEM. The results agreed well with the experimental data. However, one needs to calculate the local curvature k_n at the nodes on the body surface in order to apply this boundary. In addition, both $k_n(\nabla\phi-\vec{U}_c-\vec{\Omega}\times r_b)^2$ and $\frac{\partial}{\partial n}(\frac{1}{2}|\nabla\phi|^2)$ are all difficult to

treat in the FEM formulation. Therefore, Eq. (2.5.7) is applied for the body surface boundary condition in this thesis.

However, there is a difficulty associated with the force and acceleration calculation. In Eqs. (2.5.7) and (2.5.11), the accelerations and velocities of the floating bodies should be known in order to calculate the $\partial\phi/\partial t$. In cases with freely floating bodies, the accelerations depend on the forces acting on the floating body. In order to calculate the force, $\partial\phi/\partial t$ is necessary. They are nonlinearly coupled. In order to overcome this difficulty, some special techniques should be employed. These techniques will be discussed in the following section.

2.6. Existing methods to overcome the difficulty on calculating the force and accelerations

In order to tackle this difficulty existing in the force calculation as mentioned above, four types of methods have been suggested in literatures. They are the mode-decomposition method, the indirect method,the Dalen & Tanizawa's method and the iterative method.

The mode-decomposition method was suggested by Vingi & Brevig (1981). In this approach, the body acceleration is decomposed into several modes, i.e. the accelerations for surge (a_1), sway (a_2), heave (a_3), roll (a_4), pitch (a_5), yaw (a_6) motion and the acceleration due to velocity field. Therefore, $\partial\phi/\partial t$ can be found by using

$$\frac{\partial\phi}{\partial t} = \sum_{i=1}^{6} a_i\varphi_i + \varphi_v \tag{2.6.1}$$

where φ_i is the contribution for $\partial\phi/\partial t$ of i^{th} mode component of generalized body acceleration, φ_v is the contribution due to due to velocity field. Every mode is found by solving a boundary value problem similar to that for the velocity potential but under different boundary conditions which are independent of the acceleration. Using these modes and the body-motion equations, the body acceleration is determined. Recently, Koo (2003) , Koo & Kim (2004) used this method to simulate the response of a 2D freely floating body to nonlinear water waves. The disadvantage of this method is that exact BVPs for each mode (4 modes in two-dimensional cases or 7 modes in three-dimensional cases) are required. The CPU time, therefore, may be considerably increased if employing an iterative procedure rather than a direct solution scheme (such as Gauss Elimination) which is unlikely to be suitable for solving the corresponding linear algebraic system containing a very large number of unknowns.

The indirect method was developed by Wu & Eatock Taylor (1996). In this method, some auxiliary functions were introduced to decouple the mutual dependence between the force and the acceleration of the body. The accelerations can be obtained directly by solving similar BVPs as velocity potential before the force on the body is known. Many researchers (Koo & Kim,2004; Kashiwagi & Momoda ,1998; Kashiwagi ,2000; Wu & Eatock Taylor,2003; Wu & Hu ,2004; Wang & Wu ,2006) have used this method to simulate 2D or 3D wave-body

interaction. Similar to the mode-decomposition method, the motion is decomposed into several modes and $\partial\phi/\partial t$ is also found by using Eq. (2.6.1). However, the Haskind-Newmann relation is utilized to find the relationship between φ_v and $\varphi_i(i=1,2,3...6)$ from the radiation damping in the linear theory. φ_v is hence calculated indirectly from $\varphi_i(i=1,2,3...6)$ instead of being directly solved. The computational time is reduced compared to the mode-decomposition method because the direct evaluation of φ_v can be omitted. Koo & Kim (2004) compared the mode-decomposition method and the indirect method by using a case involving a barge-type floating body. They concluded that both methods lead to the similar results. When we use the indirect method, however, the body-surface pressure cannot be obtained.

In the method proposed by Dalen (1993) and Tanizawa (Tanizawa,1995; Tanizawa & Minami,1998; Tanizawa, Minami & Naito,1999), the body accelerations in Eq. (2.5.6) are implicitly substituted using Bernoulli's equation and thus the velocity potential and its time derivative are solved without the need to calculate accelerations of the floating bodies However, this method requires one to form a special matrix for $\partial\phi/\partial t$ which is different from the one for the velocity potential and whose properties have not been sufficiently studied. This is likely to increase the difficulty for numerically solving the algebraic equations associated with $\partial\phi/\partial t$ and also needs more CPU time for generating the special matrix. That would be the main reason for this method not to be commonly used.

Cao, Beck. & Schultz (1994) and Beck (1994) suggested an iterative method to calculate the force and acceleration at each time step as follows,

1. Solve the BVP for velocity potential and calculate the velocity of the free surface;
2. Calculate the $\frac{\partial\phi}{\partial t}, \frac{D\phi}{Dt}$ on the free surface;
3. Guess an initial acceleration of the floating body using the value at the last time step;
4. Solve the BVP for $\partial\phi/\partial t$ and calculate $\partial\phi/\partial t$ on the body surface;
5. Compute the pressure on the body surface using Bernoulli equation and integrate the pressure to get the force;
6. Correct the acceleration of the floating body by using Newton's law;
7. If the difference between the new acceleration and the old one is larger than the error tolerance, replace the old one with the new one and go to 4; otherwise, stop the iteration.

In this procedure, the need to solve extra equations in the first two methods and the problem with the third method are eliminated. In their application, the velocity of the floating body is calculated explicitly. The explicit procedure may be satisfactory if the time steps, and therefore changes in the velocity and acceleration in one step are sufficiently small; otherwise, it may degrade the accuracy and even lead to instability.

3. MATHEMATICAL MODEL AND NUMERICAL METHOD

The computational domain is chosen as a rectangular tank. Two types of methods are used to generate nonlinear waves. The first method is to generate the wave by a piston-like wavemaker which is mounted at the left end (on the negative side of the x-axis, see, Fig.3.0.1). The second method is to specify the initial condition for the position and the velocity of the particles at the free surface. Reflective and absorbing boundary conditions are implemented on the lateral boundaries (at the right end) of the tank. For the former, this boundary is considered as a fixed wall. For the latter, a damping zone with a Sommerfeld condition is applied in order to suppress the reflection, as sketched in Fig. 3.0.1. Arbitrary forms of submerged bodies, such as sand bars, on the tank-bed may be included. A Cartesian coordinate system is used with the oxy plane on the mean free surface and with the z-axis being positive upwards. A floating body is placed at x=0 initially and moored to the bed or walls of the tank.

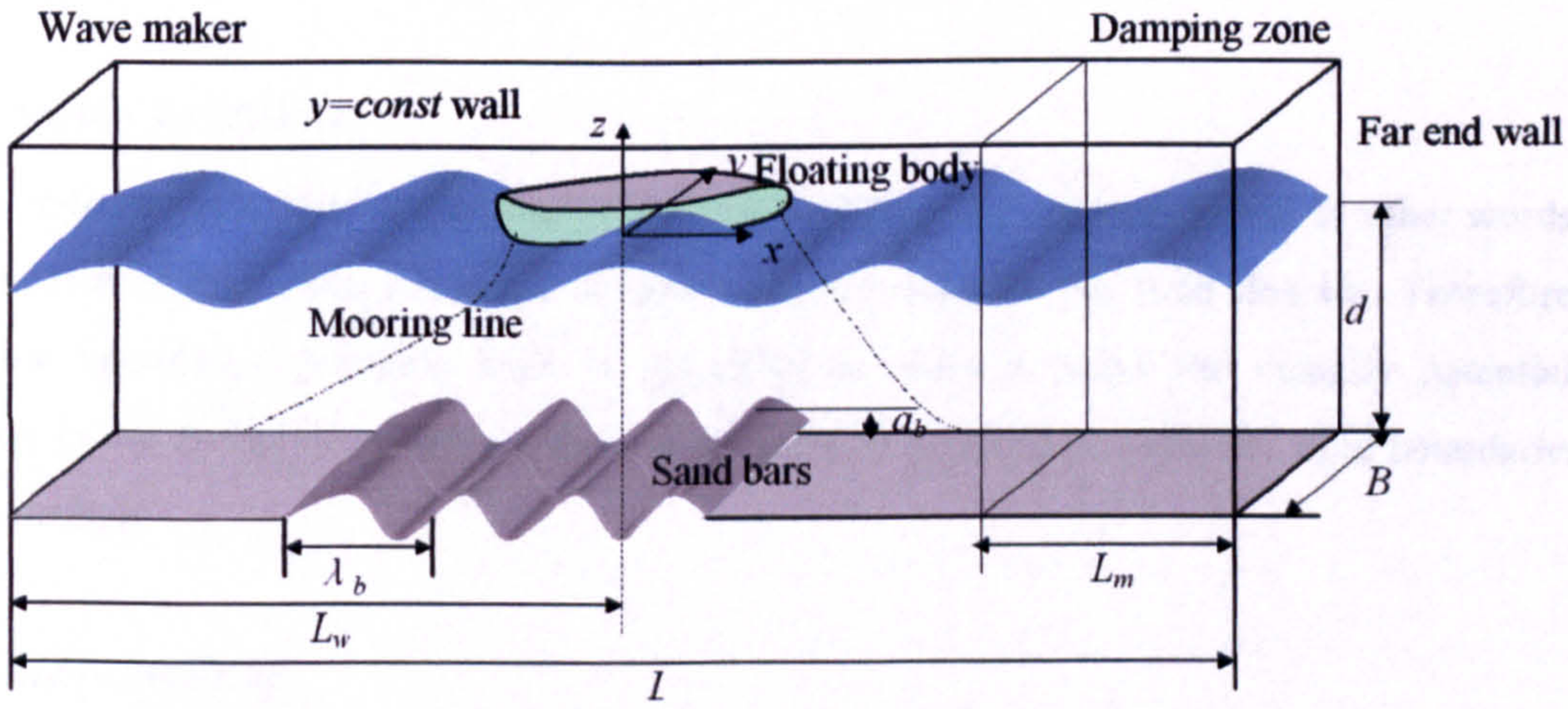

Fig. 3.0.1 Sketch of the fluid domain

(far end wall: the lateral boundaries; *y=const* wall: vertical side wall)

3.1. FNPT models for water waves

3.1.1. Governing equation

Similar to the usual FNPT Model, the fluid is assumed to be incompressible, irrotational and inviscid. The continuity equation in such a condition is

$$\nabla \vec{u} = 0 \tag{3.1.1}$$

where $\vec{u}$ is the velocity vector of the flow. The velocity potential (ϕ) is introduced and the velocity vector can be described as a spatial gradient of the velocity potential, i.e.,

$$\vec{u} = \nabla\phi \tag{3.1.2}$$

Substituting Eq. (3.1.2) into Eq. (3.1.1), the velocity potential then satisfies Laplace's equation,

$$\nabla^2\phi = 0 \tag{3.1.3}$$

in the fluid domain.

As mentioned above, Bernoulli's equation is employed in order to calculate the pressure p,

$$p = -\rho\left(\frac{\partial\phi}{\partial t} + \frac{1}{2}|\nabla\phi|^2 + gz + c\right) \tag{3.1.4}$$

This equation is the same as Eq. (2.5.1). c is an arbitrary function of time independent of spatial variable which is usually be omitted by redefining velocity potential appropriately. c is taken as zero in this work. Eq. (3.1.4) is derived by substituting Eq. (3.1.2) into the moment equation.

Once the velocity potential is obtained by solving the governing equation, i.e., Eq.(3.1.3), once can find the velocities using Eq.(3.1.2) and the pressure using Eq.(3.1.4). However, in order to find the velocities and pressure by using NS models, one needs to solve the moment equations and continuity equation together with proper boundary conditions where four variables in a three-dimensional case should be of concern. The FNPT model clearly makes the problem easier.

3.1.2. Boundary conditions

The motion of the flow in the fluid domain is controlled by the boundaries. In other words, the physical boundary determines the behaviour of the fluid in the fluid domain. Therefore, appropriate boundary conditions must be specified in order to solve the velocity potential. According to the definition of the problem, there are two types of boundaries: rigid boundaries and free surface.

On the rigid boundaries

On all rigid boundaries, such as the wavemaker, the sea bed, the vertical walls of the tank and the surface of the floating body, the fluid particles cannot go through the surface and can only move along the tangential direction of the surface. Therefore, the normal velocity of the fluid on the rigid boundaries should be equal to the normal velocity of the boundary surface at the corresponding point to the fluid particle.

$$\vec{v}_n = \vec{n}\cdot\vec{U}(t) \tag{3.1.5}$$

where $\vec{U}(t)$ is the velocity vector of the rigid boundaries. Decomposing Eq. (3.1.2), the normal velocity component can be obtained by

$$\vec{v}_n = \frac{\partial\phi}{\partial n} \tag{3.1.6}$$

where $\vec{n}$ is the unit normal vector of the rigid boundaries. The positive direction of the normal vector points to the outside of the fluid domain. Substituting Eq. (3.1.6) into Eq. (3.1.5), the velocity potential on the rigid boundary should satisfy

$$\frac{\partial \phi}{\partial n} = \vec{n} \cdot \vec{U}(t) \tag{3.1.7}$$

The normal velocity of the boundary surface must be known before this condition is employed. For the specific case illustrated in Fig.3.0.1, $\vec{U}(t) = 0$ on the sea bed and other fixed walls of the tank, and thus the velocity potential satisfies

$$\frac{\partial \phi}{\partial n} = 0 \tag{3.1.8}$$

On the wavemaker, $\vec{U}(t) = U_x(t)$ in which $U_x(t)$ is the velocity of the wave maker and so Eq. (3.1.7) can be rewritten as

$$\frac{\partial \phi}{\partial x} = \vec{U}_x(t) \tag{3.1.9}$$

However, once a free-response structure is included, the velocity of the structure will be found by Newton's law. This will be discussed in Section 3.2.

On the free surface

On the free surface $z = \zeta(x, y, t)$, both kinematic and dynamic conditions are required. The conditions may be described by several formulations, namely Eulerian, semi-Eulerian or Lagrangian. The semi-Eulerian formulation and Lagrangian formulation are usually used for the time-marching procedure. Detailed formulations of these three formulations can be found in Ma (1998). Compared to semi-Eulerian formulation in which the free-surface node is restricted to be moved in its vertical direction, the Lagrangian form makes it more realistical to move the node on the free surface and therefore is more suitable to treat a case with domain transformation, e.g., the cases involved in wave makers and/or floating bodies. In this work, the Lagrangian form is used. The kinematic condition on the free surface is

$$\frac{Dx}{Dt} = \frac{\partial \phi}{\partial x}, \frac{Dy}{Dt} = \frac{\partial \phi}{\partial y}, \frac{Dz}{Dt} = \frac{\partial \phi}{\partial z} \tag{3.1.10}$$

and the corresponding dynamic condition is

$$\frac{D\phi}{Dt} = -gz + \frac{1}{2}|\nabla \phi|^2 \tag{3.1.11}$$

where $\frac{D}{Dt}$ is the substantial (or total time) derivative following fluid particles. In Eq. (3.1.11), the atmospheric pressure has been taken as zero.

3.1.3 Initial condition

Suppose the velocity potential in the n^{th} time step has been obtained, $\nabla\phi$ can be evaluated by a mixed FD based velocity calculation scheme which is extended from the method by Ma (1998) and will be discussed in Chapter 5. Eq (3.1.11) gives $\frac{D\phi}{Dt}$ on the free surface, and hence the velocity potential on the free surface in the next time step can be found. Similarly, Eq. (3.1.10) gives the new position of the free surface in the next time step. Both of them make it possible to solve the boundary value problem in the next time step. The procedure is called a time-marching procedure and has been discussed earlier. This procedure also requires known state values in the initial time step.

The initial condition on the free surface in this problem can be expressed as

$$\begin{aligned} &\varsigma(x,y,0) = \psi(x,y) \\ &\phi(x,y,\varsigma(x,y,0),0) = \varphi(x,y) \end{aligned} \tag{3.1.12}$$

in which $\psi(x,y)$ is the initial position of the free surface and $\varphi(x,y)$ is the initial velocity potential on the free surface. If a floating body is included, its velocity and position at the starting instant must also be given.

As was mentioned at the beginning of this chapter, there are two ways to generate waves in a numerical tank. The first one is to generate waves by a piston-like wavemaker. In these applications, the flow and the floating body all start from rest, $\varphi(x,y)$ is therefore taken as 0 and $\psi(x,y)$ represents the mean free surface. In the second method, the position of and the velocity potential on the free surface are given by the special values obtained by either analytical formulation or numerical methods. In this thesis, the method is only used to generate solitary waves. In those cases, no floating bodies are included and $\psi(x,y)$, $\varphi(x,y)$ are given by Tanaka's model (Tanaka, 1986).

3.2. Motion equation of a floating body and conditions on the body surface

Eq. (3.1.7) requires the velocity on the body surface. If the translational velocity of the gravitational centre of the body $\vec{U}_c$ and the angular velocity relative to the gravitational centre $\vec{\Omega}$ are specified, the velocity at a point on the body is determined by

$$\vec{U} = \vec{U}_c + \vec{\Omega} \times \vec{r}_b \tag{3.2.1}$$

where $\vec{r}_b$ is the position vector relative to the gravitational centre (See Fig. 3.2.1). Therefore, $\vec{U}_c$ and $\vec{\Omega}$ should be known for the purpose of solving the velocity potential. If $\vec{U}_c$ and $\vec{\Omega}$ are unknown, such as those of a free-response floating body, they need to be calculated.

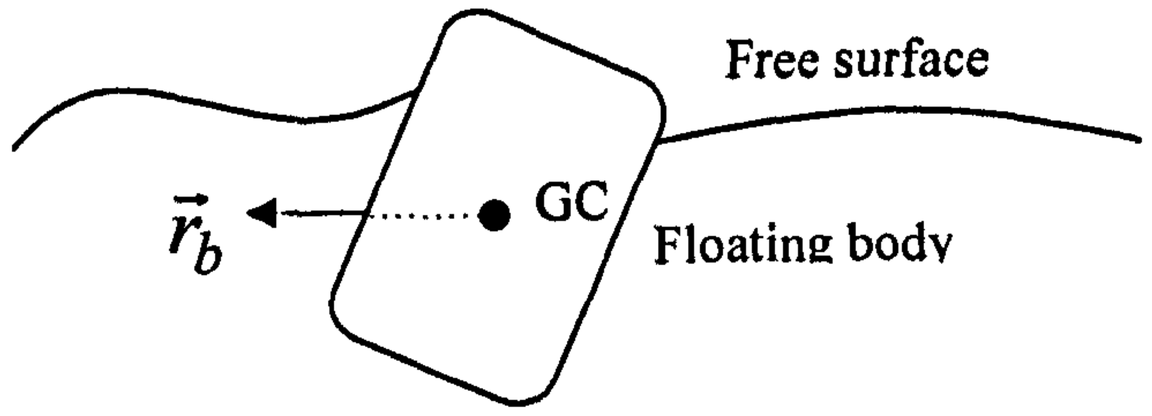

Fig. 3.2.1 Sketch of a floating body and $\vec{r}_b$ (GC: Gravitational centre)

In a general fully nonlinear time domain simulation, the motion of the floating body is governed by Newton's law. The rotational equations are formed in terms of components in a moving coordinate system whose coordinate centre is located at the gravitational centre.The following equations govern the displacements, velocities and accelerations of the floating body (see, for example, Ma, 1998; Ma & Patel, 2001).

$$[M]\frac{d\vec{U}_c}{dt} = \vec{F} \tag{3.2.2}$$

$$[I]\frac{d\vec{\Omega}}{dt} + \vec{\Omega}\times[I]\vec{\Omega} = \vec{N} \tag{3.2.3}$$

$$\frac{d\vec{S}}{dt} = \vec{U}_c \tag{3.2.4}$$

$$[B]\frac{d\vec{\theta}}{dt} = \vec{\Omega} \tag{3.2.5}$$

where $\vec{F}$ and $\vec{N}$ are the force and moment relative to the gravitational centre acting on the floating body; $\frac{d\vec{U}_c}{dt}$ (for breity, it is referred to as $\dot{\vec{U}}_c$ in this thesis)the translational acceleration of its gravitational centre; $\frac{d\vec{\Omega}}{dt}$ (for breity, it is referred to as $\dot{\vec{\Omega}}$ in this thesis) and $\vec{\Omega}$ its angular velocity and acceleration; $\vec{\theta}(\alpha,\beta,\gamma)$ the Euler angles; $\vec{S}$ the translational displacements. In Eqs. (3.2.2) - (3.2.5), $[M]$ and $[I]$ are mass and inertia matrices, respectively; and $[B]$ is the matrix formed by Euler angles and defined as,

$$[B] = \begin{bmatrix} \cos\beta\cos\gamma & \sin\gamma & 0 \\ -\cos\beta\sin\gamma & \cos\gamma & 0 \\ \sin\beta & 0 & 1 \end{bmatrix} \tag{3.2.6}$$

In 2D cases, $\alpha = 0, \gamma = 0$ and $\vec{\Omega}\times[I]\vec{\Omega} = 0$. Eqs (3.2.3) and (3.2.5) can be rewritten as

$$[I]\frac{d\vec{\Omega}}{dt} = \vec{N} \tag{3.2.7}$$

$$\frac{d\vec{\theta}}{dt} = \vec{\Omega} \tag{3.2.8}$$

Once $\vec{F}$ and $\vec{N}$ are solved, the accelerations $\frac{d\vec{U}_c}{dt}$ and $\frac{d\vec{\Omega}}{dt}$ can be found and the velocities $\vec{U}_c$ and $\vec{\Omega}$ are so obtained by integrating the accelerations, which gives the boundary condition for velocity potential on rigid boundaries. Eqs. (3.2.4) and (3.2.5) give the new position of the floating body for the next time step.

However, in a general 3D case, $\vec{\Omega}\times[I]\vec{\Omega}$ is non-zero and determined by $\vec{\Omega}$. One may calculate $\vec{\Omega}$ by integrating $\frac{d\vec{\Omega}}{dt}$ explicitly or implicitly. As is known, an implicit scheme is more stable than the explicit scheme in terms of time step. An implicit multi-step method, which will be discussed in Section 3.6., is used in this thesis to calculate $\vec{\Omega}$. $\frac{d\vec{\Omega}}{dt}$ in Eq. (3.2.3) is therefore be solved by using an iterative method.

3.3. Force calculation and the equations for $\partial\phi/\partial t$

To evaluate the accelerations and velocities of the floating body, one must calculate the force ($\vec{F}$) and moment ($\vec{N}$) acting on a body in Eqs. (3.2.2) and (3.2.3). The force and moment can be separated into two components: one due to the dynamic pressure of the fluid and the other one due to external forces ($\vec{f}_m$) and moments ($\vec{N}_m$), such as those due to mooring lines.

$$\vec{F} = \vec{f}_h + \vec{f}_m \tag{3.3.1}$$

$$\vec{N} = \vec{N}_h + \vec{N}_m \tag{3.3.2}$$

where $\vec{f}_h$ and $\vec{N}_h$ are the dynamic force and the moment acting on the body surface due to the dynamic pressure, respectively. They can be obtained by integrating the pressure p over the body surface by using Bernoulli's equation,

$$\vec{f}_h = -\rho \iint_{S_b} \left(\frac{\partial\phi}{\partial t} + \frac{1}{2}|\nabla\phi|^2 + gz \right) \vec{n} ds \tag{3.3.3}$$

$$\vec{N}_h = -\rho \iint_{S_b} \left(\frac{\partial\phi}{\partial t} + \frac{1}{2}|\nabla\phi|^2 + gz \right) \vec{r}_b \times \vec{n} ds \tag{3.3.4}$$

where S_b denotes the wetted body surface.

In this work, the external forces only come from the mooring lines, $\vec{f}_m$ and $\vec{N}_m$ hence equal to forces and moments due to mooring lines, respectively. Because this work focuses on the wave-body interaction, the mooring lines are approximated by using springs,

$$\vec{f}_m = k_m \vec{S}_m \tag{3.3.5}$$

$$\vec{N}_m = \vec{r}_m \times \vec{f}_m \tag{3.3.6}$$

in which k_m is the spring stiffness of the mooring line, $\vec{S}_m$ is the displacement of the mooring point, $\vec{r}_m$ is the position vector of the mooring point relative to the gravitational centre.

Substituting Eqs (3.3.3)- (3.3.6) into (3.3.1) and (3.3.2), the force and moment acting on the body can be described as

$$\vec{F} = -\rho \iint_{S_b} \left(\frac{\partial \phi}{\partial t} + \frac{1}{2} |\nabla \phi|^2 + gz \right) \vec{n} ds + k_m \vec{S}_m \tag{3.3.7}$$

$$\vec{N} = -\rho \iint_{S_b} \left(\frac{\partial \phi}{\partial t} + \frac{1}{2} |\nabla \phi|^2 + gz \right) \vec{r}_b \times \vec{n} ds + \vec{r}_m \times \vec{f}_m \tag{3.3.8}$$

As can be seen, the time derivative of the velocity potential ($\partial\phi/\partial t$) is required and is critical for accurately calculating forces and moments. As discussed in Section 2.5, the simple backward FD scheme may suffer from the problem of the saw-tooth instabilities (Sen, 1993). In this thesis, $\partial\phi/\partial t$ is found by solving a similar boundary value problem to that for ϕ defined in Eqs. (3.1.1)- (3.1.4) Similar to that used by Wu & Eatock Taylor (1996), Ma (1998) and Ma, Wu & Eatock Taylor (2001a), the boundary value problem for $\partial\phi/\partial t$ is defined by,

$$\nabla^2 \left(\frac{\partial \phi}{\partial t} \right) = 0 \tag{3.3.9}$$

in the fluid domain. On the free surface $z = \zeta(x, y, t)$, $\partial\phi/\partial t$ is given by

$$\frac{\partial \phi}{\partial t} = -g\zeta - \frac{1}{2} |\nabla \phi|^2 \tag{3.3.10}$$

which is based on the condition $p = 0$. Once ϕ is solved by from. Eqs. (3.1.3) (3.1.7), (3.1.10)- (3.1.11), $\nabla\phi$ can be calculated. Eq. (3.3.10) can provide the value of $\partial\phi/\partial t$ on the free surface. On a rigid boundary, particularly on a moving boundary, $\partial\phi/\partial t$ satisfies the equation (see , for example, Wu & Eatock Taylor, 1996; Ma, 1998),

$$\frac{\partial}{\partial n} \left(\frac{\partial \phi}{\partial t} \right) = [\dot{\vec{U}}_c + \dot{\vec{\Omega}} \times \vec{r}_b] \cdot \vec{n} - \vec{U}_c \cdot \frac{\partial \nabla \phi}{\partial n} + \vec{\Omega} \cdot \frac{\partial}{\partial \vec{n}} [\vec{r}_b \times (\vec{U}_c - \nabla \phi)]. \tag{3.3.11}$$

On the moving boundary without rotational motion, such as on the wavemaker, $\vec{\Omega} = 0$. Eq. (3.3.11) can be rewritten as

$$\frac{\partial}{\partial n} \left(\frac{\partial \phi}{\partial t} \right) = \dot{\vec{U}}_c \cdot \vec{n} - \vec{U}_c \cdot \frac{\partial \nabla \phi}{\partial n} \tag{3.3.12}$$

Since the normal direction of the wavemaker is negative x-direction in this thesis, the condition on the wavemaker, therefore, can be written as

$$\frac{\partial}{\partial n}\left(\frac{\partial \phi}{\partial t}\right) = -\dot{U}_{cx} + U_{cx}\frac{\partial^2 \phi}{\partial x^2} \tag{3.3.13}$$

where $\dot{U}_{cx}, U_{cx}$ are x-directional component of the translational acceleration and velocity of the wavemaker,respectively.

As mentioned above, there is a difficulty with solving Eqs. (3.3.9) to (3.3.11). As can be seen from Eq. (3.3.11), the accelerations $\vec{\dot{U}}_c$ and $\vec{\dot{\Omega}}$ should be known when solving the boundary value problem for $\partial\phi/\partial t$. However, in cases involving a free-response floating body, they are evaluated by Eqs. (3.2.2) and (3.2.3) which depends on the force and moment given by Eqs. (3.3.7) and (3.3.8). In turn, to find the force and moment, one needs $\partial\phi/\partial t$. The scheme to overcome this difficulty will be detailed in Chapter 6 below.

3.4. Radiation condition and wave absorption

Reflective or absorbing boundary conditions may be implemented on the right side of the tank. For the numerical simulation of waves where an absorbing boundary condition is used, the reflection from the far end wall is undesirable. The simplest way to ease this type of effect is to enlarge the computational domain. Obviously, this would need a very large domain to carry out a long-time simulation. An alternative approach is to remove the reflection as much as possible by using some special technique, i.e. imposing an artificial radiation condition on the boundary at the far end. To do so, many methods were developed, a detailed review can be found in Ma (1998). Here, a combination of the Sommerfeld condition with a damping zone will be employed. This technique was developed by Ma (1998) and Ma, Wu & Eatock Taylor (2001a). A brief summary is given here.

On the far end wall, the Sommerfeld condition is given

$$\frac{\partial \phi}{\partial t} + c\frac{\partial \phi}{\partial n} = 0 \tag{3.4.1}$$

where the parameter c is the phase velocity of the wave in the linear harmonic waves. The value of c is taken as

$$c = \sqrt{\frac{\tanh(k)}{k}} \tag{3.4.2}$$

in which k is evaluated by using $\omega^2 = k\tanh(k)$. Although this constant value is not consistent with the property of the fully nonlinear waves, it is easy to use. On the other hand, the combined damping zone technique will reduce the error caused by the above choice of c.

Since, in this work, the boundary condition on the free surface is defined by the Lagrangian notation, the boundary at the far end is chosen to move following the fluid particles. In the numerical experience, the far end wall is usually regarded as a rigid plane and moving with an average velocity (U_{rc}) of the x-component of the velocity of the fluid particles on the

intersection line between the boundary and the free surface. According to this assumption, the normal direction of the far end wall is x-direction, Eq. (3.4.1) can be rewritten as

$$\frac{\partial \phi_{rc}}{\partial t} = -c\frac{\partial \phi_{rc}}{\partial n} = -cu \tag{3.4.3}$$

in which subscript rc indicates the far end boundary, u is the x-directional velocity component of fluid particles. Therefore, the time derivative of the velocity potential on the far end wall can be expressed as

$$\frac{d\phi_{rc}}{dt} = \frac{\partial \phi_{rc}}{\partial t} + U_{rc}\frac{\partial \phi_{rc}}{\partial x} + v\frac{\partial \phi_{rc}}{\partial y} + w\frac{\partial \phi_{rc}}{\partial z} = -c\frac{\partial \phi_{rc}}{\partial n} + U_{rc}u + v^2 + w^2 \tag{3.4.4}$$

where v and w are the y-directional and z-directional velocity component of the fluid particles ,respectively. The time integration of Eq. (3.4.4) has been suggested by Ma (1998) as

$$\phi_{rc}|_t = \begin{cases} 0 & t \le t_1 \\ \phi_{rc}|_{t-\Delta t} + \dfrac{d\phi_{rc}}{dt}\Big|_{t-\Delta t}\Delta t & t > t_1 \end{cases} \tag{3.4.5}$$

in which $t_1 = L/(1+\beta)$ and β a coefficient which is taken as 0.2. It should be noted the Sommerfeld condition is not consistent with the free surface condition on the waterlines (intersection lines) between the free surface and the far end wall. This may lead to a numerical instability. To suppress the problem, an interpolation area is defined. In this area, the velocity potential is replaced by an interpolation function (Ma, Wu & Eatock Taylor, 2001a).

The damping zone is an area near the boundary at the far end wall. In this area, an artificial viscous term is adopted in the free surface condition. The reflection is reduced by removing the energy from the water because of the viscous terms. As used by Ma (1998) and Ma, Wu & Eatock Taylor (2001a), an artificial viscous term is only adopted to the dynamic condition because the modification to the kinematic condition may cause saw-tooth waves in the damping zone according to their testing. After being modified, the dynamic condition can be rewritten as

$$\frac{D\phi}{Dt} = -gz + \frac{1}{2}|\nabla\phi|^2 - v(x)|\phi| sign(\frac{\partial \phi}{\partial n}) \tag{3.4.6}$$

where the function *sign ()* is defined by:

$$sign(f) = \begin{cases} -1 & f < 0 \\ 0 & f = 0 \\ 1 & f > 0 \end{cases} \tag{3.4.7}$$

and $v(x)$ is a damping coefficient and is assigned as

$$v(x) = \begin{cases} \dfrac{1}{2}v_0\left[1 - \cos\left(\dfrac{\pi(x - x_d)}{L_m}\right)\right] & x \ge x_d \\ 0 & x < x_d \end{cases} \tag{3.4.8}$$

where x_d is the x-coordinate of the left end of the zone ; L_m is the length of the zone. In Ma(1998) L_m is taken as $\min(3\lambda d, 3d)$ λ is the wave length; v_0 is the magnitude of the damping coefficient which is optimised from numerical experiences by Ma(1998) as follows,

$$v_0 = 0.0496\omega^3 - 0.1751\omega^2 + 0.2352\omega - 0.0689 \qquad (3.4.9)$$

It should be noted that the frequency ω in Eq. (3.4.9) are nondimensionalised by $\sqrt{d/g}$ (more detail can be found in Chapter 7). Although the above equations are based on harmonic waves, this combined technique works well even in cases with irregular waves. That is due to the fact that the irregular waves associated with marine engineering often have a narrow band spectrum and are mainly dominated by the components near a particular frequency.

3.5. Numerical procedure and FEM formulation

The fully nonlinear interaction between waves and floating structures described in the above 3 sub-sections can be solved by a numerical procedure in a time domain. At each time step, the free surface and the potential values on it as well as velocities on all rigid boundaries, the position, velocity and acceleration of the floating structures are known, the velocity potential and its time derivative are solved by using the FEM. To do so, a computational mesh is required. Such a mesh needs to be updated at every time step in order to follow the deformation of the fluid domain during the calculation. As mentioned in Chapter 1, an unstructured mesh is usually necessary for the purpose of satisfying the need of simulating complex wave-body interaction problem. Regenerating such a mesh is time consuming. In order to overcome the problem, a method called QALE-FEM (represents Quasi Arbitrary Lagrangian Eulerian Finite Element Method) is developed in this thesis.

The main idea, which distinguishes the QALE-FEM method from the conventional FEM (Ma, 1998; Ma, Wu & Eatock Taylor, 2001a), is that the complex mesh is generated only once at the beginning and is moved at other time steps in order to conform to the motions of the free and structure surfaces. In this approach, the mesh can be generated by any generator and can have any complexity, any structure and any desired distribution. Because the mesh generator is used only once in a simulation of several thousands time steps, the CPU time spent on mesh generation is not an important matter since it may be only a small proportion of total computational time even it is quite long (say several minutes). In addition, the generator is not necessarily included in the main code. The idea of moving mesh is borrowed from the ALE formulation for the NS Model. However the velocities of the moving mesh do not need to be considered in governing equations in our approach. That is why this approach is called as quasi arbitrary Lagrangian-Eulerian finite element method (QALE-FEM). It is obvious that the technique for moving mesh in this approach is vital in order to achieve a good quality mesh at

all time steps and to avoid a large CPU requirement. A robust method has been developed herein for this purpose.

Since an unstructured mesh is used and moved by the above method, the scheme to calculate the velocity on the boundary developed by Ma (1998) and Ma, Wu & Eatock Taylor (2001a) is not applicable. A robust mixed FD scheme is therefore developed. The newly developed scheme allows one to calculate the velocity without the limitation of the mesh structure. It is, therefore, suitable to deal with the problem where a moving unstructured mesh is used.

Apart from the above developments, an iterative procedure to find the acceleration of and the force acting on the floating body is also developed. This method overcomes the difficulty associated with the implicit relationship between the force acting on and the acceleration of the floating body using an iterative procedure without the need of solving extra equations which are required by the mode-decomposition method and the indirect method. It also avoids the problem of forming a special matrix for $\partial\phi/\partial t$, whose properties have not been fully studied, in Dalen and Tanizawa's proposal. In the newly developed method, the velocity of the floating body is calculated implicitly, instead of being computed explicitly by the iterative procedure by Cao, Beck & Schultz (1994). This method is therefore more stable than the latter in cases involving floating bodies in large motion. Many numerical techniques, i.e. the scheme to estimate the initial value and the way to assign the under-relaxation coefficient, are developed to achieve overall high efficiency.

Similar to the conventional FEM, after the velocity on the free surface is found, the velocity potential on the free surface at the next time step can be estimated using Eqs. (3.1.11). This provides a Dirichlet condition for the velocity potential on the free surface,

$$\phi = f_p \tag{3.5.1}$$

where f_p is the potential value at the free surface. The acceleration of the floating body can be integrated to obtain the velocity of the floating body which provides a Newmann condition on the rigid boundary.

$$\frac{\partial\phi}{\partial n} = f_n \tag{3.5.2}$$

in which f_n is the value of normal derivative of the velocity potential on the rigid boundaries. These conditions on the boundaries enable one to solve the boundary value problems at the next time step. The problem about $\partial\phi/\partial t$ described in Eqs. (3.3.9) to (3.3.11) is also solved by using the above method with ϕ and the boundary conditions for it are replaced by $\partial\phi/\partial t$ and corresponding boundary conditions for $\partial\phi/\partial t$. For the purpose of providing the computational mesh required by the FEM, the fluid domain is discretised into a set of small tetrahedral elements as shown in Fig. 3.5.1,

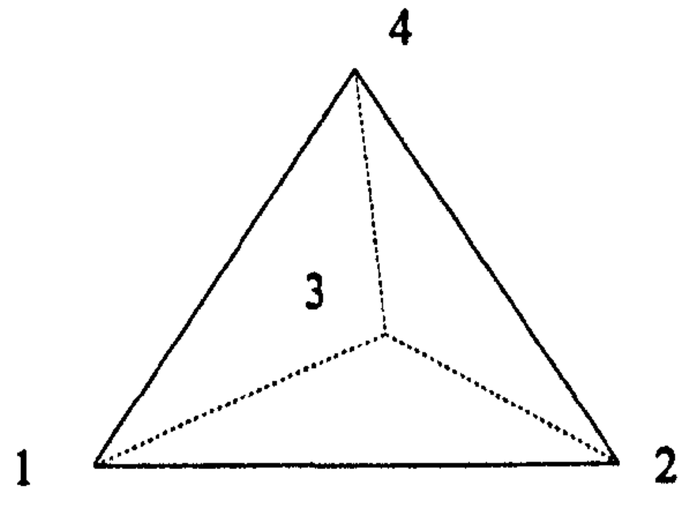

Fig.3.5.1 Sketch of a tetrahedral element (1,2,3 and 4 is the local node numbers)

The numerical procedure of the QALE-FEM method can be summarised as

1. Starts with an initial state;
2. Solve the BVP for the velocity potential described by Eqs. (3.1.3), (3.1.5) , (3.1.10) and (3.1.11);
3. Calculate the velocity of the fluid on the boundary, i.e. the free surface and the body surface;
4. Solve the BVP for $\partial\phi/\partial t$ defined by Eqs. (3.3.9)- (3.3.11);
5. Compute the force acting on the body by using Eqs (3.3.7) and (3.3.8);
6. If a free-response floating body is involved, calculate the accelerations and velocities of the floating structures by using Eqs. (3.2.2)- (3.2.5);
7. Update the position of, the velocity potential and the velocities on the free surface and the floating structures;
8. Move the mesh in order to conform to the deformation of the fluid domain;
9. Go to the next time step.

In this procedure, step 2 and step 4 are to solve the boundary value problems for velocity potential and its time derivative by FEM method, which will be discussed in this section. The velocity calculation scheme in step 3 will be discussed in Chapter 5. The iterative procedure to find the force (step 5) acting on and the acceleration (step 6) of the free-response floating body will be discussed in Chapter 6. A time integration scheme is developed to update the fluid domain in step 7 and will be discussed in Section 3.6. The method to move the mesh in step 8 will be discussed in Chapter 4.

3.5.1. FEM formulation for ϕ

As in the usual finite element models (see, for example, Ma,1998;Ma,Wu & Eatock Taylor,2001a), the velocity potential is expressed in terms of a shape function, $N_J(x,y,z)$:

$$\phi = \sum_J \phi_J N_J(x,y,z) \tag{3.5.3}$$

in which ϕ_J is the velocity potential at Node J. Using the Galerkin method, the Laplace equation and the boundary conditions are discretised as follows,

$$\iiint_{\forall} \nabla N_I \cdot \sum_{\substack{J \\ J \notin S_P}} \phi_J \nabla N_J d\forall = \iint_{S_n} N_I f_n dS - \iiint_{\forall} \nabla N_I \cdot \sum_{\substack{J \\ J \in S_P}} (f_p)_J \nabla N_J d\forall \tag{3.5.4}$$

where S_P represents the Dirichlet boundary on which the velocity potential f_p is known and S_n represents the Numann boundary on which the normal derivative of the velocity potential f_n is known. Eq. (3.5.4) can further be written in the matrix form:

$$[A]\{\phi\} = \{B\} \tag{3.5.5}$$

where

$$\{\phi\} = [\phi_1, \phi_2, \phi_3, \ldots, \phi_I, \ldots]^T \qquad (I \notin S_P) \tag{3.5.6}$$

$$A_{IJ} = \iiint_{\forall} \nabla N_I \cdot \nabla N_J d\forall \qquad (I \notin S_P, J \notin S_P) \tag{3.5.7}$$

$$B_I = \iint_{S_n} N_I f_n dS - \iiint_{\forall} \nabla N_I \cdot \sum_{J \in S_P} (f_p)_J \nabla N_J d\forall \qquad (I \notin S_P) \tag{3.5.8}$$

A and B are coefficient matrices. From Eqs. (3.5.7) and (2.5.8), it can be found that these matrices depend on the definition of the shape function and therefore the shape function affects the accuracy of the calculation. Linear, quadratic or higher-order polynomial shape functions may be used. For the cases with 3D wave-structure interaction, Ma (1998) and Ma, Wu & Eatock Taylor (2001a) have shown that the linear shape function is relatively simple and leads to sufficiently accurate results if a fine enough mesh is employed. In this work, a linear shape function is used.

$$N_I(x,y,z) = \begin{cases} N_i^{e_k}(x,y,z) & I \in e_k \\ 0 & I \notin e_k \end{cases} \tag{3.5.9}$$

where I is any global node number, $N_i^{e_k}(x,y,z)$ is the local shape function for element e_k and is written as

$$N_i^{e_k} = \frac{\forall_i}{\forall_{e_k}} = \frac{1}{6\forall_{e_k}}(a_i + b_i x + c_i y + d_i z) \qquad (i = 1,2,3,4) \qquad x,y,z \in e_k \tag{3.5.10}$$

in which $\forall_{e_k}$ is the volume of the element, can be given as follows:

$$\forall_{e_k} = \frac{1}{6}\det\begin{vmatrix} 1 & x_1 & y_1 & z_1 \\ 1 & x_2 & y_2 & z_2 \\ 1 & x_3 & y_3 & z_3 \\ 1 & x_4 & y_4 & z_4 \end{vmatrix} \tag{3.5.11}$$

$\forall_i$ is the volume of a tetrahedron where node i of the element is replaced by (x,y,z). The coefficient matrices of the algebraic Eq. (3.5.5) are hence integrated over the elements.

$$A_{IJ} = \sum_k \iiint_{e_k} \nabla N_I \cdot \nabla N_J d\forall \qquad (I \notin S_P, J \notin S_P) \tag{3.5.12}$$

$$B_I = \sum_k \iint_{\Delta S_n(e_k)} N_I f_n dS - \sum_k \iiint_{e_k} \nabla N_I \cdot \sum_{J \in S_P} (f_p)_J \nabla N_J d\forall \qquad (I \notin S_P) \tag{3.5.13}$$

where $\sum_k$ is the sum taken over all the elements, and $\Delta S_n(e_k)$ represents the triangular surface of element e_k.

An element e_k is discussed below. At this element, shape function $N_J(x, y, z)$ is linear, the gradient ∇N_J is constant. Substituting Eq. (3.5.9) into (3.5.12),

$$\iiint_{e_k} \nabla N_I \cdot \nabla N_J d\forall = \begin{cases} \dfrac{1}{36\forall_{e_k}} (b_i b_j + c_i c_j + d_i d_j) & I, J \in e_k \\ 0 & I \notin e_k \text{ or } J \notin e_k \end{cases} \tag{3.5.14}$$

in which *i* and *j* are the local node numbers of node *I* and node *J* in the element e_k, respectively.

Eq. (3.5.13) results from the contribution of the boundary condition, i.e. Dirichlet condition on S_p and Numann condition on S_n. When the element contains *I* and *J* with *J* being on S_p, get

$$\iiint_{e_k} \nabla N_I \cdot \sum_{J \in S_P} (f_p)_J \nabla N_J d\forall = \frac{1}{36\forall_{e_k}} (b_i b_j + c_i c_j + d_i d_j)(f_p)_j \tag{3.5.15}$$

otherwise

$$\iiint_{e_k} \nabla N_I \cdot \sum_{J \in S_P} (f_p)_J \nabla N_J d\forall = 0 \tag{3.5.16}$$

When one of the triangle surfaces of the element is part of the boundary S_n and contains node *I*.

$$\iint_{\Delta S_n(e_k)} N_I f_n dS = \iint_{\Delta S_n(e_k)} N_i^{e_k} f_n dS \tag{3.5.17}$$

otherwise

$$\iint_{\Delta S_n(e_k)} N_I f_n dS = 0 \tag{3.5.18}$$

Eq. (3.5.17) can be analytically integrated if f_n is assumed to be constant or linear on $\Delta S_n(e_k)$.

If f_n is constant on $\Delta S_n(e_k)$,such as on the wave maker,

$$\iint_{\Delta S_n(e_k)} N_i^{e_k} f_n dS = \frac{\Delta S^{e_k}}{3} f_n \tag{3.5.19}$$

in which ΔS^{e_k} is the area of $\Delta S_n(e_k)$. While, if f_n is linear on $\Delta S_n(e_k)$,

$$\iint_{\Delta S_n(e_k)} N_i^{e_k} f_n dS = \frac{\Delta S^{e_k}}{3} \left[\frac{(f_n)_i}{2} + \frac{(f_n)_j}{4} + \frac{(f_n)_k}{4} \right] \tag{3.5.20}$$

where subscript *i,j,k* denote local node number. $(f_n)_i$ is the nodal values of f_n at node *i*.

Once the contributions from each element are known, the coefficient matrices in Eq. (3.5.4) can be formed by summing them properly. Eq. (3.5.4) is then solved by using a conjugate gradient iterative method with the SSOR (Symmetric Successive Over-Relaxation algorithm) pre-conditioner and optimised parameter(see Ma, 1998 for details).

It should be noted that the boundary conditions on the free surface and on the rigid boundary are different. The nodes on the waterline must satisfy both simultaneously. This is known as the singularity problem on the waterlines which has been discussed in Chapter 2. In order to solve this problem, two types of method were used in the applications where BEM is used. One was suggested by Lin, Newman and Yue (1984) in which both the free surface condition and the body surface condition are employed at one point. The other one was discussed by Wang, Yao and Tulin (1995), in which every single intersection points at the waterlines are considered as two points. However, in the FEM, the free surface condition has appeared on the right side of the formulation. This can ease the well-known singularity problem at the waterline between the free surface and rigid boundaries and so special treatment is not required, as pointed by Wu and Eatock Taylor (1994) and Ma (1998).

3.5.2. FEM formulation for $\partial\phi/\partial t$

The problem about $\partial\phi/\partial t$ described in Eqs. (3.3.9) to (3.3.11) is also solved by using the above method with ϕ and the boundary conditions for it are replaced by $\partial\phi/\partial t$ and corresponding boundary conditions for $\partial\phi/\partial t$. However, the normal derivative of $\partial\phi/\partial t$ on the Newmann condition (Eq. (3.3.11)) contains a second-order derivative of velocity potential ($\frac{\partial\nabla\phi}{\partial n}$). This term is unknown and difficult to integrate in a FEM formulation. One may use a backward FD scheme if an interpolating method is employed to find the velocity potential and the velocity at points on its normal direction. For example at node *a* on the body surface as shown in Fig. 3.5.2, $\frac{\partial\nabla\phi}{\partial n}$ may be calculated by

$$\left(\frac{\partial\nabla\phi}{\partial n}\right)_a = \frac{(\nabla\phi)_a - (\nabla\phi)_{a'}}{l_n} \tag{3.5.21}$$

in which point *a'* is located in the normal direction (n_a) of node a with distance of l_n. Subscript *a* and *a'* denotes the value at nodes *a* and *a'*, respectively. Of course, one may also use other FD formulation, such as the 3-point formulation. But, no matter which formulation is chosen, one must find points on the normal direction of node *a*. $\nabla\phi$ at point *a'* can be calculated by a numerical formulation using the velocity potential in the fluid domain. To do so, this point should be in the fluid domain.

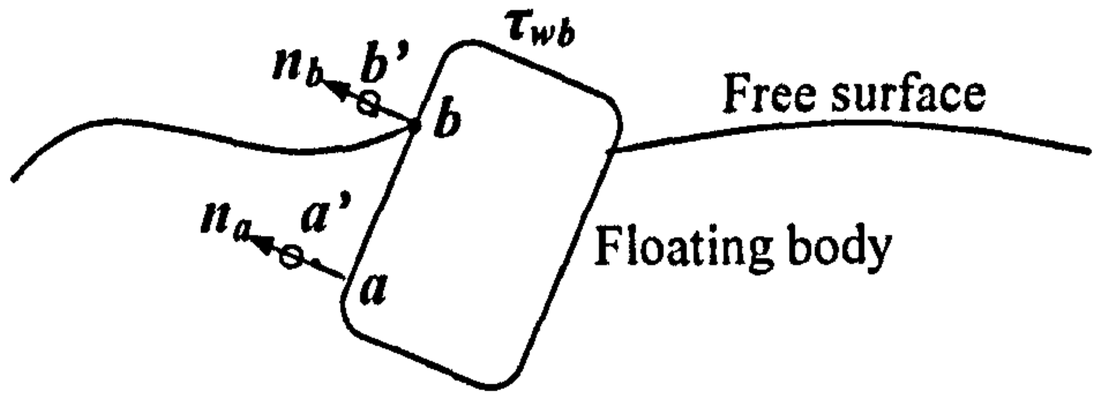

Fig. 3.5.2 Sketch of nodes on the body surface and their normal direction

However, in some cases, we cannot find these points in the fluid domain, e.g. the nodes on the waterlines (node b shown in Fig.3.5.2). For these nodes, it is impossible to find a point on its normal direction (n_b) in the fluid domain. Therefore, it may not possible to calculate the term $\frac{\partial \nabla \phi}{\partial n}$ by using a backward difference scheme. In this case, one cannot give a proper boundary condition for $\partial\phi/\partial t$ on the body surface.

In order to overcome the above problem, $\frac{\partial \nabla \phi}{\partial n}$ is expanded as

$$\frac{\partial \nabla \phi}{\partial n} = \frac{\partial}{\partial n}\left(\frac{\partial \phi}{\partial n}\vec{n} + \frac{\partial \phi}{\partial \tau_1}\vec{\tau}_1 + \frac{\partial \phi}{\partial \tau_2}\vec{\tau}_2\right) = \frac{\partial^2 \phi}{\partial n^2}\vec{n} + \frac{\partial}{\partial \tau_1}\left(\frac{\partial \phi}{\partial n}\right)\vec{\tau}_1 + \frac{\partial}{\partial \tau_2}\left(\frac{\partial \phi}{\partial n}\right)\vec{\tau}_2 \qquad (3.5.22)$$

where $\vec{\tau}_1, \vec{\tau}_2$ are two tangential unit vectors of the body surface. The second-order normal derivative of the velocity potential at the nodes on the body surface is converted to a function of the tangential derivative using the relationship,

$$\frac{\partial^2 \phi}{\partial n^2} = -\left(\frac{\partial^2 \phi}{\partial \tau_1^2} + \frac{\partial^2 \phi}{\partial \tau_2^2}\right) \qquad (3.5.23)$$

This formulation is based on the fact that the velocity potential satisfies Laplace's equation in the fluid domain (Eq. 3.1.3). Substituting Eq.(3.5.23) into Eq. (3.5.22),

$$\frac{\partial \nabla \phi}{\partial n} = -\left(\frac{\partial^2 \phi}{\partial \tau_1^{\,2}} + \frac{\partial^2 \phi}{\partial \tau_2^{\,2}}\right)\vec{n} + \frac{\partial}{\partial \tau_1}\left(\frac{\partial \phi}{\partial n}\right)\vec{\tau}_1 + \frac{\partial}{\partial \tau_2}\left(\frac{\partial \phi}{\partial n}\right)\vec{\tau}_2$$

$$= -\left[\frac{\partial}{\partial \tau_1}\left(\frac{\partial \phi}{\partial \tau_1}\right) + \frac{\partial}{\partial \tau_2}\left(\frac{\partial \phi}{\partial \tau_2}\right)\right]\vec{n} + \frac{\partial}{\partial \tau_1}\left(\frac{\partial \phi}{\partial n}\right)\vec{\tau}_1 + \frac{\partial}{\partial \tau_2}\left(\frac{\partial \phi}{\partial n}\right)\vec{\tau}_2 \qquad (3.5.24)$$

In this equation, $\frac{\partial \phi}{\partial n}$ is the normal velocity component which satisfies the boundary condition for velocity potential on the rigid boundary, i.e. Eq. (3.1.7). $\frac{\partial \phi}{\partial \tau_1}$ and $\frac{\partial \phi}{\partial \tau_2}$ are the tangential velocity components which can be found by using the velocity calculation scheme discussed later.

For nodes on the body surface but not lying on the waterlines, the fluid particles are always distributed on both side of its tangential direction. Therefore, it is possible to find the tangential derivative of the velocity by using a central FD scheme. For nodes on the waterline, we can find the fluid particles at least on one side of its tangential direction and therefore can calculate the tangential derivative of the velocity by using backward FD scheme. Hence, the difficulty discussed above is solved. Furthermore, the accuracy of the central FD scheme is higher than the backward FD scheme in cases with same mesh size and so Eq. (3.5.24) may lead to higher accuracy than direct calculation of $\frac{\partial \nabla \phi}{\partial n}$. Based on this, the boundary condition for $\partial\phi/\partial t$ on the wavemaker (Eq. (3.3.14)) can be rewritten as

$$\frac{\partial}{\partial n}\left(\frac{\partial \phi}{\partial t}\right) = -\dot{\vec{U}}_c - \vec{U}_c\left(\frac{\partial^2 \phi}{\partial x^2} + \frac{\partial^2 \phi}{\partial z^2}\right) \tag{3.5.25}$$

On other rigid boundaries, the boundary condition (Eq. (3.3.11)) is rewritten as

$$\frac{\partial}{\partial n}\left(\frac{\partial \phi}{\partial t}\right) = [\dot{\vec{U}}_c + \dot{\vec{\Omega}} \times \vec{r}_b - \vec{\Omega} \times \vec{U}_c] \cdot \vec{n} - \frac{\partial}{\partial \vec{n}}[(\dot{\vec{U}}_c + \dot{\vec{\Omega}} \times \vec{r}_b) \cdot \nabla \phi]. \tag{3.5.26}$$

where $\vec{r}_b$ is the position vector relative to the gravitational centre(See Fig. 3.2.1). The derivation can be found in Ma (1998). However, the last term of Eq.(3.5.26) includes a normal derivative of $[(\dot{\vec{U}}_c + \dot{\vec{\Omega}} \times \vec{r}_b) \cdot \nabla \phi]$. It is difficult to numerically calculate and therefore needs to be rearranged. For this purpose, let Γ be the last term of Eq. (3.5.26)

$$\Gamma = -\frac{\partial}{\partial \vec{n}}[(\dot{\vec{U}}_c + \dot{\vec{\Omega}} \times \vec{r}_b) \cdot \nabla \phi] \tag{3.5.27}$$

which is then expanded as

$$\Gamma = -\frac{\partial}{\partial \vec{n}}(\dot{\vec{U}}_c + \dot{\vec{\Omega}} \times \vec{r}_b) \cdot \nabla \phi - \frac{\partial \nabla \phi}{\partial n} \cdot (\dot{\vec{U}}_c + \dot{\vec{\Omega}} \times \vec{r}_b). \tag{3.5.28}$$

Since $\frac{\partial \vec{r}_b}{\partial \vec{n}} = \vec{n}$, Eq. (3.5.28) can then be rewritten as

$$\Gamma = -(\dot{\vec{\Omega}} \times \vec{n}) \cdot \nabla \phi - \frac{\partial \nabla \phi}{\partial n} \cdot (\dot{\vec{U}}_c + \dot{\vec{\Omega}} \times \vec{r}_b) \tag{3.5.29}$$

Finally, substituting Eq. (3.5.29) into (3.5.26) gives

$$\frac{\partial}{\partial n}\left(\frac{\partial \phi}{\partial t}\right) = [\dot{\vec{U}}_c + \dot{\vec{\Omega}} \times \vec{r}_b - \vec{\Omega} \times \vec{U}_c] \cdot \vec{n} - (\dot{\vec{\Omega}} \times \vec{n}) \cdot \nabla \phi - \frac{\partial \nabla \phi}{\partial n} \cdot (\dot{\vec{U}}_c + \dot{\vec{\Omega}} \times \vec{r}_b). \tag{3.5.30}$$

Substitute this equation into the corresponding equation of Eq. (3.5.17) in the FEM formulation for $\partial\phi/\partial t$ and split the contribution into two parts: one including $\frac{\partial \nabla \phi}{\partial n}$ and the rest, i.e.

$$\iint_{\Delta S_n(e_k)} N_l f_n dS = B_{n1}^{e_k} + B_{n2}^{e_k} \tag{3.5.31}$$

where

$$B_{n1}^{e_k} = \iint_{\Delta S_n(e_k)} N_i^{e_k} f_{n1} dS \tag{3.5.32}$$

$$B_{n2}^{e_k} = \iint_{\Delta S_n(e_k)} N_i^{e_k} f_{n2} dS \tag{3.5.33}$$

in which

$$f_{n1} = [\dot{\vec{U}}_c + \dot{\vec{\Omega}} \times \vec{r}_b - \vec{\Omega} \times \vec{U}_c] \cdot \vec{n} - (\dot{\vec{\Omega}} \times \vec{n}) \cdot \nabla\phi \tag{3.5.34}$$

$$f_{n2} = -\frac{\partial \nabla\phi}{\partial n} \cdot (\dot{\vec{U}}_c + \dot{\vec{\Omega}} \times \vec{r}_b) = -\frac{\partial \nabla\phi}{\partial n} \cdot \vec{U} \tag{3.5.35}$$

$B_{n1}^{e_k}$ can be calculated by using the same formulation as Eq. (3.5.19) where f_n is replaced by f_{n1}. Substitute Eq. (3.5.24) into Eqs. (3.5.33) and (3.5.35),

$$B_{n2}^{e_k} = \iint_{\Delta S_n(e_k)} N_i^{e_k} \left[\left(\frac{\partial \phi_{\tau_1}}{\partial \tau_1} + \frac{\partial \phi_{\tau_2}}{\partial \tau_2} \right) U_n - \frac{\partial \phi_n}{\partial \tau_1} U_{\tau_1} - \frac{\partial \phi_n}{\partial \tau_2} U_{\tau_2} \right] dS \tag{3.5.36}$$

For brevity, $\phi_{\tau_1}, \phi_{\tau_2}$ and ϕ_n represent $\frac{\partial \phi}{\partial \tau_1}$, $\frac{\partial \phi}{\partial \tau_2}$ and $\frac{\partial \phi}{\partial n}$,respectively. $U_n, U_{\tau_1}, U_{\tau_2}$ are normal and tangential velocity components, respectively. Using Stoke's theory, Eq. (3.5.36) can be rewritten as

$$B_{n2}^{e_k} = -\oint_{sb} - N_i (U_{\tau_2} \phi_n - U_n \phi_{\tau_2}) d\tau_1 + N_i (U_{\tau_1} \phi_n - U_n \phi_{\tau_1}) d\tau_2$$

$$- \iint_{\Delta S_n(e_k)} \left[\phi_{\tau_1} \frac{\partial (N_i U_n)}{\partial \tau_1} + \phi_{\tau_2} \frac{\partial (N_i U_n)}{\partial \tau_2} - \phi_n \frac{\partial (N_i U_{\tau_1})}{\partial \tau_1} - \phi_n \frac{\partial (N_i U_{\tau_2})}{\partial \tau_2} \right] dS \tag{3.5.37}$$

in which sb denotes the boundary of $\Delta S_n(e_k)$. Let $B_{n21}^{e_k}$ and $B_{n22}^{e_k}$ be the former and latter term, respectively,

$$B_{n21}^{e_k} = -\oint_{sb} - N_i (U_{\tau_2} \phi_n - U_n \phi_{\tau_2}) d\tau_1 + N_i (U_{\tau_1} \phi_n - U_n \phi_{\tau_1}) d\tau_2 \tag{3.5.38}$$

$$B_{n22}^{e_k} = - \iint_{\Delta S_n(e_k)} \left[\phi_{\tau_1} \frac{\partial (N_i U_n)}{\partial \tau_1} + \phi_{\tau_2} \frac{\partial (N_i U_n)}{\partial \tau_2} - \phi_n \frac{\partial (N_i U_{\tau_1})}{\partial \tau_1} - \phi_n \frac{\partial (N_i U_{\tau_2})}{\partial \tau_2} \right] dS \tag{3.5.39}$$

$B_{n21}^{e_k}$ denotes the contribution from the waterline. In this thesis, triangular elements are used and the normal direction in an element is constant. Once the normal unit vector is found, the tangential unit vector in each element is found by $\vec{\tau}_1 \perp \vec{n}$, $\vec{\tau}_1 // \vec{e}_x$, $\vec{\tau}_2 \perp \vec{n}$ and $\vec{\tau}_2 // \vec{e}_y$ where $\vec{e}_x$ and $\vec{e}_y$ are the unit vectors in the x- and y-directions, respectively. In this local normal-tangential coordinate system, $B_{n21}^{e_k}$ and $B_{n22}^{e_k}$ can be calculated by

$$B_{n21}^{e_k} = -\begin{cases} \frac{1}{3}|\tau_{1i} - \tau_{1j}|(\psi_i + \frac{1}{2}\psi_j) + \frac{1}{3}|\tau_{2i} - \tau_{2j}|(\vartheta_i + \frac{1}{2}\vartheta_j) & i, j \in S_w \\ 0 & otherwise \end{cases} \tag{3.5.40}$$

and

$$B_{n22}^{e_k} = -\frac{\Delta S^{e_k}}{3}(-\frac{\phi_{\tau_1 i}\Omega_{\tau_2 i}}{2} - \frac{\phi_{\tau_1 j}\Omega_{\tau_2 j}}{4} - \frac{\phi_{\tau_1 j}\Omega_{\tau_2 j}}{4} + \frac{\phi_{\tau_2 i}\Omega_{\tau_1 i}}{2} + \frac{\phi_{\tau_2 j}\Omega_{\tau_1 j}}{4} + \frac{\phi_{\tau_2 k}\Omega_{\tau_1 k}}{4})$$

$$-\frac{c^n{}_i}{6}\left[(U_n\phi_{\tau_2} - U_{\tau_2}\phi_n)_i + (U_n\phi_{\tau_2} - U_{\tau_2}\phi_n)_j + (U_n\phi_{\tau_2} - U_{\tau_2}\phi_n)_k\right]$$

$$-\frac{b^n{}_i}{6}\left[(U_n\phi_{\tau_1} - U_{\tau_1}\phi_n)_i + (U_n\phi_{\tau_1} - U_{\tau_1}\phi_n)_j + (U_n\phi_{\tau_1} - U_{\tau_1}\phi_n)_k\right] \tag{3.5.41}$$

where

$$\psi = -U_{\tau_2}\phi_n + U_n\phi_{\tau_2} \text{ and } \vartheta = U_{\tau_1}\phi_n - U_n\phi_{\tau_1} \tag{3.5.42}$$

i,j and k is the local node number in the element.; $b^n{}_i = \tau_{2j} - \tau_{2k}; c^n{}_i = \tau_{1k} - \tau_{1j}$ and τ_1, τ_2 are the tangential coordinate values. S_w denotes the waterline. The derivations of these equations are given in Appendix A.

3.6. Time integration scheme

In the time marching procedure described above, many physical quantities, need to be updated in order to provide the new condition at the next time step. All of these quantities are given in terms of time derivatives,

$$\frac{dy}{dt}(t) = f(t) \tag{3.6.1}$$

where y represents the physical quantities, i.e. the following four types of physical quantities in the time marching procedure described above,

1) The position (x,y,z) of the free surface in Eq. (3.1.10)
2) The velocity potential (ϕ) on the new free surface in Eq. (3.1.11)
3) The translational ($\vec{U}_c$) and angular ($\vec{\Omega}$) velocity of the floating body
4) The translational displacement $\vec{S}$ and the Euler angles $\vec{\theta}(\alpha,\beta,\gamma)$ of the floating body in Eqs. (3.2.4) and (3.2.5)

A time integration scheme is therefore required to find the value of y in the next time step,

$$y^n = y^{n-1} + \int_{n-1}^{n} f(t)dt \tag{3.6.2}$$

in which superscript n and n-1 represents the n^{th} and $(n\text{-}1)^{th}$ time steps, respectively. The information in n^{th} time step may or may not be taken into account to treat $\int_{n-1}^{n} f(t)dt$. If the

information in the current time step is considered, the scheme is implicit; otherwise, the scheme is explicit.

In order to achieve high computational efficiency, the following criteria are used to choose the time integration scheme,

- It must be accurate and stable;
- Not requiring sub-step calculations;
- Not updating the fluid domain in the calculation at one time step; saving the CPU time spent not only on this but also on forming the new coefficient matrix for FEM.

To do so, two types of methods are commonly used. One is based on the Runge-Kutta method. The other one is the multi-step method (see, Gear,1971). In the Runge-Kutta method, every time step is separated into several sub-steps (3 sub-steps in a general 4^{th}-order Runge-Kutta scheme). This method therefore requires three sub-step calculations at one time step forward Koo (2003) and Koo & Kim (2004) used a 4^{th}-order Runge-Kutta scheme is generally used to update the position and the velocity of the floating body. In each sub-step, the geometry of the computational domain may or may not be updated. If it is not updated, it is called a frozen coefficient method; otherwise, it is called a fully updated method. The CPU time spent on updating in the fully updated method is roughly equal to 4 times that in the frozen coefficient method. However, the frozen coefficient may not lead to stable and reasonable results for problems with large motions of floating bodies, as indicated by Koo & Kim (2004). Based on this, the frozen method doesn't satisfy the first and the second criteria, while the fully updated method doesn't satisfy the second and the third criteria. The Runge-Kutta method is therefore excluded in this work.

In the multi-step method, a Taylor expansion is used to treat $\int_{n-1}^{n} f(t)dt$. If constant time step is used (Gear,1971), Eq. (3.6.2) is therefore rewritten as

$$y^n = y^{n-1} + f^{n-1}\Delta t + \frac{1}{2}\left(\frac{df}{dt}\right)^{n-1}\Delta t^2 + \sum_{i=3}^{m}\frac{\left(\frac{d^{(i-1)}f}{dt^{(i-1)}}\right)^{n-1}\Delta t^r}{i!} + o(\Delta t^{m+1}) \qquad (3.6.3)$$

in which superscript *(i)* represents i^{th}-order derivative. y^n is calculated by y, its first-order time derivative (f)and its higher-order time derivative $\left(\frac{d^{(i-1)}f}{dt^{(i-1)}}\right)^{n-1}, i \geq 2$ without the need of separating every time step into several sub-steps. However, $\left(\frac{d^{(i-1)}f}{dt^{(i-1)}}\right)^{n-1}, i \geq 3$ in this thesis is unknown and $\left(\frac{df}{dt}\right)^{n-1}$ may or may not be known. Due to this fact, the above four types of

physical quantities are separated into two groups: one whose second-order time derivative is unknown, i.e. the first three types of physical quantities listed above, and one whose second-order time derivative is known, i.e. the last type of physical quantities.

For the physical quantities in the first group

In first group, all the higher-order time derivatives are expressed as a FD scheme of f. Either an explicit Adams-Bashforth method or an implicit Adams- Moulton method may be used (Gear,1971). The standard explicit Adams-Bashforth method is given by

$$y^n = y^{n-1} + \Delta t \sum_{i=0}^{r} \beta_{ri} f^{n-1-i} \tag{3.6.4}$$

in which r+1 is the number time steps which is taken into account in Eq. (3.6.2), β_{ri} is the linear coefficient, the superscript n and n-1 represent the time step .The standard implicit Adams- Moulton method is given by

$$y^n = y^{n-1} + \Delta t \sum_{i=0}^{r} \beta^*_{ri} f^{n-i} \tag{3.6.5}$$

where β^*_{ri} is the linear coefficient. Details on how to calculate β_{ri} and β^*_{ri} are given by Gear (1971). As discussed by Gear (1971), Eq. (3.6.5) requires larger time step than Eq. (3.6.4) to get stable results if the same r is chosen. It is also shown that the stability of both schemes gets worse as r increases. In addition, the memory required for storing the information at previous time steps is also increased as r increases. Therefore, the Adams-Bashforth method with r=1 and Adams- Moulton method with r=2 are commonly used. The former formulation is

$$y^n = y^{n-1} + f^{n-1}\Delta t + \frac{\left(f^{n-1} - f^{n-2}\right)}{2}\Delta t + o(\Delta t^3) \tag{3.6.6}$$

and the latter one is given by,

$$y^n = y^{n-1} + \frac{\Delta t}{12}(5f^n + 8f^{n-1} - f^{n-2}) + o(\Delta t^4) \tag{3.6.7}$$

The accuracy of Eq. (3.6.6) has been investigated by Ma (1998) and Ma, Wu & Eatock Taylor (2001a) using the case with fixed cylinders. Their results have shown that this explicit scheme is sufficiently accurate. The implicit scheme (Eq.3.6.7) has higher accuracy than Eq. (3.6.6). However, the implicit scheme requires an iterative procedure. During the iterative procedure, y^n in each sub-step of the iteration should be corrected in the next sub-step. This method is hence not suitable for updating the free surface since the position of the free surface and hence the fluid domain will be updated in the iterative procedure which is not expected. Therefore, Eq. (3.6.6) is used to update the free surface. Furthermore, because of the iterative procedure, the computational cost of the implicit scheme is more than that of the explicit method. For the purpose of achieving high computational efficiency, Eq. (3.6.6) is also used to

deal with other physical quantities in the first group unless the iterative procedure is required for other aims, i.e. for a freely responding floating body. In such case, the force acting on and the acceleration of the floating body are calculated iteratively in order to decouple their mutual dependency. The implicit method here does not affect the whole computational efficiency.

Based on the above discussion, it is summarised that Eq. (3.6.6) is used to update the position of the free surface and the implicit scheme (Eq.3.6.7) is used to deal with the velocity of the floating bodies. However, for the velocity potential on the new free surface, the explicit scheme (Eq. 3.6.6) is used in cases without free-response floating bodies, but the implicit scheme (Eq.3.6.7) is used in cases with free-response floating bodies where an iterative procedure is used to find the force acting on and the acceleration of the floating body.

For the physical quantities in the second group

In the second group, the second-order time derivative $f^{(1)}$ of the physical quantities, i.e., the translational displacement and the Euler angles, is known. y^n is therefore expressed as a function of $\frac{df}{dt}$ and f, for example, the implicit scheme as following,

$$y^n = y^{n-1} + f^{n-1}\Delta t + \frac{\Delta t^2}{2}\left(\frac{df}{dt}\right)^{n-1} + \frac{\Delta t^3}{6}\frac{\left(\frac{df}{dt}\right)^{n} - \left(\frac{df}{dt}\right)^{n-2}}{2\Delta t} \tag{3.6.8}$$

or the explicit scheme as following,

$$y^n = y^{n-1} + f^{n-1}\Delta t + \frac{\Delta t^2}{2}\left(\frac{df}{dt}\right)^{n-1} + \frac{\Delta t^3}{6}\frac{\left(\frac{df}{dt}\right)^{n-1} - \left(\frac{df}{dt}\right)^{n-2}}{\Delta t} \tag{3.6.9}$$

The above two equations are based on the 3rd order Taylor expansion with $\frac{d^2 f}{dt^2}$ approximated by a FD scheme. As discussed above, the implicit scheme requires iteration in which y^n is corrected at every sub-step. If Eq. (3.6.9) is used, the translational displacement and the Euler angle are changed at every sub-step of the iteration. As a result, the position of the floating body is changed as well. That implies that the coefficient matrices for the algebraic equations should be re-calculated at every sub-step of the iteration and therefore the third criteria above is not satisfied. Due to this, Eq. (3.6.8) is used to update the position of the floating body in this thesis.

4. MESH MOVING SCHEME FOR QALE-FEM METHOD

As indicated in Chapter 3, in the QALE-FEM the mesh is generated only once at the beginning of the calculation and is moved to accommodate the large variation of the fluid domain without need of any mesh regeneration at every time step. The vital task of the QALE-FEM method is to develop a scheme to control the nodal motion of the mesh at all other time steps.

Compared to other fluid-structure interaction problems, e.g. those in aerodynamic problems, a defining characteristic of the fluid domain in the wave-structure problem is that there is a free surface which is unknown and moving during the whole calculation. The deformation of the domain caused by the motion of the free surface is very large in cases with nonlinear large water waves. These make the mesh in a fluid domain with free surface become more difficult to conform to the deformation of the fluid domain using the existing techniques. On the other hand, the position of nodes on the free surface depends on the Lagrangian dynamic and kinematic condition, which usually causes the nodes to get too close to or too far from each other than in the initial state. In some cases, this may result in the appearance of negative elements/element overlap. All these problems are undesirable for the FEM method. For this reason, the nodes on the free surface should be redistributed and the mesh moving scheme for the interior nodes in the QALE-FEM method should also consider the change of the free surface.

In this work, the initial mesh is generated by an in-house mesh generator based on the mixed Delaunay triangulation and advancing front technique (see, for example, Frey, Borouchaki & George, 1998). In order to achieve high efficiency and accuracy of computation, the method to move the mesh should satisfy the following criteria:

- It must create satisfactory element shapes at all time steps.
- It must preserve reasonable refinement and distribution in regions of interest, such as those close to the free surface and structures.
- It must be computationally efficient.

4.1. Existing methods for moving computational mesh

Many researchers published various methods to control the motion of meshes in the ALE formulation for the NS model. Often-used methods include the empirical formulation method (Donea, Giuliani & Halleux,1982), the trigonometric function method (Huerta & Liu, 1988; Kjellgren & Hyvarinen, 1998), the method based on the solution of Laplace's equation to find the velocity of mesh developed by Lohner & Yang (1996), the equipotential method (Souli, Ouahsine & Lewin, 2000), the weighted average method (Aymone, Bittencourt & Creus, 2001),

the isoparametric mapping method (Gadala, Movahhedy & Wang, 2002), the transfinite mapping method (Gadala, 2004). Besides these, a self-adaptive mesh technology was developed recently and applied widely in NS models (an example sees Li, Tang & Zhang, 2002). The main concept below this is to map the fluid domain into a fixed region by solving a coupled Poisson type mesh equation, so that the governing equations can be solved in the fixed mapping domain. These methods either tend to make the mesh uniform, need a special mesh structure or require much computational time. So they are not perfect options satisfying the above criteria.

On the other hand, in the community of researchers who use ALE formulation for NS models, a fictitious elastic solid or dashpot/spring is assumed to exist in the whole mesh system. The displacement of nodes is therefore solved by a static equilibrium equation which results from the summation of forces at every node. This method is called the dynamic mesh algorithm (Zeng & Eigher, 2005). When this algorithm is implemented in conjunction with the NS models in ALE formulation, solution mapping from the previous mesh to the updated mesh is avoided (Huerta & Liu, 1988). This assumption forms the basis of two kinds of methods.

One is called elastic analogy method. The elements are regarded as elastic and the deforming spatial domain is treated as a mass of elastic material so that the boundary displacements are spread into the mesh through elastic forces. A few researchers have used this method to deal with free surface problems. Souli & Zolesio (2001) and Behr & Abraham (2002) used this method to simulate free surface problems; Souli, Ouahsine & Lewin (2000) and Zhang& Hisada (2001) applied this method to treat fluid-structure interaction problems with structural buckling and large domain changes. However, the static equation in the elastic analogy method is complex and the CPU time spent in forming as well as solving such equations is longer than the spring analogy method discussed below. This method hence doesn't satisfy the above criteria properly. This is also the reason why this method is not widely used.

The other one is called the spring analogy method and has been mainly applied to aerodynamic problems without a free surface. The main concept behind the method is that nodes in a mesh are considered to be connected by springs. The whole mesh is then deformed like a spring system. The boundary displacements therefore propagate into the mesh by virtue of a static equilibrium condition requiring that the sum of spring forces at each interior node is constant during the whole calculation. The spring system may comprise linear springs along each edge of elements (see, for example, Batina,1989; Yang & Lee, 1996; Anderson, 1997) or may consist of both linear and torsional springs (Farhat .et al., 1998, 2002; Degand & Farhat, 2002; Burg,2004; Bottasso, Detomi, & Serra, 2005), the latter applying a moment to nodes. The sketches of the linear and torsional spring are shown in Fig.4.1.1.

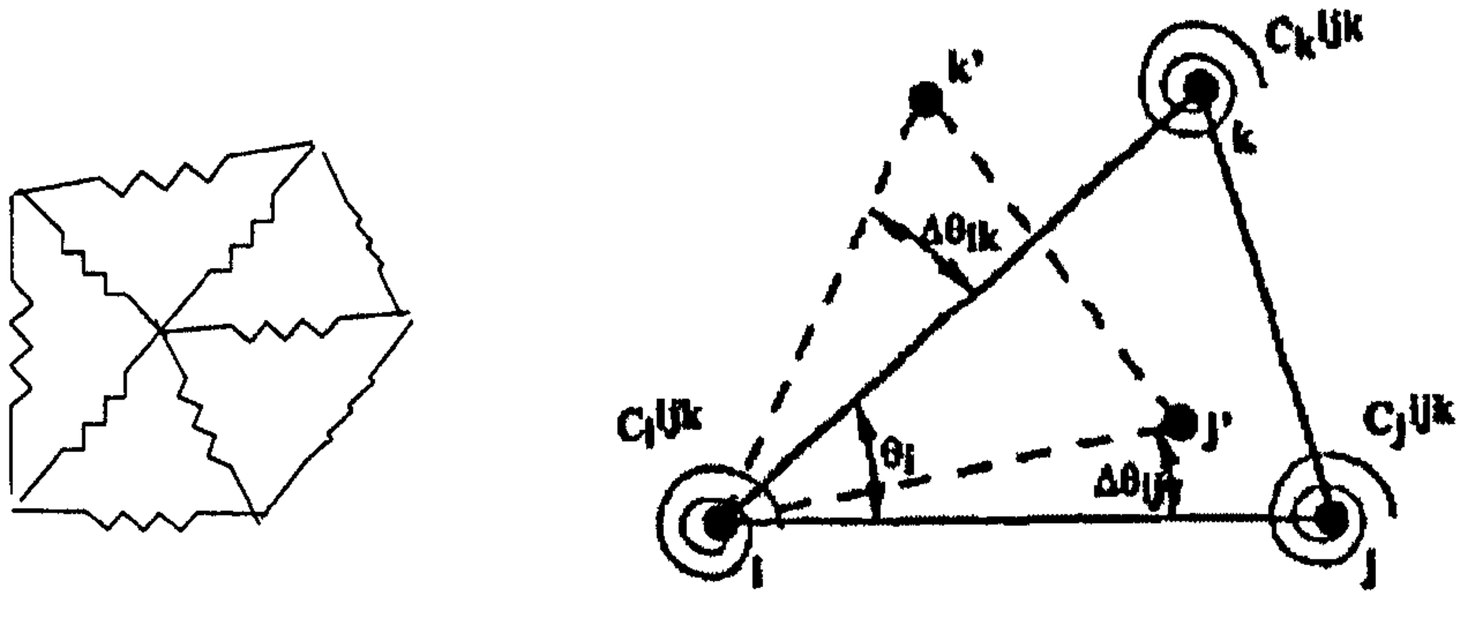

(a) linear (b) torsional (Farhat, Degand & Koobus et al ,1998)

Fig. 4.1.1 Sketches of linear spring and torsional spring systems

4.1.1. Linear spring analogy

In the traditional linear spring analogy method, linear springs are only attached to the edge of every element and the spring system in the initial condition is in a static equilibrium state. Once the boundary is moved, the nodal displacement on the boundary introduces spring forces that subsequently displace interior nodes to make the whole spring system reach static equilibrium. It is assumed that the resultant force acting on every interior node in static equilibrium at every time step is equal to that in the initial state, i.e.,

$$\vec{F}_{si}^{\,n} = \vec{F}_{si}^{\,0} \tag{4.1.1}$$

where $\vec{F}_{si}$ is the resultant force acting on the i^{th} interior node, superscript *0* and *n* represent the initial status and the n^{th} time step, respectively. Using the above equation, the nodal displacement can be obtained. Two types of springs, i.e. vertex spring and segment spring, are commonly used in the linear spring analogy method.

Vertex springs

Vertex springs are always under tension unless the spring length is zero, the assumed force for this type of spring can be described as

$$\vec{f}_{ij} = k_{ij}(\vec{x}_j - \vec{x}_i) \tag{4.1.2}$$

where f_{ij} is the spring force between node i and node j; $\vec{x}$ is the spatial coordinate and k_{ij} is the spring stiffness of spring (i,j). The resultant force acting on i^{th} node is hence given as

$$\vec{F}_{si} = \sum_{j=1}^{N_i} k_{ij}(\vec{x}_j - \vec{x}_i) \tag{4.1.3}$$

in which N the number of nodes which connect to node i. Since $\vec{x}$ can be expressed as

$$\vec{x} = \vec{x}^{\,0} + \Delta\vec{r} \tag{4.1.4}$$

in which $\vec{x}^0$ is the initial spatial coordinate; $\Delta\vec{r}$ the displacement of the node, Eq. (4.1.3) is therefore rewritten as

$$\vec{F}_{si} = \sum_{j=1}^{N_i} k_{ij}(\vec{x}_j^0 + \Delta\vec{r}_j - \vec{x}_i^0 - \Delta\vec{r}_i) = \sum_{j=1}^{N} k_{ij}(\vec{x}_j^0 - \vec{x}_i^0) + \sum_{j=1}^{N} k_{ij}(\Delta\vec{r}_j - \Delta\vec{r}_i) \tag{4.1.5}$$

Substitute Eq. (4.1.3) into Eq. (4.1.1), we can get

$$\sum_{j=1}^{N} k_{ij}(\Delta\vec{r}_j - \Delta\vec{r}_i) = 0 \tag{4.1.6}$$

The iterative formulation to calculate the displacement of the node i is therefore written as

$$\Delta\vec{r}_i = \sum_{j=1}^{N_i} k_{ij}\Delta\vec{r}_j \Big/ \sum_{j=1}^{N_i} k_{ij} \tag{4.1.7}$$

Segment springs

Segment springs have zero tension at initial length, the spring force between two nodes i and j can be calculated using the displacements of these two nodes, i.e.

$$\vec{f}_{ij} = k_{ij}(\Delta\vec{r}_j - \Delta\vec{r}_i) \tag{4.1.8}$$

The resultant force acting on i^{th} node is hence given as

$$\vec{F}_{si} = \sum_{j=1}^{N_i} k_{ij}(\Delta\vec{r}_j - \Delta\vec{r}_i) \tag{4.1.9}$$

Initially, the displacements of all nodes are zero, the initial resultant force acting on every node is therefore equal to zero. Substituting Eq. (4.1.9) into Eq. (4.1.1) gives

$$\sum_{j=1}^{N} k_{ij}(\Delta\vec{r}_j - \Delta\vec{r}_i) = 0 \tag{4.1.10}$$

This equation is the same as Eq. (4.1.6) and the iterative formulation for displacement by using segment springs is so the same as Eq. (4.1.7). That means the formulation of segment springs and that of the vertex springs are exactly same. No matter which spring is used, the same results are obtained.

Spring stiffness

If the spring stiffness is given, the nodal displacement can be found using Eq. (4.1.7). It is observed in Eq. (4.1.2) or Eq. (4.1.8) that for a specified force f_{ij}, a larger value of the spring stiffness means a small deformation of the spring. The spring stiffness represents the capability to resist the deformation caused by the external force. If the springs in one area are relatively stiffer than those in other areas, the elements in this area are more difficult to deform. The definition of the spring stiffness requires that the springs in the regions of interest, which are

usually near the moving boundaries, should be relatively stiffer than those in the rest of the area so that the elements in those regions have higher capability to resist the deformation caused by the motion of the boundaries.

In the traditional linear spring analogy method used in computational aerodynamics, the stiffness is taken as the inverse of the distance between two nodes (e.g. Batina, 1989), i.e.,

$$k_{ij} = 1/l_{ij} \tag{4.1.11}$$

where l_{ij} is the distance between i^{th} node and j^{th} node. Eq. (4.1.11) has been used by many researchers, such as Yang & Lee (1996), Anderson (1997) , Burg (2004). This definition of k_{ij} is justified by the fact that if two nodes tend to get closer during the mesh motion, the spring attached to the edge they belong to becomes stiffer and therefore prevents them from colliding. Furthermore, the distance between every two nodes is relatively smaller in the regions of interest than that in the rest of the fluid domain. The spring stiffness is therefore larger in those regions. The linear spring analogy method with this definition of the spring stiffness is referred as the conventional spring analogy method in this thesis.

The distinct advantages of the linear spring analogy system include requiring little CPU time and being very simple to implement. The system can be and has been successful in cases without extremely large distortion of elements and without nearly flat elements (Yang & Lee, 1996; Anderson, 1997; Burg, 2004). However, a major drawback of this approach is the lack of control of the collapse mechanisms due to the fact that linear spring forces in the conventional spring analogy method are not affected by angular or by volume changes of the element. Element inversion may occur in the cases with very severely distorted or nearly flat elements (Tezduyar, Behr & Liou, 1992).

4.1.2. Torsional spring analogy

In order to apply the spring analogy method to cases with very severely distorted or nearly flat elements, Farhat, Degand & Koobus et al (1998) attached torsional springs to the vertexes of every element (Fig.4.1.1b) in a 2D case. The stiffness of the torsional spring is defined as

$$C_i^{ijk} = 1/\sin^2\theta_i^{ijk} \tag{4.1.12}$$

where C_i^{ijk} is the torsional stiffness associated with the facing angle θ_i^{ijk} that has node i as its vertex on the triangle Δijk. This definition of the spring stiffness is based on the fact that if θ_i^{ijk} is close to 0 or 180^0, C_i^{ijk} is close to infinite and therefore prevents the element from inversing. The moment M^{ijk} generated by the torsional spring acting on every node in the triangle can be written as

$$M^{ijk} = C^{ijk}\Delta\theta^{ijk} \tag{4.1.13}$$

where

$$M^{ijk} = \begin{bmatrix} M_i^{ijk} & M_j^{ijk} & M_k^{ijk} \end{bmatrix}^T \tag{4.1.14}$$

$$C^{ijk} = \begin{bmatrix} C_i^{ijk} & 0 & 0 \\ 0 & C_j^{ijk} & 0 \\ 0 & 0 & C_k^{ijk} \end{bmatrix} \tag{4.1.15}$$

and $\Delta\theta^{ijk}$ is the rotational displacement

$$\Delta\theta^{ijk} = \begin{bmatrix} \Delta\theta_i^{ijk} & \Delta\theta_j^{ijk} & \Delta\theta_k^{ijk} \end{bmatrix}^T \tag{4.1.16}$$

In order to combine the torsional spring moment with the linear spring force expressed as Eq. (4.1.2) or (4.1.8), the rotational displacement in Eq. (4.1.13) is converted into the formulation of the nodal translational displacement by

$$\Delta\theta^{ijk} = R^{ijk}\Delta r^{ijk} \tag{4.1.17}$$

where R^{ijk} is the conversional matrix, Δr^{ijk} the matrix describes the translational displacements of node i,j and k. Eq. (4.1.13) therefore can be converted into a set of equivalent forces,

$$F_{torsional}^{ijk} = \left[\left(R^{ijk}\right)^T C^{ijk} R^{ijk}\right]\Delta r^{ijk} = K_{torsional}^{ijk}\Delta r^{ijk} \tag{4.1.18}$$

in which $F_{torsional}^{ijk}$ is the force generated by the torsional springs. The torsional spring and the linear spring are therefore combined into a single network of springs. For each edge sharing nodes i and j, the total artificial spring force F_{total}^{ij} is

$$F_{total}^{ij} = K_{linear}^{ij}\Delta r^{ij} + \sum_{ij} B_{ij}^{ijk} K_{torsional}^{ijk}\Delta r^{ijk} \tag{4.1.19a}$$

and

$$K_{linear}^{ij} = \frac{1}{l_{ij}}\left[E_{ij}\right] \tag{4.1.19b}$$

in which $[E_{ij}]$ is a matrix based on the Euler angle of spring ij ; Δr^{ijk} the matrix describes the translational displacements of node i and j; B_{ij}^{ijk} is a Boolean operator that extracts from a vector associated with a triangle ijk the subcomponent associated with the edge ij; $\sum_{ij}$ represents the summation of all the elements sharing edge ij. It is also assumed that the total spring force acting on every edge of the element is constant during the mesh moving procedure, the nodal displacement can be solved by using Eq. (4.1.19).

This method has been extended to 3D cases by Farhat, Degand & Koobus et al (2002) and Degand & Farhat (2002). All their results demonstrated that the torsional spring analogy may retain the mesh quality during the calculation even in cases with severely distorted and/or nearly flat elements. However, there are two additional matrices, i.e. R^{ijk} and E_{ij}, which have to be

calculated each time step at high computational cost. Furthermore, there are 3 torsional springs in the 2D case with triangle element and up to 12 torsional triangles in 3D cases with tetrahedron elements. Such a number of torsional springs complicate the formulation and force transformation. On the other hand, the conversional matrix R^{ijk} is obtained under the assumption that both the angular and the translational nodal displacements are sufficiently small. Hence, this method requires a sufficiently small time step to satisfy the above assumption. Therefore, its computational efficiency is undoubtedly low and the torsional spring analogy method does not satisfy the criteria given above.

For the same purpose, i.e., enhancing the ability of preventing the near flat element from collapsing, Bottasso, Detomi & Serra (2005) developed a ball-vertex spring analogy method. The main idea is to introduce additional linear spring that resists the motion of a mesh vertex towards its opposite face (see the dashed spring in Fig. 4.1.2). The position of each mesh vertex is found by forming its equilibrium under the combined effect of its edge-connected springs together with the additional ball-vertex springs. This method avoids the force transformation and displacement conversion and therefore has higher computational efficiency than the torsional spring analogy method. However, the additional springs also introduce additional computational cost.

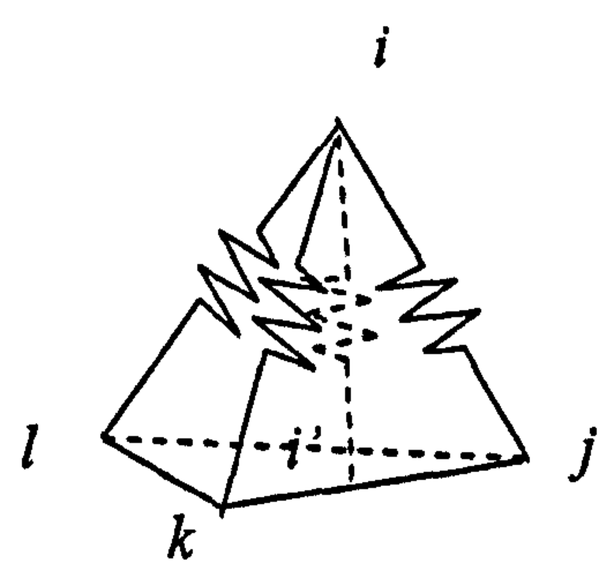

Fig. 4.1.2 Linear springs in the ball-vertex spring analogy method
(*i*' is the projected point of node *i* on the plane *j-k-l)*

The effect from the angular or volume changes of the elements may be considered in the linear spring system through modifying the spring stiffness of the linear spring (Blom, 2000; Zeng & Eigher, 2005). To do so, Blom (2000) developed a semi-torsional spring analogy method for 2D cases. In Blom's method the angular information is incorporated into the spring stiffness as

$$k_{ij}^{semi-torsional} = \frac{k_{ij}^{linear}}{\theta^{ij}} \tag{4.1.20}$$

where θ^{ij} is the angle facing the edge (*i,j*) on an element as shown in Fig.4.1.3b; k^{linear} is the linear spring stiffness and can be calculated by using Eq. (4.1.11). Though there were still many problems associated with this formulation, e.g. for each edge *i-j* there may be two different θ^{ij} in two connected elements (triangles *i-j-k* and *j-l-i* in Fig.4.1.3b) sharing edge *i-j*, Blom (2000) provided a novel idea to enhance the capability of the linear spring analogy method for cases with very severely distorted and/or nearly flat elements by taking into account the facing angle in the spring stiffness.

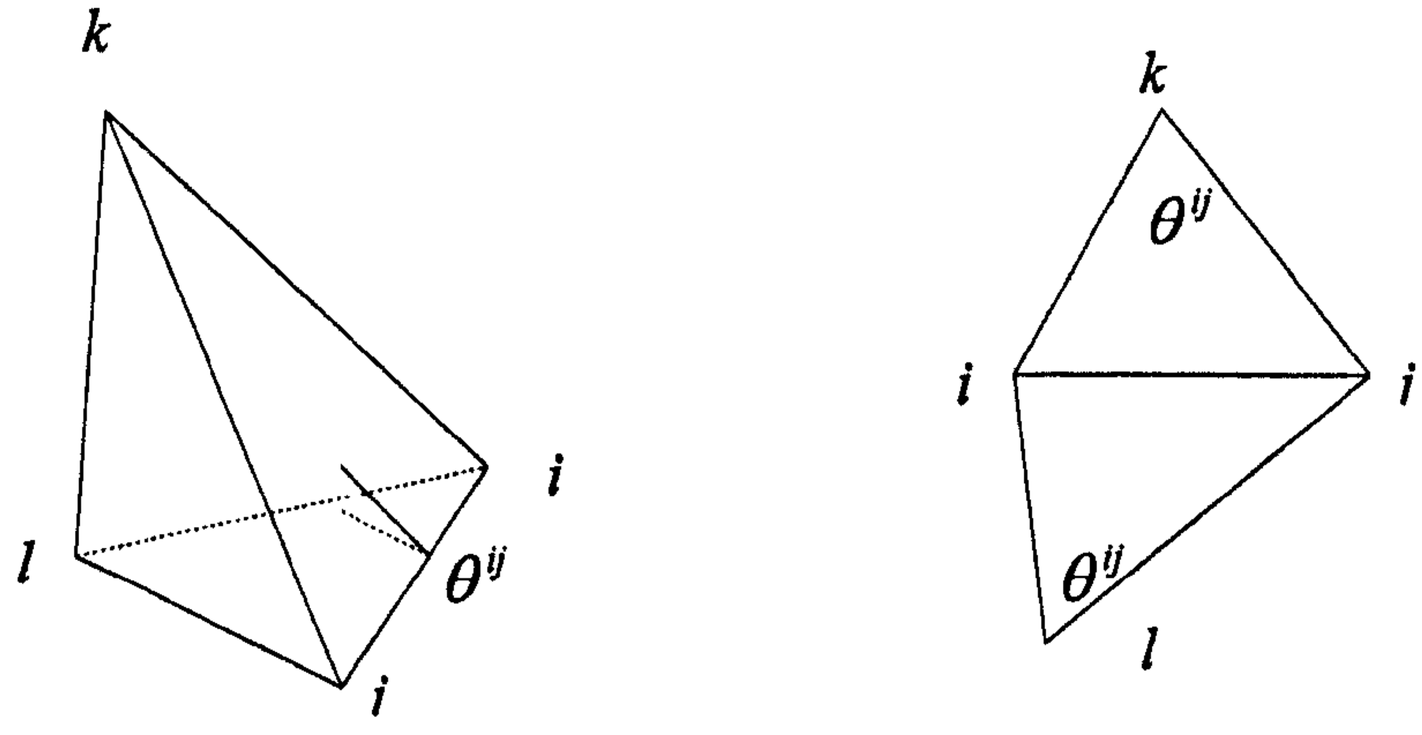

Fig.4.1.3 Facing angles in an 2D or 3D element
(a: 3D tetrahedron element; b: 2D triangle element)

Based on Bolm's contribution, Zeng & Eigher (2005) developed a new semi-torsional approach for 3D dynamic unstructured mesh problems. In their application, the spring stiffness is defined as

$$k_{ij} = \frac{1}{l_{ij}^2} + \kappa \sum_{m=1}^{NE_{ij}} \frac{1}{\sin^2 \theta_m^{ij}} \tag{4.1.21}$$

where NE_{ij} is the number of elements sharing edge *i-j*, θ_m^{ij} is the facing angle which faces the edge *i-j* on the m^{th} element sharing the edge (see Fig. 4.1.3a), κ is a coefficient and is assigned to be 1 in their applications. Once the facing angles sharing edge become *i-j* smaller, the second term ($\sum_{m=1}^{NE_{ij}} \frac{1}{\sin^2 \theta_m^{ij}}$) of Eq. (4.1.21) becomes larger and the spring *i-j* therefore become stiffer which prevents the facing angle from becoming smaller. Compared to the traditional spring analogy method, the semi-torsional approach considers the angular and the volume changes of the element, it therefore has higher capability to resolve the problem with large deformation caused by the moving boundaries. This formulation has been successfully applied to update the

unstructured mesh in 3D cases without free surfaces. However, once a free surface is involved, many associated problems will arise as mentioned before.

In this thesis, a spring analogy method based on the semi-torsional approach is extended to move the computational mesh during the calculation, since this method can achieve resonable quality of the mesh for all time steps and avoid excessive computational time spent on the mesh moving procedure. In order to overcome the difficulties associated with the free surface, as well as the moving rigid boundary, the following strategies are adopted to move the mesh:

- considering the interior nodes and boundary nodes separately;
- considering the nodes on the free surface and on rigid boundaries separately;
- considering the nodes lying on the waterlines and others separately;
- using relatively stiffer springs near the moving boundaries, such as the free surface and the moving rigid boundaries.

The first three strategies separate the nodes into 4 groups: interior nodes, nodes on the free surface but not lying on the waterlines (referred as inner-free-surface nodes), the nodes on the waterlines and the nodes on the body surface but not lying on the waterlines (referred as inner-body-surface nodes). Different methods are employed for moving different nodes. The last strategy is due to the fact that in the region where the springs are stiffer, the elements are more difficult to deform and therefore have higher capability to resist the external forces generated by the deformation of the boundaries. This strategy also ensures the newly developed model satisfies the second criterion.

4.2. New method in the QALE-FEM method to move the interior nodes

4.2.1. Numerical method

A linear spring analogy method is used to move the interior nodes. As discussed above, the spring stiffness should be assigned a larger value near the moving boundaries, such as the free surface and the moving rigid boundaries. To do so, two additional coefficients are introduced to correct the spring stiffness corresponding to Eq. (4.1.21). The spring stiffness is given as

$$k_{ij} = \left(\frac{1}{l_{ij}^2} + \kappa \sum_{m=1}^{NE_{ij}} \frac{1}{\sin^2 \theta_m^{ij}} \right) \Psi^{fs} \Psi^{bs} \tag{4.2.1}$$

where Ψ^{fs}, Ψ^{bs} are the additional correction coefficients associated with free surface and the moving rigid boundaries, respectively. These two coefficients are close to 1 when the springs are far from the moving boundaries and become larger if the spring is closer to the moving boundaries.

1) Correction coefficient Ψ^{fs}

In the initial mesh used here, the elements on the free surface are located at the mean free surface. The vertical coordinate, therefore, can be used to evaluate the distance between the spring and the free surface. Wu & Eatock Taylor (1994, 1995) suggested an exponential function based formulation to determine the distance between the horizontal surfaces near the free surface when using a structured mesh. Using this idea, Ψ^{fs} is defined as

$$\Psi^{fs} = e^{\gamma_f |1+(z_i+z_j)/2d|} \tag{4.2.2}$$

in which z_i and z_j are the vertical coordinates of Nodes I and J, respectively; d is the water depth; and γ_f is an coefficient that should be assigned a larger value if the springs are required to be stiffer at the free surface. Obviously, Ψ^{fs} is larger for springs near the free surface according to Eq. (4.2.2).

2) Correction coefficient Ψ^{bs}

In this thesis, Ψ^{bs} is defined as ,

$$\Psi^{bs} = e^{\gamma_b(\hat{w}_i+\hat{w}_j/2)} \tag{4.2.3}$$

in which γ_b plays the same role as γ_f but is used to adjust the spring stiffness near the body surface. The two coefficients may be different but in the present work, these two coefficients are taken to have the same values. $\hat{w}$ is a weight function and is determined by,

$$\hat{w} = \begin{cases} 0 & d_f > D_f \\ 1 - d_f / D_f & d_f \le D_f \end{cases} \tag{4.2.4}$$

where d_f is the minimum distance from the node concerned to the body surface as shown in Fig. 4.2.1. ; D_f is the distance between the body surface and the boundary of the near-body-region and is defined as,

$$D_f = \varepsilon d_{c\max} \tag{4.2.5}$$

where d_{cmax} is the maximum distance from the gravitational centre to the wetted body surface and depends on the relative position of the floating body to the free surface. In this thesis ε = 1.5 is used.

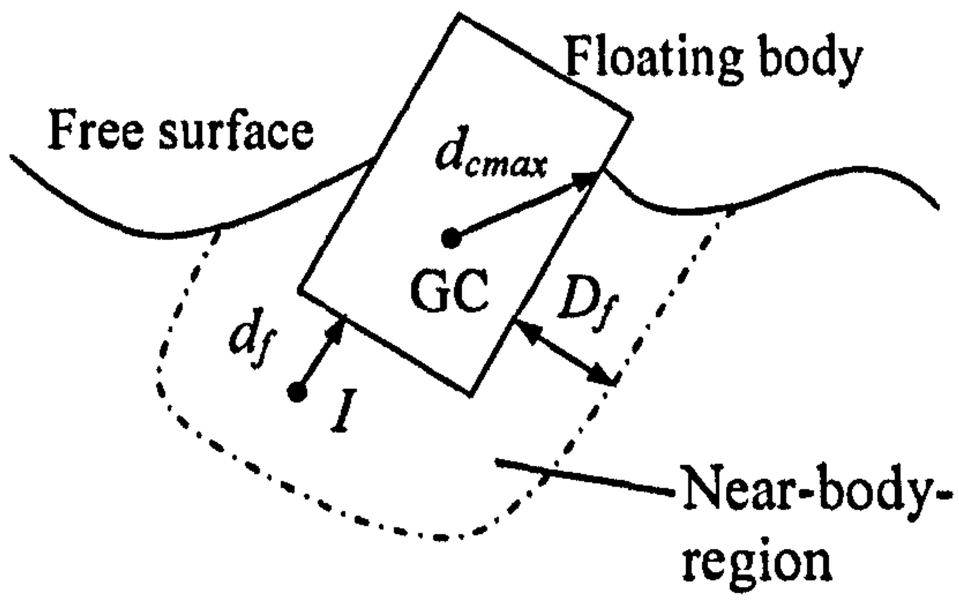

Fig.4. 2. 1 Region near moving body surface (GC: Gravitational centre)

It should be noted that Eq. (4.2.4) is suitable not only for floating bodies, but also for any moving rigid boundary, such as the moving sea bed. In that case, a similar coefficient as Ψ^{bs} should be taken into account when calculating spring stiffness.

4.2.2. Element quality and mesh quality

The quality of the mesh plays an important role in assessing the efficiency of a moving mesh scheme. In order to assess the quality of the mesh, a quality coefficient q_i (Cavendish, Field & Frey ,1995; Lewis, Zheng & Gethin,1996) for a single element I is defined

$$q_i = \frac{3R_i}{R_c} \tag{4.2.6}$$

where R_i, R_c are the inradius and circumradius of the element, respectively. This coefficient is based on the fact that the best tetrahedron/triangle element is the regular tetrahedron/triangle whose circumradius is three times of the inradius. The range of this coefficient is from 0 to 1. It equals to 1 for regular tetrahedrons/triangles and 0 for elements whose 4/3 points are located in a same plane. Obviously, smaller values of this coefficient mean the element is flatter and the quality of the element is lower. Since this coefficient q_i is used to assess the quality of a single element, it is called element quality.

After the element quality is found, the quality of the mesh is given by

$$Q_s = M / \sum_{i}^{M} \frac{1}{q_i} \tag{4.2.7}$$

where Q_s is the mesh quality; M the number of the elements in the fluid domain. This coefficient represents the aggregate quality of all the elements of the mesh and so is called mesh quality in this work. As discussed above, the linear spring analogy method may not work in cases with nearly flat elements, the minimum element quality $q_{\min}$ is also calculated to assess the mesh moving scheme.

4.2.3. Numerical tests

In order to optimize the parameters, i.e. κ , γ_b and γ_f in Eq. (4.2.1), a numerical investigation is then carried out. As discussed above, γ_b and γ_f play similar roles and can be assigned the same value. Furthermore, the spring surface is more difficult to deal with than the rigid boundaries. As long as the correction coefficient for the free surface works well , the correction coefficient for the body surface should also work. Due to this reason, only κ and γ_f are investigated. To do so, the case which artificially specifies the free surface without floating bodies is used here and Ψ^{bs} is therefore assigned to be 1 in these cases. Two factors,

the term $\sum_{m=1}^{NE_{ij}} \frac{1}{\sin^2 \theta_m^{ij}}$ and γ_f in the correction coefficient Ψ^{fs}, therefore need to be tested. The effect of the correction coefficient Ψ^{bs} , will be discussed in Chapter 8 and Chapter 9 by using cases of long-period calculations.

The initial meshes are 3D unstructured. The free surface in the initial mesh is the mean free surface. A sketch of the mesh is shown as Fig.4.2.2. The length and the width of the tank are 12 and 1 respectively. The mesh size is taken as $\Delta x = \Delta y = 0.075$. The mesh quality ($Q_s$) of the initial mesh is 0.69 and the minimum quality is 0.12.

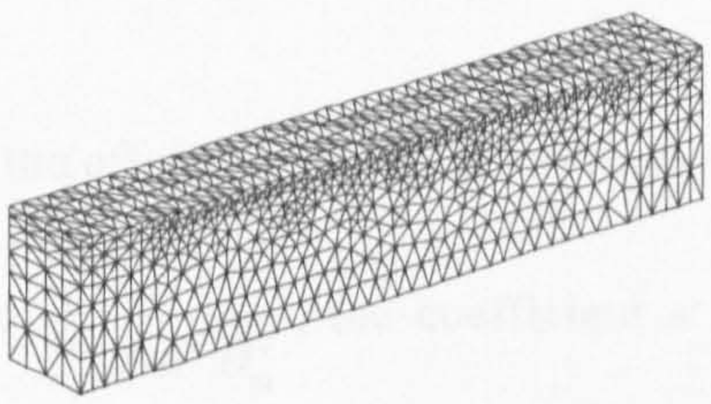

Fig.4.2.2 Illustration of the initial mesh used in the test cases for spring analogy stiffness

The deformation of the free surface is artificially given by specifying the position of the nodes on the free surface. After the free surface is deformed, the spring analogy method with different definition of the spring stiffness is applied to move the interior nodes. Two tests are carried out in this sub-section to investigate the effectiveness of the method. One is to specify the nodal position on the free surface using a periodic sinusoidal function and the other one is to assign an artificial overturning wave profile on the free surface. It should be noted that the deforming procedure is separated into 50 sub-steps to ensure the deformation of the free surface as well as the displacement of the node are small enough. This operation is not needed in a time domain simulation because the deformation of the boundaries in each time step is relatively small.

In the first test, the wave profile is specified by

$$z = 0.3\sin[\pi(x - L/2)] + 1 \tag{4.2.8}$$

This profile is close to that of a monochromatic wave and therefore may represent the free surface in an actual simulation. In this artificial case, the wave length is 2 and the wave height is 0.6. The steepness here is larger than that in the actual case without overturning wave. As long as the method present in this chapter works this case, it may have the ability to deal with all actual cases without wave overturning.

In order to investigate the efficiency of the spring analogy method with different spring stiffness, the mesh on the vertical wall where y=0.5 is visualized. This is due to the fact that the case described by Eq. (4.2.8) is obviously y-coordinate independent and therefore the boundary mesh on the vertical wall can indicate the whole quality of the mesh. Fig. 4.2.3 shows the initial mesh on the wall where y=0.5.

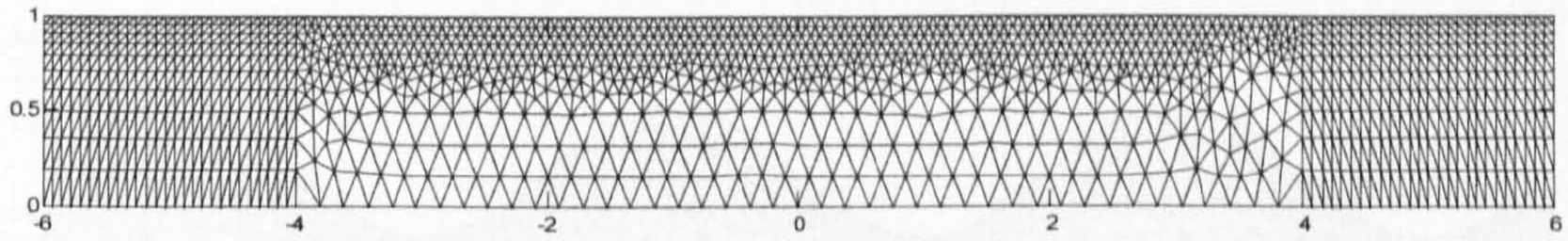

Fig.4.2.3. Initial mesh on the vertical boundary (y=0.5)

(Thick curve: free surface)

First of all, a case is run to test the effectiveness of the correction coefficient Ψ^{fs}. In order to eliminate the effect of the term $\sum_{m=1}^{NE_{ij}} \frac{1}{\sin^2 \theta_m^{ij}}$, the coefficient κ in Eq. (4.2.1) is taken as 0 and $\gamma_f = 1.7$ is used for the correction coefficient Ψ^{fs}. Fig. 4.2.4 shows the mesh after being moved.

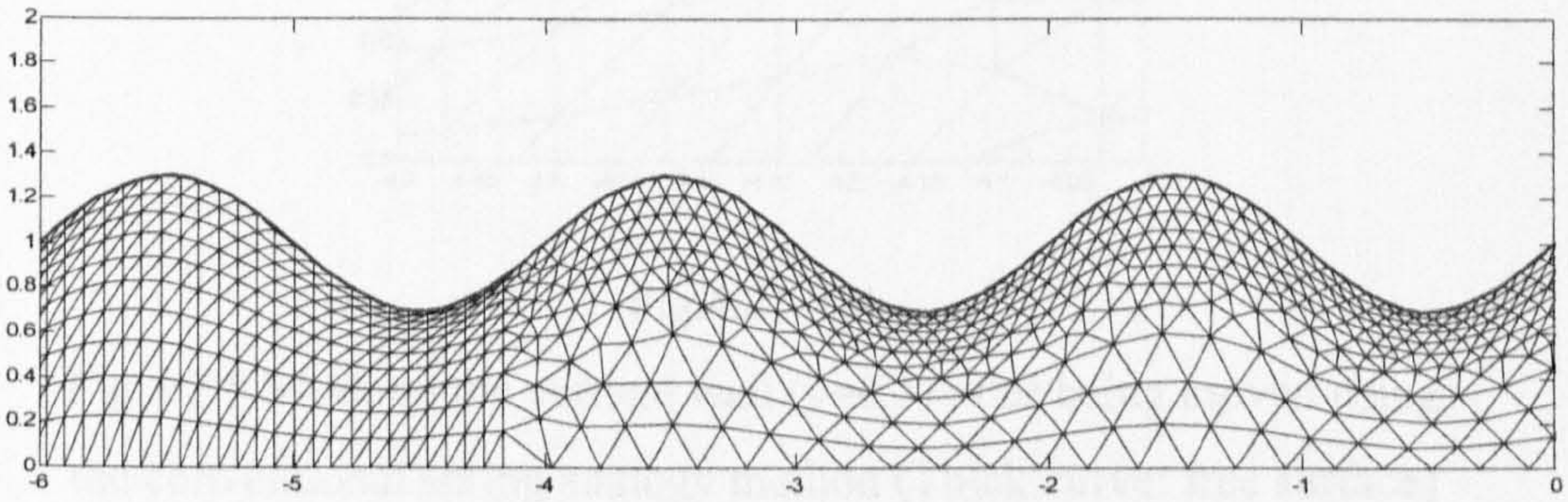

Fig.4.2.4 (a)

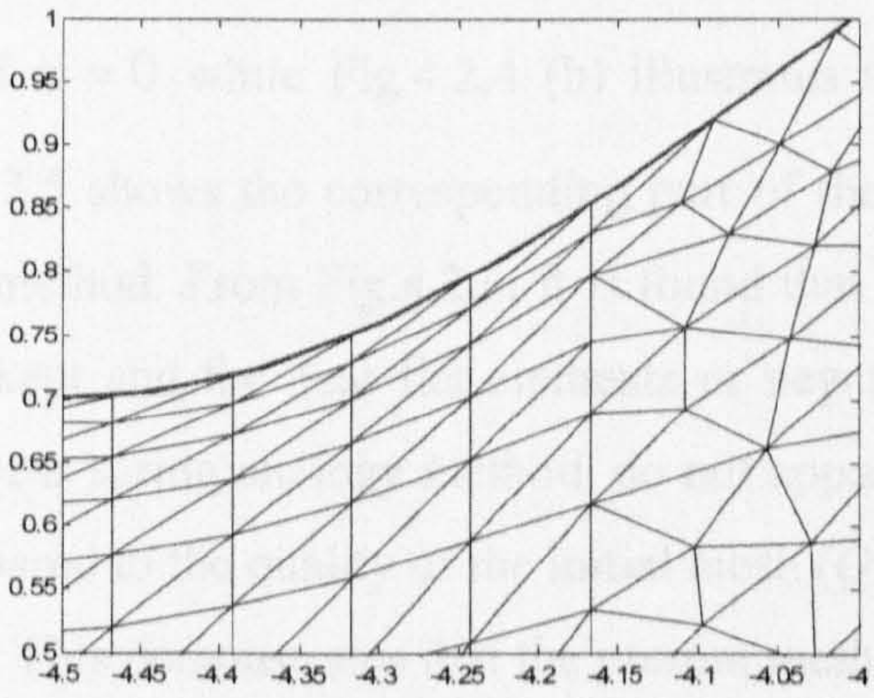

Fig.4.2.4 (b)

Fig.4.2.4 Mesh on the vertical wall (y=0.5) after being moved ($\gamma_f = 1.7$, $\kappa = 0$)

(Thick curve: free surface)

For the purpose of comparison, another case where the spring stiffness is given by the conventional definition, i.e. Eq. (4.1.11), is also run. The meshes after being moved in this case are plotted in Fig. 4.2.5.

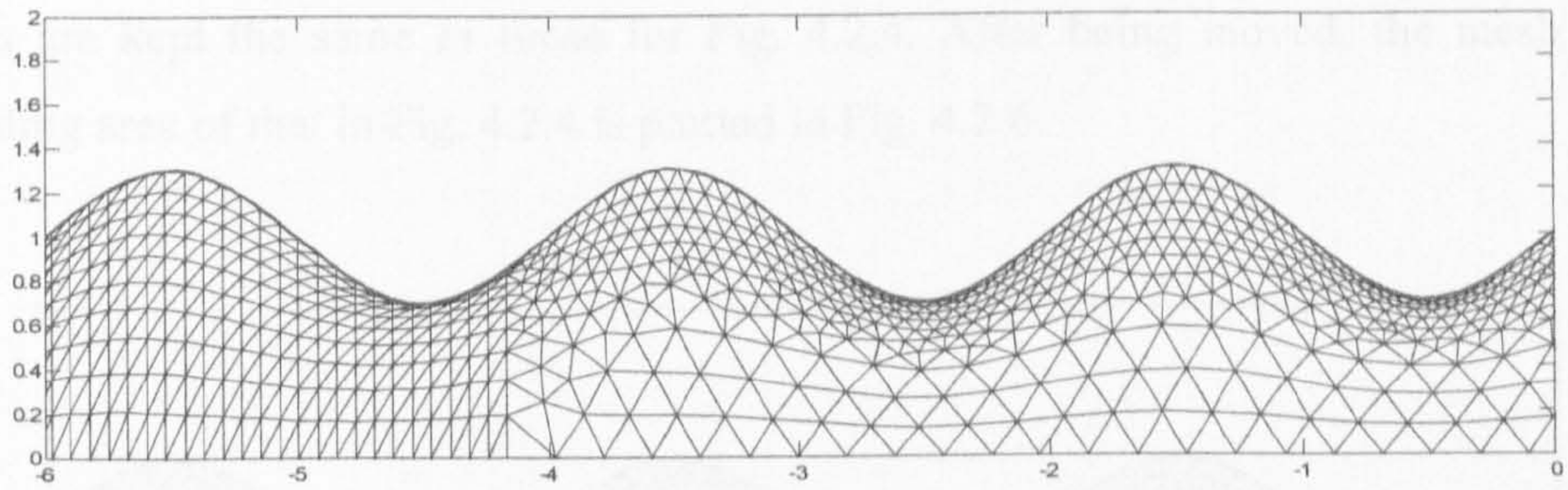

Fig.4.2.5 (a)

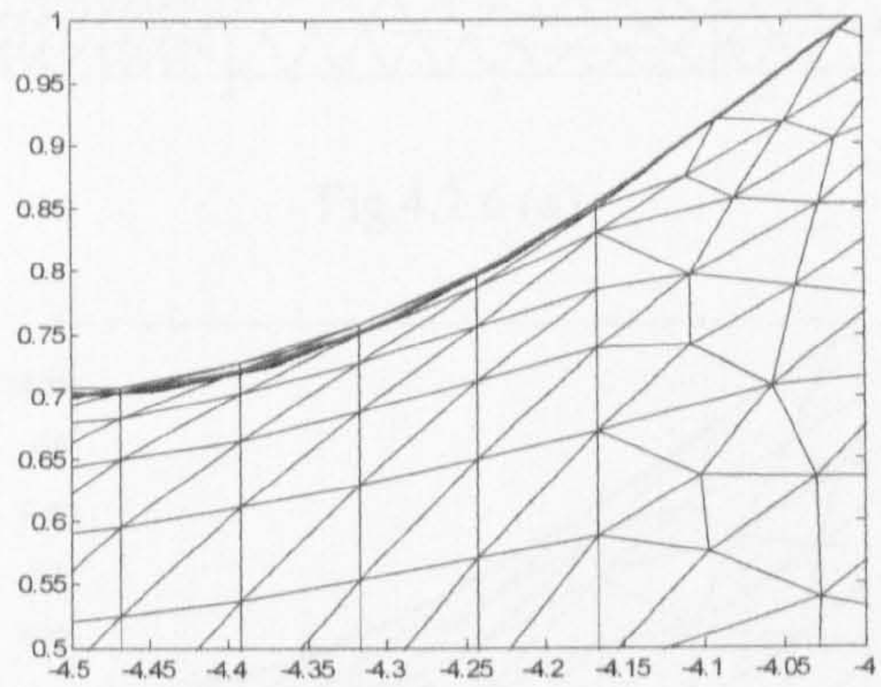

Fig.4.2.5 (b)

Fig.4.2.5 Mesh on the vertical wall (y=0.5) after being moved using the conventional spring analogy method (Thick curve: free surface)

Fig.4.2.4 (a) shows a part of the mesh on the vertical wall (y=0.5) moved using the present method with $\gamma_f = 1.7$ and $\kappa = 0$ while Fig.4.2.4 (b) illustrates the enlarged mesh in areas near a wave trough. Fig.4.2.5 shows the corresponding part of the mesh moved by using the traditional spring analogy method. From Fig.4.2.4, it is found that the original refinement and the nodal distribution are kept and the near flat elements or negative elements, which are of concern when using the linear spring analogy method, do not appear. The mesh quality in this figure is about 0.60. Compared to the quality of the initial mesh (Q_s=0.69), the decrease of the mesh quality is very slight. This demonstrates that the present method works well for this case. However, in case where the conventional spring analogy method is used, the elements near the wave troughs become very flat (see, Fig.4.2.5a). Many interior nodes in some regions (Fig.4.2.5b) moved outside of the fluid domain and negative elements appeared. This implies

that the conventional spring analogy method failed to provide a satisfactory mesh by moving nodes in this case and therefore may not be able to treat the case with steep waves in this work.

Another case is run to test the effect of the term $\sum_{m=1}^{NE_{ij}} \frac{1}{\sin^2 \theta_m^{ij}}$. In this case κ=1, all other parameters are kept the same as those for Fig. 4.2.4. After being moved, the mesh on the corresponding area of that in Fig. 4.2.4 is plotted in Fig. 4.2.6.

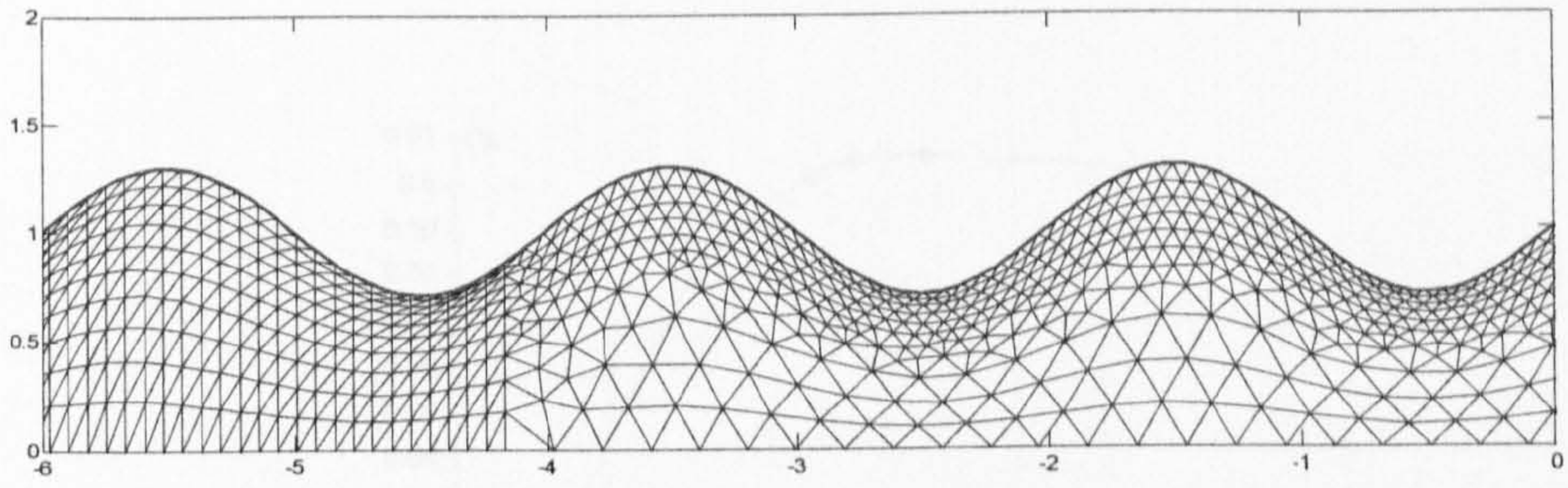

Fig.4.2.6 (a)

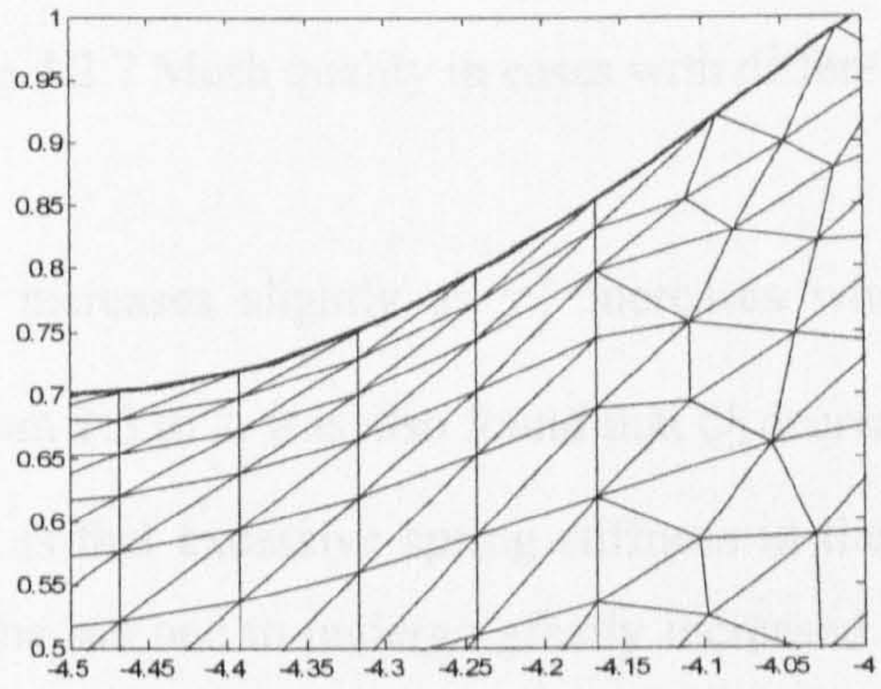

Fig.4.2.6 (b)

Fig.4.2.6 Mesh on the vertical wall (y=0.5) after being moved ($\gamma_f = 1.7$, $\kappa = 1$)

(Thick curve: free surface)

From this figure, it is found that the shape of elements and the nodal distribution are similar to those shown in Fig. 4.2.4 and the negative elements do not appear. The mesh quality in Fig.4.2.6 is about 0.61 which is 1.5% higher than that in Fig.4.2.4. This means the term $\sum_{m=1}^{NE_{ij}} \frac{1}{\sin^2 \theta_m^{ij}}$ contributes in keeping the quality of the mesh when a spring analogy method is employed but the effectiveness is not evident. However, additional computational cost is

required in order to calculate $\sum_{m=1}^{NE_{ij}} \frac{1}{\sin^2 \theta_m^{ij}}$. For the purpose of achieving high computational efficiency, this term is not considered in cases without overturning waves.

An advanced test is then carried out to optimise the value of γ_f. The parameters in Eq. (4.2.1) and the initial mesh are same as those in Fig. 4.2.4 except γ_f ranging from 0.5 to 3 in this case. The mesh qualities in cases with different γ_f are shown in Fig. 4.2.7.

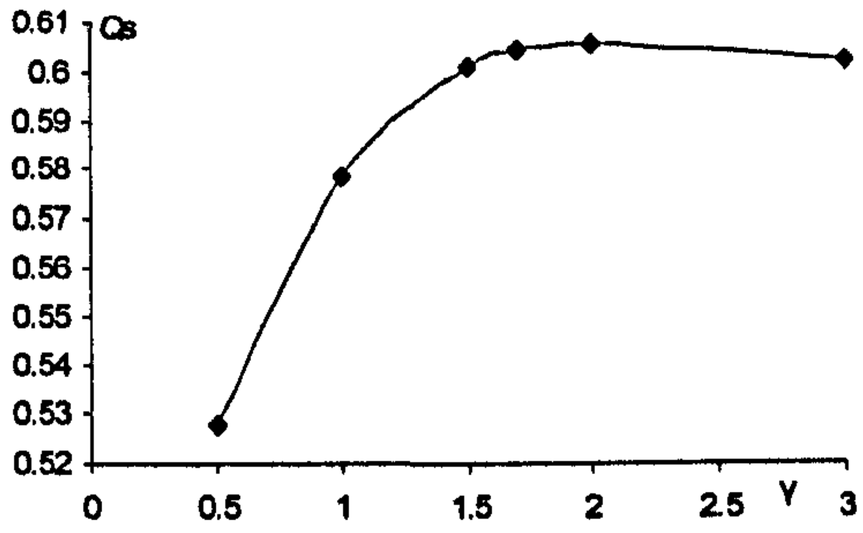

Fig.4.2.7 Mesh quality in cases with different γ_f

It is observed that Q_s increases slightly as γ_f increases when $\gamma_f < 1.5$ and increases slowly when γ_f ranges from 1.5 to 2. It is also found that Q_s decreases when γ_f is larger than 2. The most likely reason is that excessive spring stiffness in the area near the free surface causes the elements near the sea bed to undergo greatly increased external tension, due to the free surface deformation, and consequently become distorted. The value of γ_f is taken as 1.7 but further numerical tests may be needed to choose the value of γ_f based on the wave steepness.

As discussed, the free surface in the above test may only represent that in cases without an overturning wave. Once the overturning wave occurs, the free surface profile near the overturning jet would be very sharp. This may result in negative elements appearing in this region. In order to investigate the ability of the present spring analogy method, the second test is then carried out. In this test, the free surface is artificially assigned a overturning wave jet, whose profile is duplicated from Grilli, Guyenne & Dias (2001), as shown in Fig. 4.2.8. The crest almost reaches 0.7. Two cases are run. γ_f in both cases is given as 1.7 while κ is 0 and 1, respectively. The meshes after being moved in these two cases are plotted as Fig.4.2.9 and Fig.4.2.10.

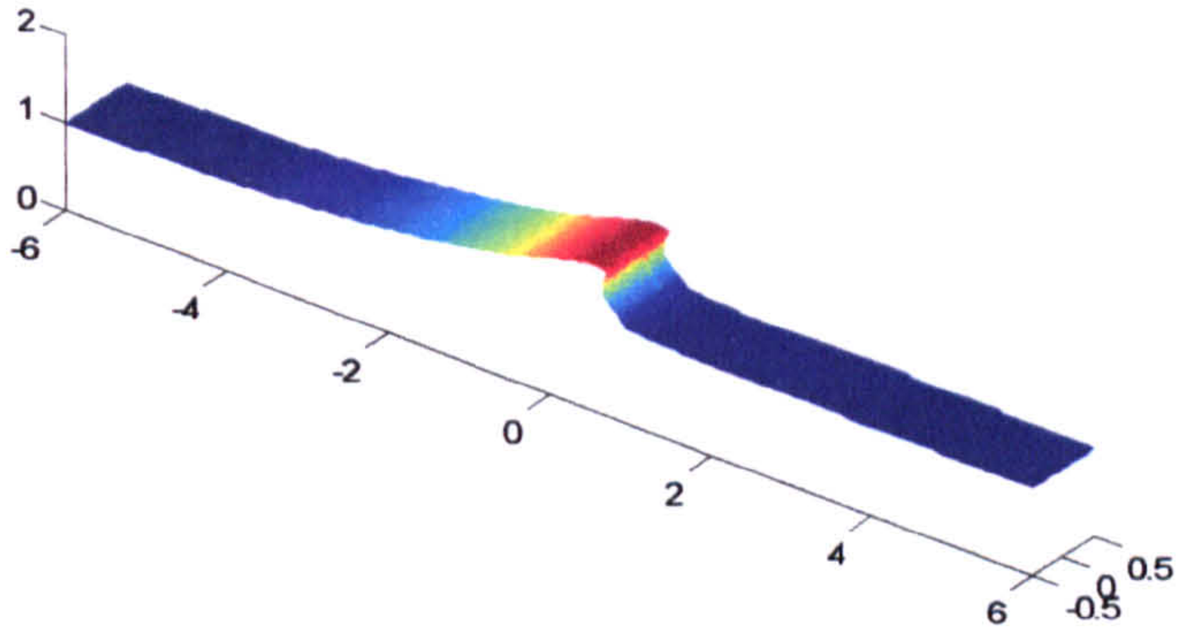

Fig.4.2.8 Assumed free surface profile in the case with an overturning wave

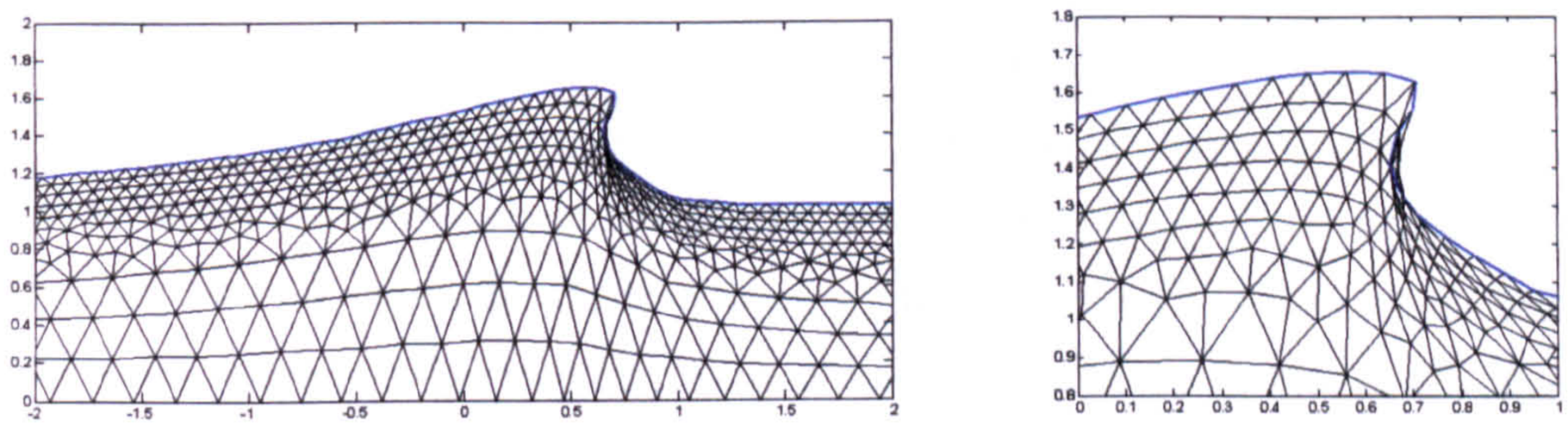

(a) (b)

Fig.4.2.9 2D mesh on the vertical wall in the case with an assumed overturning wave (γ_f=1.7, κ=0) (Thick curve: free surface)

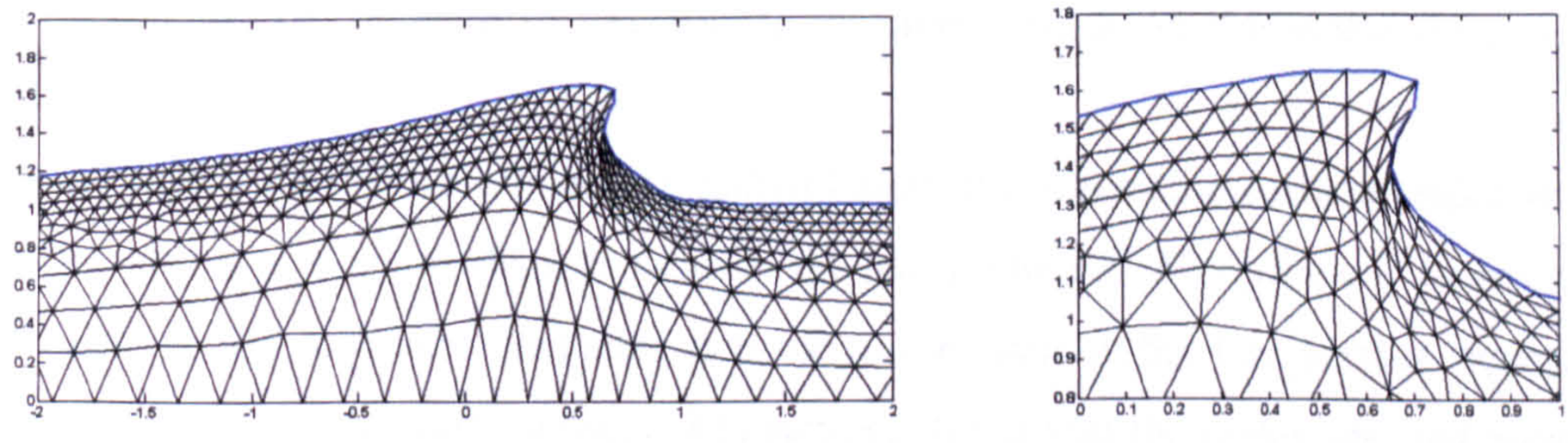

(a) (b)

Fig.4.2.10 2D mesh on the vertical wall in the case with an assumed overturning wave (γ_f=1.7, κ=1) (Thick curve: free surface)

Fig. 4.2.9 (a) shows a part of the mesh on the vertical wall (y=0.5) after being moved in case with γ_f=1.7, κ=0 and Fig.4.2.9 (b) illustrates the enlarged mesh in region near the overturning

jet. Fig.4.2.10 shows the corresponding part of the mesh in case with γ_f=1.7, κ=1. From these figures, it is observed that: without term $\sum_{m=1}^{NE_{ij}} \frac{1}{\sin^2 \theta_m^{ij}}$ in the spring stiffness (κ=0), there are negative elements in the mesh near the overturning jet (see Fig.4.2.9b); with term $\sum_{m=1}^{NE_{ij}} \frac{1}{\sin^2 \theta_m^{ij}}$ in the spring stiffness (κ=1), this phenomenon did not occur (see Fig. 4.2.10b). These results demonstrated that the term $\sum_{m=1}^{NE_{ij}} \frac{1}{\sin^2 \theta_m^{ij}}$ plays an important role in keeping the refinement of the mesh and the distribution of the nodes in this test. Therefore, κ should be non-zero in cases with overturning waves.

4.3. Moving nodes on the free surface

Special attention must be paid to nodes on the free surface because they play a decisive part in producing results of high accuracy for water wave problems. In order to track precisely the free surface, the node positions on the surface are determined by physical boundary conditions in Eq. (3.1.10), i.e., following the fluid particles, at most time steps. However, as indicated above, the nodes updated in this way may become too close to or too far from each other. To prevent this from happening, these nodes are relocated at specified interval (e.g., every 40 time steps). As pointed out in Section 4.1.2, they are grouped into those on curved waterlines, such as the intersecting line between the free surface and vertical walls or the wavemaker, and those that do not lie on the waterlines, when being relocated. The nodes in the latter group are called inner-free-surface nodes. In this section, only the method to move inner-free-surface nodes is presented. The scheme to redistribute the nodes lying on the water lines will be presented in Section 4.4.

Once the nodes on the waterlines are redistributed, the inner-free-surface nodes will be moved by the spring analogy method, as used for the interior nodes. Nevertheless, there exists a difficulty. That is how to ensure the nodes after moving remain on the free surface represented by discrete points. For simplicity, a method to achieve this is that the nodes are first moved in the projected plane of the free surface, i.e., calculating the values of x and y of the new position of every node using the spring analogy system. After the x- and y-directional coordinates of the new position are obtained, the elevations of the free surface corresponding to them are evaluated by an interpolating method.

It is well-known, for an FEM method, the mesh should be finer in the region where the gradients of the physical quantities, e.g, the elevation, are larger (Li, Tang & Zhang, 2002). In this aspect, the objective for the projected mesh on x-y plane after being moved is that more

nodes distribute in the area where the gradient of the free surface is relatively larger. In order to achieve this objective, the local gradient of the free surface is taken into account. The spring stiffness in moving the nodes in x- and y- directions, therefore, is determined, respectively, by:

$$k_{ij}^{(x)} = \frac{1}{l_{ij}^2}\sqrt{1+\left(\frac{\partial \varsigma}{\partial x}\right)^2} \quad \text{and} \quad k_{ij}^{(y)} = \frac{1}{l_{ij}^2}\sqrt{1+\left(\frac{\partial \varsigma}{\partial y}\right)^2} \,. \tag{4.3.1}$$

where $\frac{\partial \varsigma}{\partial x}$ and $\frac{\partial \varsigma}{\partial y}$ are the local slopes of the free surface in the x- and y-directions, respectively.

Inclusion of free-surface slopes in the spring stiffness ensures that the spring forces acting on a node are proportional to relative displacements between nodes measured along the curved free surface rather than along horizontal directions. For brevity, this method is called 'Global method' herein.

In order to test the effectiveness of the 'Global method', a case is run. In this case, the initial mesh used is similar to Fig.4.2.2 with width of 4 and length of 6. The mesh on the free surface is shown in Fig.4.3.1 (a) . In order to check whether the above objective for moving nodes in x-y plane, the projected mesh on this plane is also plotted in Fig. 4.3.1 (b).

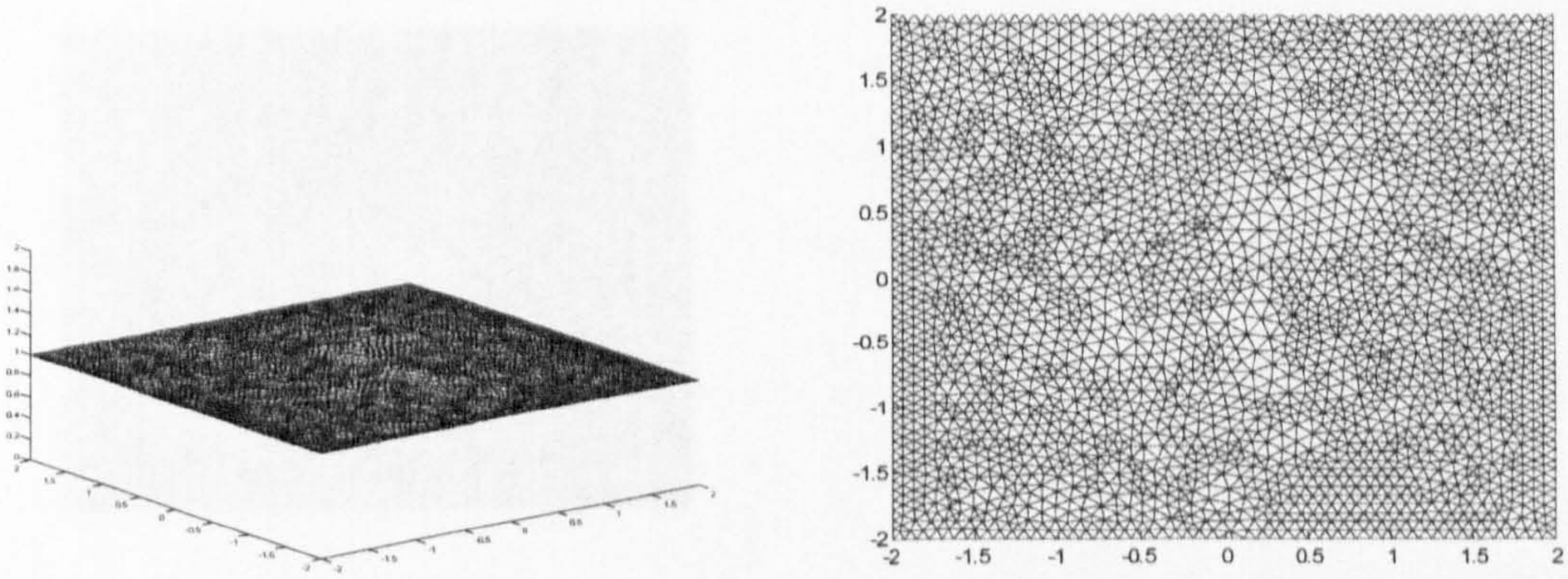

(a) whole mesh on the free surface (b) projected mesh on x-y plane

Fig.4.3.1 Initial mesh on the free surface

.

The free surface is now given an assumed profile which satisfies

$$z = 1 + 2e^{-10(x^2+y^2)} \tag{4.3.2}$$

and a part of the free-surface mesh near the peak of the elevation is shown in Fig. 4.3.2 (a). The 'Global method' is then used to redistribute the inner-free-surface nodes. The corresponding mesh after adaptation is shown in Fig.4.3.2 (b). It is observed that more nodes are moved to the region near the peak area and the nodes in the whole domain are therefore distributed more uniformly along the curved free surface.

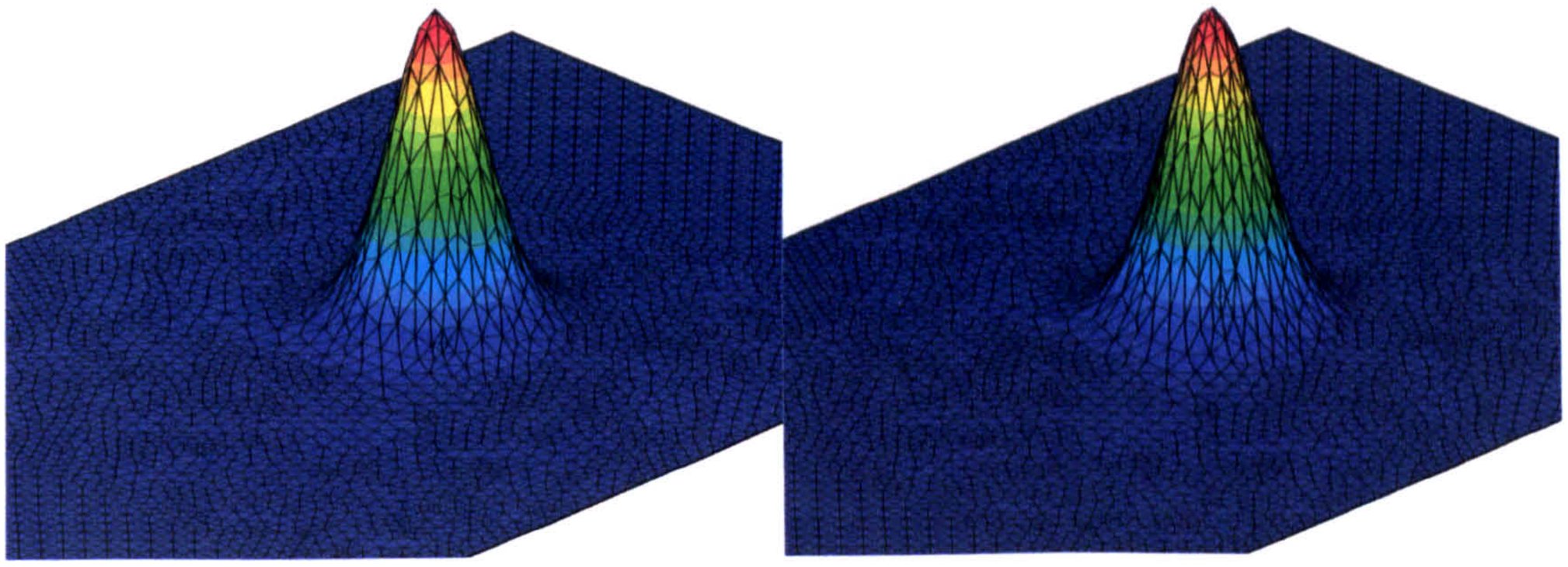

(a) before being redistributed (b) after being redistributed

Fig.4.3.2 Mesh on the free surface near the peak area

Analysis is also made for the projected mesh on the *x*-*y* plane. The mesh near the peak area projected to the *x*-*y* plane is plotted as Fig.4.3.3 where Fig.4.3.3 (a) is that before being redistributed and Fig.4.3.3 (b) after being redistributed.

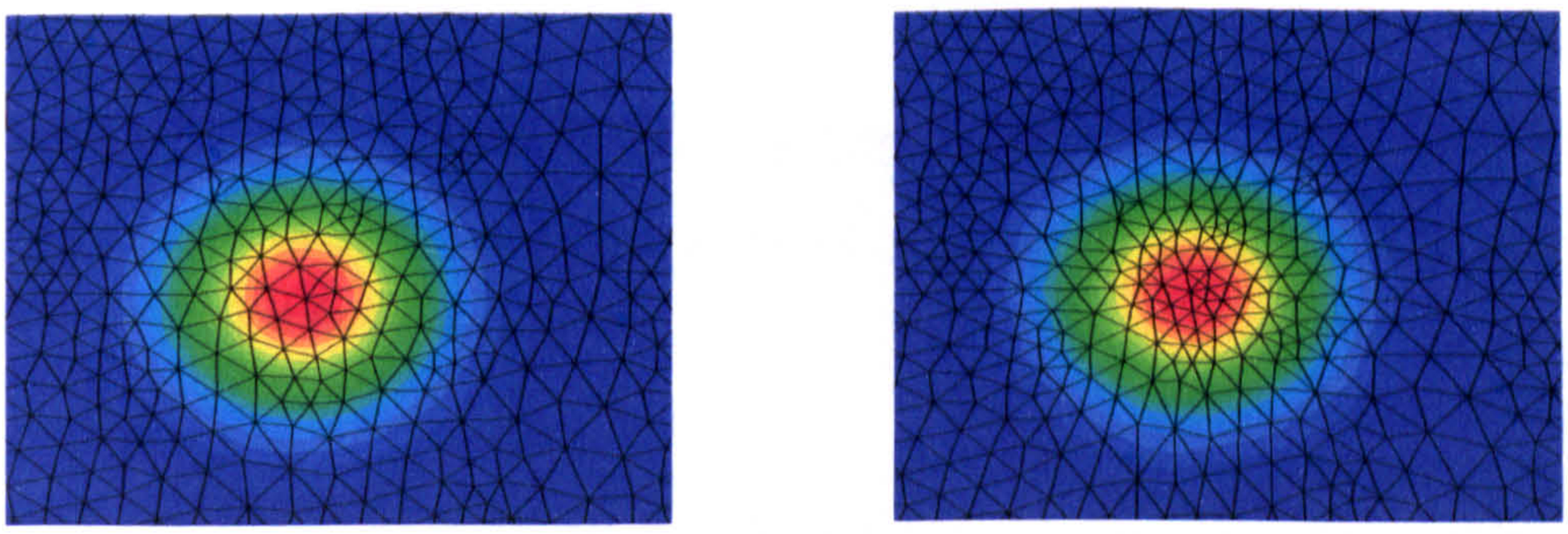

(a) before being redistributed (b) after being redistributed

Fig.4.3.3 Projected mesh on the *x*-*y* plane

It is also found from Fig.4.3.3 (b) that on the projected mesh on the *x*-*y* plane the nodal distribution is tighter near the peak area where the gradient of the free surface is larger than on other regions, as expected. This method can achieve the objective for move inner-free-surface nodes described above.

It should be noted, however, that this approach is obviously subject to a condition that the free surface must have only one intersecting point with any vertical line; in other words, it can be expressed by a single-valued function. Once the free surface is a multi-valued function of *x*- and *y*-coordinate, i.e. when overturning waves occur, the above approach is not applicable. In

such cases, a spring analogy method (called 'Local method') based on the local normal-tangential coordinate system is developed and adopted to move the nodes. The derivation and investigation of this method will be presented in Section 4.5.

4.4. Redistributing nodes on the waterlines

The nodes on the waterlines will be re-distributed by adopting the principle of the self-adaptive mesh (Davies & Venkatapathy, 1999). The basic idea is to make the weighted arc-segment lengths between two successive nodes a constant along the curved waterlines, i.e.

$$\varpi_i \Delta s_i = C_s \tag{4.4.1}$$

where ϖ is a weighting function, Δs_i the arc-segment length between two successive nodes and C_s a constant. The value of C_s is determined by using the fact that the total length of the curved waterline (L_s), should equal the sum of all arc-segment lengths, which gives

$$C_s = L_s \Big/ \sum \frac{1}{\varpi_i} = L_s / \chi_s \tag{4.4.2}$$

where $\chi_s = \sum \frac{1}{\varpi_i}$. Therefore, if the weighting function is given, the arc-segment lengths can be evaluated by

$$\Delta s_i = \frac{L_s}{\varpi_i \chi_s}. \tag{4.4.3}$$

The distribution of Δs_i is controlled by the weighting function. An arc-segment tends to be smaller for a larger value of the weighting function or vice versa. Davies & Venkatapathy. (1999) used the weight function as

$$\varpi = 1 + \alpha \tilde{f}^{\beta} \tag{4.4.4}$$

where α and β are two coefficients and $\tilde{f}$ is the function of the gradient of a variable, such as velocity. For the applications considered in this thesis, $\tilde{f}$ is taken as a function of the curvature of the curved waterline and is given by

$$\varpi_i = 1 + \alpha \left[(\kappa_i - \kappa_{\min}) / (\kappa_{\max} - \kappa_{\min}) \right]^{\beta} \tag{4.4.5}$$

where κ_i is the curvature of the curve Δs_i; $\kappa_{\max}$ and $\kappa_{\min}$ are the maximum and minimum curvatures of the waterline, respectively. It is suggested by Davies & Venkatapathy (1999) that the coefficient α is determined by the arbitrarily-specified maximum ($\Delta s_{s\max}$) and minimum ($\Delta s_{s\min}$) length of the arc-segment elements, i.e.

$$\alpha = \frac{\Delta s_{s\max}}{\Delta s_{s\min}} - 1. \tag{4.4.6}$$

In our applications, it is expected that the arc-segment length is smaller in areas of shorter waves and is larger in areas of longer waves. Hence it is reasonable to specify

$$\frac{\Delta s_{s\max}}{\Delta s_{s\min}} = \frac{L_{\max}}{L_{\min}} \tag{4.4.7}$$

where $L_{\max}$ and $L_{\min}$ are the maximum and minimum wave lengths, respectively, which can be roughly estimated for problems considered. It should be noted that α subjected to Eq. (4.4.7) becomes zero for waves with single wavelength and so the arc-segment lengths are a constant after the nodes are re-distributed. Such a distribution of nodes is reasonable for these cases. The evaluation of β is not so straightforward. As indicated by Davies & Venkatapathy (1999), this value is determined in such a way that the minimum length of arc-segment elements obtained by Eq. (4.4.3) is approximately equal to the specified Δs_{smin}. To achieve this, iteration must be performed. According to numerical tests, a value of β in the range of 0.5 ~1.0 can lead to a satisfactory distribution of Δs_i when $L_{\max}/L_{\min}<10$.

In order to investigate the above method for redistributing nodes on the waterline, test cases are carried out for both 2D curves and 3D curves. The initial nodes on the curves are assigned a new assumed position and the above method is then used to redistribute the nodes.

In the 2D case, the nodes are distributed evenly on a straight line from x= -4 to x= 4, initially. The curve is then assigned to be satisfied

$$z = -2\sec h(5x) \tag{4.4.8}$$

The above method is therefore used to redistribute the nodes. The new position of every node is shown in Fig. 4.4.1. For the purpose of comparison, those of nodes before being redistributed are also plotted together.

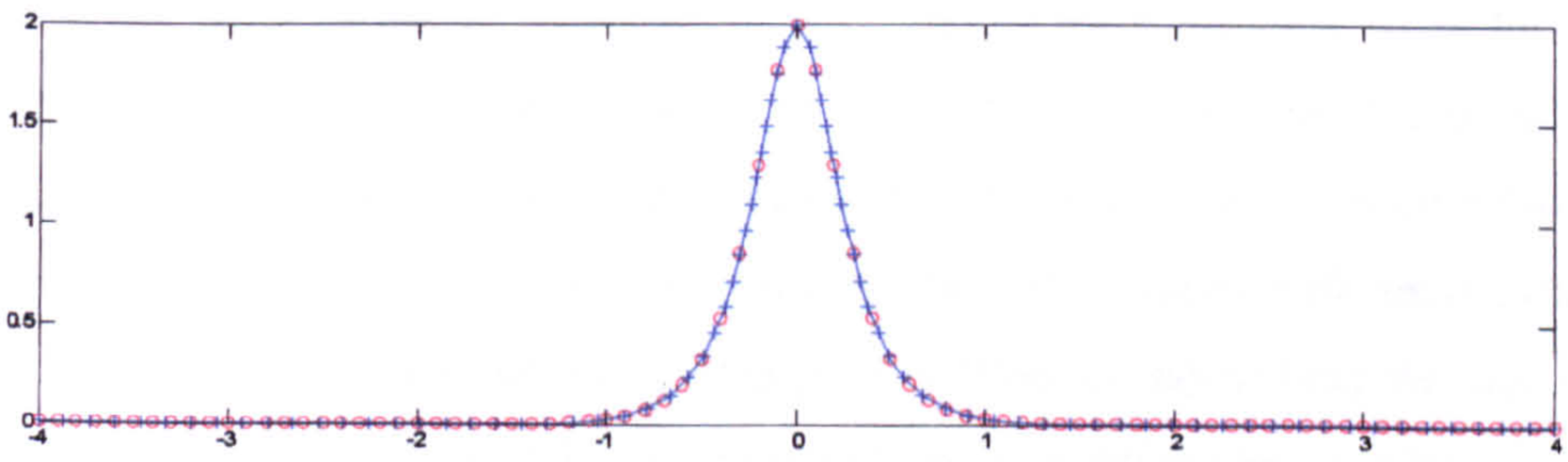

Fig.4.4.1 Initial nodes and those after being redistributed on a 2D curve
('o': before redistributed; '+': after redistributed)

It is observed from this figure that more nodes are moved to the region where the gradient of z is larger, i.e. near the peak (-1<x<1). The curved distance between every two nodes is redistributed to be proportional along the curve. As a result, the x-directional distance between every two nodes is self-adaptive with respect to the gradient of z. This implies that the method

to redistribute the nodes on 2D waterlines leads to better nodal distribution and is therefore effective.

A similar conclusion is achieved in a 3D case. Here, the nodes are distributed equidistantly along a 3D curve as following

$$x^2 + y^2 = 1 \quad \text{and} \quad z = 0 \tag{4.4.9}$$

initially and then are moved along z-direction to

$$z = 2\sin(\pi x) \tag{4.4.10}$$

Finally, the nodes are redistributed by using the above method. The results are shown in Fig.4.4.2. Similar to Fig. 4.4.1, the nodal distribution on the curve before being redistributed is also plotted together for the purpose of comparison.

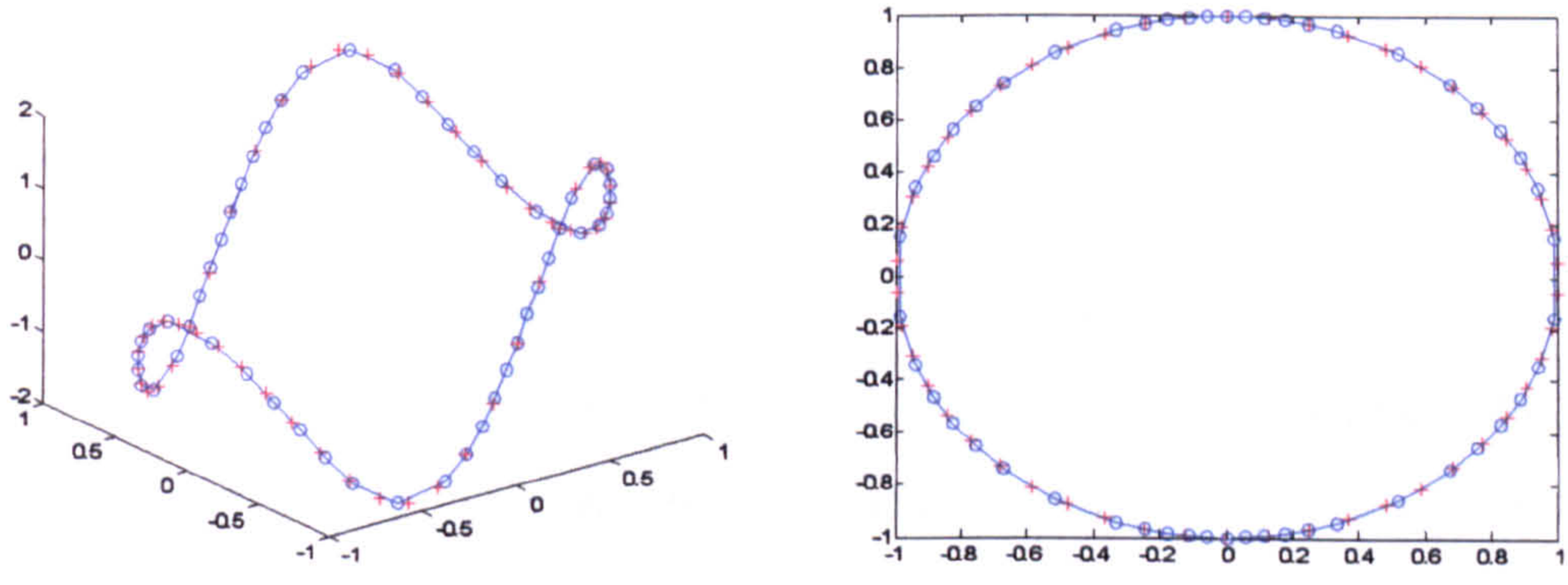

(a) 3D curve (b) projected curve on x-y plane

Fig.4.4.2 Initial nodes and those after being redistributed on a 3D curve

('+': before redistributed; 'o': after redistributed)

Fig.4.4.2 (a) shows the 3D spatial distribution of the nodes on the waterlines, while Fig.4.4.2 (b) is its projected figure on x-y plane. Similar to the 2D case, it is found that, after being redistributed, more nodes are moved to the region where the gradient of z (see the top and bottom regions of Fig. 4.4.2 (b)) and the nodal distribution in the region with small gradient of z become sparse. This demonstrates that the present method to redistribute the nodes on the waterlines can deal with both 2D and 3D problems and leads to satisfactory results.

4.5. Moving nodes on the body surface

The wetted body surface is time-dependent in the problems considered here. In order to conform to the change of the wetted body surface, the nodes on the surface must also be moved at each time step. The principle for doing so is similar to that for moving the nodes on the free surface, i.e., splitting the nodes into two groups: nodes on the waterline and nodes lying on the body surface but not on the waterline, the later called inner-body-surface nodes. They are moved according to the physical condition and must also be moved in order to prevent nodes

becoming too close to or too far from each other. The inner-body-surface nodes may appear to be moved by the same approach for moving inner-free-surface nodes, i.e., projecting the nodes onto a horizontal plane, moving the nodes in it by using the spring analogy method and then finding the new positions of nodes on the body surface by interpolation. However, this is not always possible for floating body surfaces, particularly when they undergo angular motions, such as roll and/or pitch which cause two intersecting points exist on a vertical line. Therefore, one cannot actually use the same approach as for moving the inner-body-surface. A new approach is developed here.

In this new approach, the spring analogy method is applied in a local coordinate system formed by the local tangential and normal lines. In this local coordinate system, the body surface is single–valued. This means there is only one intersecting point between the body surface and a line parallel to the local normal line (and, of course, perpendicular to the local tangential line). Say a node i is first moved along the tangential line by

$$\Delta\vec{r}_{i\tau} = \sum_{j=1}^{N_i} k_{ij}\Delta\vec{r}\cdot\vec{\tau}_i \Big/ \sum_{j=1}^{N_i} k_{ij} \tag{4.5.1}$$

where $\vec{\tau}_i$ is the tangential direction at node i. After that, the new position of the nodes on the body surface is found by interpolation in the local coordinate system. The spring stiffness in Eq. (4.5.1) is taken as $k_{ij} = 1/l_{ij}^2$. This approach is referred as 'Local method' in this thesis.

It should be noted that at a sharp corner, there will be no unique tangential and normal lines and so the above approach fails. To overcome the difficulty, two simple ways are applied in this work. One is to prescribe a node at the corner and the other is to smooth the corner. Either way works well and gives similar results based on the numerical tests.

It should also be pointed out that this method may be used to move the nodes on the free surface. Since this method can deal with the surface which can be expressed as a multi-valued function of (x,y). Therefore, it eliminates the limitation of the 'Global method' to cases involving non-overturning waves. According to the numerical investigation in this work, the CPU time required by the 'Local method' is almost 3 times more than that required by the 'Global method'. The computational efficiency of the 'Local method' is relatively lower than the 'Global method'. This is because additional CPU time is required by the 'Local method' to calculate the normal and tangential directions at each node on the free surface at each sub-step of the spring analogy method. Therefore, the 'Global method' is used to move the inner-free-surface nodes in cases without overturning waves. Once the overturning wave occurs, the 'Local method' is used. A subroutine is written to automatically choose the method.

4.6. Surface fitting and physical quantities updating

As mentioned above, the nodes on the boundaries are restricted on the surface when they are moved. In order to make sure the nodes after being moved are still on the surface, an interpolating method is needed to fit the surface. This method should be highly efficient and accurate enough for the free surface problem. On the other hand, after the mesh is moved, the physical quantities, such as velocity potential and velocity, at the nodes in the new position also should be updated for the next time step. To do so, two interpolating methods are used: the shape function approach and the moving least square method.

4.6.1. Shape function approach

This method based on the shape function was used by by Ma, Wu & Eatock Taylor (2001a,b) and Ma (1998) to estimate the free surface elevations (i.e. coordinate z) and to approximate other physical quantities, such as velocity on the free surface, at every node after being redistributed. To do so, one needs to find which element each new node belongs to by using the coordinate x and y of the new nodes. After that, the value of z is estimated using the shape function defined in this element.

In order to find the element where the new node J is located, the following vector is defined in each element (i,j,k),

$$VJ_1 = \{x_J - x_i, y_J - y_i\}$$
$$VJ_2 = \{x_J - x_j, y_J - y_j\}$$
$$VJ_3 = \{x_J - x_k, y_J - y_k\}$$
$$Vji = \{x_j - x_i, y_j - y_i\}$$
$$Vkj = \{x_k - x_j, y_k - y_j\}$$
$$Vik = \{x_i - x_k, y_i - y_k\}$$

where x,y and z are the coordinates of corresponding nodes denoted by the subscripts. If new node J is inside of the element (i,j,k) , J and every node in this element should be in the same side of its corresponding facing line, e.g. J and node i in the same side of line j-k. This condition leads to the following requirement.

$$\begin{cases} VJ_i \times Vji \geq 0 \\ VJ_j \times Vkj \geq 0 \\ VJ_k \times Vik \geq 0 \end{cases} \tag{4.6.1}$$

Once the element e^k which satisfies Eq. (4.6.1) is found, e^k must contains node J and hence the wave elevation and other physical quantities (f^*) are therefore approximated by

$$f^* = \sum_{i=1}^{3} N_i^{e_k} f_i \tag{4.6.2}$$

in which f represents the physical quantities, e.g. wave elevation and velocity, which need to be approximated , subscript i represents the local node number in e^k . The accuracy of Eq. (4.6.2) clearly depends on the shape function $N_i^{e_k}$. The shape function used in both Ma, Wu & Eatock Taylor (2001a,b) ,Ma (1998) and this thesis is a linear function. Thus, this method is a linear approximation of the free surface. The shape function approach in the present work is only used to treat the case with linear waves.

4.6.2. Moving least squares method

Alternatively, a method based on the moving least squares (MLS) method, in which the positions of the nodes after being moved are determined by using the information at a group of old nodes in such a way that the error is minimised. This method has been frequently used to form the interpolating function in Meshless methods and the details about it may be found in, e.g. Atluri, & Zhu (1998), Ma (2005). Only a brief introduction to MLS is presented here.

Introduction of MLS

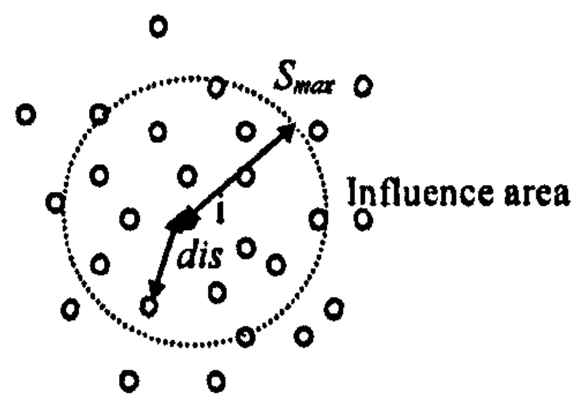

Fig.4.6.1 Sketch of the moving least squares method

Fig.4.6.1 shows a sketch of the MLS method. In this figure, the variable $f(x,y)$ is known at the points marked as hollow circles. These points are called sampling points in this section. The solid point is the point where the variable f should be approximated (called interpolating point in this section). It is assumed the variable $z=f(x,y)$ satisfies the following equation using n sampling points in a sub-domain (influence area in Fig.4.6.1) ,

$$f(x,y)=\sum_{i=1}^{n} a_i(x,y)p_i(x,y)=P^T(x,y)a(x,y) \tag{4.6.3}$$

where $P(x,y)=[p_1(x,y),p_2(x,y),\ldots,p_m(x,y)]^T$ is a basis function with m self-contained multinomial, the rank of MLS is maximum rank of the multinomial in the basis function.

$$P(x,y)=[1,x,y,x^2,xy,y^2,x^3,x^2y,xy^2,y^3,\ldots]^T \tag{4.6.4}$$

Based on the above definition, m=6 for a 2-order MLS models, m=10 for a 3-order MLS models. $a(x,y)=[a_1(x,y),a_2(x,y),\ldots,a_m(x,y)]^T$ is the coefficient matrix. Consider the weighted scattered weak form as follows,

$$J = \sum_{i=1}^{n} w_i [f(x,y)_i - z_i]^2 = \sum_{i=1}^{n} w_i [P^T(x_i, y_i) a(x_i, y_i) - z_i]^2 \tag{4.6.5}$$

where z_i is the value of ith node and z_i=z (x_i,y_i) , w_i is the weight of ith node. a (x,y) can be calculated using the principle of least squares method, i.e.

$$\frac{\partial J}{\partial a} = A(x,y)a(x,y) - B(x,y)Z = 0 \tag{4.6.6}$$

in which

$$A(x,y) = \sum_{i=1}^{n} w_i P(x_i, y_i) P^T(x_i, y_i) \tag{4.6.7}$$

$$B(x,y) = [w_1 P(x_1, y_1), w_2 P(x_2, y_2), \ldots, w_n P(x_n, y_n)]^T \tag{4.6.8}$$

$$Z = [z(x_1, y_1), z(x_2, y_2), \ldots, z(x_n, y_n)] \tag{4.6.9}$$

then , a (x,y) is given

$$a(x,y) = A^{-1}(x,y)B(x,y)Z \tag{4.6.10}$$

Substituting Eq. (4.6.10) into Eq. (4.6.3), the following fitting function is obtained,

$$f(x,y) = P^T(x,y)A^{-1}(x,y)B(x,y)Z \tag{4.6.11}$$

The weight of ith node is based on the distance and can be defined as Atluri, & Zhu (1998)

$$w(s) = \begin{cases} 2/3 - 4s^2 + 4s^3 & s \le 0.5 \\ 4/3 - 4s + 4s^2 - 4/3s^3 & 0.5 < s \le 1 \\ 0 & s > 1 \end{cases} \tag{4.6.12}$$

where $s = dis / s_{\max}$ and dis is the distance between the interpolating point and sampling points around it. $s_{\max}$ is the radius of influence area. The value of $s_{\max}$ should be different in order to solve different problems. In the free surface problem, the calculation of $s_{\max}$ should consider the wave length and/or local slope of the free surface. In this thesis, it is taken as

$$S_{\max} = \delta d_{\max} \tag{4.6.13}$$

in which $d_{\max}$ is the maximum distance between the interpolating point and the sampling points. δ is a coefficient which is taken as 1.2. Once the number of sampling points is given, one can calculate the distance between the interpolating point and all the sampling points. $d_{\max}$ can be found and so $s_{\max}$ can be determined by Eq. (4.6.13). Based on this, the problem about the definition of the influence area is converted to a problem of determining the value of n. Therefore, the value of n and m are the key factors which affect the efficiency of the MLS.

It should be noted that if z is not a single-valued function of (x,y) in the sub-domain (influence area), i.e. there are two or more intersecting points in a vertical line, for example the free surface in a case with an overturning wave, the above method does not work. As discussed

in Section 4.5, in such a sub-domain, the normal coordinate as well as other physical quantities always can be expressed as a single-valued function of tangential coordinates. In order to solve this problem, the above method should be carried out in the local normal tangential coordinate system and x,y coordinates in Eqs. (4.6. 2-12) are therefore replaced by the tangential coordinate.

Numerical investigation

In order to investigate the efficiency of MLS method, numerical tests were carried out using a PC (Pentium Ⅳ 2.53G, 1G RAM). In these numerical investigations, a surface is assumed to satisfy the following functions,

$$z = 0.5\sin(2\pi x/5) + 0.75\sin(2\pi y/0.5) \tag{4.6.14}$$

in the domain Ω:{$0 \le x \le 10, -0.5 \le y \le 0.5$}, the nodes are distributed randomly. The computational error is defined

$$err = \left[\sum_{i=1}^{N}(z_i^{exact} - z_i^{fitted})^2\right]^{1/2} \tag{4.6.15}$$

where $z_i^{exact}, z_i^{fitted}$ are exact value and fitted value, *err* denotes absolute error of whole domain. For every point to be approximated, n nearest nodes are searched as the sampling points for the MLS method. In this test case, n=50 is used. For the purpose of comparison, some other published methods (Burden & Fairs, 2004), i.e, Shepard method, Fourier transform method, m-order least squares method (LSM), are also used. The results are shown in Table. 4.6.1

Table 4.6.1 Comparison between different interpolating methods

Method	Rank	Err	CPU time (s)
Shepard method		1.37	0.14
Fourier transform		0.75	0.48
LSM	2	0.73	0.53
	3	0.73	0.77
MLS	1	2.14	0.14
	2	1.41	0.19
	3	4.04D-2	0.36
	4	7.73D-3	0.76

It can be found that the MLS method is the most accurate of all the models being investigated. It also can be observed in Table. 4.6.1, the accuracy of the MLS and the CPU time increase when the rank (m) and the number of nodes (n) increases, as expected.

In order to optimize m and n, more test cases are carried out. The exact solution of the surface is the same as that used in Table. 4.6.1, n varies from 20 to 80, m=3, m=6 and m=10 are used respectively in this investigation. The results can be found in Fig 4.6.2 and Fig 4.6.3.

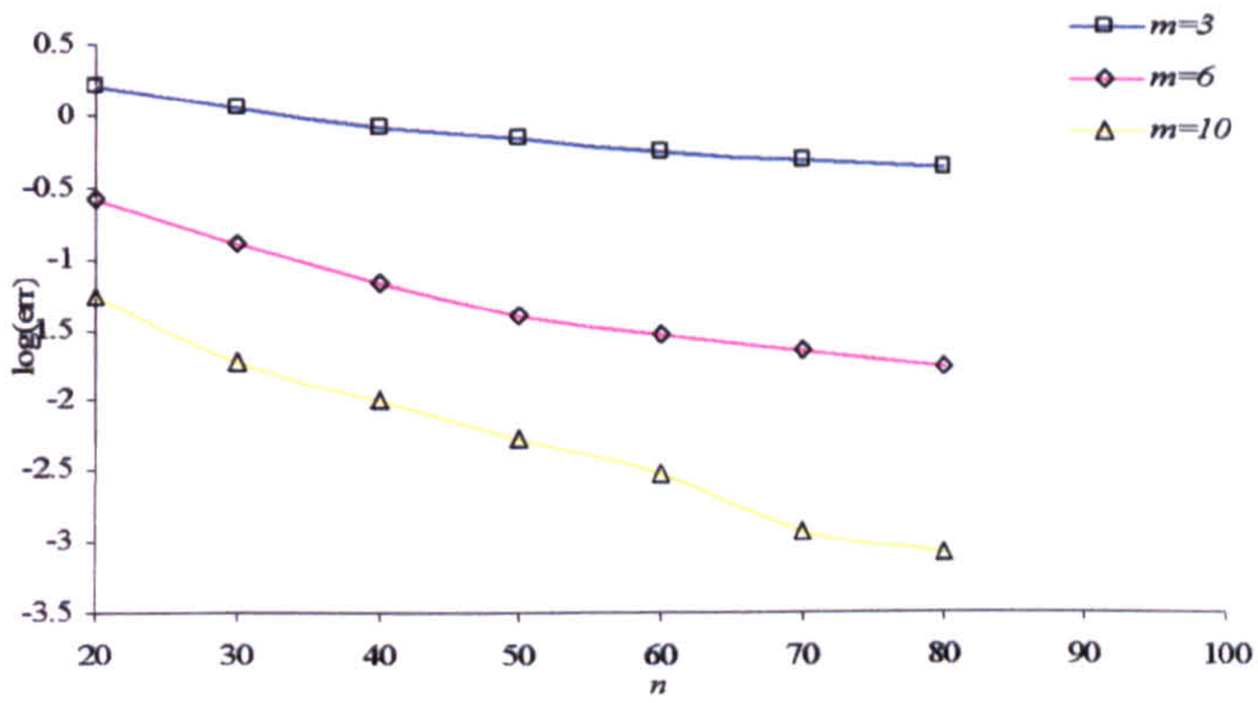

Fig. 4.6.2 Error of MLS for different n and m

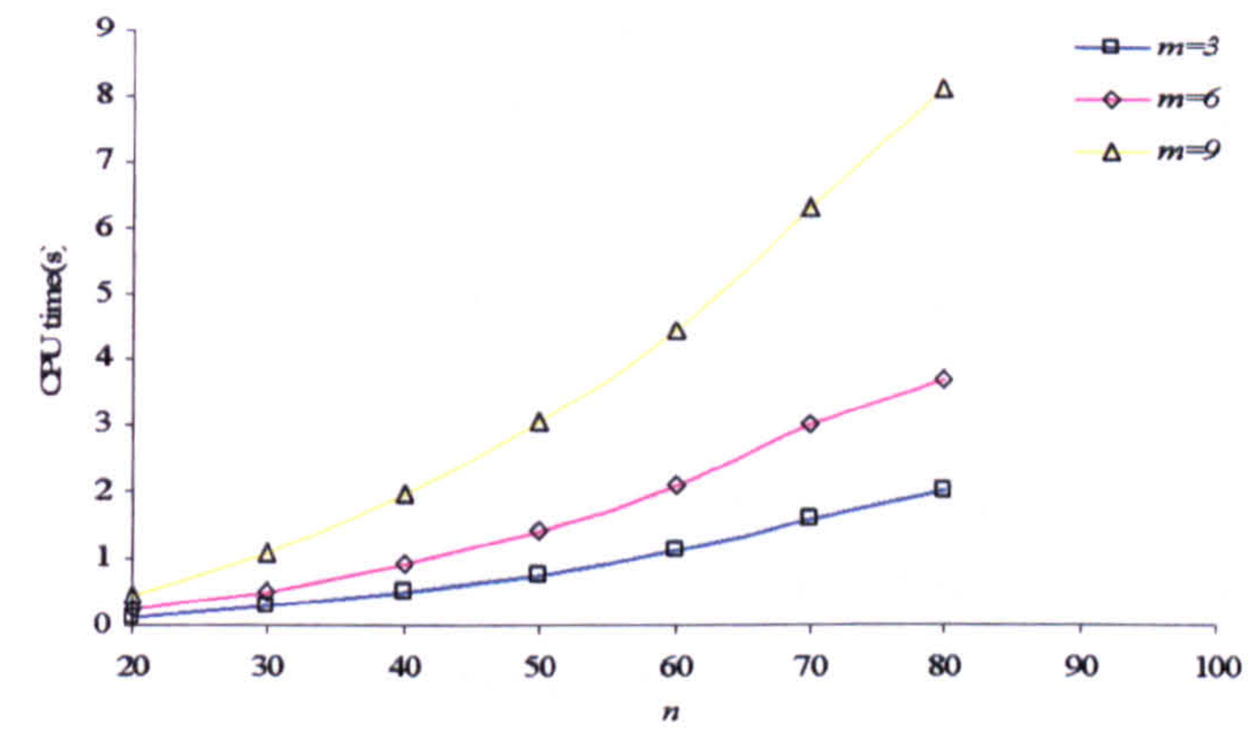

Fig. 4.6.3 CPU time spend on MLS for different n and m

Fig.4.6.2 and Fig.4.6.3 show the error of and the CPU time required by the MLS with different n and m. From Fig. 4.6.1.it is observed that the accuracy increases as the number of nodes (n) as well as the increase of m. It is also found, from Fig. 4.6.3, that the CPU time increases dramatically when m>6. In this thesis, m=6 are chosen. On the other hand, different values of n do not affect the accuracy evidently when n>50.

Choice of n

The definition of the influence area should consider the wave length for water wave problem. Therefore when choosing the value of n, one needs to take the wave length into account. Usually, the nodal density of the computational mesh used for water wave problem should also consider the wave length. In other words, the mesh size (the scalar of the element Δs_e) on the free surface should be the a function of the wave length , i.e. $\Delta s_e = \lambda / \sigma$ in which λ is the

wave length, σ is a coefficient. In the numerical simulation in Chapters 8,9 and 10, the mesh size on the free surface follows the above strategy.

Due to this fact, n in this work may be chosen according to the topological relationship of the mesh which is shown in Fig. 4.6.4.

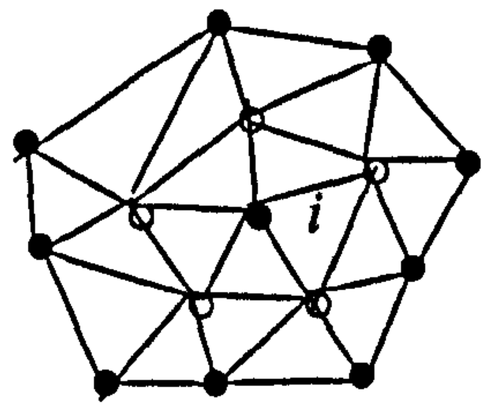

Fig.4.6.4 Node i and the nodes around it
(hollow: first-layer nodes of i; solid: second-layer nodes of i)

Fig.4.6.4 shows a node i and the nodes around it. The nodes connected to node i are marked as first-layer nodes around node i in this thesis (see the hollow circle in Fig.4.6.4). The nodes connected to the first-layer nodes around node i but not belonging to first-layer nodes or itself are marked as second-layer nodes around node i (see the solid circle in Fig. 4.6.4). The rest may be deduced by analogy, i.e. k^{th} –layer nodes are those connected to $(k\text{-}1)^{th}$-layer nodes but not belonging to all the nodes on the lower layer.

Based on this definition, once the nearest node of the interpolating point is found, one may choose k layers nodes to form the influence area and n is therefore the number of those chosen nodes. The main advantages of this approach are

1) There is no need to calculate the distance between the interpolating point and all the nodes on the free surface in order to find the sampling nodes in the influence area for the MLS;
2) It ensures the sampling points are usually distributed surrounding the interpolating point, except on the boundary.

This approach is so used in this thesis and numerical tests indicate k=2 is sufficiently accurate for the cases in this thesis and the procedure to find the nearest node will be discussed in the following section.

4.6.3. Method to find the nearest node

As mentioned above, it is necessary to find the nearest node to the interpolating point in order to form the influence area for the MLS method. The simplest way is calculate the distance between the interpolating point and all the nodes on the free surface. It is time-consuming task if the number of nodes on the free surface is very large. Alternatively, this problem may be converted to finding the element where the interpolating point is located. Once such an element

is found, the nearest node should be one of the three nodes of the element because of the topological relationship of the computational mesh. To find the element, Ma (1998) developed a method given in Eq. (4.6.1). In this method, all elements on the free surface is searched in order to find an element satisfying Eq. (4.6.1). In this aspect, this method is not effective particularly in 3D case where the elements on the free surface are very large. On the other hand, this method is clearly based on the assumption that the surface can be expressed as a single-valued function of (x,y). As discussed above, this assumption may not be true. A method based on an iterative procedure under local normal-tangential coordinate system is developed and presented here.

Consider a node J on the free surface or body surface, the normal and tangential directions $(\vec{\tau}_1, \vec{\tau}_2, n)$ of node J can be found. The tangential displacement of this node in the spring analogy method is determined by Eq. (4.5.1). The projected point (J') of node J on the tangential plane $(\vec{\tau}_1 - \vec{\tau}_2)$ after displacement can therefore be obtained. This procedure is illustrated in Fig. 4.6.5. In this local normal-tangential coordinate system, in order to judge whether the point is located at an element or not, the coordinate values (x,y) in the 6 vectors of Eq. (4.6.1) are replaced by the local tangential coordinates$(\vec{\tau}_1, \vec{\tau}_2)$. An initial searching node is selected as J, i.e. $N_n^0 = J$, the searching procedure to find the nearest node of point J' is expressed as follows

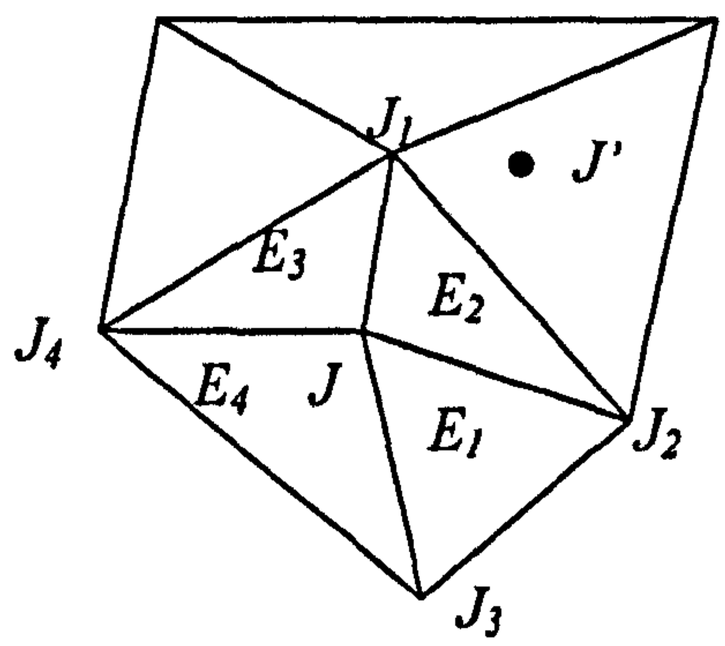

Fig.4.6.5 Sketch of the way to find the nearest node

1) Convert the Cartesian coordinate value (x,y,z) at nodes around N_n^k into normal-tangential coordinate system defined by $(\vec{\tau}_1, \vec{\tau}_2, n)$;

2) Search the elements sharing N_n^k (see, for example, E_1, E_2, E_3, and E_4 for node J in the Fig. 4.6.5). Eq. (4.6.1) is used to judge whether J' is located at one of the elements. If yes, record the element number E_n^u and go to step 4) otherwise go to step 3)

3) From the nodes connecting to N_n^k (for example, J_1, J_2 ,J_3 and J_4 for node J in Fig.4.6.5) , find a nearest node N_n^{k+1}, go to step 1)

4) Find the nearest node from those of element E_n^u and mark it as N_n^u.

Once N_n^u and E_n^u are obtained, it is easy to apply MLS or the shape function to fit the surface. This method is carried out in a local domain, i.e. only the elements around the node *J*. The normal coordinate value is always expressed as a single-valued function of two tangential coordinates. In addition, in the spring analogy method, the displacement of each node is very small, i.e. smaller than the distance between two successive nodes. Node N_n^0 is close to the node N_n^u or may be the node N_n^u. One may need only 1 to 2 iterative steps to find the solution N_n^u, E_n^u. The efficiency of this procedure is much higher than the one used by Ma (1998).

4.6.4. Special treatment for nodes on the boundary

Numerical investigation also found that the difference between the exact solution and the value approximated by using MLS method is larger for the interpolating point near the boundary. That is because the distribution of the sampling points is unsymmetrical according to the interpolating point (see, Fig. 4.6.6 as an example).

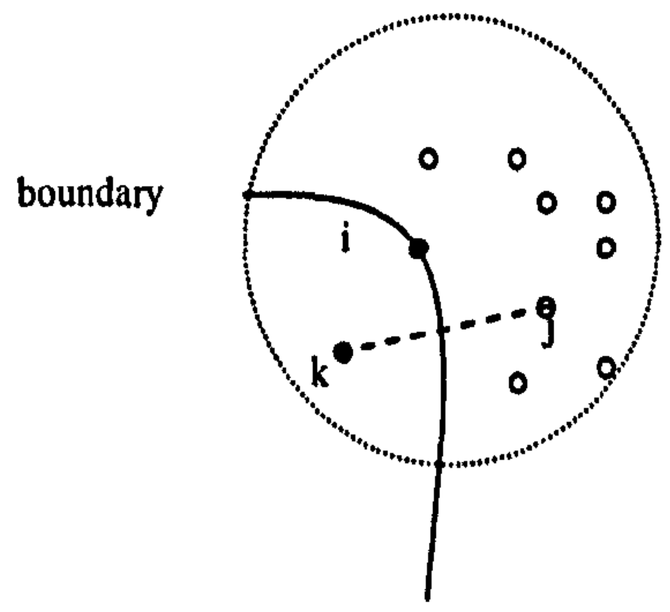

Fig.4.6.6 A point near the boundary and the nodes around it
(solid: the interpolating point *i*; hollow: the sampling points around point *i*
Dotted circularity: the influence area.)

Usually, the boundary of the free surface, i.e. the waterlines between the free surface and the floating bodies, the wave maker and the far end wall, are paid more interest in the wave-structure interaction problem. In order to achieve higher accuracy for the MLS when being applied to treat the boundaries, two approaches are used in this thesis.

The first one is so called symmetrical-point method which is widely in Meshless Computational Fluid Dynamics (SPH), e.g. Monagghar (1994), Debroux, Prakash & Cleary (2001). Fig. 4.6.4 shows the sketch. The solid point is the interpolating point *i* which will be approximated, the hollow points are the nodes around it, the dotted circularity is its influence area. For every node *j*, we can find its symmetrical point with respect to boundary (marked as *k* in Fig. 4.6.4). If the boundary condition is taken as

$$\frac{\partial f}{\partial n} = c \tag{4.6.16}$$

where *f* is the physical quantity to be approximated, *n* is the normal direction of the boundary. This physical quantity at artificial node *k* (f_k) can be found based on a central FD scheme, i.e.

$$f_k - f_j = c\Delta r_{jk} \tag{4.6.17}$$

in which Δr_{jk} is the distance between node *j* and node *k*. For example, on the vertical wall (*y*=const) wall of the numerical tank, *c*=0 and therefore $f_k = f_j$.

However, a difficulty associated with this method is that the symmetrical points are difficult to find when the shape of the boundary is complicated, such as curved 3D surface. In this thesis, the method is only adopted for the nodes near the plane boundary, i.e. *y*=const wall, the wave maker and the far end wall of the numerical tank. In those cases, the artificial symmetrical points are shown as Fig. 4.6.7.

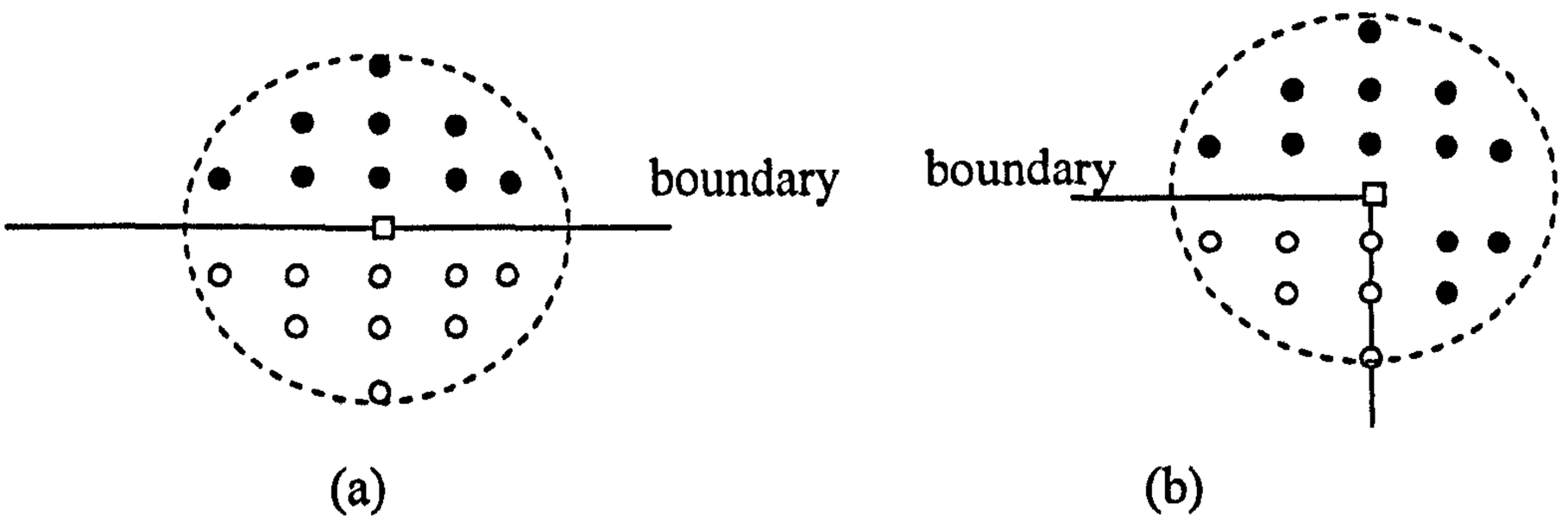

Fig.4.6.7 nodes and their symmetrical nodes

(solid circle: the artificial symmetrical nodes; hollow circle: the nodes in the influence area; Square: the point need to be approximated; Dotted circularity: the influence area.)

The second approach is to fit the boundaries using the nodes on the boundaries. To do so, a curvilinear coordinate ξ is used. Suppose the nodes on the curve are arranged in the same direction along the curve. ξ is defined as the curvilinear distance along the curve which is shown in Fig. 4.6.8.

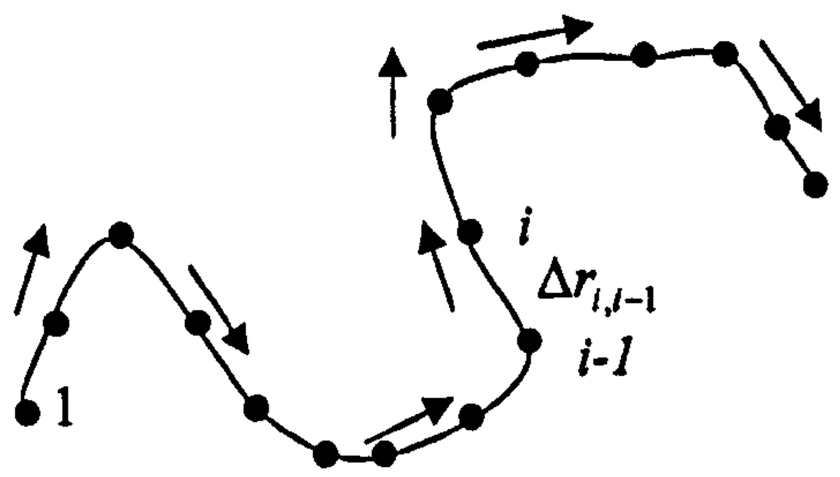

Fig.4.6.8 Sketch of nodes on a curve
(solid circle: nodes; arrow: the direction of the curve)

For ξ at n^{th} node can be obtained by

$$\xi_n = \sum_{i=1}^{n-1} \Delta r_{i,i+1} \tag{4.6.18}$$

in which $\Delta r_{i,i+1}$ is the arc-segment length between i^{th} node and $(i+1)^{\text{th}}$ node. For every node on the curve, an exclusive ξ is calculated by using Eq. (4.6.18) and the value of ξ increases along the curve. The x-,y- and z-coordinates of the curve therefore may be expressed as a single-valued function of ξ, i.e.

$$x = x(\xi), y = y(\xi), z = z(\xi) \tag{4.6.19}$$

by using the discrete nodes on the curve. If we know the value of ξ at the interpolating point, the x-,y- and z-coordinates can be approximated by using an appropriate interpolating method, e.g., the linear interpolating method or the MLS method. For example, for a interpolating point where ξ equals to ξ_{int}, it is necessary to find a node i on the curve that satisfies

$$(\xi_{i+1} - \xi_{\text{int}}) > 0 \text{ and } (\xi_{\text{int}} - \xi_i) > 0 \tag{4.6.20}$$

If a linear interpolating method is used, the x-,y- and z-coordinates can be approximated as

$$x = [x_i(\xi_{i+1} - \xi_{\text{int}}) + x_{i+1}(\xi_{\text{int}} - \xi_i)]/(\xi_{i+1} - \xi_i) \tag{4.6.21}$$

$$y = [y_i(\xi_{i+1} - \xi_{\text{int}}) + y_{i+1}(\xi_{\text{int}} - \xi_i)]/(\xi_{i+1} - \xi_i) \tag{4.6.22}$$

$$z = [z_i(\xi_{i+1} - \xi_{\text{int}}) + z_{i+1}(\xi_{\text{int}} - \xi_i)]/(\xi_{i+1} - \xi_i) \tag{4.6.23}$$

This method is only used in cases with linear waves. For the cases with steep waves, the MLS method, which is similar to Eqs. (4.6.3)- (4.6.12), is employed herein.

In the same way, we may use this method to approximate other physical quantities. The distinct advantage of this method is that the physical quantities including x-,y- and z-coordinate can always expressed as a single-valued function of ξ. However, the curve does not fit unless the value of ξ of the interpolating point is known, otherwise, this method fails. In this work, it

is only used to fit the water lines when the nodes on it are redistributed by using the method described in Section 4.4.

5. VELOCITY CALCULATION SCHEME

It is crucial in simulating water waves to evaluate the fluid velocities on the free surface because they are required to update the information on the surface every time step. The velocity at a node may be estimated by using a FD technique from the velocity potentials at this node and nodes connected to it. Ma, Wu & Eatock Taylor (2001a) suggested that the horizontal components of the velocities at nodes on the free surface are evaluated separately from their vertical components. For estimating the vertical component, they developed a three-point formula that needs the velocity potentials at the node considered and at two other nodes on the same vertical line as this node, which are next but just below the free surface. After the vertical component is found, the horizontal components are computed by averaging those given by the difference of the velocity potentials at all neighbour nodes on the free surface. This approach is very efficient and accurate. However, it is limited to structured meshes with vertical grid lines. In this section, the above approach will be extended to unstructured meshes generally without vertical grid lines.

5.1. Velocity calculation formula for nodes on the free surface

As indicated in Section 2.3, the approach (traditional 3-point method) developed by Ma, Wu & Eatock Taylor (2001a) is only applicable to meshes with special structure, i.e. there must be two nodes on the vertical line starting from the node on the free surface. This condition is different to be satisfied in case with moving unstructured mesh unless a mesh with special structure is employed. In order to remove this limitation, a new approach is developed. The basic idea of this approach is similar to that used by Ma,Wu & Eatock Taylor (2001a). The main differences are that

(1) the vertical line is replaced by a normal line perpendicular to the free surface at the node considered;

(2) the two nodes on the vertical line are replaced by two points on the normal line, which do not necessarily coincide with any nodes;

(3) the normal component of the velocity is found before computing the components in tangential directions.

Consider Node I on the free surface of an unstructured mesh with nodes J_k (k=1, 2, 3, ... , m) as its neighbours on the free surface. A normal line is drawn from Node I to the inner domain and two points P_{I1} and P_{I2} are chosen on this line, as shown in Fig. 5.5.1. The distance between I and P_{I1} is h_{I1} and the distance between P_{I1} and P_{I2} is h_{I2}. The normal component ($\vec{v}_n$) of the velocity at Node I is calculated by

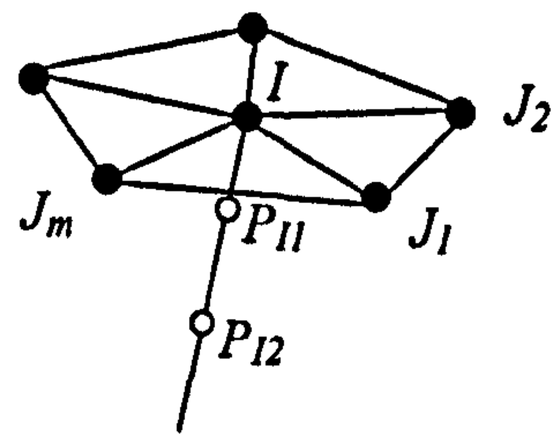

Fig. 5.1.1 Sketch of nodes around Node *I*

$$\vec{v}_n = \left[\frac{2}{3h_{I1}} \left(\frac{2h_{I1} + h_{I2}}{h_{I1} + h_{I2}} + \frac{1}{2} \right) \phi_I - \left(\frac{2}{3h_{I2}} + \frac{1}{h_{I1}} \right) \phi_{P_{I1}} + \frac{2}{3h_{I2}} \left(\frac{h_{I1}}{h_{I1} + h_{I2}} \right) \phi_{P_{I2}} \right] \vec{n} \,. \tag{5.1.1}$$

where $\vec{n}$ is the unit normal vector of the free surface at Node *I*. This equation is similar to Eq. (2.4.1), which is obtained by the combination of a two-point (weighted by 1/3) and a three-point (weighted by 2/3) differential formula. Nevertheless, $\phi_{P_{I1}}$ and $\phi_{P_{I2}}$ here are not nodal values and may be found using the method discussed in subsection 5.2 below. The normal vector is taken as the average of the normal vectors of all surface elements (such as I-J_1-J_2) with Node *I* as one of their nodes, i.e.,

$$\vec{n} = \sum_{i=1}^{M} \vec{n}_i s_i \Big/ \sum_{i=1}^{M} s_i \tag{5.1.2a}$$

where M is the number of surface elements with Node *I* as one of their nodes, s_i and $\vec{n}_i$ are the area and the normal vector of every element, and

$$\vec{n}_i = (\vec{x}_I - \vec{x}_{J_1}) \times (\vec{x}_I - \vec{x}_{J_2}) / | (\vec{x}_I - \vec{x}_{J_1}) \times (\vec{x}_I - \vec{x}_{J_2}) | \tag{5.1.2b}$$

in which $\vec{x} = \{x, y, z\}$ is the vector type of coordinate, the subscripts I, J_1 and J_2 denote the nodes of the element.

In order to estimate the velocity in the tangential directions, the unit tangential vector ($\vec{\tau}$) is required. The vector may be determined using

$$\vec{\tau}_x \perp \vec{n}, \ \vec{\tau}_x // \vec{e}_x, \ \vec{\tau}_y \perp \vec{n} \ \text{and} \ \vec{\tau}_y // \vec{e}_y$$

The tangential components of the velocity are related to the difference of the velocity potential between any pair of nodes containing Node *I* and one of Nodes $J_1, J_2, \ldots\ldots, J_m$ by

$$\vec{v}_{\tau_x} \cdot \vec{l}_{IJ_k} + \vec{v}_{\tau_y} \cdot \vec{l}_{IJ_k} = \vec{l}_{IJ_k} \cdot \nabla\phi - \vec{v}_n \cdot \vec{l}_{IJ_k} \ (k=1, 2, 3, \ldots\ldots, m) \tag{5.1.3}$$

where $\vec{l}_{IJ_k}$ is the unit vector from Node *I* to Node J_k; $\vec{v}_{\tau_x}$ and $\vec{v}_{\tau_y}$ represent the velocity components in $\vec{\tau}_x$ and $\vec{\tau}_y$ directions, respectively. The derivation of this equation is similar to Eq. (2.3.3) but replacing *x*-, *y*- and *z*-directional vectors with the normal and tangential vectors. Obviously, the number of equations in Eq. (5.1.3) equals the number of free-surface nodes connected to Node *I* (*m*).

Generally, for every node on the free surface, at least 2 free-surface nodes are connected to it. Therefore, the number of equations in Eq. (5.1.3) is usually larger than 2, the number of unknowns ($\vec{v}_{\tau_x}$ and $\vec{v}_{\tau_y}$). In order to use all the equations and enhance the accuracy, the least squares method is adopted to solve Eq. (5.1.3) and so find $\vec{v}_{\tau_x}$ and $\vec{v}_{\tau_y}$ .Once the three components are obtained, the velocity components in *x*-, *y*- and *z*-directions can readily be computed by projecting them on these directions.

In this method, two points are chosen for the purpose of calculating the normal velocity components. This implies Eq. (5.1.1) may be applied to any cases with moving unstructured mesh without the limitation of the mesh structure. However, P_{I1} and P_{I2} are not the nodal points and so the velocity potentials at those points cannot be given directly by the FEM method. Therefore an interpolating method is required to approximate the velocity potentials at those two points. This method will be discussed in the following section. Furthermore, these two points may be difficult to find for nodes in some special region of the free surface, i.e. those near the body surface and sharp crest, different methods are developed to specially handle those nodes. These special treatments will be presented in Section 5.3 and 5.4.

5.2. Velocity potential at points P_{I1} and P_{I2}

There are two issues associated with the velocity potential at Points P_{I1} and P_{I2}, involved in the above velocity computations. One is how to choose the positions of the points and the other is how to estimate the values of the potential at these points. According to the numerical experience, Point P_{I1} should be located in the element connected to Node *I* and Point P_{I2} should be in another element next to the previous element in the normal direction. This is rational from simple reasoning. If the two points are too close to Node *I* so that they fall into one element, the values of potential calculated at these points are based mainly on the information of one element and so the estimated difference by using these values may possess low accuracy .i.e. one order lower than the shape function defined for solving velocity potential. In this thesis, a linear shape function is used. The accuracy may not be high enough. On the other hand, if the points are too far from each other or from Node *I*, the error of velocity estimated using Eq. (5.1.1) may also be big because the error increases with distances between them. That is because the accuracy of the FD scheme is in the order of $(\Delta h)^2$. So, h_{I1} and h_{I2} in Eq. (5.1.1) can be determined by:

$$h_{I1} = h_{I2} = \varepsilon \hbar \,, \tag{5.2.1}$$

where ε is the coefficient and $\hbar$ is the distance from Node *I* to the intersecting point of the normal line I-P_{I1}-P_{I2} with the element surface formed by other three interior nodes of the element connected to Node *I*. In order to ensure the two points are in the desired elements, ε is most likely to be a value in the range of 0.6 ~ 0.9. Numeical tests show that the value of $\hbar$ does not necessarily have to be calculated every time step. In fact, it is calculated only at the first

time step for cases presented in the following chapters. The detail and results of those numerical tests will be discussed in Chapter 7.

With the values of h_{I1} and h_{I2} determined, the values of the velocity potential at Points P_{I1} and P_{I2} can be estimated by some interpolating methods. To do so, a straightforward method is to use the shape function, i.e. using Eq. (3.5.3) to approximate the velocity potential once the element where Points P_{I1} or P_{I2} located. Alternatively, one may also use the MLS method. In this method, an influence domain is defined for each point (P_{I1} or P_{I2}) and the nodes in the influence domain are found. By using these nodes and the velocity potentials on them, one can estimate the velocity potential by using a similar formulation shown in Section 4.6.2. As discussed in Section 4.6., the former method needs less computational time but gives less accurate values, particularly in cases with large gradients. The latter requires more computational time but results in more accurate potential values. If the waves to be simulated are very steep, the latter should be used; otherwise the former would be the better choice. Because the steep waves are studied here, the latter one is used.

Similar to the MLS described in Section 4.6, for each point J (P_{I1} or P_{I2}) , n_{inf} layers of nodes around its nearest node are found to form the influence domain. Therefore, one must find the nearest node for point J. The procedure to find the nearest node in this section is similar to the one used to find the node on boundary mesh in Section 4.6.3, i.e,

1) start from the initial searching node N_n^0 (Node I);

2) For every element sharing N_n^k, judge whether the point is located in this element. If there is one, record it as E_n^u and go to 4; otherwise go to 3;

3) Find the nearest one from the nodes connected to N_n^k and mark it as N_n^{k+1}. Go to 2);

4) Find the nearest one from the nodes in E_n^u and record it as N_n^u.

In this procedure, an important step is to judge whether the point J is inside of the element or not. For this purpose, the main idea of the approach, which is used to treat 2D problem presented in Section 4.6.1, is extended to treat the 3D problem with tetrahedron elements. Fig. 5.2.1 shows a tetrahedron element in the fluid domain

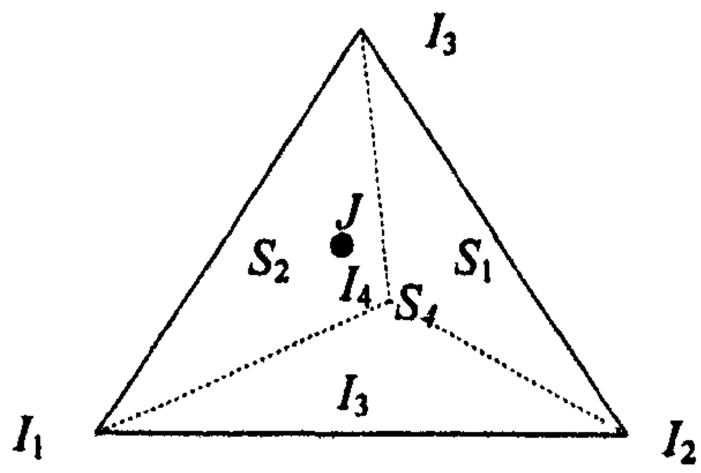

Fig.5.2.1 Nodes and facing surfaces in a tetrahedron element (black point: Point J)

In this figure, I_1, I_2, I_3 and I_4 are its vertexes and S_1, S_2 S_3 and S_4 are the face surfaces of nodes I_1, I_2, I_3 and I_4, respectively. Once the Point J is located in this element, Point J and I_k (k=1,2,3,4) should be on the same side of surface S_k. Therefore, the following equations should be satisfied,

$$\left\{\left[(\vec{x}_{I_2}-\vec{x}_{I_3})\times(\vec{x}_{I_4}-\vec{x}_{I_2})\right]\cdot(\vec{x}_J-\vec{x}_{I_2})\right\}\left\{\left[(\vec{x}_{I_2}-\vec{x}_{I_3})\times(\vec{x}_{I_4}-\vec{x}_{I_2})\right]\cdot(\vec{x}_{I_1}-\vec{x}_{I_2})\right\}\geq 0 \tag{5.2.2a}$$

$$\left\{\left[(\vec{x}_{I_1}-\vec{x}_{I_4})\times(\vec{x}_{I_3}-\vec{x}_{I_1})\right]\cdot(\vec{x}_J-\vec{x}_{I_1})\right\}\left\{\left[(\vec{x}_{I_1}-\vec{x}_{I_4})\times(\vec{x}_{I_3}-\vec{x}_{I_1})\right]\cdot(\vec{x}_{I_2}-\vec{x}_{I_1})\right\}\geq 0 \tag{5.2.2b}$$

$$\left\{\left[(\vec{x}_{I_4}-\vec{x}_{I_1})\times(\vec{x}_{I_2}-\vec{x}_{I_4})\right]\cdot(\vec{x}_J-\vec{x}_{I_4})\right\}\left\{\left[(\vec{x}_{I_4}-\vec{x}_{I_1})\times(\vec{x}_{I_2}-\vec{x}_{I_4})\right]\cdot(\vec{x}_{I_3}-\vec{x}_{I_4})\right\}\geq 0 \tag{5.2.2c}$$

$$\left\{\left[(\vec{x}_{I_2}-\vec{x}_{I_1})\times(\vec{x}_{I_3}-\vec{x}_{I_2})\right]\cdot(\vec{x}_J-\vec{x}_{I_2})\right\}\left\{\left[(\vec{x}_{I_2}-\vec{x}_{I_1})\times(\vec{x}_{I_3}-\vec{x}_{I_2})\right]\cdot(\vec{x}_{I_4}-\vec{x}_{I_2})\right\}\geq 0 \tag{5.2.2d}$$

Since the numbered order of nodes on every element of the mesh is the same, i.e., clockwise or anti-clockwise, the second term ($\left\{\left[(\vec{x}_{I_2}-\vec{x}_{I_3})\times(\vec{x}_{I_4}-\vec{x}_{I_2})\right]\cdot(\vec{x}_{I_1}-\vec{x}_{I_2})\right\}$) of Eq. (5.2.2a) has the same sign for all elements. For example, in this work, it is always negative. Therefore, Eq. (5.2.2a) can be rewritten as

$$\left\{\left[(\vec{x}_{I_2}-\vec{x}_{I_3})\times(\vec{x}_{I_4}-\vec{x}_{I_2})\right]\cdot(\vec{x}_J-\vec{x}_{I_2})\right\}\leq 0 \tag{5.2.3a}$$

Similarly the rest of Eq. (5.2.2) can be written as

$$\left\{\left[(\vec{x}_{I_1}-\vec{x}_{I_4})\times(\vec{x}_{I_3}-\vec{x}_{I_1})\right]\cdot(\vec{x}_J-\vec{x}_{I_1})\right\}\leq 0 \tag{5.2.3b}$$

$$\left\{\left[(\vec{x}_{I_4}-\vec{x}_{I_1})\times(\vec{x}_{I_2}-\vec{x}_{I_4})\right]\cdot(\vec{x}_J-\vec{x}_{I_4})\right\}\leq 0 \tag{5.2.3c}$$

$$\left\{\left[(\vec{x}_{I_2}-\vec{x}_{I_1})\times(\vec{x}_{I_3}-\vec{x}_{I_2})\right]\cdot(\vec{x}_J-\vec{x}_{I_2})\right\}\leq 0 \tag{5.2.3d}$$

Once the nearest node of Point J is found, the fluid domain can be determined by using n_{inf} layers of nodes around it. The MLS method therefore can approximate the velocity potential in the influence domain by using

$$\phi(x,y,z)=P^T(x,y,z)A^{-1}(x,y,z)B(x,y,z)F \tag{5.2.4}$$

where F is the matrix formed by the velocity potential at every node in the influence domain. This formulation is similar to Eq. (4.6.10) but has been extended to 3D cases. The matrices A and B are obtained by solving $m\times m$ linear equations formed by the least squares method. This is the most time-consuming task in the MLS procedure. In order to calculate the velocity at each node on the free surface, matrices A and B should be calculated twice, one for point P_{I1}, the other one for point P_{I2}. This approach is called 'Method 1'. A possible way to improve the computational efficiency for velocity calculation is to find the velocity potential at point P_{I2} by

using the same matrices A and B in Eq. (5.2.4) for point P_{I1}. This is based on the following two facts,

1) The distance between the two points is small even when ε=0.9 because the nodes are tightly distributed near the free surface;
2) $\phi_{P_{I2}}$ plays less important role in Eq. (5.1.1) than $\phi_{P_{I1}}$. Even so, there is a relatively large error in $\phi_{P_{I2}}$, the error for the normal velocity component is still small.

This approach to approximate $\phi_{P_{I2}}$ using the same interpolating formulation as that of $\phi_{P_{I1}}$ is called 'Method 2'. In this approach, one needs to calculate matrices A and B only once. As a result, the computational cost is reduced. The comparison between these two methods will be investigated in the following section.

5.3. Numerical Validation

In order to validate the velocity calculation scheme, a case with a y-directionally averaged solitary wave in a tank is investigated. The wave elevation velocity and the velocity potential on the free surface are given by Tanaka's method (Tanaka,1986), which has been widely used by many researchers, such as Grilli & Svendsen (1990), Grilli, Subramanya(1994), Grilli & Skourup(1998), Grilli, Guyenne & Dias (2000,2001), Fochesato & Dias (2006). The FEM formulation described as Eqs. (3.5.3)- (3.5.8) is used to solved this boundary value problem and gives the velocity potential at every node on the fluid domain. Then, the above velocity calculation scheme is used to solve the velocity at the free surface. The results are compared with the results by Tanaka (1986). The relative error E_r is defined as

$$E_r = \frac{\|u_{cal} - u_a\|}{\|u_a\|} \tag{5.2.4}$$

where u_{cal} and u_a are the present numerical results and the results by Tanaka (1986), respectively. $\|f\| = \int_{A_e} f^2 dA$ in which f represent u_{cal} - u_a or u_a in Eq. (5.2.4), A_e is the area over which the error is estimated.

A case with wave amplitude of A=0.6d is run in a tank with length of 18d and width of 2d. The mesh is unstructured as shown in Fig. 4.2.2. The mesh size is taken as $\Delta x = 0.05d$ and $\Delta y = 0.075d$ on the free surface. The initial wave crest in x-direction (x_0) is located at $5.7d$ from the left side (the position of the wavemaker in Fig. 3.0.1). The main aim of this test is to validate the present velocity calculation scheme, only the results at $t = 0$ are not affected by the error existing in the time integrating scheme, meshing moving procedure and other numerical technique. The results of velocity at $t = 0$ are shown in Fig. 5.3.1. The accuracy of the long-period calculation in this case will be discussed in the end of this section.

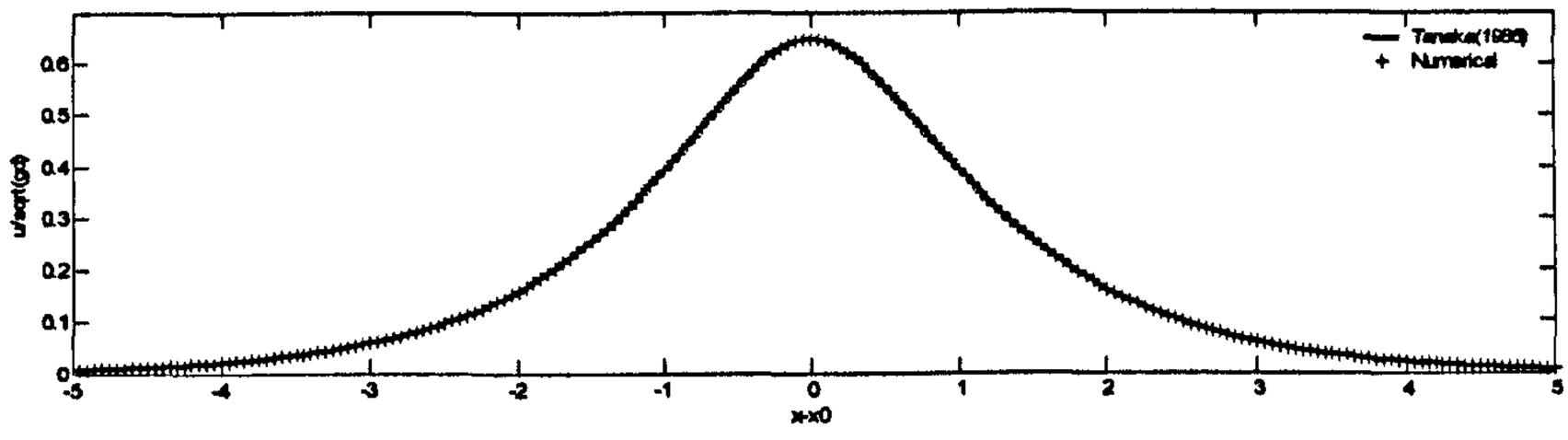

Fig.5.3.1 (a) Horizontal velocity component (y=0)

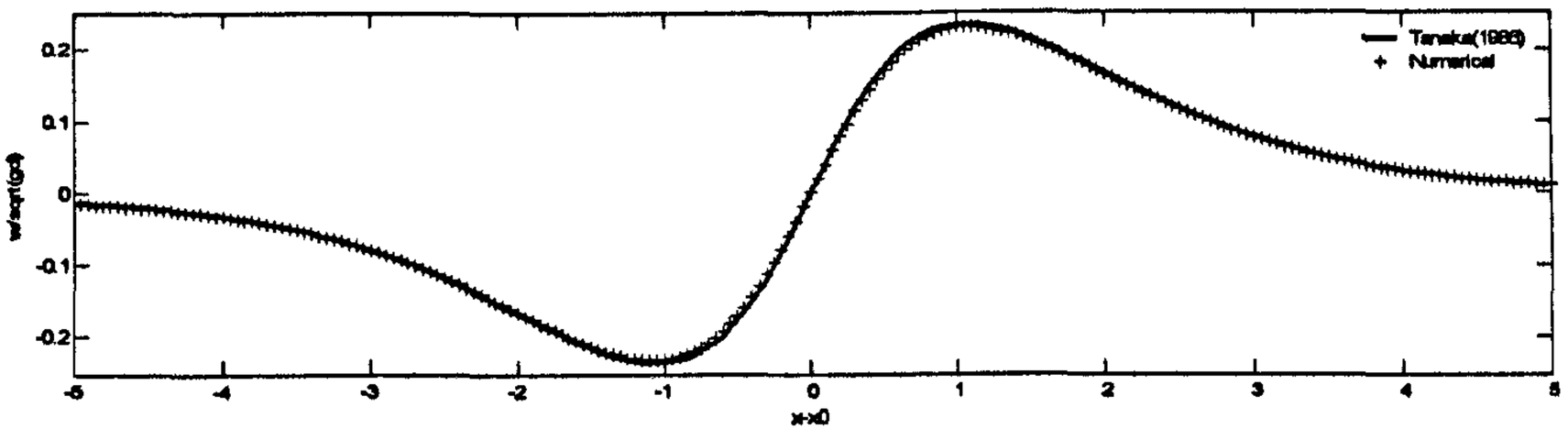

Fig.5.3.1 (b) Vertical velocity component (y=0)

Fig.5.3.1 Comparison of velocity components between numerical results and Tanaka's results (A=0.6d, $t = 0$,n_{inf}=2, ε =0.9 velocity is nondimensionlised by $\sqrt{gd}$, x coordinate is nondimensionlised by d , 'Method 1' for velocity calculation)

Fig.5.3.1 gives the velocity components at the centre of the tank obtained by using the method described above. For the purpose of comparison, the results from Tanaka (1986) are also plotted as well. In this calculation, the recovery technique, which will be presented in Section 5.7, is applied. From this figure, it is found that both the horizontal velocity component and the vertical velocity component obtained by the above numerical method agree well with those calculated by Tanaka's model. The relative error for the horizontal velocity component is less than 0.5% and that for vertical component is less than 1%. These results indicate that the velocity calculation scheme here is accurate enough. Further validation will be given in Chapter 7 , where the numerical waves generated by a wave maker are compared with analytical solution, experimental data and the results from other numerical methods.

In the above case, n_{inf}=2. Different values of n_{inf} are also investigated for this reason. The results are plotted as Fig.5.3.2 It can be found from this figure that no evident difference exists between the results by using different n_{inf} . For the purpose of achieving high computational efficiency, n_{inf}=2 is used in this thesis.

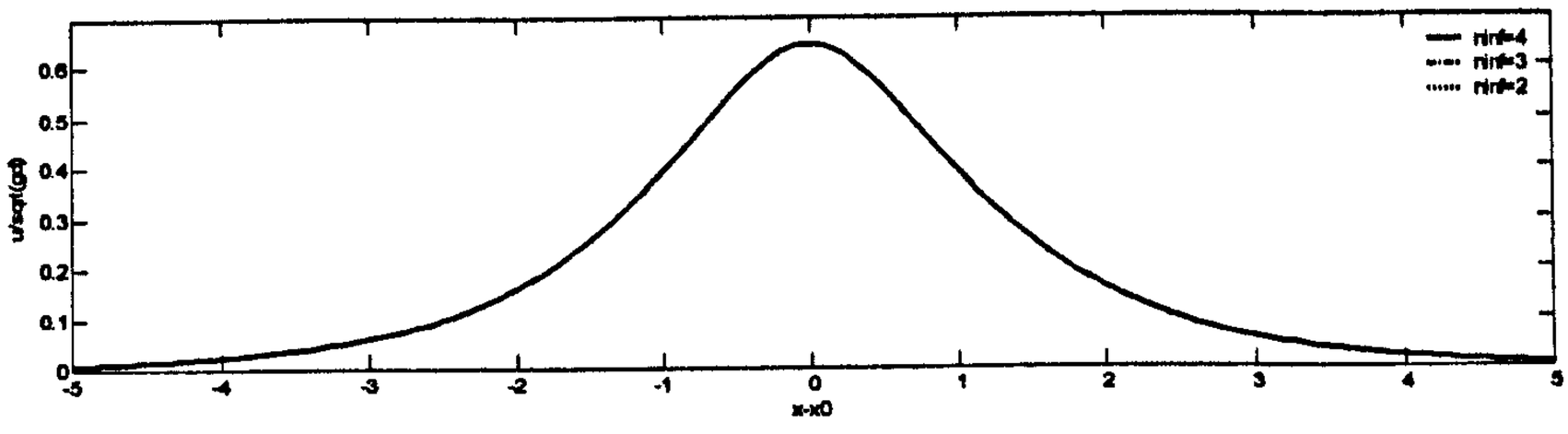

Fig.5.3.2 (a) Horizontal velocity component (y=0)

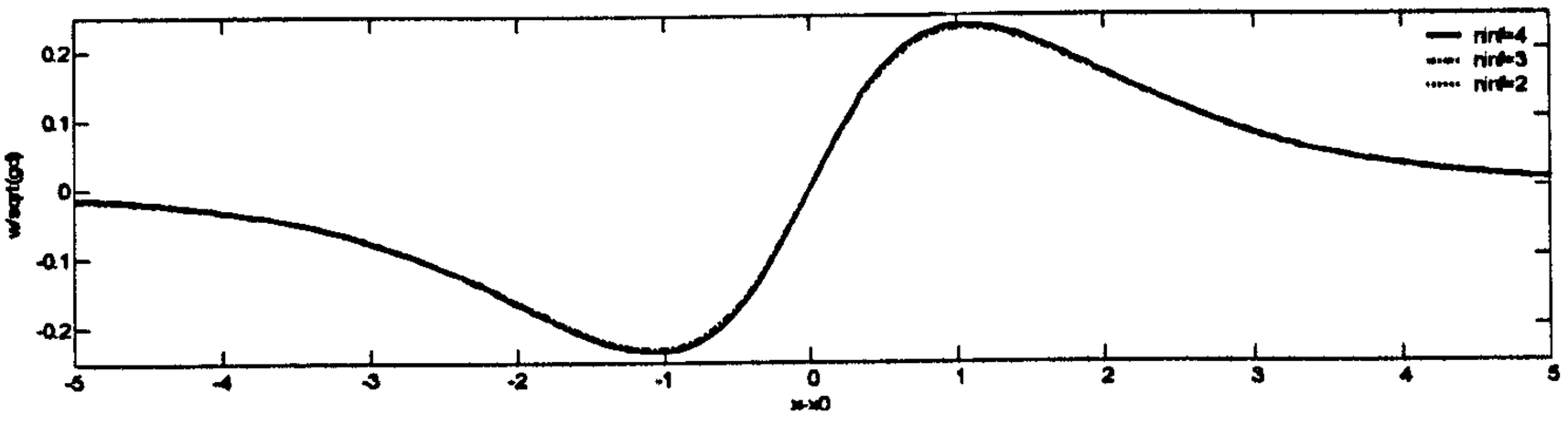

Fig.5.3.2 (b)Vertical velocity component (y=0)

Fig.5.3.2 Comparison of velocity components using different n_{inf} (A=0.6d, $t = 0$,n_{inf}=2, ε =0.9 velocity is nondimensionlised by $\sqrt{gd}$, x coordinate is nondimensionlised by d ; 'Method 1' for velocity calculation)

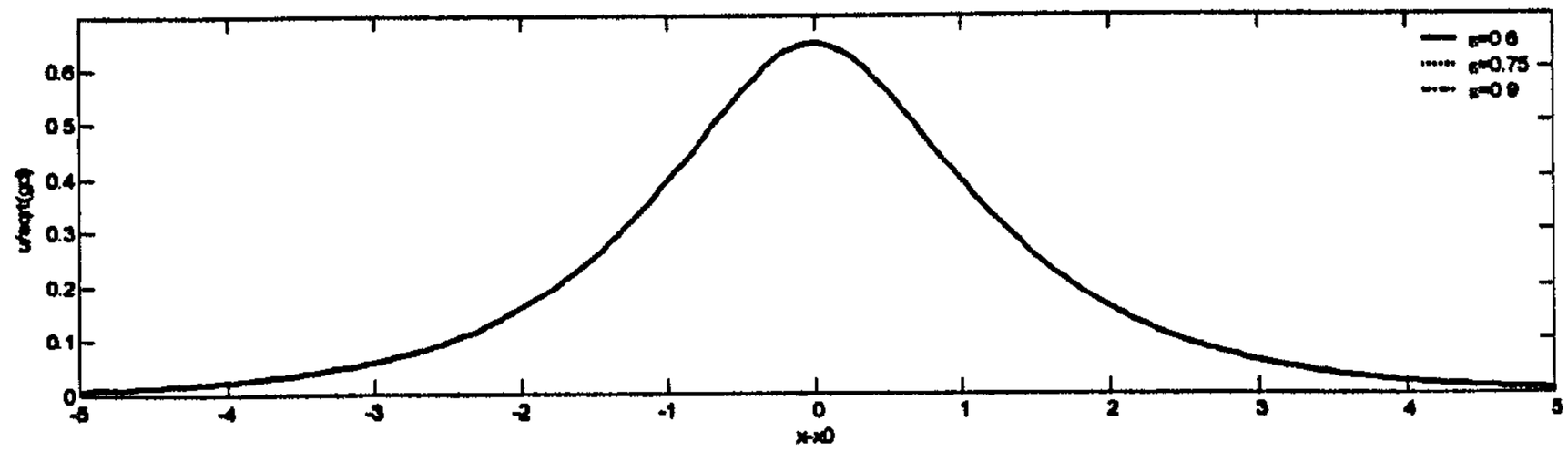

Fig.5.3.3 (a) Horizontal velocity component (y=0)

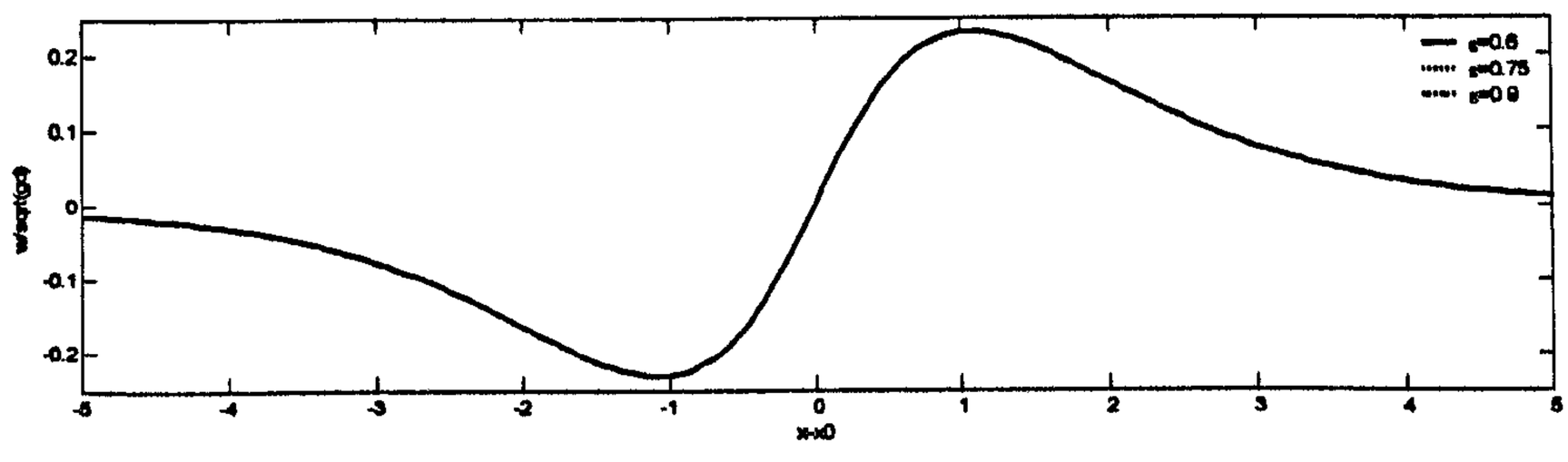

Fig.5.3.3 (b)Vertical velocity component (y=0)

Fig.5.3.3 Comparison of velocity components using different ε (A=0.6d, $t = 0$,n_{inf}=2, ε =0.9 velocity is nondimensionlised by $\sqrt{gd}$, x coordinate is nondimensionlised by d 'Method 1' for velocity calculation)

Numerical tests show that ε in Eq.(5.2.1) may be a value in the range of 0.6 ~ 0.9 and that numerical results obtained are not sensitive to its specific value (Fig. 5.2.3). In this work, ε=0.9 is used unless P_{I1} or P_{I2} is outside the fluid domain. In that case, a special treatment will be applied. Details of the special treatment will be discussed in Section 5.5.

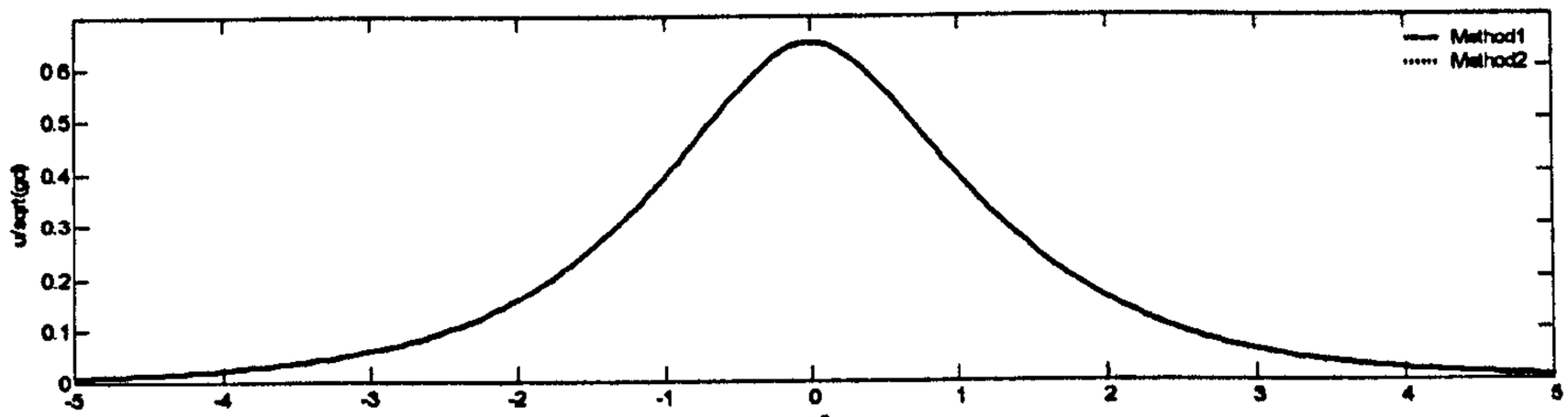

Fig.5.3.4 (a) Horizontal velocity component (y=0)

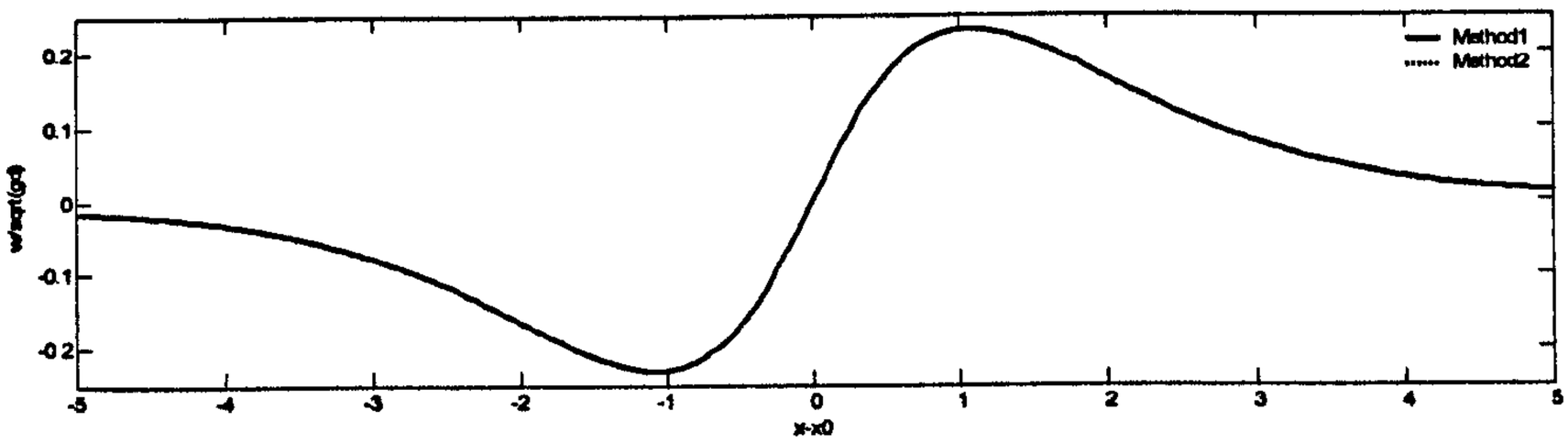

Fig.5.3.4 (b) Vertical velocity component (y=0)

Fig.5.3.4 Comparison of velocity components using different methods to approximate the velocity potential at point P_{I2} (A=0.6d , t = 0 , n_{inf}=2, ε =0.9 velocity is nondimensionlised by $\sqrt{gd}$, x coordinate is nondimensionlised by d)

In the above investigation, 'Method 1' is used to find the velocity potential at both point P_{I1} and P_{I2} . Comparison between the results obtained by 'Method 1' and 'Method 2' is also made. The case is the same as that in Fig. 5.3.1. The velocity components obtained by different methods are plotted in Fig.5.3.4. From this figure, it is observed that there are no evident differences between the results obtained from these two methods. Since the 'Method 2' requires less CPU time than 'Method 1' , 'Method 2' is used in this thesis. More investigations in cases with different wave steepness will be carried out to compare these two methods. The results will be discussed in Chapter 7.

. As is known, on a time domain simulation, the velocity on the free surface will give the new position and the velocity potential of the free surface at the next time step by using the time marching procedure described in Chapter 3.The error in the velocity might be brought to the next time step through such a procedure. In other words, the error may be accumulated. In order to investigate the velocity calculation scheme in a long-period calculation, the case with solitary wave propagating on a numerical tank is run. The initial parameters used in this case are same

as that used in Fig. 5.3.4 and 'Method 2' is used to approximate the velocity potential at those two points. The time step is taken as $\Delta t = 0.025\sqrt{d/g}$. Fig. 5.3.5 shows the comparison of the velocity on the free surface between the present numerical results and the results obtained by Tanaka's model (Tanaka, 1986) at $t = 5.0\sqrt{d/g}$.

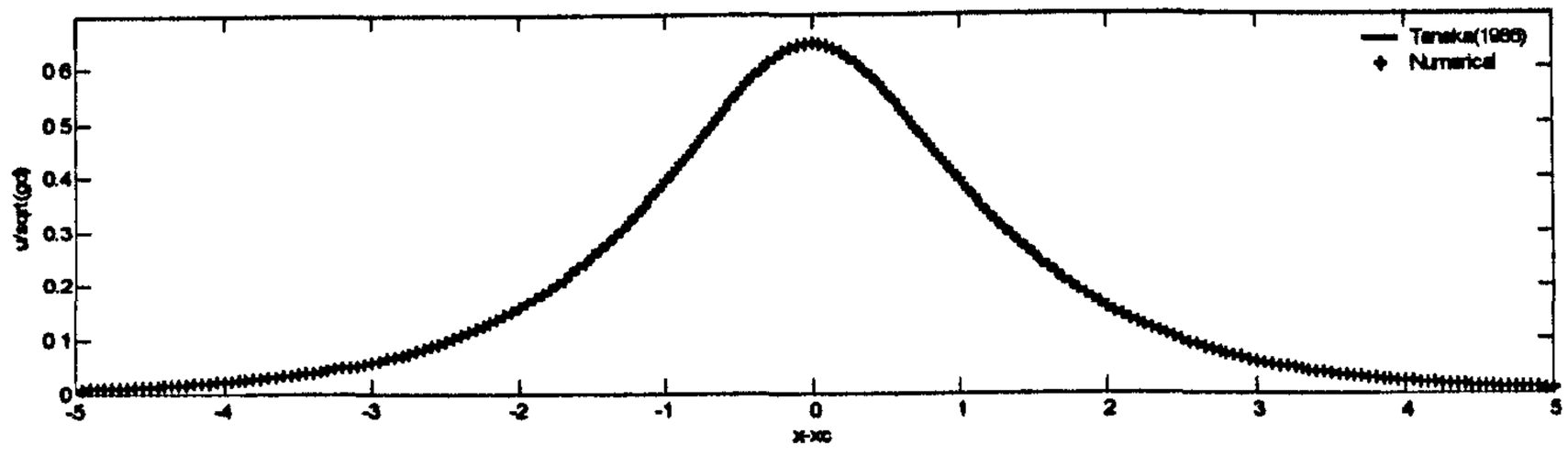

Fig.5.3.5 (a) Horizontal velocity component (y=0)

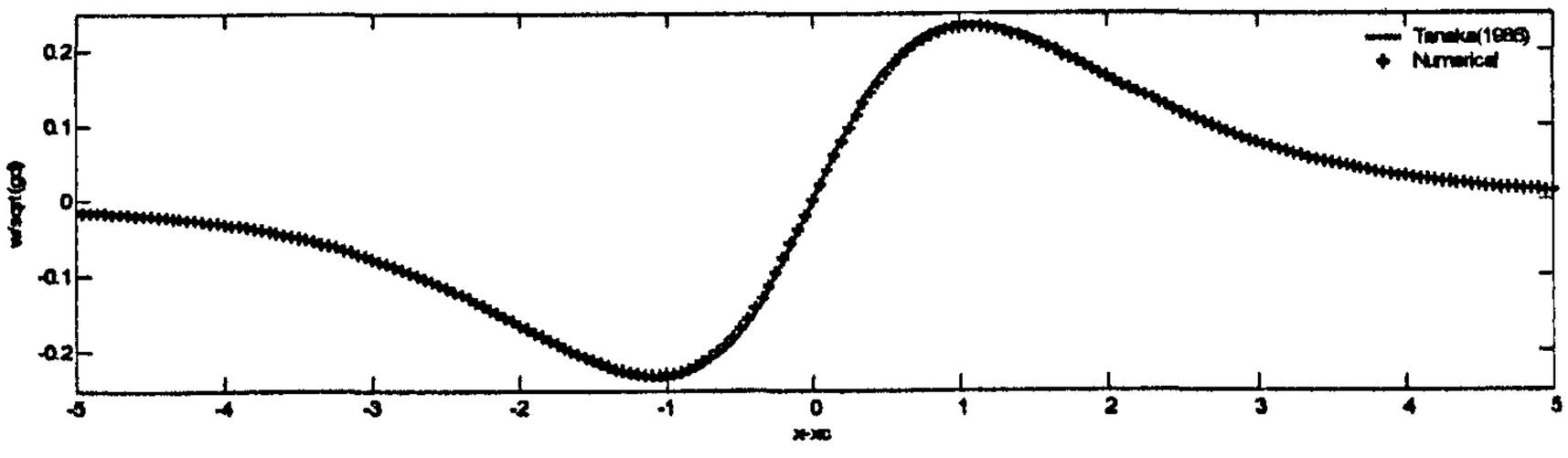

Fig.5.3.5 (b) Vertical velocity component (y=0)

Fig.5.3.5 Comparison of velocity components between numerical results and Tanaka's results (A=0.6d, $t = 5.0\sqrt{d/g}$,n_{inf}=2, ε =0.9 velocity is nondimensionlised by $\sqrt{gd}$, x coordinate is nondimensionlised by d; xc is the position of the wave crest , 'Method 2' for velocity calculation)

Good agreement is achieved both for horizontal velocity component and vertical velocity component. The relative errors for these two components are all less than 1% .It is also can be seen from Fig. 5.3.1 and Fig. 5.3.5 that the profiles of the velocity component centred at the crest of the solitary waves in different instance are almost the same. That is because solitary waves should keep permanent form while propagating on a flat sea bed. Fig. 5.3.6 shows the wave profiles at $y=0$ at different time steps. It is observed that the wave form is almost the same at different instance. This result indirectly gives evidence that the current velocity calculation scheme is accurate enough.

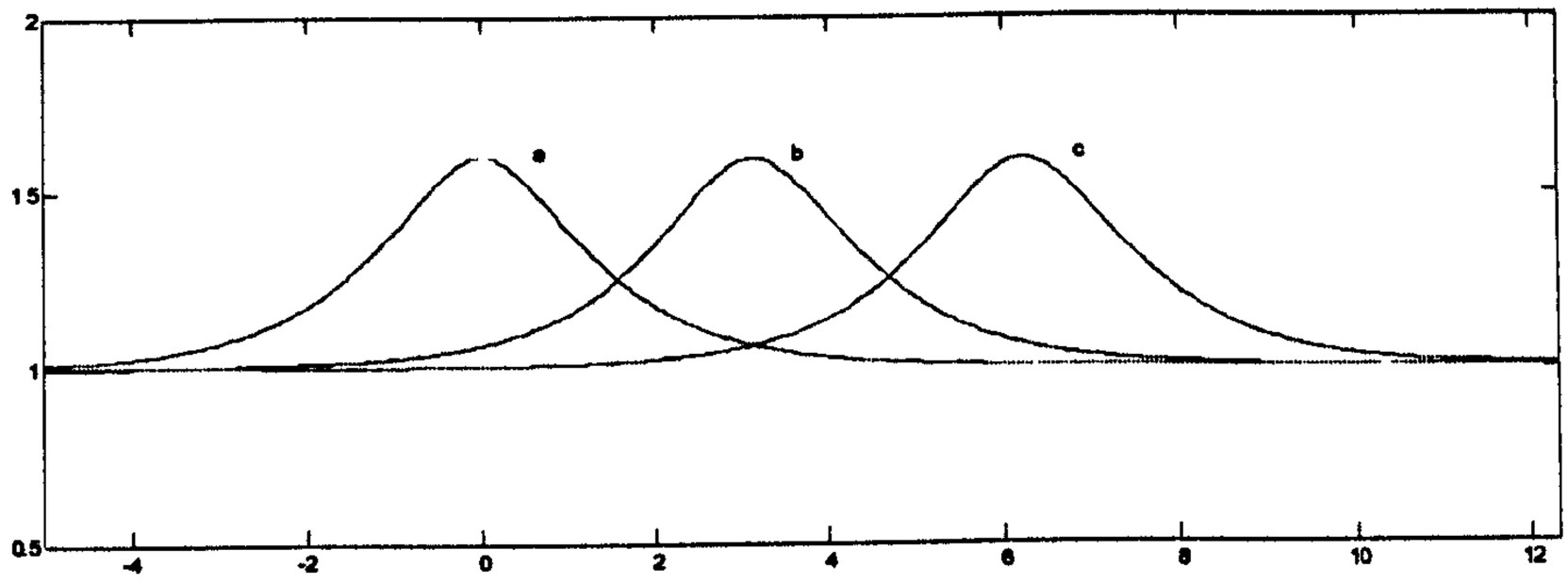

Fig. 5.3.6 Wave profile in different time instance (redistribute nodes once per 20 time steps)

(a: $t = 0$;b: $t = 2.5\sqrt{d/g}$;c: $t = 5.0\sqrt{d/g}$)

.

5.4. Special treatment for nodes near solid boundaries

It may become impractical to use the above method to calculate the velocity for nodes near a solid boundary because the normal line I-P_{I1}-P_{I2} may intersect with the solid boundary (see Fig. 5.4.1). If this happens, either Point P_{I2} is placed outside the fluid domain if h_{I1} and h_{I2} are still estimated by Eq. (5.2.1) or the two points (P_{I1} and P_{I2}) are contracted into one element. Both situations may degrade the results.

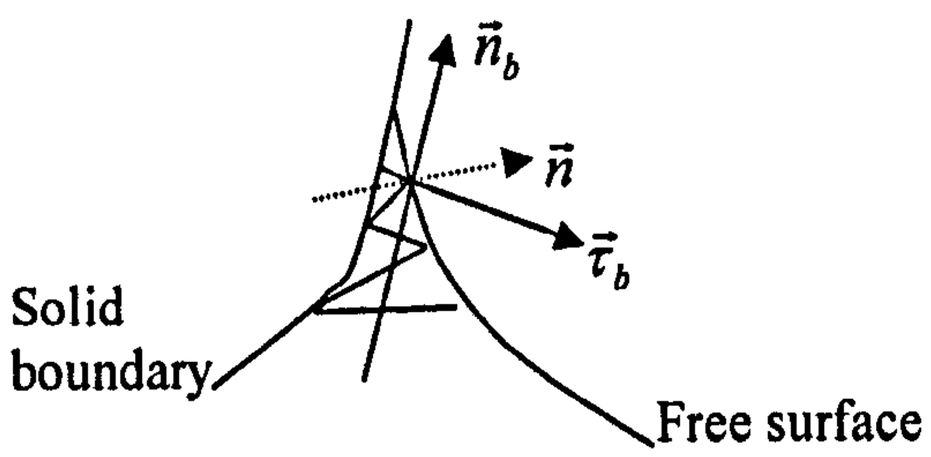

Fig.5. 4.1 Nodes near a solid boundary

In order to avoid such problems, it is proposed that the normal line (coinciding with vector $\vec{n}$ in Fig. 5.1.1) at a node near a solid boundary is replaced by a line (coinciding with vector $\vec{n}_b$) obtained by rotating the normal line to the direction perpendicular to the normal vector, passing the node considered, of the boundary surface. Correspondingly, $\vec{\tau}$ is replaced by $\vec{\tau}_b$ that is determined by $\vec{n}_b$, $\vec{e}_x$ and $\vec{e}_y$ using the similar method to that for $\vec{\tau}$. After doing so, Eqs. (5.1.1) and (5.1.3), by substituting $\vec{n}_b$ and $\vec{\tau}_b$ for $\vec{n}$ and $\vec{\tau}$, are still used to compute the velocity at the node. Using this treatment, the velocity components in x-, y-, and z-directions are directly obtained when the solid boundary is vertical, e.g. on the wave maker and the far end wall.

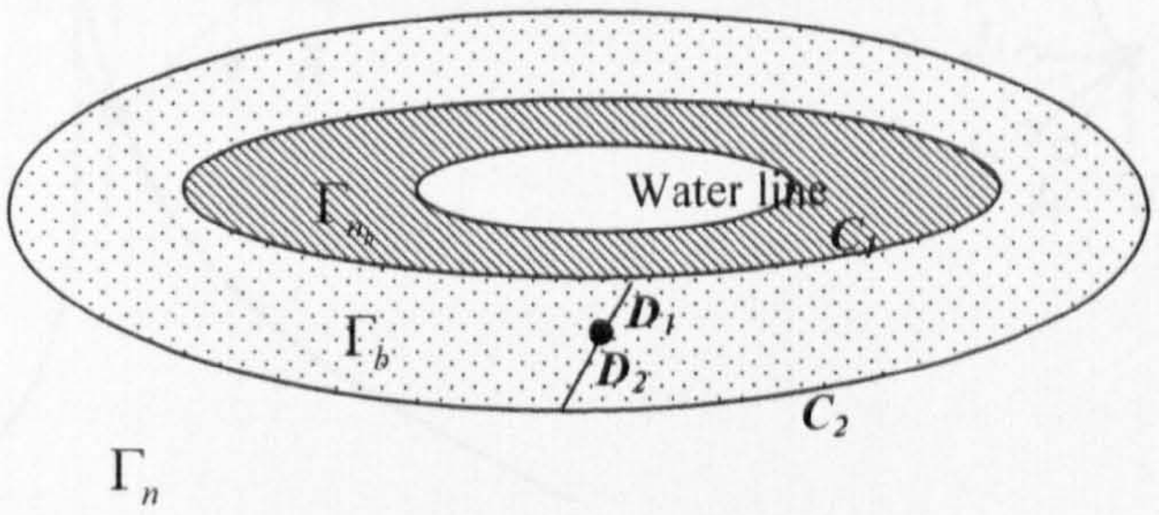

Fig.5.4.2 Sketch of buffering areas around the floating body

Let Γ_{n_b} denote the area (shaded area in Fig.5.4.2) where the above special treatment is applied, Γ_n the rest of the free surface. On the intersecting curve (C_1) between Γ_{n_b} and Γ_n, the velocity may not be continuous because of the above special treatment. To avoid this happening, a buffering area Γ_b (dotted area in Fig.5.4.2) is defined outside of Γ_{n_b}. For the nodes in this area, both the general method (the result from this method is $\vec{v}_r$) and the above special treatment (the result from this method is $\vec{v}_s$) are used to calculate the velocity. The ultimate velocity at node i in this area is

$$\vec{v} = D_1\vec{v}_s + D_2\vec{v}_r /(D_1 + D_2) \tag{5.2.4}$$

where D_1 is the distance between the node i and the curve C_1. D_2 is the distance between the node i and the curve C_2 which is the intersecting curve of Γ_b and Γ_n.

However, if $\vec{n}_b$ is very close to $\vec{\tau}$, the above approach to calculate velocity at nodes near the rigid boundary may not work. The reason is that once the angle between $\vec{n}_b$ and $\vec{\tau}$ is very small, the coefficients for tangential velocity components in LSM equation formed by Eq. (5.1.3) are much smaller than those for normal velocity components and therefore such a LSM formulation may result in relatively large error for the tangential velocity components. In order to solve this problem, another special treatment is suggested. This treatment will discussed in the following section and also used to the nodes near crests of the free surface.

5.5. Special treatment for nodes near crests of the free surface

Similarly, point P_{I2} and point P_{I1} may be outside of the fluid domain or the two points are contracted into one element near the crest when waves are very steep or overturning. Therefore, a special treatment is also needed in such cases.

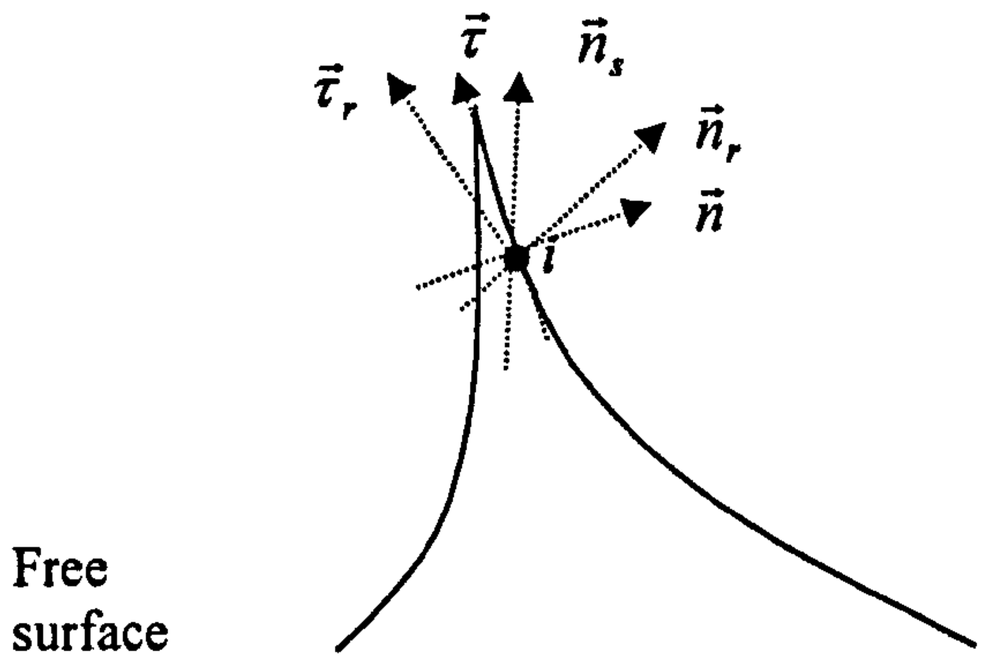

Fig.5.5.1 Nodes near the crest and its neighbours

Obviously, the replacement vector $\vec{n}_b$ does not exist in the above principle. Instead of $\vec{n}_b$, one may find the vector $\vec{n}_s$ which is parallel to the tangential direction of the free surface on the other side of the crest (Fig. 5.5.1a) . However, $\vec{n}_s$ may still be too close to $\vec{\tau}$, particularly when the crest is overturning. To overcome this problem, another vector $\vec{n}_r$ in place of $\vec{n}$ is used and defined as below (see Fig.5.4.1) . Suppose the node i on the free surface, $J_1,J_2,J_3,.....J_M$ are the interior nodes connected with it. The angle α_{iK} between $\vec{n}$ and each vector $\vec{x}_i - \vec{x}_{J_K}$ (K =1,2,...M) can be found by using the following formula

$$\cos\alpha_{iK} = \vec{n}\cdot(\vec{x}_i - \vec{x}_{J_k}) / \left|\vec{n}\cdot(\vec{x}_i - \vec{x}_{J_k})\right| \tag{5.5.1}$$

From these nodes ($J_1,J_2,J_3,.....J_M$), $J_{K\min}$ is the node where $\alpha_{iK\min} = \min\{\alpha_{i1},\alpha_{i2},...,\alpha_{iM}\}$. So , $\vec{n}_r$ is chosen as

$$\vec{n}_r = (\vec{x}_i - \vec{x}_{J_{K\min}}) / \left|\vec{x}_i - \vec{x}_{J_{K\min}}\right| \tag{5.5.2}$$

Therefore, $\vec{n}_r$ is closest to $\vec{n}$ so that it has largest angle with $\vec{\tau}$ and therefore ease the problem described above. Similarly, $\vec{\tau}$ is replaced by the corresponding $\vec{\tau}_r$ of $\vec{n}_r$. $\hbar$ in Eq. (5.2.1), is also updated by using the distance between node i and node $J_{K\min}$, and ε =0.6.

Since node $J_{K\min}$ is an interior node, there are at least two nodes connected to it. Therefore, this approach ensures there are two layers of elements along $\vec{n}_r$ of node i so that one can avoid point P_{I2} or point P_{I1} from being outside of the fluid domain as long as the mesh near the free surface is fine enough.

5.6. Velocity calculation at nodes on the body surface

The normal velocity at nodes on a rigid boundary is known when solving the BVP for velocity potential. According to the body surface boundary condition, Eq. (3.1.4), the velocity component in the normal direction can be found by

$$\vec{v}_n = \vec{n} \cdot \vec{U}(t) = \vec{n} \cdot (\vec{U}_c + \vec{\Omega} \times \vec{r}_b) \tag{5.6.1}$$

For the purpose of calculating the tangential components of the velocity, the nodes on the body surface are separated into two groups: inner-body-surface nodes and nodes on the waterlines. Different methods are applied.

5.6.1. Inner-body-surface nodes

For the inner-body-surface nodes, the corresponding tangential vectors need to be defined. Both are in the surface of the boundary and determined by

$$\vec{\tau}_x \perp \vec{n},\ \vec{\tau}_x // \vec{e}_x,\ \vec{\tau}_y \perp \vec{n} \text{ and } \vec{\tau}_y // \vec{e}_y. \tag{5.6.2}$$

After that, one can use the same method as that for nodes on the free surface. To do so, the nodes J_k (k=1, 2, 3, ... , m) in Fig.5.1.1 are replaced by the neighbour nodes on the body surface. Eq. (5.1.3) is then used to calculate the tangential velocity components.

5.6.2. Nodes on waterlines

However, at the nodes on the waterline, Eq. (5.1.3) becomes similar to a backward scheme due to unsymmetrical distribution of nodes around the waterline and so becomes less accurate than at the inner-body-surface nodes. Therefore, the two tangential components need special consideration. In this case, the tangential velocity components are replaced by another two orthogonal vectors, one is tangent to the waterline (τ_w) and the other (n_w) is perpendicular to it (Fig. 5.6.1)

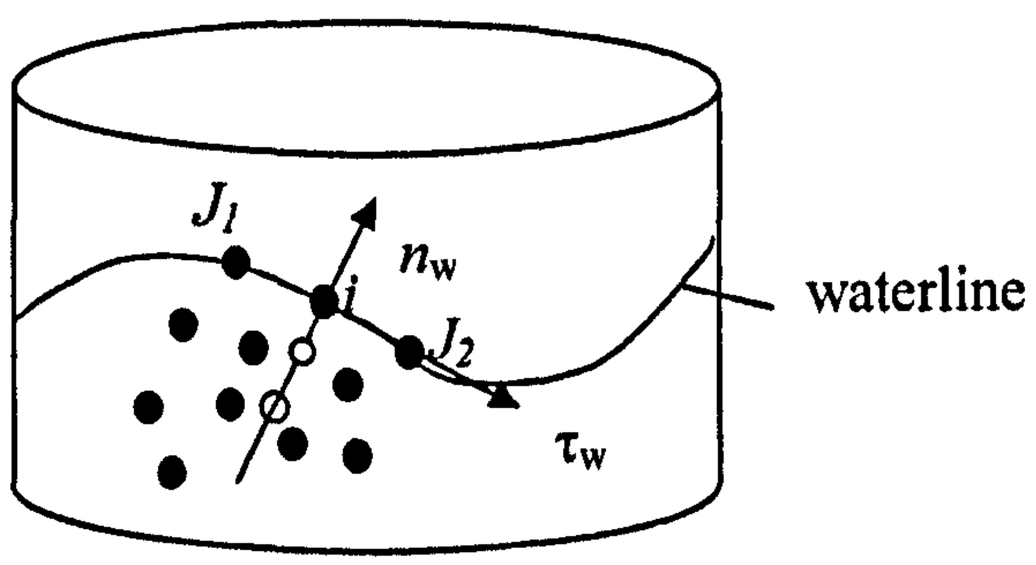

Fig.5.6.1 Nodes on the body surface and water line

Velocity component ($\vec{v}_{\tau_w}$) in the direction of $\vec{n}_w$

The velocity component in the direction of vector $\vec{n}_w$ is estimated by using a three-point method similar to Eq. (5.1.1) . The three points contained the node *i* on the waterline and the other two points (marked as empty circles in Fig.5.5.1) on the line $\vec{\tau}_y$. The velocity potentials at these two points are interpolated by using the body-surface nodes around them. A LSM method defined by Eqs. (4.6.3)- (4.6.9), is employed to do so. Therefore, Eq. (5.1.1) can give the velocity component in the direction of $\vec{n}_w$

Velocity component ($\vec{v}_{\tau_w}$)in the direction of $\vec{\tau}_w$

After the velocity component in the direction of $\vec{n}_w$ is found, the velocity component in the direction of $\vec{\tau}_w$ can be estimated by using the velocity potential at two neighbour nodes (J_1 and J_2) . The simplest way is to apply the central difference scheme,

$$\vec{v}_{\tau_w} = \frac{\phi_{J_1} - \phi_{J_2}}{l_{12}} \cdot \vec{\tau}_w \tag{5.6.3}$$

in which $l_{12} = \left|\vec{X}_{J_1} - \vec{X}_{J_2}\right|$ is the distance between node J_1 and node J_2; v_{τ_x} is the model of vector $\vec{v}_{\tau_x}$. However, in order to consider the the direction of the vector from the node *i* to node J_1 and J_2, a scheme based on the concept of directional derivative is used here,

$$\frac{\partial \phi}{\partial \vec{l}} = \frac{\partial \phi}{\partial n}\frac{\partial n}{\partial \vec{l}} + \frac{\partial \phi}{\partial \tau_w}\frac{\partial \tau_w}{\partial \vec{l}} + \frac{\partial \phi}{\partial n_w}\frac{\partial n_w}{\partial \vec{l}} = \vec{v}_n \frac{\partial n}{\partial \vec{l}} + \vec{v}_{\tau_w}\frac{\partial \tau_w}{\partial \vec{l}} + \vec{v}_{n_w}\frac{\partial n_w}{\partial \vec{l}} \tag{5.6.4}$$

where $\vec{l}$ is the directional vector from one of the two neighbour nodes (J_1 and J_2) pointing to the other. A central difference scheme is used to replace the partial derivatives in Eq. (5.6.4). This equation is therefore rewritten as

$$v_{\tau_w} l_{12}^{\tau_w} = \frac{\phi_{J_1} - \phi_{J_2}}{l_{12}} - v_n l_{12}^n - v_{n_w} l_{12}^{n_w} \tag{5.6.5}$$

in which v_n, v_{τ_w}, v_{n_w} are the models of the velocity components $\vec{v}_n, \vec{v}_{\tau_w}, \vec{v}_{n_w}$ respectively; $l_{12}^n, l_{12}^{\tau_w}, l_{12}^{n_w}$ are the three components of vector $\vec{l}_{12}$ in $\vec{n}$, $\vec{n}_w$ and $\vec{\tau}_w$ directions, respectively.

It should be noted that in cases with sharp corners on the waterline (node *i* in Fig.5.6.2a), the normal vector is not continuous. The normal velocity component in the body surface condition, i.e., Eq. (3.1.4), should be equal to $\vec{v}_{n1}$ and $\vec{v}_{n2}$ (Fig 5.6.2b). Due to this fact, the velocities at these nodes are difficult to find, particularly in cases where there is an incident angle between the incident wave and the floating bodies (Fig5.6.2b). The problems associated with the sharp corners may be one of the reasons why the nonlinear interaction between the

water waves and the free-response floating structure with an incident angle cannot been found in the public domain.

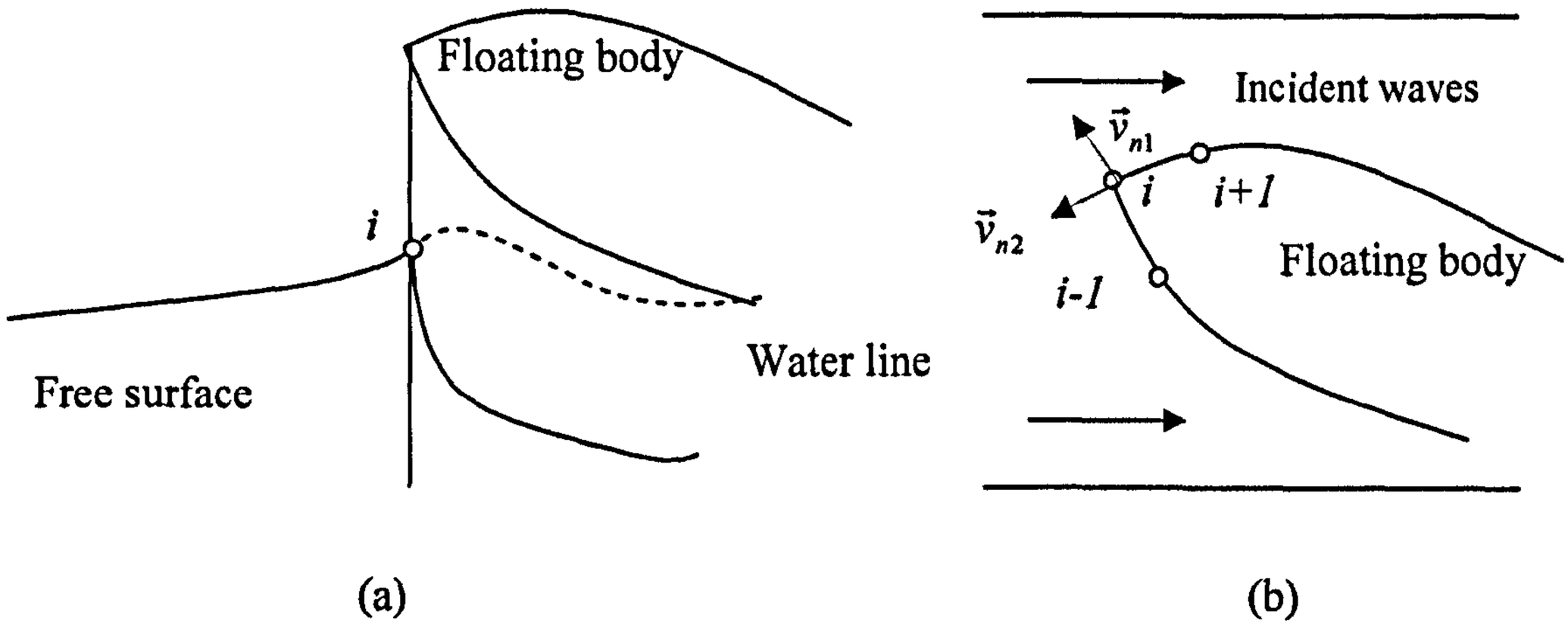

Fig.5.6.2 Sketch of corner problems associated with floating bodies

To overcome this difficulty, the velocity at a node at a sharp corner is approximated using that at the nodes around it by the same MLS method as used in Section 4.6.2. For each node *i* on the sharp corner of the body surface (Fig. 5.6.2b), two layers of nodes around node *i* are found to form the influence domain. Eqs. (4.6.3)- (4.6.9) with m=6 give the approximated value of velocity at this node. The basis for this approach is from the patch recovery technique as used by Ma (1998) and Ma, Wu & Eatock Taylor (2001a). That is based on the fact that the velocity is continuous and therefore may be described as a multinomial of coordinative in a small sub-domain, such as the influence domain in this approach. It should be noted that once an overturning wave occurs near the sharp corner, the MLS method in this approach should be carried out in a local-normal coordinate system, as discussed in Section 4.6.3. But the interaction between the floating body and the overturning wave is not considered in this work.

5.7. Smoothing and recovery techniques

As mentioned in Section 2.4, the finite element solution usually suffers from an oscillating error (so called saw-tooth problem, Fig. 5.7.1). For the purpose of removing this oscillation, two techniques are widely used by the researchers. One is the smoothing technique, the other is the patch recovery technique.

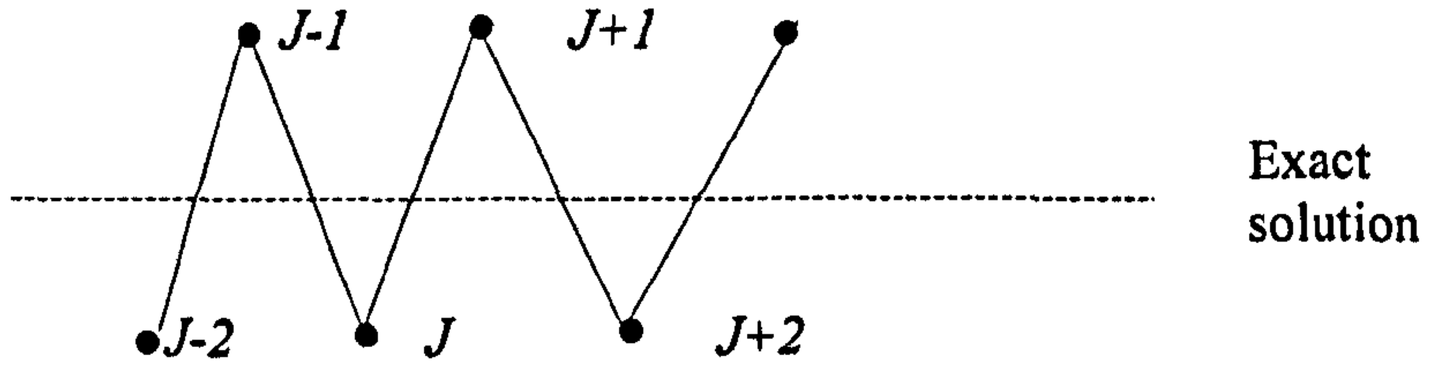

Fig. 5.7.1 Sketch of the smoothing technique

5.7.1 Smoothing technique

Like Ma (1998) & Ma, Wu & Eatock Taylor (2001a,b), a 5-point smoothing scheme is used to smooth the velocity at the nodes on the waterlines. The details of this scheme can be found in the above references, here only a brief summary is given.

For five equally-spaced points, the relevant formula is written as

$$\overline{w}_J = \frac{1}{16}(-w_{J-2} + 4w_{J-1} + 10w_J + 4w_{j+1} - w_{j+2}) \tag{5.7.1}$$

where w is the function to be smoothed and $\overline{w}$ is the smoothed value. Subscripts in Eq. (5.7.1) indicate node numbers. *J-2,J-1,J+1,J+2* are located at both side of the node J as shown in Fig.5.7.1. The numerical investigation by Ma (1998) has proved that this scheme is very efficient. However, the approach is only applicable for the nodes on a straight line with equal space between every two connected nodes. In order to deal with the problem with variable node space, Koo & Kim (2004) extend the above 5-point smooth scheme as

$$\overline{w}_J = a_{J-2}w_{J-2} + a_{J-1}w_{J-1} + a_J w_J + a_{J+1}w_{J+1} + a_{J+2}w_{J+2}) \tag{5.7.2}$$

and

$$a_{J-2} = \frac{-\Delta s_{J-1}\Delta s_{J+1}}{2\Delta s_{J-2}(\Delta s_{J+2} - \Delta s_{J-2})} \tag{5.7.3a}$$

$$a_{J-1} = \frac{-\Delta s_{J+1}}{2(\Delta s_{J-1} - \Delta s_{J+1})} \tag{5.7.3b}$$

$$a_J = \frac{\Delta s_{J-1}\Delta s_{J+1}}{2\Delta s_{J-2}\Delta s_{J+2}} + \frac{1}{2} \tag{5.7.3c}$$

$$a_{J+1} = \frac{-\Delta s_{J-1}}{2(\Delta s_{J-1} - \Delta s_{J+1})} \tag{5.7.3d}$$

$$a_{J+2} = \frac{\Delta s_{J-1}\Delta s_{J+1}}{2\Delta s_{J+2}(\Delta s_{J+2} - \Delta s_{J-2})} \tag{5.7.3e}$$

in which

$$\Delta s_{J-2} = x_{J-2} - x_J ; \Delta s_{J-1} = x_{J-1} - x_J ; \Delta s_{J+1} = x_{J+1} - x_J ; \Delta s_{J+2} = x_{J+2} - x_J \qquad (5.7.4)$$

The coefficients $a_{J-2}, a_{J-1}, a_J, a_{J+1}$ and a_{J+2} depend on a single coordinate value, x or y. Therefore, this approach is not applicable to 3D curved water lines. In order to extend the smoothing technique to this work, the arc-segment length between two successive nodes on these waterlines is considered when calculating the coefficients for each nodes in Eq. (5.7.2) and Eq. (5.7.4) is replaced by

$$\Delta s_{J-2} = s_{J-2,J-1} + s_{J-1,J} ; \Delta s_{J-1} = s_{J-1,J} ; \Delta s_{J+1} = s_{J+1,J} ; \Delta s_{J+2} = s_{J+2,J+1} - s_{J+1,J} \qquad (5.7.5)$$

where $s_{I,K}$ is the arc-segment length between node I and K (I, K=J-2, J-1, J, J+1 and J+2). This approach is only used to smooth the velocity on the waterlines of the floating body. It should be noted that only the tangential velocity components at the nodes on the waterlines need to be smoothed because the normal components are known.

5.7.2 Recovery technique

For other nodes on the free surface, a patch recovery technique (Ma, 1998; Ma, Wu & Eatock Taylor, 2001a) is used here. In this method, the velocity at a node i is assumed to be fitted by a polynomial over a patch on the free surface. This approach works well in case without overturning wave. As mentioned in Section 2.4.2, this approach is based on the assumption that the surface can be expressed as $z=f(x,y)$ where f is a single-valued function. In many cases, such as the body surface and the free surface with overturning wave, this assumption is not corrected as being discussed in Section 4.5.

In order to avoid this problem happening, the patch recovery approach is carried out in a local normal-tangential coordinate ($\vec{\tau}_x, \vec{\tau}_y, \vec{n}$) system, where only one intersection point exists in the normal direction, defined by using the same method as Section 4.5. The patch is therefore projected to $o\tau_x\tau_y$ plane and therefore the velocity on the patch is assumed to satisfy the following linear function of τ_x, τ_y,

$$w_i^* = a + b\tau_x + c\tau_y \qquad (5.7.6)$$

and the velocity in the superconvergent point J (J=1,2,3,...M) is estimated by

$$w_J^s = a^s + b^s \tau_{x_J} + c^s \tau_{y_J} = \sum_{j=1} N_j w_j \qquad (5.7.7)$$

where N_j is the shape function. The coefficient a^s, b^s, c^s is calculated,

$$\begin{bmatrix} a^s \\ b^s \\ c^s \end{bmatrix} = \begin{bmatrix} \alpha_1 & \beta_1 & \gamma_1 \\ \alpha_2 & \beta_2 & \gamma_2 \\ \alpha_3 & \beta_3 & \gamma_3 \end{bmatrix} \begin{Bmatrix} w_1 \\ w_2 \\ w_3 \end{Bmatrix} \qquad (5.7.8)$$

in a triangle element where the node number is in turn *l*-*m*-*n* ($l, m, n = 1,2,3$),

$$\alpha_l = \frac{1}{2\Delta}(\tau_{x_m}\tau_{y_n} - \tau_{y_m}\tau_{x_n}) \tag{5.7.9}$$

$$\beta_l = \frac{1}{2\Delta}(\tau_{y_m} - \tau_{y_n}) \tag{5.7.10}$$

$$\gamma_l = -\frac{1}{2\Delta}(\tau_{x_m} - \tau_{x_n}) \tag{5.7.11}$$

in which Δ is the area of this element.

The least squares method is therefore used to solve the equations of Eq. (5.7.6). As mentioned above that the local normal-tangential recovery technique requires more CPU time than the original one by Ma (1998) , therefore it only may be used to recover the velocity on the body surface in this work. For the velocity on the free surface, the method developed by Ma (1998) is applied unless overturning waves occur.

6. ITERATIVE PROCEDURE FOR CALCULATING FORCE

In this work, $\partial\phi/\partial t$, involved in Eqs. (3.3.3) and (3.3.4) for estimating the forces on floating bodies, is calculated by solving a boundary value problem defined in Eqs. (3.3.10)-(3.3.12). In order to find $\partial\phi/\partial t$ at the n^{th} time step, the boundary conditions on the free surface require the wave elevation and the velocity on the free surface. In this time step, the wave elevation can be found by using the velocity on the free surface at $(n\text{-}1)^{th}$ time step by using a time marching scheme based on Eq. (3.1.7). The velocity on the free surface at this time step can be found by using the scheme described in Chapter 5 after the BVP problem for the velocity potential is solved. However the boundary condition on the body surface requires the velocity and the accelerations of the floating bodies. There is a difficulty with doing so due to the nonlinear coupling between the body and wave motions. In order to tackle this difficulty, four types of methods have been suggested in the literature. Those are the indirect method, the mode-decomposition method, the Dalen & Tanizawa's method and the iterative method.

As discussed in Section 2.6, in the mode-decomposition and the indirect method, the motion is decomposed into several modes and so the equations have to be solved for the purpose of modelling different modes of motion. While, the Dalen & Tanizawa's method requires a special matrix for $\partial\phi/\partial t$. This may increase the difficulty for numerically solving the algebraic equations associated with the BVP of $\partial\phi/\partial t$.

Apart from the CPU time spent on every time step, the overall efficiency also depends on the time marching procedure. As discussed in Section 3.6, either explicit or implicit multi-step method may be used to estimate the velocity of the floating body but the latter is better in terms of stability. Unfortunately, the body velocity is estimated from the acceleration at previous time steps (or sub-steps) in all existing methods; i.e., the corresponding procedure is explicit. The explicit procedure requires sufficiently small time step to ensure a stable calculation. In cases involving a floating body with large motion, the existing methods either used very small time steps or separated one time step into several sub-steps, such as a 4^{th}-order Runge-Kutta with fully updated explicit or frozen coefficient. The former required more time steps to achieve a specified long period calculation and the latter required sub-step calculations. The overall computational coefficient of both approaches is relatively low. Whereas, if an implicit scheme is used, one may use a relatively long time step without sub-step calculation because the stability of the implicit method is better than explicit method with respect to same accuracy (Gear, 1971).

Because the main aim of this work is to investigate the response of the floating bodies to nonlinear waves, the motion of the floating bodies in those cases will be relatively large, e.g.,

the wave-induced response near the resonance area. Therefore, an implicit method is used to integrate the velocity of the floating body.

One may also use an implicit method to update the position of and the velocity potential on the free surface. To do so, the position of the free surface also needs to be updated during a time step. Therefore, the coefficient matrix for the FEM should be updated. This results in additional computational cost. Based on the numerical investigation by Ma, Wu & Eatock Taylor (2001b), the explicit formula (Eq.3.6.1) is accurate and stable for updating the information on the free surface.

In order to integrate implicitly the velocity of the floating body, an iterative procedure is required. In this aspect, the iterative method for $\partial\phi/\partial t$ may be more suitable for this work than any other methods. An improved iterative procedure, called Iterative Semi Implicit Time Integration Method for Floating Bodies (ISITIMFB), is developed. It incorporates the advantages and overcomes some of the disadvantages of other methods. This method has the following features

(a) Using the acceleration in the current step to estimate the body velocity, i.e., it is implicit, distinguishing it from all other methods discussed above;

(b) Not requiring sub-step calculations, different from the fully updated Runge-Kutta method;

(c) Eliminating the necessity of solving the extra equations as in the indirect method and the mode-decomposition method and the need to generate a special matrix in the Dalen & Tanizawa's method, getting rid of the main disadvantages of all three;

(d) not updating the positions of the free surface and the floating body during the iteration to find the acceleration and force, saving the CPU time spent not only on this but also on forming the new coefficient matrix.

The details of the method are described in the following section.

6.1. Iterative procedure

Suppose that all calculations until $t=t_{n-1}$ have been completed and so the velocity potential and its time derivative on the free surface, the positions of all boundaries including the free surface and the body surface have been obtained through updating. To find the fluid and body velocities at time t_n, the following procedure is used.

1) Predict the body acceleration $\vec{A}^{n(0)}$ at time t_n by curve fitting of accelerations at previous time steps using a least squares method and estimate the corresponding body velocity by using the Adams-Moulton method as follows,

$$\vec{U}_b^{n(0)} = \vec{U}_b^{n-1} + \frac{\Delta t}{12}(5\vec{A}_b^{n(0)} + 8\vec{A}_b^{n-1} - \vec{A}_b^{n-2}) \tag{6.1.1}$$

where $\vec{A}^{n(0)}$ and $\vec{U}_b^{n(0)}$ represent the predicted values of translational or angular body accelerations and velocities, respectively, at the current time step, which are used as the initial values of iteration.

2) Solve the boundary value problem for ϕ using $\vec{U}_b^{n(0)}$ in Eq. (6.1.1) for the boundary condition on the body surface.

3) Calculate the fluid velocity and the time derivative of the velocity potential on the free surface.

4) Calculate the fluid velocity $\vec{V}_b^{n(0)}$ on the body surface.

5) Using the following loop to find the acceleration of and forces on the body:

(a) Solve the boundary value problem for $\left(\frac{\partial \phi}{\partial t}\right)^{n(k)}$ using $\vec{A}^{n(k-1)}, \vec{U}_b^{n(k-1)}$ and $V_b^{n(k-1)}$ in its boundary condition on the body surface (Eq. (3.3.12)), where the subscript n (k-1) represent the variables at time t_n but at k-th iteration (k=1,2,3.....);

(b) Calculate the forces or moments $\vec{F}^{n(k)}$ and so the acceleration

$$\vec{A}_b^{n(k)} = [M]^{-1}\left[\alpha^n \vec{F}^{n(k)} + (1-\alpha^n)\vec{F}^{n(k-1)}\right]; \tag{6.1.2}$$

in which the mass matrix $[M]$should be replaced by the matrix of the moment of inertia $[I]$, (Eq. (3.2.7)), if the angular acceleration and moment are concerned;

(c) Estimate the new body velocity using the similar method to Eq. (6.1.1)

$$\vec{U}_b^{n(k)} = \vec{U}_b^{n-1} + \frac{\Delta t}{12}(5\vec{A}_b^{n(k)} + 8\vec{A}_b^{n-1} - \vec{A}_b^{n-2}); \tag{6.1.3}$$

(d) Solve the boundary value problem for ϕ using $\vec{U}_b^{n(k)}$ in Eq. (3.1.6) for the boundary condition on the body surface;

(e) Calculate the new fluid velocity $\vec{V}_b^{n(k)}$ on the body surface;

(f) Check if the relative error of accelerations (or forces) is smaller than the control error; if not, go to a); otherwise go to 6).

6) Update the position of the body using the final body velocity and acceleration in the above loop by using the 3rd order Taylor expansion,

$$\vec{S}_b^{n+1} = \vec{S}_b^{n} + \vec{U}^{n(u)}\Delta t + \frac{\Delta t^2}{2}\dot{\vec{U}}^{n(u)} + \frac{\Delta t^3}{6}\frac{d\dot{\vec{U}}^{n(u)}}{dt} \tag{6.1.4}$$

where $\vec{S}_b^{n+1}$ is the translational or annular displacement of the body to be used for the calculation of the next time step; $\vec{U}^{n(u)}$ and $\vec{\dot{U}}^{n(u)}$ represent the final values of body velocities and accelerations (translational or annular) in the above loop, respectively; and $\frac{d\vec{\dot{U}}^{n(u)}}{dt}$ is calculated using the FD scheme $\frac{d\vec{\dot{U}}^{n(u)}}{dt} = \left(\vec{\dot{U}}^{n(u)} - \vec{\dot{U}}^{n-1(u)}\right) / \Delta t$.

7) Calculate the fluid velocity on the free surface using the final velocity potential in the above loop.

8) Update the time derivative of the velocity potential on and the positions of the free surface using the same method as in Ma (1998) and Ma, Wu & Eatock Taylor (2001a), i.e.Eq. (3.6.1)

9) Go to the next time step.

As can be seen, an under-relaxation in Eq. (6.1.2) is employed in the iterative loop from (a) to (f) to improve the convergence rate. The value of α^n is determined by

$$\alpha^n = \frac{A_b^{n-1(u)} - A_b^{n-1(0)}}{A_b^{n-1(1)} - A_b^{n-1(0)}} \tag{6.1.5}$$

where $A_b^{n-1(u)}$ is the final value of the acceleration in the iteration at the previous step. This expression is proposed by considering the fact that if one had known α^{n-1}, the solution for $A_b^{n-1(u)}$ would have been found in one iteration through (a) to (f) and by assuming that $\alpha^n \approx \alpha^{n-1}$. After the iterative procedure is finished in one time step, Eq. (3.6.1) is used to update the geometry of the free surface.

This iterative procedure is distinguished from one in Cao, Beck & Schultz (1994) in three aspects.

(1): The velocity potential (and so the fluid velocity) is obtained in Cao, Beck & Schultz (1994) by assuming that the body velocity in Eq. (3.1.4) is estimated using the acceleration at the previous time step and thus the boundary value problem for ϕ is solved only once, i.e. without Step (d), in the above loop. Therefore the procedure in Cao, Beck & Schultz (1994) is actually an explicit method.

(2): The relaxation scheme in Eq. (6.1.2) and the corresponding relaxation coefficient in Eq. (6.1.5) are employed in this thesis while it is not clear whether any relaxation is adopted in Cao, Beck & Schultz (1994).

(3): The body velocity used in Eq. (3.1.4) is continually updated here by employing the scheme as given in Eqs. (6.1.1) and (6.1.3), while it needs to be evaluated only once in Cao, Beck & Schultz (1994).

It has been pointed out that the body and free surface positions are not updated in the iteration loop in the above procedure. That is why this method is classified as 'Semi Implicit'. In this aspect, it is similar to the frozen coefficient method. However, this procedure has not been found to suffer the instability problem associated with the frozen coefficient method; instead, it has been found to exhibit the similar stable behaviour to that of the full updated Runge-Kutta method. Numerical demonstration of this will be given below.

6.2. Prediction of the body acceleration $\vec{A}^{n(0)}$

The efficiency of the iterative procedure is decided by the iteration count (or the number of iterations) in the above loop - the smaller iteration counts the more efficient the procedure. One may understand that the iteration count for a specified accuracy depends on the quality of the predicted velocity in Eq. (6.1.1) and three values of the acceleration in Eq. (6.1.3). Better prediction of the velocity and closer values of the acceleration should lead to the smaller number of iterations. The quality of the predicted velocity and the values of the acceleration are in turn determined by the time step, the amplitude of the body motions and the natural frequency of the system.

In order to predict the $\vec{A}^{n(0)}$ with high quality, a least squares prediction method is used here. The detail can be found in Whittle (1963). Suppose the acceleration of the floating body at n^{th} time step is obtained. A polynomial $f(t)$ can be found by using the sampling points $(n,n-1,n-2,n-2,\ldots n-m+1)$ based on the principle of least squares method (see Fig.6.2.1), the predicted acceleration of the floating body at $(n+1)^{th}$ time step is given by $f(t_{n+1})$. The number of sampling points in this method affects the accuracy in predicting the acceleration. In this work, 5 points are used.

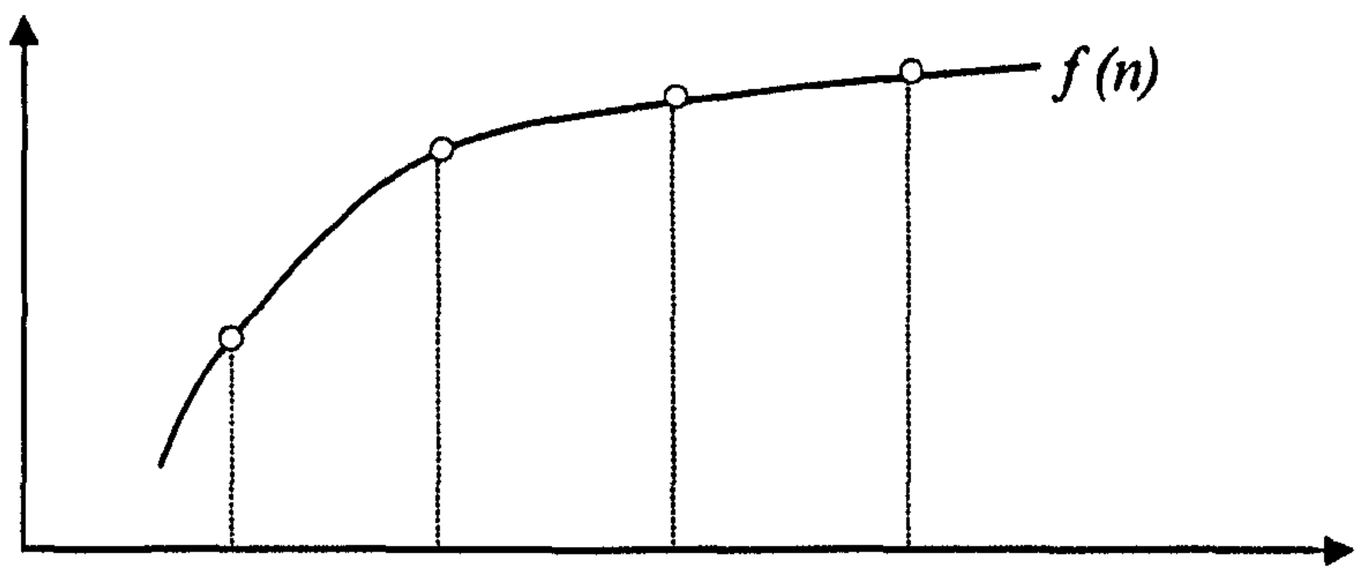

Fig.6.2.1 sketch of the least squares prediction

As has been known, the time step undoubtedly affects the accuracy of the prediction of $\vec{A}^{n(0)}$ Usually, smaller time step leads to relatively accurate predicted results and therefore results in

less iteration count for the ISITIMFB procedure. On the other hand, for a given wave and the shape of the body, the largest motion amplitude is related to the natural period. Therefore, the two most important factors affecting the iteration count may be the time step and the natural period. Their effects are to be investigated in Section 8.2.1. Apart from this, the mesh size may affect the iteration count as well, because it affects the convergence rate of the FEM. This effect will be discussed in Chapter 9.

7. WAVES GENERATED BY A WAVEMAKER

In this Chapter, the QALE-FEM method is validated by comparing its numerical predictions with analytical solutions and published results from other methods and experiments. Two kinds of problems are considered: one is nonlinear water waves (regular and random) generated by a wavemaker in a tank; and the other is the interaction between the water waves and periodic bars on the tank-bed. Some of the results have been published in Yan & Ma (2005) and Ma & Yan (2006), more results are given in this chapter. All parameters with a length scale are nondimensionalised by the water depth d and other parameters by

$$t \to \tau\sqrt{d/g} \quad \text{and} \quad \omega \to \omega\sqrt{g/d}\,. \tag{7.0.1}$$

7.1. Waves propagation in a flat tank

Water waves generated by a piston wavemaker in the tank with flat sea bed are considered in the first instance. In the past decade, the problem has been widely studied by many researchers using different numerical tools. Many interesting and valuable results were given, such as the analytical solution by Eatock Taylor, Wang & Wu (1994), the numerical simulation by Ma (1998) and Ma, Wu & Eatock Taylor (2001a,b), the experimental research by Nestegard (1999). In this section, the QALE-FEM method is used to simulate the waves propagating in a flat-bottom tank.

The waves may be monochromatic, bichromatic and random depending on the motion of the wavemaker. The meshes used are similar to that in Fig. 7.1.1 but much finer.

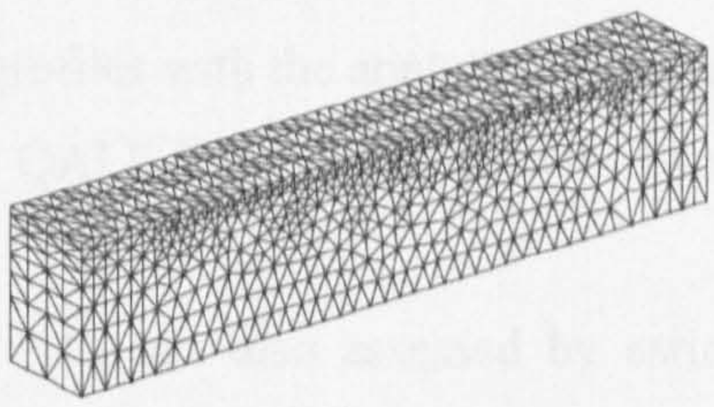

Fig.7.1.1 Illustration of initial mesh used for wavemaker problems

7.1.1. Monochromatic waves

The cases with monochromatic waves are firstly modelled In these cases, the motion of the wavemaker is governed by

$$S_w(\tau) = -a\cos(\omega\tau), \tag{7.1.1}$$

$$U_w(\tau) = a\omega\sin(\omega\tau), \tag{7.1.2}$$

where $S_w(\tau)$ is the displacement of the wavemaker, $U_w(\tau)$ is its velocity, a and ω are respectively its amplitude and frequency.

When the amplitude of the wavemaker is very small, the steepness of the generated waves is also very small. The numerical results for such a case can be compared with the linearised analytical solution by Eatock Taylor, Wang & Wu (1994). For this purpose, a case with a =0.0041 and ω=1.45 is simulated in a tank of length $L \approx 14.7$. The mesh is unstructured and the number of elements is about 78060. The time step is 0.021666, about 200 steps in each period. The wave profiles at two different instants (t=10T and 15T, where T =2π/ω is the period) are plotted in Fig. 7.1.2, which shows that the numerical results are in very good agreement with the corresponding analytical solution.

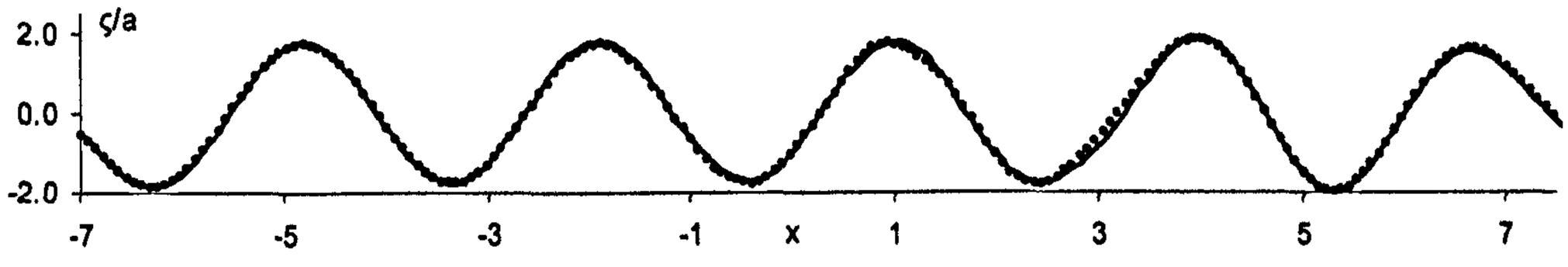

(a) $\tau = 10T$

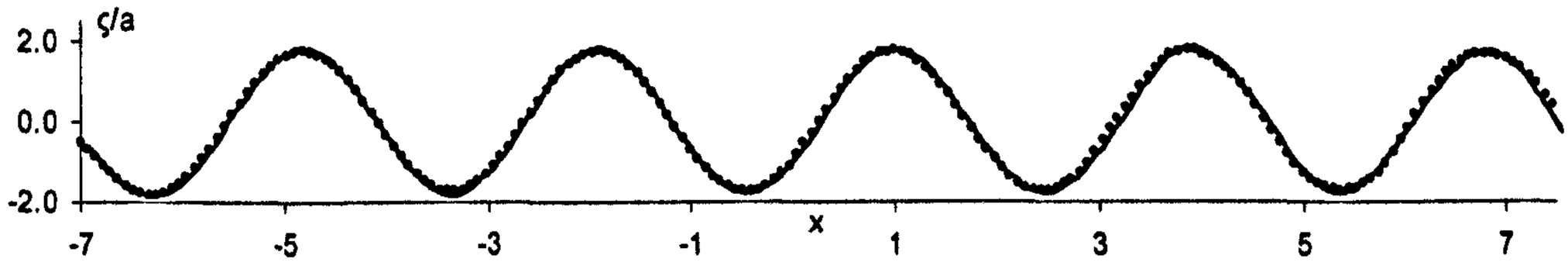

(b) $\tau = 15T$

Fig. 7.1.2 Comparison of wave profiles with the analytical solution for ω=1.45 and a=0.0041 (Solid line: QALE-FEM; Dots: analytical solution)

The numerical results in Fig. 7.1.2 are also assessed by estimating relative errors. The relative error (E_r) is defined as:

$$E_r = \frac{\|\varsigma - \varsigma_a\|}{\|\varsigma_a\|} \tag{7.1.3}$$

where $\|\varsigma\| = \int_{A_e} \varsigma^2 dA$, ς_a is an analytical wave elevation and A_e is the area over which the error is estimated. Because the accuracy of the waves within the damping zone should not be of concern, A_e equals the area of the free surface minus the part of the damping zone. The relative

errors evaluated in this way for the results in Fig. 7.1.2 are less than 0.5%. It is also found that the wave profile at $\tau = 10T$ and that at $\tau = 15T$ are almost the same.

The wave histories recorded at different positions at the above cases are plotted in Fig 7.1.3. The figure shows that the numerical results are in very good agreement with the corresponding analytical solutions, although the error is slightly greater near the damping zone. The cases with other frequencies are also carried out. The results for all of them show a similar agreement with the analytical solution to that seen in Fig. 7.1.2 and 7.1.3.

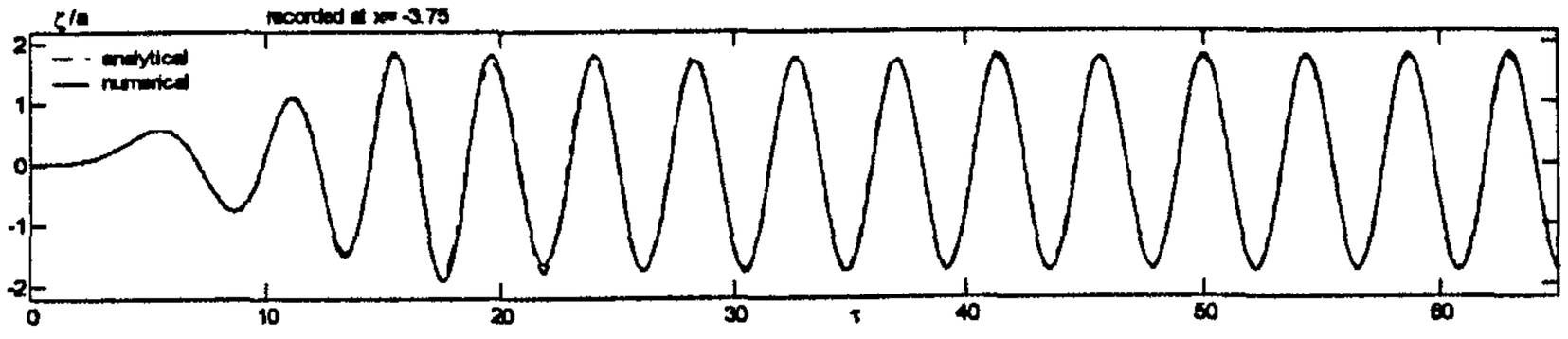

(a) wave history recorded at x= -3.75

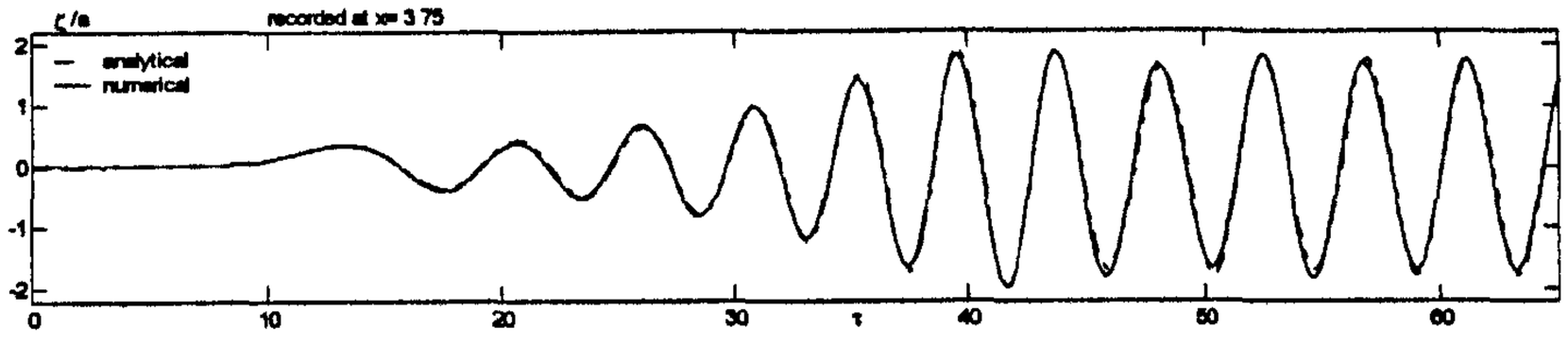

(b) wave history recorded at x=3.75

Fig.7.1.3. Comparison of the wave history with the analytical solution at x= -3.75 and x=3.75 for the case with ω=1.45 and a=0.0041

The behaviour of the QALE-FEM is then investigated by simulating waves of a larger amplitude and strong nonlinearity. The amplitude of the wavemaker is taken as 0.082. The frequency (ω) and tank length are the same as that in Fig. 7.1.2. The steepness of the generated waves is about 0.08. For such steep waves, the analytical solution mentioned above should not be considered valid. In order to validate the QALE-FEM in this case, its results are compared with those obtained by using conventional FEM described in Ma (1998) and Ma, Wu & Eatock Taylor (2001b). The length of the time step (also 200 steps in each period) is the same in both methods, whereas the type of mesh and the number of elements are different. When using the conventional FEM, the mesh is structured and the number of elements is 75264. When using the QALE-FEM, the mesh is unstructured and the number of elements is about 78060. The latter is also tested using a larger number of elements (133632) but no significant difference in results was found. The wave profiles at time $\tau = 10T$ and $15T$ from these two methods are depicted in Fig. 7.1.4. The agreement between them is quite good. The relative error estimated by the same method for Fig. 7.1.2 is found to be less then 1%.

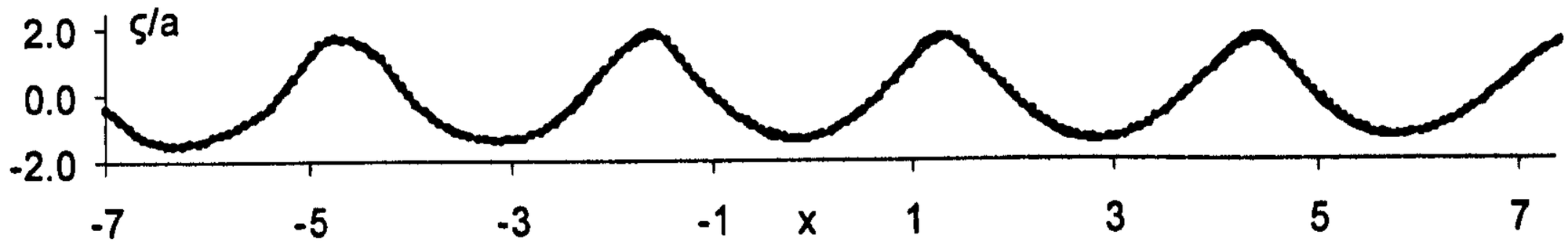

(a) $\tau = 10T$

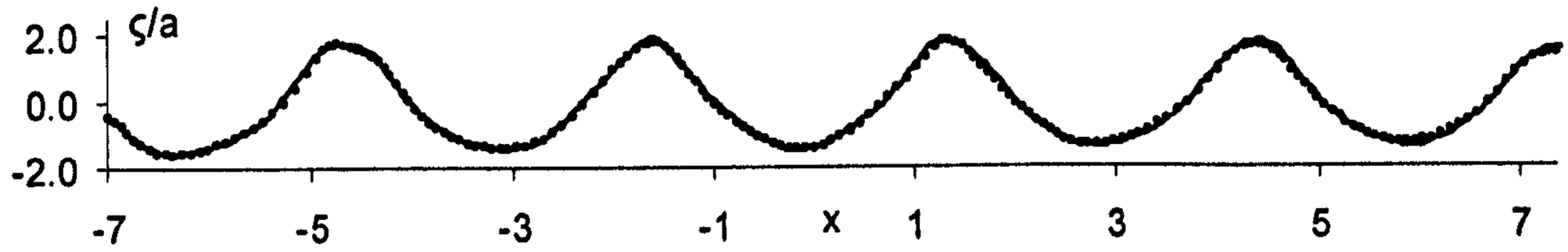

(b) $\tau = 15T$

Fig. 7.1.4 Comparison of wave profiles for ω=1.45 and a=0.082 (Solid line: QALE-FEM; Dots: conventional FEM (Ma, Wu & Eatock Taylor,2001b))

As a periodic wave, its repeatability is a very important property. Ma (1998) has investigated the repeatability of the periodic waves and concluded that his results had good repeatability. The above agreement between the results by QALE-FEM and his results also give a proof that the modelling waves by QALE-FEM also have good repeatability.

7.1.2. Bichromatic waves

The QALE-FEM has also been used to simulate bichromatic waves. These waves are generated by the following motion of the wavemaker

$$S_w(\tau) = -a_1 \cos(\omega_1 \tau) - a_2 \cos(\omega_2 \tau) \tag{7.1.4}$$

$$U_w(\tau) = a_1 \omega_1 \sin(\omega_1 \tau) + a_2 \omega_2 \sin(\omega_2 \tau) \tag{7.1.5}$$

where a_1 and a_2 are the amplitudes corresponding to the components with frequencies ω_1 and ω_2, respectively.

As an example, the values for these parameters are assigned as a_1=0.016, a_2=0.5a_1, ω_1=1.45 and ω_2= 2.03. The tank has the same length and the mesh is the same as for Fig.7.1.4. The time step is about 0.01548, about 200 steps in each period given by $2\pi/\omega_2$. For this case, the wave history recorded at a fixed point is plotted in Fig.7.1.5, together with the results from the conventional FEM. It can be seen that the results from the two methods are in very good agreement in the other area (Fig. 7.1.5a) and the relative error is in the same level as for Fig. 7.1.4.

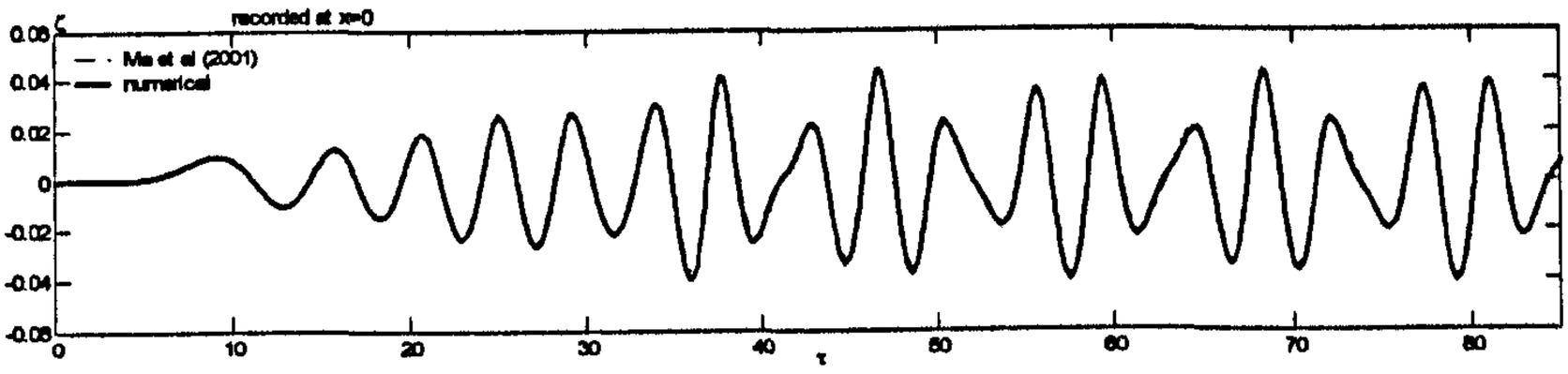

(a) Recorded at x=0

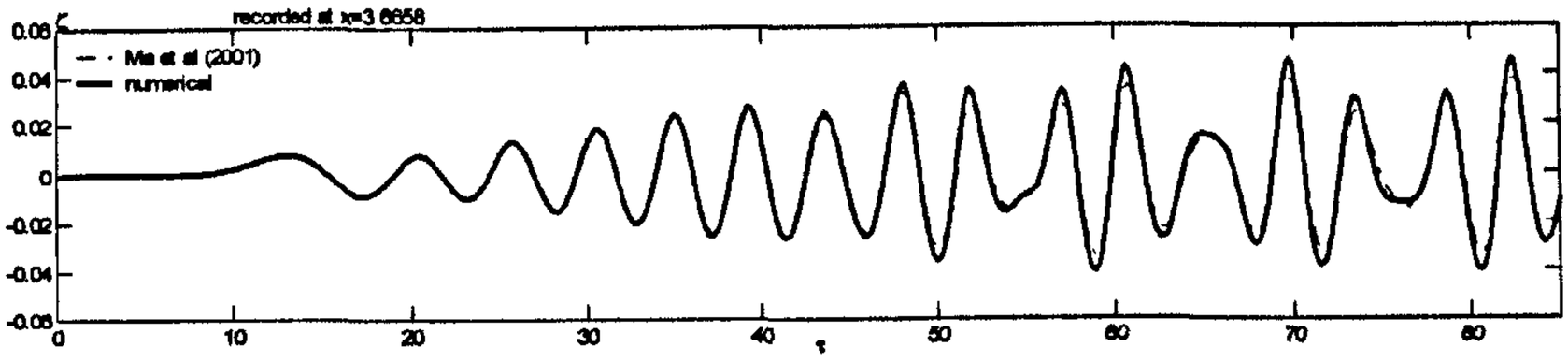

(b) Recorded at x=3.6658

Fig.7.1.5 Comparison of wave histories for a_1=0.016, a_2=0.5a_1, ω_1=1.45 and ω_2= 2.03
(Solid line: QALE-FEM; Dotted lines: conventional FEM (Ma, Wu & Eatock Taylor,2001b))

7.1.3. Random waves

The QALE-FEM is also used to simulating random waves. In order to compare with the experimental results given by Nestegard (1999), the same motion of the wavemaker as those described in Nestegard (1999) is used, which is specified by a Fourier series with different scaling factors (α_{random}). The Fourier series is shown in Fig. 7.1.6.

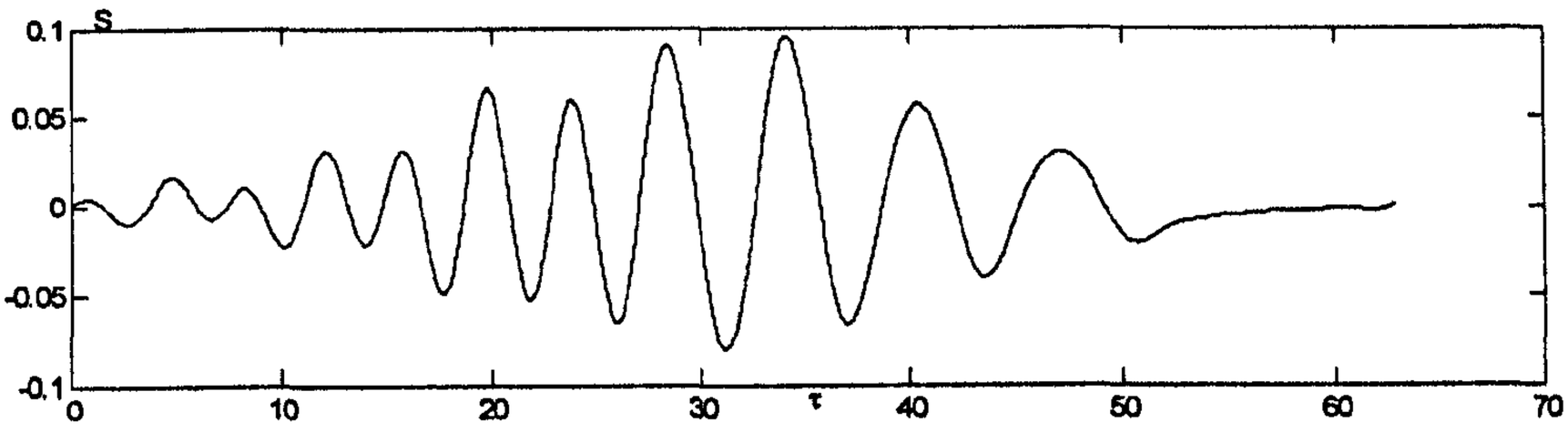

Fig.7.1.6 Fourier series used to generate random waves

The water waves generated by this motion are focused at a point in the tank to form a large and steep wave. To model this case, the tank length is chosen as 20. The time step is about 0.0242 and the number of elements is 183,240. Fig. 7.1.7 shows the wave histories recorded at $x = 3.436$ (where the wave is expected to focus) together with the experimental data provided by Nestegard (1999) for the scaling factors equal to 0.612 and 0.749. It can be seen that the agreement of the numerical results with the experimental data is satisfactory. Particularly the largest wave crests are excellently predicted by the numerical analysis.

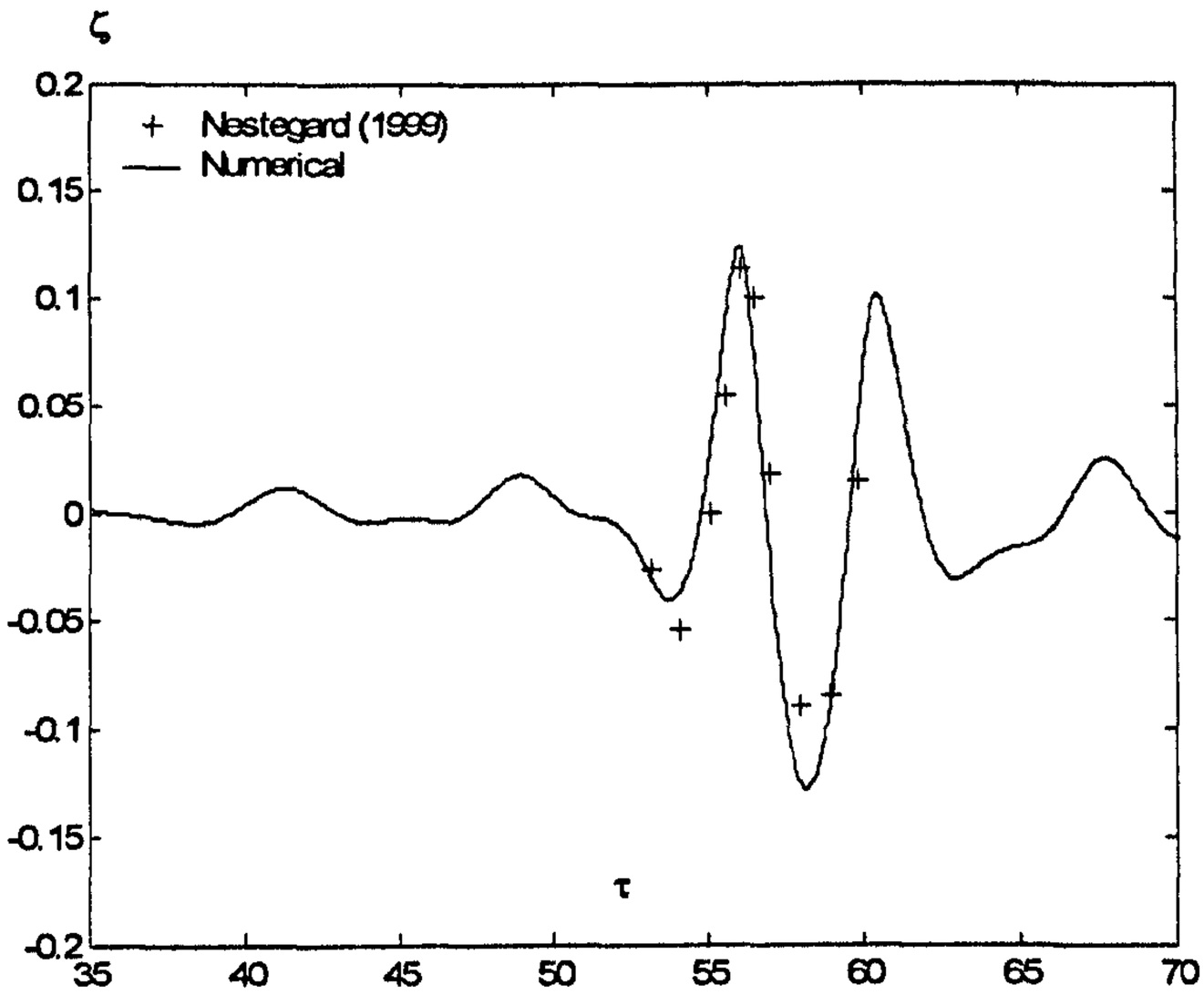

Fig.7.1.7 (a) ($\alpha_{random} = 0.612$)

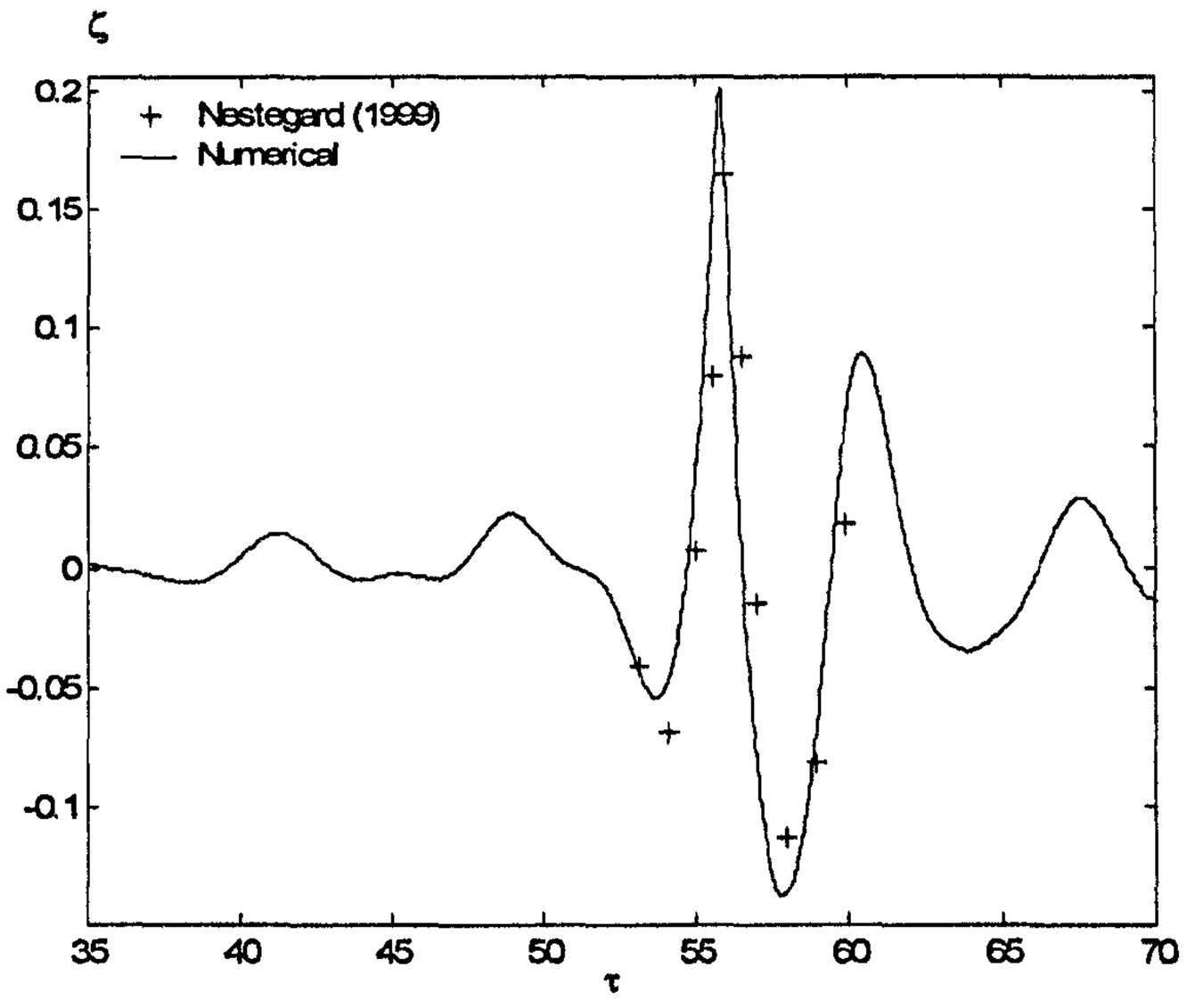

Fig.7.1.7 (b) ($\alpha_{random} = 0.749$)

Fig.7.1.7 Comparison of wave histories at x =3.436 with measured data given by Nestegard (1999)

In this section, the newly developed QALE-FEM method has been validated by comparing its numerical predictions with published analytical solutions, experimental data and results from other methods. Monochromatic, bichromatic and random waves are generated by a wavemaker and their propagation is modelled. The results given by the present method agree well with published data. This implies that the present QALE-FEM method has similar accuracy with the conventional FEM.

7.2. Convergence investigation

The above test cases have given excellent results in cases with different wave amplitudes. In those cases, the time steps are very small, e.g. *T*/200. The initial mesh used is also same for those cases. As has been known, the mesh size and the time step are two important factors which affect the convergence behaviour. Ma (1998) suggested that 40 divisions in each length and 200 time steps per wave period may be required to obtain convergent results by using a structured mesh. The convergence property of QALE-FEM is most likely to be different because a moving unstructured mesh is used. In order to investigate the convergence behaviour, an investigation is carried out in a tank with length equal to 12. For convenience, the monochromatic waves are used in these cases. The convergence prosperities in terms of different time steps, mesh size are tested. Different wave amplitudes are used. Convergence is examined by comparing the wave history recorded at different points. The mesh is generated with different divisions along the length (*dx*), but the divisions along the width is fixed because the resulting wave is now *y*-independent. Other parameters of the test cases are shown in Table.7.2.1. For each case in Table.7.2.1, two amplitudes of the wave maker are used, i.e. 0.0041 and 0.082 for $\omega = 1.45$, 0.0041 and 0.035 in for $\omega = 2.0$.

Table 7.2.1 Parameters for cases for convergence investigation

Δt	$\omega = 1.45, L$=12				$\omega = 2.0, L$=10			
	dx=0.058	*dx=0.073*	*dx=0.097*	*dx=0.146*	*dx=0.031*	*dx=0.039*	*dx=0.052*	*dx=0.078*
T/200	A1	B1	C1	D1	E1	F1	G1	H1
T/150	A2	B2	C2	D2	E2	F2	G2	H2
T/100	A3	B3	C3	D3	E3	F3	G3	H3
T/64	A4	B4	C4	D4	E4	F4	G4	H4
T/32	A5	B5	C5	D5	E5	F5	G5	H5

7.2.1. Convergence *vs* different time steps

In order to investigate the effect of the time step on the convergence, cases with $\Delta t = T/200, T/150, T/100, T/64$ and $T/32$ as shown in Table. 7.2.1 are carried out. Fig.7.2.1 shows the results of case a=0.035, $\omega = 2.0$. In these case, L=10, *dx=0.052* (G1 to G5), i.e. about 30 nodes per wave length along the *x*-direction. It is observed that there are no evident differences between the results in case $\Delta t < T/64$ from Fig.7.2.1a and 7.2.1b. However, the results for $\Delta t = T/32$ seems different to that for $\Delta t = T/200$ (Figs. 7.2.1c and 7.2.1d).

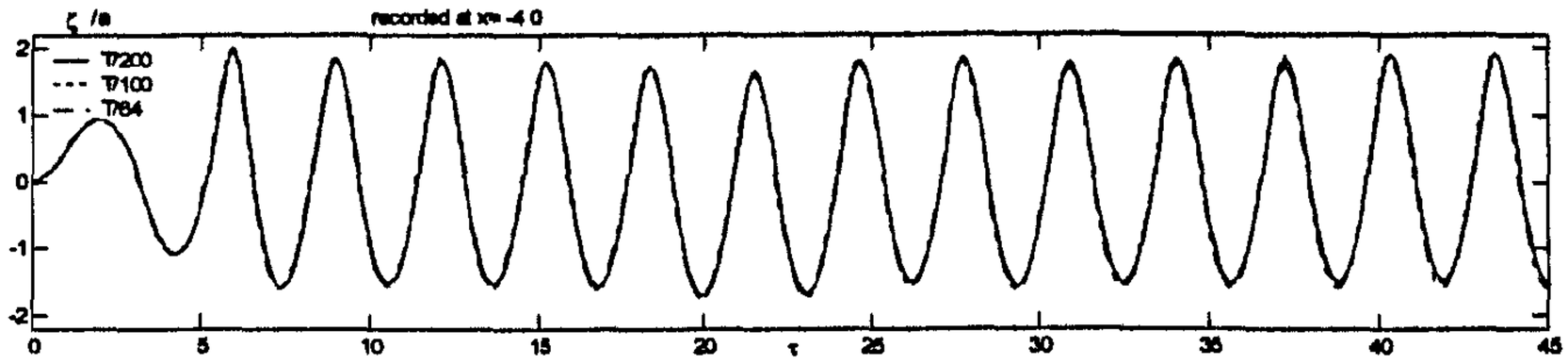

Fig.7.2.1 (a) recorded at x= -4

Fig.7.2.1 (b) recorded at x=0

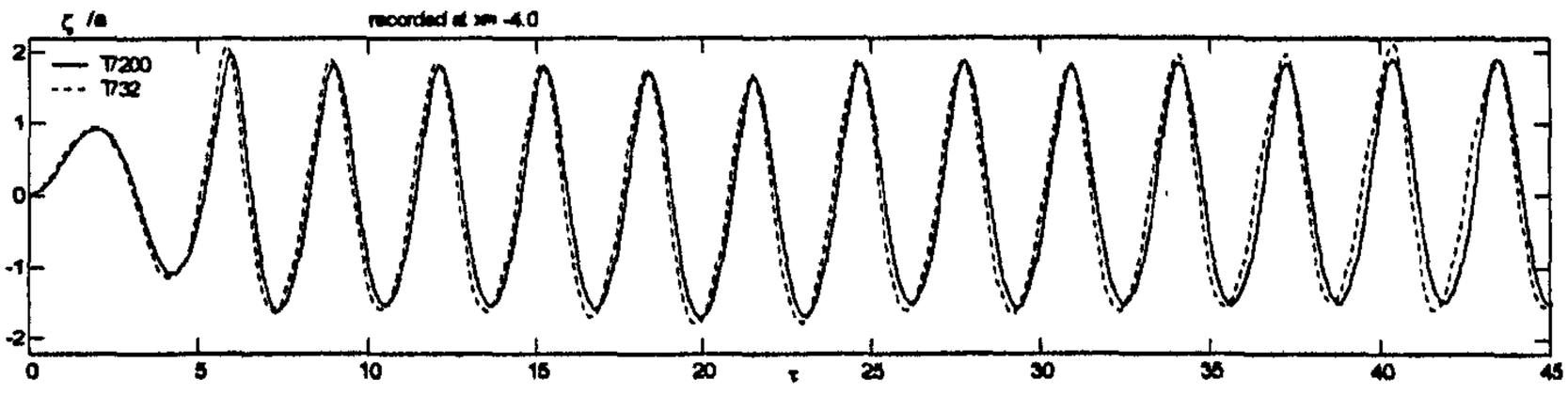

Fig.7.2.1 (c) recorded at x= -4

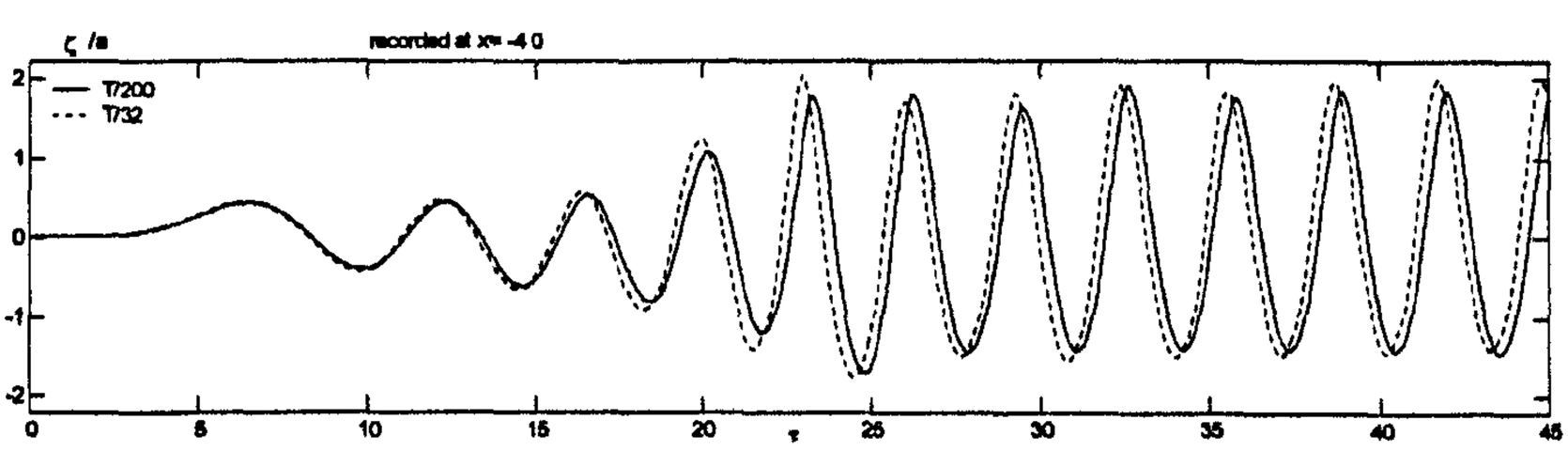

Fig.7.2.1 (d) recorded at x=0

Fig.7.2.1 Time histories of the wave elevations in cases with different time steps

(a=0.035, $\omega = 2.0$)

The results of cases with smaller wave amplitude are also investigated and plotted as Fig.7.2.2. From this figure, it is found that the results for $\Delta t = T/32$ are very close to those for $\Delta t = T/200$ when the wave amplitude is smaller. Based on these tests, one may use $\Delta t = T/32$ for case with small waves and $\Delta t = T/64$ for steeper waves. Similar conclusions are obtained for other cases in Tab.7.2.1.

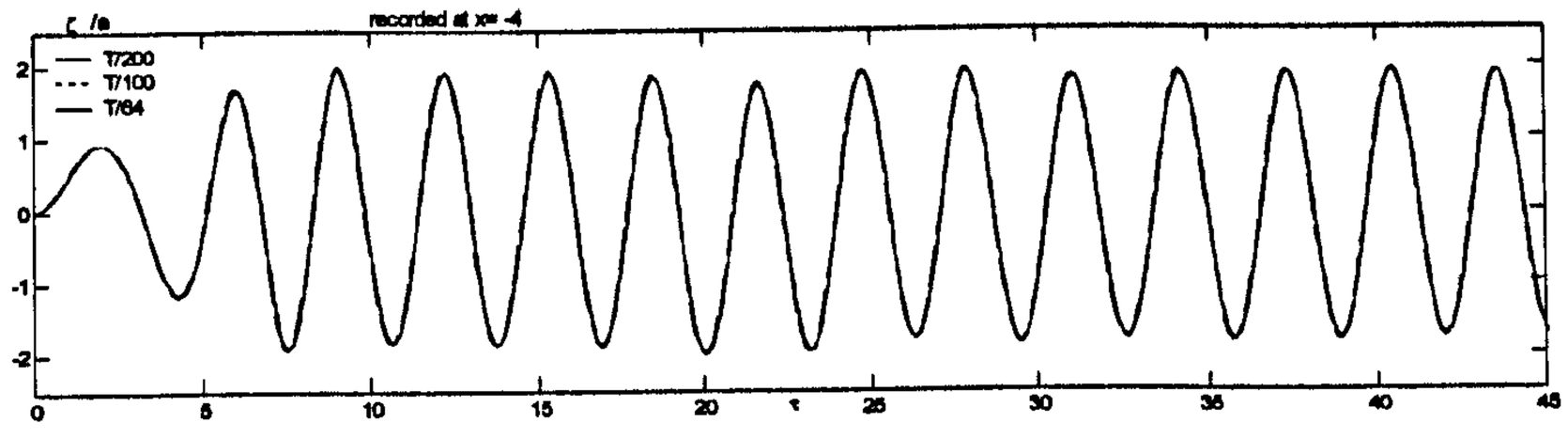

Fig.7.2.2 (a) recorded at x= -4

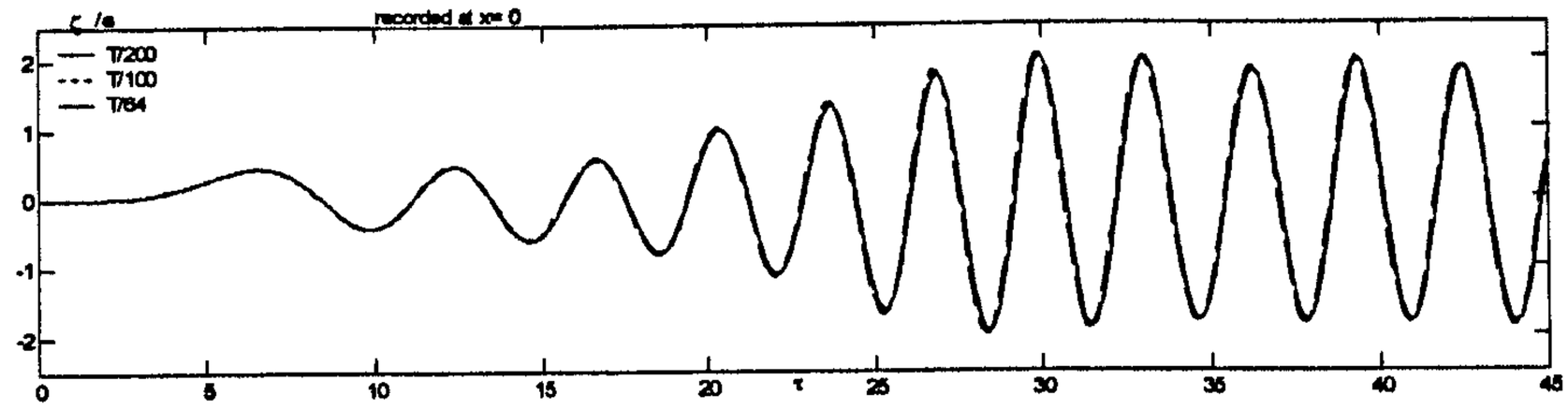

Fig.7.2.2 (b) recorded at x=0

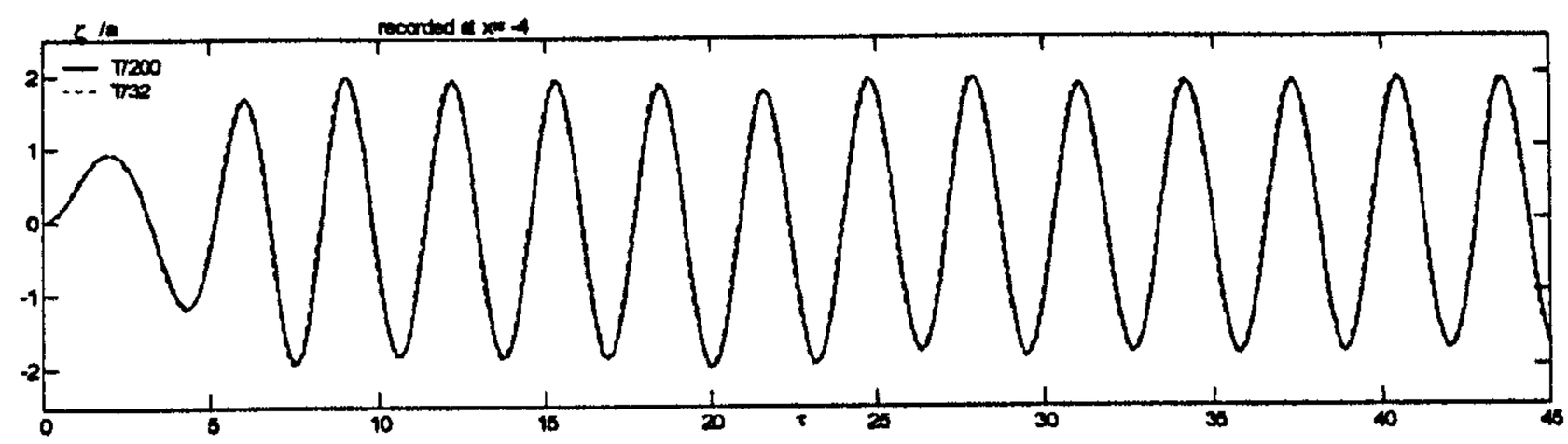

Fig.7.2.2 (c) recorded at x= -4

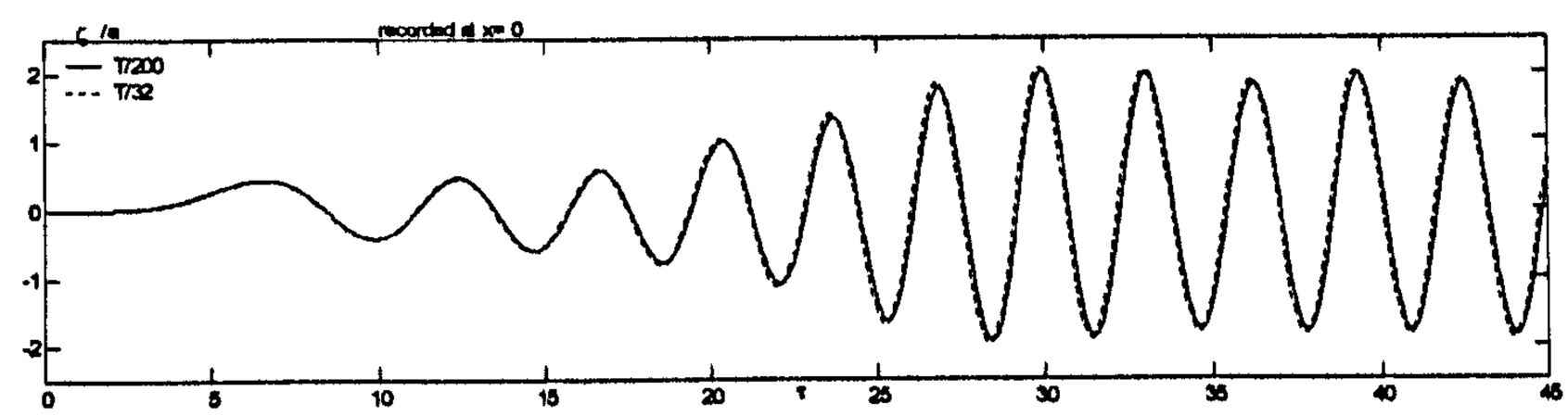

Fig.7.2.2 (d) recorded at x=0

Fig.7.2.2 Time histories of the wave elevation in cases with different time steps

(a=0.0041, $\omega = 2.0$)

7.2.2. Convergence *vs* different mesh size

On the other hand, the mesh size also affects the convergence property. In order to investigate the relation between convergence and mesh size, cases with different mesh size are investigated as shown in Table. 7.2.1. In these cases, the divisions along the x-direction are chosen as 20, 30,40 and 50 per wavelength, respectively. The corresponding mesh size in the x-

direction can be found in Table. 7.2.1., i.e. 0.146, 0.097, 0.073 and 0.058 for cases with $\omega = 1.45$ and 0.078, 0.052, 0.039 and 0.031 for cases with $\omega = 2.0$. Fig. 7.2.3 shows the time history of the wave elevation for different mesh sizes and different time steps in case a=0.035, $\omega = 2.0$, while Fig.7.2.4 shows the corresponding case with smaller wave amplitude of those in Fig.7.2.3.

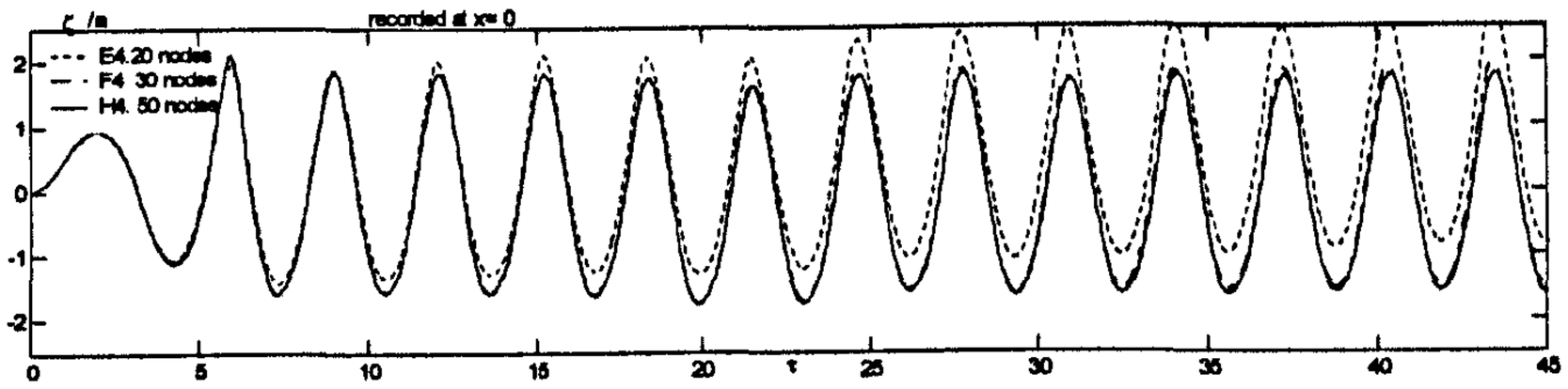

(a) recorded at x= -4 $\Delta t = T/64$

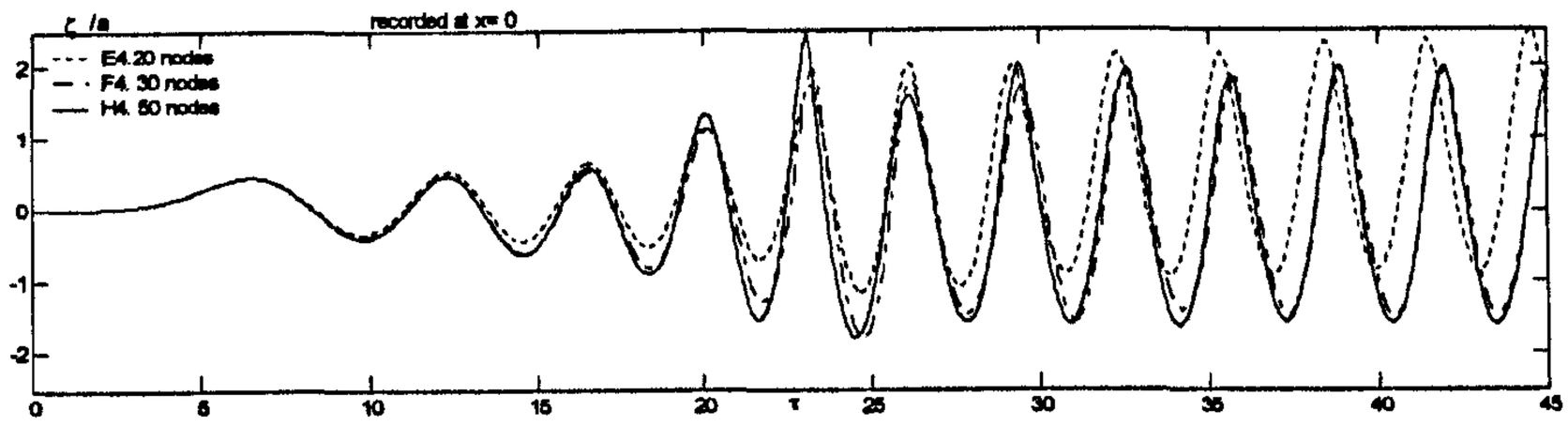

(b) recorded at x=0 $\Delta t = T/64$

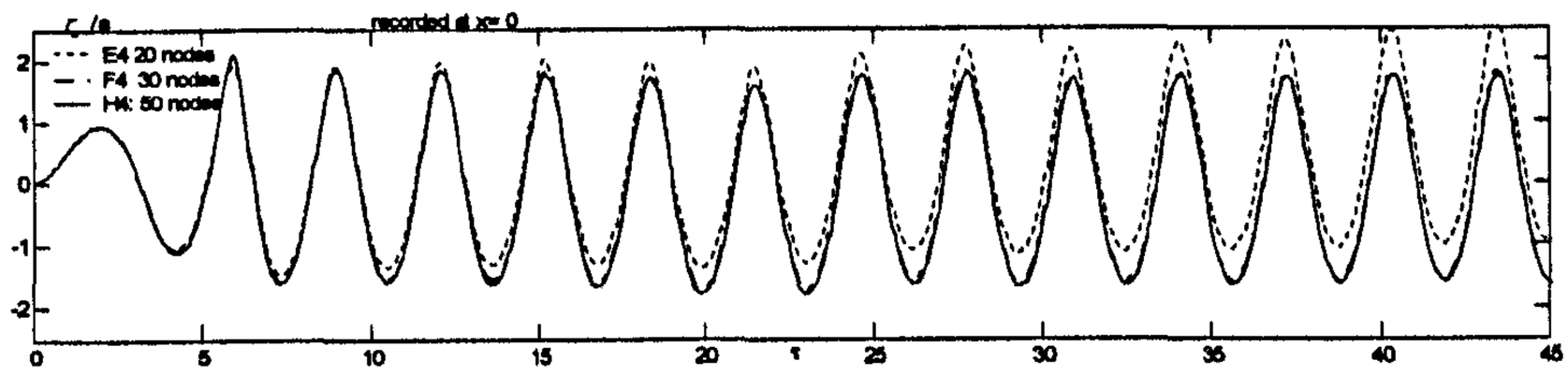

(c) recorded at x= -4 $\Delta t = T/100$

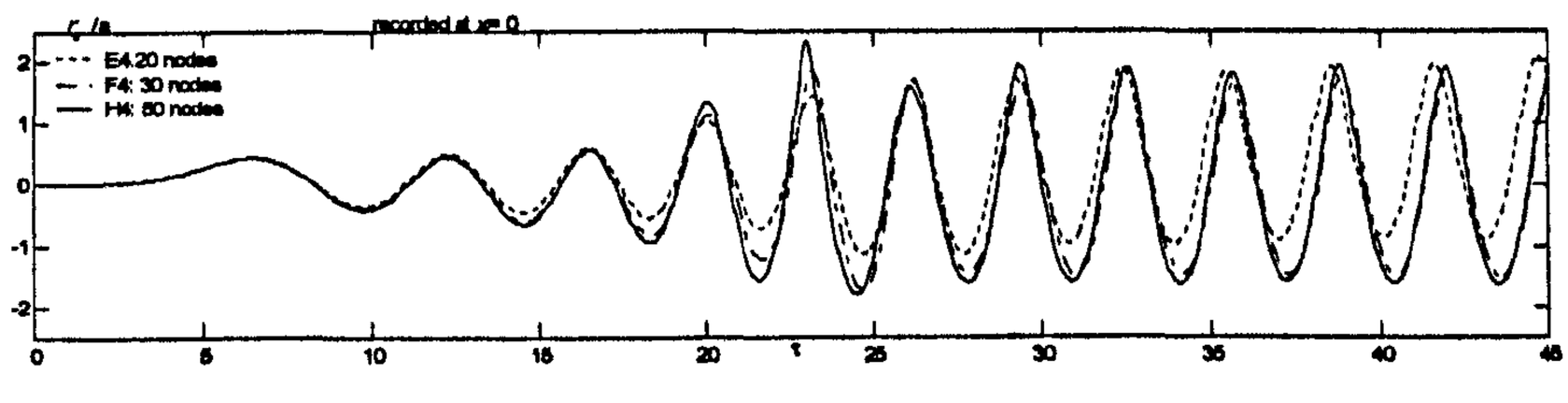

(d) recorded at x=0 $\Delta t = T/100$

Fig.7.2.3. Time histories of the wave elevation in cases with different mesh sizes and different time steps (a=0.035, $\omega = 2.0$)

From Fig. 7.2.3a and 7.2.3b, it is observed that in cases with a=0.035, $\omega = 2.0, \Delta t = T/64$, there are no evident difference between the results from cases where 30 or more nodes are distributed in a wavelength along the x-direction on the free surface. However, when the x-directional size (Δx) is 0.078 (about 20 nodes per wavelength), the results seem not convergent (dotted curve in Fig. 7.2.3). This means the results with mesh size of 0.078 are not convergent. Similar results can be obtained in case with a=0.035, $\omega = 2.0, \Delta t = T/100$ from Fig. 7.2.3c and 7.2.3d.

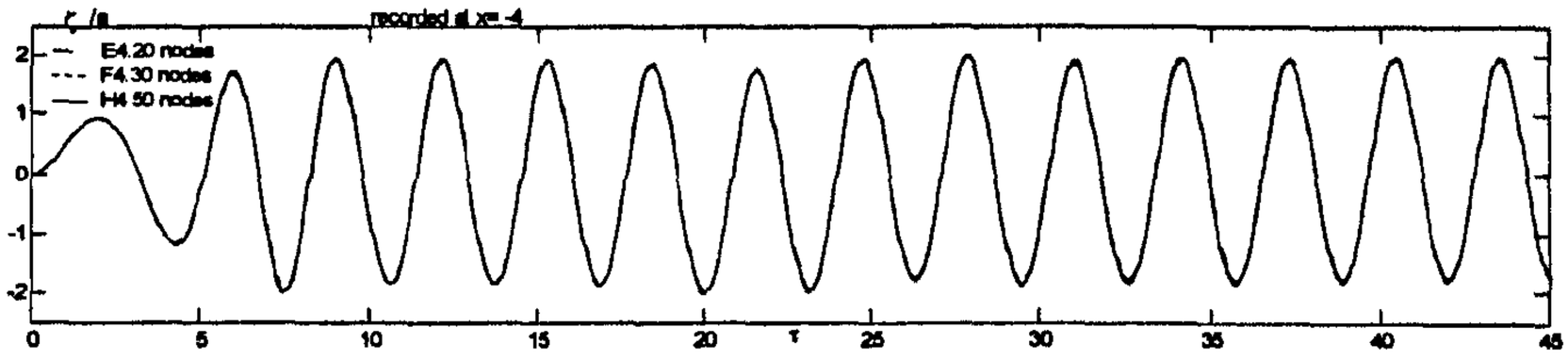

(a)recorded at x= -4 $\Delta t = T/64$

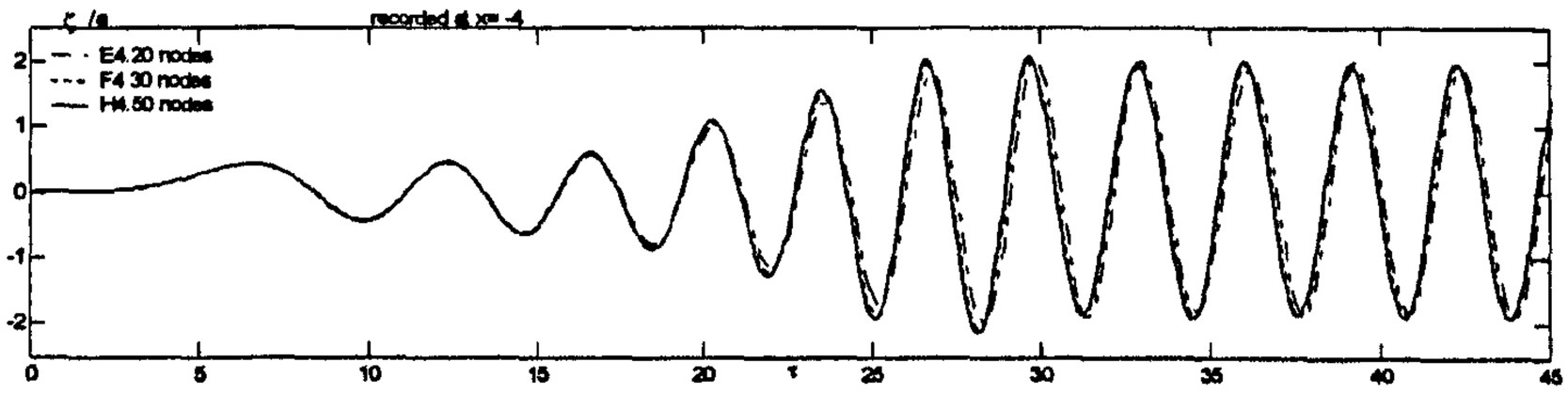

(b)recorded at x=0 $\Delta t = T/64$

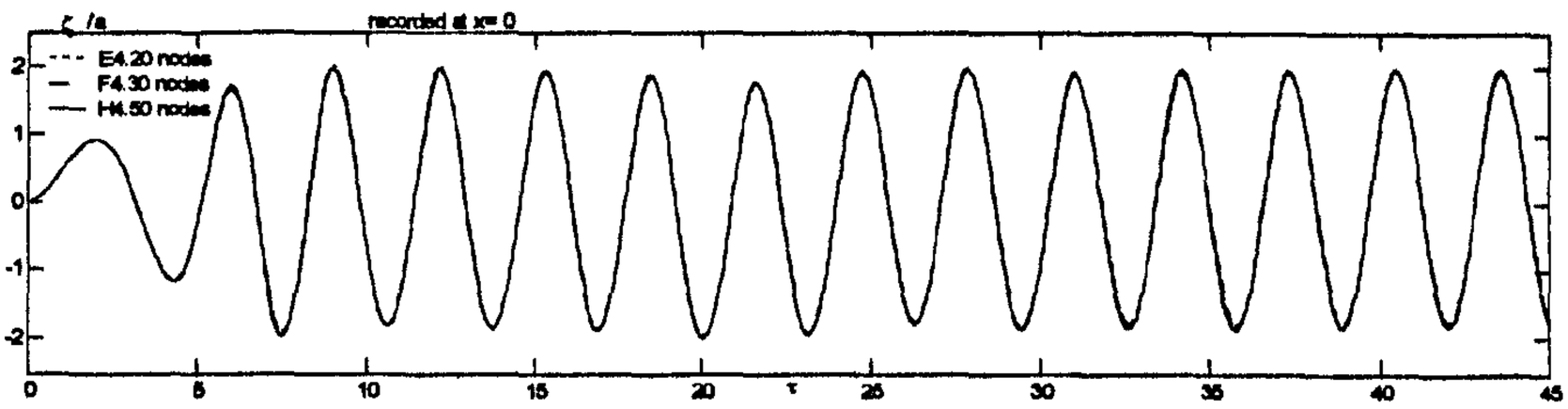

(c) recorded at x= -4 $\Delta t = T/100$

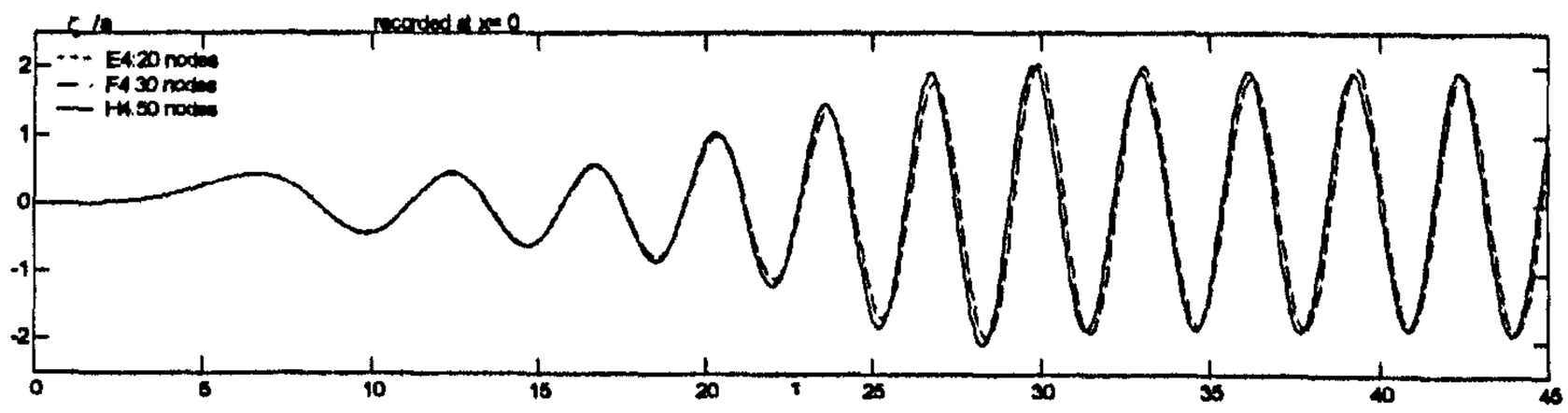

(d) recorded at x=0 $\Delta t = T/100$

Fig.7.2.4. Time histories of the wave elevation in cases with different mesh sizes and different time steps (a=0.0041, $\omega = 2.0$)

However, in cases with small wave amplitudes, the difference between the results for $\Delta x \approx \lambda/20$ and those for $\Delta x \leq \lambda/30$ is smaller. Not like that in Fig 7.2.3, the results for

$\Delta x \approx \lambda/20$ is still convergent in this figure. This implies for case with very small steepness, e.g., linear waves, the mesh size with $\Delta x \approx \lambda/20$ may be small enough to get a convergent result. Because this work focuses on the nonlinear waves, at least 30 nodes in a wave length are required. It should be noted that the conclusion mentioned above may not work in a case involving a floating body, since the convergence rate of the ISITIMFB procedure also needs to be investigated for the same purpose. Those investigations will be presented in Chapters 8 and 9.

7.3. Investigation on some numerical techniques

7.3.1. Investigation of different velocity calculation methods

In Section 5.3, comparison has been given between two velocity calculation methods in the case of solitary wave. More investigations of periodic waves are made in this section to test these two approaches. To do so, similar cases as B3 in Table 7.2.1 are used. In these cases, $\omega = 1.45, L = 12$, the time step is taken as $T/100$ and the mesh size on the free surface is taken as $\Delta x \approx \lambda/30$, the wave amplitudes are taken as 0.082 and 0.1, respectively. Both 'Method 1' and 'Method 2' are used to approximate $\phi_{P_{12}}$.

Fig.7.3.1 shows the wave history recorded at x= -4 in case with a=0.082. For comparison, the result from the conventional FEM by Ma (1998) is also plotted together. It is found that the difference between the results for 'Method 1' and those for 'Method 2' is negligible. Both results agree well with those from Ma (1998).

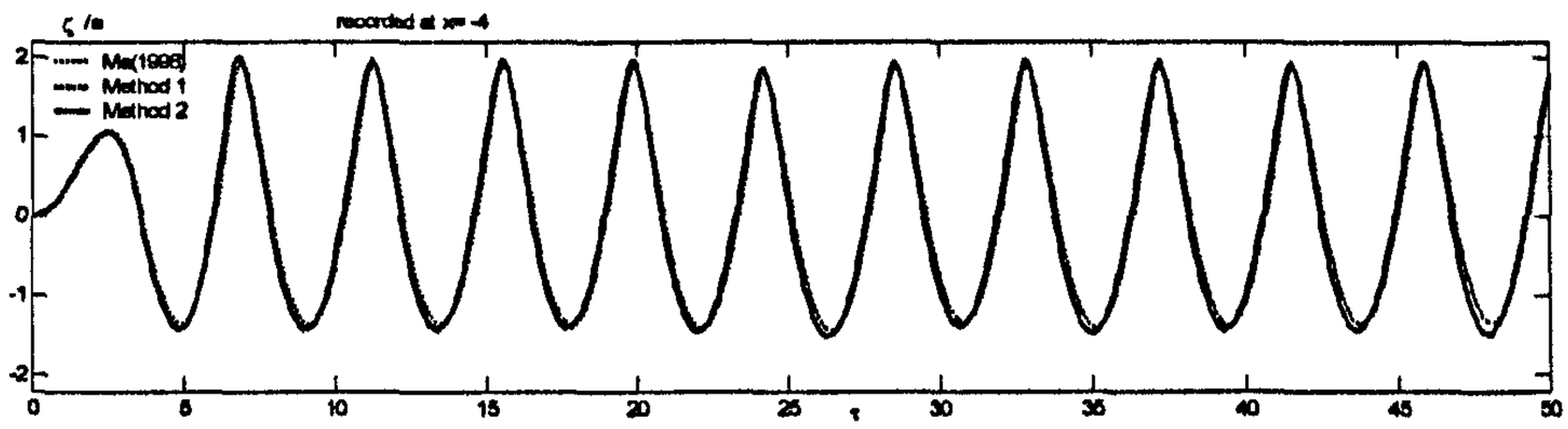

Fig.7.3.1 Comparison of the wave history recorded at x= -4 in case with different methods to approximate $\phi_{P_{12}}$ (a=0.082, $\omega = 1.45$, $\Delta t = T/100$, the time step used in Ma (1998) is T/200)

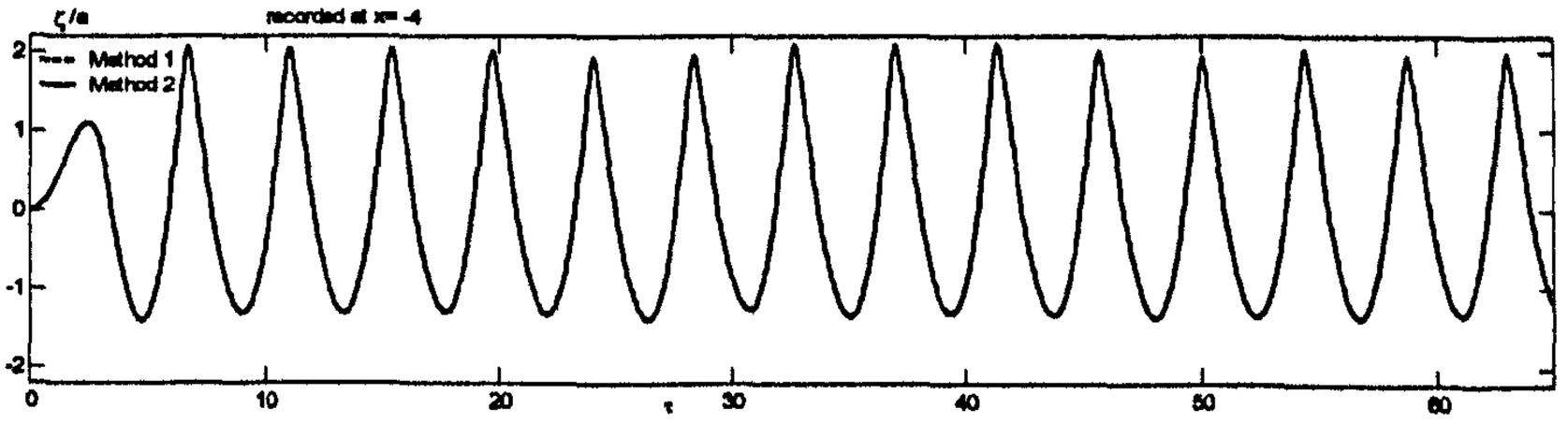

Fig.7.3.2 Comparison of the wave history recorded at x= -4 in case with different methods to approximate $\phi_{P_{12}}$ (a=0.1, $\omega = 1.45$, $\Delta t = T/100$)

In the case with a=0.10, Fig. 7.3.2 illustrates the wave history recorded at the same points as Fig. 7.3.1. It is also found that the difference between these two results is negligible. To further compare these two methods, the wave profiles in different instances are plotted as Fig. 7.3.3. These figures all show excellent agreement between the results from different velocity calculation schemes.

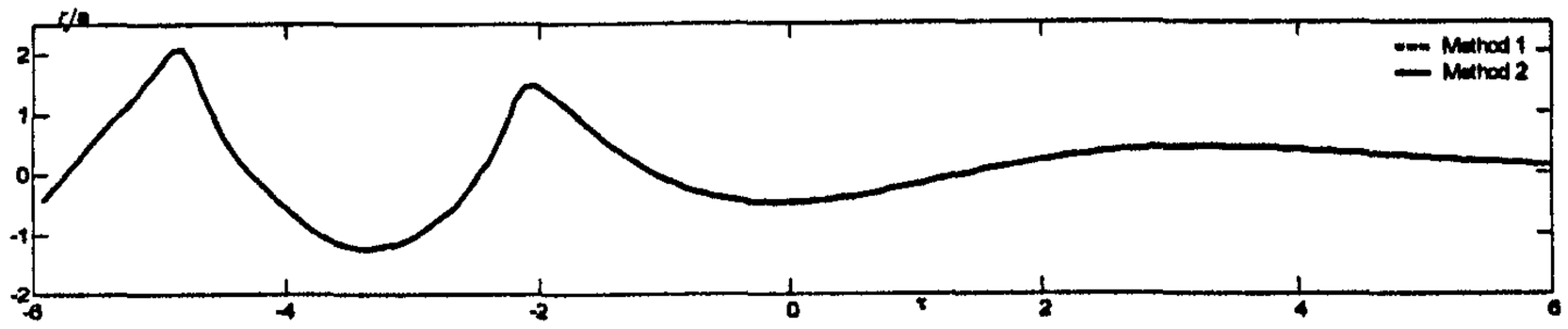

Fig.7.3.3 (a) wave profile at $\tau = 11.2658$

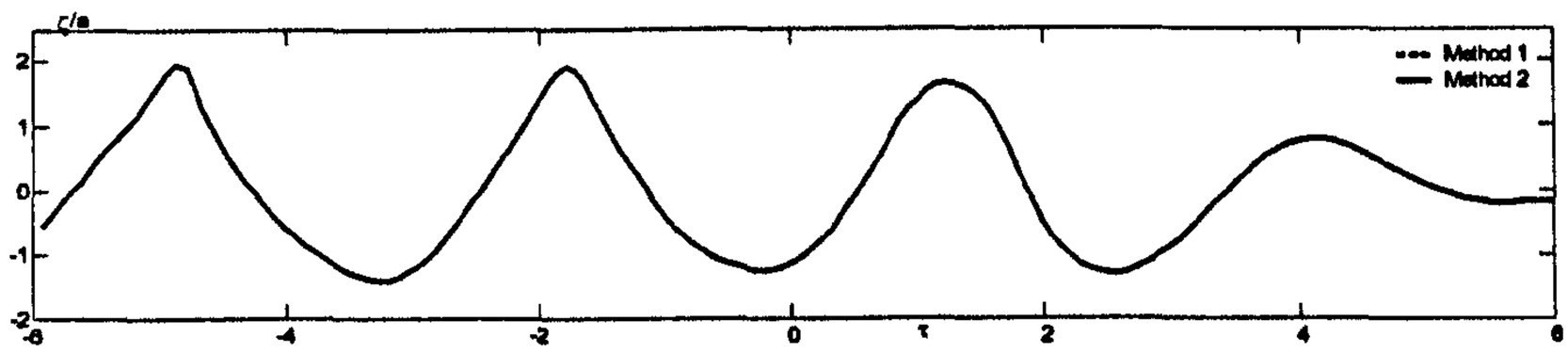

Fig.7.3.3 (b) wave profile at $\tau = 24.2648$

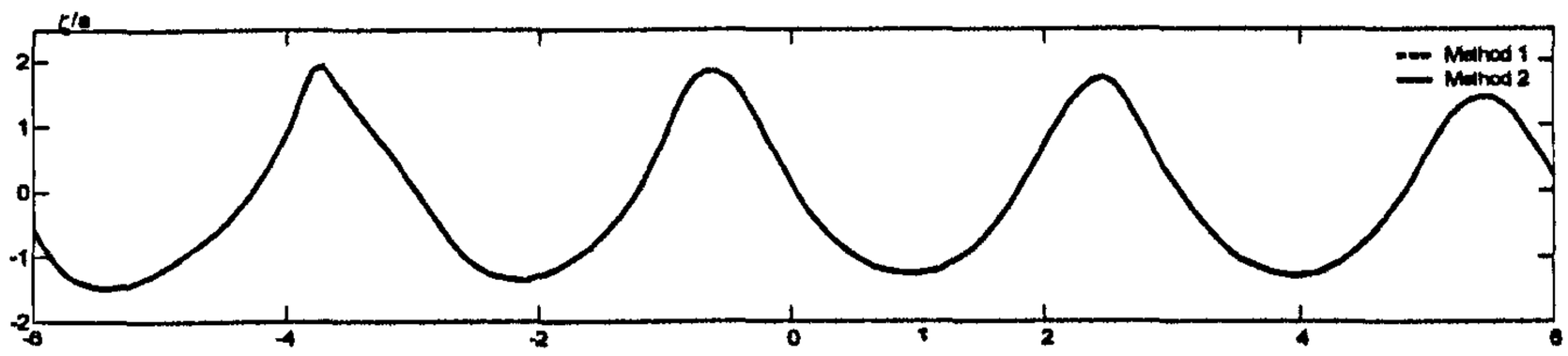

Fig.7.3.3 (c) wave profile at $\tau = 47.662$

Fig.7.3.3 Wave profiles at different instance (a=0.1, $\omega = 1.45, \Delta t = T/100$)

. As a result of these investigations, 'Method 2' is used to approximate $\phi_{P_{12}}$ in the following application, since this method requires less CPU time than the other. It should be noted that in case with an overturning wave, the 'Method 2' may not give results of the same accuracy as 'Method 1'. Because in such a case, the spatial derivatives of the velocity potential near the free surface, particularly near the overturning jet (crest), are larger than those in the above two cases, therefore the interpolating function of the MLS for $\phi_{P_{11}}$ and that for $\phi_{P_{12}}$ are quite different. In these cases, 'Method 1' should be used.

One may also find that for the case with a=0.1, $\omega = 1.45, \Delta t = T/100$, Fig. 7.3.2 and Fig. 7.3.3 did not give the results by Ma (1998). The reason is that a structured mesh with vertical lines in z-direction is used in his study. When the waves become steeper, the element near the

free surface might be close to flat (Fig. 7.3.4a). Once some elements near the free surface become close to flat, it is difficult for Ma (1998) to obtain convergent results.

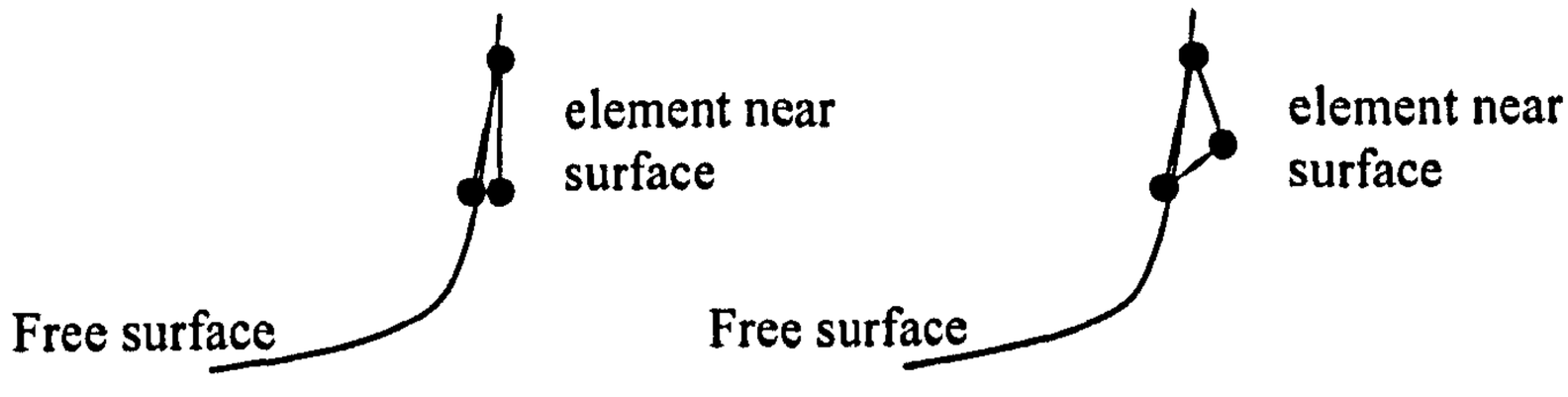

(a) structured mesh (b) unstructured mesh

Fig.7.3.4 Sketch of an element near the free surface

With the QALE-FEM method, the above phenomena, i.e, near flat element, may not appear since an unstructured mesh is used (Fig. 7.3.4b). Therefore the QALE-FEM method may give convergent results for these cases similar to Fig. 7.3.2.

7.3.2. Investigation of absorbing boundaries

In this work, a Sommerfeld condition with a damping zone near the far end wall is used to reduce the reflection from the far end wall. This technique is the same as that in Ma (1998). Ma (1998) has investigated the efficiency of this technique in cases with structured meshes. However, in this work, the mesh is unstructured and is moving at every time step. This technique to absorb the reflection may not work. In order to validate it, numerical investigations are necessary. The numerical validation in Section 7.1 indicated that the results (wave history or wave profile) using QALE-FEM agree well with those by the conventional FEM in Ma (1998). These validations gave indirect evidence that this technique works well in the application of QALE-FEM. Further comparison between the results obtained by using tanks with different widths is made in this section.

To do so, a bichromatic wave with a_1=0.016, a_2=0.75a_1, ω_1=1.45 and ω_2= 2.175 is generated in a short tank with L=*15* and a long tank with L=*30* respectively. In these cases, there are about 30 nodes in a wavelength of the wave component of ω_2= 2.175. The time step is taken as 0.0043 (T_1/100). Fig. 7.3.5 shows the wave history recorded at a point. It is observed that the wave generated in a short tank is close to that generated in a longer tank. This implies that the method for the radiation condition works well in this case. The reflection from the far end wall is very small. The wave profiles in different instances are shown in Fig.7.3.6. It is observed that after long-time simulation, the wave profiles in tanks with different widths show little difference. This results support the conclusion, i.e. the current technique to remove the reflection, in advance.

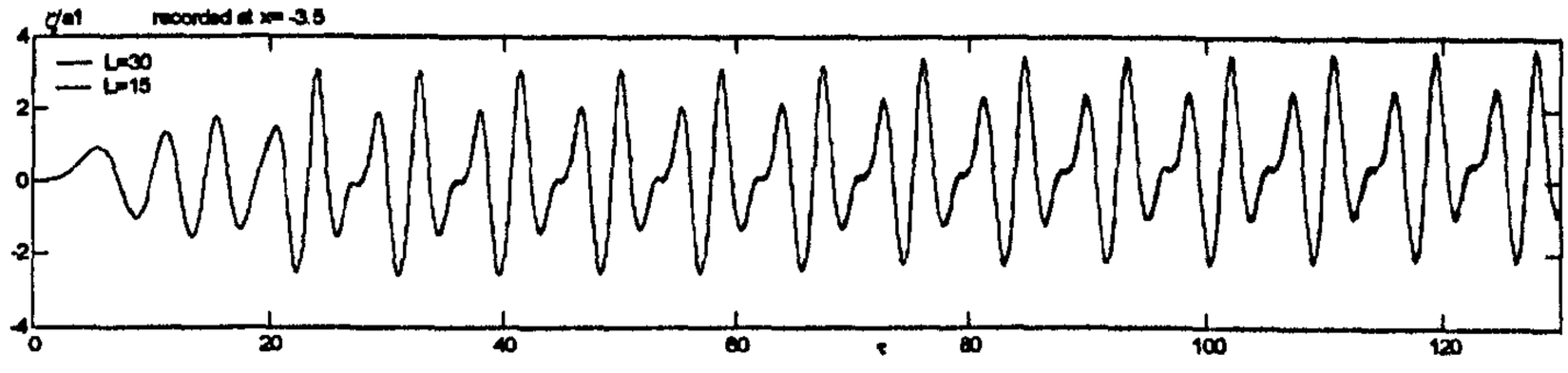

Fig.7.3.5 Wave histories recorded at x= -3.5

(a_1=0.016, a_2=0.75a_1, ω_1=1.45 and ω_2= 2.175)

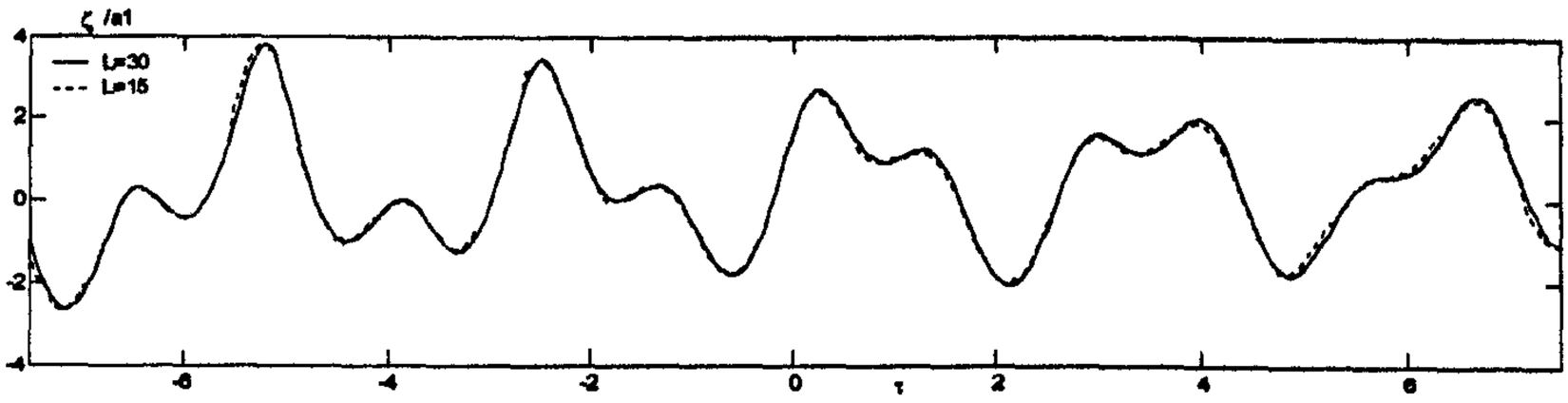

Fig. 7.3.6 (a) τ=95.33

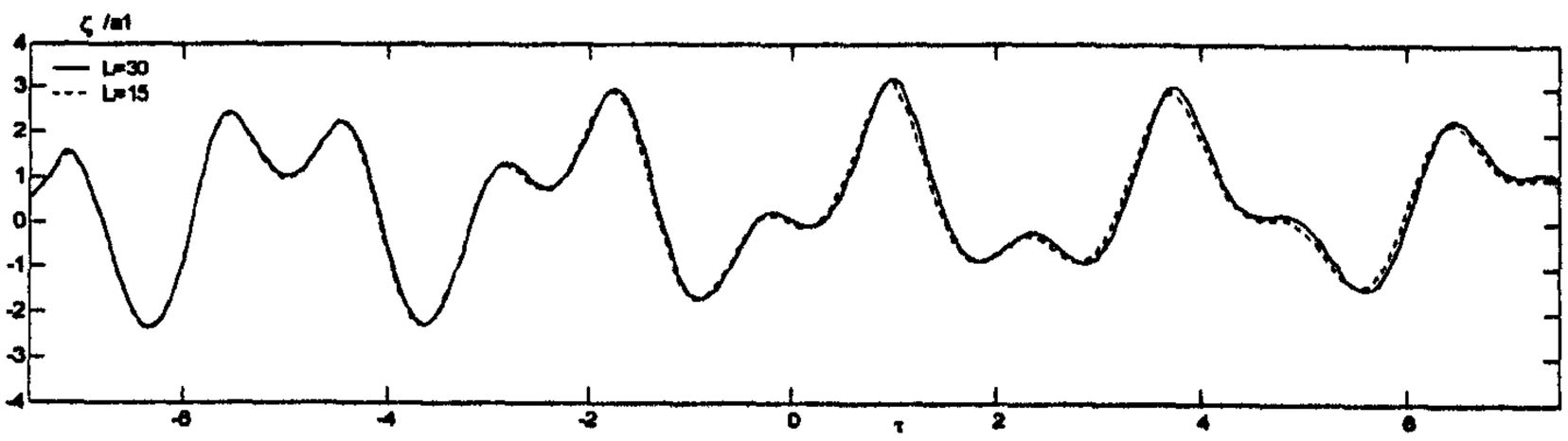

Fig. 7.3.6 (b) τ=100.10

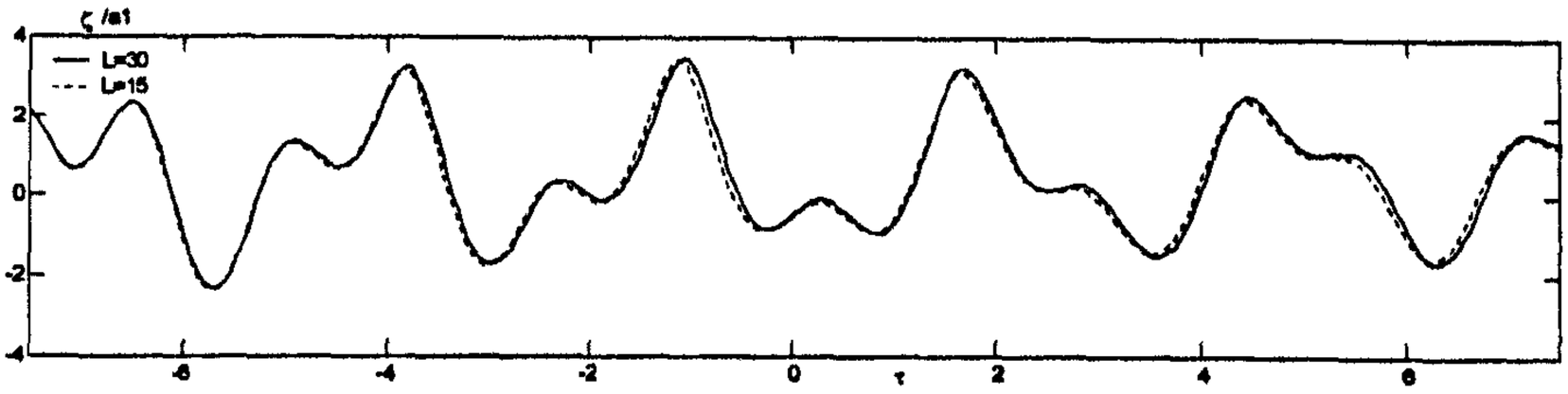

Fig. 7.3.6 (c) τ=110.06

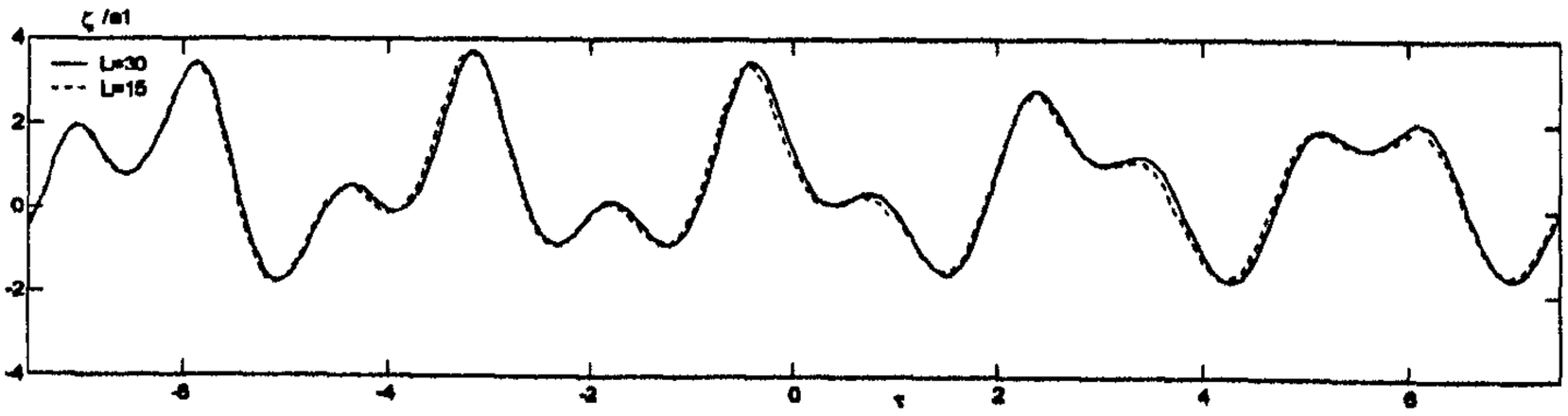

Fig. 7.3.6 (d) τ=120.03

Fig. 7.3.6 Wave profiles in different instances

(a_1=0.016, a_2=0.75a_1, ω_1=1.45 and ω_2= 2.175)

7.3.3. Numerical investigation on wider tanks

The main aim of this work is to simulate 3D wave-body interaction. In those cases, the tank requires larger width than those in the above validations where the tank of B=0.15. Before we apply the QALE-FEM to 3D problem, it is necessary to investigate all the techniques, e.g., recovery technique, work well in such a wider tank. To do so, many cases are carried out in a tank with L=12, B=2. The meshes are unstructured in these cases; the x-directional and y-directional mesh sizes on the free surface are taken as $\Delta x = \Delta y \approx \lambda/30$, respectively. The nonlinear waves are generated by using Eqs. (7.1.1) and (7.1.2) with a=0.082, $\omega = 1.45$. The time step is $\Delta\tau = T/64$. The wave history recorded at different points in the central line (y=0) are compared with those obtained by using a narrow tank with L=12, B=0.15. The results are shown in Fig. 7.3.7.

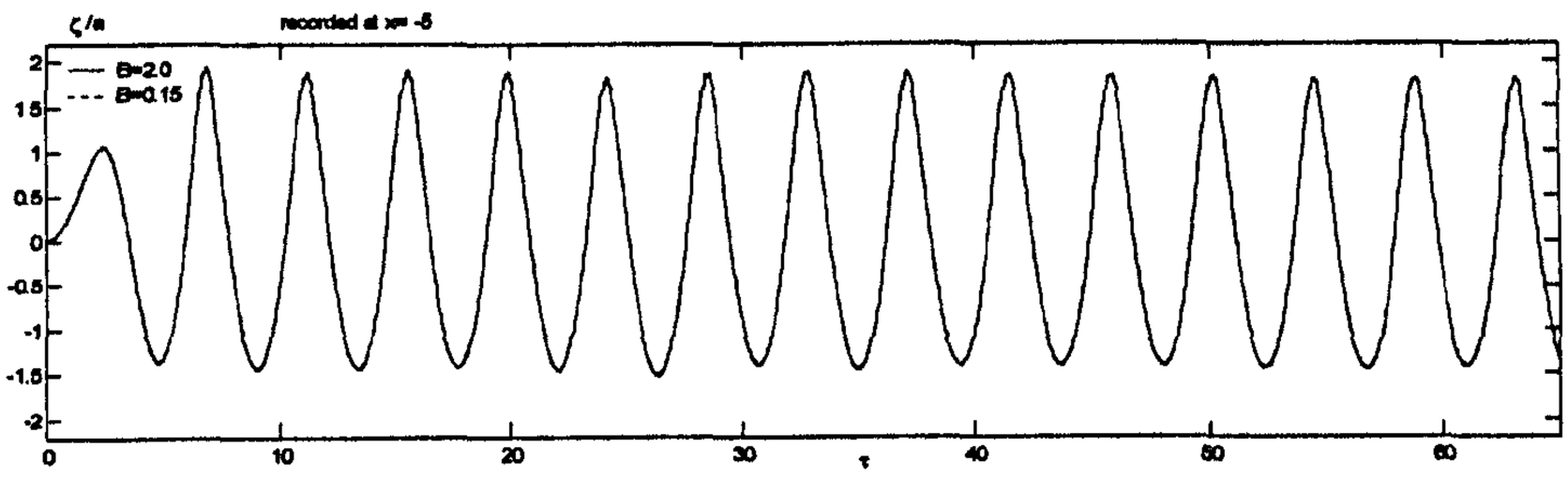

(a) wave history record at x= -5,y=0

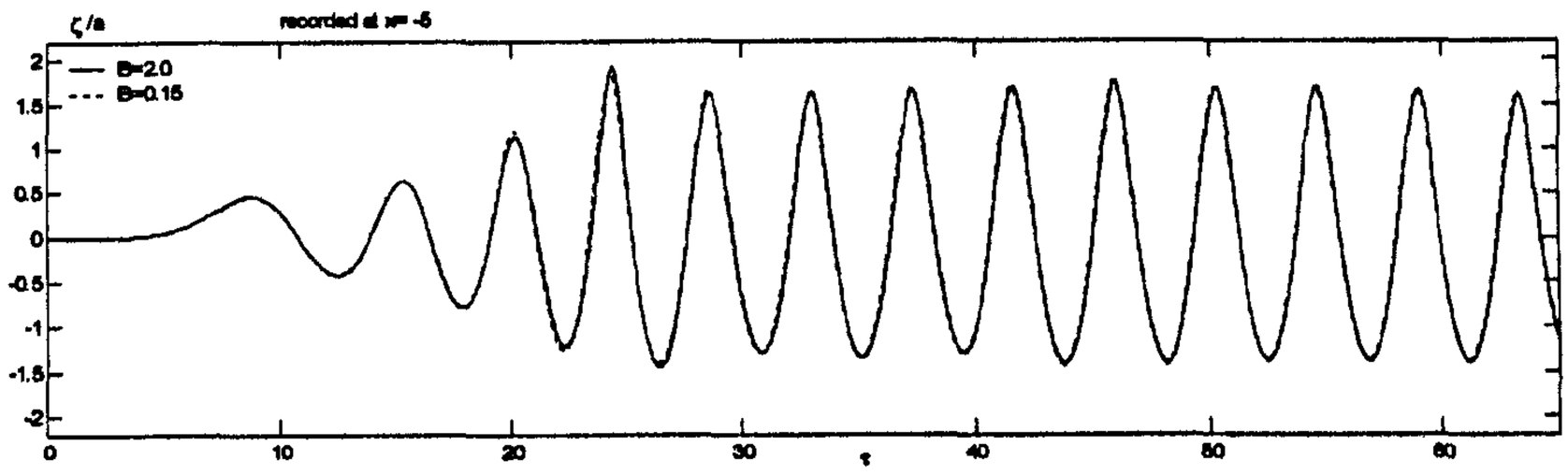

(b) wave history record at x= -1,y=0

Fig.7.3.7 Comparison of the wave histories obtained by different tanks (a=0.082, $\omega = 1.45$, $\Delta t = T/64$ for QALE-FEM and $\Delta t = T/200$ for conventional FEM by Ma, 1998)

It is observed that there is no evident difference between the results obtained in case with wide tank and with narrow tank. This implies that in cases with wider tank the QALE-FEM method still leads to satisfactory results. The corresponding wave profiles in different instances are plotted in Fig.7.3.8. It is found that the free surface in different instances is all very smooth. There is no 'saw-tooth' phenomenon. These results also support the statement that the patch

recovery technique used can successfully remove the 'saw-tooth' problem associated with the velocity calculation.

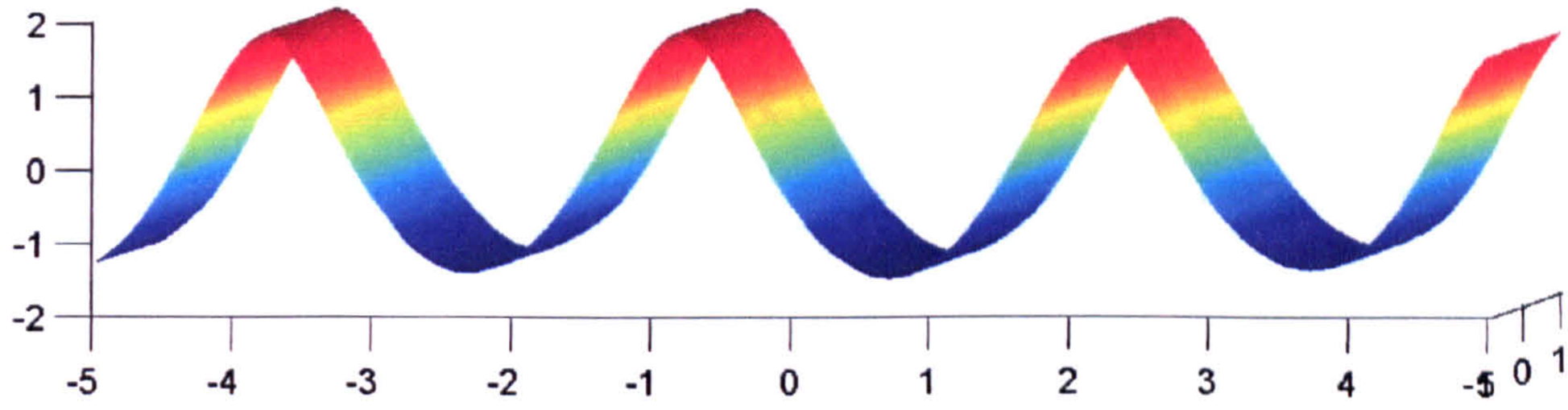

Fig.7.3.8 (a) $\tau = 10T$

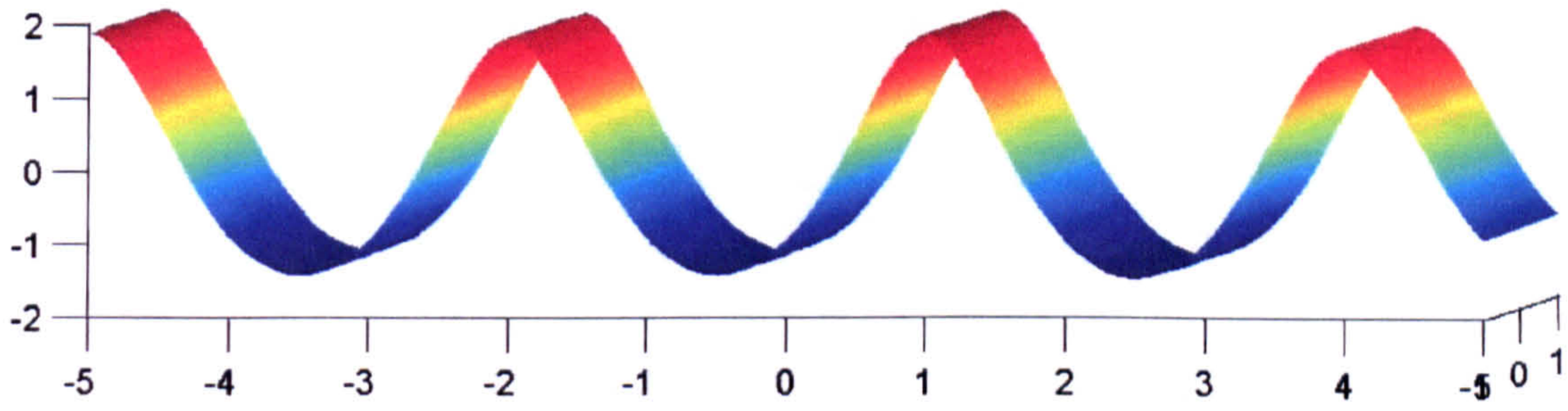

Fig.7.3.8 (b) $\tau = 10.5T$

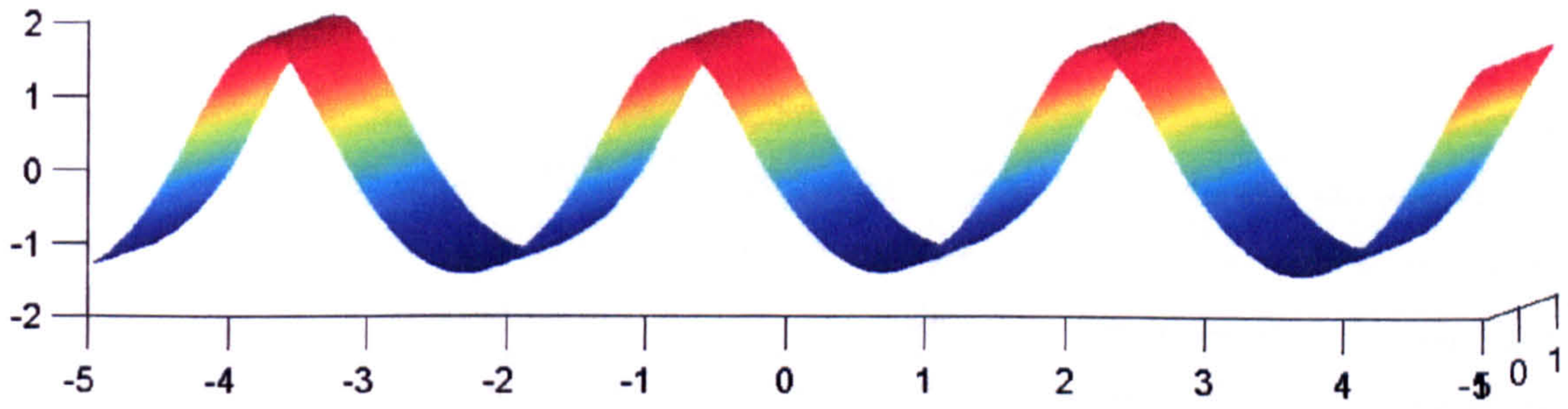

Fig.7.3.8 (c) $\tau = 15T$

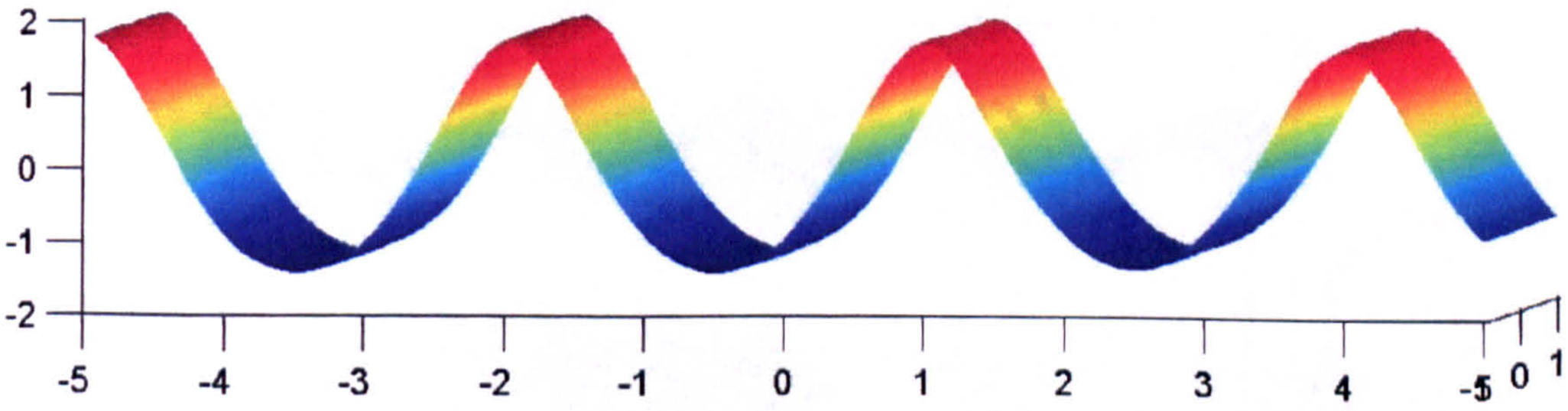

Fig.7.3.8 (d) $\tau = 15.5T$

Fig.7.3.8 Free surface profiles in different instances

(a=0.082, $\omega = 1.45$, $\Delta t = T/64$, L=12, B=2.0)

7.4. Reflection due to periodic bars on the sea bed

The QALE-FEM is now employed to simulate the interaction between waves and periodic bars on the seabed. Since the experimental demonstration by Heathershaw (1982), the problem has been studied by many researchers using various mathematical models with particular attention paid to Bragg resonance that leads to large reflecting waves. These models were developed by making various approximations, including linear perturbation approach by Davies, & Heathershaw (1984), multiple scale analysis by Mei (1985), mild-slope approach by Chamberlain & Porter (1995), fully linear analysis by Porter & Porter (2003) and so on. The results obtained from these models agreed well with experiments carried out by Heathershaw (1982) and Davies & Heathershaw (1984) in cases with small surface wave and bar wave steepness. Liu & Yue (1998) performed a fully nonlinear analysis using a spectral method and pointed out that the nonlinear effects may cause the downshift of reflection coefficient curves compared with results from the simplified models such as in Mei (1985).

In this section, the numerical results obtained by using the QALE-FEM will be compared with published experimental data and analytical/numerical solutions, with particular attention paid to the reflecting wave properties near the Bragg resonance. The main purpose of the comparisons is to further validate the new numerical method. Apart from this, certain results corresponding to larger wave amplitudes will also be presented in order to illustrate the nonlinear effects on the reflection.

The two cases to be considered are the same as those in Heathershaw (1982), i.e., bar patches with 4 and 10 sinusoidal bars on the seabed, respectively. The wave generator motions are as specified by Eqs. (7.1.1) and (7.1.2). The sketch of the fluid domain in this case is shown in Fig.7.4.1a. For ease of description, the side of the bar patch near the wavemaker is called the front side, and the other side the lee side. The initial meshes used are similar to that illustrated in Fig. 7.4.1b but much finer.

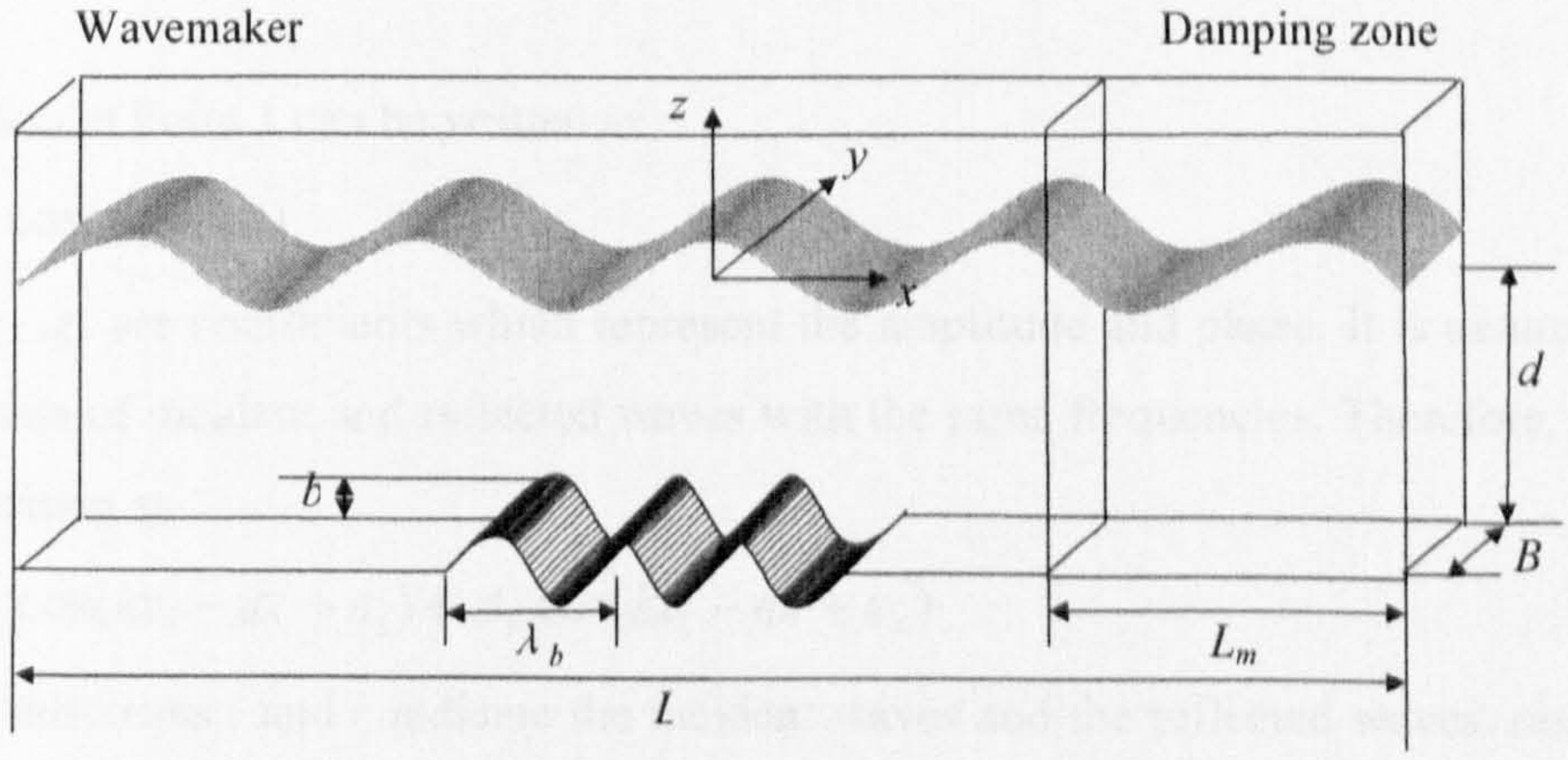

Fig.7.4.1 (a) Sketch of fluid domain

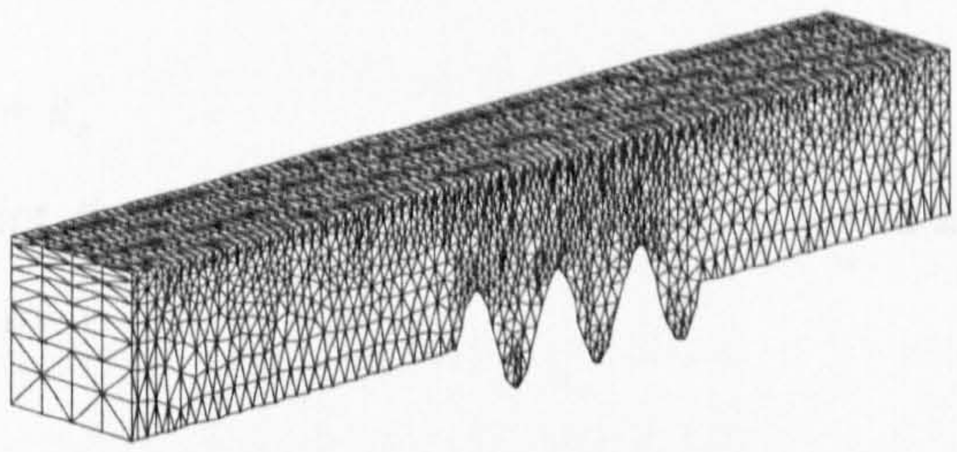

Fig.7.4.1 (b) typical initialized mesh

Fig.7.4.1 Typical initialized mesh for the Bragg scattering problem

The reflection coefficients, defined by $K_r = A_r/A_i$, where A_r and A_i are the amplitudes of reflecting and incident waves, are calculated from wave histories recorded at a series of points along the tank (see Fig. 7.4.2) by using the same method as in Heathershaw (1982). Suppose there are two gauges with distance of Δl to record the wave elevations,

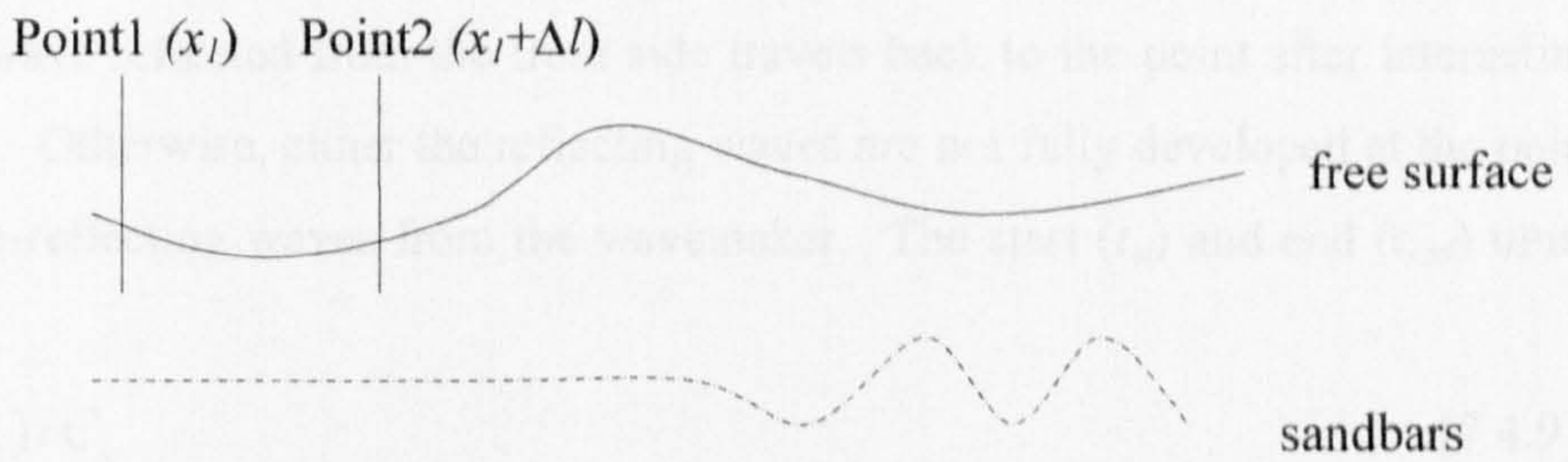

Fig. 7.4.2 sketch for calculating the reflection coefficient

The elevation at Point 1 can be written as

$$\varsigma_1 = c_1 \cos(g_1 + \omega t) \tag{7.4.1}$$

in which c_1 ,g_1 are coefficients which represent the amplitude and phase. It is assumed that the wave consists of incident and reflected waves with the same frequencies. Therefore, Eq. (7.4.1) can be rewritten as

$$\varsigma_1 = A_i \cos(kx_1 - \omega t + \varepsilon_i) + A_r \cos(kx_1 - \omega t + \varepsilon_r) \tag{7.4.2}$$

where the subscripts i and r indicate the incident waves and the reflected waves, respectively. ε are constant. Expand Eq. (7.4.2),

$$\varsigma_1 = A_1 \cos \omega t + B_1 \sin \omega t \tag{7.4.3}$$

and

$$A_1 = A_i \cos G_r + A_r \cos G_r ; B_1 = A_i \sin G_i - A_r \sin G_r \tag{7.4.4}$$

where

$$G_i = kx_1 + \varepsilon_i ; G_r = kx_1 + \varepsilon_r \tag{7.4.5}$$

similarly, for the second Point, the elevation recorded can be described as

$$\varsigma_2 = A_2 \cos \omega t + B_2 \sin \omega t \tag{7.4.6}$$

and

$$\begin{aligned} A_2 &= A_i \cos(k\Delta l + G_r) + A_r \cos(k\Delta l + G_r) \\ B_2 &= A_i \sin(k\Delta l + G_i) - A_r \sin(k\Delta l + G_r) \end{aligned} \tag{7.4.7}$$

From Eqs. (7.4.1) to (7.4.7), the amplitude of the incident wave and reflected wave can be obtained by

$$\begin{aligned} A_i &= \frac{1}{2|\sin k\Delta l|}\left[(A_2 - A_1 \cos k\Delta l - B_1 \sin k\Delta l)^2 + (B_2 + A_1 \sin k\Delta l - B_1 \cos \Delta l)^2\right]^{1/2} \\ A_r &= \frac{1}{2|\sin k\Delta l|}\left[(A_2 - A_1 \cos k\Delta l + B_1 \sin k\Delta l)^2 + (B_2 - A_1 \sin k\Delta l - B_1 \cos \Delta l)^2\right]^{1/2} \end{aligned} \tag{7.4.8}$$

Once A_i and A_r is obtained, the reflection coefficient can be estimated.

For the purpose of computing the reflection coefficients, the time history to be used at a point must start from the time when the wave reflected from the lee side has arrived at the point and end before the wave reflected from the front side travels back to the point after interacting with the wavemaker. Otherwise, either the reflecting waves are not fully developed at the point or affected by the re-reflecting waves from the wavemaker. The start (t_{st}) and end (t_{end}) times may be estimated by

$$t_{st} = (L_{wp} + 2L_{bp2})/C_g \tag{7.4.9}$$

$$t_{end} = (3L_{wp} + 2L_{bp1})/C_g \tag{7.4.10}$$

where C_g is the group velocity of the water wave; L_{wp} is the distance from the wavemaker to the point considered; L_{bp1} and L_{bp2} are the distances from the point to the front and lee sides of the bar patch, respectively.

7.4.1. Reflection coefficient as the function of wave frequencies

First considered are the cases with small wave amplitudes. For these cases, the water waves are generated by small amplitudes (a=0.02 for 4 bars and 0.005 for 10 bars) and the resulting wave steepness (H/λ, where H and λ are the water wave height and length, respectively) is less than 0.002. In order to compare our results with experimental data in Heathershaw (1982), the dimensionless bar wave number (k_b) is assigned a value of $\pi/10$, the ratios of the bar amplitude

(a_b) to the water depth are taken respectively as $a_b/d = 0.32$ for 4 bars and $a_b/d = 0.16$ for 10 bars. The wave histories recorded at two points about 5 bar-lengths before the front side of the bar patch are used.

The reflection coefficients near the resonant condition ($2k/k_b = 1$, where k is the water wave number) are presented in Fig.7.4.3 together with experimental data from Heathershaw (1982). For the case with 10 bars, the nonlinear numerical results from Liu & Yue (1998) and analytical results from the simplified model (David & Heathershaw, 1984) are also included. For the case with 4 bars, the analytical results from Porter & Porter (2003) are plotted apart from the experimental and our numerical results. From Fig.7.4.3a for the case of 4 bars, it can be seen that the numerical results obtained by using the QALE-FEM method agree well with the analytical results given in Porter & Porter (2003) and satisfactorily with experimental data in Heathershaw (1982). Fig.7.4.3b for 10 bars indicated that the present numerical prediction almost coincide with those of Liu & Yue (1998) and are closer to the experimental data than the analytical solution based on simplified model (Mei,1985) on the side of $2k/k_b > 1$. When $2k/k_b < 1$, the present results differ with those of Liu & Yue (1998) but are closer to the experimental data of Heathershaw (1982) and the analytical results from the simplified models (Mei, 1985).

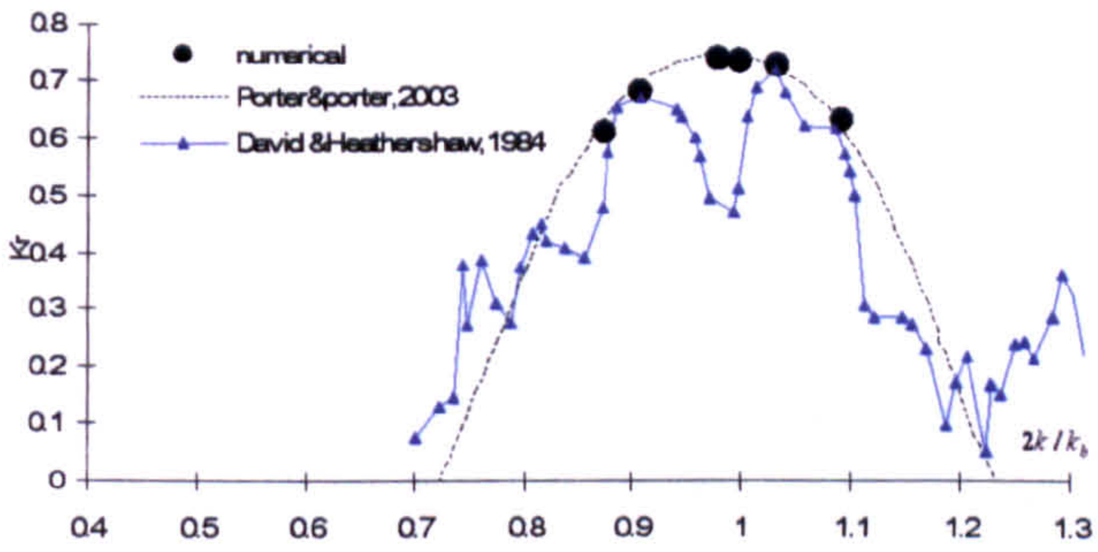

(a) Four bars, $a_b/d = 0.32$

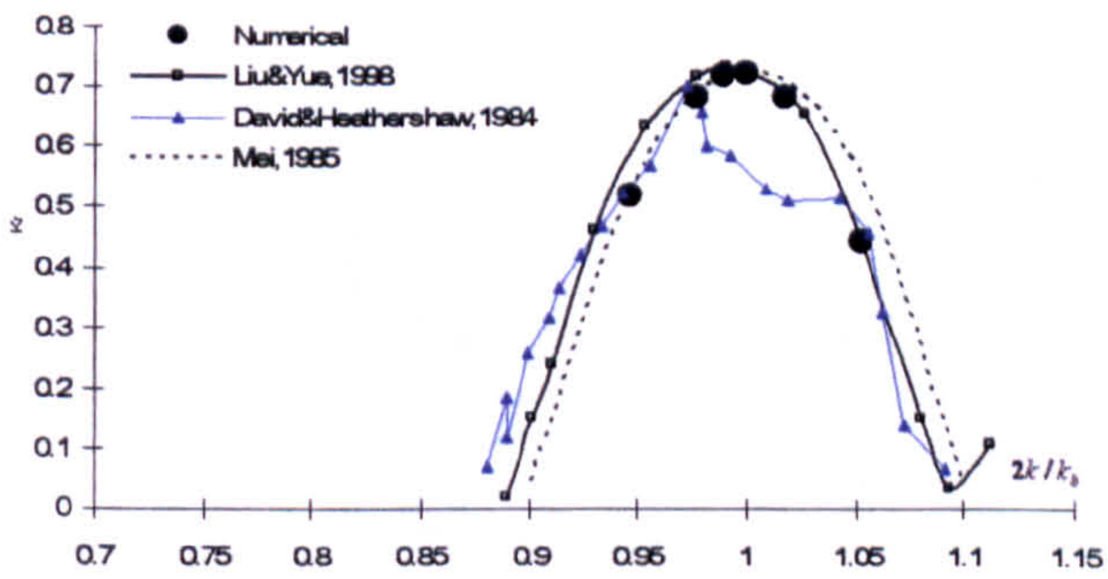

(b) Ten bars, $a_b/d = 0.16$

Fig.7.4.3 Reflection coefficients ($K_r = A_r/A_i$ with A_r and A_i being the amplitudes of reflection and incident waves, respectively) with $k_b d = \pi/10$

One may also find that in the region $2k/k_b$ close to 1, the reflection coefficients calculated by the numerical results including the present results are all different to the experimental data, though the difference between the numerical results are small. In this region, the resonance is very strong. Viscosity may play very important role and therefore reduces the reflection. However, all the numerical methods present in this figure are based on potential theory which is inherently inviscid.

To further show the properties of the reflected waves, the wave profiles at different instances for 4 bars are plotted in Fig.7.4.4, in which the coordinate system is shifted so that its origin is at the centre of the bar patch and the bar patch is located in the range of $-2 < x/\lambda_b < 2$ ($\lambda_b = 2\pi/k_b$). It can be observed that when the incident wave reaches the bars, the reflected wave begins to be produced. The reflected wave propagates towards the wavemaker, is superposed onto the incident wave and makes the resultant wave before the front side ($x/\lambda_b = -2$) higher than the incident wave. It can also be observed that the wave after the lee side ($x/\lambda_b = 2$) is considerably smaller than the wave before the front side, as expected. The wave profiles at different instants for 10 bars are shown in Fig. 7.4.5. Similar phenomena are found in cases with 10 bars.

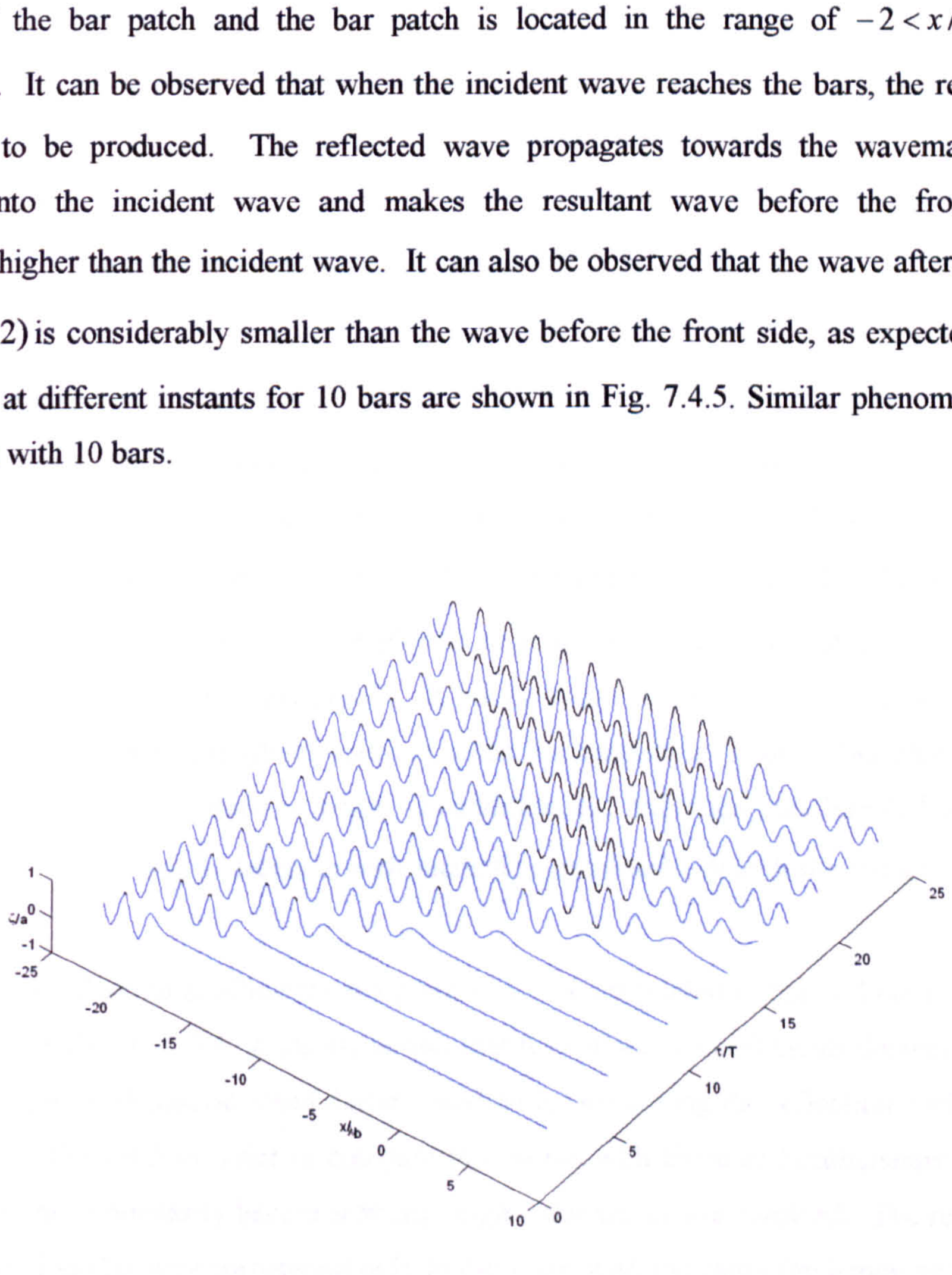

Fig.7.4.4 Wave profiles at different instances for 4 bars

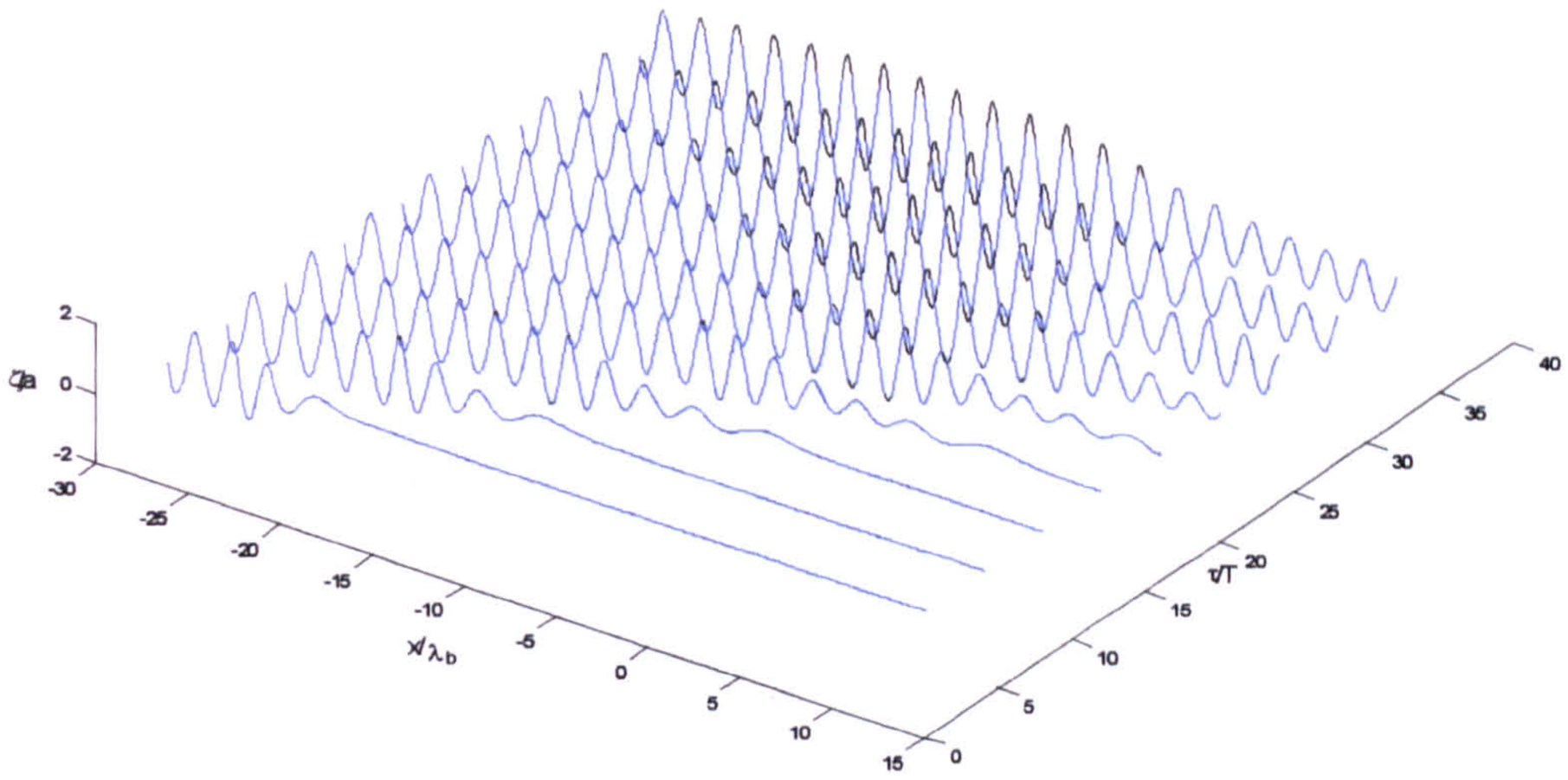

Fig.7.4.5 Wave profiles at different instances for 10 bars

7.4.2. Nonlinear effects

In order to investigate the nonlinear effects, the case with 4 bars is simulated with different amplitudes. All other parameters except for the amplitude are the same as those for Fig.7.4.4. The reflection coefficients corresponding to $2k/k_b \approx 1$ are presented in Fig.7.4.6. In Fig. 7.4.6a, the coefficients at different positions are plotted together with the experimental results and analytical solution from Heathershaw (1982). It can be seen that the reflection coefficients are close to those of the linear analytical solution when the amplitude is small but close to the measured data when the amplitude is larger. In addition, the reflection coefficients before the front side ($x/\lambda_b = -2$) tend to decrease with increasing amplitude, though the reduction is not very significant.

The numerical reflection coefficients at a point x/λ_b= -4 are plotted in Fig. 7.4.6b in order to show the trend clearly. Fig. 7.4.6b clearly shows that the reflection coefficients decrease as the amplitudes increase. It should be noted that the method for estimating the reflection coefficients is the same as in Fig.7.4.3 in order to compare the results with those in Heathershaw (1982). However, when the nonlinearity becomes strong, high order waves are involved. The reflection coefficients found in this way correspond only to the wave with the same frequency as the first order wave and do not include the reflection of high order waves.

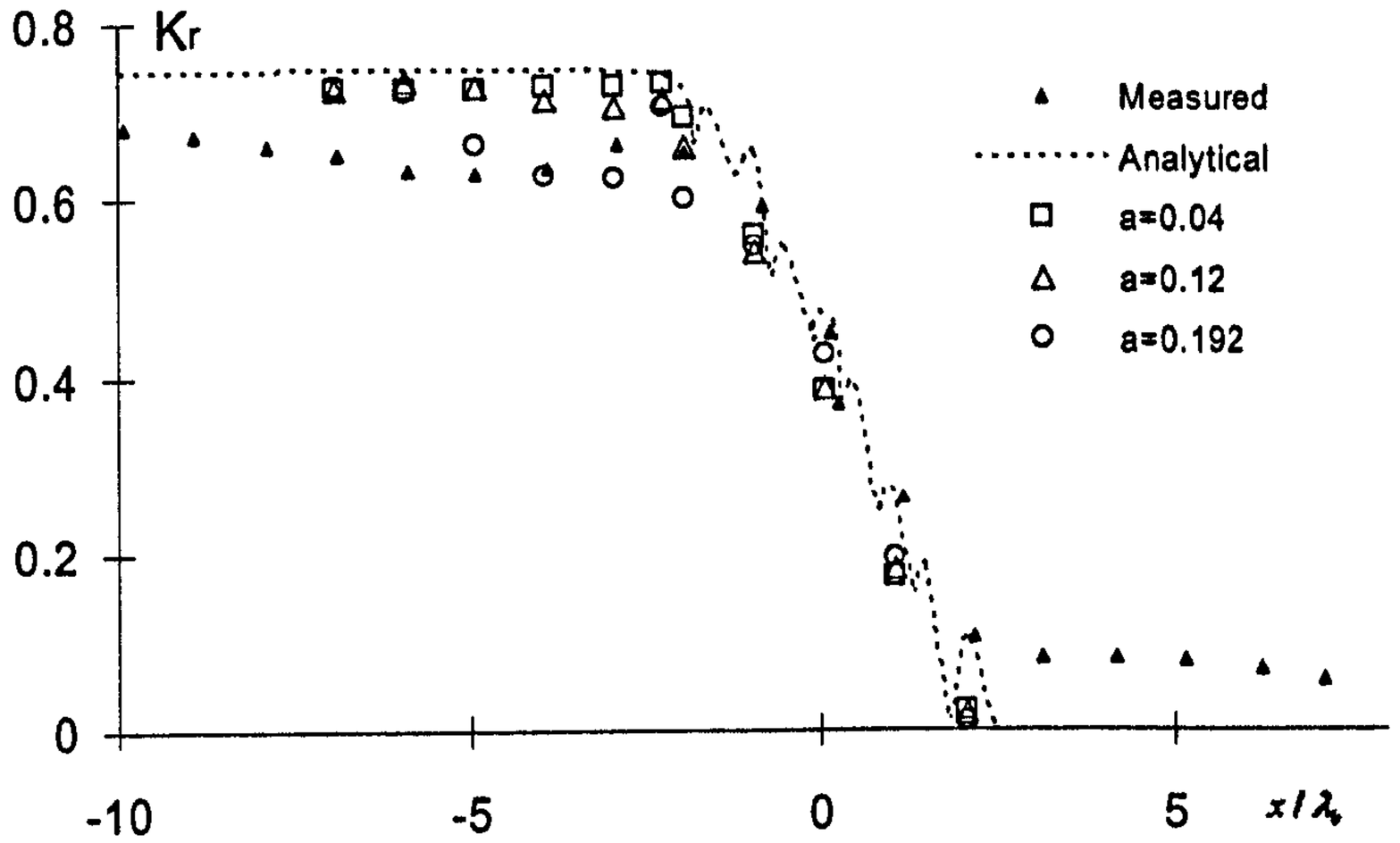

(a) K_r at different positions

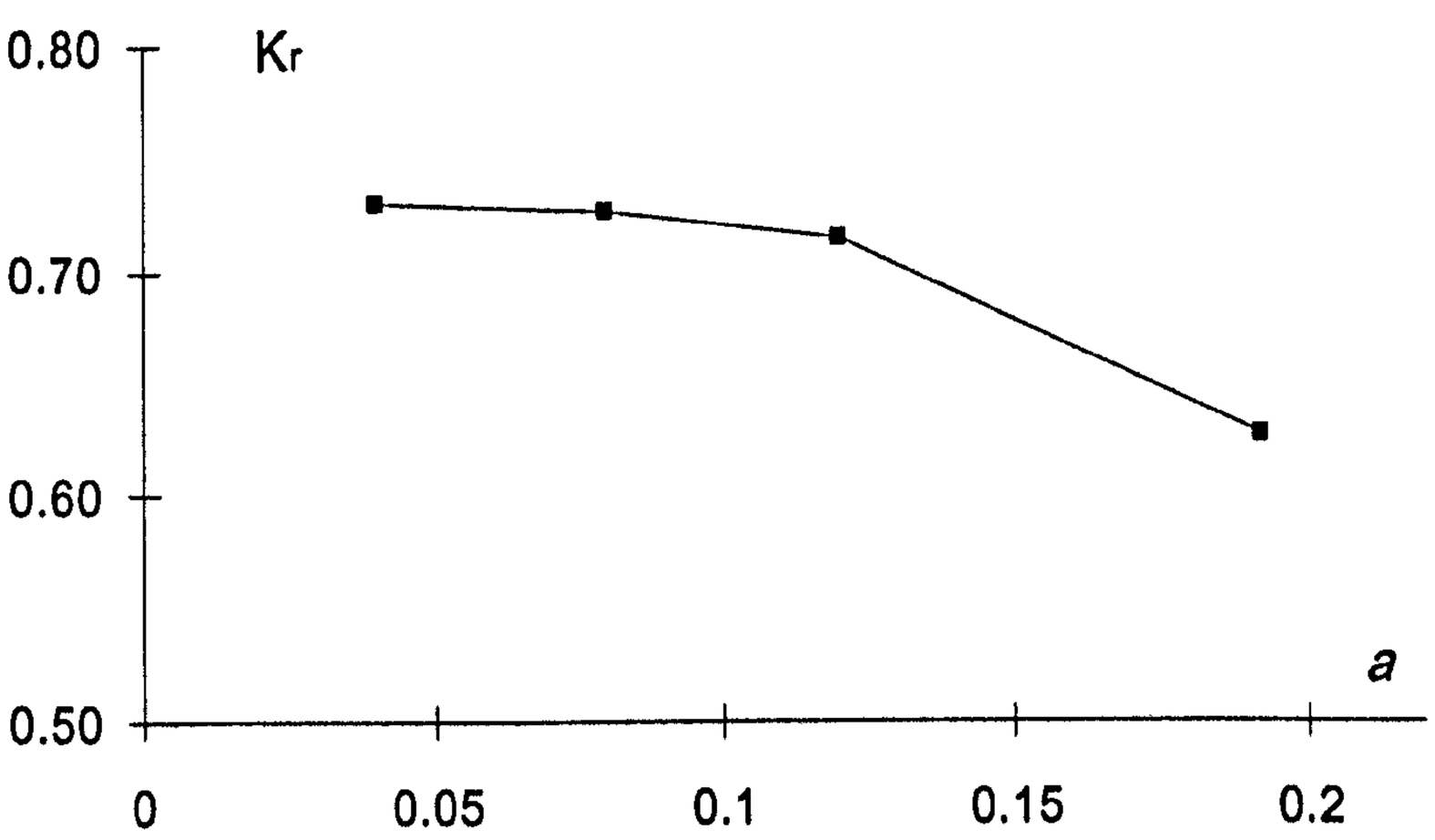

(b) K_r at $x/\lambda_b \approx -4$

Fig. 7.4.6 Nonlinear effects on reflection coefficients at $2k/k_b \approx 1$ for 4 bars

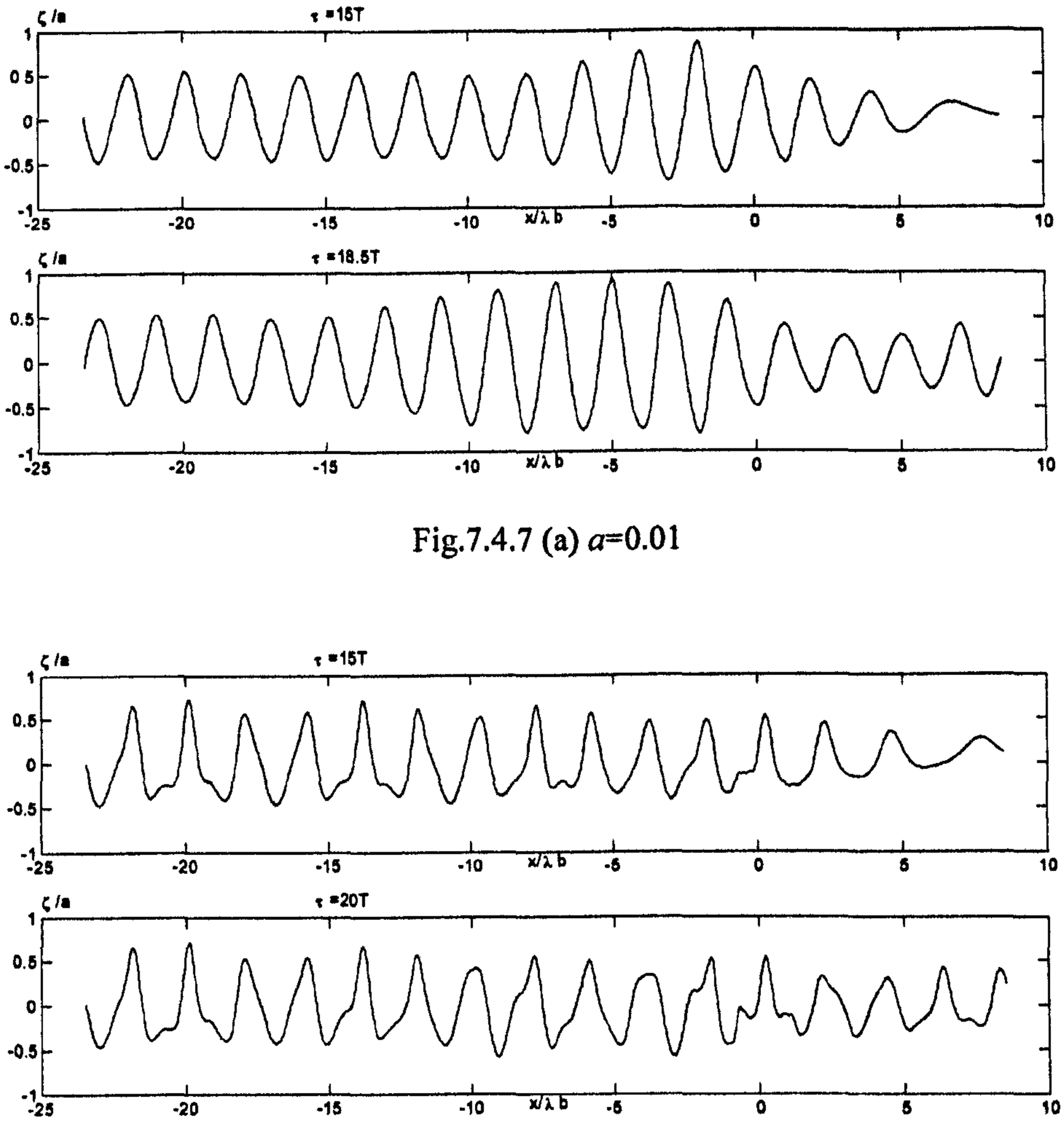

Fig.7.4.7 (a) a=0.01

Fig.7.4.7 (b) a=0.192

Fig.7.4.7 Wave profiles corresponding to different amplitudes for 4 bars

In order to look at overall reflection of nonlinear waves by the bar patch, the shapes of wave profiles for the same case are illustrated in Fig.7.4.7. In this figure, the wave profiles for smaller and larger amplitudes are depicted to show the different reflection properties. As can be seen, the wave profiles to the left of the bar patch for the smaller amplitude seems to be formed by superimposing two harmonic waves with the same length travelling in opposite directions (so the wave become higher) but the shape is still similar to the shape of harmonic waves. For the larger amplitude, the wave amplitude on the left of the bar batch seems not to be changed dramatically by the reflection waves, instead, the shape of the waves is significantly modified. More wave profiles corresponding to different amplitudes for 4 bars of the case in Fig.7.4.7 are given in Fig.7.4.8.

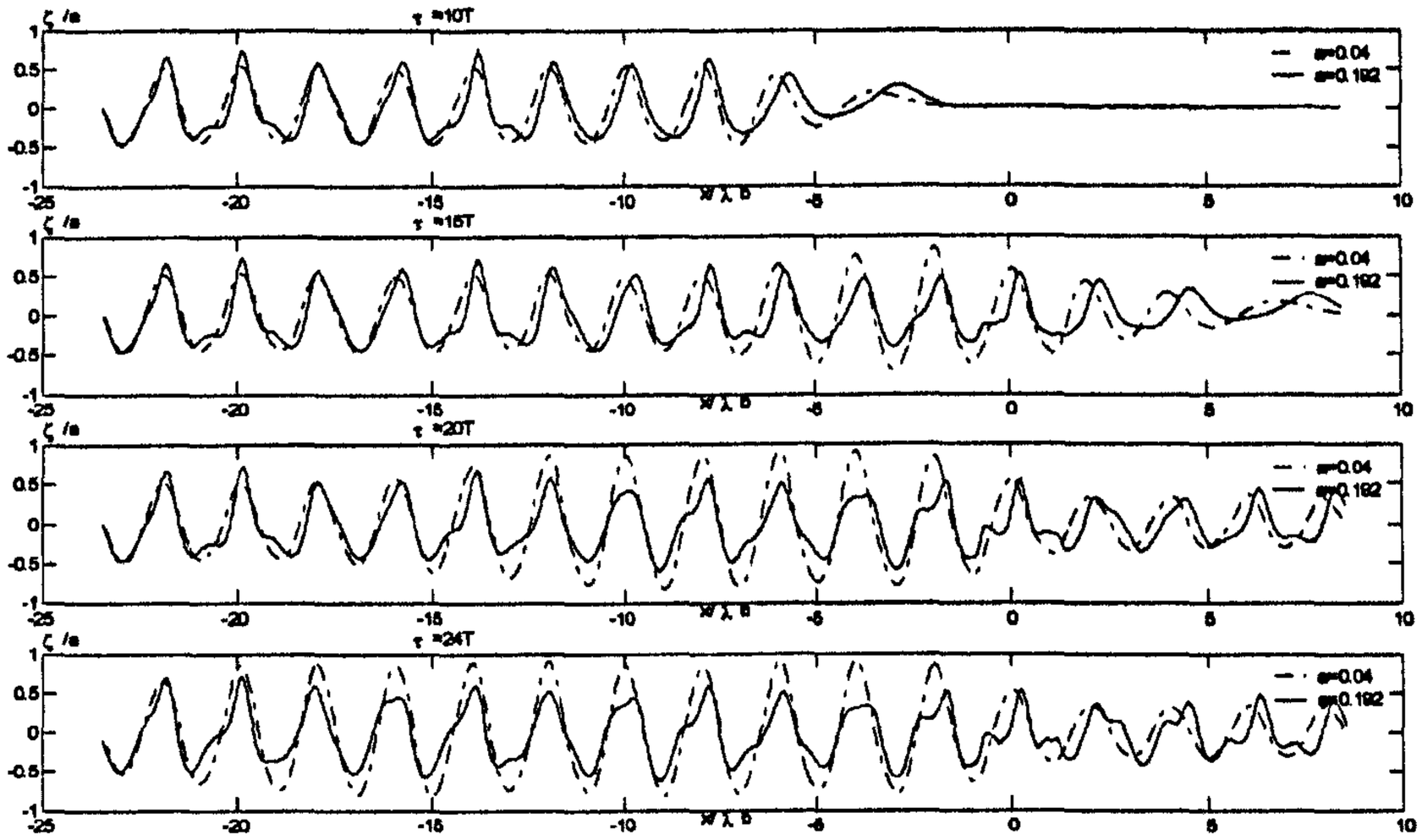

Fig.7.4.8 Wave profiles in different instances
corresponding to different amplitudes for 4 bars

7.5. Computational efficiency of mesh moving scheme and mesh quality

A significant development in this work is to move, instead of re-generating, the unstructured mesh at every time step when simulating water waves based on the FNPT Model. As pointed out in Chapter 4, the mesh obtained should have satisfactory element shapes and preserve the reasonable refinement and distribution in regions of interest, such as those close to the free surface and the bars on the tank-bed at all time steps. But Chapter 4 only investigated the effectiveness of the new developed spring analogy method by using some artificial cases in one step. The mesh quality during a long-period calculation is also of concern. In this section, investigations for cases without floating bodies are considered. The mesh quality in case with floating bodies will be assessed and discussed in Chapter 8 and Chapter 9.

In order to show the quality of mesh moved by using the method discussed in Chapter 4, a case of nonlinear water waves without bars is tested, in which, a=0.082, ω=1.45 and L = 14.7. The fluid domain is discretised into about 133,632 elements. The time-step length is taken as $\Delta t=T/64$. The results of the wave elevation have been validated in Section 7.1.1. The computational mesh at different time is shown in Fig. 7.5.1. It is observed that the mesh quality remains high throughout the simulation. It should be noted that the mesh used in this case near the wave maker is structured. This result means the above mesh moving scheme can be applied to unstructured mesh, structured mesh or a mixed mesh as shown in this figure.

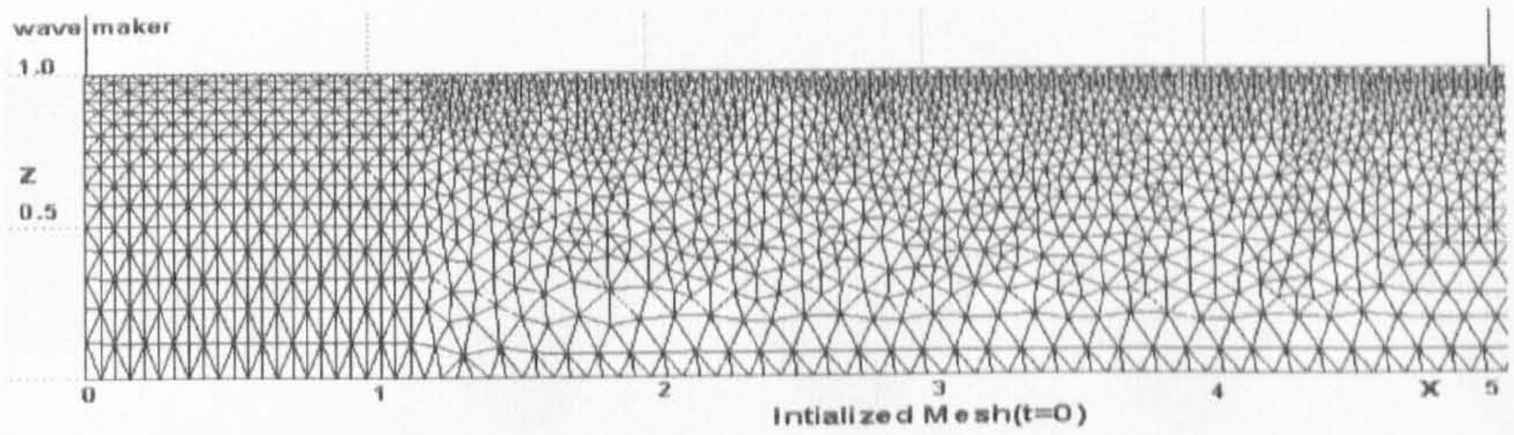

(a) $\tau = 0$

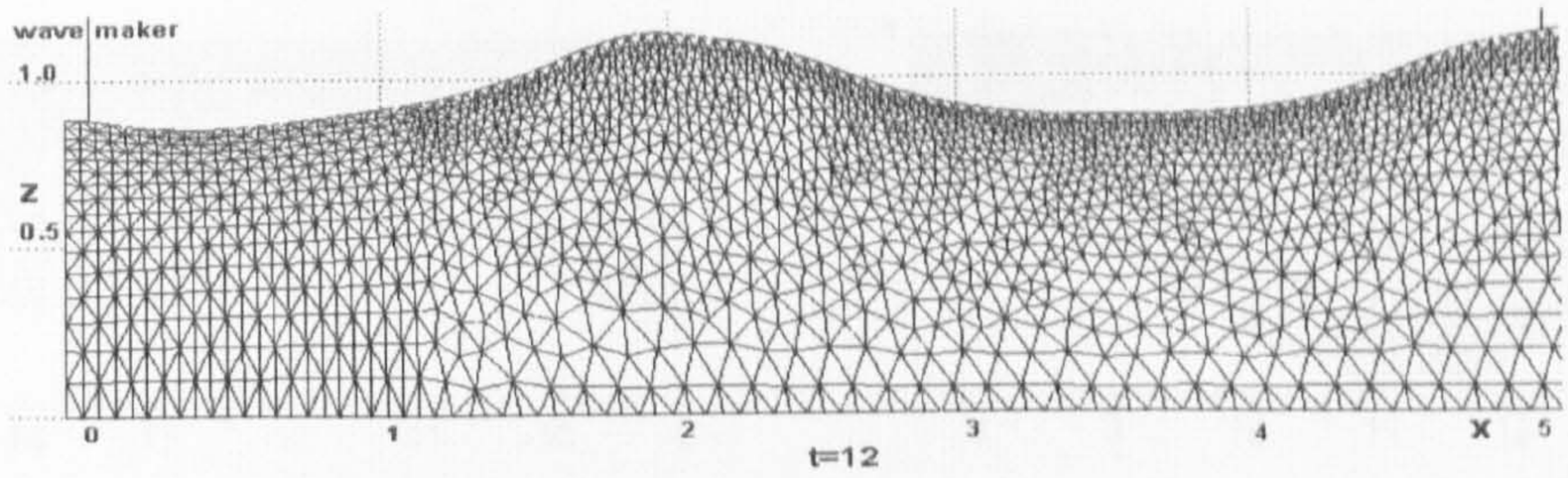

(b) $\tau = 12$

(b) $\tau = 48$

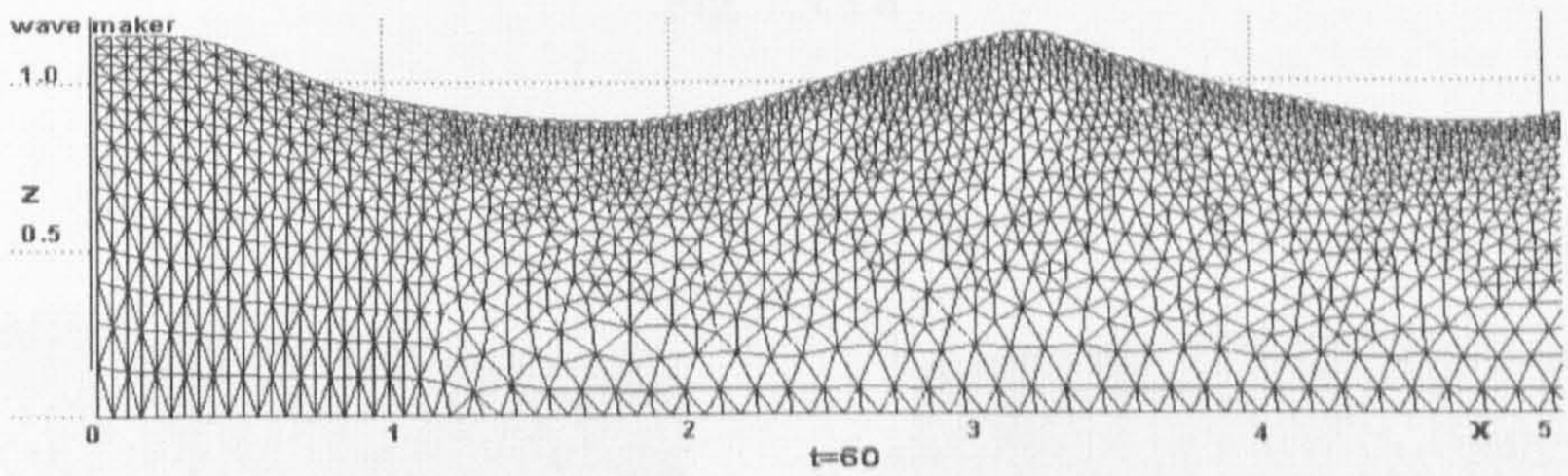

(d) $\tau = 60$

Fig.7.5.1 Mesh in different instances in case with flat sea bed
(a=0.082, ω=1.45 , L = 14.7, $\triangle t$=T/64)

Another case considered here is the case with 4 bars as shown in Fig.7.4.8 with a=0.192. Fig. 7.5.2 and Fig. 7.5.3 shows the initial mesh and a mesh during the calculation, respectively.

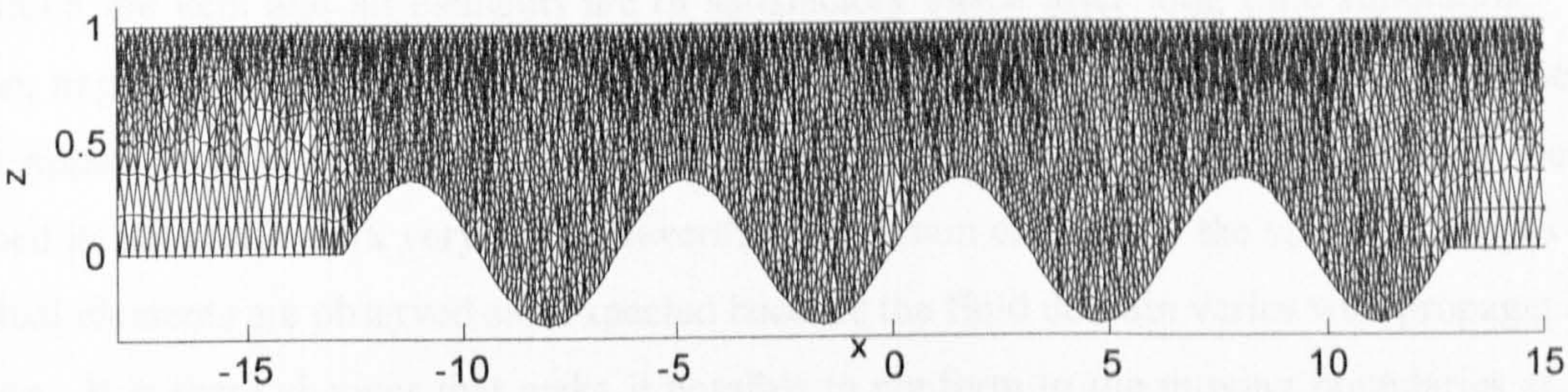

Fig. 7.5.2a

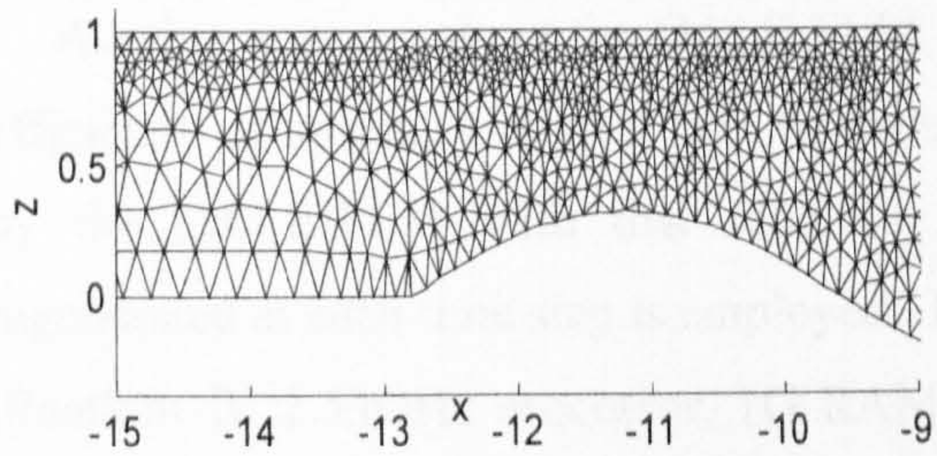

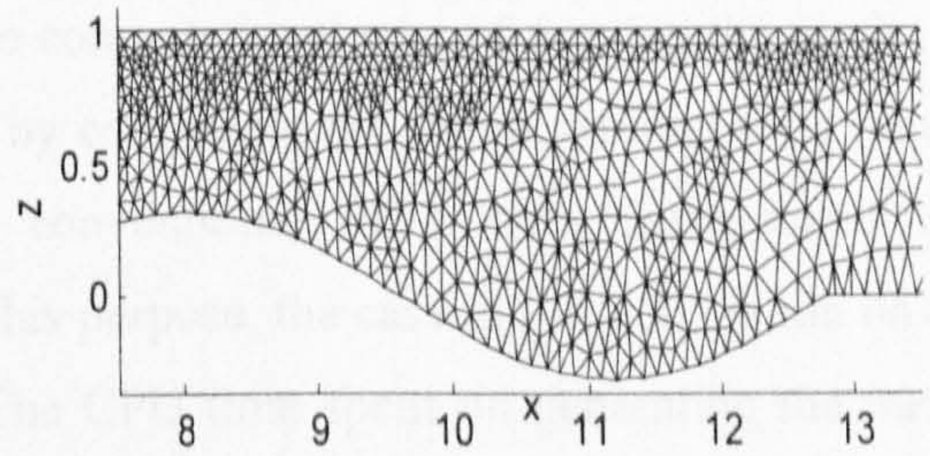

Fig. 7.5.2b

Fig.7.5.2 Initial mesh for 4 bars

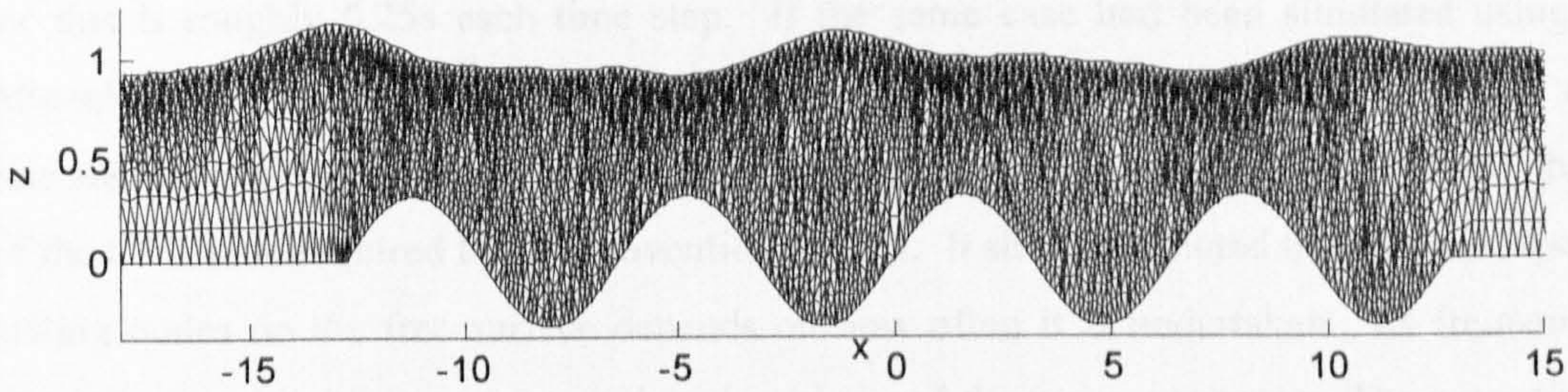

Fig. 7.5.3 a

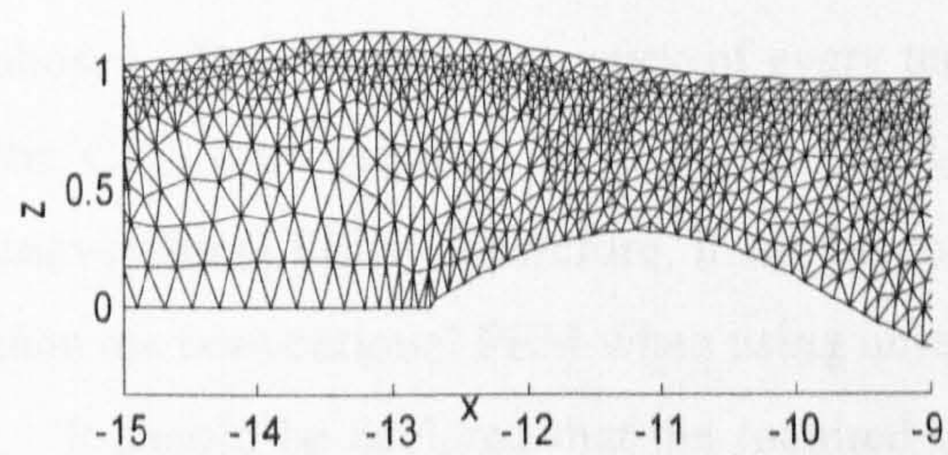

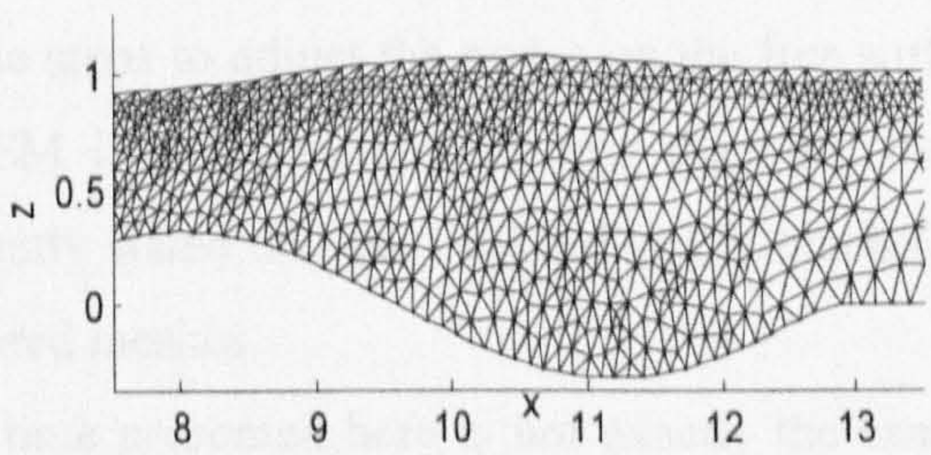

Fig. 7.5.3 b

Fig. 7.5.3 Mesh at $\tau \approx 332$ (4 bars, a=0.192)

Fig. 7.5.2a shows a part of the initial unstructured mesh while Fig. 7.5.2b illustrates the enlarged mesh in areas near the two sides of the bar patch. Fig. 7.5.3 depicts the corresponding part of the mesh at about $\tau = 332$. These figures demonstrate that the original refinement and

distribution are kept and all elements are of satisfactory shape after long time simulation. In addition, negative elements, which are of concern when using the linear spring analogy method, do not appear in the simulation. This implies that the techniques used for moving mesh described in Section 3 work very well. Nevertheless, certain changes in the sizes and shapes of individual elements are observed and expected because the fluid domain varies with propagation of waves. It is these changes that make it possible to conform to the moving boundaries at all time steps and so to achieve satisfactory results.

Another concern about the QALE-FEM is the computational cost of moving the mesh. The efficiency of moving the mesh can be deduced by comparing the computational time required by the QALE-FEM with that required if a conventional FEM with unstructured mesh regenerated at each time step is employed. For this purpose, the case in Fig.7.5.3 is run on a PC (Pentium Ⅳ 2.53GHz processor, 1G RAM). The CPU time spent on generating the mesh is about 53s. After the mesh is generated, the CPU time spent on all the other calculations is on average about 3s each time step, including 0.09s for moving interior nodes and 0.25s for adjusting all nodes on the free surface. In this simulation, adjustment of nodes on the free surface is performed every 40 time steps and takes about 9s each time, so the additional CPU time for this is roughly 0.25s each time step. If the same case had been simulated using a conventional FEM with the same mesh regenerated at each time step, the total CPU time on each time step would have been about 60s. This implies that the QALE-FEM requires less than 10 % of the CPU time required by the conventional FEM. It should be noted that the time spent on adjusting nodes on the free surface depends on how often it is undertaken. Its frequency depends on the number of time steps used each period and the wave steepness. The more time steps in each period, the less frequently adjustment has to be performed. On the other hand, the steeper the waves, the more often adjustment is needed. According to the experience so far, the adjustment frequency is unlikely to be less than every ten time steps if a reasonable time step is chosen. Even with a frequency of every ten time steps to adjust the nodes on the free surface, the CPU time required by using the QALE-FEM is still considerably less than that by the conventional FEM. Therefore, it can be confidently stated that the QALE-FEM is much faster than the conventional FEM when using unstructured meshes.

It should be declared that the required CPU time presented here is not exactly the same as that presented in Ma & Yan (2006). That is because the computer code is optimized and the computational cost now is cheaper than Ma & Yan (2006).

8. NONLINEAR INTERACTION BETWEEN 2D FLOATING BODIES AND STEEP WAVES

In this chapter, the QALE-FEM method is used to simulate the nonlinear interaction between 2D floating bodies and steep waves. A sketch of this problem is given in Fig.8.0.1.

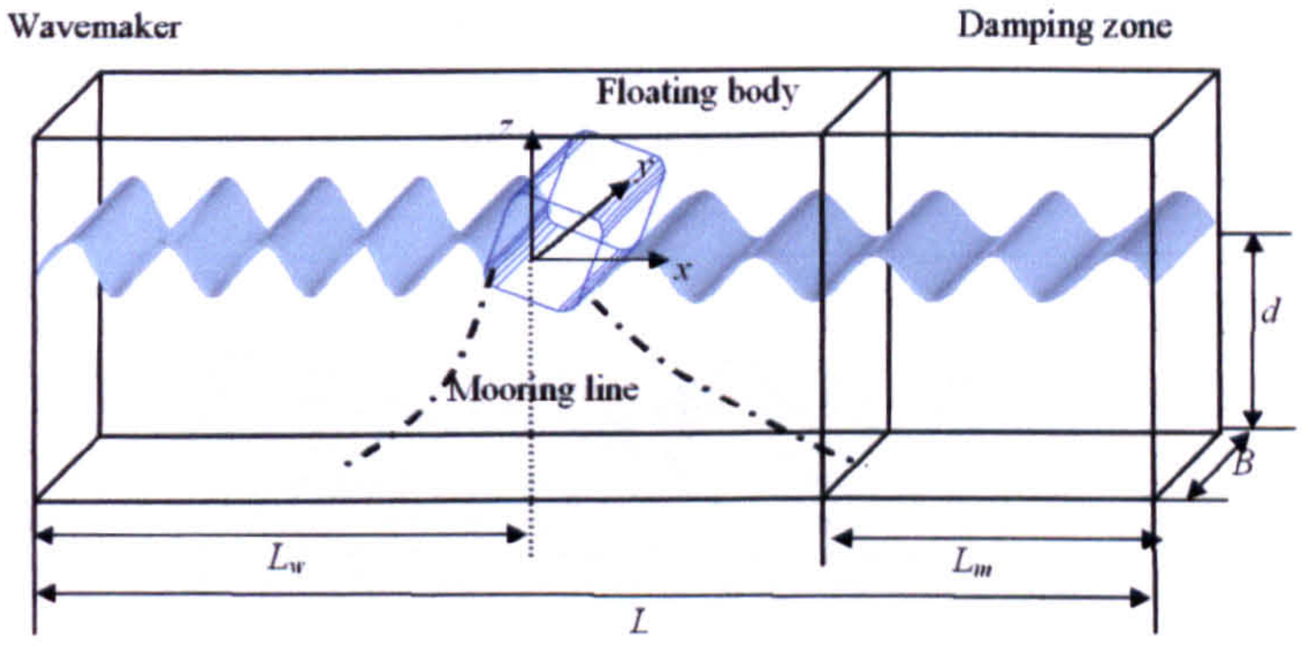

Fig.8.0.1 Sketch of fluid domain with floating bodies

Some of the results are validated by comparing the numerical results with analytical solutions and published works. Some of the results in this chapter have been published in Yan & Ma (2006), more results are presented here. Unless mentioned otherwise, all parameters with a length scale are nondimensionalised by the water depth d and other parameters by

$$t \to \tau\sqrt{d/g} \text{ and } \omega \to \omega\sqrt{g/d}\ . \tag{8.0.1}$$

8.1. Waves generated by a 2D forced-motion floating body

Although the main aim of this chapter is to simulate cases involving 2D free-response floating bodies, the case for a 2D body in forced motions is investigated in the first stage in order to validate the force calculation, in which the iteration loop discussed in the previous section becomes unnecessary since the body acceleration does not need to be found. The body in these cases is formed with a circular cylinder as the submerged part and vertical walls above it, as shown in Fig.8.1.1 (a). The dimensionless radius of the cylinder ($\overline{R}_b$) is 0.25. The initial mesh around the body is similar to that in Fig. 8.1.1 (b) but much finer.

The displacement (η) of the body is specified by

$$\eta(\tau) = a_b \sin(\omega_b \tau) \tag{8.1.1}$$

where a_b and ω_b are the amplitude and circular frequency of the motion, respectively. The velocity corresponding to Eq. (8.1.1) is

$$\vec{U}_c(\tau) = a_b\omega_b \cos(\omega_b\tau) \tag{8.1.2}$$

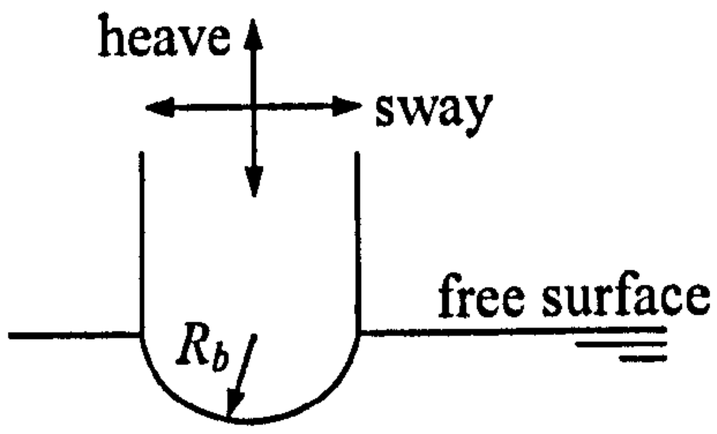

(a) floating body

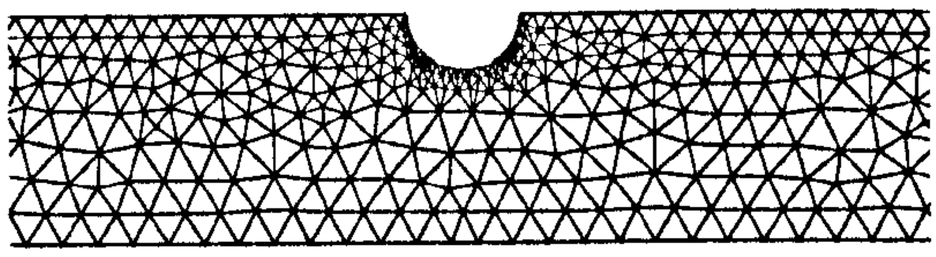

(b) initial mesh near the body

Fig.8.1.1 Sketch of body motions and illustration of the initial mesh

This implies that the floating body suddenly gains a finite value of velocity from rest, which is not only practically impossible but also can result in a numerical difficulty (Eatock Taylor, Wang & Wu, 1994; Eatock Taylor, 2005). To avoid this, the velocity $\vec{U}_c$ is ramped as in Eatock Taylor (2005) and given by

$$\vec{U}_c(\tau) = a_b\omega_b \cos(\omega_b\tau)(1 - e^{\beta\tau}) \tag{8.1.3}$$

$$\beta = -\chi\omega_b / 2\pi \tag{8.1.4}$$

where χ is a coefficient. The larger the value of χ, the shorter the time is, during which the effects of the ramp function persist, though the value does not affect the final results. In this thesis, $\chi = 5$ is used.

8.1.1. Convergence properties of force calculation

When the amplitude of the harmonic motion is small, the hydrodynamic force can be evaluated by summing the analytical added mass and radiation damping forces (Faltinsen,1990). In this section, the force estimated by the added mass and radiation damping is used for comparison with numerical results to verify the QALE-FEM method. For the numerical

simulation, the total tank length is taken as $L \approx 30$ with the length from the wavemaker to the body taken as $L_w \approx 15$ (Fig. 8.0.1). The motion amplitude in Eqs. (8.1.3) and (8.1.4) is assigned as $a_b = 0.01$. The mesh is unstructured and there are about 35 elements on the free surface in each wave length. The time step is taken as $T/128$, where T is the wave period. The x-direction hydrodynamic force (divided by $\rho g d^2$) in the forced sway and the z-direction hydrodynamic force (also divided by $\rho g d^2$) in the forced heave are plotted in Fig.8.1.2 for three cases with different values of ξ, where $\xi = \omega_b^2 \overline{R}_b$ is the frequency parameter.

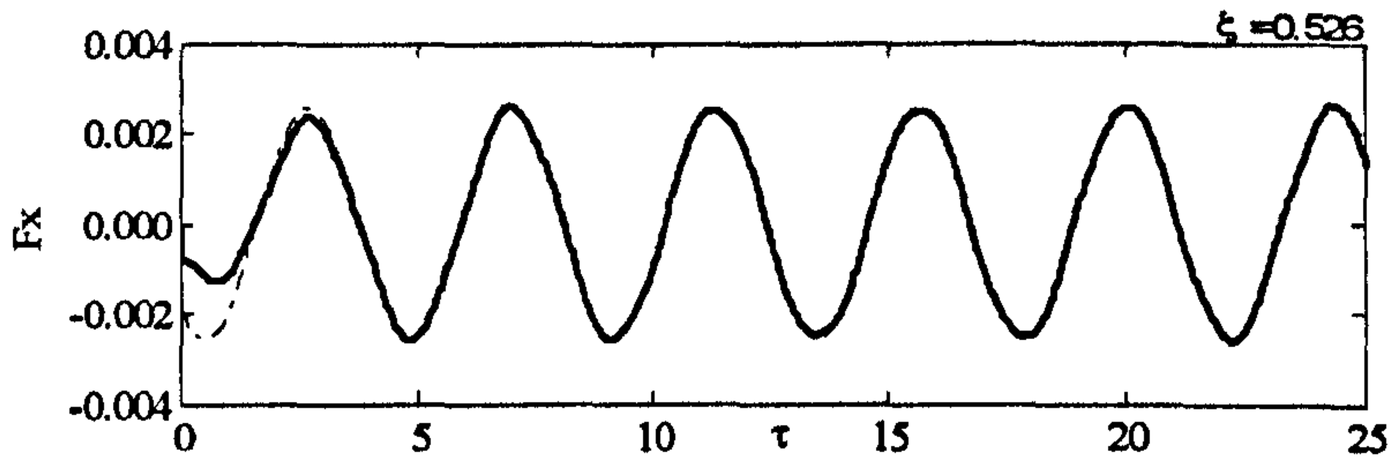

Fig.8.1.2 (a) forced sway $\xi = 0.526$

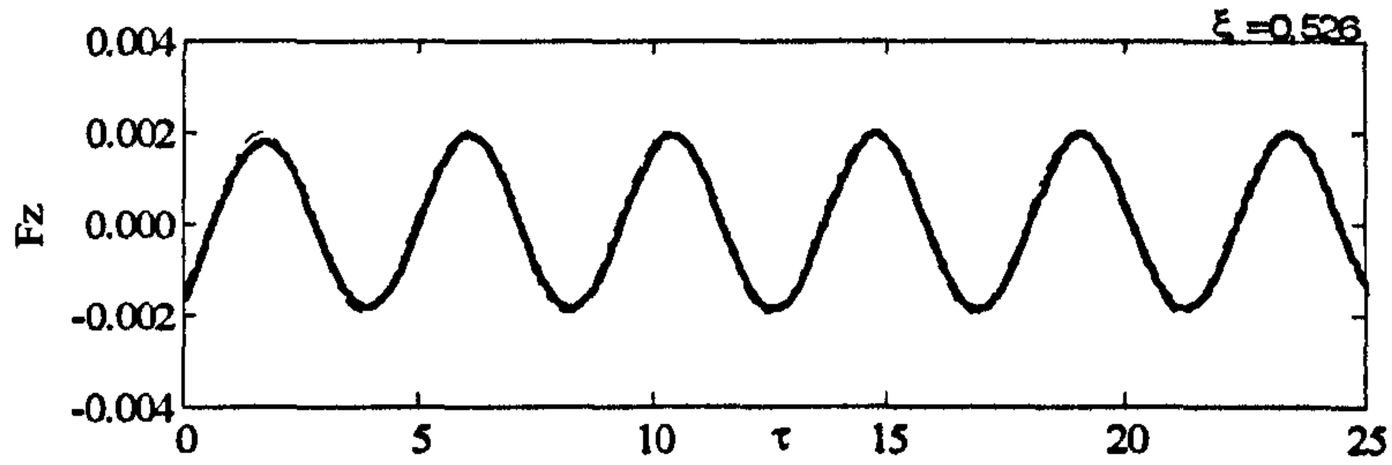

Fig.8.1.2 (b) forced heave $\xi = 0.526$

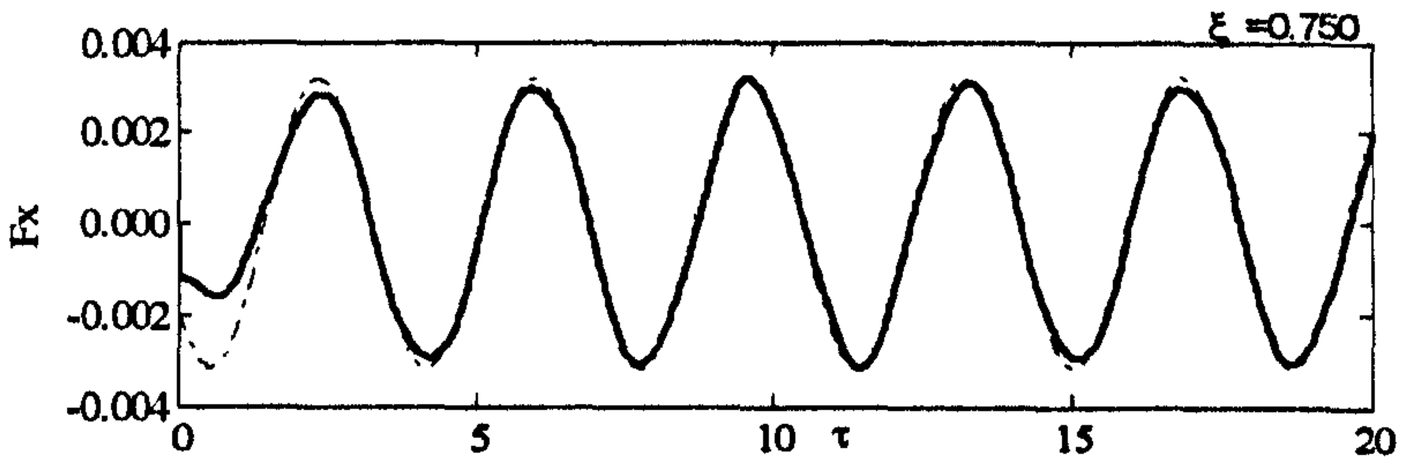

Fig.8.1.2 (c) forced sway $\xi = 0.750$

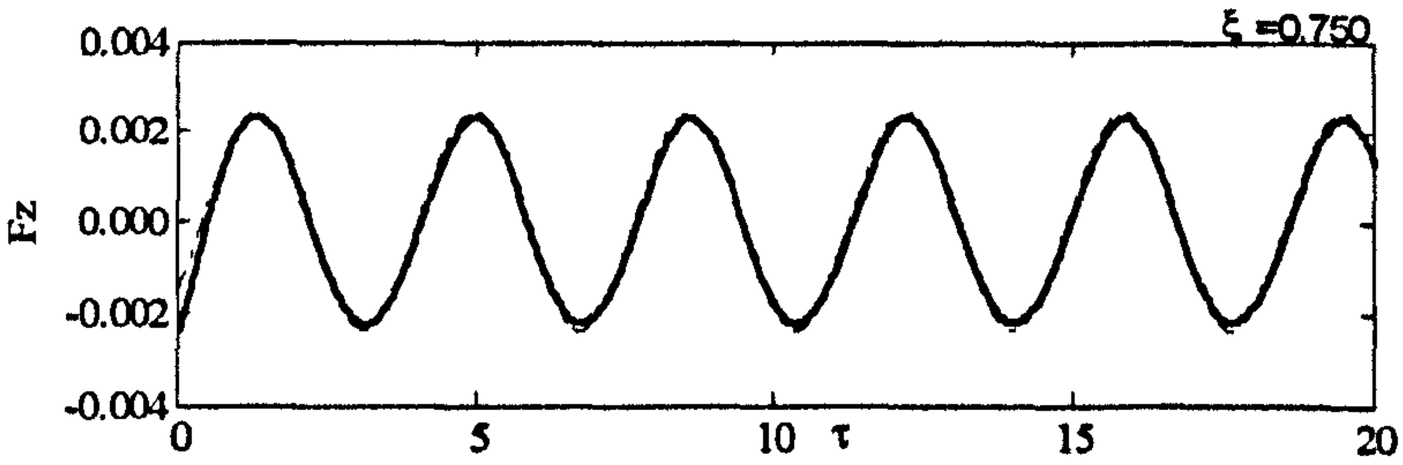

Fig.8.1.2 (d) forced heave $\xi = 0.750$

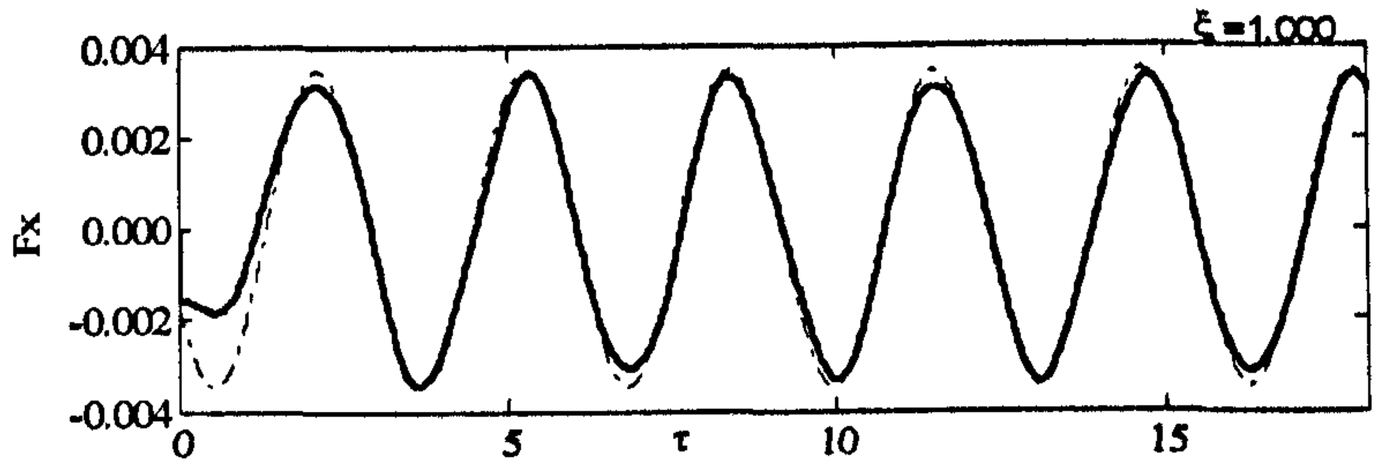

Fig.8.1.2 (e) forced sway ξ=1.0

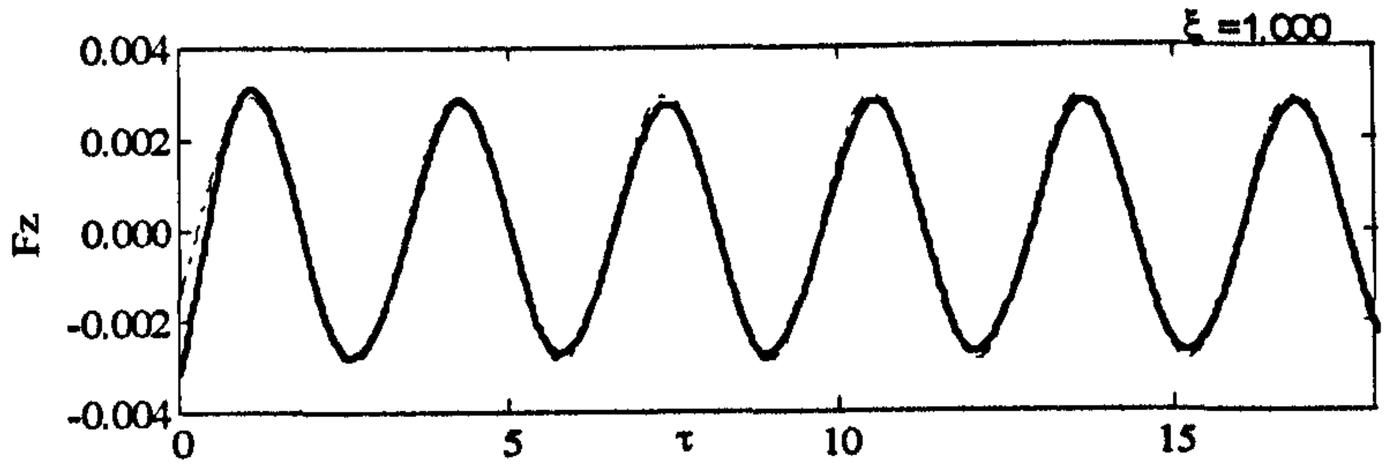

Fig.8.1.2 (f) forced heave ξ=1.0

Fig.8.1.2 Comparison of force histories for cases for forced sway/heave with analytical solution (Solid line: numerical results, Dot line: analytical solution (Faltinsen, 1990)

It can be seen that the numerical results agree very well with the analytical ones in all the cases, except in the transient period when the difference is expected because the analytical forces are evaluated for steady state but not for the transient stage. To quantitatively show the accuracy of the numerical results, the relative error (E_r) for the results in Fig. 8.1.2 is evaluated by:

$$E_r = \frac{\|f_n - f_a\|}{\|f_a\|} \tag{8.1.5}$$

where $\|f\| = \int_{A_e} f^2 dA$; f_n and f_a are the numerical and analytical forces, respectively; and A_e is the duration over which the error is estimated. Because the accuracy of the forces within the transient period should not be of concern, A_e is taken as the total duration of simulation minus the transient period (about half of wave period). The relative errors evaluated in this way for all the cases in Fig. 8.1.2 do not exceed 0.5%.

The characteristics of the relative error are further investigated by considering different time steps and different mesh sizes. For this purpose, the relevant parameters are taken as $a_b = 0.01$ and $\xi = 0.75$ (the corresponding wave length is about $\lambda \approx 2.0$), which are the same as the second case in Fig 8.1.2. It should be noted that the investigation on how numerical errors are affected by time steps is relatively easy but not on how they are related to mesh sizes. That is because the errors depend on both mesh sizes and mesh structures and also because it is impractical to consider all possible mesh structures as the unstructured meshes are used in this

paper. Apart from these, the mesh sizes constantly change with time for water wave problems. To eliminate the difficulty, a representative mesh size (*ds*) is used, which is defined as the distance between nodes on the free surface when the water is at rest. The initial mesh structures are almost the same in all cases considered, which feature that the nodes on the free surface, the tank bed and the body surface are uniformly distributed; the distance between nodes on the free surface is roughly twice of that on the body surface and half of that on the tank bed; and the distance between nodes in the vertical direction gradually decrease from the bed to the free surface.

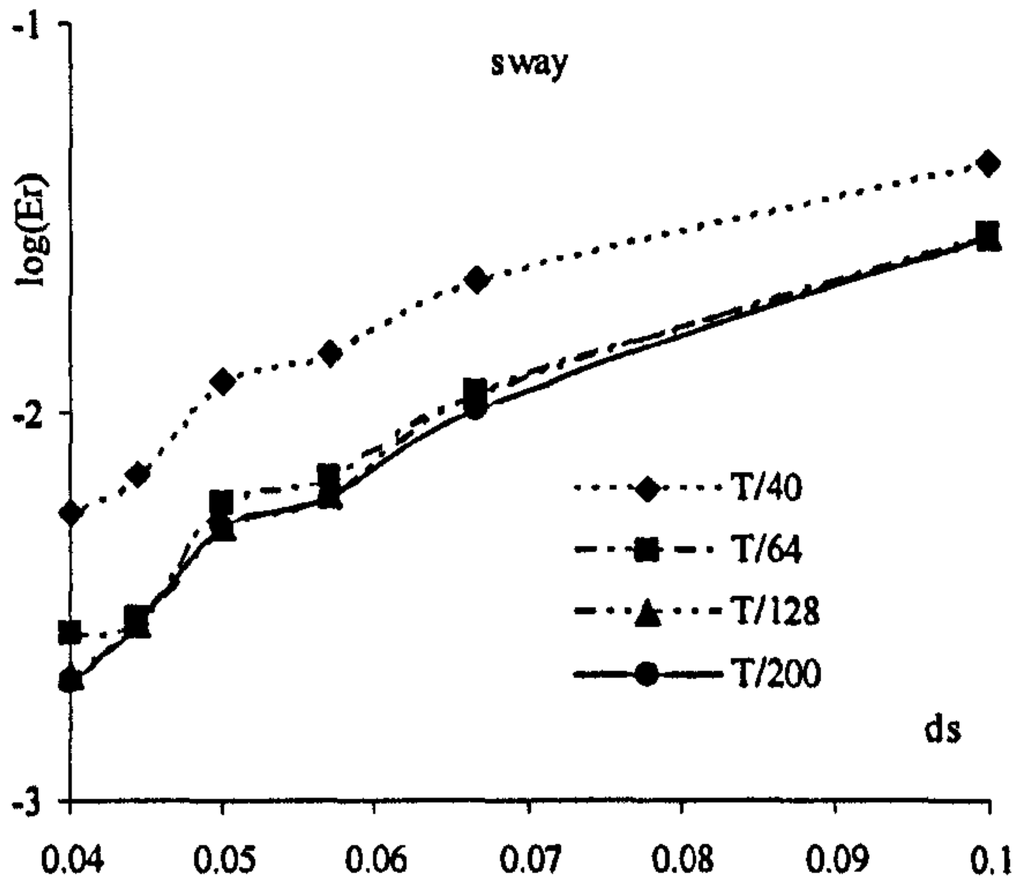

(a) Sway

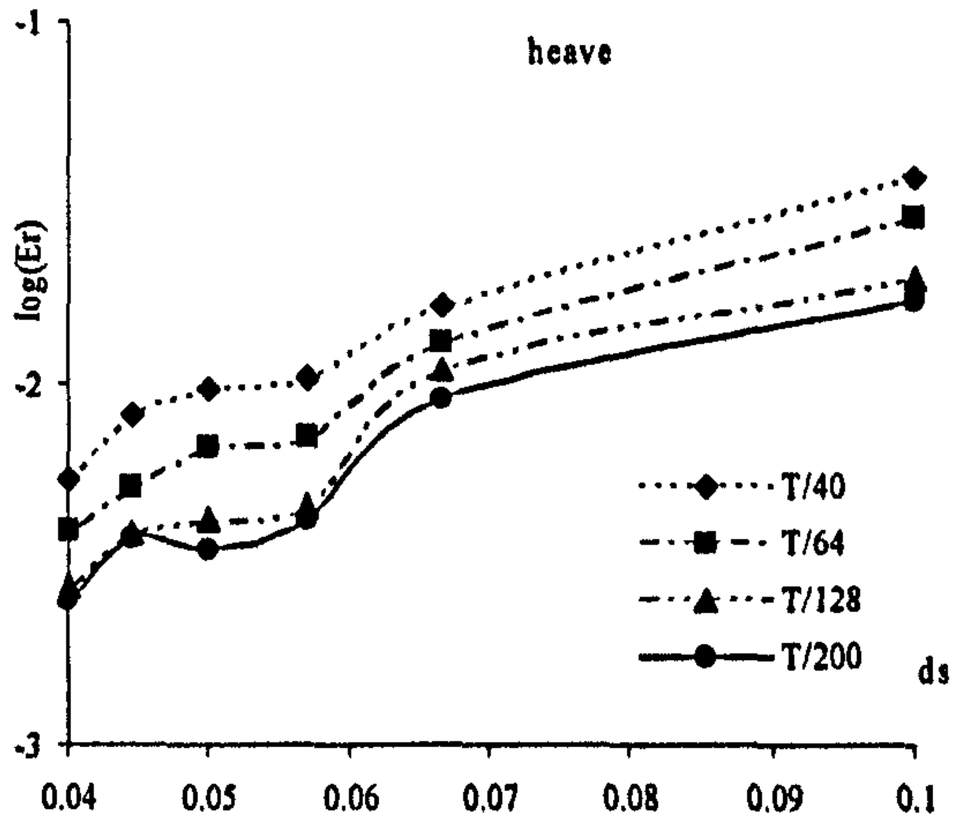

(b) Heave

Fig. 8.1.3 Relative errors for different meshes and different time steps

The relative errors corresponding to different time steps and different representative sizes (ds) are presented in Fig. 8.1.3a and Fig. 8.1.3b for sway and heave, respectively. In these figures, the time step is given as the wave period (T) divided by a number. It is observed that the relative errors reduce with the decrease in mesh sizes and/or time steps, as expected. Particularly in the ranges of $0 < ds < 0.057$ (about 35 elements in over one wave length) and $0 < dt < T/64$, the relative errors are less than 0.8% for all these cases. This implies that the numerical results with a specified accuracy are achievable by using a sufficiently fine mesh and small time step.

8.1.2. Forced motion with larger amplitudes

In order to investigate the nonlinear effects on waves generated by the forced-motions of the floating body, the cases similar to Fig. 8.1.1 but with larger amplitudes are simulated. The wave histories recorded on the left hand side of the body for the case with forced sway (a_b=0.123) is depicted in Fig.8.1.4 together with that for a_b=0.0041. Fig.8.1.5 shows the wave histories for the forced heave, in which the solid line is the wave history for a_b=0.082, while the dotted line is that for a_b=0.0041. In both figures, the wave elevations are divided by the motion amplitude (a_b).

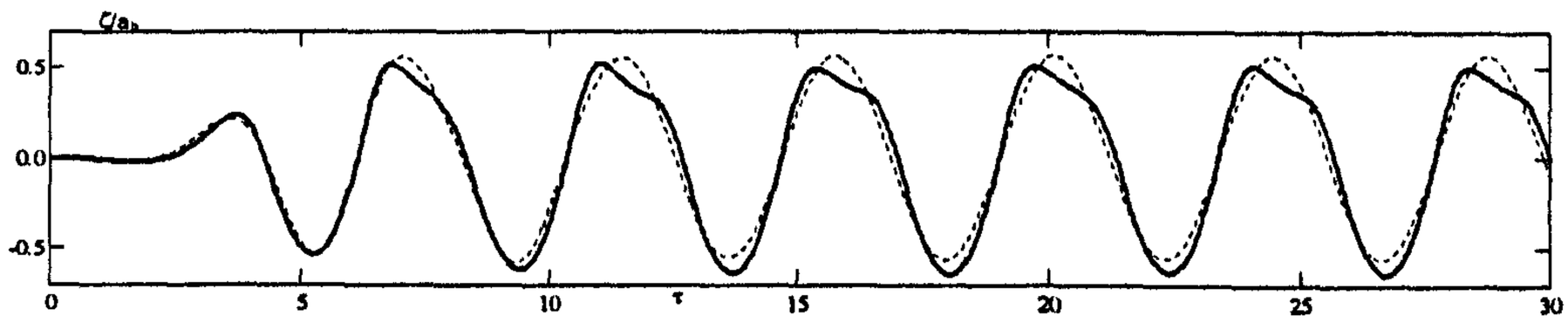

Fig.8.1.4 Wave history recorded at x= -1 due to forced sway

(L=30, ω_b=1.45, $\xi = 0.75$, solid line: a_b=0.123, dot line: a_b=0.0041)

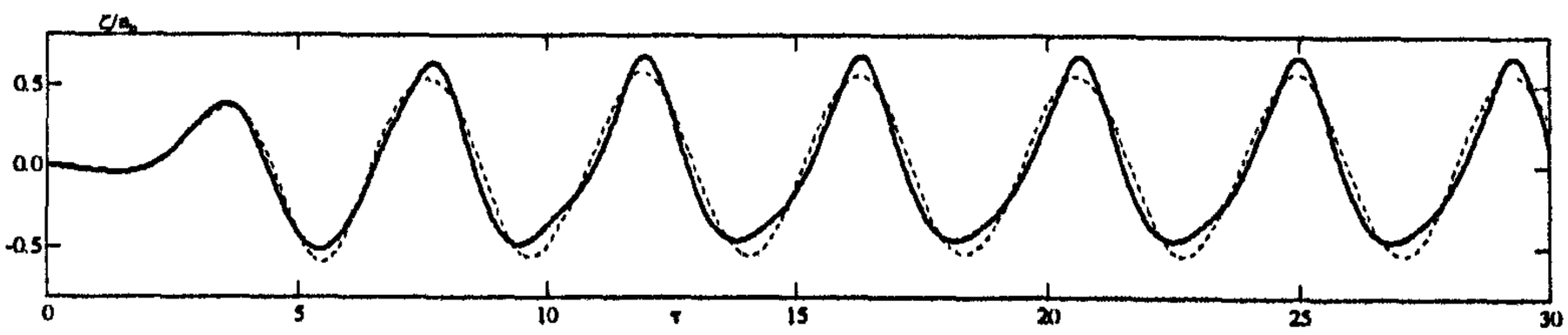

Fig.8.1.5 Wave history recorded at x= -1 due to forced heave

(L=30, ω_b=1.45, $\xi = 0.75$, solid line: a_b=0.082, dot line: a_b=0.0041)

It can be observed that the wave height seems not to be changed dramatically while the shape of the wave history curve becomes more complicated as the amplitudes of motions becomes larger in the cases for forced sway. In the cases for forced heave, the wave history

becomes sharper at crests and flatter at troughs with the increase of the motion amplitudes. All are typical features of nonlinear waves.

To show how well the mesh conform to the variation of the body and free surfaces, the mesh configurations for forced sway motions at some time steps are given in Fig. 8.1.6. From these figures, it can be seen that the mesh quality near the body surface is maintained even though the motion of the floating body is large.

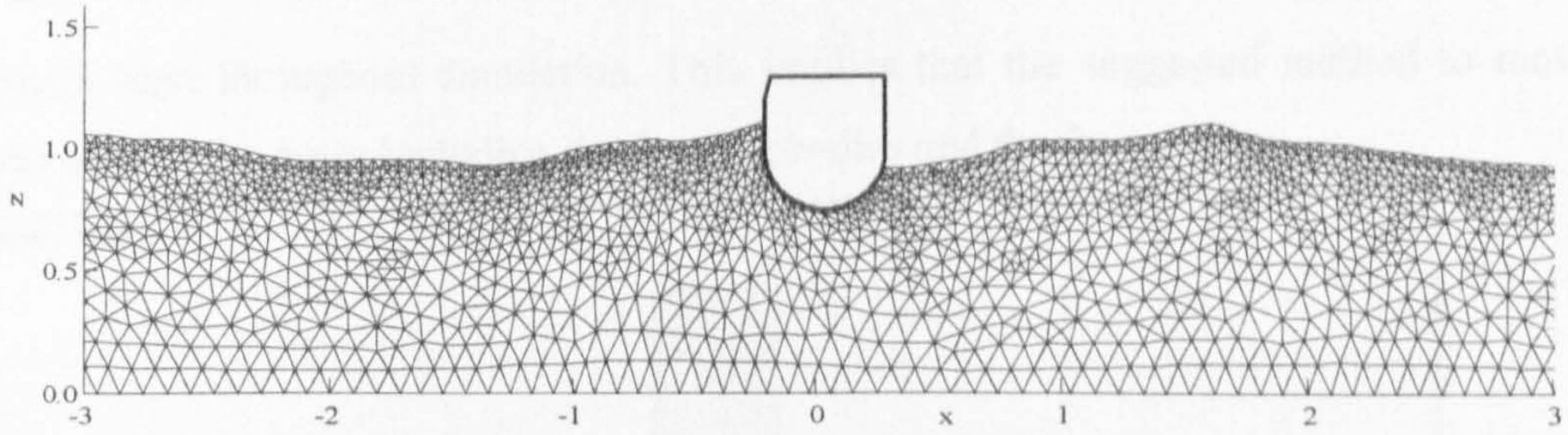

(a)$\tau \approx 14.50$

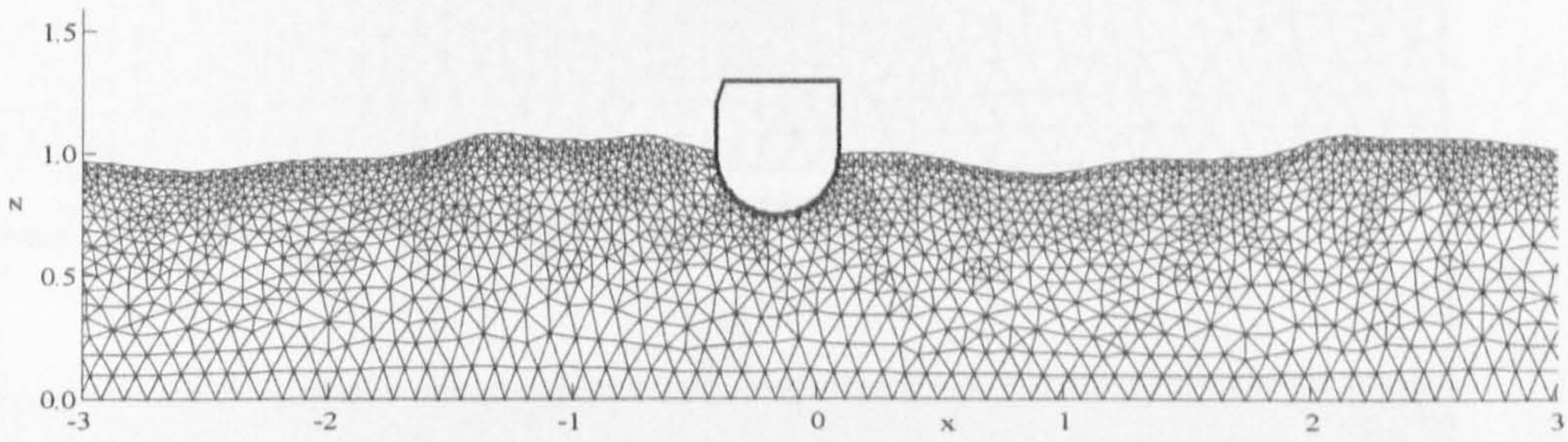

(b)$\tau \approx 15.80$

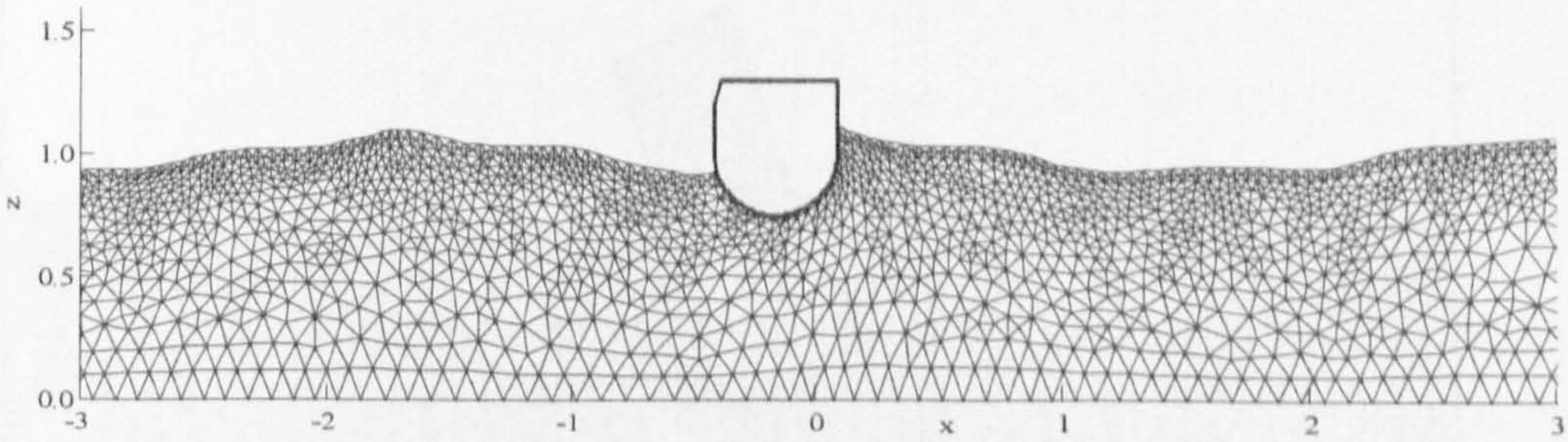

(c)$\tau \approx 16.66$

Fig.8.1.6 Mesh configurations for forced sway motion

(L=30, ω_b=1.45, $\xi = 0.75$ a_b=0.123)

Cases with forced roll motion are also investigated. For a circular cylinder, the normal velocity on the body surface is zero in the case with a roll motion with respect to the centre of the circle. Therefore, the wave generated by such a motion is small. In order to investigate the

mesh moving scheme in the case with roll motion, the circular cylinder is replaced by a barge-type floating body. The mesh is similar to Fig. 8.1.6. The width of this body is $0.25d$ and the draft of the body is $0.5d$ as being seen in Fig.8.1.7a. The motion of the floating body is now described as

$$\Omega_c(\tau) = a_b \omega_b \cos(\omega_b \tau)(1 - e^{\beta\tau}) \tag{8.1.6}$$

where Ω_c is the angular velocity of the floating body. An example of case with forced-roll motion is shown Fig. 8.1.7. In this case, $\omega_b = 1.45, a_b = -0.123rad$. It is found that the mesh quality remain high throughout simulation. This implies that the suggested method to move nodes works well in the cases including the floating bodies and the free surface.

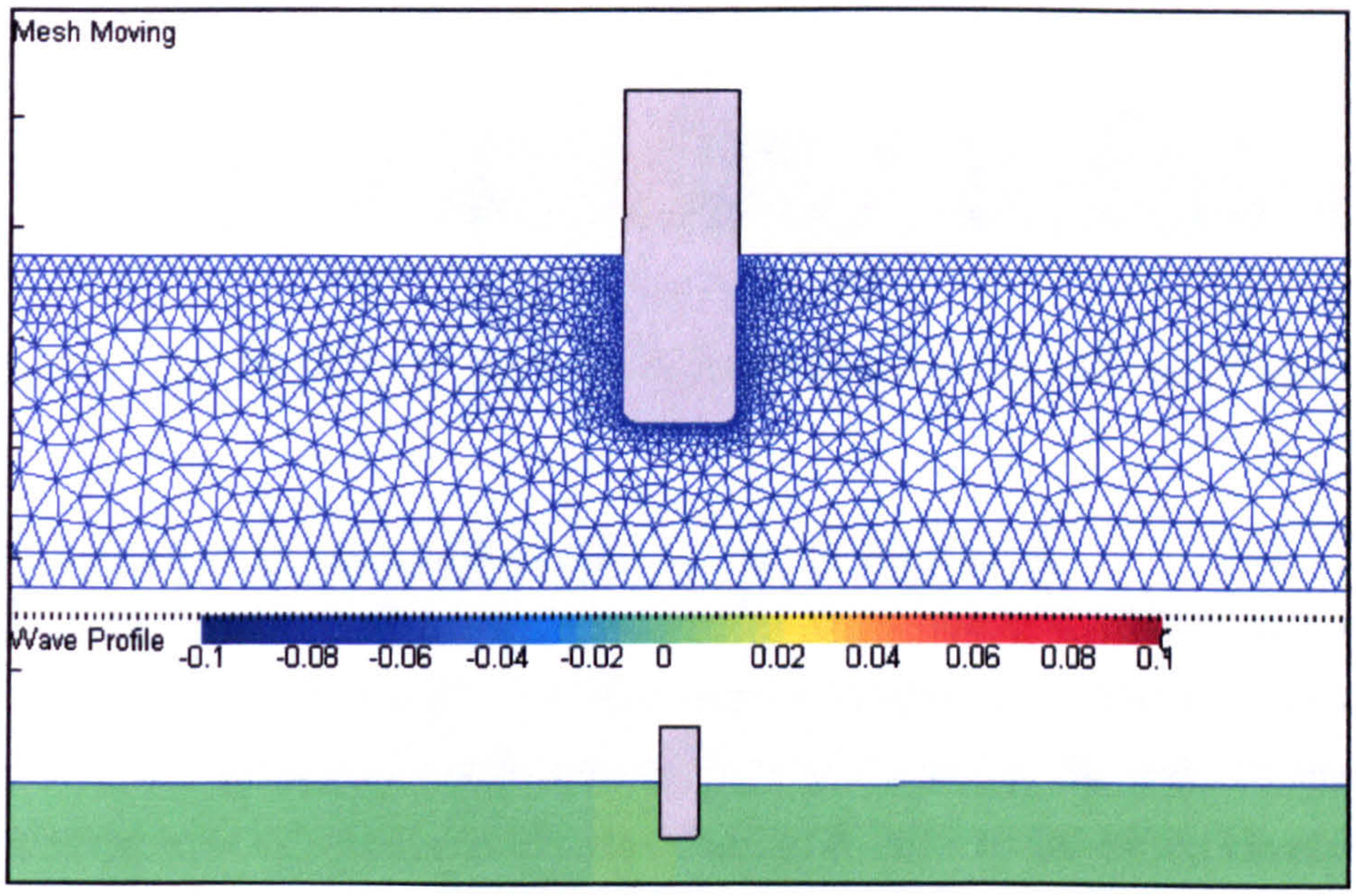

Fig.8.1.7 (a): Initial mesh

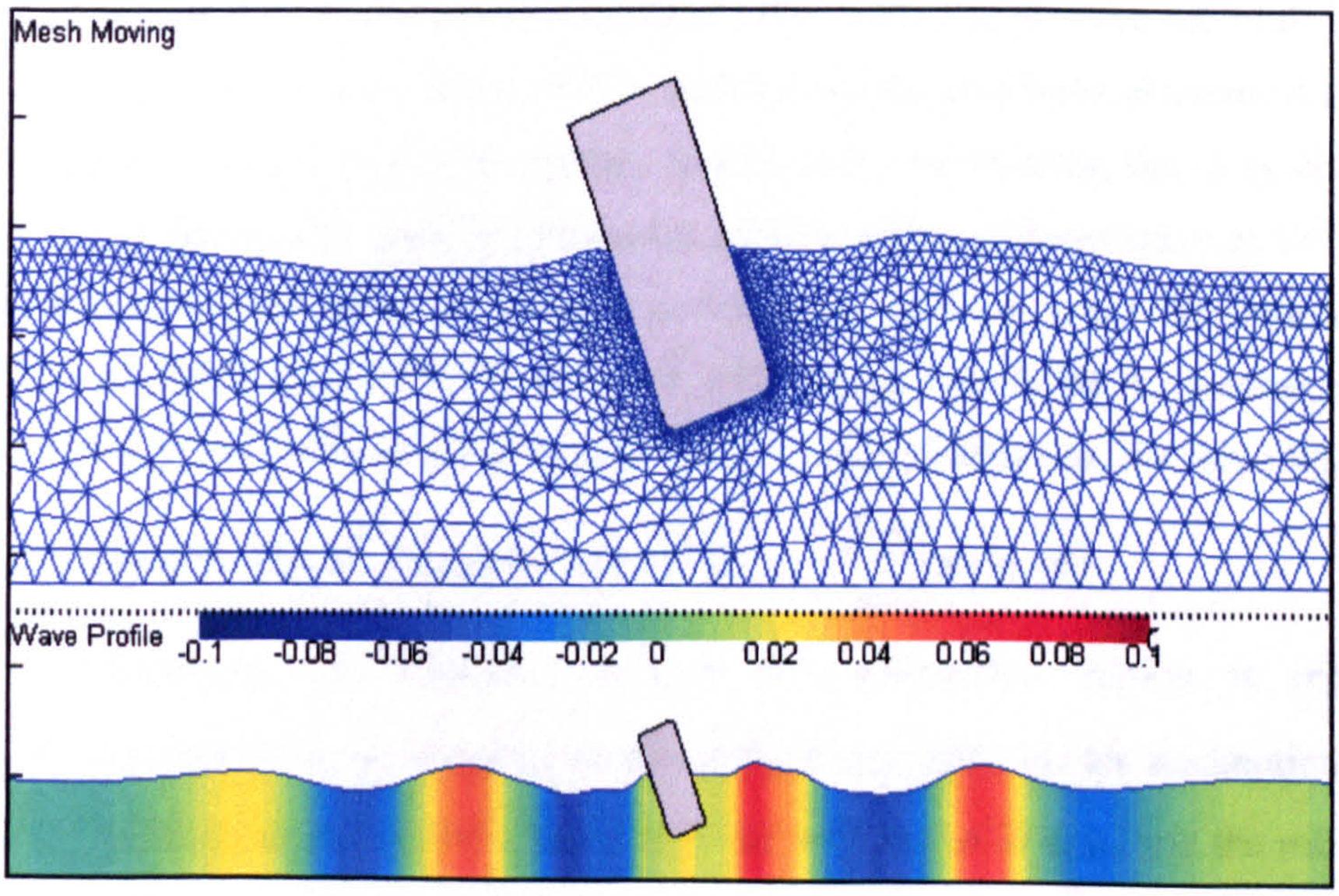

Fig.8.1.7 (b): $\tau = 3.75T$

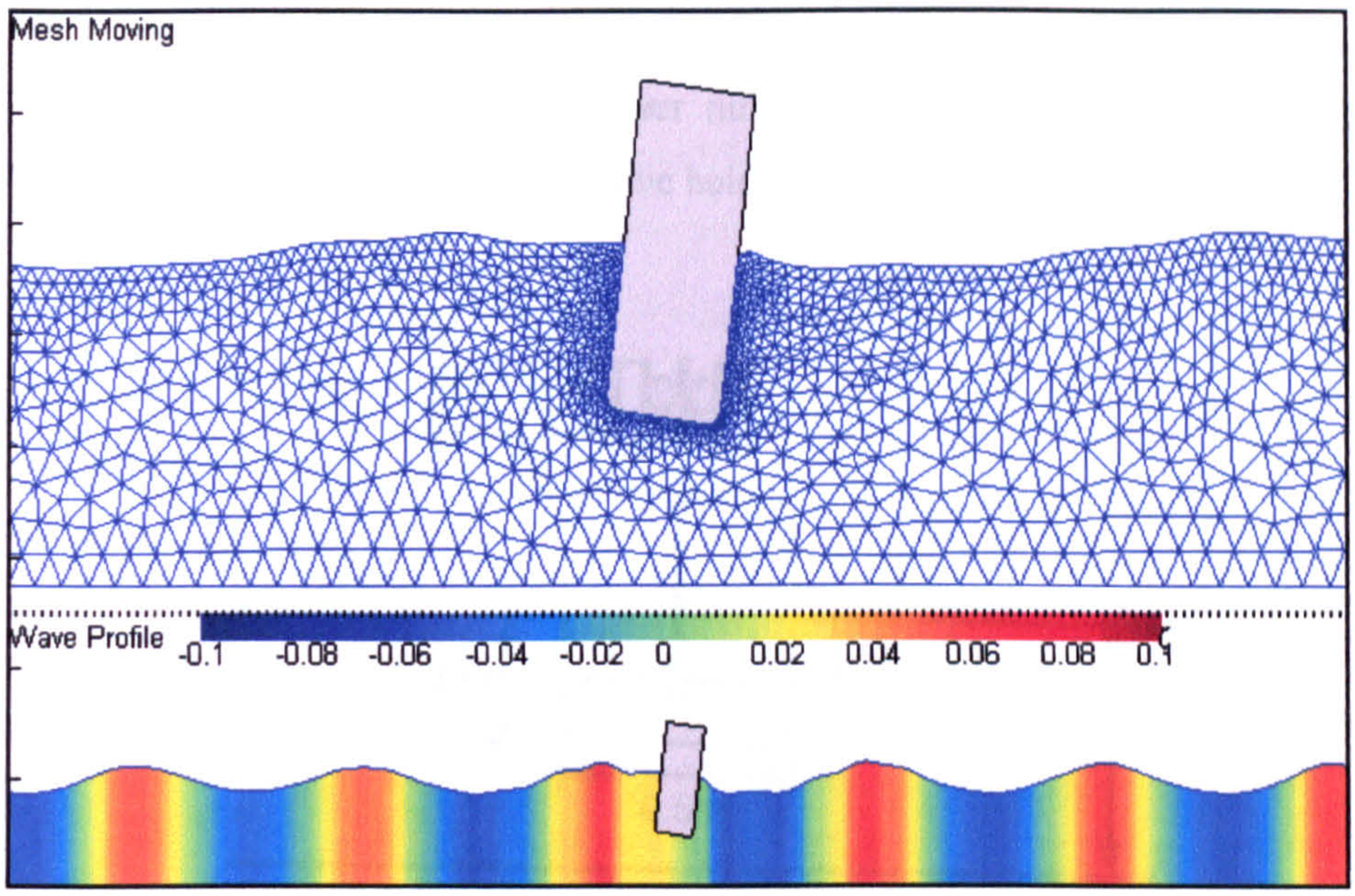

Fig.8.1.7 (c): $\tau = 7.25T$

Fig.8.1.7 Wave profiles and mesh around the floating body with forced-roll motion

8.2. Free-response of 2D moored floating structures to steep waves

After being validated using cases for forced-motions, the QALE-FEM method is now applied to simulate the motions of a 2D free-response floating body. The incident waves are generated by a wavemaker in a tank and the body is moored to the walls of the tank, as illustrated in Fig. 8.0.1. The initial mesh used is similar to Fig 8.1.1 (b) but the circular cylinder is changed to a barge-type floating body. For this body, the mass is 125kg; the moment of inertia about the gravitational centre is 4.05 kg·m^2; the width (B_b) is 0.5m; the draft is 0.25m; the local radius of round corner of the body is 0.064m and the gravitational centre is located at 0.885m measured from the keel of the barge. In this work, the mooring line is modelled by a horizontal spring through the gravitational centre with the spring stiffness taken as 197.58 N/m. These parameters and the shape of the body are chosen to be consistent with those in Koo & Kim (2004) and Tanizawa (1995) whose results will be used to validate the present numerical model. A sketch of this problem is shown as Fig.8.2.1. In the simulations, the mean water depth of the tank is equal to the wave length determined by $\lambda = \frac{2\pi g}{\omega^2}\tanh(2\pi)$.

In the following, the frequency (ω) of the wavemaker motion is represented by $\xi = \omega^2 B_b / 2g$; the force is nondimensionalised by using $\rho g d^2$ on the assumption that the length of the 2D body in the direction parallel to the wavemaker is unit; and the roll angle is nondimensionalised by $(\omega_w{}^2 / g)A_w$, where A_w is the amplitudes of incident waves. Other

parameters are nondimensionalised by the same way as in previous sections. The numerical results are compared with experimental results of Nojiri & Murayama (1975), the analytical solution given in Koo & Kim (2004), other numerical results of Koo & Kim (2004) and Tanizawa (1995). Two different incident wave height results are also compared.

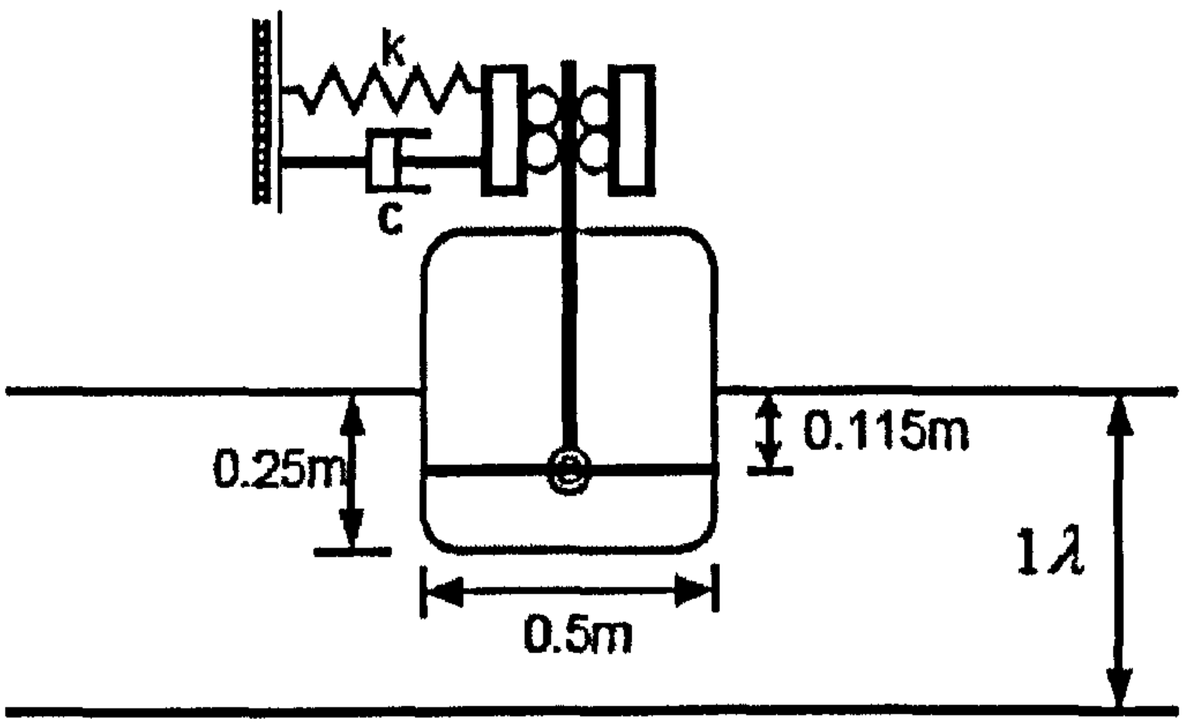

Fig.8.2.1 Sketch of surface piercing single barge simulation (Koo & Kim ,2004).

(Radius of barge round corner=0.064m, width=0.5m, draft=0.25m)

8.2.1. Wavemaker ramp function and artificial damping technique

It is well known that the waves generated by a wavemaker in a tank are characterised by a transient wave profile in the front part of a wave train even though the motion of the wavemaker is purely harmonic. The transient wave profile often consists of several waves with different lengths and heights and a larger wave crest separating the transient and steady parts in the wave train. If one aims to investigate the properties of steady-sate responses, such as RAOs, of floating bodies, the transient waves and corresponding body responses are useless and hence they should be suppressed in order to reduce computational cost. Three methods may be used for this purpose. The first one is to apply wavemaker ramp functions that reduce the wave heights in the transient part. The second is to add artificial viscosity in the dynamic equations of floating bodies (called artificial damping technique), which diminishes the transient body responses. The third method is the combination of the first and the second ones. Details about them are given below.

Two wavemaker ramp functions are investigated. The first one is similar to those in Eatock Taylor, Wang & Wu (1994) and Eatock Taylor (2005). The wavemaker motion corresponding to the first ramp function, called 'Ramp1', is governed by

$$S_w(\tau) = -a\cos(\omega\tau), \tag{8.2.1}$$

$$U_w(\tau) = a\omega\sin(\omega\tau), \tag{8.2.2}$$

$$\dot{U}_w(\tau) = a\omega^2\cos(\omega\tau)(1-e^{\beta\tau}) \tag{8.2.3}$$

where S_w, U_w and $\dot{U}_w$ are the displacement, velocity and acceleration of the wavemaker respectively; and the coefficient β is the same as that in Eq. (8.1.3) with ω_b replaced by ω. In this approach, the generated wave is not modified by the ramp function because the velocity of the wavemaker and so the velocity potential are not affected. The ramping is only performed on the acceleration of the wavemaker, which implies that the value of $\partial\phi/\partial t$ and so forces on bodies are ramped. The wavemaker motion corresponding to the second ramp function, called 'Ramp2', is governed by

$$S_w(\tau) = -a\cos(\omega\tau)r(\tau), \tag{8.2.4}$$

$$U_w(\tau) = \partial S_w / \partial\tau \quad , \tag{8.2.5}$$

$$\dot{U}_w(\tau) = \partial U_w / \partial\tau \tag{8.2.6}$$

$$r(\tau) = \begin{cases} 1 & \tau > T_f \\ \left[1 - \cos(\pi\tau / T_f)\right]/2 & \tau \le T_f \end{cases} \tag{8.2.7}$$

where T_f is the cut-off time of the ramp function and is determined by

$$T_f = \kappa L_w / C_g \tag{8.2.8}$$

in which κ is a coefficient between 0 and 1; and C_g is the group velocity of waves.

The efficiency of Ramp1 and Ramp 2 are investigated with $\xi = 1$, $a = 0.0016$, $L \approx 15$ and $L_w \approx 10$. The mesh used is unstructured with about 35 elements on the free surface in each wavelength. For the Ramp2, $\kappa = 0.25$ and $\kappa = 0.5$ are adopted for two cases, respectively.

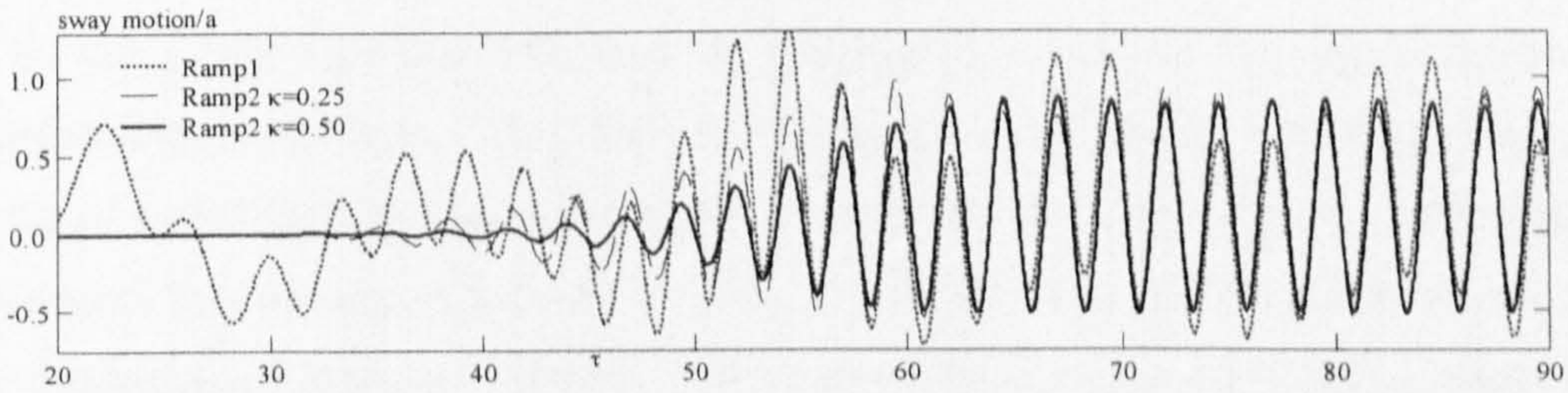

Fig.8.2.2 Sway motion using different ramp functions

Fig. 8.2.2 shows the sway motions obtained by using different ramp functions. It can be observed that Ramp2 can make the calculation become steady sooner than Ramp1, though its effectiveness depends on the value of κ. However, that the waves at the wavemaker generated by using Ramp2 during period $\tau < T_f$ are not the incident waves desired, implying that the waves at the floating body do not become the desired incident waves until $\tau > T_f + L_w / C_g$. In addition, even after the desired incident waves arrive at the floating body, its responses exited by undesired waves do not disappear immediately and so take extra time (T_e) to become those

excited by the desired waves. As a result, the time history of motions during the time $\tau < T_f + L_w / C_g + T_e$ should not be considered when estimating RAOs. Based on this analysis, it is obvious that the shorter the sum of $T_f + T_e$, the less CPU time is required for estimating RAOs. As can be seen in Fig. 8.2.2, the transient period becomes longer, indicating that T_e becomes larger, with T_f being shorter (i.e., smaller κ) when using the Ramp2 only. Therefore, the reduction in T_f does not necessarily lead to the reduction in the sum of $T_f + T_e$.

The other option left is to reduce T_e by using the artificial damping technique mentioned above. With this technique, the motion equation, e.g., Eq. (3.2.2), is modified to

$$[M]\dot{U}_c + \beta_a U_c = F \tag{8.2.9}$$

where β_a is the artificial damping coefficient. It is given by

$$\beta_a(\tau) = \begin{cases} 0 & \tau > T_d \\ \alpha\beta_c[1+\cos(\pi\tau / T_d)]/2 & \tau \le T_d \end{cases} \tag{8.2.10}$$

where β_c is the critical damping corresponding to a motion component (such as sway or heave); α is a coefficient; and T_d is the time during which the artificial damping is active.

In this case, the natural frequencies in heave and roll motion are much higher than wave the frequency of the incident wave. The transient effect is not evident in these two motions and therefore those two motion modes can become steady soon. So, this type of artificial damping coefficient is only added to sway motion in this section. In order to investigate the effect of different α, the same cases as Fig.8.2.2 are carried out.

From Fig. 8.2.2, one may find that there is long-period oscillation existing in the sway motion (particularly, dotted curve), that is due to the transient response of the floating body and should be suppressed. One may also find that that this type of oscillation disappears after long – period calculation by damping of the sway motion. The larger the maximum displacement, the slower the oscillations disappear. The maximum sway displacement can be used to assess the CPU time required to reach steady state. In the investigation for the choice of α, the maximum sway displacements in cases with different values of α are calculated and the results are plotted in Fig. 8.2.3.

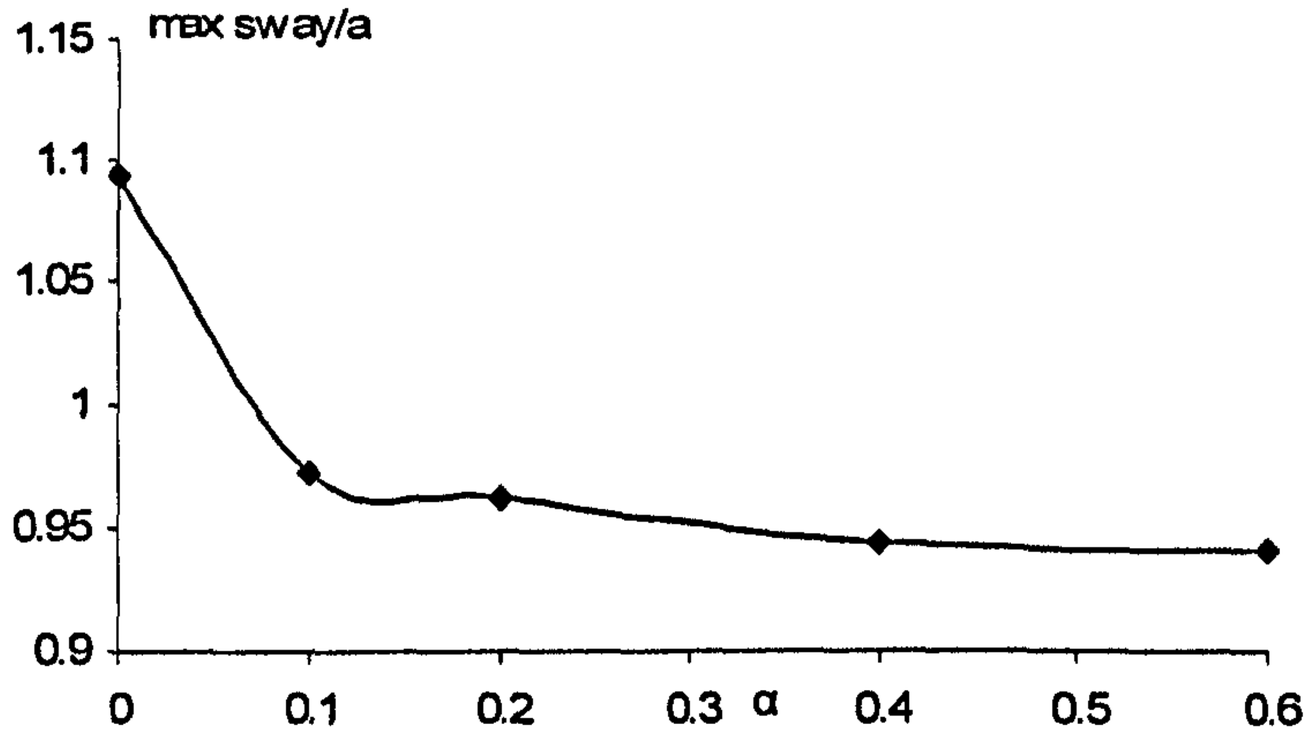

Fig.8.2.3 Maximum displacement in cases with different α

($\varpi = 0.25$ and $T_d = L_w / C_g$)

From this figure, it is seen that the maximum sway displacement decrease with the increase of α. The rate of decrease is large when α <0.1, but slows down when α >0.1. Particularly when α >0.4, the maximum displacements are almost the same as for α =0.4 and α =0.6 As a result of this investigation, α is best taken as 0.5. Although this technique may be used alone, we will only discuss numerical results obtained by combining it with the Ramp2.

To show the effectiveness of the combined method, the two cases for the Ramp2 with $\kappa = 0.25$ and $\kappa = 0.5$ in Fig.8.2.2 are considered again but in the first case, both the Ramp2 with $\kappa = 0.25$ and the artificial damping technique with $\alpha = 0.5$ are applied. Fig. 8.2.4 gives the results, in which the dashed line denotes the result from the combined method while the solid line represents the result obtained by only using the Ramp2 with $\kappa = 0.5$. It is interesting to see that the response by the combined method using $\kappa = 0.25$ becomes steady at about $\tau = 60$, approximately two wave periods earlier than that by the Ramp2 alone with $\kappa = 0.5$, which is steady at about $\tau = 65$. However, as shown in Fig. 8.2.2, the response corresponding to $\kappa = 0.25$ becomes steady much later than that to $\kappa = 0.5$ when using the Ramp2 alone. This indicates that the combined method is more effective in suppressing the transient response.

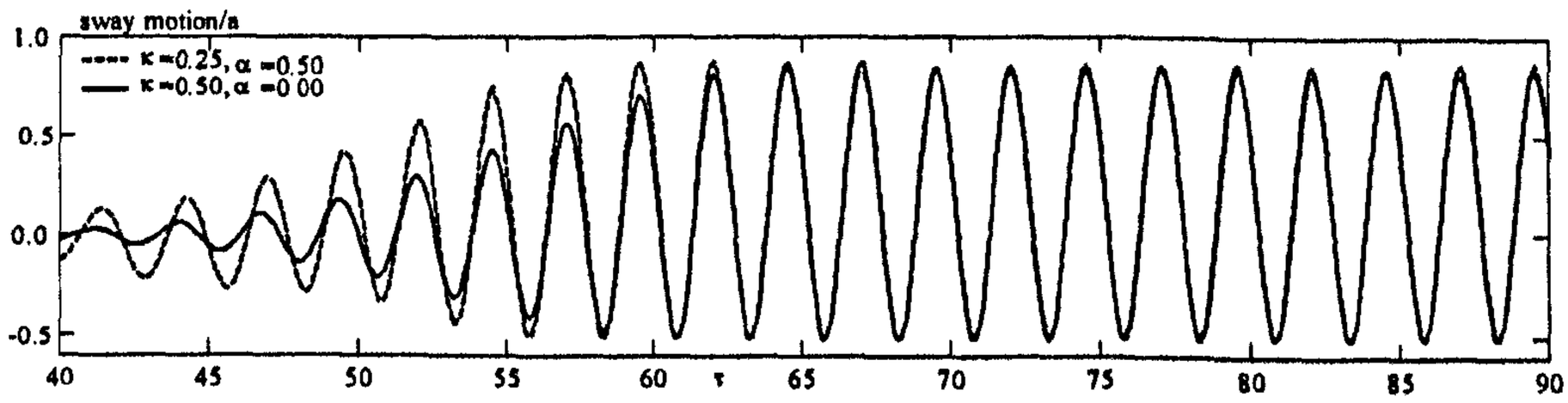

Fig.8.2.4 Sway motion by using artificial damping technique

Apart from these given above, the hydrodynamic forces acting on the body obtained by using different ramp functions and/or the artificial damping technique are also investigated. The results are plotted in Fig.8.2.5. It shows that no matter which method is used, the hydrodynamic force acting on floating body tends to the same steady-state limit. This result indirectly indicates that the wavemaker ramp function and artificial damping technique do not affect the RAOs. This implies, the ramp function together with artificial damping technique can get the actual RAOs using less CPU time. Therefore, the highest computational efficiency may be obtained.

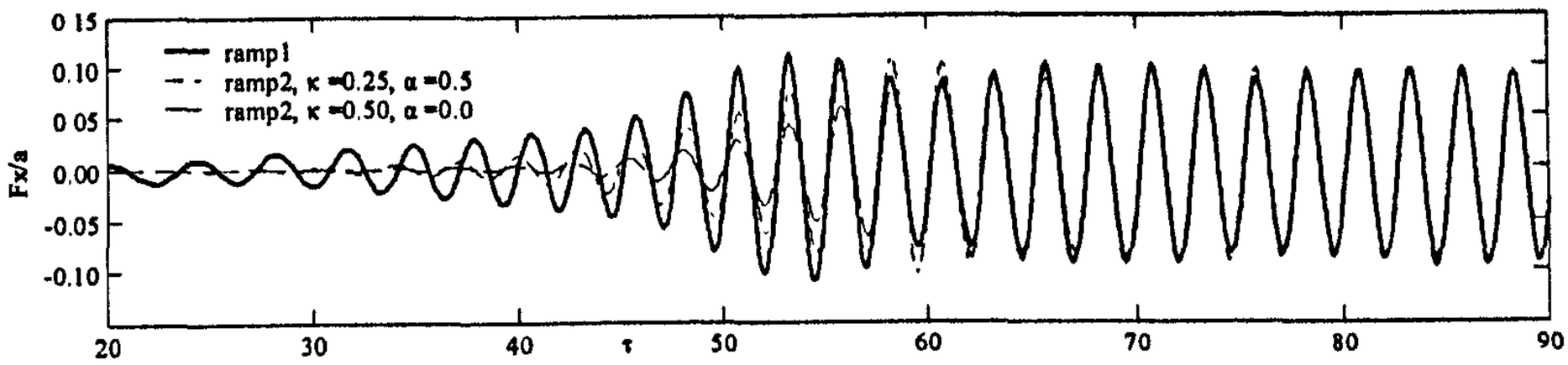

Fig.8.2.5 Hydrodynamic force in cases with different ramp functions

8.2.2. Convergence properties of the ISITIMFB

One of developments in this work is the suggestion of the ISITIMFB procedure to find the forces and the motions of the floating body. Its convergence properties, i.e. the iteration count to achieve a specified accuracy, are presented and discussed in this subsection for the following case: the barge is similar to the one described at the beginning of Section 8.2; the length of the numerical tank is taken as $L \approx 13$ with $L_w \approx 8$; and the dimensionless incident wave height generated is about 0.018 and the frequency parameter is $\xi = 0.4$. Similar to above cases, the mesh used is unstructured with about 35 elements on the free surface in each wavelength. As has been discussed in Chapter 6, the two most important factors affecting the iteration count are the time step and the natural period (frequency) of the system. Thus we mainly look at the convergence properties by changing the time step and the natural period in the following.

The results for different time steps are presented by three curves in Fig 8.2.6 (a), which correspond to three specified relative errors: 0.1%, 0.5% and 1%. In the figure, there are two rows of numbers under the horizontal axis. The first row represents the number of time steps in each wave period and the second row gives the length of the time step, i.e. the period divided by the number in the first row. In these cases, the mass of the floating body is the same as before, i.e. 125 kg. Under this condition, the value of ξ based on the natural frequency is about 0.5 ~ 0.6 as shown by the experimental data in Nojiri & Murayama (1975). One may observe from this Figure that the iteration count for a specified error decreases with the increase in the number of time steps in each period as expected. One may also observe that the convergence can be

achieved within 10 iterations when the control error is 1% and the number of time steps in each period is larger than 64; and that reducing the control errors leads to a slight increase in iteration number. It should be noted that the wave frequency is near the natural frequency in these cases. For other cases (not presented) where the wave frequencies are much larger than the natural frequency, the convergence properties are better than those shown here.

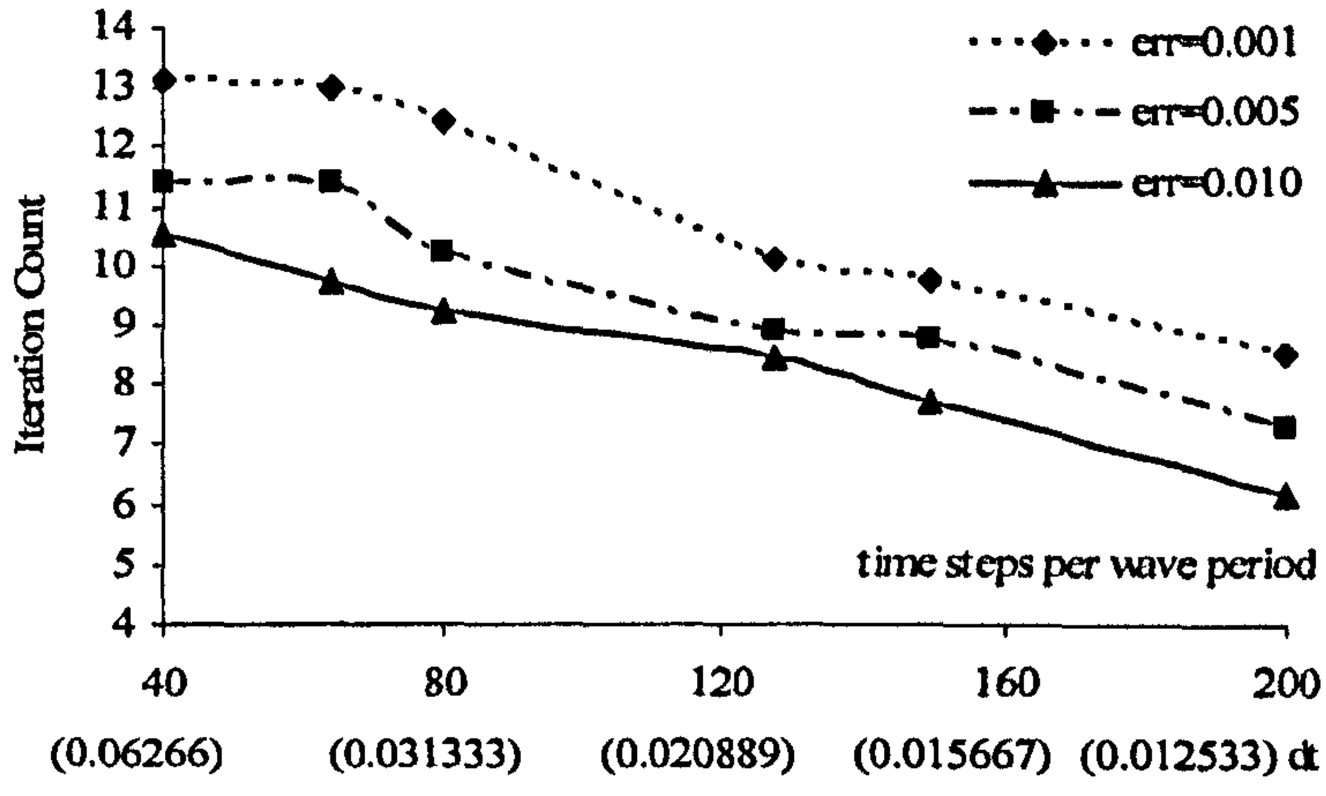

(a) iteration count *vs* time step

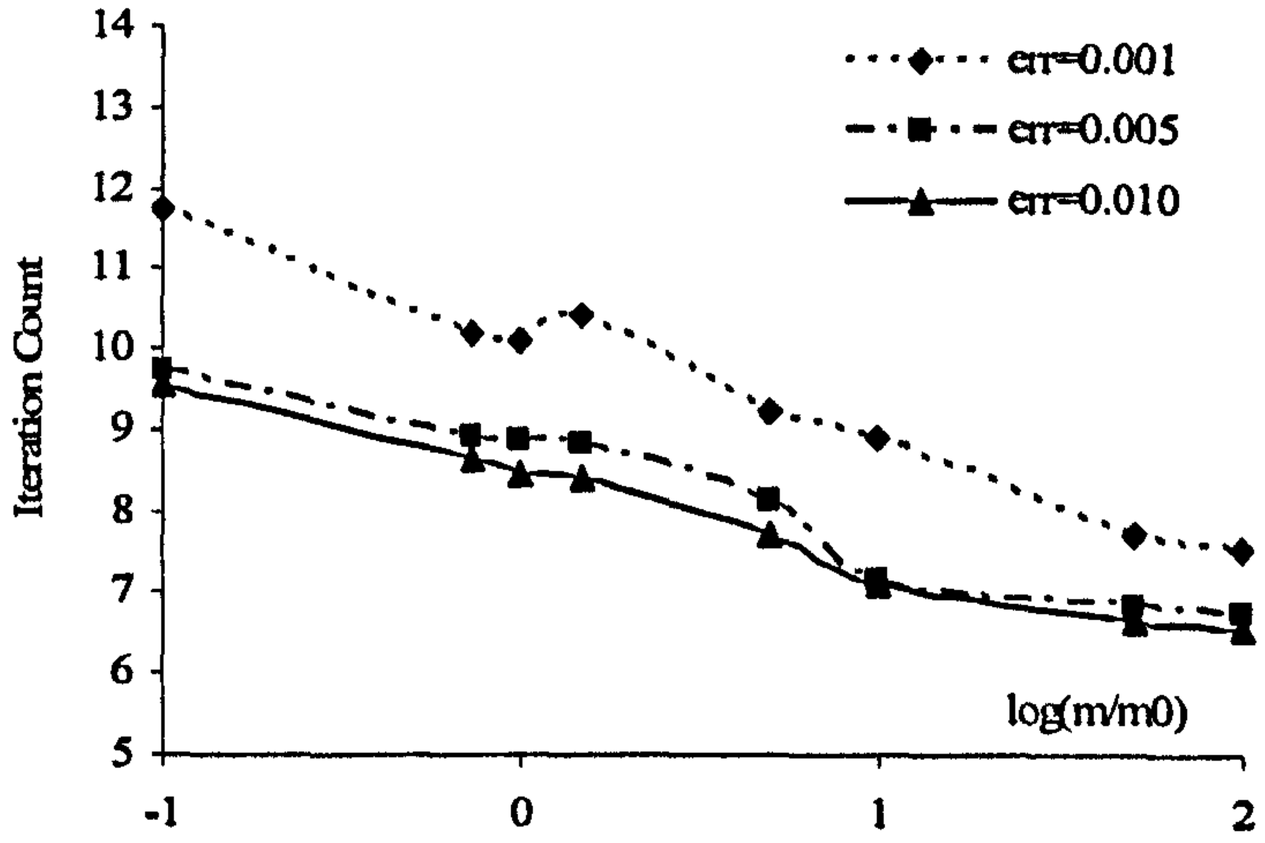

(b) iteration count *vs* mass

Fig.8.2.6 Iteration counts for different time steps and different masses
(err: the control iterative error)

The results corresponding to the different natural frequencies at three different control errors are depicted in Fig. 8.2.6b, which are obtained by artificially changing the mass in the range of $0.1m_0 \le m \le 100m_0$ (m0: the mass for Fig. 8.2.6a) without changing the mooring stiffness and the shapes of the floating body (i.e., the restoring coefficient being roughly fixed). Under this condition, the square of the natural frequency should be inversely proportional to the

mass; and on this basis, the iteration count is plotted against the ratio of the mass to m_0 rather than the frequency in the figure. The time step is taken as $T/128$ and all other parameters are the same as those in Fig.8.2.6 (a). The results in Fig 8.2.6b indicate that the iteration count varies with the change in mass or natural frequency but only in a small range for a large range of change in mass. Similar to Fig. 8.2.6a, the difference in the iteration count does not change dramatically when the control error changes from 0.1% to 1%. In addition, the iteration count is smaller than 10 over the range of mass investigated when the control error is 1%.

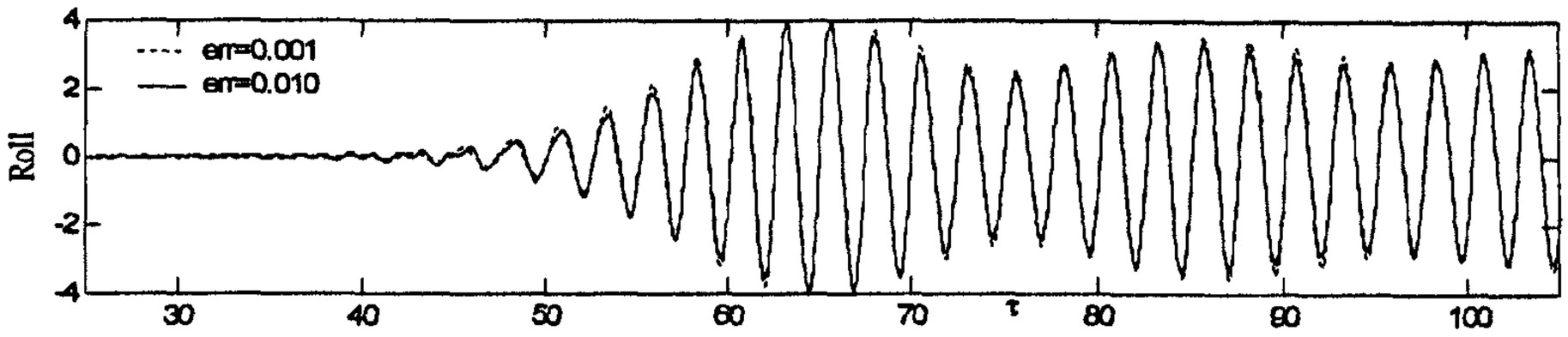

Fig.8.2.7 Comparison of roll histories for different control errors ($dt = T/64$)

Another point that needs to be discussed is how the control error in the ISITIMFB procedure affects the computed responses. Fig. 8.2.7 shows the comparison of roll motions obtained by using two different control errors for the cases of $\Delta t = T/64$ in Fig. 8.2.6. It can be seen that the difference between the results is negligible. Therefore, one may consider the control error of 1% is acceptable in engineering practice but it is recommended that the computed results are compared with those by using a smaller control error such as 0.5%, which is followed when acquiring the numerical results in the thesis.

8.2.3. Comparison with other force calculation methods

In this subsection, the ISITIMFB procedure is firstly compared with a fully explicit method obtained by replacing Eq. (6.1.1) with an explicit Adams-Bashforth scheme (see, William Gear C, 1971),

$$\vec{U}_b^{n(k)} = \vec{U}_b^{n-1} + \frac{\Delta t}{2}(3\vec{A}_b^{n-1} - \vec{A}_b^{n-2}). \tag{8.2.1}$$

For the fully explicit method, the iteration is not needed. The time step is taken as $T/200$ and $T/64$; and other parameters are the same as those used in Fig.8.2.7. The results are plotted in Fig. 8.2.8. From Fig. 8.2.8 (a), it is observed that the ISITIMFB leads to similar results to the fully explicit integration procedure when the time step is small ($T/200$). However, when the time step becomes larger ($T/64$), the results from the ISITIMFB have negligible difference from those for smaller time steps while the results from the fully explicit integration procedure pose evident disagreement with those using smaller time step (Fig.8.2.8 (b)). This indicates that the ISITIMFB proposed in this thesis can give more accurate results at the same time step or can

use larger time steps for specified accuracy and so needs less CPU time for a given period of simulation than the explicit method.

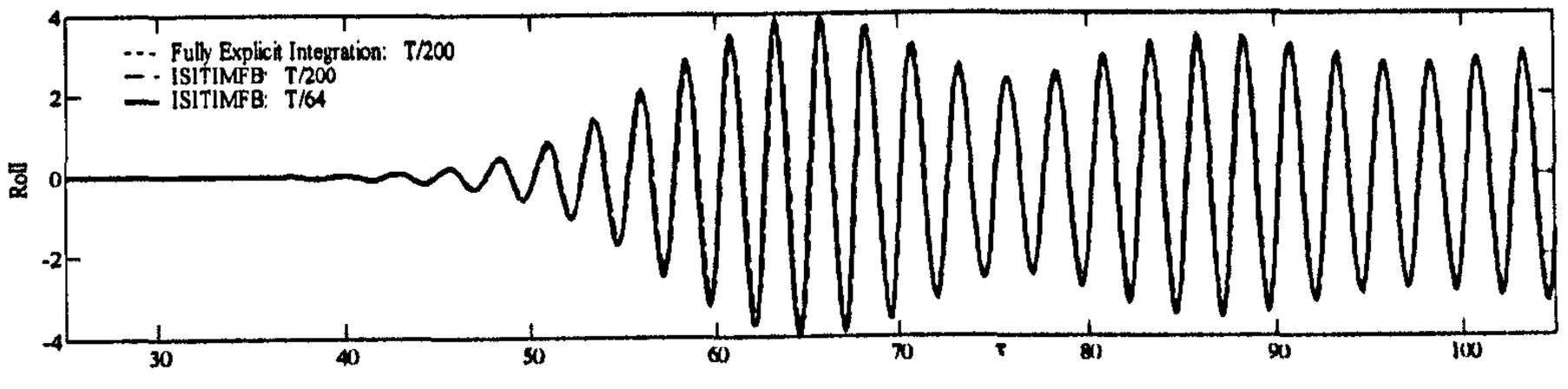

(a)

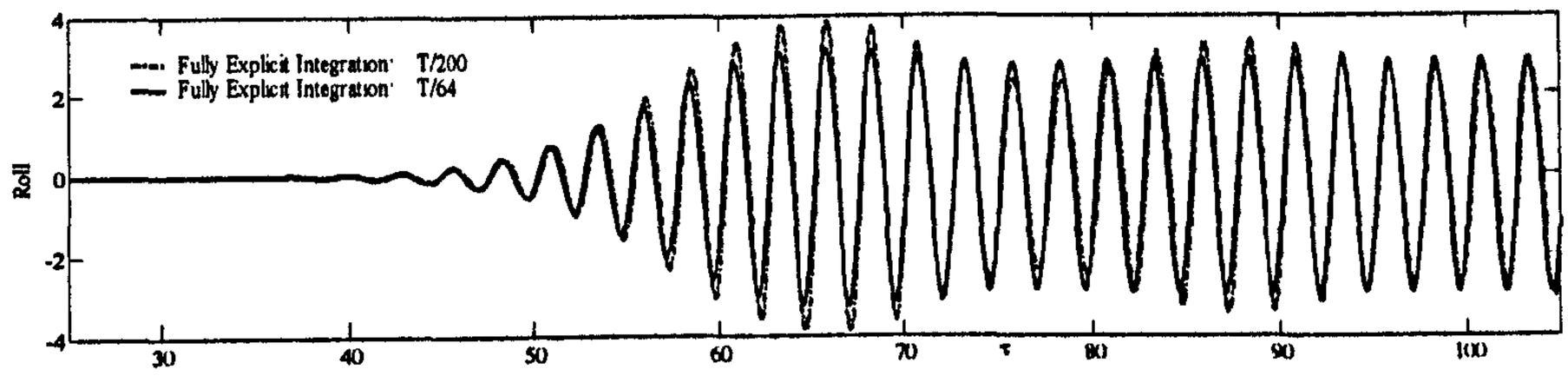

(b)

Fig.8.2.8 Comparison of roll motions from the ISITIMFB and explicit procedures

Secondly, to demonstrate the behaviour of the ISITIMFB, its results are compared with those from fully-updated and frozen-coefficient 4th-order Runge-Kutta schemes (Koo & Kim, 2004) and shown in Fig. 8.2.9, using the same parameters except for the wave height and the time step as for Fig. 8.2.8. To consider the same case as in Koo& Kim (2004), the dimensionless incident wave height of 0.0025 and the time step $\Delta t = T/40$ are used here.

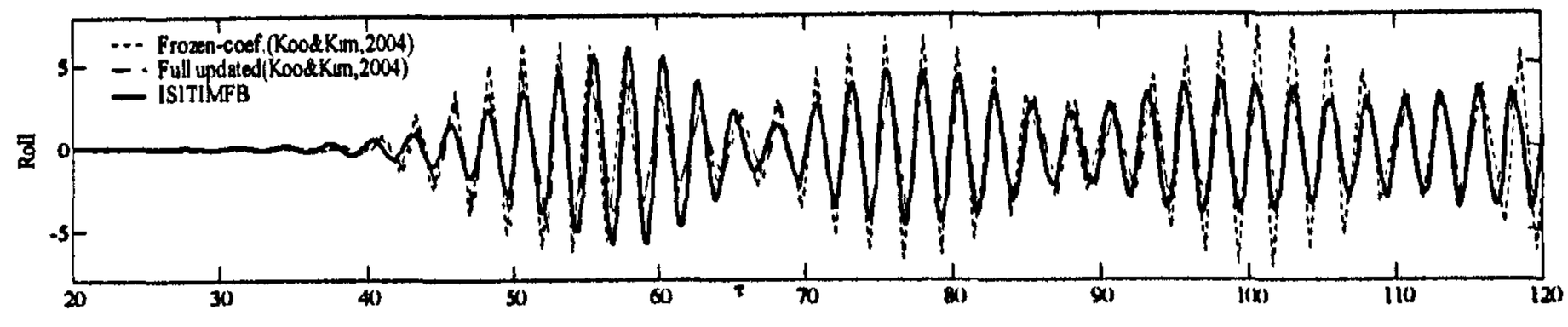

Fig.8.2.9 Comparison of roll motions from ISITIMFB and other methods

(Frozen-coefficient scheme: $\Delta t = T/128$; ISITIMFB and Fully updated Runge-Kutta method: $\Delta t = T/40$)

As can be seen, the presented procedure leads to steady-state results that agree well with those from the full-updated Runge-Kutta method while the frozen-coefficient Runge-Kutta scheme does not give similar results even when the time step is as small as *T*/128. The results for the frozen-coefficient Runge-Kutta scheme also tend to be unstable as indicated by Koo & Kim (2004). This clearly demonstrates that the ISITIMFB can alleviate the instability problem

of the frozen-coefficient method and can be as accurate and robust as the full-updated Runge-Kutta method but without the need of multiple updating of fluid domain geometries and so of the coefficient matrix in one time step forward.

8.2.4. RAOs of sway, heave and roll motions

To further validate the QALE-FEM method in the cases with a floating body, the RAOs of sway, heave and roll motions of the barge are compared with the linear solution from frequency domain analysis as given in Koo & Kim (2004), Maruo (1960) and the experimental data in Nojiri & Murayama (1975). In the numerical simulations, Ramp2 together with the artificial damping technique is employed, for which the associated parameters are taken as $\kappa = 0.25$, $T_d = L_w / C_g$ and $\alpha = 0.5$; as in above sections, the unstructured mesh is adopted with about 30 elements on the free surface in each wavelength and the time step is taken as $\Delta t = T/128$. For all cases considered here, the amplitudes of the wavemaker are adjusted properly so that generated incident wave heights are either 0.01m or 0.07m, which are the same as those in the cited publications.

The RAOs of sway, heave and roll motions corresponding to different incident waves are plotted in Fig. 8.2.10 together with the results from other publications. They are estimated by performing the FFT analysis on the steady-state portion of the time histories of corresponding motions. As can been seen, the present numerical results are closer to the linear solution when the incident waves are small (0.01m) but closer to the experimental data when the wave height becomes larger (0.07m). This is reasonable because the experimental data for the larger wave height contain nonlinear effects that are taken into account by the nonlinear numerical simulations but not by the linear solution.

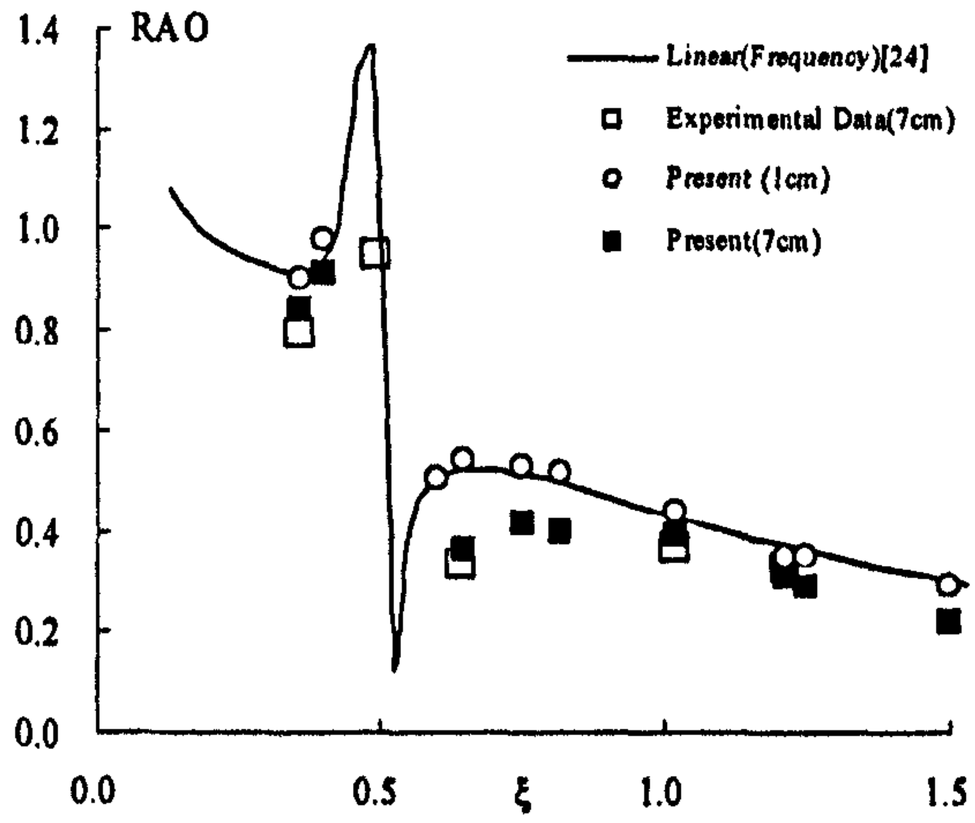

Fig.8.2.10 (a) RAO of sway motion

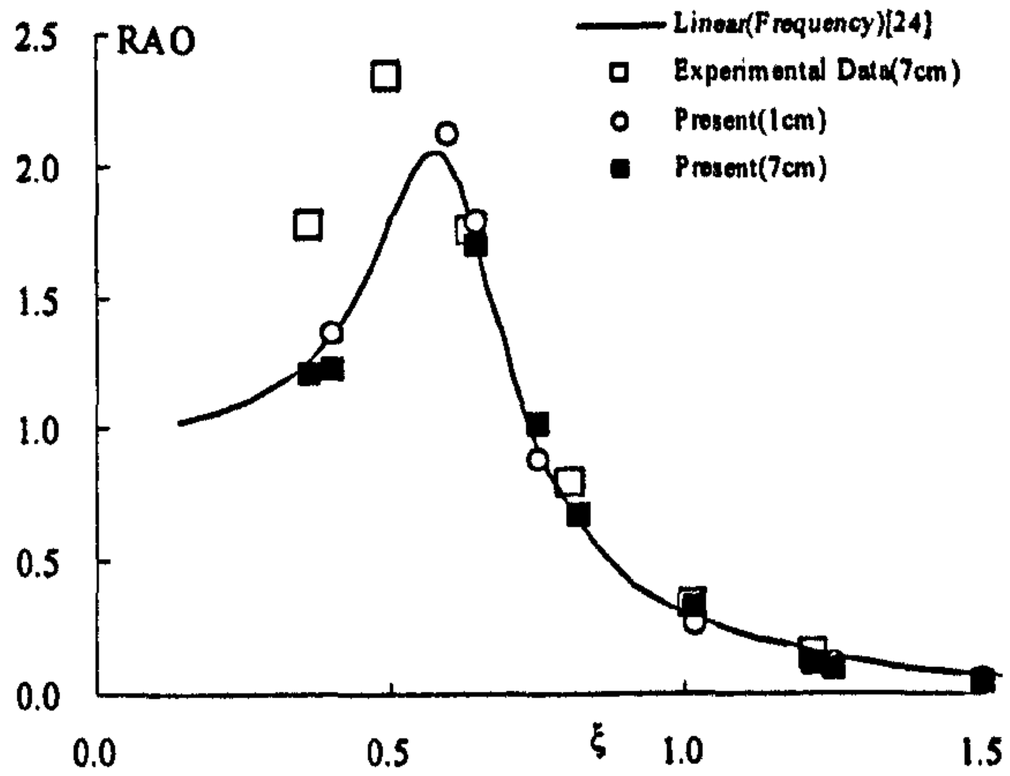

Fig.8.2.10 (b) RAO of heave motion

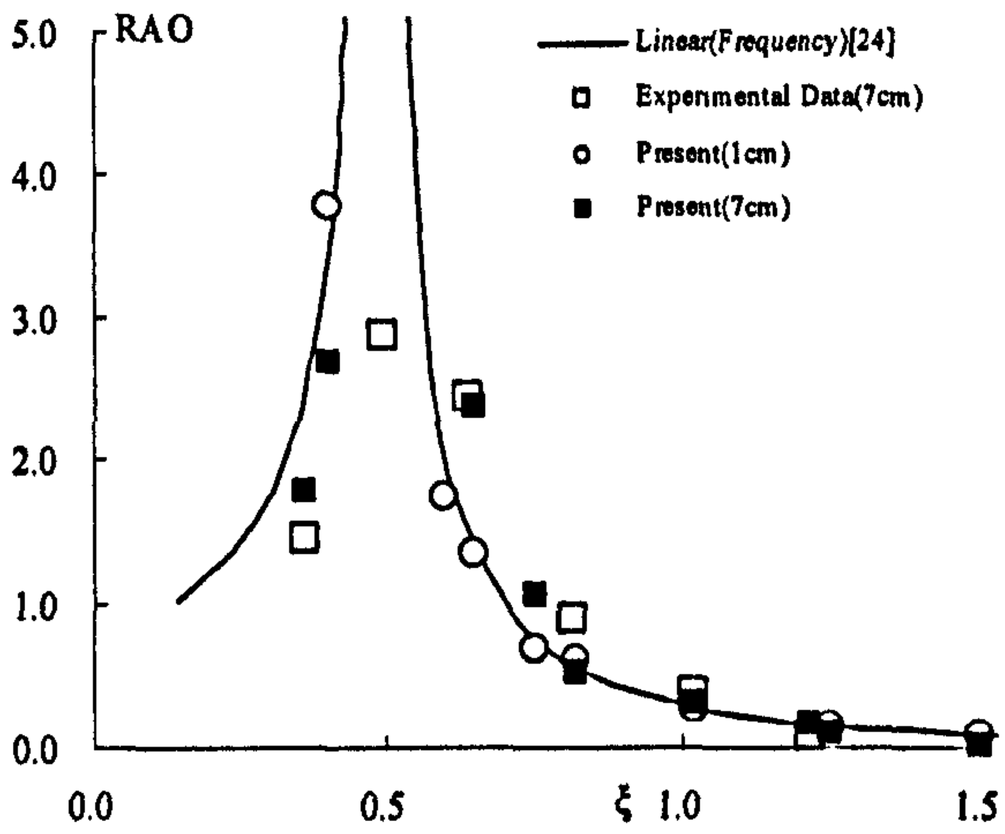

Fig.8.2.10 (c) RAO of roll motion

Fig.8.2.10 RAOs of sway, heave and roll as a function of ξ

However, the difference between experimental data and numerical results is obvious in the area near resonance frequencies. That may be due to the fact the viscosity is not considered in numerical simulations whereas it is inevitable in experiments. To demonstrate that the conjecture might be true, an empirical damping force is added into the roll equation, which is formed by a damping coefficient multiplying the roll velocity. The value of the damping coefficient is taken as 1.5% or 2.8% of the critical damping coefficient in two different simulations. It should be noted that the empirical damping added here plays different rules and is for different purposes from the artificial damping discussed above. The empirical damping here is applied from the start to the end of simulations to approximate the real viscosity and so affects the amplitudes and RAOs even after the motions become steady. The artificial damping discussed in Section 8.2.1 is applied in a specified simulation period from the start in order to

suppress the transient responses and does not affect the amplitudes and RAOs after motions become steady.

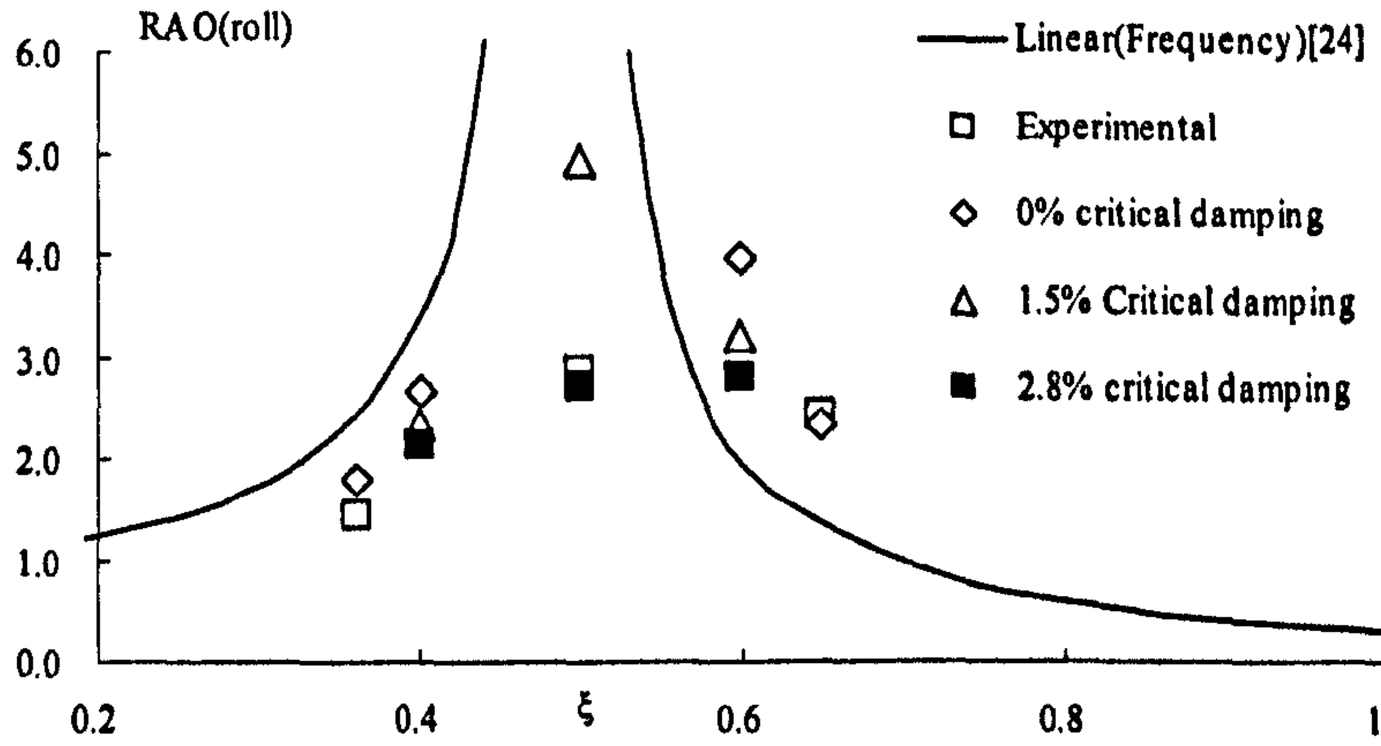

Fig. 8.2.11 RAO of roll motion in cases with roll artificial damping

The RAOs of the roll motion near the resonant frequency obtained by using different empirical damping for the same cases in Fig. 8.2.10 are shown in Fig.8.2.11 together also with the linear solution and the experiment data. It can be seen that when the empirical roll damping is 2.8% of the critical damping, our numerical results agree quite well with the experimental data in the resonant area in this case. One may envisage, therefore, that with an appropriate empirical roll damping, our numerical method can give satisfactory result even when viscosity is important.

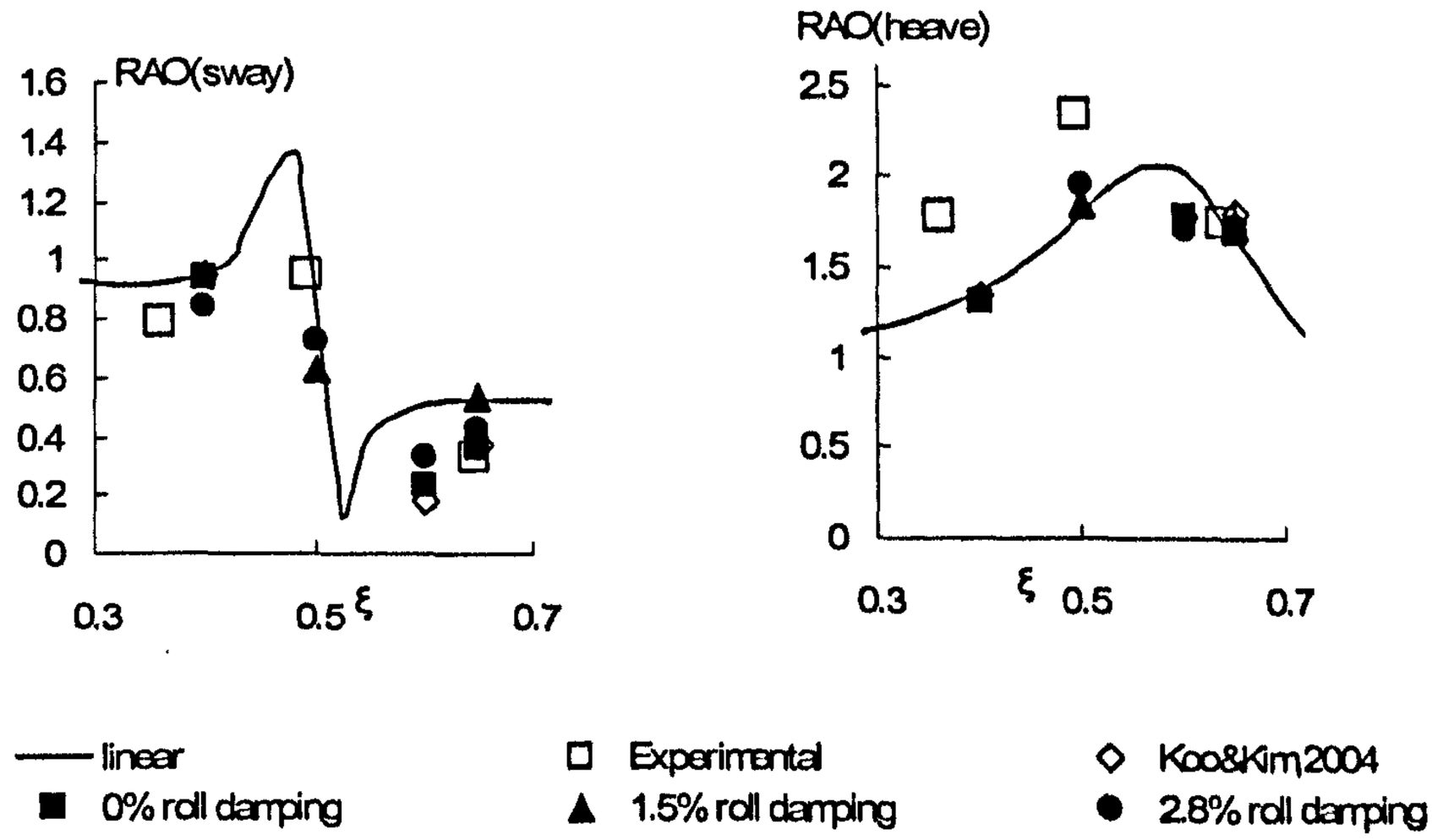

Fig. 8.2.12 RAOs of sway and roll in cases with empirical roll damping

The empirical roll damping not only affects the roll motion, but also affects the sway and heave motion. The corresponding RAOs of sway and heave motion of the case in Fig.8.2.11 are shown in Fig. 8.2.12. This is reasonable, because every mode of the motion is dependent on the other. To show further effect on the motion history caused by additional artificial roll damping, one example of body-motion history is plotted as Fig. 8.2.13. It is observed that the roll motion is decreased by artificial damping which also changes the RAOs of sway motion composition, whereas the heave motion seems not to change.

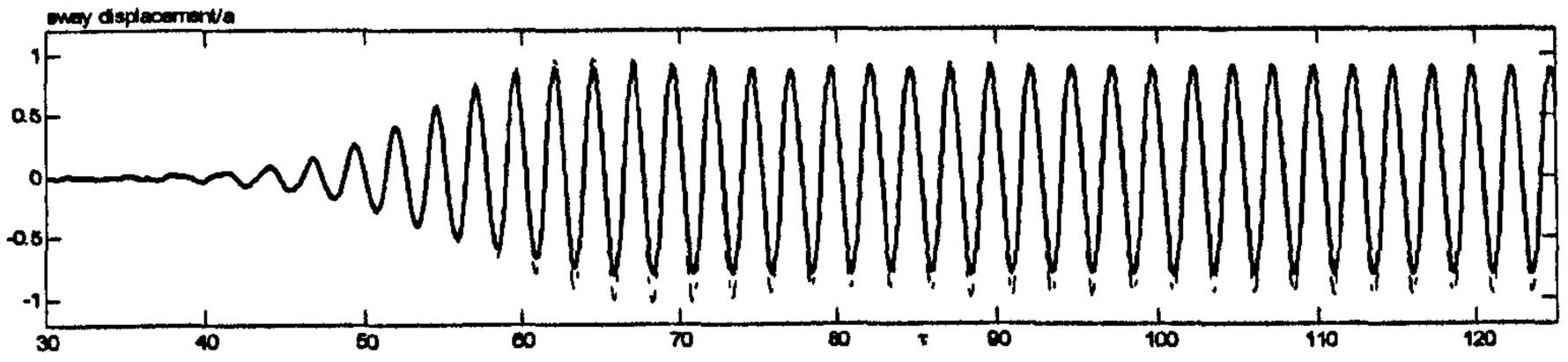

Fig.8.2.13 (a)sway

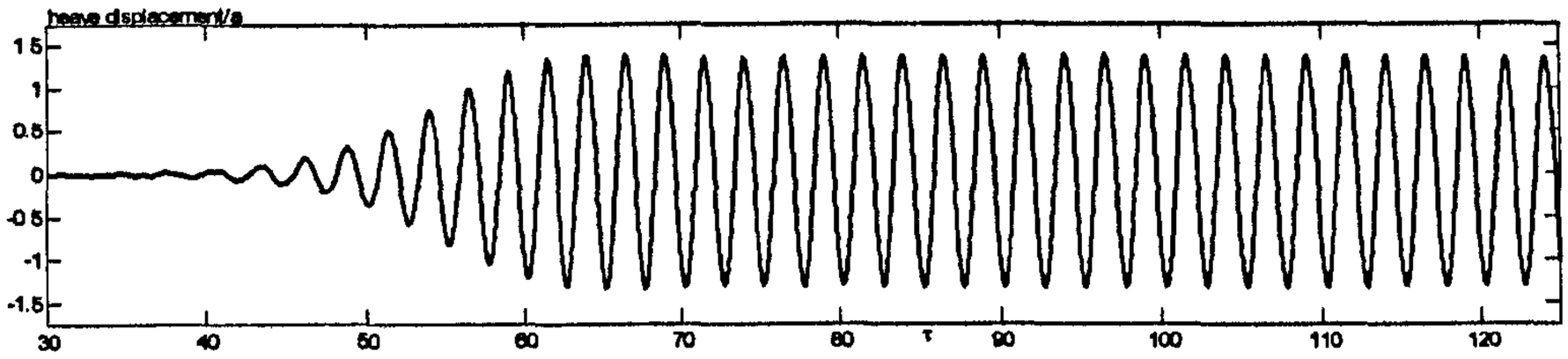

Fig.8.2.13(b)heave

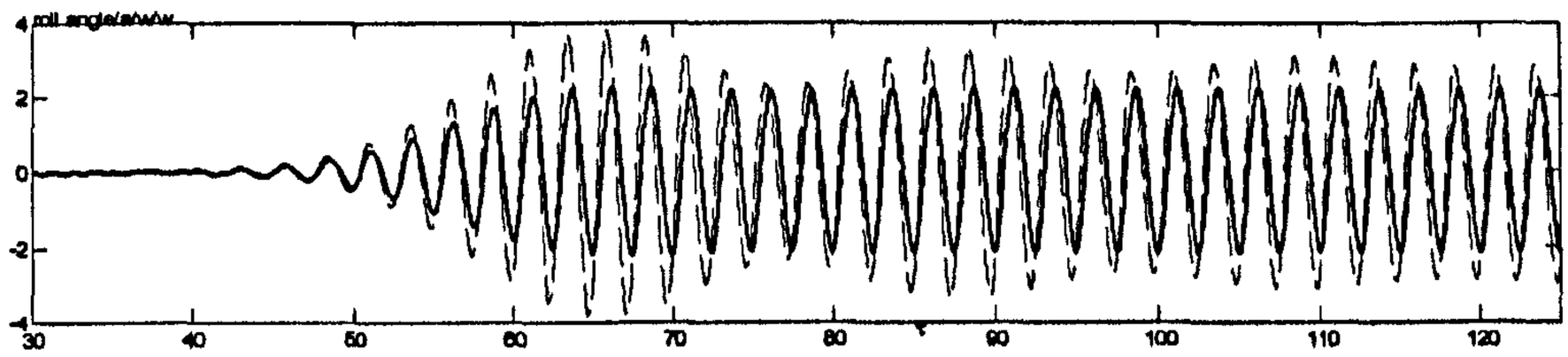

Fig.8.2.13(c) roll

Fig.8.2.13 Simulated floating body motions in cases with different artificial roll damping ($\xi = 0.4$;solid line: 2.8% critical roll damping; dash line: 0% critical roll damping)

The cases in Figs. 8.2.11 and 8.2.12 are also simulated using different meshes, different iterative control errors and different time steps. Some results are shown in Fig. 8.2.14, from which one can see that the difference between them is very small. This implies that the numerical errors due to selecting different mesh sizes, time steps and iterative control errors are negligible for the results in these two figures.

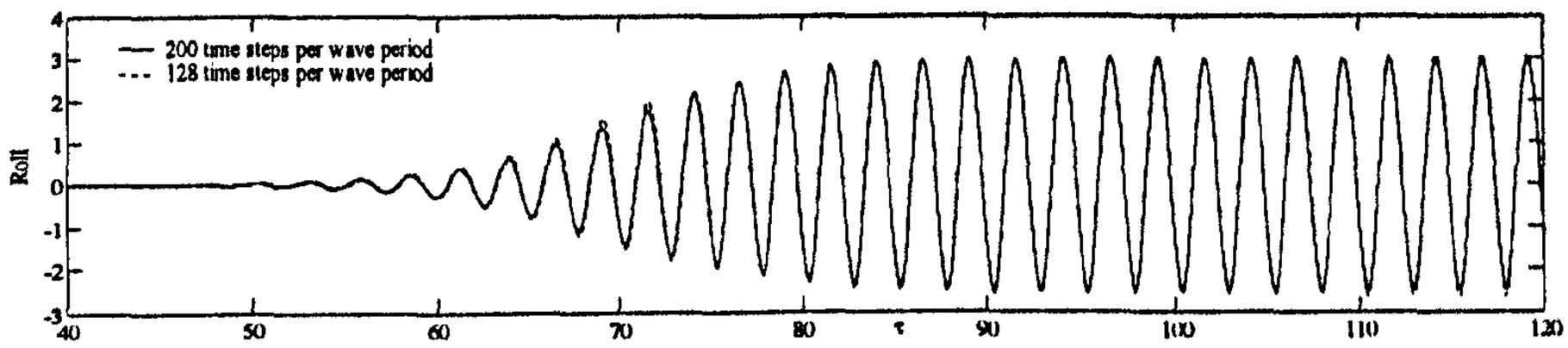

(a) different time steps (iterative control error is taken as 0.005,30 nodes per wave length)

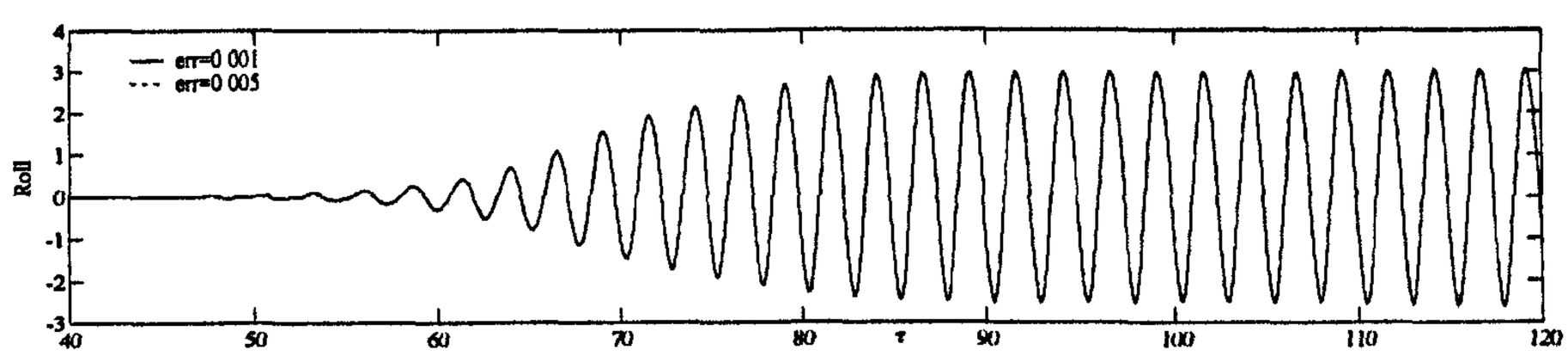

(b) different iterative control errors ($\Delta t = T/128$,30 nodes per wave length)

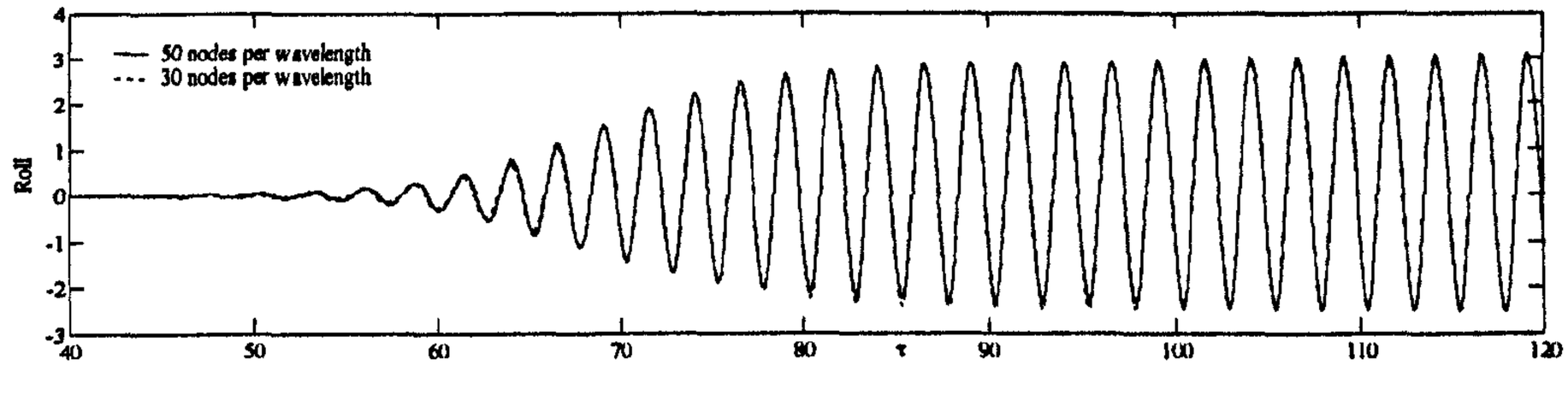

(c) different meshes ($\Delta t = T/128$,iterative control error is taken as 0.005)

Fig.8.2.14 Roll motion in terms of different time steps, iterative control error and meshes ($\xi = 0.5$, the wave height is 0.07m)

8.2.5. Transient responses of floating bodies

So far, discussions on responses of floating bodies to waves have been focused on the RAOs and how to calculate them in a more efficient way. In this section, some results are presented for transient responses of floating bodies, which are also used to show the nature of nonlinear interaction between floating bodies and waves. For the cases considered in this section, the tank length is $L \approx 10$ with $L_w \approx 5$ and the frequency parameter is $\xi = 0.65$ that is near the resonant value as seen in Fig. 8.2.10. The generated wave heights are about 7cm. In these applications, Ramp1 (Eq.8.2.1-3) is used to govern the motion of wave-maker. For the purpose of validation, the results are firstly compared with those from the same case in which Ramp2 is used. This is similar to Fig.8.2.4 but the incident waves here are much steeper than that in Fig. 8.2.4. The result is shown in Fig.8.2.15. It can be observed that that no matter which ramp function, Ramp1 or Ramp2, is used, the force and moment acting on body tend to the same results except

for the region where the wave-maker ramping function still affects the incident waves (i.e. the first four periods in Fig.8.2.15). This result indirectly indicates that the RAOs simulated by using Ramp1 are the same as when Ramp2 is used. It is also observed that the force and moment acting on the floating body has evident nonlinearity.

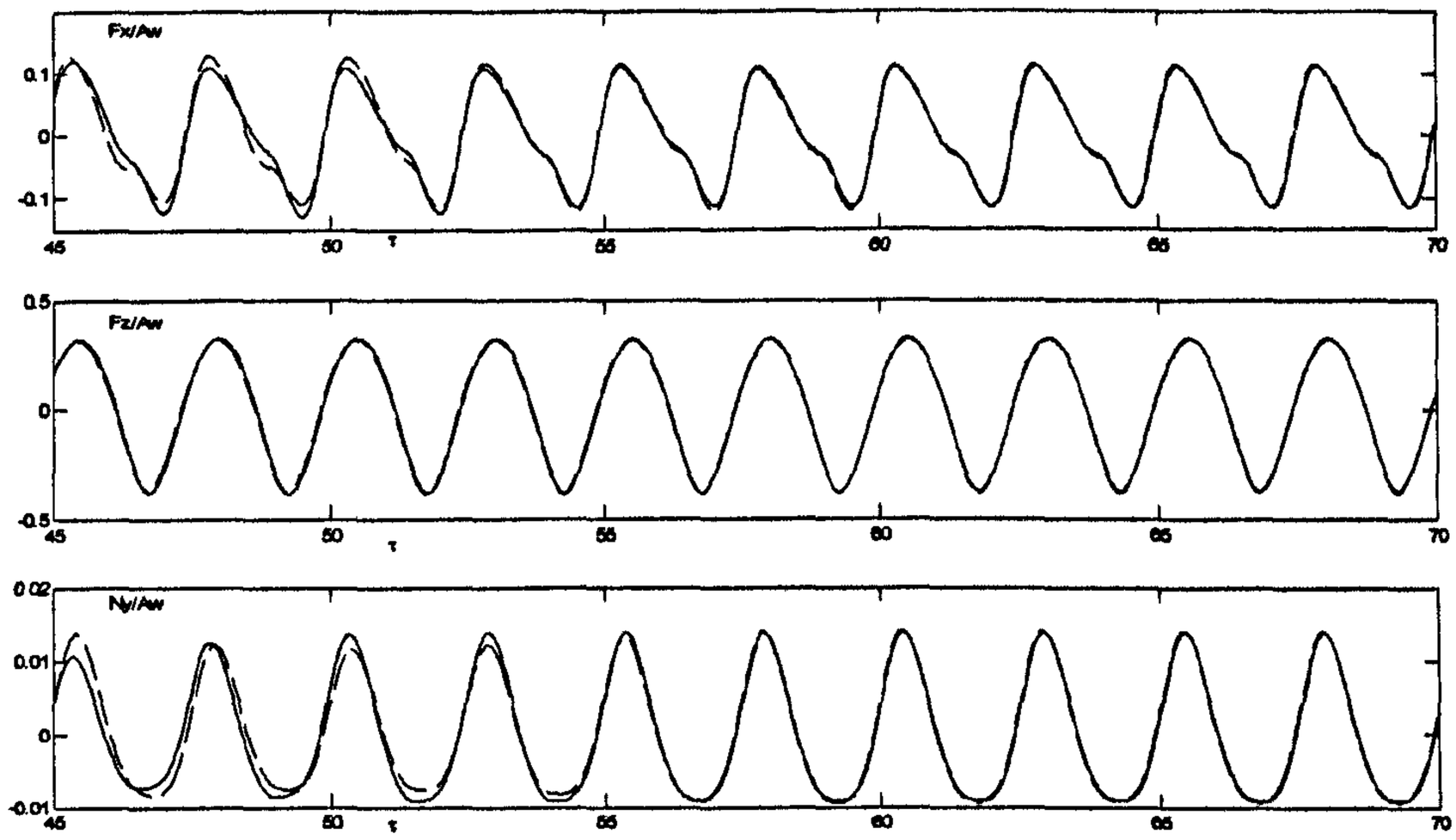

Fig.8.2.15 Force and moment acting on the floating body according to different wave-maker ramp function ($\xi = 0.65$, wave height is taken as 7cm. solid: Ramp1; Dash: Ramp2)

The wave elevations and body responses are shown in Fig.8.2.16, which illustrates how the body responds to the transient waves. One may see that the body motion, particularly the roll angle in this case, is dramatically larger when the front part of the wave trains just reaches the body than those in other instances and so larger than those predicted by using RAOs (see Fig.8.2.16 c,e).

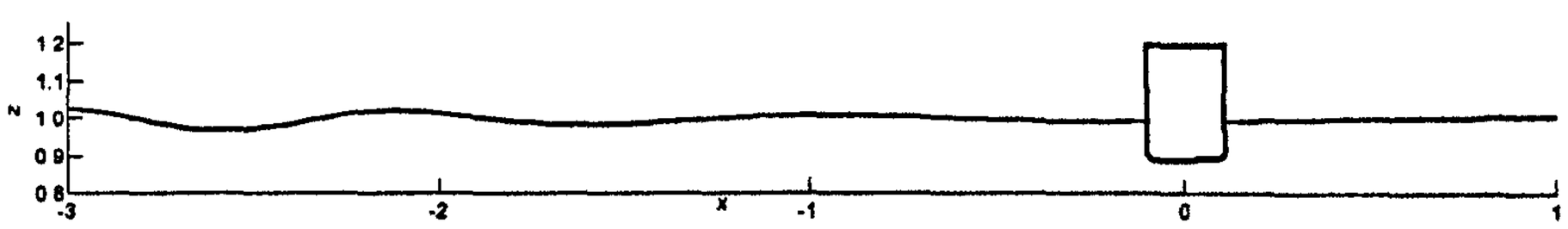

Fig.8.2.16 (a) τ≈18.17

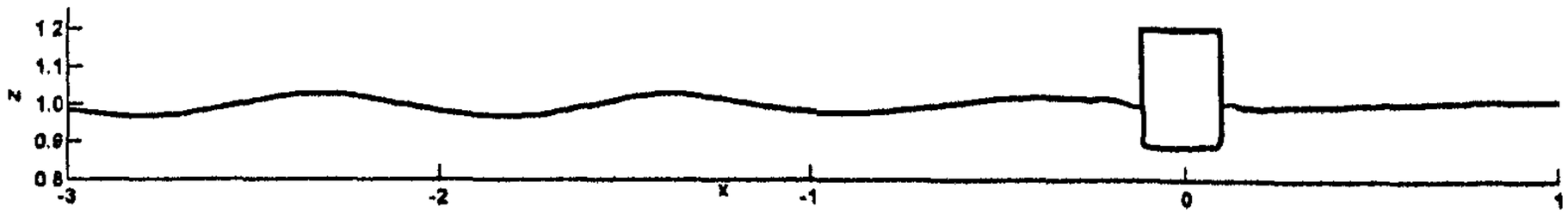

Fig.8.2.16 (b) τ≈25.07

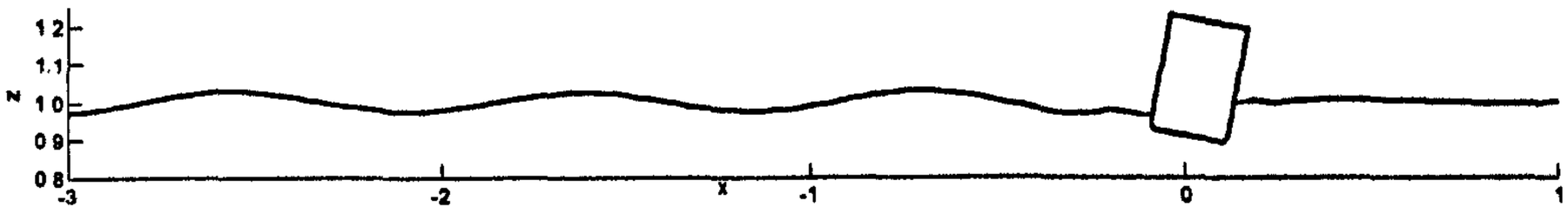

Fig.8.2.16 (c) $\tau \approx 34.47$

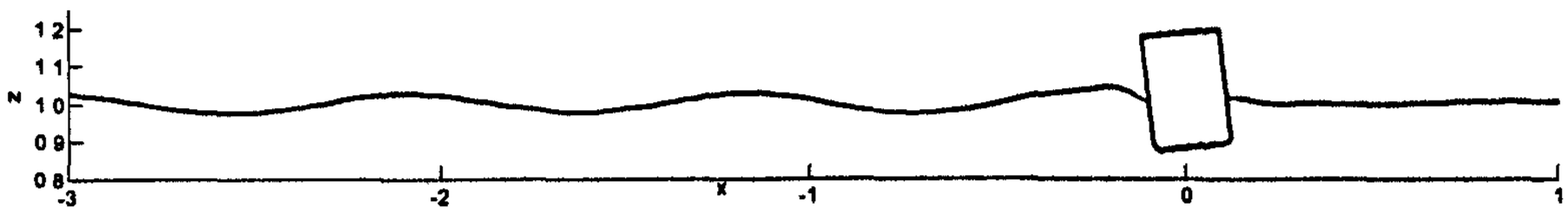

Fig.8.2.16 (d) $\tau \approx 35.72$

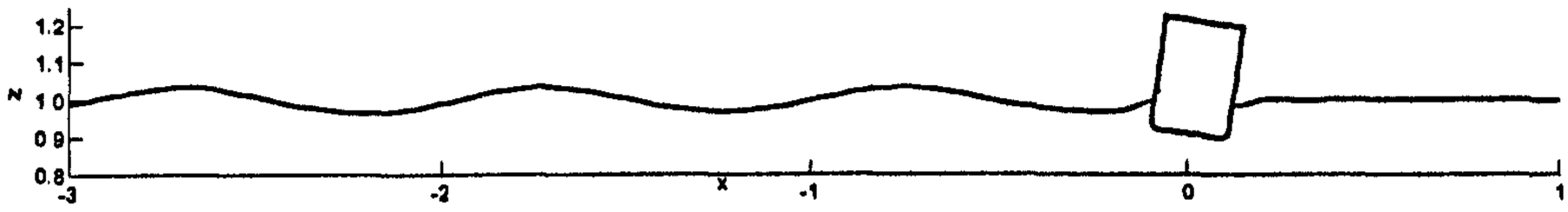

Fig.8.2.16 (e) $\tau \approx 51.39$

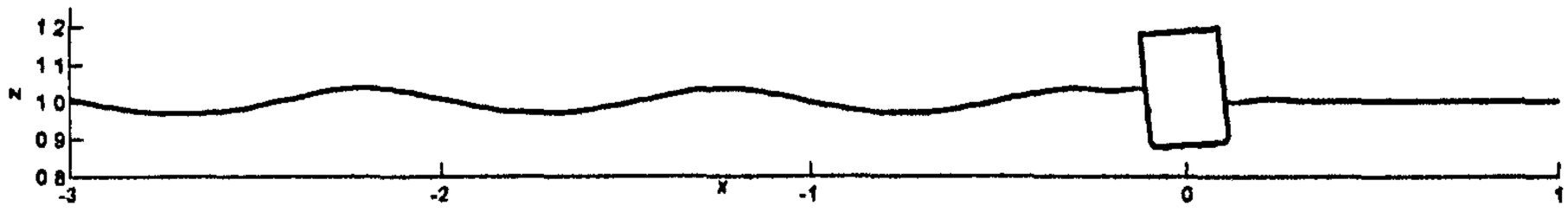

Fig.8.2.16 (f) $\tau \approx 52.64$

Fig.8.2.16 Wave elevation and body motion ($\xi = 0.65$, the wave height is about 7cm)

It is clearer in Fig. 8.2.17, where the roll time history is plotted. This implies that the transient responses rather than RAOs should be considered in design in order to check if a floating body is safe when it is subjected to transient waves.

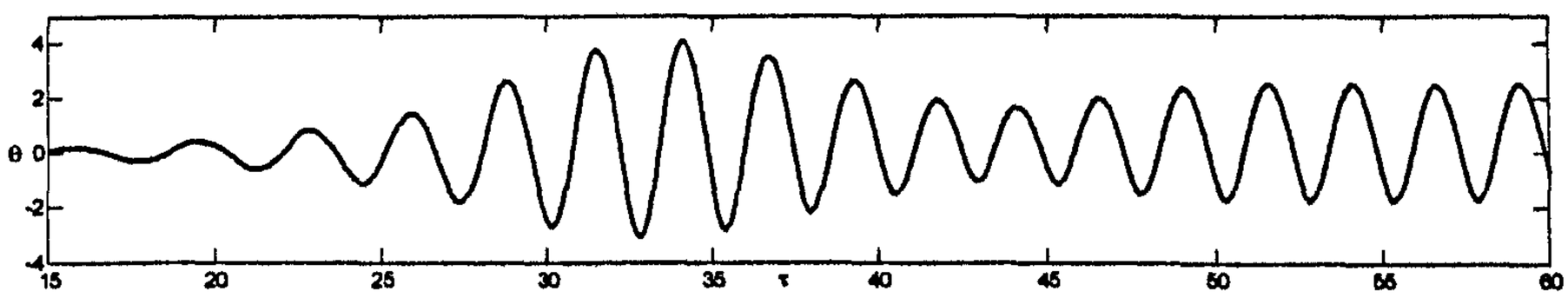

Fig.8.2.17 Time history of roll for the wave height of 7cm and $\xi = 0.65$

To show the effect on wave elevation due to the motion of floating body, the wave run-up recorded at the water line of the floating body is plotted as Fig.8.2.18. It can be observed that the wave run-up in the lee side of the floating body becomes much smaller than incident wave. This mainly be because that the incident wave is reflected by the floating body and make the waves to the lee side of the body become smaller. It is also found that the wave run-up recorded

at both sides of the body seem to be combined by various components of waves and therefore show evident characteristic of nonlinear waves.

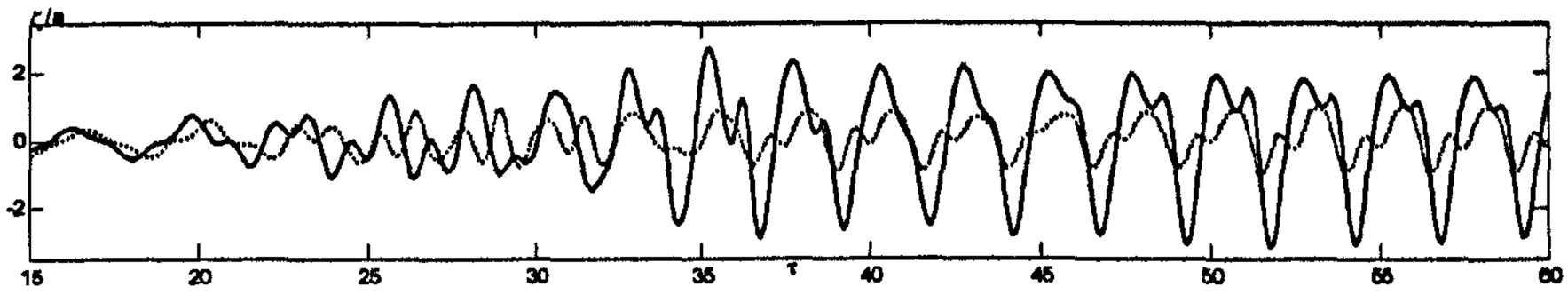

Fig.8.2.18 wave run-up recorded at waterline

($\xi = 0.65$, actual wave height is taken as 7cm. solid line: front side; dot line: lee side)

To further show the nonlinearity involved in this case, the sway force and roll moment acting on the floating body is plotted in Fig.8.2.19. Similar to Fig.8.1.15, it can be observed that all the curves are quite complex. For the sway force, the curve in one wave period is not symmetric about the apex point in that period. For the roll moment, the curve exhibits sharper high crests and flatter and shallower troughs. All are features of nonlinearity.

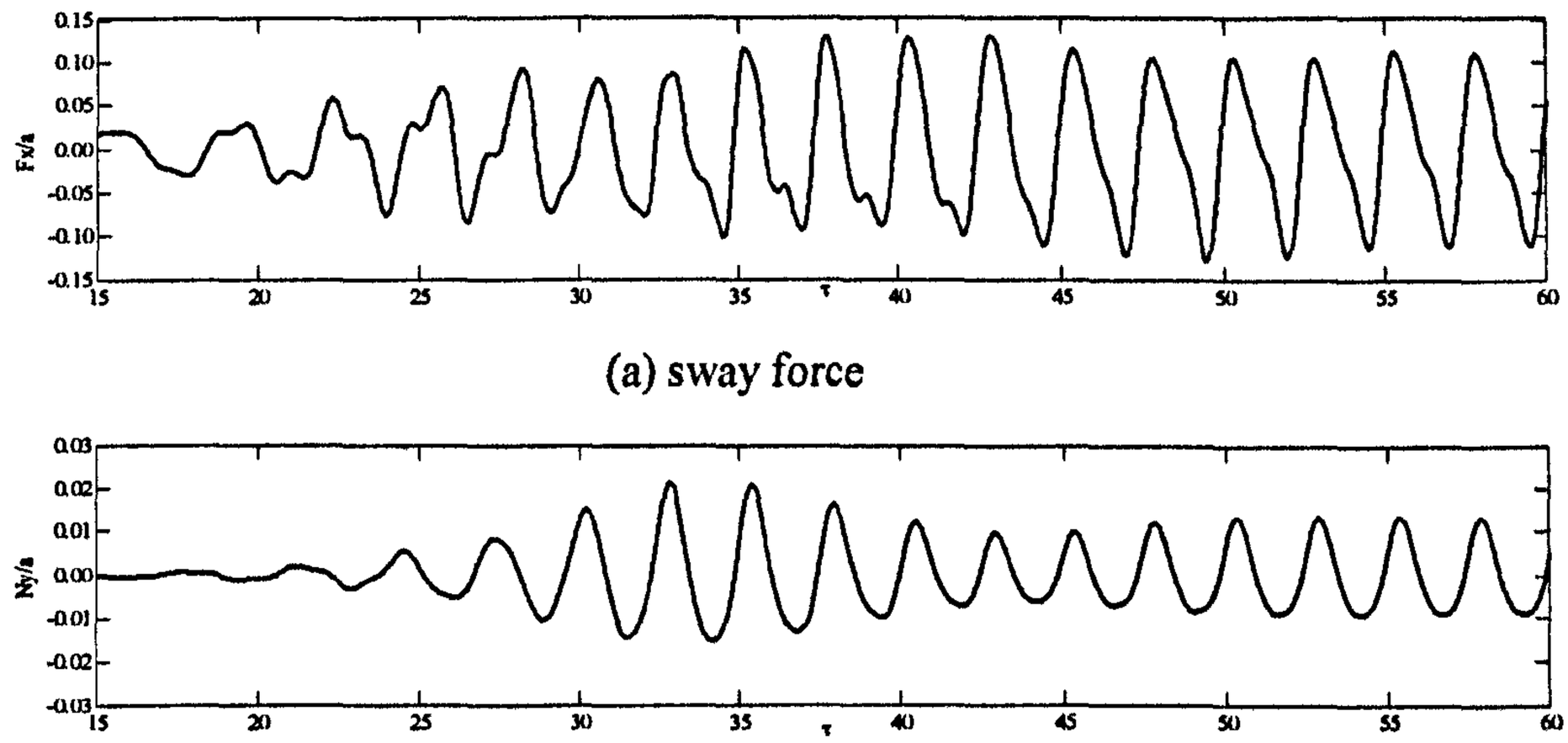

(a) sway force

(c) roll moment

Fig.8.2.19 Force and moment acting on the floating body

($\xi = 0.65$, the wave height is about 7cm)

8.2.6. The effect of sand bars on transient responses of floating bodies

The QALE-FEM method is then applied to the case with a floating body and periodic bars on the seabed. In this case, the incident wave height is 7cm and the frequency parameter of $\xi = 0.65$, 3 sinusoidal bars are mounted in front side of the floating body whose amplitude (a_b) and wavelength ($\lambda_b = 1$) are taken as 0.5 and 1 respectively. The force acting on the floating bodies is plotted as Fig. 8.2.20. For the purpose of comparison, the results from the case without bars are also plotted. It can be observed that the sway forces in these two cases are

different. This change is because of the reflection by the sand bars on the seabed. Because the floating body is located in the lee side of the bar patches, the wave is reduced by the bars as discussed in Section 7.4. The force acting on the floating body is therefore reduced.

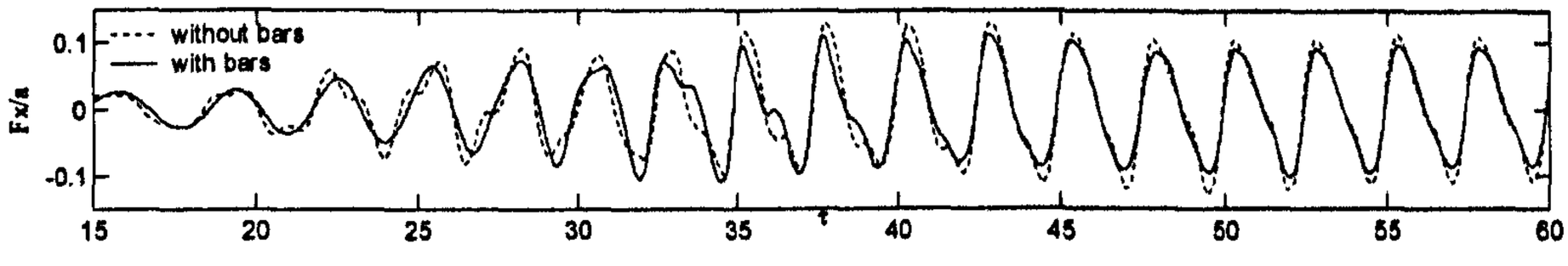

Fig.8.2.20 Comparison of sway forces acting on the floating body with and without sandbars ($\xi = 0.65$, the wave height is about 7cm)

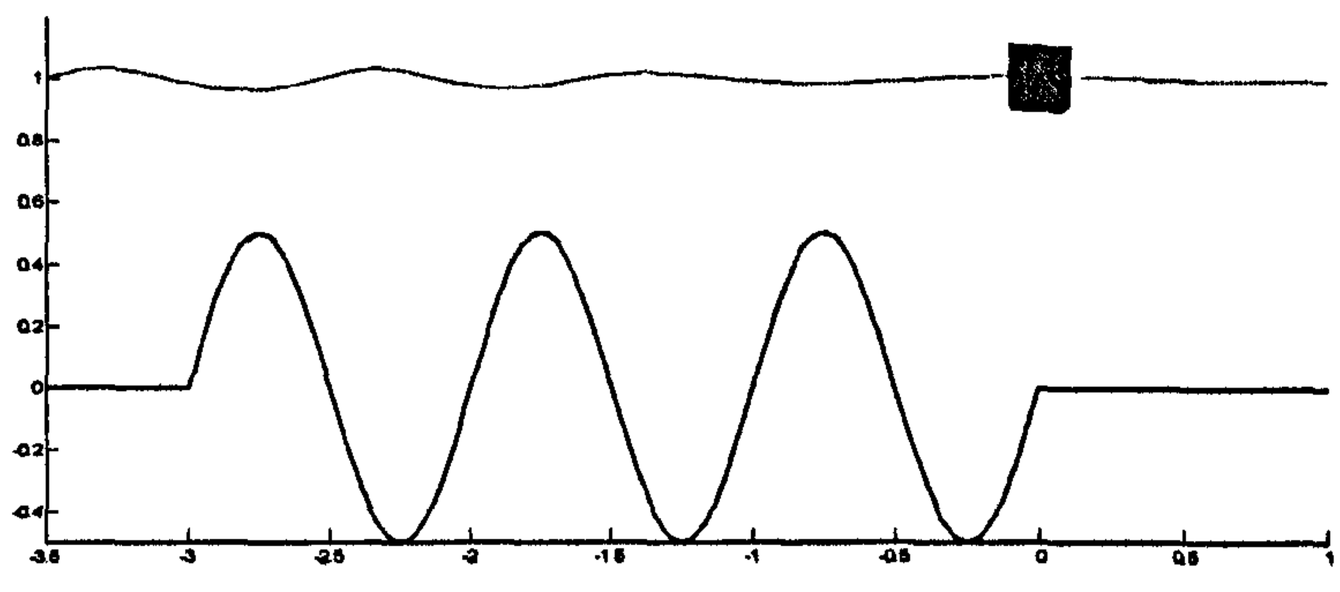

Fig. 8.2.21 (a) $\tau \approx 20.05$

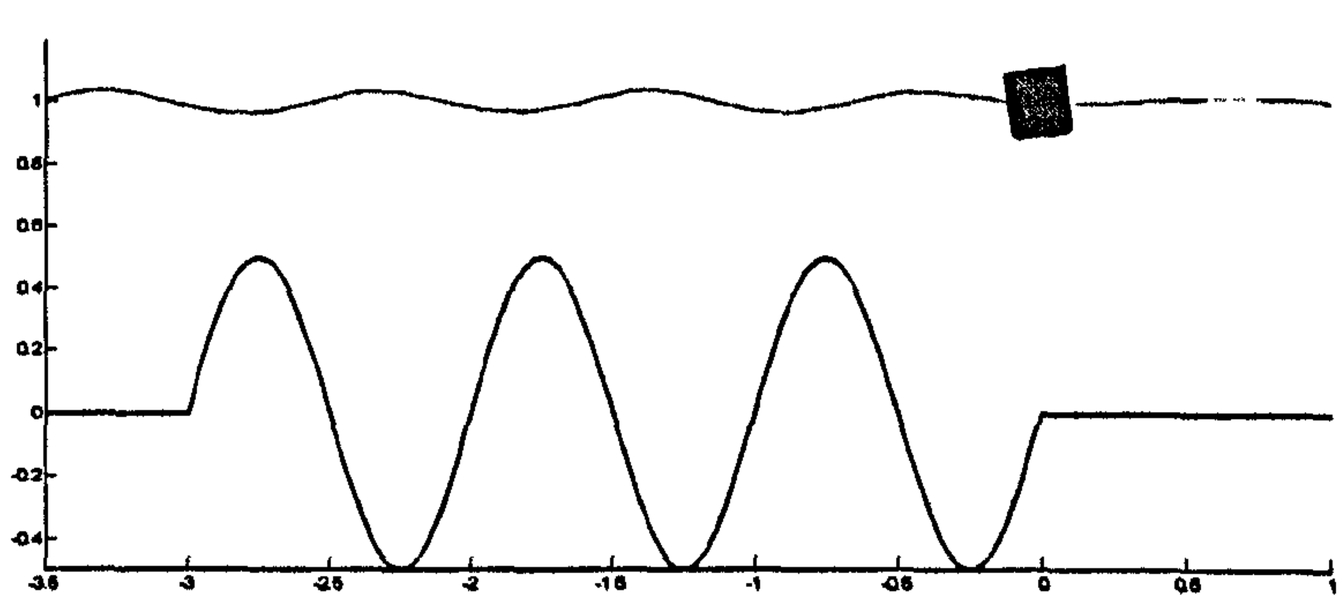

Fig. 8.2.21 (b) $\tau \approx 27.57$

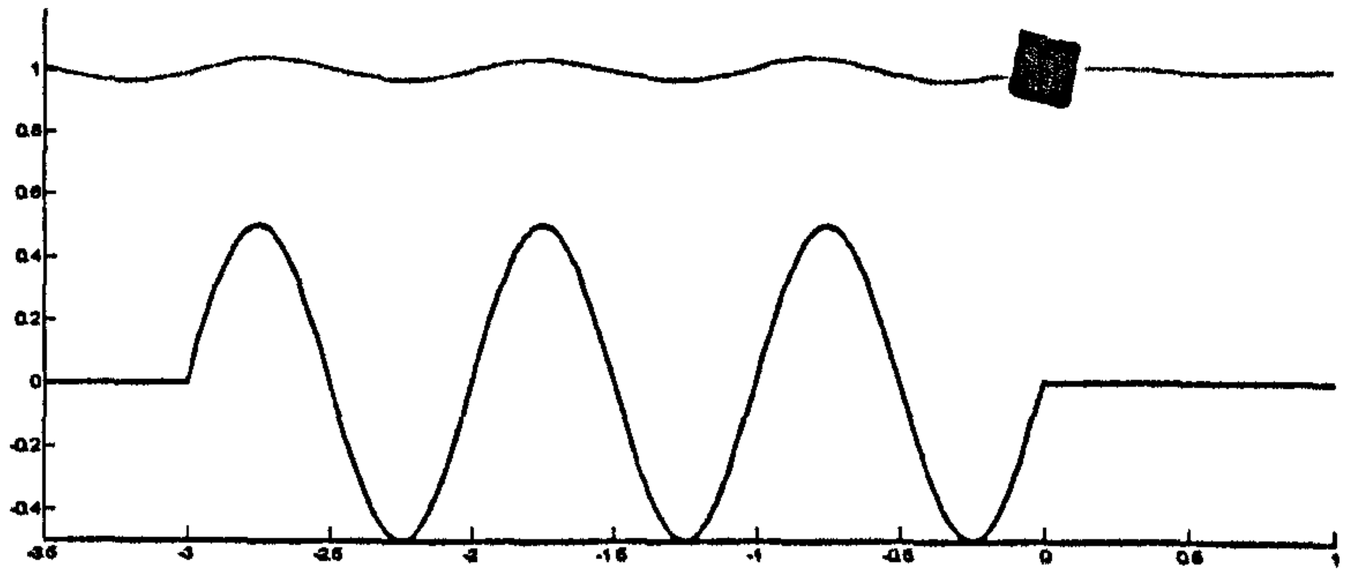

Fig. 8.2.21 (c) $\tau \approx 29.08$

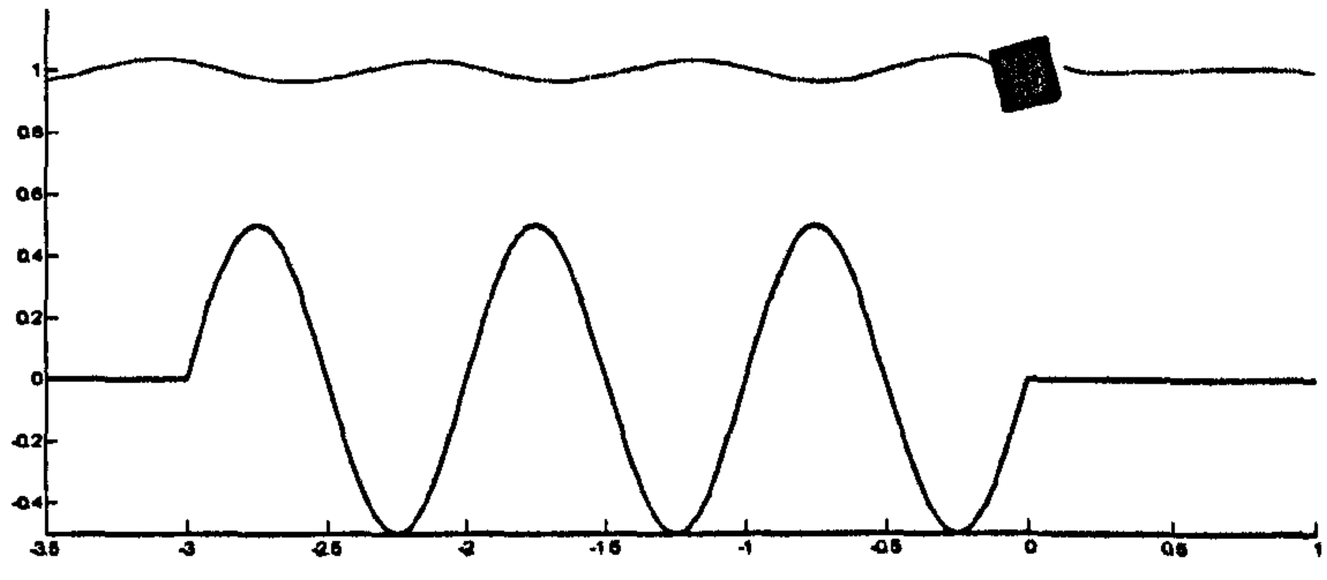

Fig. 8.2.21 (d) $\tau \approx 33.09$

Fig. 8.2.21 wave elevation and body motion ($\xi = 0.65$, wave height is about 7cm, the bar patch is located from -3~0, a_b=0.5, $\lambda_b = 1$)

To further show the wave elevations and body responses, some snapshots are shown in Fig. 8.2.21, which illustrates how the body responds to the transient waves. As the wavelength of the incident wave is short in this case, the effect from the bars is not very evident. When the wavelength becomes close to Bragg resonance condition, the reflection caused by bars might becomes more evident.

In order to demonstrate this, the test cases involving 10 sand bars with $a_b/d = 0.16$ on the sea bed are carried in a tank with length is 68. The bar patch is located from -16 to 16 with the centre being located at x=0. The wave maker is mounted at x= -44. $2k/k_b$ in this case is equal to 1 in which the Bragg resonance happens. The amplitude and the frequency of the wave maker are taken as 0.1 and 0.86026, respectively. The floating body in this case is the same as that used in Fig.8.2.20. The initial positions of the floating body are located at x= -18 (before the sand bar, named as 'Case 1'), x=0 (in the middle of sandbar patch, named as 'Case2') and x=18 (after sandbar patch, named as 'Case 3'). For the sake of comparison, the case without sand bars is carried out. The floating body in this case is located at x=0 and wave maker is mounted at x= -26. This case is named 'Case0' in the following investigation. The time histories of the motion in these cases are shown in Figs. 8.2.22 -8.2.24. For the purpose of comparison, the results from 'Case 0' are also plotted together.

Fig. 8.2.22 shows the response of the floating body located at the front of the bar patch. It can be seen that all the motion modes become larger by the reflection from the sandbars. It also found that the phase of the motion is also changed by the sandbars. Fig. 8.2.23 shows the response of the floating body located in the middle of the bar patch. It is observed that the sway motion is reduced since the incident wave is reflected by the bar patch. However, the amplitude of the heave motion seems not change dramatically, but the phase is changed by the reflected waves. The sandbar also affects the roll motion and makes the roll more complicated than the one without bar patch. The response of the floating body located at the lee side of the bar patch

is plotted as Fig. 8.2.24. It is observed that all the three motion modes seem be reduced by the reflection of the bar patch.

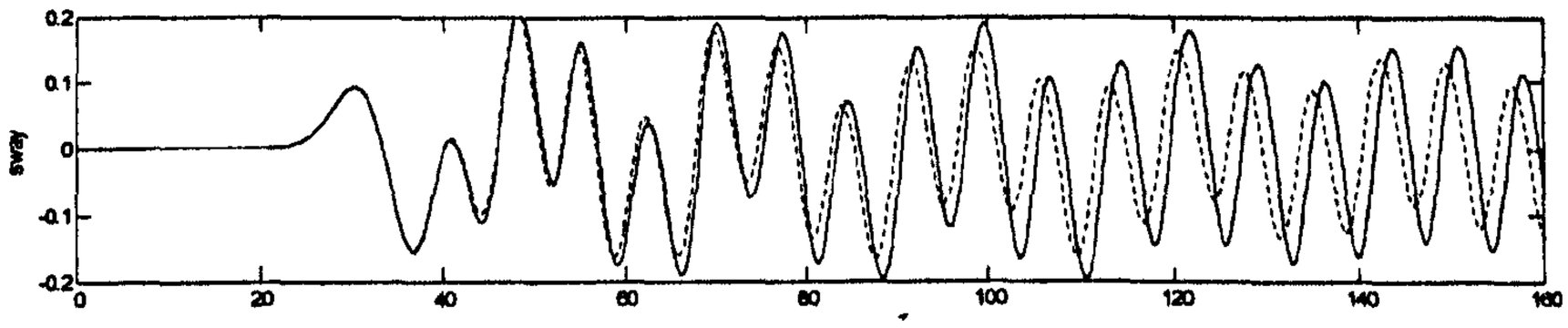

Fig.8.2.22 (a) sway

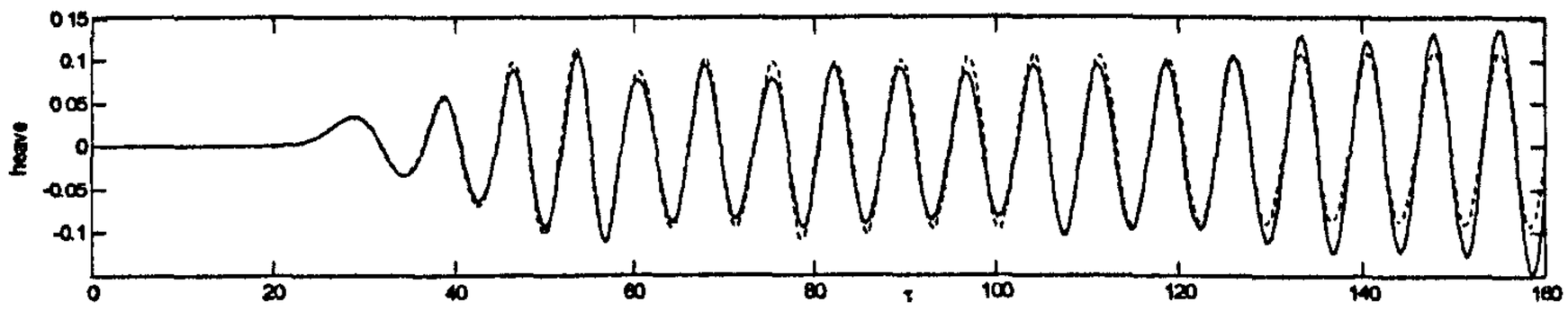

Fig.8.2.22 (b) heave

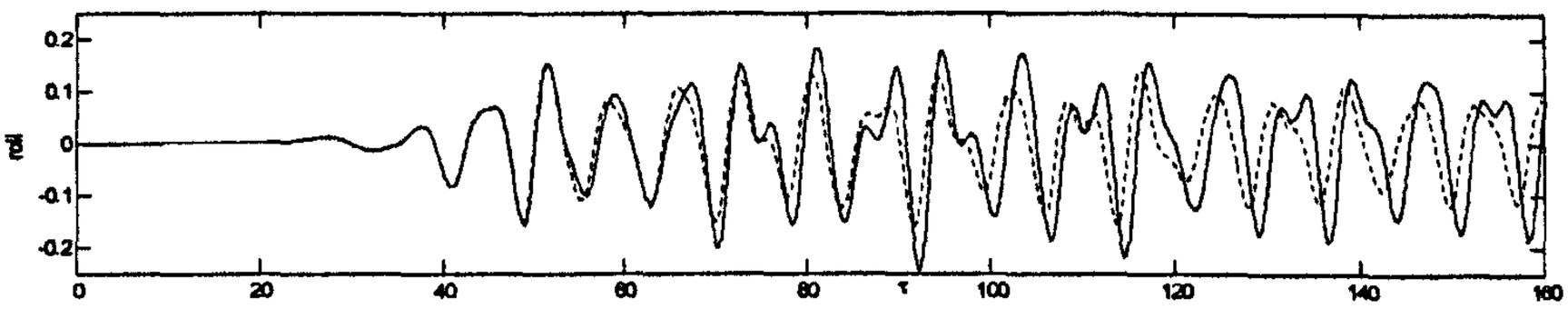

Fig.8.2.22 (c) roll

Fig.8.2.22 Time histories of motions in 'Case1'

(solid: floating body located in the front of the bar patch; dot: without sand bar)

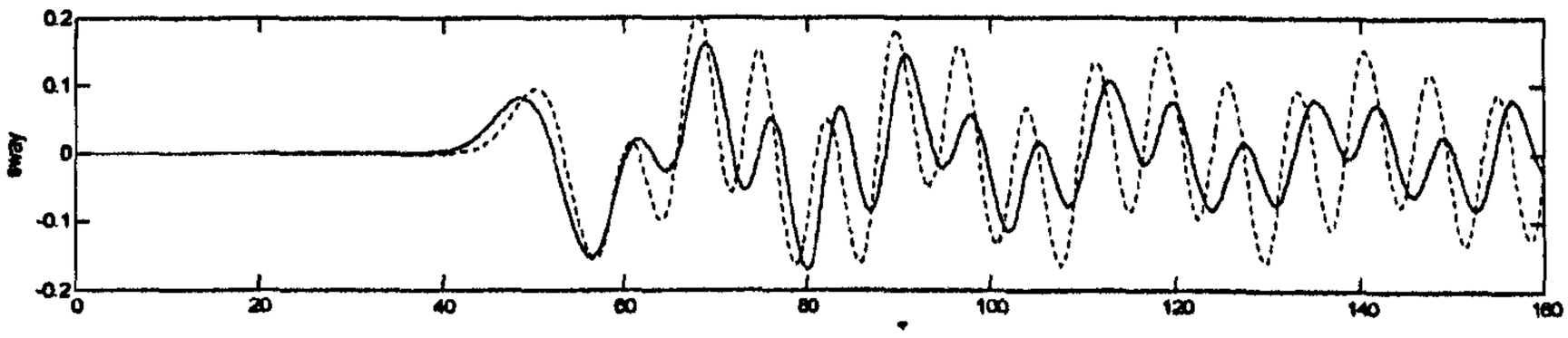

Fig.8.2.23 (a) sway

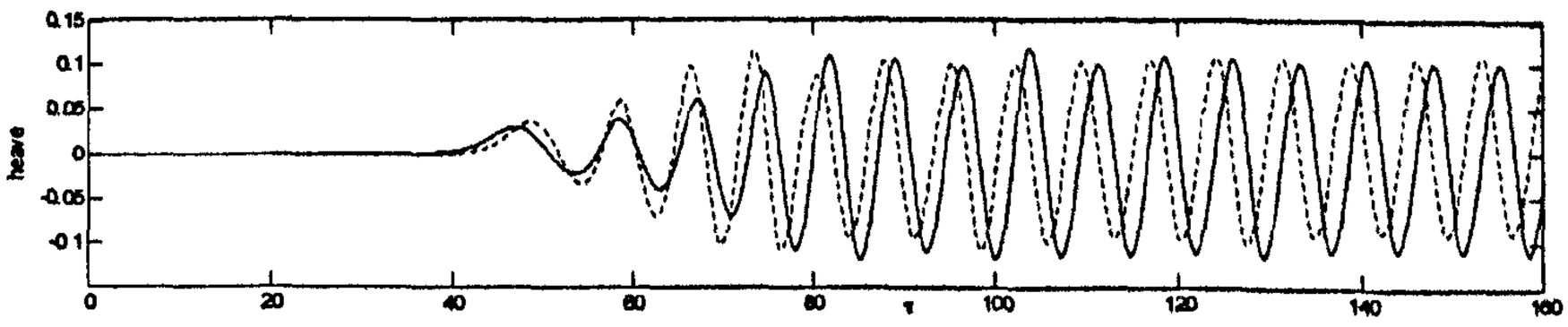

Fig.8.2.23 (b) heave

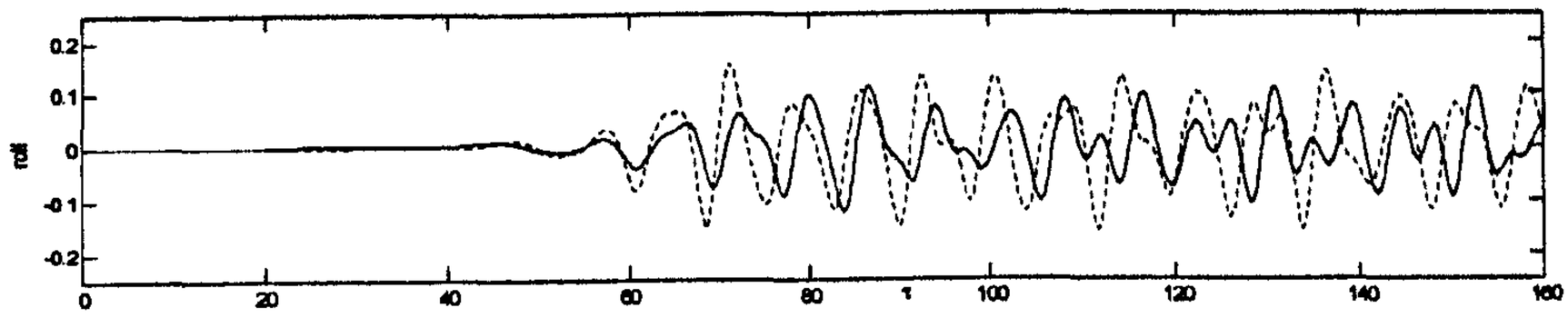

Fig.8.2.23 (c) roll

Fig.8.2.23 Time histories of motions in 'Case2'

(solid: floating body located in the middle of the bar patch; dot: without bar)

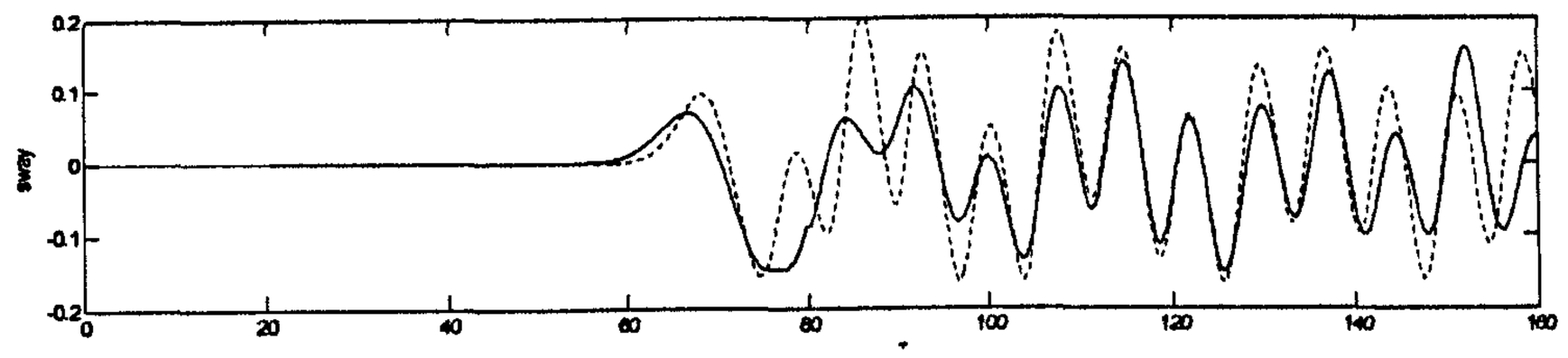

Fig.8.2.24 (a) sway

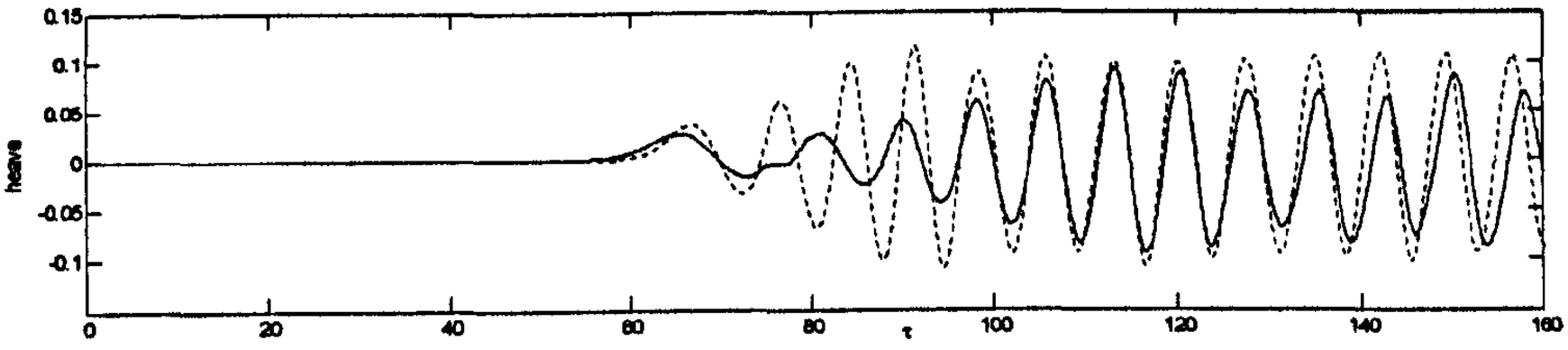

Fig.8.2.24 (b) heave

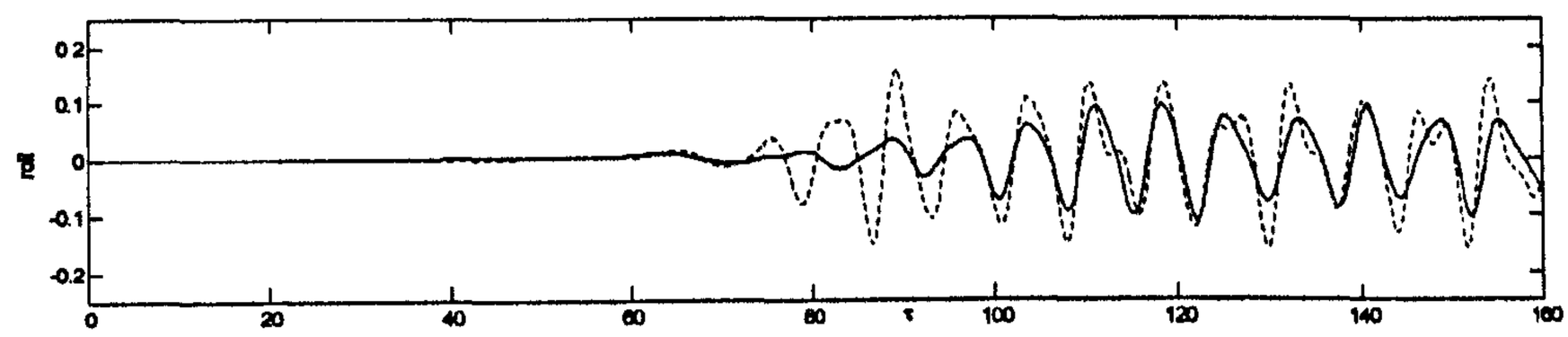

Fig.8.2.24 (c) roll

Fig.8.2.24 time histories of motions in 'Case3'

(solid: floating body located at the lee of the bar patch; dot: without bar)

8.3. Mesh quality around the floating body

In the QALE-FEM method, the unstructured mesh is moved according to the motion of the boundaries. In order to satisfy the requirement of the FEM solver, the mesh must of high quality throughout simulation. As indicated in Chapter 7, without floating bodies, the mesh quality can be retained. With the inclusion of floating bodes, their motions, particularly large angular motions, can make the mesh near body surfaces undergo large variations and so it is necessary to check if the methodology for moving meshes in the QALRE-FEM could also produce good

quality of meshes in these cases. Some illustrations have been given for the cases with forced motions in Figs.8.1.6 and 8.1.7 . Apart from these, extensive investigations have also been made for the cases associated with free-response floating bodies during the development of the method. Two cases will be presented in this section to demonstrate the effectiveness of the method in producing good meshes at all time steps.

In the first case, the same floating body described in Section 8.2 is used, which is subjected to a wave of height 7cm with frequency parameters $\xi = 0.65$ in a tank of L=10. This case is run on a PC (Pentium Ⅳ 2.53GHz processor, 1G RAM). The fluid domain is discretised into about 129,732 elements and 28,725 nodes.

Figs. 8.3.1-3 presents the mesh at different instances, where the lower column illustrates the enlarged mesh in the vicinity of the body surface. Fig.8.3.1 depicts the initial unstructured mesh while Fig. 8.3.2 and Fig. 8.3.3 show the meshes in the same area but after quite long time simulation. These figures demonstrate that the original refinement and distribution are maintained well and all the elements retain satisfactory shape during the simulation. In addition, negative elements, which are of concern when using the linear spring analogy method, do not appear. On the other hand, the CPU time spent on moving the mesh at each time step is on average about 1s, including 0.01s for moving mesh on the body surface, approximately the same as the CPU time spent on sandbar problems in Chapter 7. The CPU time spent on all calculations in one step is about 5s on average. It indicates that the method used to move mesh in the QALE-FEM in cases with floating bodies is as efficient as in cases without floating bodies. It also indicates that useful results for a problem like these may be obtained in several hours by using a normal PC.

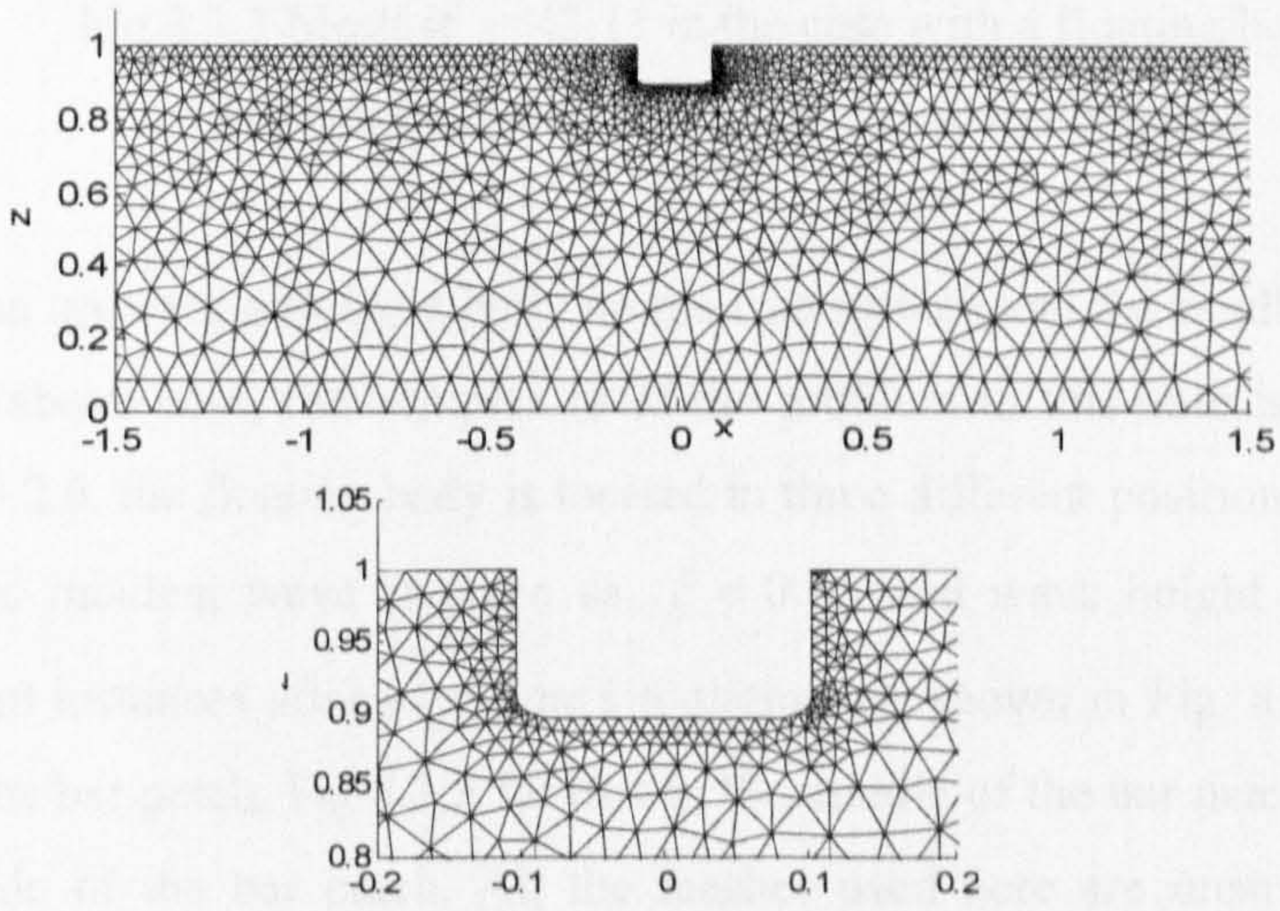

Fig.8.3.1 Initial mesh in the case with a floating body (τ=0.0) (Top: mesh around body; Down: enlarged mesh)

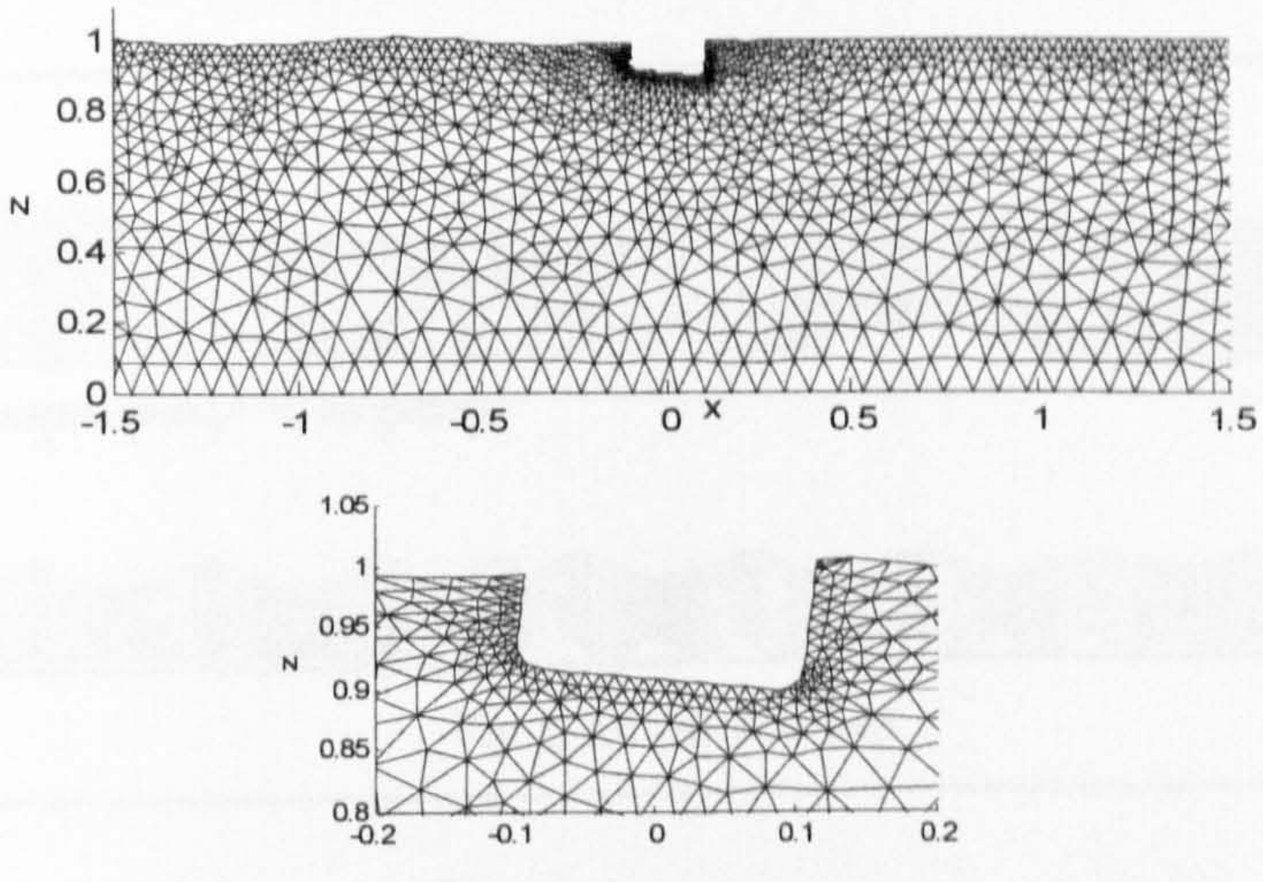

Fig.8.3.2 Mesh at $\tau \approx 39.6$ in the case with a floating body

(Top: mesh around body; Down: enlarged mesh)

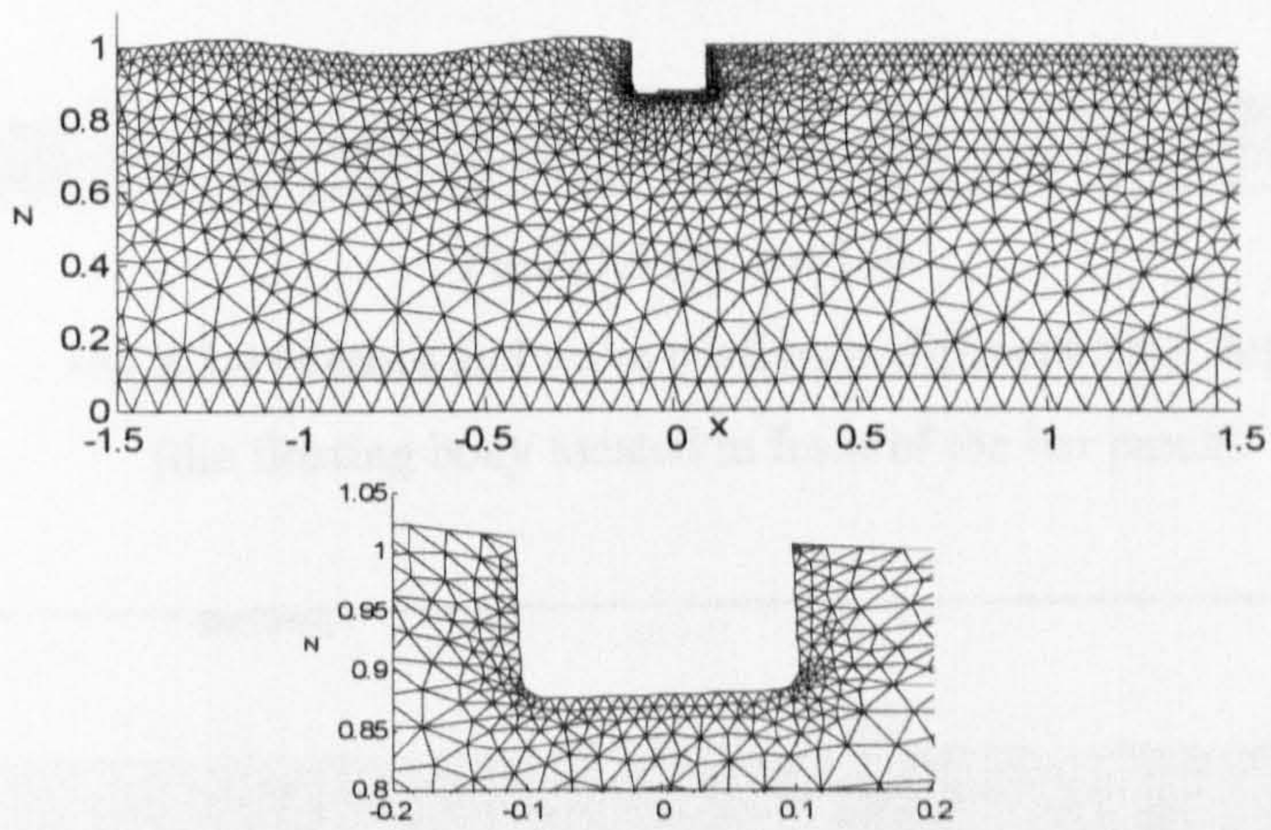

Fig.8.3.3 Mesh at $\tau \approx 43.11$ in the case with a floating body

(Top: mesh around body; Down: enlarged mesh)

The second case involves a floating body on the free surface and the sandbars on the sea bed. Compared to the above case, the complexity of the problem in this case is higher. Similar to those in Section 8.2.6, the floating body is located in three different positions as shown in Figs. 8.2.21-8.2.23. The incident wave is taken as $\xi = 0.65$ and wave height is about 7cm. The meshes in different instances after long time simulation are shown in Fig. 8.3.4 for the floating body in front of the bar patch, Fig 8.3.5 for that in the middle of the bar patch and Fig. 8.3.6 for that in the lee side of the bar patch. All the meshes used here are unstructured with about 200,000 elements and 45,000 nodes. For the purpose of describing the wave profiles at the corresponding time steps, the free surface and the position of the floating body are all plotted together.

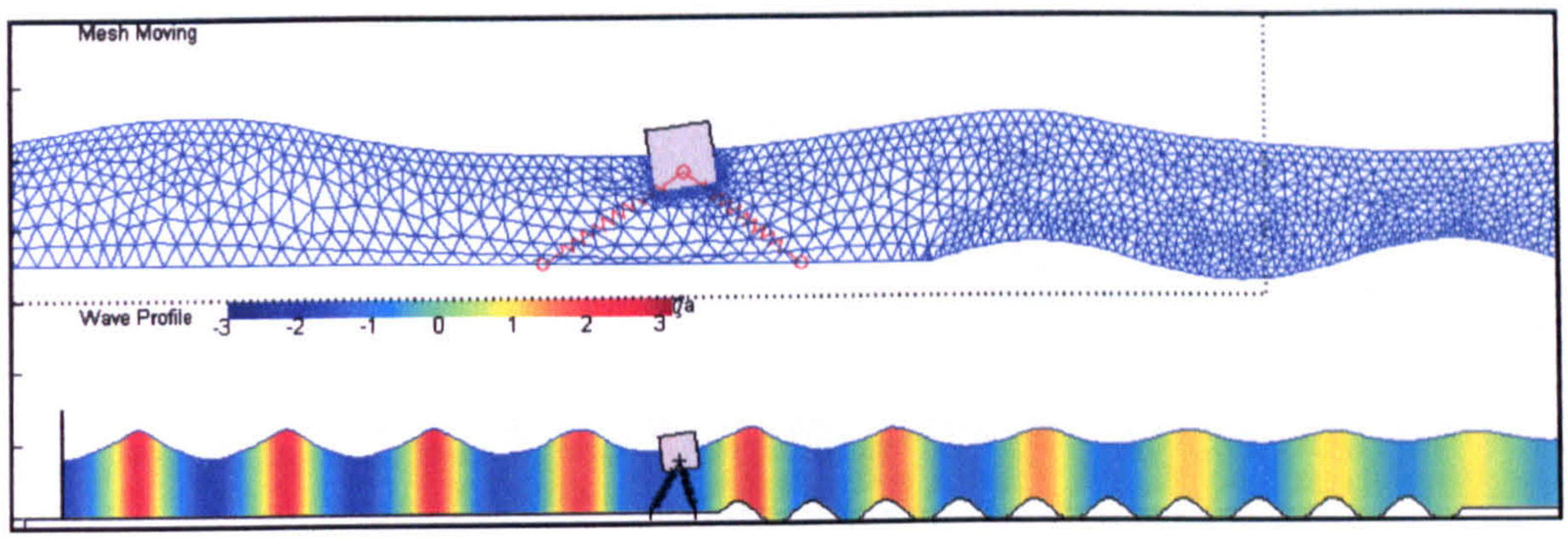

Fig.8.3.4 (a) $\tau \approx 145$

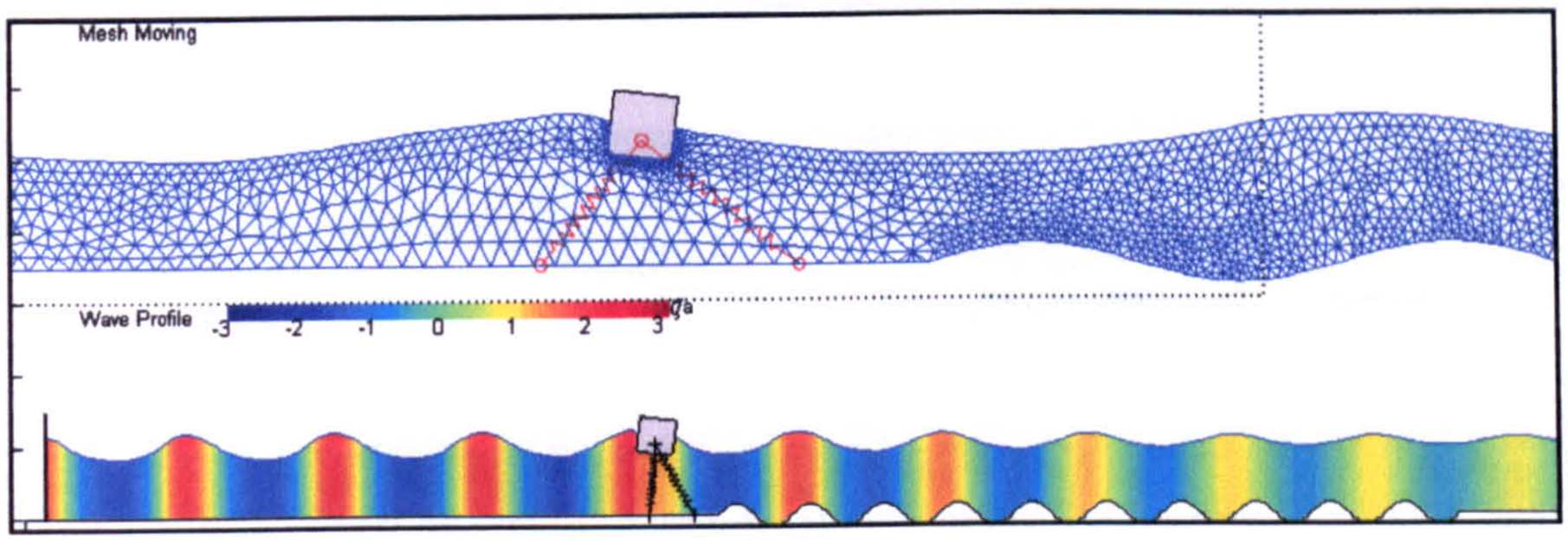

Fig.8.3.4 (b) $\tau \approx 150$

Fig.8.3.4 Meshes and wave profiles at different time steps

(the floating body located in front of the bar patch)

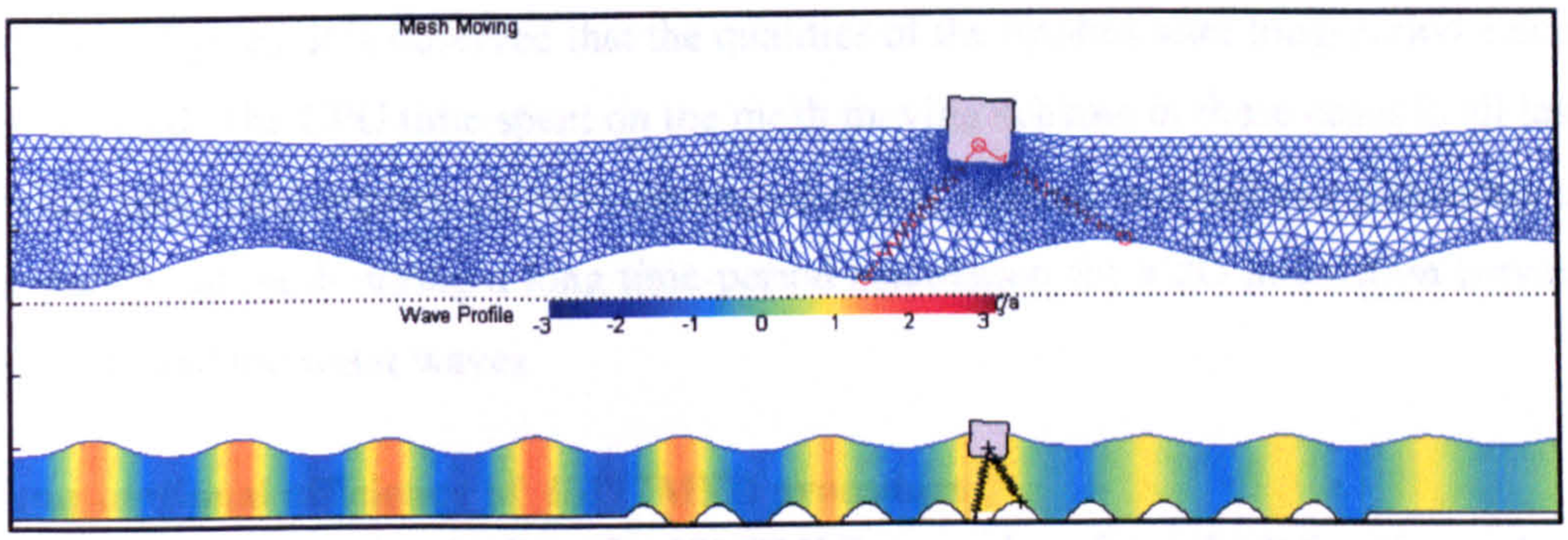

Fig.8.3.5. (a) $\tau \approx 145$

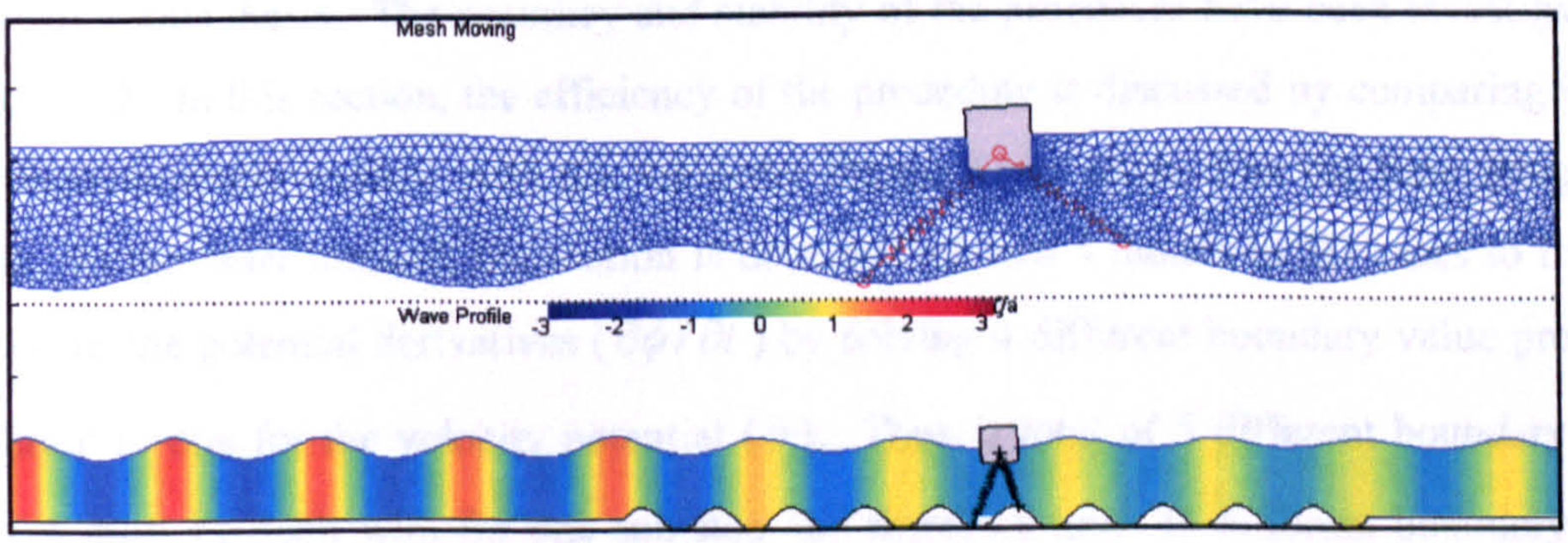

Fig.8.3.5. (b) $\tau \approx 150$

Fig.8.3.5 Meshes and wave profiles at different time steps

(the floating body located in the middle of the bar patch)

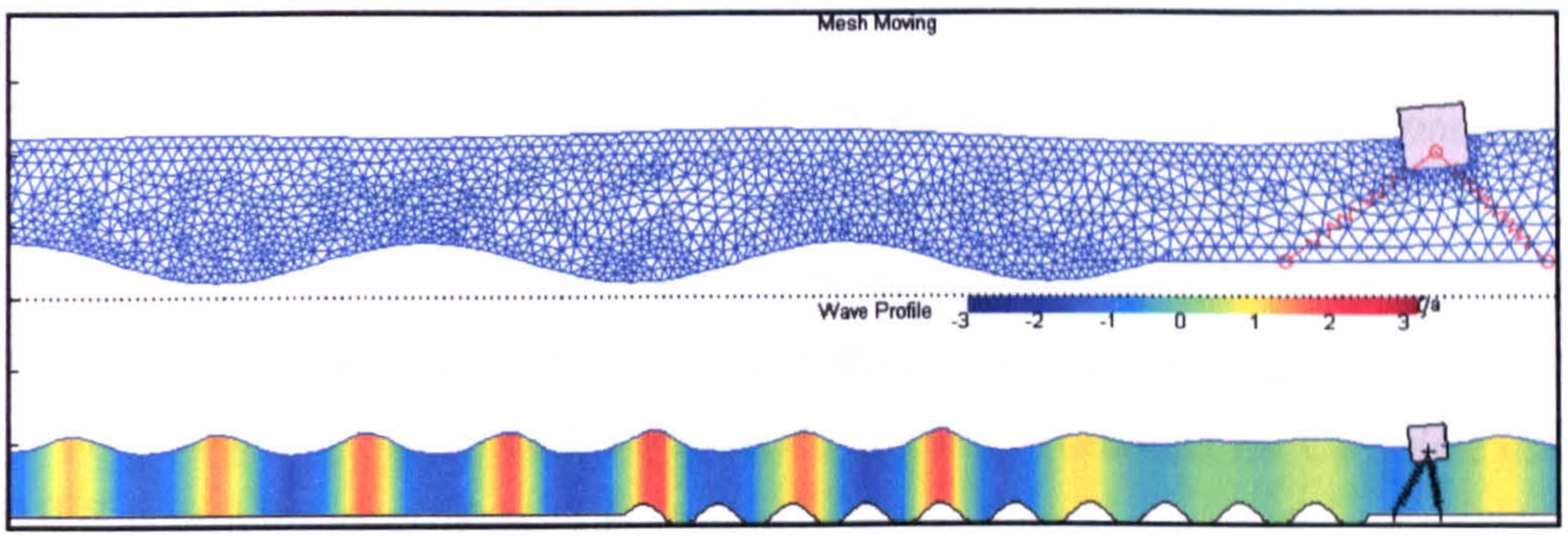

Fig.8.3.6. (a) $\tau \approx 145$

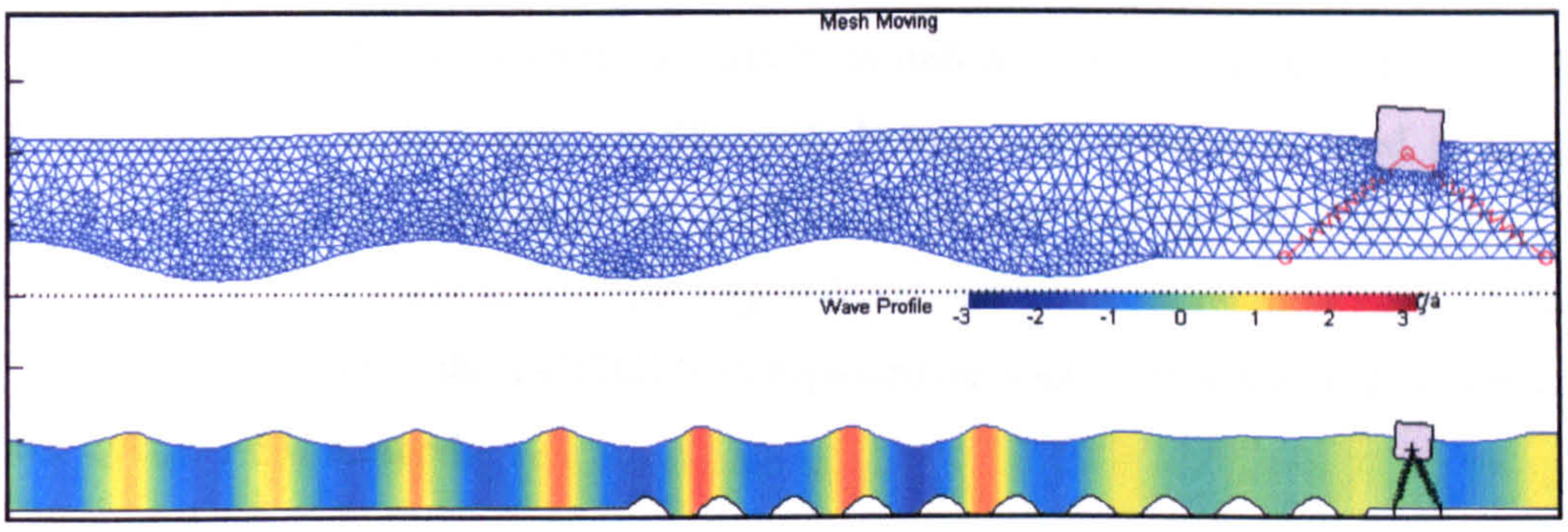

Fig.8.3.6. (b) $\tau \approx 150$

Fig.8.3.6 Meshes and wave profiles at different time steps

(the floating body located at the lee side of the bar patch)

From these figures, it is observed that the qualities of the meshes after long-period calculation are still retained. The CPU time spent on the mesh moving scheme in those cases is all less than 1s per time step. This implies the new-developed spring analogy method can efficiently update the computational mesh during a long time-period calculation for a 2D interaction between the floating body and the water waves.

8.4. Computational efficiency of ISITIMFB procedure

For cases with floating bodies, the ISITIMFB procedure for calculating forces has been developed in this thesis. The accuracy and stability of the procedure have been investigated in Section 7.2.2. In this section, the efficiency of the procedure is discussed by comparing it with mode-decomposition method with the 4th-order Runge-Kutta method as the time integration scheme. In the latter method, the motion is decomposed into 4 modes in 2D cases to find the solution for the potential derivatives ($\partial\phi/\partial t$) by solving 4 different boundary value problems in addition to one for the velocity potential (ϕ). Thus, a total of 5 different boundary value problems must be dealt with for one sub-step and therefore total 20 different boundary value problems for calculating ϕ and $\partial\phi/\partial t$ need to be solved in one time step forward. In addition,

updating of the coefficient matrix is necessary to achieve stable solution as discussed in Section 8.2.

On the other hand, when using the ISITIMFB, the number of iterations in one step forward is on average 7 for the case in Fig. 8.1.1 by using the control error of 1% in the procedure and so about 15 boundary value problems need to be solved without the necessity of updating the coefficient matrix. Therefore, for this case, the CPU time required by the ISITIMFB is less than 75% of that required by the mode-decomposition method. Although the CPU time used by the ISITIMFB is problem-dependent, it is more efficient as long as the number of iterations in the ISITIMFB is less than 10; this may not be exceeded in many cases unless choosing a control error and a time step that are unnecessary small, as indicated in Section 8.2 In addition, if the mode-decomposition method with the 4th-order Runge-Kutta scheme is used in the present QALE-FEM method, the calculation of velocities on the free surface with unstructured meshes must be performed five times in one time step forward, which likely requires considerable more CPU time. Consequently, the ISITIMFB is a procedure that is efficient and is best matched with the QALE-FEM method.

9. FREE-RESPONSE OF 3D MOORED FLOATING STRUCTURES TO STEEP WAVES

In this section, the QALE-FEM method is used to simulate the nonlinear interaction between 3D floating bodies and steep waves. A sketch of this problem is shown as Fig.3.0.1. Three types of floating bodies are considered in this chapter, i.e. SPAR, barge-type floating bodies and Wigley Hull ships. Some of the results are validated through comparison with analytical solutions and published results. Unless mentioned otherwise, all parameters with a length scale are nondimensionalised by the water depth d and other parameters by

$$t \to \tau\sqrt{d/g} \text{ and } \omega \to \omega\sqrt{g/d}\,. \tag{9.0.1}$$

As in previous cases, the initial mesh is unstructured. An example of the mesh near the body surface is shown as Fig. 9.0.1.

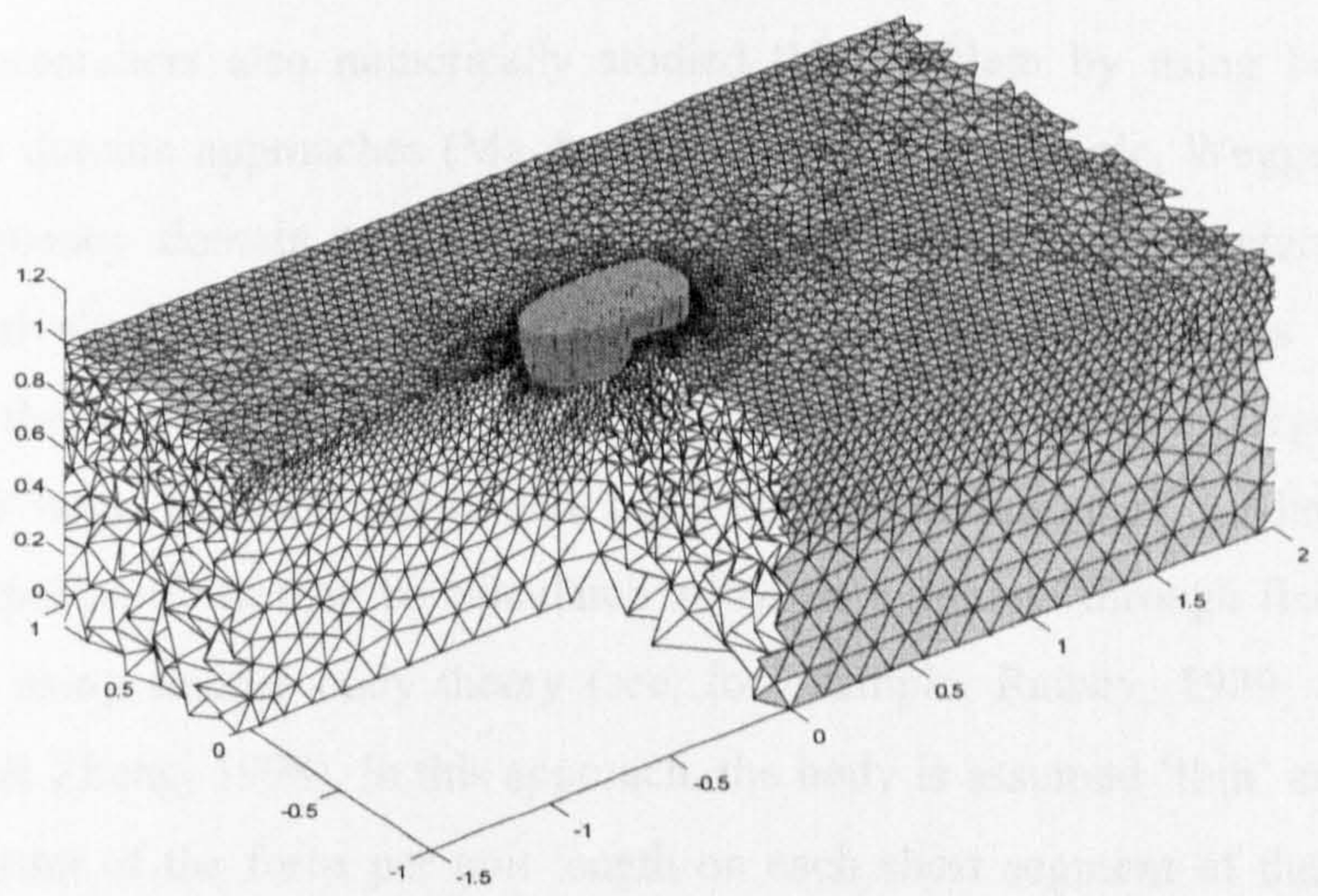

Fig.9.0.1 The initial mesh near the 3D floating body

9.1. Free response of a moored SPARs to monochromatic waves and bichromatic waves

The spar platform is basically a large floating vertical cylindrical structure which may be moored by mooring lines. A sketch of this problem is shown in Fig.9.1.1. The advantages of this type of floating structure for oil and gas production operations is that a SPAR is more economically efficient than a bed mounted structure. Due to this fact, the nonlinear interaction between the moored spar platforms and water waves has attracted much interest recently. A detail review can be found in Ma & Patel (2001).

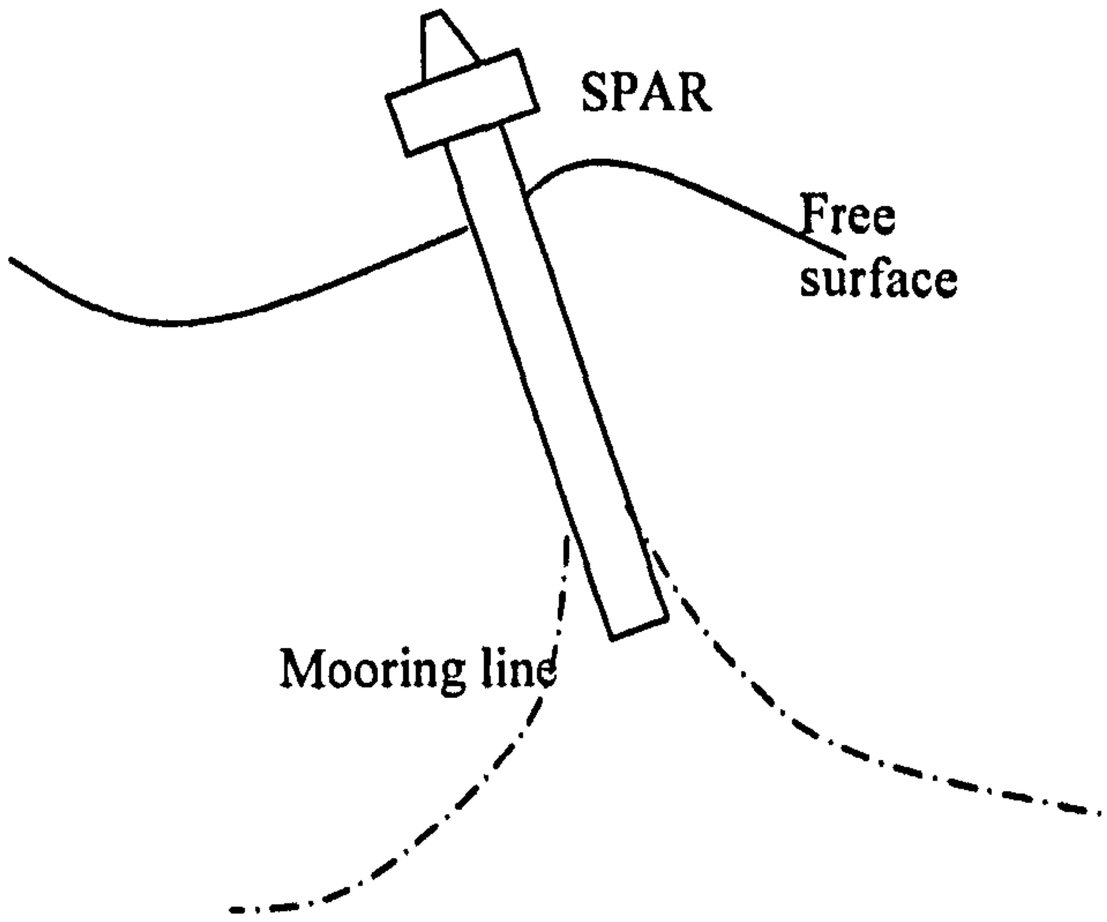

Fig.9.1.1 Sketch of a moored spar platform

Two experimental studies are reported by Weggel et al (1997) and Carpenter , Leonard & Yim (1995). Many researchers also numerically studied this problem by using both frequency domain and time domain approaches (Ma & Patel, 2001). For example, Weggel et al (1997) presented a frequency domain technique and gave the statistical parameters of the spar response at relatively low computational cost. However, this technique is based on the assumption that the wave is very small, and therefore may be subject to large errors when dealing with the large incident waves and large motion of the spars. Alternatively, the response of the spar platform may be calculated in the time domain through finding the wave forces evaluated using slender body theory (see, for example, Rainey, 1989; Kim & Chen, 1994; Ran, Kim & Zheng, 1998). In this approach, the body is assumed 'thin' and the force is obtained by the sum of the force per unit length on each short segment of the slender body ignoring the effects of structures on waves. Ma & Patel (2001) also employed this method but consider nonlinear forces which were neglected before. Their results are compared with the experimental studies by Weggel et al (1997). However, to author's knowledge, the fully nonlinear model for the free response of the SPARs is still rare in the publications.

In this section, the QALE-FEM method is used to simulate the free response of a moored spar to monochromatic waves and bichromatic waves. The dimensional parameters of the spar platform for this study are shown in Table. 9.1.1. The mooring line in this simulation is considered as a nonlinear spring with its stiffness taken as 191kN/m up to an offset of 13.7m and 398kN/m at offsets larger than this.

Table 9.1.1 Principal particulars of the spar platform

Diameter ($2R_0$)	40.5m
Initial draft (D_r)	198.2m
Mass	2.6×10^8 kg
Radius of gyration (pitch and roll)	62.33m
Centre of gravity from keel	92.4m
Fairleads from keel	92.6m
Density of water	1025kg/m^3
Water depth	900m

9.1.1. Comparison with experimental data

In these cases, the waves are generated by a wave maker. The motion of the wave maker is governed by Eqs. (8.2.1) – (8.2.3) for monochromatic waves and the following equations for bichromatic waves,

$$S_w(\tau) = -a_1\cos(\omega_1\tau) - a_2\cos(\omega_2\tau) \tag{9.1.1}$$

$$U_w(\tau) = a_1\omega_1\sin(\omega_1\tau) + a_2\omega_2\sin(\omega_2\tau) \tag{9.1.2}$$

$$\dot{U}_w(\tau) = \left[a_1\omega^2{}_1\cos(\omega_1\tau) + a_2\omega^2{}_2\cos(\omega_2\tau)\right](1-e^{\beta\tau}) \tag{9.1.3}$$

The numerical results will be compared with the experimental results by Weggel et al (1997). The transient responses of the spar platform are investigated as in their work. The cases are run in a numerical tank with L=8, B=1. The mesh is unstructured with mesh size on the free surface is given by $\Delta x = \Delta y \approx \lambda/30$ (roughly 30 nodes in a wavelength). The time step is taken as T/128.

It should be noted that in such deep water (900m), the nondimensionalised diameter of the spar platform is very small (0.045). There are two associated problems. The first one is that the mass of a small body results in a larger iteration count for the ISITIMFB procedure as indicated in Section 8.2.2. The second one is that the mesh near the body surface should be very fine to ensure there are enough nodes on the body surface. Both can reduce the computational efficiency. To overcome these problems, the water depth used to nondimensionalise the physical quantities is shortened to 300m. This is based on the assumption that the effect on the response of the floating body from the seabed is negligible when the water depth is large enough, say, larger than one wave length. To ensure this assumption is acceptable, several cases with deeper water are also considered. The results will be discussed in Section 9.1.2.

The first case presented here is for the response of the spar to an incident monochromatic wave with the dimensional wave height being 6m and the dimensional period being 14s. The pitch of spar subjected to the monochromatic wave is shown as Fig 9.1.2. For the purpose of comparison, the experimental results which are duplicated from Weggel, Roesset & Davies, et al (1997), are also plotted together. From this figure, it is observed that the numerical results in this case are close to the experimental data.

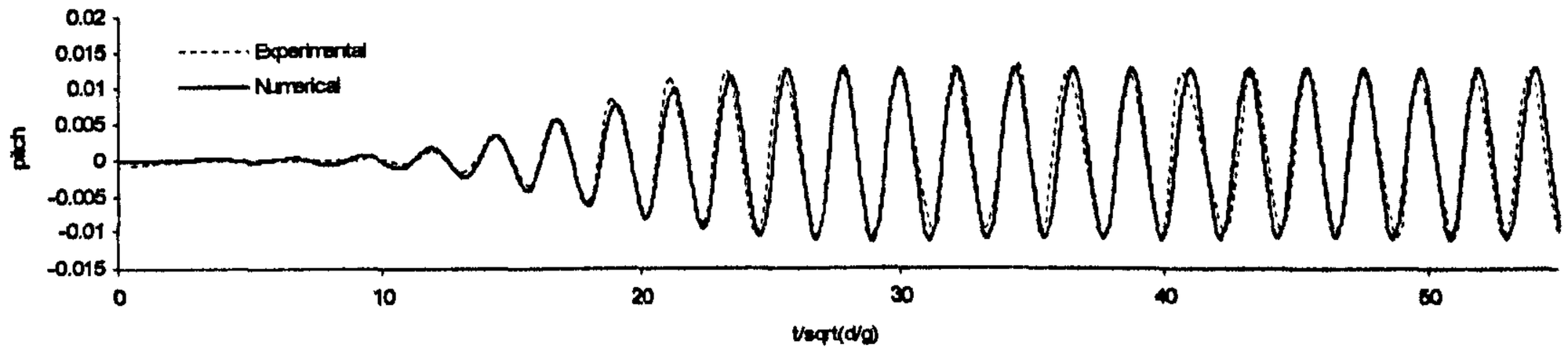

Fig.9.1.2 Comparison with experimental results for pitch of spar subjected to monochromatic waves (experimental results are duplicated from Weggel et al ,1997)

Another case is for the spar subjected to bichromatic waves with dimensional periods and amplitudes being (16s, 17.5s) and (6m, 6m), respectively. The pitch of the spar is shown in Fig.9.1.3. It is also found the numerical results agree satisfactorily with the experimental data.

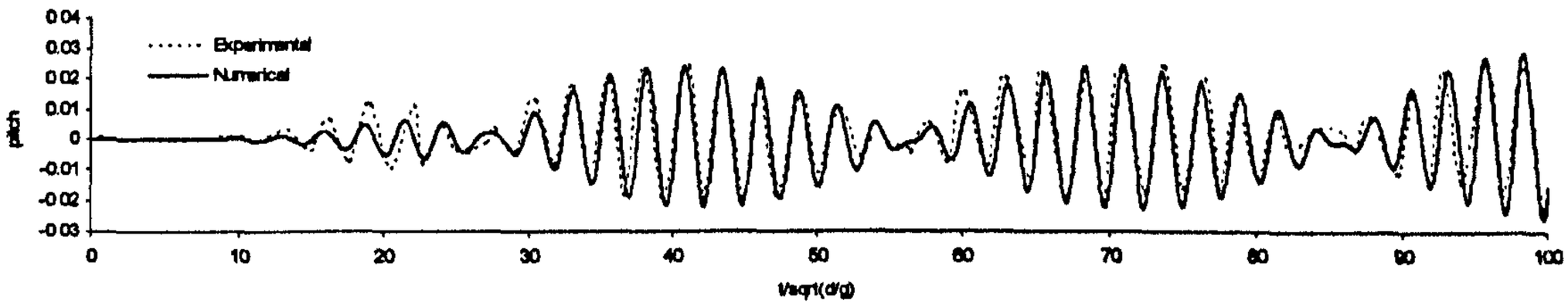

Fig.9.1.3 Comparison with experimental results for pitch of spar subjected to bichromatic waves (experimental results are duplicated from Weggel et al ,1997)

9.1.2. Effect of the water depth

As mentioned above, the water depth used to nondimensionalise the physical quantities is shortened to 300m. To investigate the effect of this treatment, the case with the water depth of 400m is also carried out. The results are shown in Fig 9.1.4 for monochromatic waves and Fig. 9.1.5 for bichromatic waves and compared with those in Fig.9.1.2 and 9.1.3, respectively.

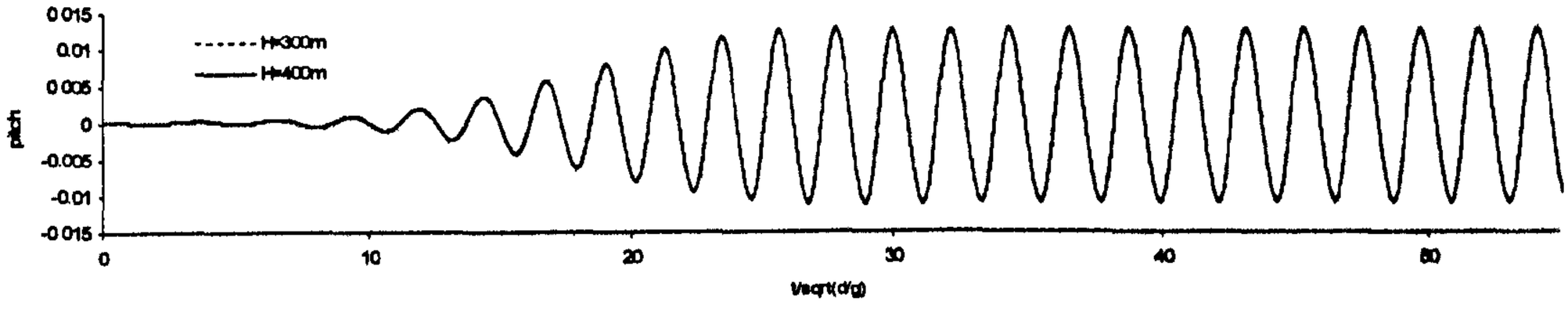

Fig.9.1.4 Comparison of pitch of spar subjected to a monochromatic wave at different water depths

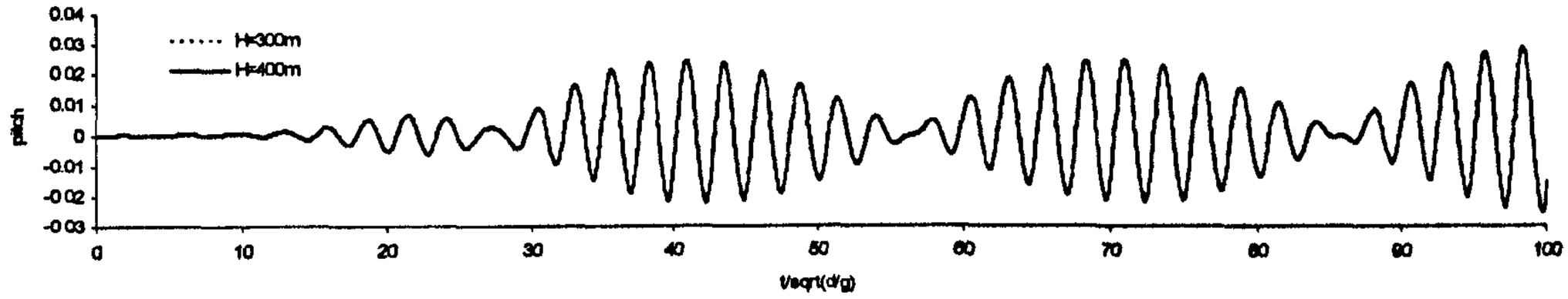

Fig.9.1.5 Comparison of pitch of spar subjected to a bichromatic wave at different water depths

These two figures show that there are no obvious differences between the results with different water depths. This implies that the effect from the seabed is indeed negligible in the above cases and the treatment, i.e. using shortened water depth, is therefore acceptable.

9.1.3. Effect of the width of tanks

In a 3D case, the reflection from the *y*=const wall (side vertical walls of the tank) should be removed. One may also use Sommerfeld condition with damping zone techniques to ease the reflection. However, in this application, the simplest way, using a larger domain, is employed. Though the numerical results showed in Fig.9.1.2 and Fig.9.1.3 show high consistency with the experimental data, it is necessary to investigate the effects of these walls. Because the width of the experimental tank is not mentioned in Weggel .et al (1997), these effects are numerically studied by using different width of the tank.

For this purpose, the same cases in Fig.9.1.2 and Fig. 9.1.3 are investigated in a wider tank (*B*=2). The resultant surge and pitch history are plotted in Fig 9.1.6 and Fig. 9.1.7.

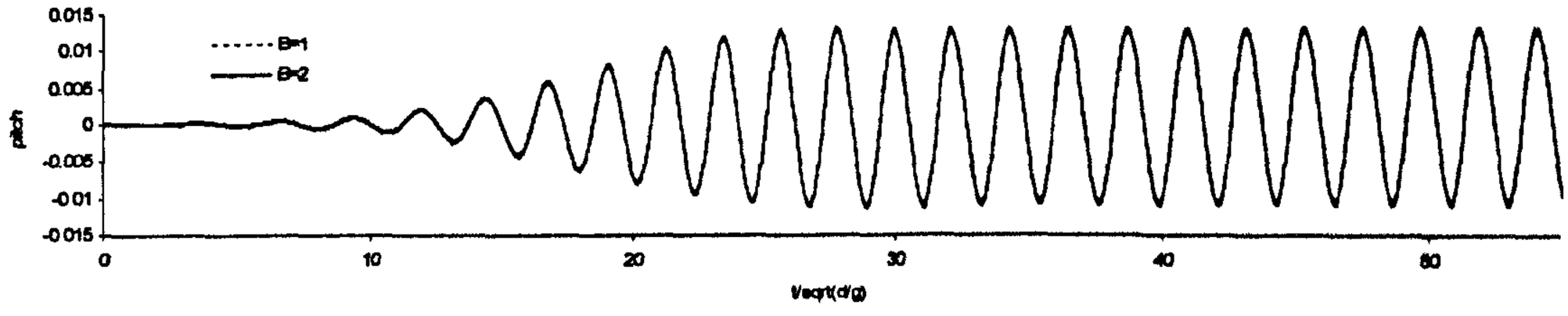

Fig.9.1.6 Comparison of surge of spar subjected to a monochromatic wave in tanks with different widths

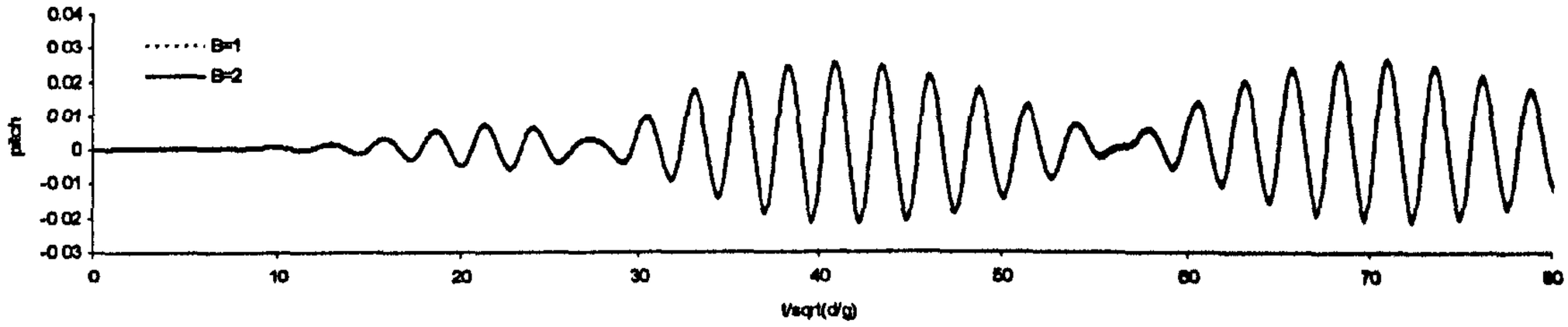

Fig.9.1.7 Comparison of pitch of spar subjected to a bichromatic wave in tanks with different widths

It is observed that the difference is very small. Therefore, the tank used in this application is considered as wide enough. The width of the tank used in Fig. 9.1.2 and Fig. 9.1.3 is about 10 times of the radius of the floating body. In the following investigations, similar principle is used. For cases with different floating bodies, more investigation may be made.

9.2. Convergence properties investigation

Similar to 2D cases, investigations on the convergence property of the QALE-FEM in 3D cases are also carried out. The case in Fig. 9.1.5 is used here. Two main factors, the time step and the mesh size, are considered in this investigation. The cases are defined in Table 9.2.1. The pitch histories of the spar platform for those cases are compared.

Table 9.2.1 Test cases in convergence property investigation

Case No.	Mesh size on the free surface	Time step
C1	$\Delta x = \Delta y \approx \lambda/30$	$T/200$
C2	$\Delta x = \Delta y \approx \lambda/30$	$T/128$
C3	$\Delta x = \Delta y \approx \lambda/30$	$T/64$
D1	$\Delta x = \Delta y \approx \lambda/20$	$T/128$
D2	$\Delta x = \Delta y \approx \lambda/40$	$T/128$

Fig.9.2.1 shows the pitch histories for the cases with different time steps. The mean mesh size on the free surface is taken as $\Delta x = \Delta y \approx \lambda/30$ and the time steps are given by $T/200$ (C1), $T/128$ (C2) and $T/64$ (C3), respectively.

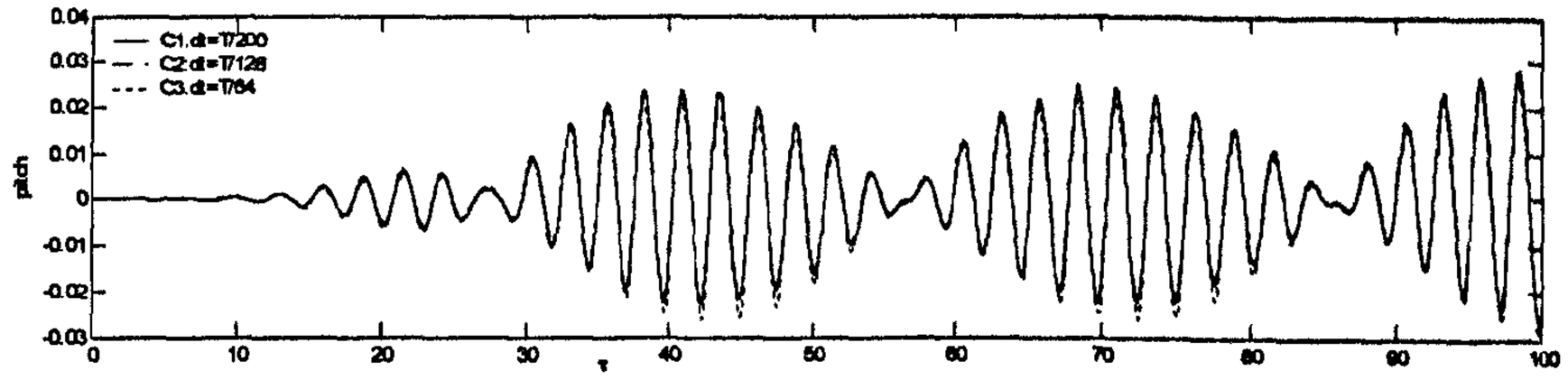

Fig.9.2.1 Pitch histories in cases with different time steps

From this figure, it is observed that the difference between the result of case (C1) with time step being $T/128$ and that of case (C2) with time step being $T/200$ is negligible. But, the result for the case with time step of $T/64$ is slightly different from the results of other two cases. However, there is no evident difference between the case with time step of $T/64$ and that with time step of $T/200$, as concluded in the convergence studies for 2D cases in Section 8.2.2. This implies the 3D cases require relatively smaller time step than 2D cases to get a convergent result. This is reasonable because the interaction between the waves and a 3D freely floating body makes the waves around the floating body become more complicated than that in a 2D case. The QALE-FEM method needs therefore smaller time step to achieve the same accuracy. Based on this, the time step in the 3D cases is taken as $T/128$ in this work.

For studying the convergence properties with different mesh sizes, the time step is taken as $T/128$ and the mesh sizes are ranged from $\lambda/40$ to $\lambda/20$ .The pitch histories of the spar platform are plotted in Fig. 9.3.2.

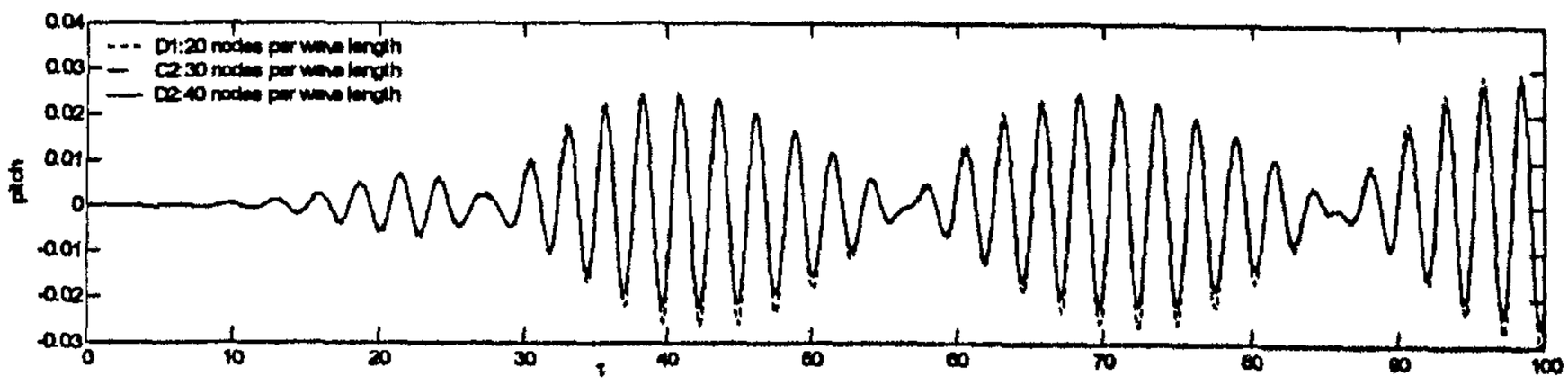

Fig.9.2.2 Pitch histories in cases with different mesh sizes

It is observed that the difference between the results in cases with the mesh size of $\lambda/30$ and $\lambda/40$ is negligible. But the case with mesh size of $\lambda/20$ leads to slightly different results from other two. This implies that in the 3D case, the mesh size should be smaller than $\lambda/30$.

This conclusion is the same as that arrived at in the 2D case. Thus, the mesh size in the 3D cases is taken as roughly $\lambda/30$ in this work.

Apart from convergence properties, the iteration counts of the ISITIMFB in these cases are also investigated. The results are plotted as Fig. 9.2.3.

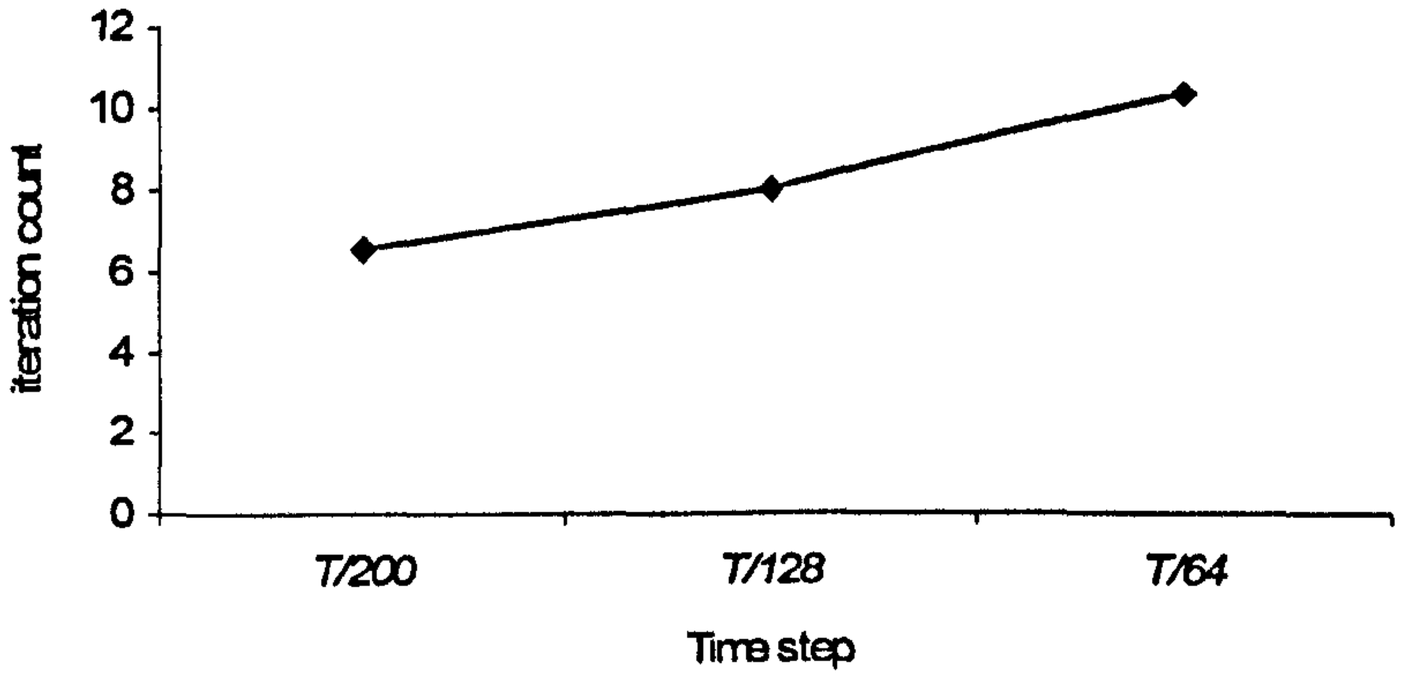

Fig. 9.2.3 (a) different time steps (mesh size : $\lambda/30$)

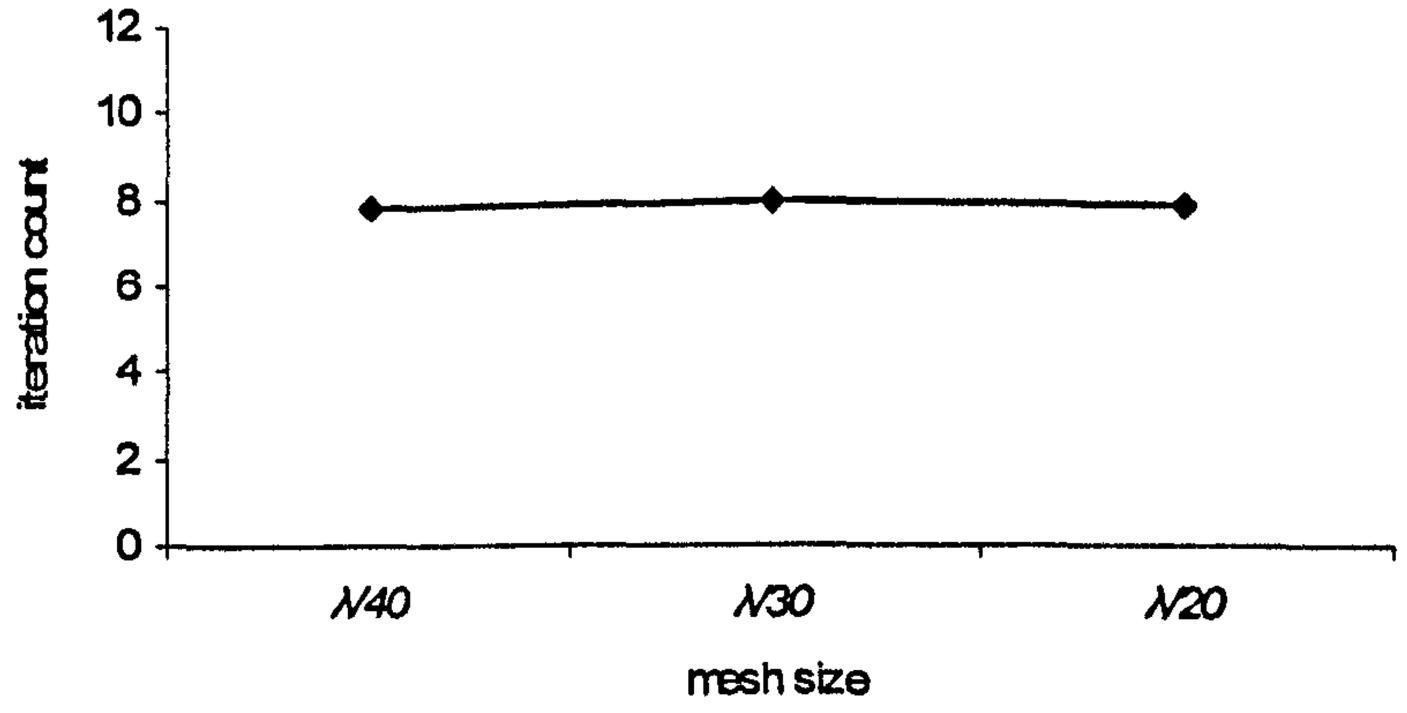

Fig. 9.2.3 (b) different mesh sizes ($\Delta t = T/128$)

Fig. 9.2.3 Iteration counts in cases with different time steps and mesh sizes

Fig. 9.2.3 (a) shows the iteration counts in the cases with different time steps while Fig.9.2.3 (b) illustrates the iteration counts in the case with different mesh sizes. It is observed from Fig.9.2.3 (a) that the iteration count increases with increasing time step, i.e. about 6 for $\Delta t = T/200$ (case C1), 8 for $\Delta t = T/128$ (case C2) and 11 for $\Delta t = T/64$ (Case C3). These results are similar to those for the 2D cases shown in Fig. 8.2.5 (a). Fig. 9.2.3 (b) demonstrates that the mesh sizes affect the iteration count slightly. In all these three cases, the iteration counts are close to 8.

The iterative control error in the ISITIMFB used in the above simulations is taken as 0.5%. As discussed in Section 8.2.2, this value is appropriate in most of the 2D cases. To confirm that this value is still small enough in 3D cases, different control errors are used foro Case C2

($\Delta x = \Delta y \approx \lambda/30, \Delta t = T/128$). The pitch histories in the cases with different control errors are plotted as Fig.9.2.4.

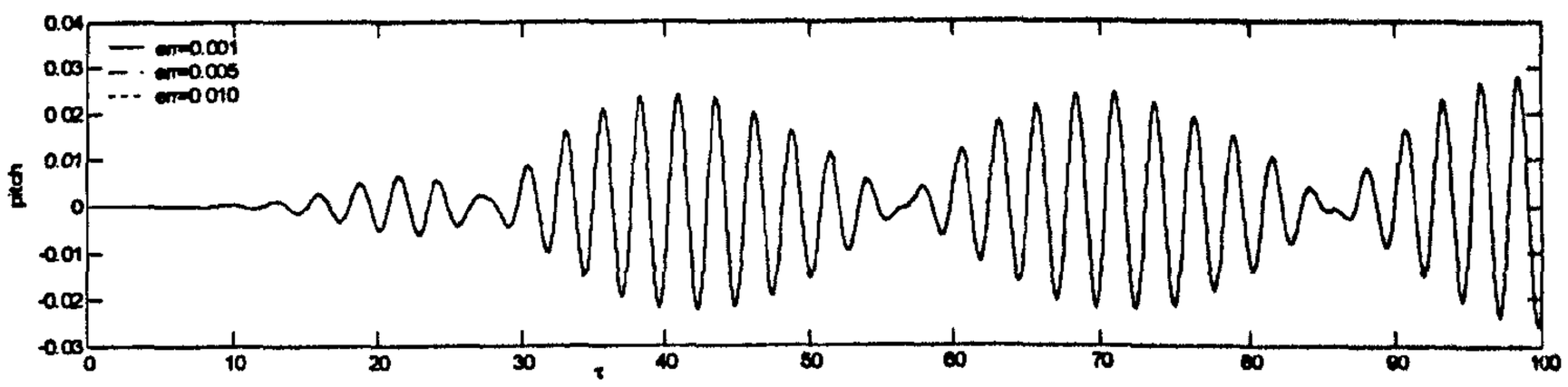

Fig.9.2.4 Pitch histories in cases with different control errors of the ISITIFMB

It can be seen that the difference between them is negligible. Therefore, the 0.5% is also small enough even in 3D cases. This value of the control error will be adopted in all the cases described in this chapter.

9.3. RAOs of surge, heave and pitch of a barge-type floating body

Compared to the spar platform, the barge-type floating body is longer relative to its draft and therefore is closer to a real ship. The interaction between the waves and the floating barge-type body has attracted much attention. An important 3D experimental study has been done by Shashikala, Sundaravadivelu & Ganapathy (1997). In their study, the response of a barge elastically moored to a fixed support for regular and random waves in head sea condition is investigated. The influence of the location of the mooring point and the stiffness of the mooring line is also explored. In addition, they also proposed a FEM solution based on the assumptions that the motion of the floating barge as well as the incident waves is linear and the submerged body surface is taken as the initial body surface beneath the still water plane. Their linear numerical results are close to the experimental data. However, in the region where the frequency of the incident wave is close to the natural frequency, the difference between their numerical results and the experimental data is relatively large. One possible reason is that, in the case near the natural frequency, the nonlinearity associated with the wave-body system is strong and therefore the above assumptions are not true. In this section, the RAOs of sway, heave and roll motions of the 3D moored barge are modelled by the QALE-FEM method. The results are compared with the experimental data and the linear numerical results. The nonlinearity associated with the problem is also presented. The sketch of experimental set up in the above reference is shown in Fig 9.3.1 and the dimensional parameters associated with the floating barge are given in Table 9.3.1.

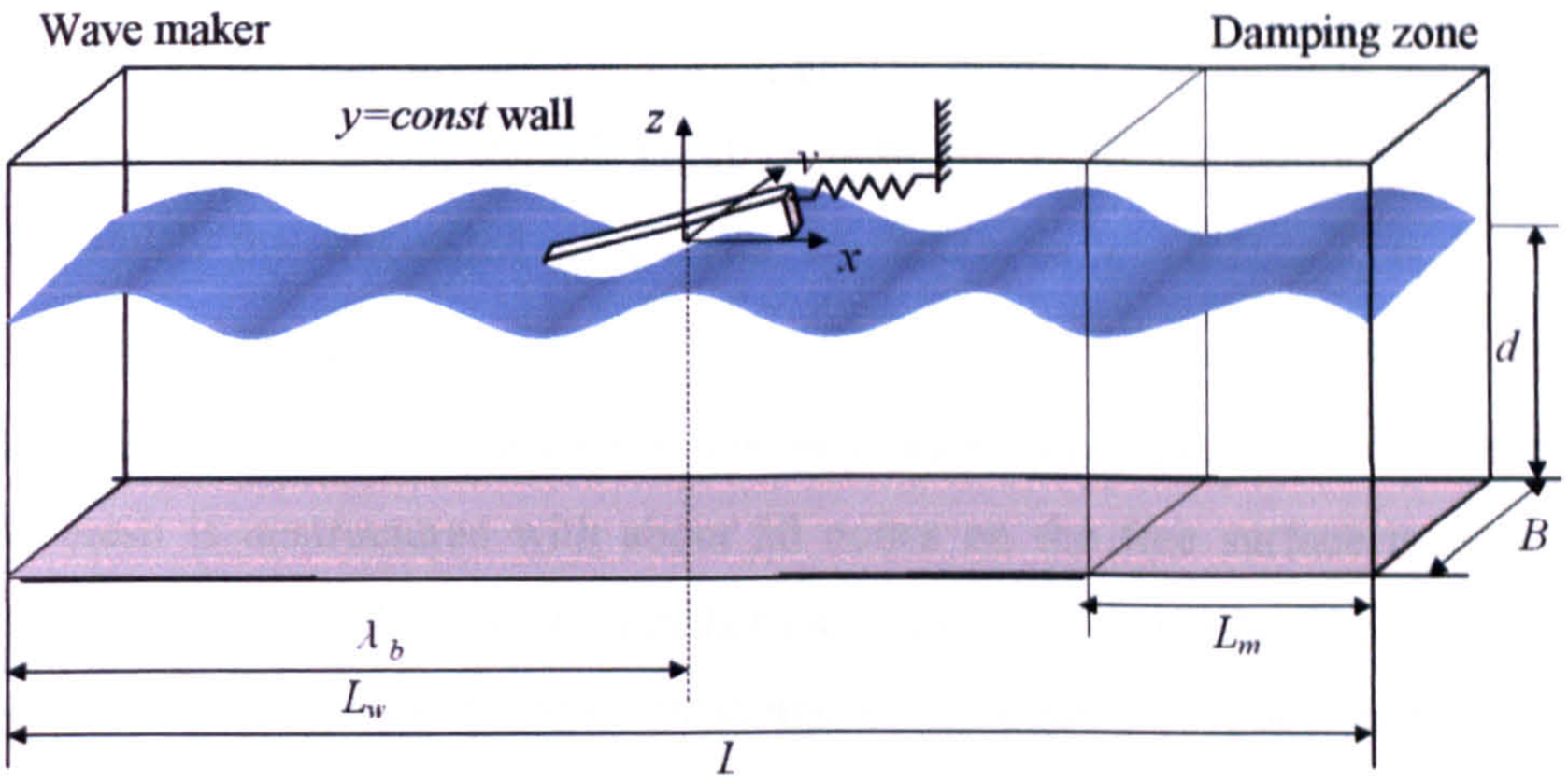

Fig.9.3.1 Sketch of the interaction between a barge-type floating body and water waves

Table 9.3.1 Details of the experiment on cases with barge-type bodies

Water depth (d)	2.35m
Length (L_b)	2m
Breadth (B_b)	0.4m
Draft (D_r)	0.1m
Mass (M)	80kg
Volume (V)	0.08m^3
Center of gravity above hase (KG)	0.09m
Longitudinal metacentric height (GMl)	3.2475m
Transverse metrcentric height	0.09338m
Mass moment of inertia about longitudinal axis	1.68kg·m^2
Mass moment of inertia about transverse axis	38.17kg·m^2
Mass moment of inertia about vertical axis	38.31kg·m^2
Center of mass from water level	0.01m
Center of buoyancy from water level	0.05m
Natural period in heave	0.902s
Natural period in pitch	1.0s
Stiffness of mooring lines	10N/mm
Mooring point from the centre of mass	80mm

The response amplitude operator (RAO) was given in Shashikala .et al.'s experiments by

Surge RAO (m/m)=Surge amplitude/Wave amplitude

Heave RAO (m/m)=Heave amplitude/Wave amplitude

Pitch RAO (rad/m)=Pitch amplitude/Wave amplitude

In the numerical simulation, the RAOs are estimated by performing the FFT analysis on the steady-state portion of the time histories of corresponding motions. In order to get the steady-state solution in a shorter time, Ramp2 together with the artificial damping technique is employed, for which the associated parameters are taken as $\kappa = 0.25$, $T_d = L_w / C_g$ and $\alpha = 0.5$, as in Section 8.2.4.

All the cases considered here are carried out in a numerical tank with L=9, B=2. The computational mesh is unstructured with about 30 nodes on the free surface in each wave length. The wave are generated by the wavemaker located at x= -5 initially. The amplitudes of the wavemaker are adjusted properly so that generated incident wave steepness equals 0.02. The time step is taken as T/128.

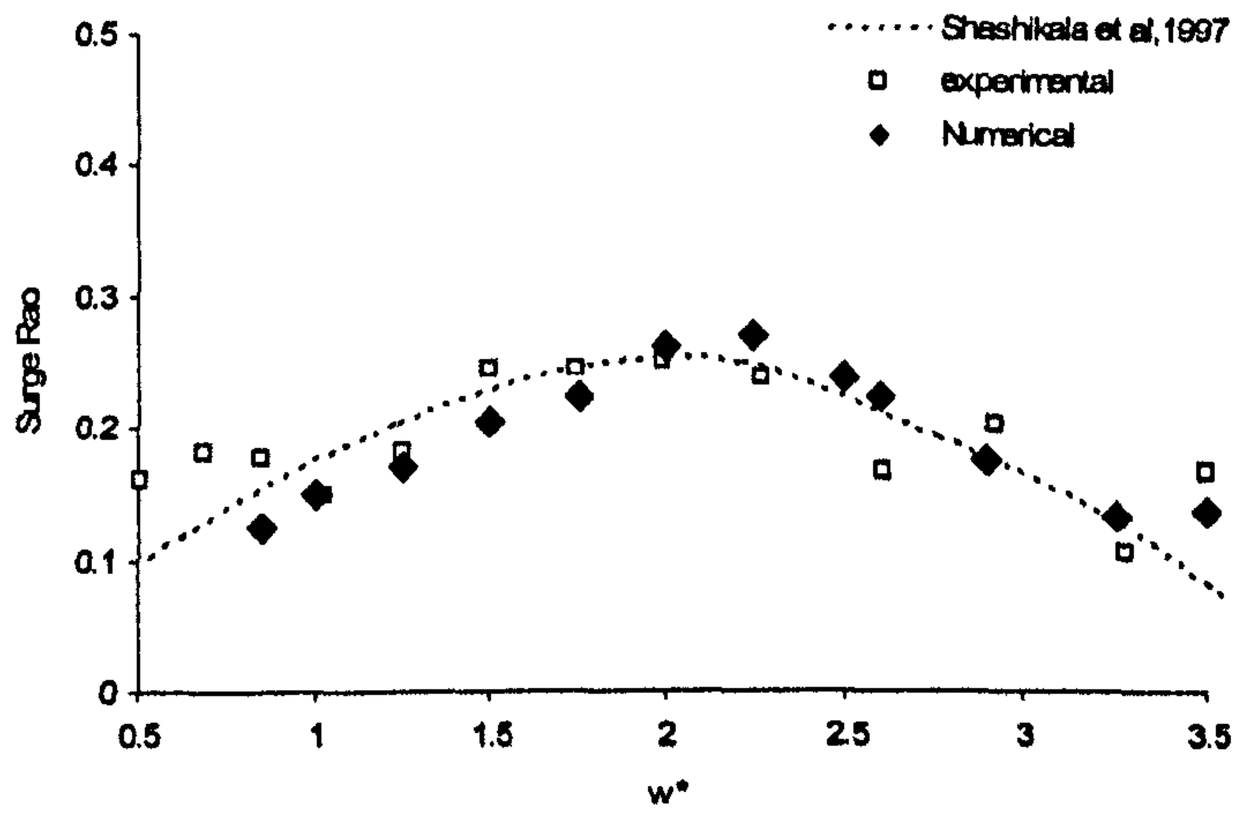

Fig.9.3.2 (a) Surge RAO

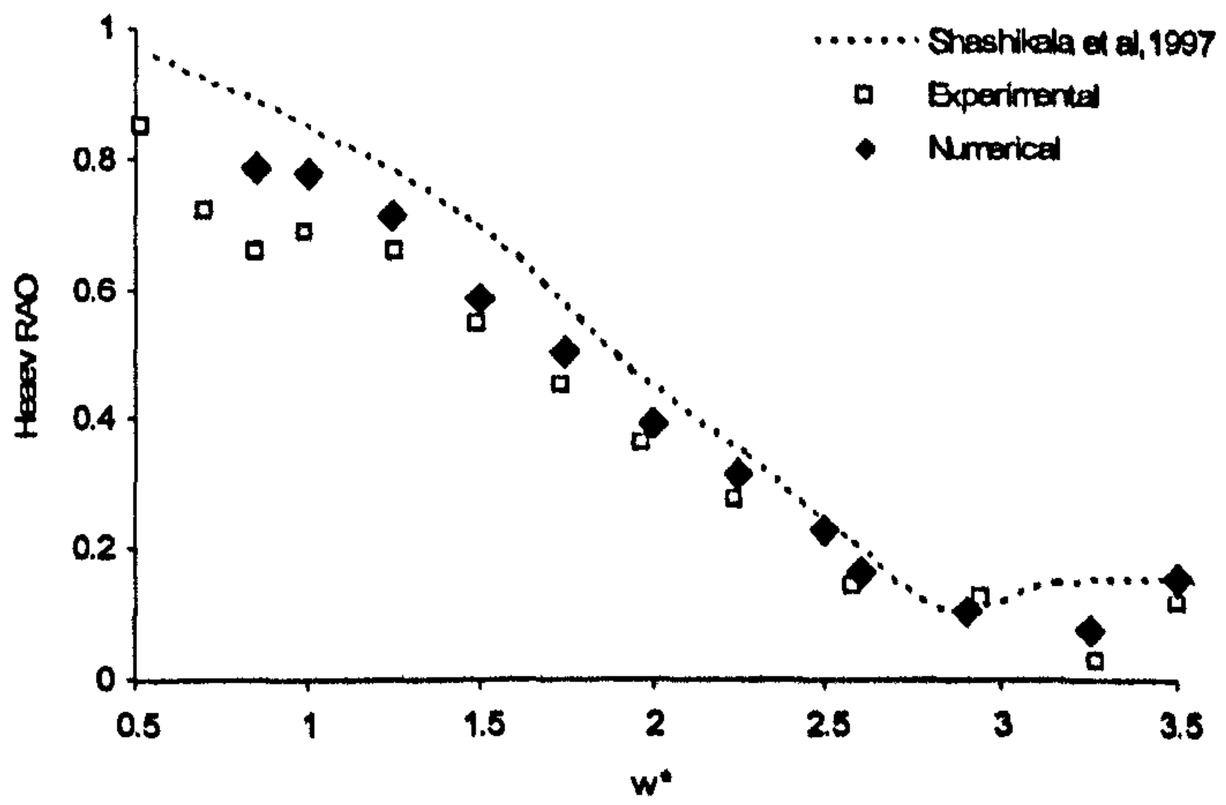

Fig.9.3.2 (b) Heave RAO

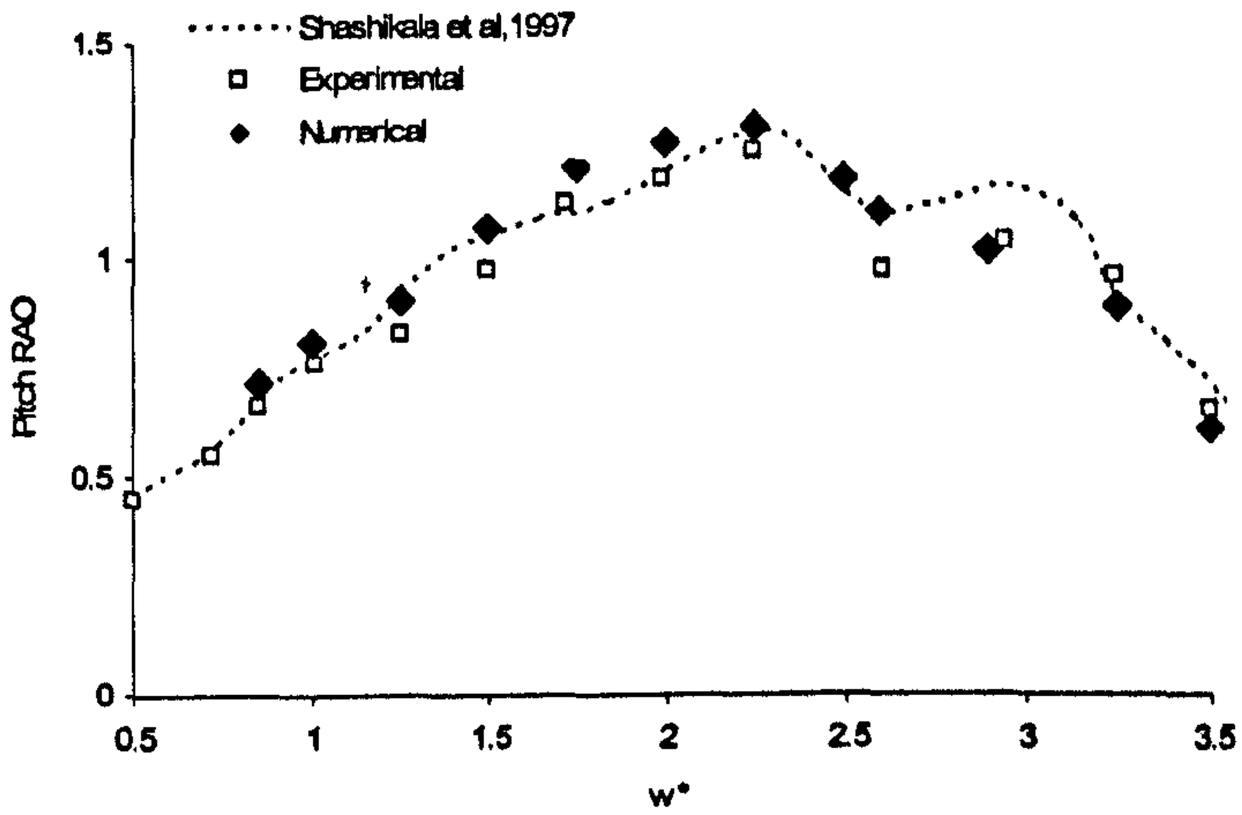

Fig.9.3.2 (c) Pitch RAO

Fig.9.3.2 Comparison of response of barge in regular waves

The RAOs of surge, heave and pitch motions corresponding to different incident waves as a function of $\omega^* = \omega^2 L_b / 2g$ are plotted in Fig. 9.3.2 together with the results from the references. From these figures, the present numerical results are closer to the experimental data than the linear numerical results by Shashikala, Sundaravadivelu & Ganapathy (1997). That is reasonable because the linear numerical model assumed both the waves and floating body motion are linear.

It is found from Fig. 9.3.2 (a) that the peak RAO for surge is located at $\omega^* \approx 2.2$, about 1/6 dimensionless natural frequency of surge (12.75). The RAO for pitch reaches peak value when ω^* is close to 2, about half of the natural frequency of pitch ($\omega^* = 4.05$). The heave response reduces to a very low value at ω^* equal to 3.0 and increase as ω^* further increases. However, the reason why the heave response is smallest when ω^* is close 3.0 still needs to be further studied. It is also observed that the difference between the linear solution and the experimental data is relatively large in this area.

To show the nonlinearity, the surge force acting on the floating body in case with $\omega^* = 2.9$ is plotted in Fig. 9.3.3.

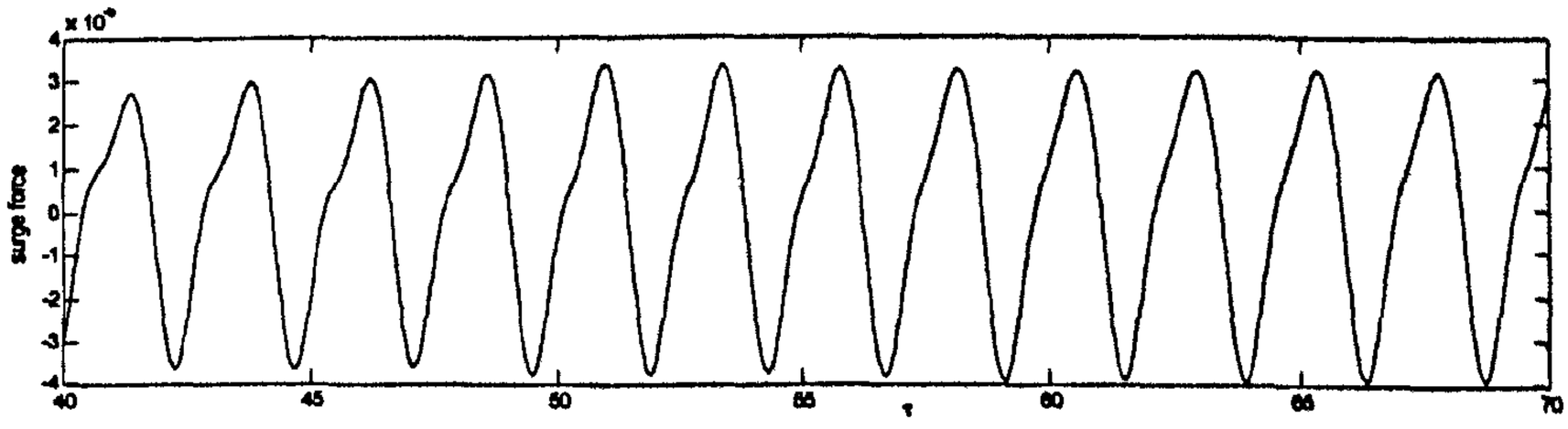

Fig.9.3.3 Surge force acting on the floating barge in case with $\omega^* = 2.9$

This figure shows the nonlinearity associated with the history of the surge force, i.e., the curve in one wave period is not symmetric about the apex point in that period. This may be the reason why the linear numerical solution shows large differences to the experimental data near that frequency area for the surge motion. The motion history of the floating body in this case is shown in Fig. 9.3.4.

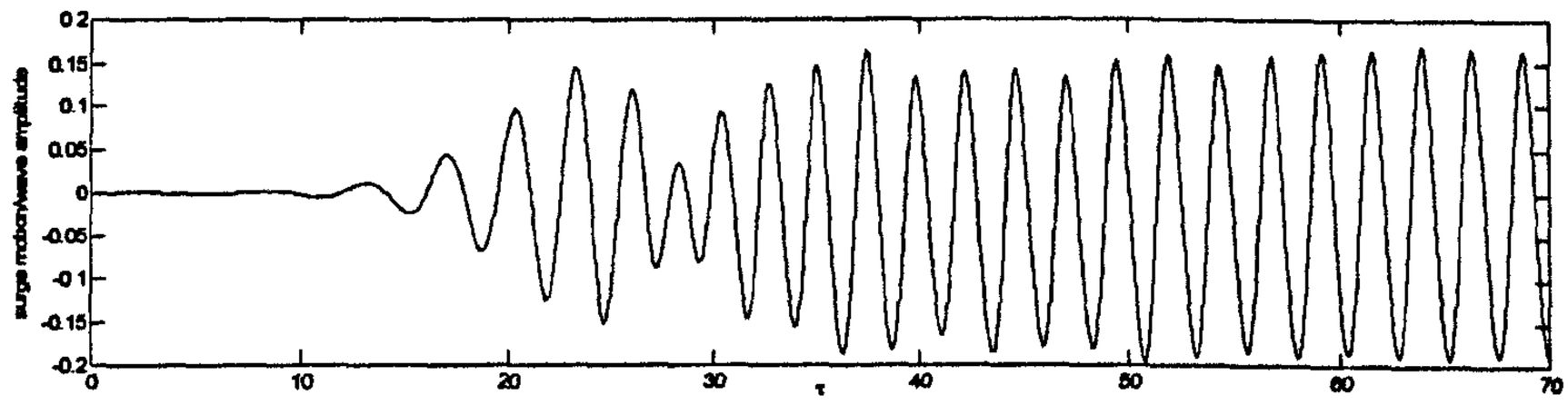

Fig.9.3.4 (a) surge motion

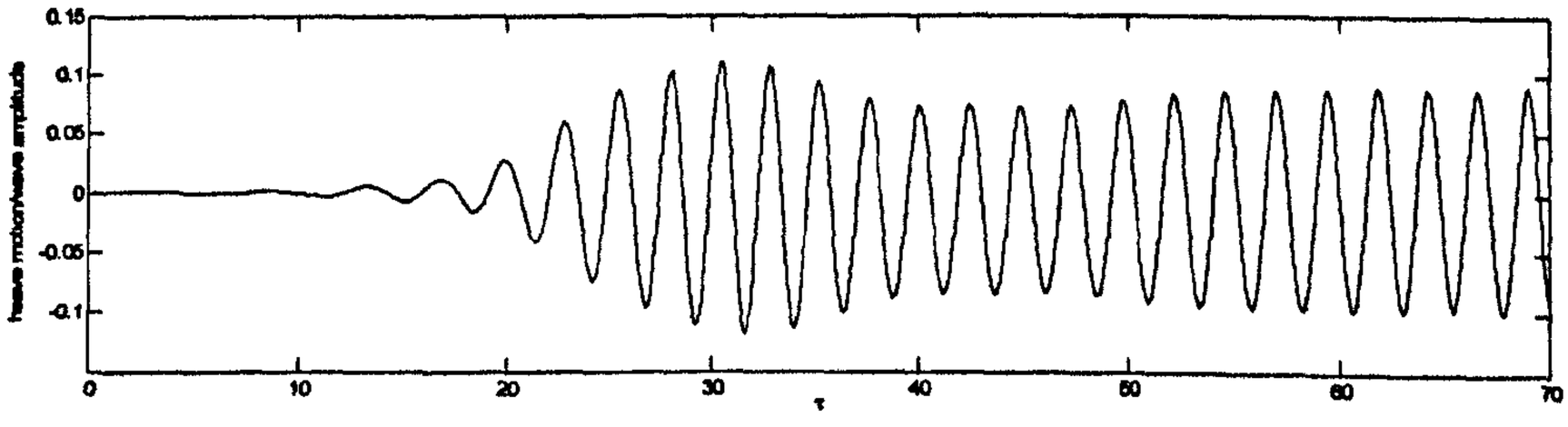

Fig.9.3.4 (b) heave motion

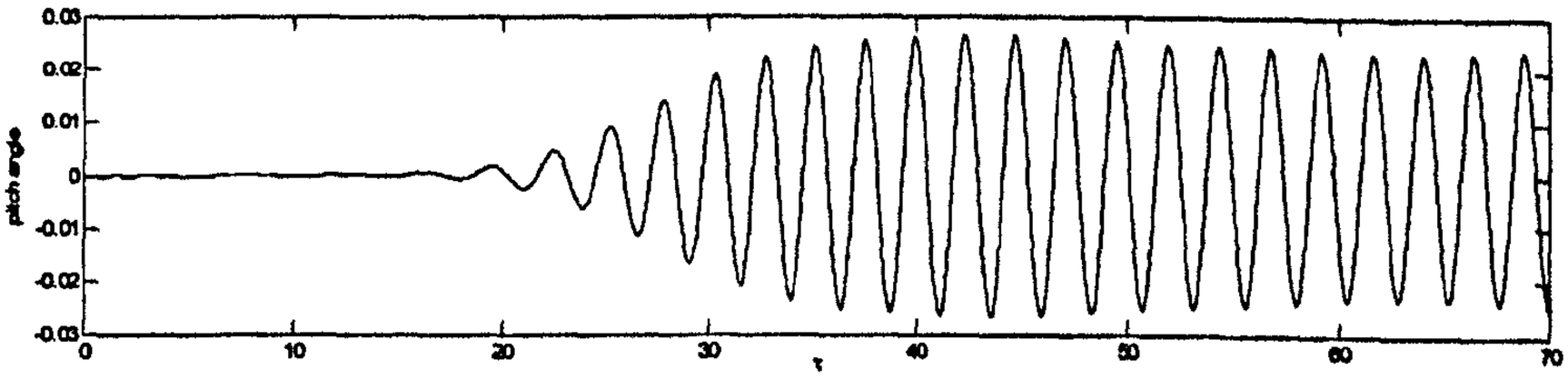

Fig.9.3.4 (c) pitch angle

Fig.9.3.4 Response of the floating barge in case with $\omega^* = 2.9$

9.4. Response of a Wigley Hull to nonlinear waves and the effect of incident angles

The QALE-FEM method is now applied to simulate the transient behaviour of the Wigley Hull due to a steep wave. The shape of the Wigley Hull used here can be described as

$$\eta = (1-\varsigma^2)(1-\xi^2)(1+0.2\xi^2)+\varsigma^2(1-\varsigma^8)(1-\xi^2)^3 \tag{9.4.1}$$

in which

$$\xi = 2x/L_b, \eta = 2y/B_b, \varsigma = z/D_r \tag{9.4.2}$$

where L_b, B_b, D_r are the length, breadth and draft of the Wigley Hull. Compared to the floating barge, Wigley Hull resembles a real ship more closely than a barge-type floating body and therefore is widely used in either experimental investigation or numerical simulation. (Qiu, 2001). A sketch of the Wigley Hull is shown in Fig.9.4.1.

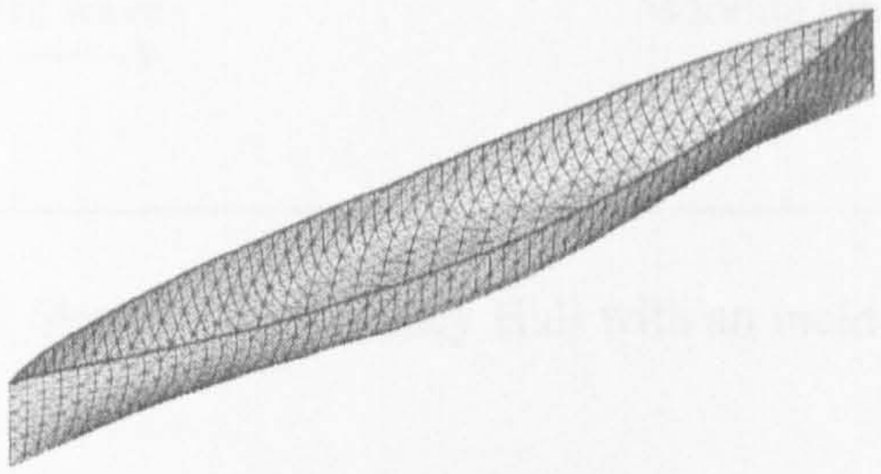

Fig.9.4.1 Wigley Hull and the mesh on its surface

In order to investigate the nonlinearity associated with the wave-Wigley Hull system, waves with different amplitudes are used. Two factors which affect the response of the Wigley Hull to the incident waves are also investigated and discussed.

The first one is the natural frequency of the Wigley Hull. Different natural frequencies lead to different response of the floating bodies to the same incident waves. From the results of RAOs shown in Section 8.2.4, it has been found that the motion becomes relatively large and the resonance may occur when the frequency of the incident wave is close to the natural frequency. In order to investigate the effect of the natural frequency, Wigley Hulls with different moment of inertias are used in this investigation. Another parameter which may affect the natural frequency of the floating body is the mooring line. Results obtained by Shashikala, Sundaravadivelu & Ganapathy (1997) have already indicated that the RAOs of the motion change as the spring stiffness changes. Naturally, different stiffness of the mooring line leads to different natural frequencies of the floating body. For example, the natural frequency on surge motion (ω_{surge}) of the Wigley Hull with mooring lines can be roughly estimated in most cases by

$$\omega_{surge} = \sqrt{k_m / M} \tag{9.4.3}$$

where M is summation of the mass and the added mass. Once the spring stiffness is changed, ω_{surge} is also changed. The effect of the mooring line will also investigated in Section 9.4.2.

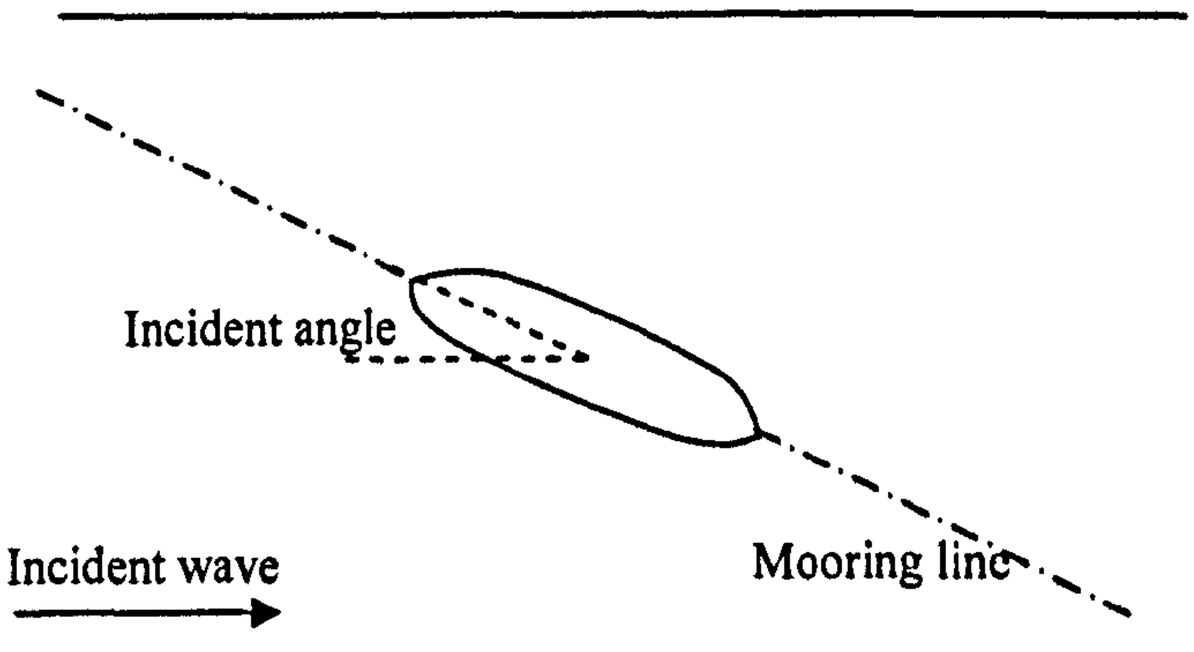

Fig.9.4.2 Sketch of the Wigley Hull with an incident angle

The second factor is the incident angle of the Wigley Hull. The incident angle is the angle between the incident wave and the central vertical plane of the hull as shown in Fig. 9.4.2. A Wigley Hull in such a condition has 6 degrees of freedom and is therefore more difficult to simulate. Fully nonlinear simulations of this problem are still rare. One possible reason is the singularity problem associated with the sharp corner of the body surface. In Section 9.4.3, the effect of the incident angle is investigated.

9.4.1. Response of the Wigley Hull to steep waves

The nonlinear response of the Wigley Hull to waves with different steepness is investigated. In this case, a Wigley Hull with L_b=1.0,B_b=0.2,D_r=0.15 is used. The dimensionless mass and the pitch moment of inertia are taken as 0.01677 and 0.035 respectively. The centre of gravity is located at 0.125 below the water level and the incident angle is taken as 0. Two linear springs are moored at both the head and the end of the Wigley Hull and located at z=1.0 (the water level) initially as shown in Fig.9.4.2. The tank used in these cases has length of 12 and width of 2, 10 times of the breadth of the hull. The waves are generated by a wave maker located at x= -7. For the purpose of investigating the transient response of the Wigley Hull, ramp function 'Ramp 1' is used here. The mesh is unstructured and the mesh size on the free surface is roughly $\Delta x \approx \lambda/30, \Delta y \approx \lambda/30$. The motion of the wave maker is governed by Eqs. (8.2.1)- (8.2.3) with $\omega = 1.7691$, a=0.0041 and 0.025, respectively. The wave roughly equals to 2, two times the length of the Wigley Hull. The time step is T/128. The spring stiffness is taken as 0.005. In order to analysis the steady motion of the Wigley Hull, a damping coefficient of 0.005 in surge is applied to absorb transient motions. The response of the Wigley Hull due to different waves is plotted in Fig. 9.4.3.

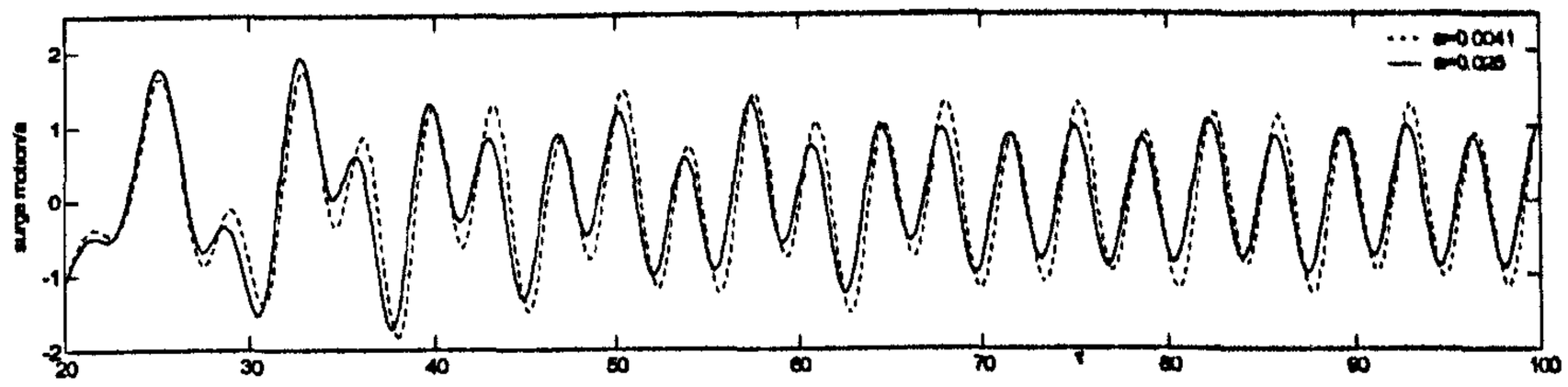

Fig.9.4.3 (a)surge

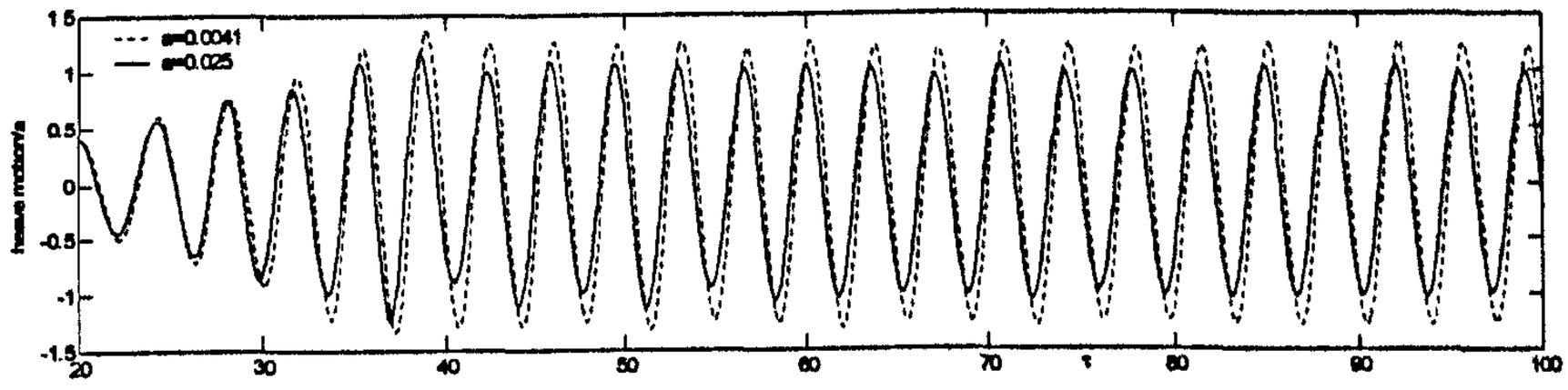

Fig.9.4.3 (b)heave

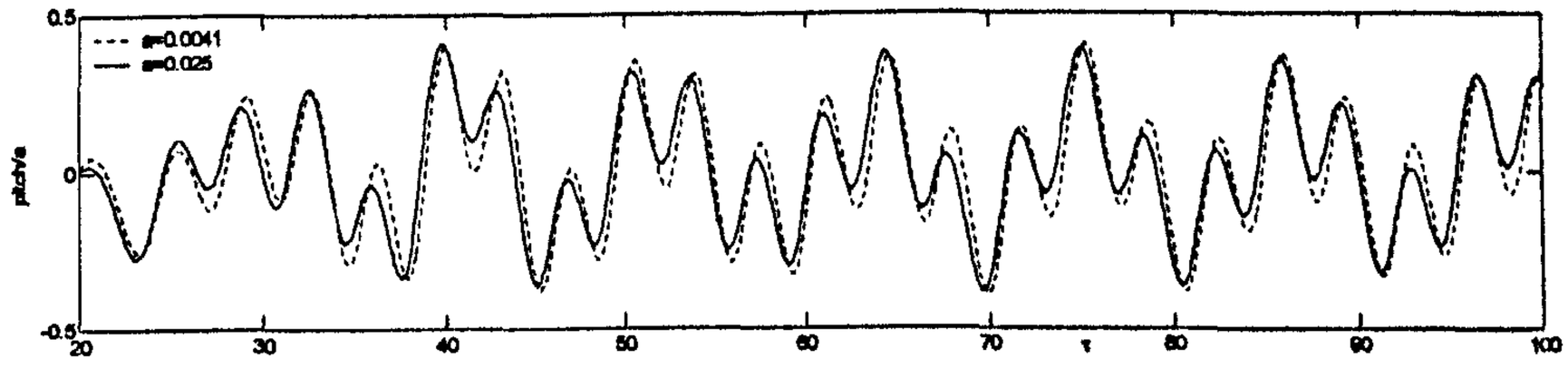

Fig.9.4.3 (c) pitch

Fig.9.4.3 Response of the Wigley Hull to waves with different steepness ($\omega = 1.7691$)

From this figure, it is observed from Fig. 9.4.3 (c) that there is long-period oscillation existing in the pitch motion. The period, roughly equals to 14.2, of this oscillation is almost 4 times that of the incident wave. This period is almost equal to the natural frequency for the pitch motion of the hull and is therefore due to the transient effect. It is also found that the response of the Wigley Hull to the steeper wave (a=0.025) is slightly in advance of that to the linear wave (a=0.0041). That is because the steeper wave travels faster than the linear wave, as indicated in Section 7.1.1. To further show the nonlinearity involved in this case, the run-up recorded in the front and lee sides of the waterline in case with a=0.025 is shown in Fig. 9.4.4.

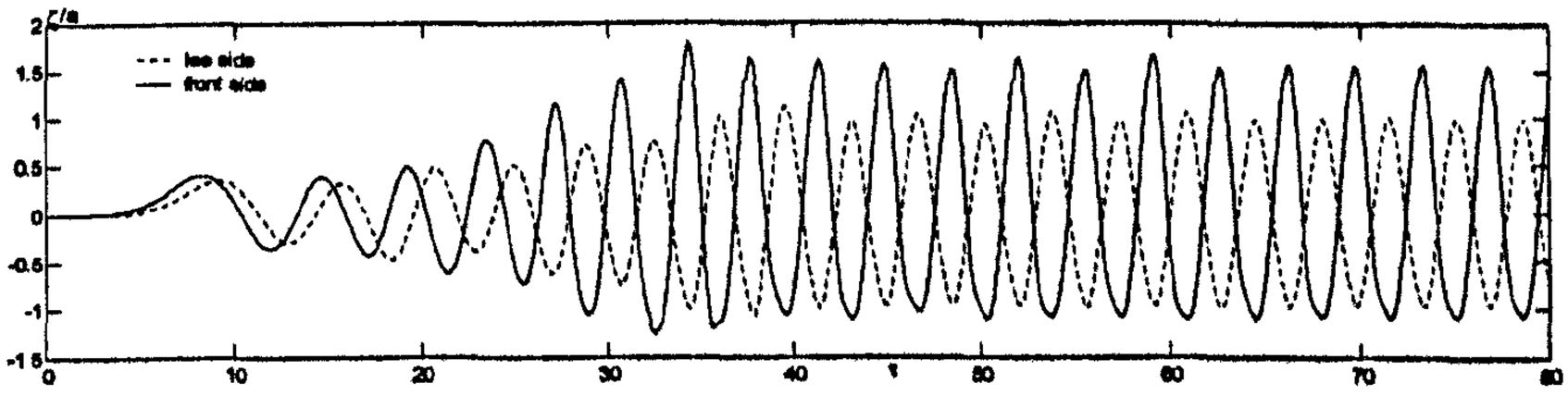

Fig. 9.4.4 Wave run-up recorded at the waterline (a=0.025, $\omega = 1.7691$)

This figure clearly demonstrates that the wave run-up at the front side of the Wigley Hull is larger than that at the lee side of the Wigley Hull. As seen, the wave profile contains nonlinear characteristic such as sharp crests and flat troughs. In addition, one may also find that the wave run-up on the front side seems roughly half a period in advance of that in the lee side. That is because the wave length of the incident wave is twice the length of the Wigley Hull. It takes about half a period for the wave to propagate from the front side to the lee side

It should be noted that the reflection from the side walls, e.g. y=const wall, may affect the response of the hull. Before further investigations are made, the effect from the width of the tank is tested. The Wigley Hull used in this test is the same as that used in Fig. 9.4.3. The width of the tank is taken as 2 (equal to $10B_b$) and 3, respectively. The amplitude of the motion of the wavemaker is a=0.025. All other parameters in these cases are the same as those in Fig. 9.4.3. Since the reflected waves from side walls need time before affecting the response, long-time simulation is required. In this investigation, $60T$ results are obtained. The response of the Wigley Hull for different widths of numerical tanks is plotted as Fig. 9.4.5.

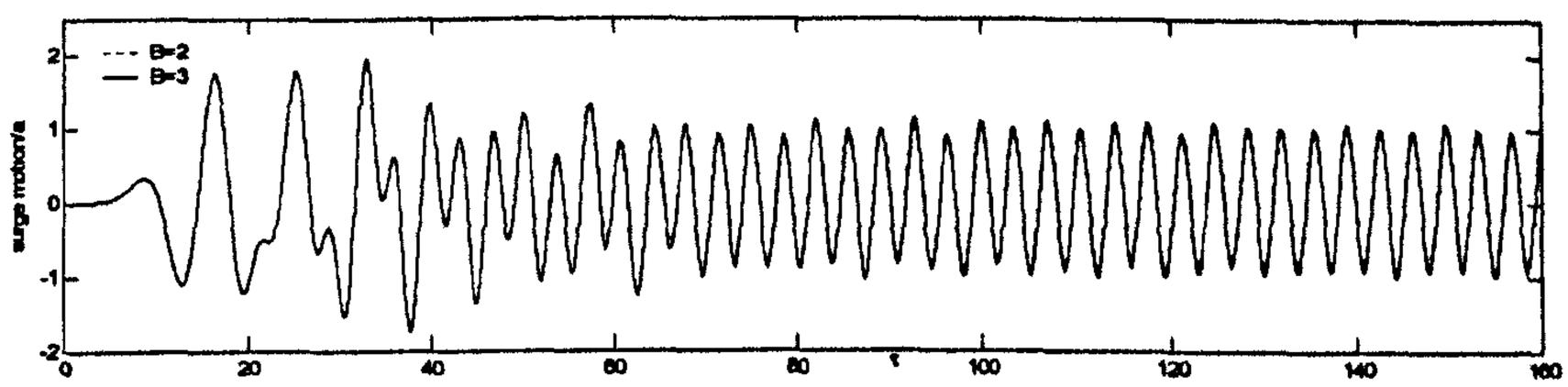

Fig. 9.4.5 (a) surge

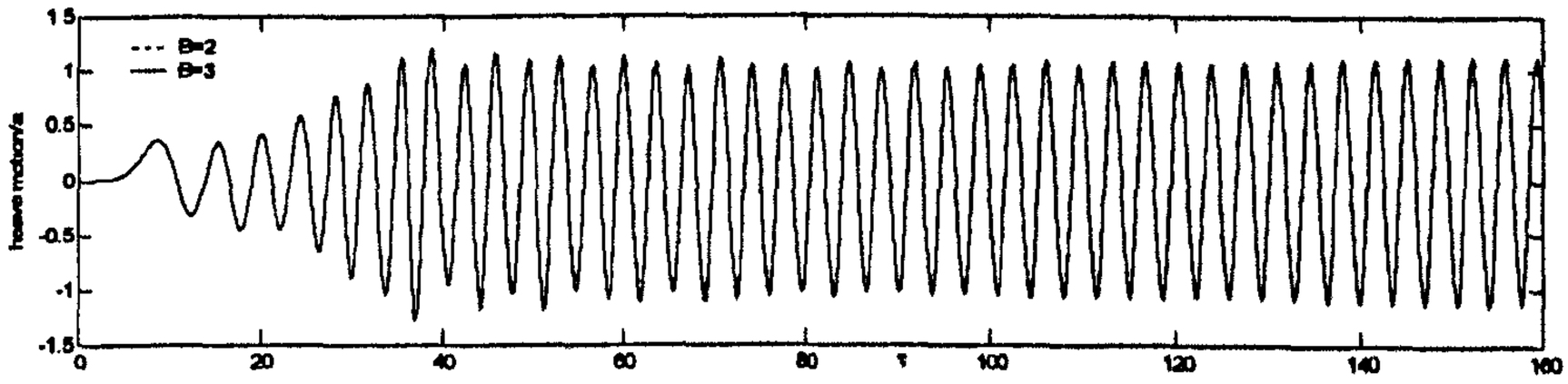

Fig. 9.4.5 (b) heave

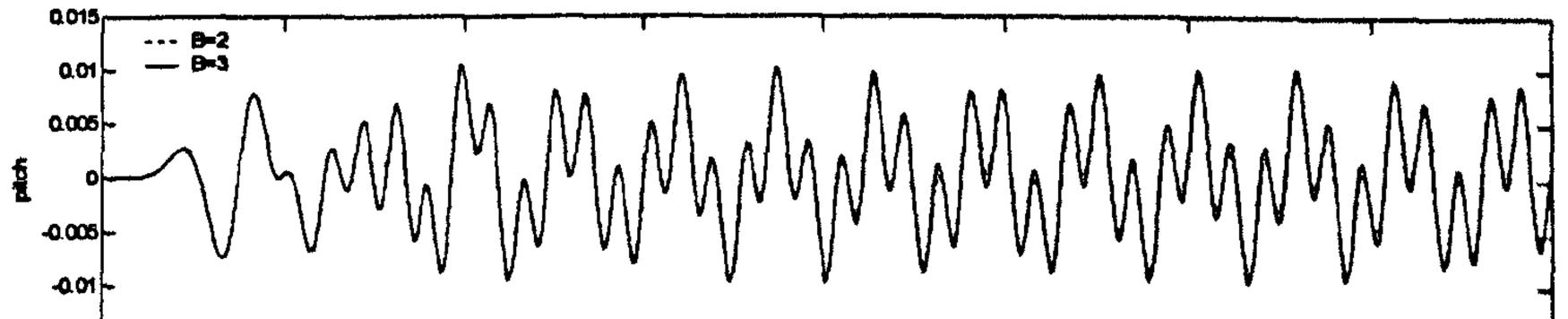

Fig. 9.4.5 (c) pitch

Fig. 9.4.5 Response of the Wigley Hull in cases with tanks of different widths ($\omega = 1.7691$, a=0.025; k_m=0.005)

This figure clearly shows that the difference between the results obtained in wider and calculated narrower tanks is negligible, even after 40 periods of calculation ($\tau > 142$). This implies that the results for B=2 are acceptable.

9.4.2. Different response for cases with different natural frequencies

The effect of the natural frequency is then investigated. As mentioned above, there are two ways to change the natural frequency of the Wigley Hull. The first one is to change the mass or moment of inertia. To do so, a case with a different moment of inertia is run. The shape of the Wigley Hull is the same as that used in Fig. 9.4.3 but the moment of inertia is given as I_y=0.015. The natural frequency for the pitch motion in this case is roughly 7.0. All other parameters are the same as those used for Fig. 9.4.3. The response of the hull is shown in Fig. 9.4.6. For the purpose of comparison, the corresponding result (I_y=0.035)is also plotted together.

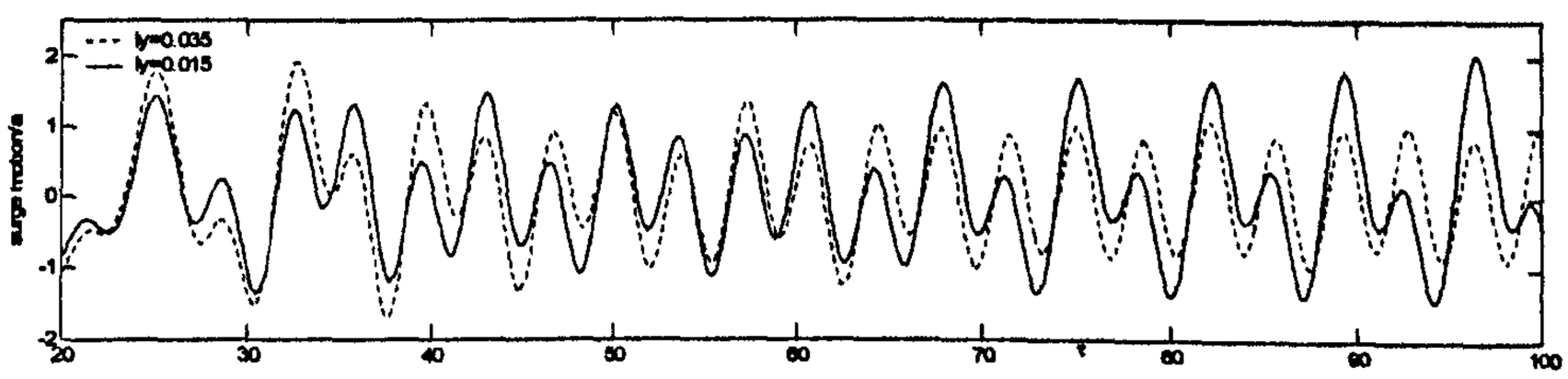

Fig. 9.4.6 (a) surge

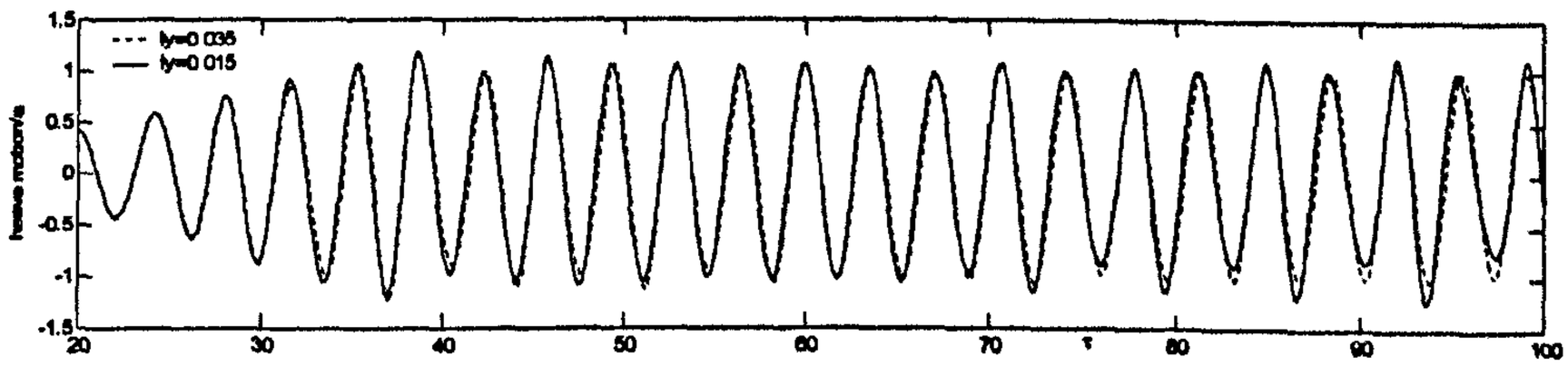

Fig. 9.4.6 (b) heave

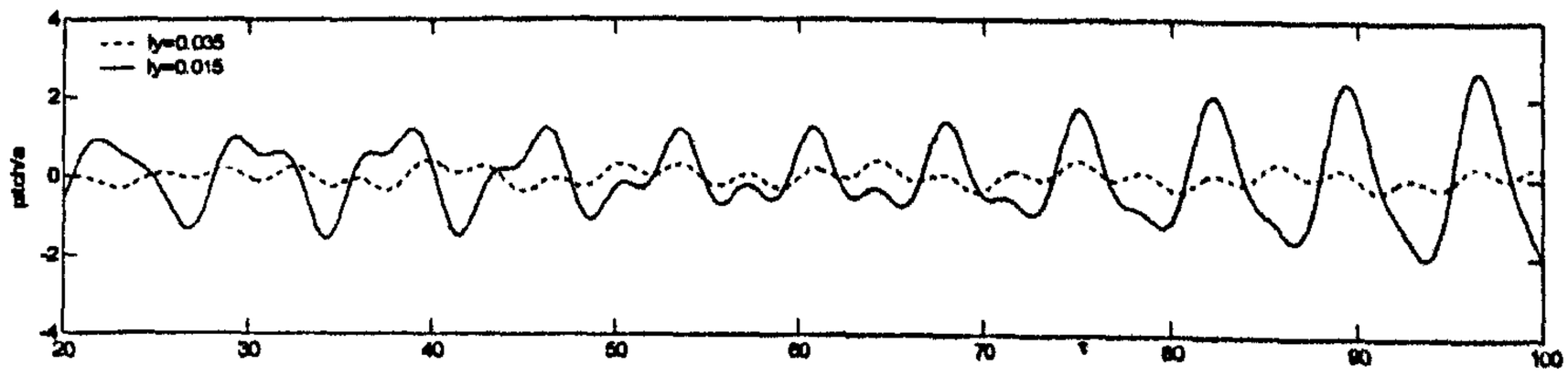

Fig. 9.4.6 (c) pitch

Fig. 9.4.6 Response of the Wigley Hull in casse with different moments of inertia ($\omega = 1.7691$, a=0.03)

It is found from this figure that the pitch motion for I_y=0.015 increases dramatically compared to that for I_y=0.035. This is because the natural frequency (roughly 1.0) for pitch of

the Wigley Hull in this case is much closer to the frequency of the incident wave than that in Fig. 9.4.3. It is also found that the response of pitch angle when $\tau > 80$ keeps increasing which indicates resonance behaviour. This also affects the surge because of coupling and makes it different from the one in Fig. 9.4.3. However, the heave motion seems to remain the same.

Another factor, which affects the natural frequency of the Wigley Hull, is the effect of the mooring line. This is also investigated. In this investigation, the stiffness of the lines, which are attached at 0.1 below the water level, is 0.00025. The incident wave is generated by using $\omega = 1.7691$ and a=0.03. All other parameters are the same as those used in Fig. 9.4.3. The time history of the motion of the Wigley Hull is shown in Fig.9.4.7, which illustrates how the Wigley Hull responds to the transient waves.

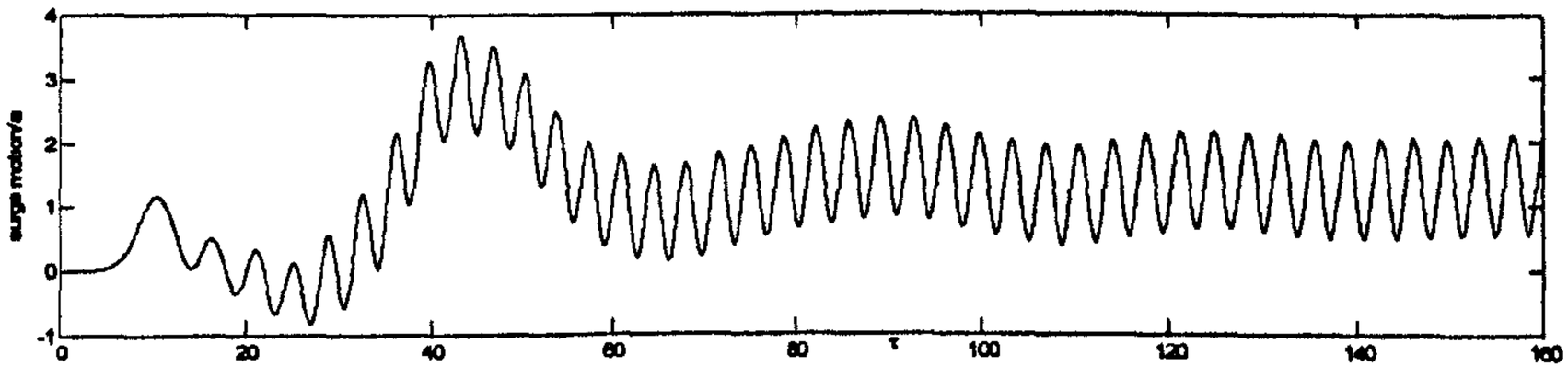

Fig.9.4.7 (a) Surge

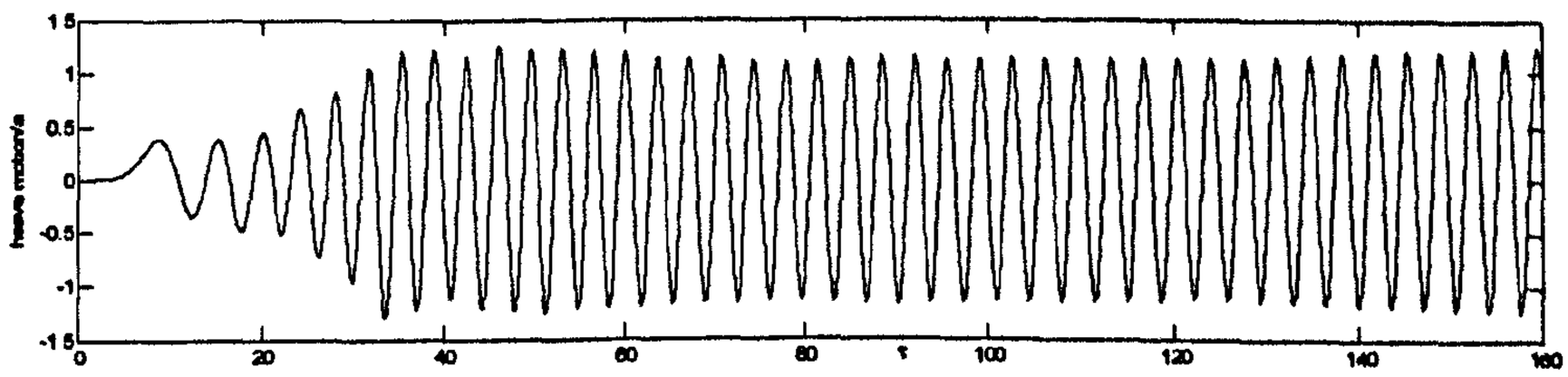

Fig.9.4.7 (b)Heave

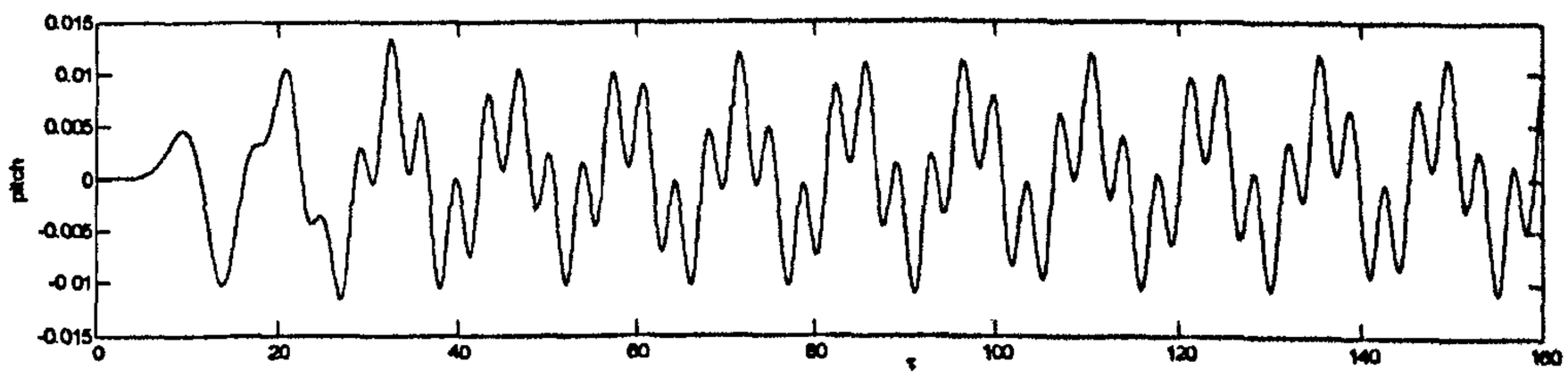

Fig.9.4.7 (c)Pitch

Fig.9.4.7 Response of the Wigley Hull due to a monochromatic wave

($\omega = 1.7691$, a=0.03, the spring stiffness is taken as 0.00025)

It is found that long-period oscillations exist in both surge and pitch motions. These oscillations are due to the transient effects. It is also found that such a long-period oscillation

in surge disappears with time goes because damping is added in surge motion, whereas this oscillation in pitch motion does not seem to disappear since the damping of this mode of motion is zero. One may also find from Fig. 9.4.7 that the transient effect may result in a larger motion than the steady-state wave. This conclusion is consistent with that in Section 8.2.5 and implies that the transient responses rather than RAOs may be considered in design.

In order to further investigate the effect of mooring line on the response of the floating body, a case with stiffer mooring line is considered. The spring stiffness is 0.015, ω_{surge} is 1.33 and the other parameters are the same as in Fig. 9.4.6. The surge motion of the Wigley Hull is shown in Fig. 9.4.8. For the purpose of comparison, the results in Fig.9.4.7, where ω_{surge} is roughly 0.18, are also plotted.

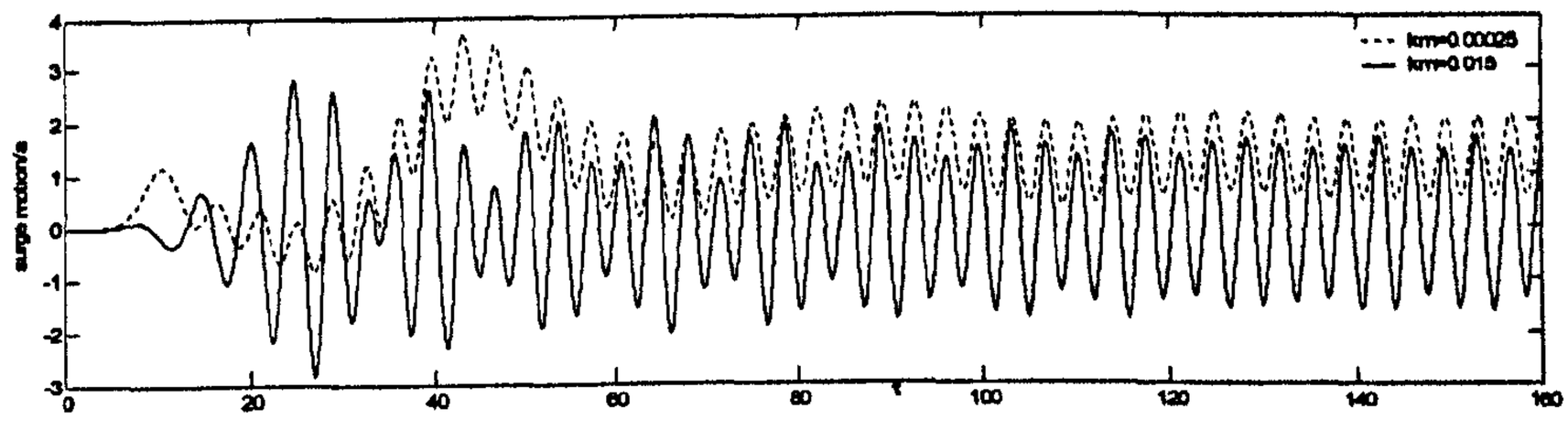

Fig. 9.4.8 Surge motion of the Wigley Hull with different stiffness of the mooring line ($\omega = 1.7691$, a=0.03)

It can be seen from this figure that the amplitude of the steady surge motion ($\tau > 120$) in this case is larger than that shown in Fig. 9.4.7. That is because the frequency of the incident wave (1.7691) is closer to the natural frequency (1.33) in this case than that (0.18) shown in Fig. 9.4.6. The transient response ($\tau < 60$) of the Wigley Hull depends on the mooring line stiffness. It is also found that the mean positions of the surface motion in case with different different mooring line stiffness are different. In the case with a soft mooring line (k_m=0.00025) is about 1.5a from the initial position. However, the surge motion for stiffer mooring line (k_m=0.015) is almost centred at the initial position. The displacement of the mean position of the surge motion is due to the drift force, which is different in those two cases. In addition, in the case with k_m=0.015, the spring force is much larger than the drift force and therefore restricts the floating body motions to oscillations about the initial position.

Results about heave and pitch motion are shown in Fig. 9.4.9. It is shown that the steady heave motions become smaller with an increase in spring stiffness. This is mainly because the incident wave frequencies in both cases are far from the natural frequency of the heave motion. In this situation, stronger stiffness restricts the motion as indicated by Shashikala, Sundaravadivelu & Ganapathy (1997). It is also found, from Fig. 9.4.9b, that the value of the

pitch motion in the case with stiffer mooring line (k_m=0.015) is larger than that for soft one (k_m=0.00025). Apart from the value, the profiles of the pitch motion for different mooring lines are also different. For the results for k_m=0.00025, the profile seems to be formed by superimposing two harmonic motions with different periods. One is the period of the incident wave and the other one is the natural period. However, those for k_m=0.015 seems nonperiodic and combined by various components of motions.

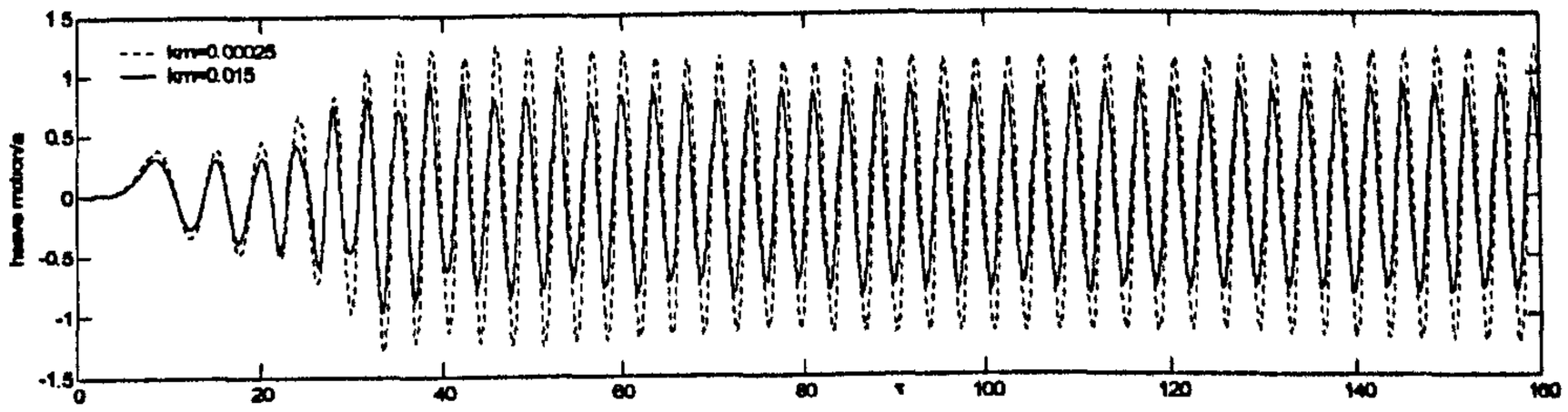

Fig. 9.4.9 (a) heave

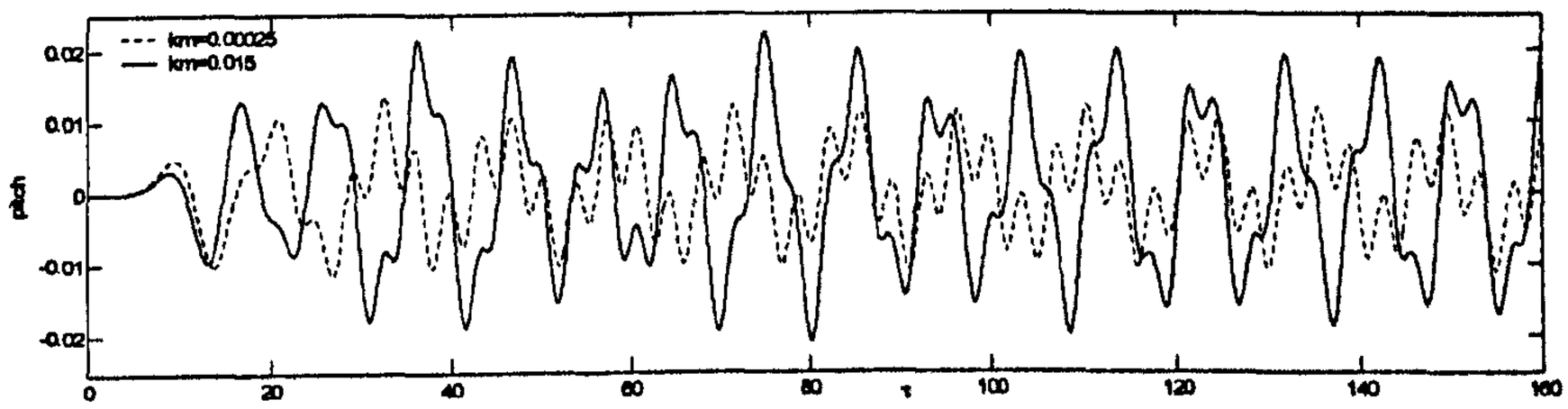

Fig. 9.4.9 (b) pitch

Fig.9.4.9 Response of the Wigley Hull with different stiffness of the mooring line ($\omega = 1.7691$, a=0.03)

9.4.3. Effects of different incident angles

The QALE-FEM method is now applied to investigate the effect of the incident angles on the response of the Wigley hull. In these cases the incident angles between the incident waves and the Wigley hull are taken from 0 to 30^0. The Wigley Hull used in this case is the same as that used in Fig. 9.4.3 and Fig. 9.4.4. The moments of inertia in roll, pitch and yaw motion are taken as I_x=0.035, I_y=0.035, I_z=0.1 respectively.

In the above investigations, the width of the tank is taken as roughly 10 times the width of the floating body. The numerical tests have demonstrated that with such a choice of the width, the side wall reflection may be negligible. However, as the incident angle of the Wigley Hull increasesl, the projected hull area increases and so incident waves are scattered more significantly. Therefore, wider tanks may be required than in the case of zero incident angles. Tests are run to investigate the effect of tank width. In these tests, the incident angle of is taken

as 30^0. The widths of the tanks are chosen as B=2, B=3 and B=5, respectively. The responses of the Wigley Hulls simulated by using the numerical tanks with different widths are plotted as Fig. 9.4.10.

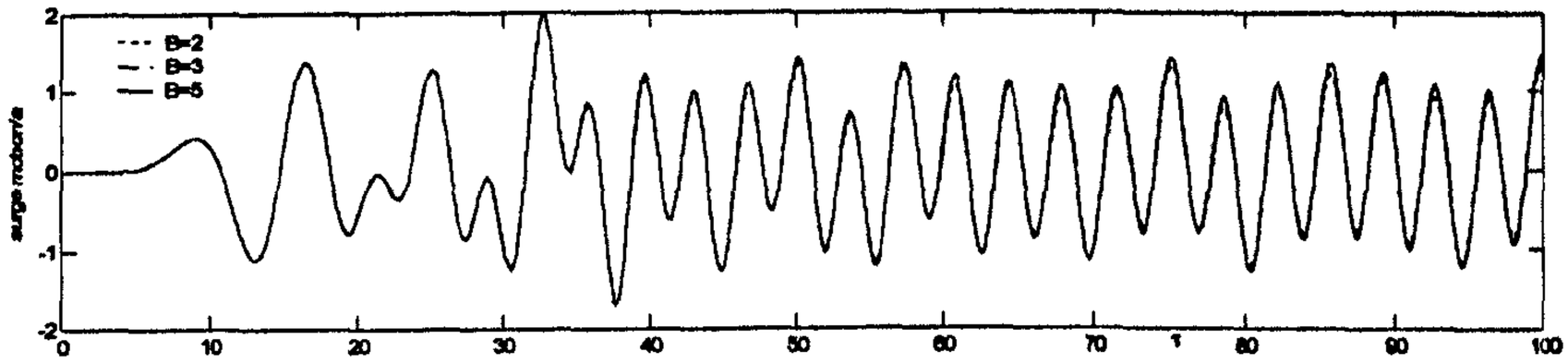

Fig. 9.4.10 (a) surge

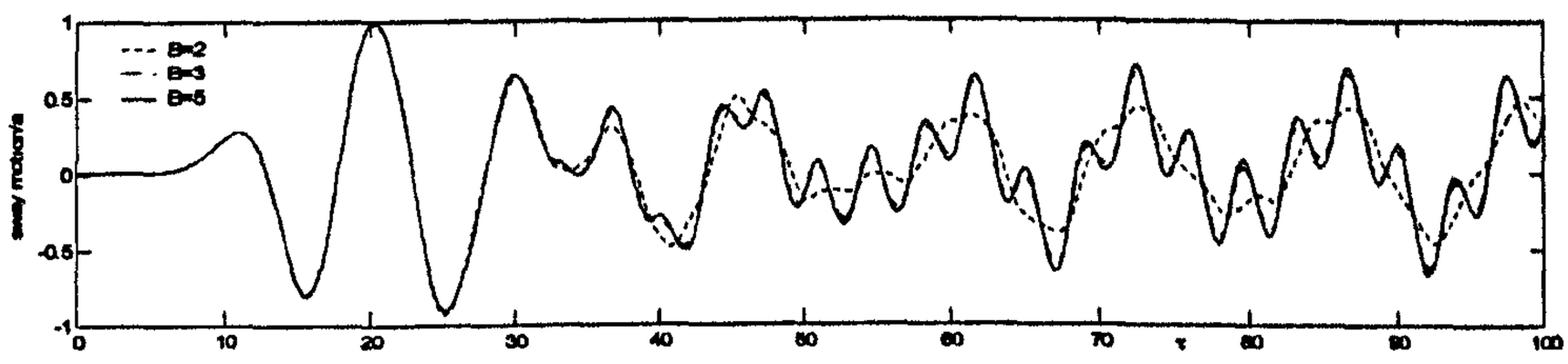

Fig. 9.4.10 (b) sway

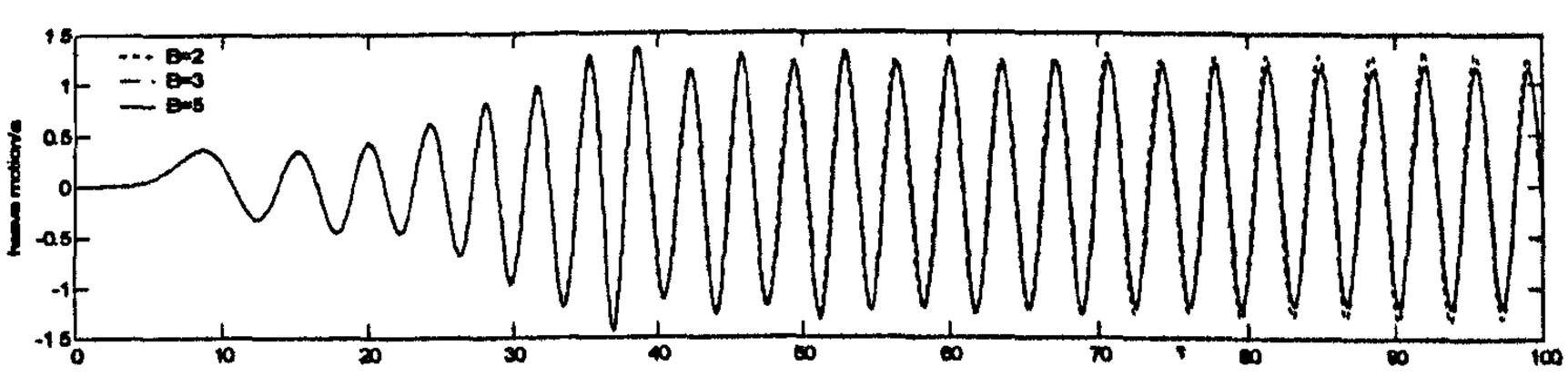

Fig. 9.4.10 (c) heave

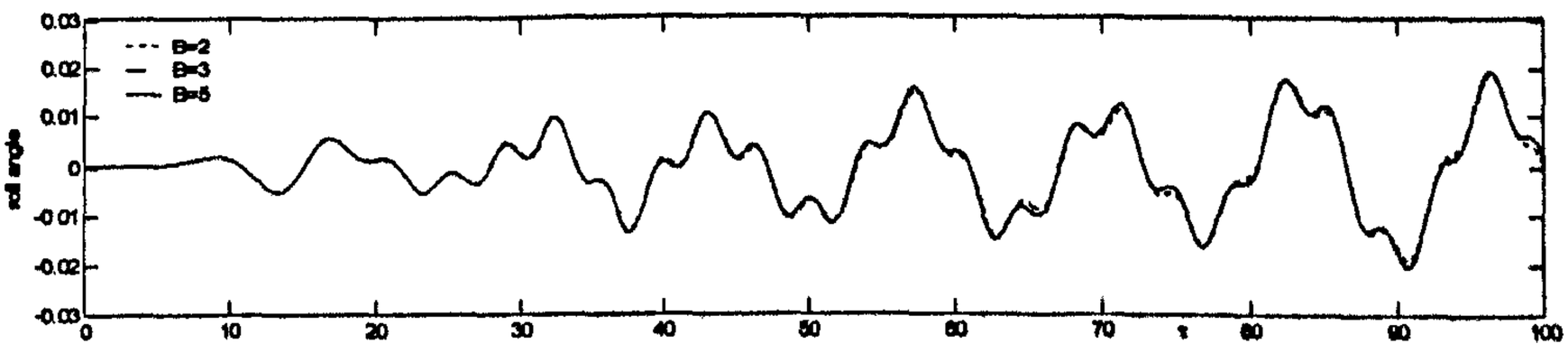

Fig. 9.4.10 (d) roll

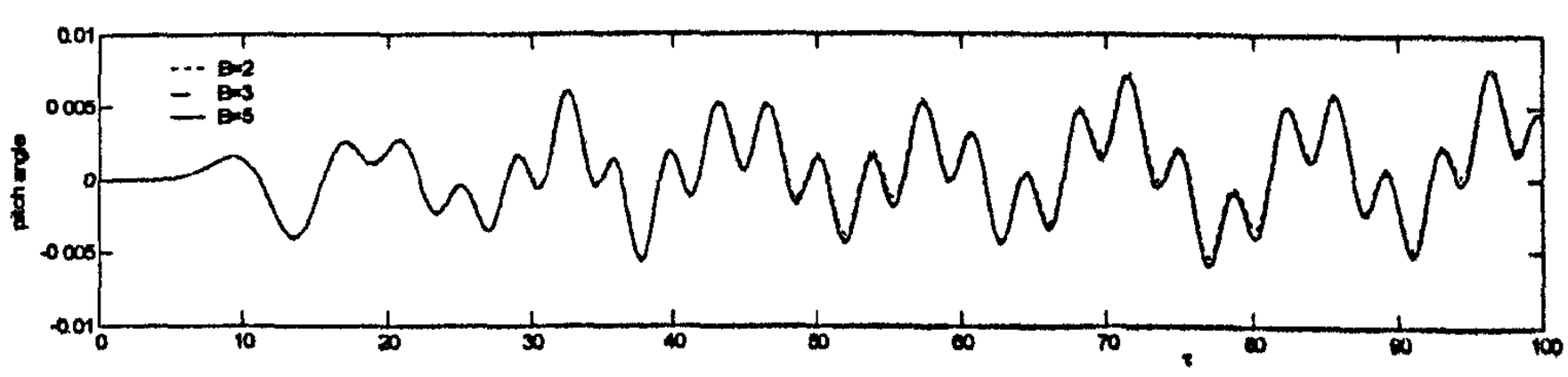

Fig. 9.4.10 (e) pitch

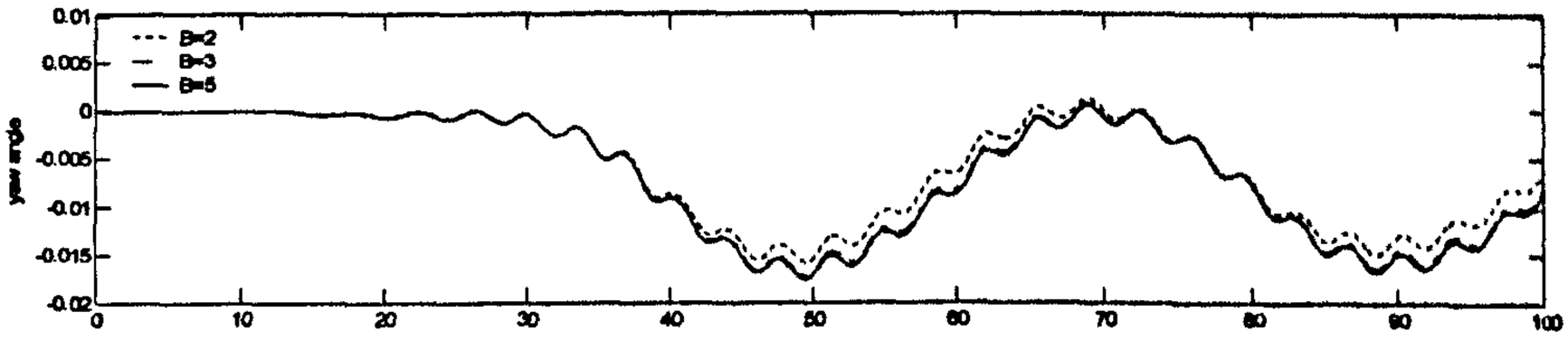

Fig. 9.4.10 (f) yaw

Fig.9.4.10 Response of the Wigley hull in tanks with different widths ($\omega = 1.7691$, a=0.025, incident angle is 30^0)

It can be seen that the results from the case with tank of B=2 are significantly different from those from the case with tank of B=5 when $\tau > 30$, while the difference is negligible when $\tau < 30$. This difference is of course due to the reflection from side walls. It is also found that the difference between those results is more evident for sway and yaw motion. That may be because these two components are more sensitive to the reflection from the side walls. On the other hand, the results from the case with the tank of B=3 is much closer to those from the case with the tank of B=5. Based on this investigation, the width of the tank is taken as B=3. It should be noted that this choice of the width of the tank is for the cases considered in this section. If the shape of the floating body is different or the incident angles are larger then 30^0, more investigation should be carried in order to determine the proper width.

The effect of incident angles is then investigated. In this case, the width of the tank is taken as B=3. The incident angles are 15^0, 20^0 and 30^0, respectively. The response of the Wigley Hull due to a monochromic wave is plotted as Fig. 9.4.11 for surge, heave & pitch and Fig. 9.4.12 for sway, roll & yaw. For the purpose of comparison, the results in Fig 9.4.3, where the incident angle equals to 0, are also plotted together in Fig. 9.4.10 but not in Fig 9.4.11 because sway, roll and yaw are zero in case with zero incident angles.

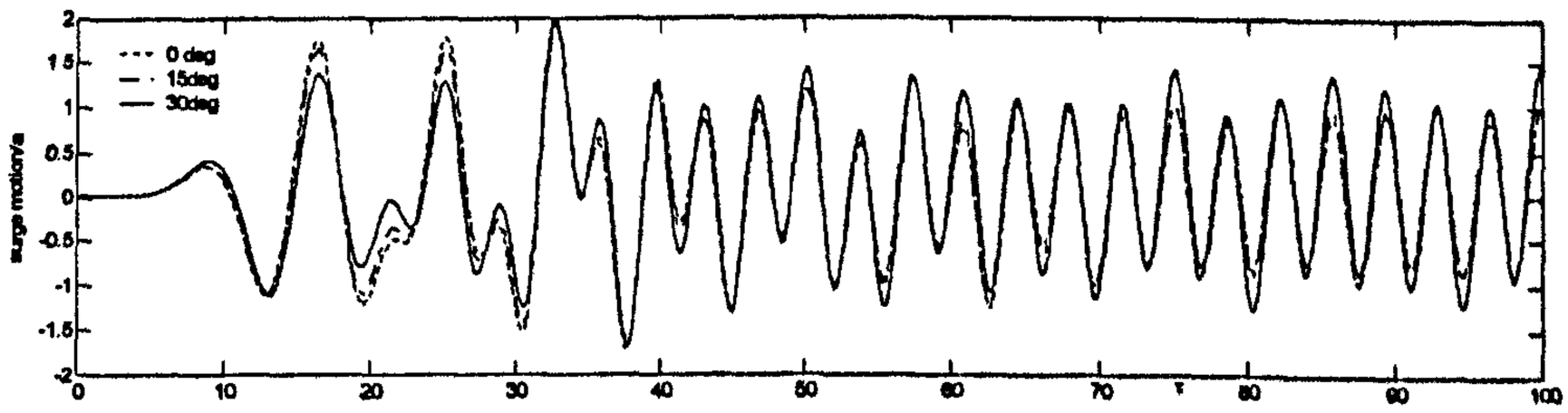

Fig.9.4.11 (a) surge

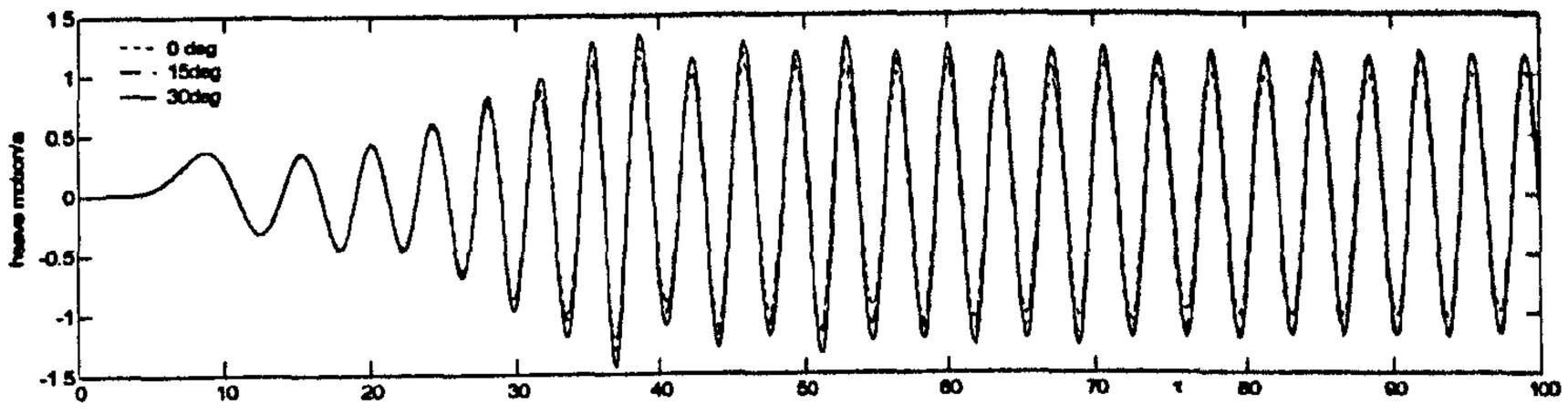

Fig.9.4. 11 (b) heave

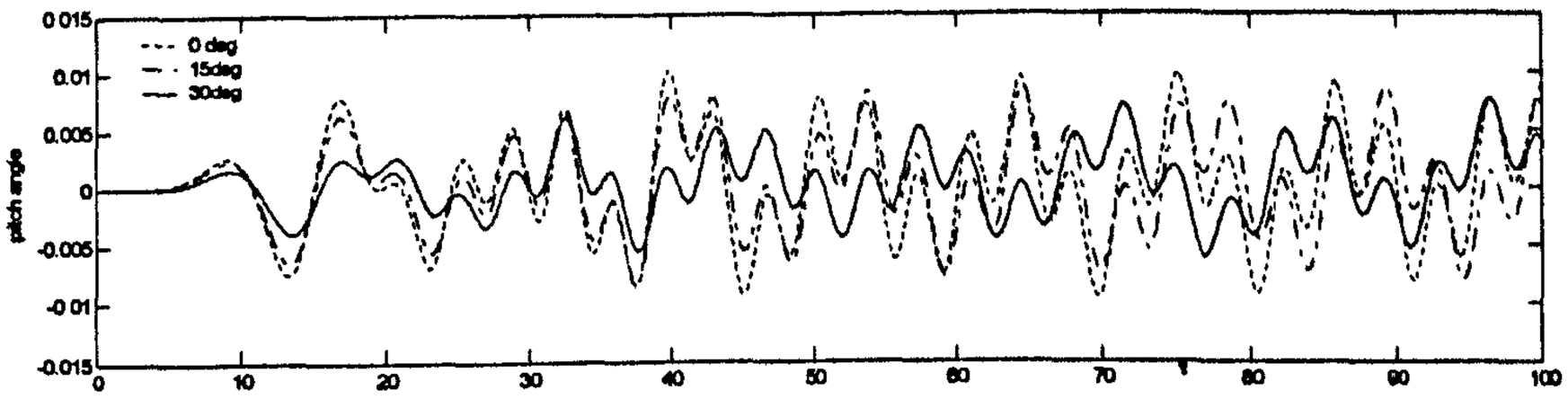

Fig.9.4. 11 (c) pitch

Fig.9.4.11 Surge, heave and pitch of the Wigley hull with different incident angles

($\omega = 1.7691$, a=0.025)

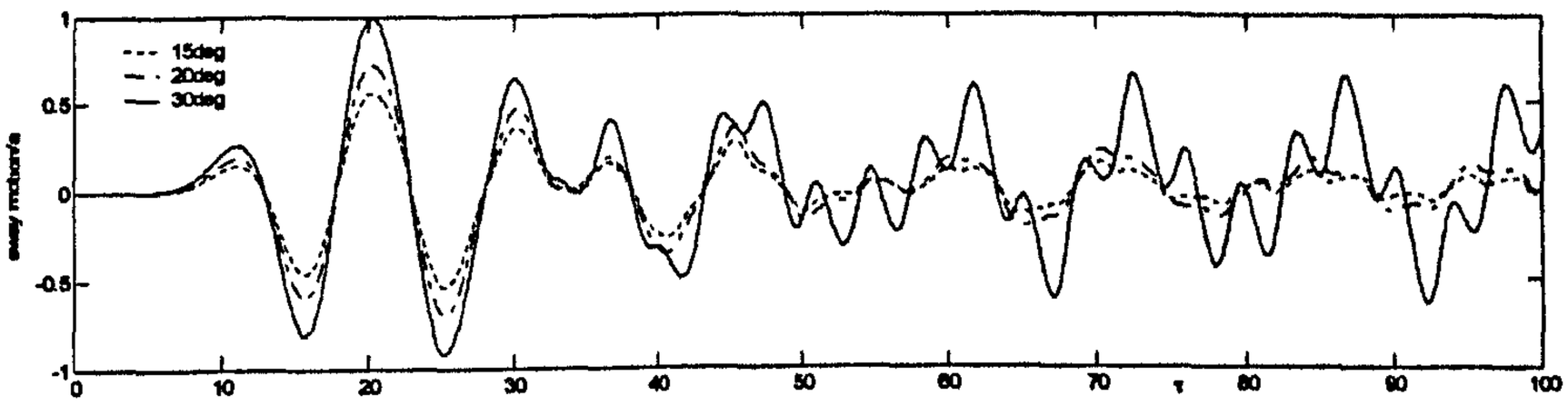

Fig.9.4.12 (a) sway

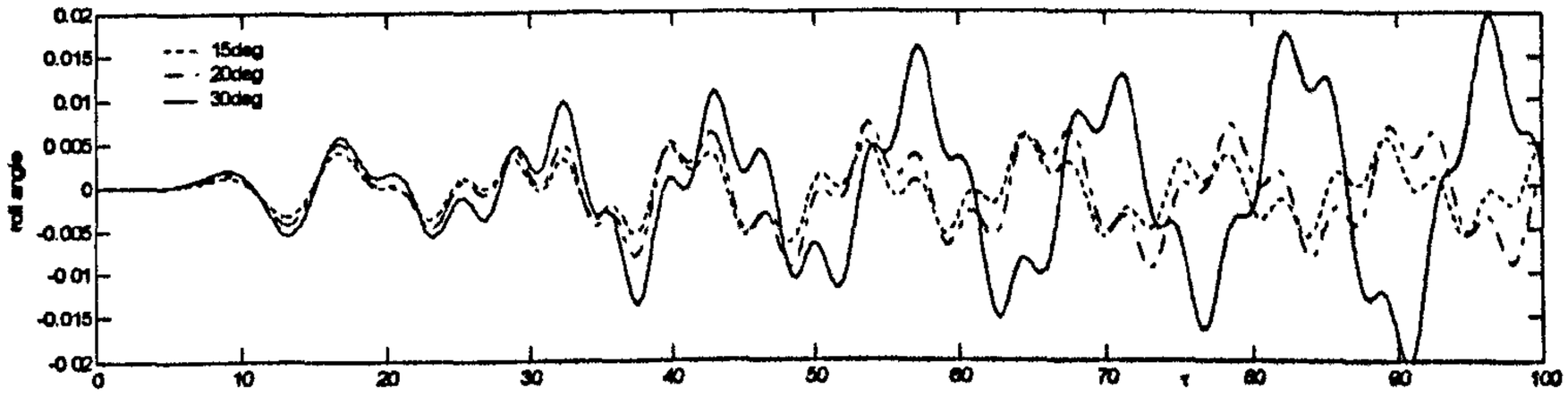

Fig. 9.4.12 (b) roll

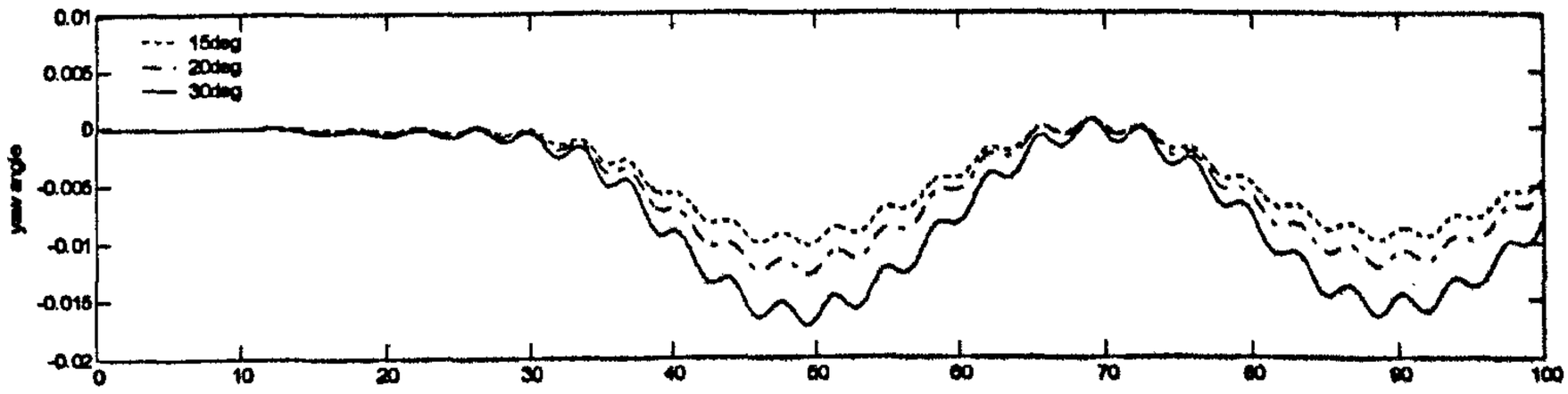

Fig. 9.4.12 (c) yaw

Fig. 9.4.12 Sway, roll and yaw of the Wigley hull with different incident angles

($\omega = 1.7691$, a=0.025)

It can be seen that all these three components of the motions are different as the incident angles vary. The surge and heave increase slightly with incident angle and the associated increase in hull project area Therefore, the wave force acting on the Wigley hull and so the translational motion of the Wigley hull increases. Similar phenomena are also found in sway shown in Fig. 9.4.12 (a). To further investigate the force acting on the body, Fig. 9.4.13 is plotted. It is found that hydrodynamic force in either surge direction or sway direction increases with incident angle, thus supporting the above comment.

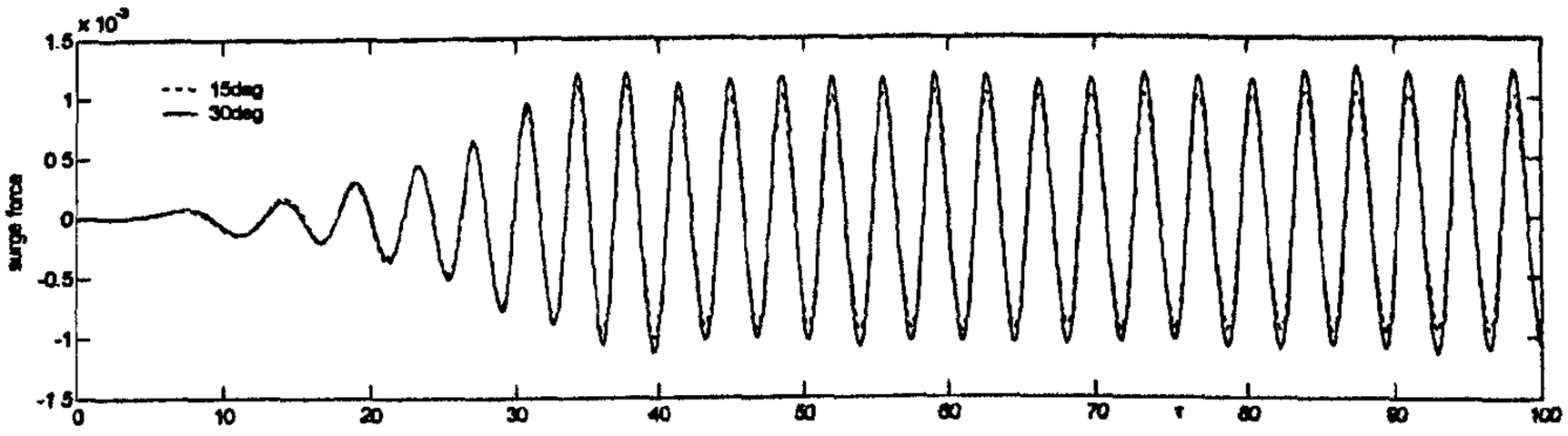

Fig. 9.4.13 (a) surge force

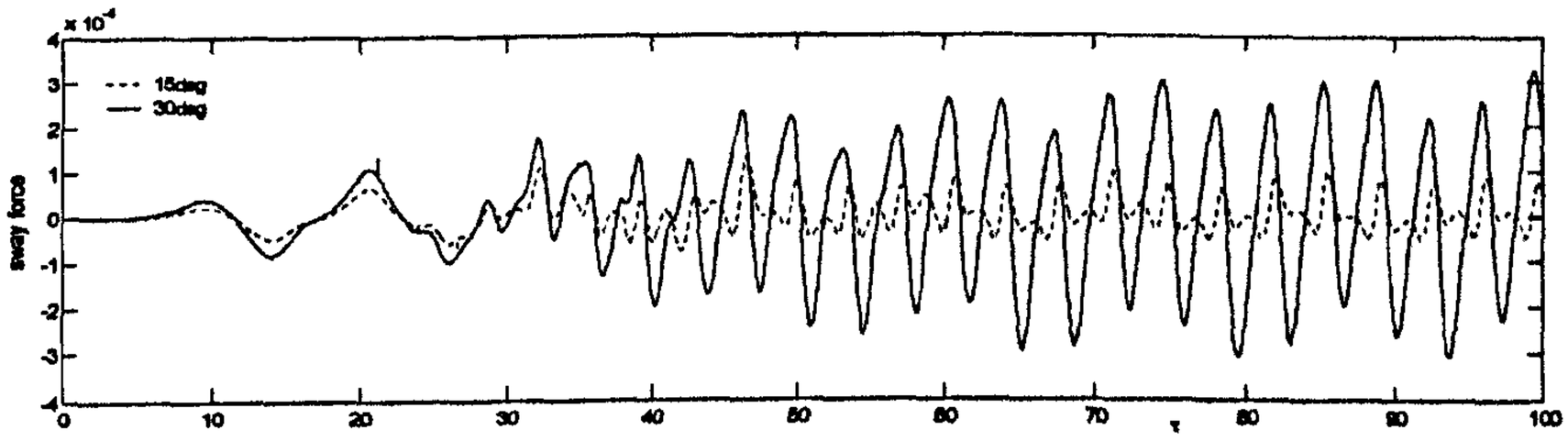

Fig. 9.4.13 (b) sway force

Fig. 9.4.13 Hydrodynamic sway forces acting on the Wigley Hull in case with different incident angles ($\omega = 1.7691$, a=0.025)

On the other hand, the pitch (Fig. 9.4.11c) and roll motion (Fig. 9.4.12b) show large differences in cases with different incident angles. These differences embody two aspects, i.e. the phase and the maximum value. In the first aspect, the time to get a peak of the motion is different in cases with different incident angles. This is because the phase difference between the wave-excited motion and the motion due to the transient effect, which combine to form the pitch or the roll motion, is different. This is mainly due to the fact that the time when the incident wave reaches the front side as well as the lee side of the Wigley Hull is different in cases with different incident angles. In the latter aspect, the maximum value of the pitch motion decreases while that of the roll motion increase with the incident angle increases. That is reasonable. When the incident angle is 0, the fluid domain is symmetrical according to the direction of roll, therefore the roll motion is 0 but the pitch motion is largest. However, when the incident angle equals 90^0, the fluid domain is symmetrical with respect to the direction of

pitch, therefore the pitch motion is 0 and the roll motion is largest. Due to this fact, when the incident angle changes from 0 to 90^0, the pitch motion should decrease from largest to 0, while the roll motion should increase from 0 to largest. It is also found from Fig 9.4.12c that the yaw motions in all of these cases are quite small, since this motion is restricted by the mooring line. It is also observed that the maximum yaw angle increase as the incident angle increases.

Apart from the response of the Wigley Hull, the incident angle also affects waves around the hull. In order to show these effects of the incident angles, the wave elevations in the cases shown in Fig. 9.4.11 with different incident angles are compared. Figs. 9.4.14 to 9.4.17 show some snapshots of the free and the floating body in different instances.

It is found from these figures that no matter whether the incident angle is zero or not, the wave around the Wigley hull are scattered or reflected by the hull. Such scattered or reflected waves complicate the wave elevation around the hull. However, a significant difference between these two cases is that the Wigley Hull with non-zero incident angles makes the waves unsymmetrical. In particular, the wave elevations near the port of the hull are different to that near the starboard of the hull (Fig. 9.4.15a, 9.4.16a and 9.4.17a). To further show this phenomena, the waterlines in different instances in the case with the incident angle of 30^0 is plotted in Fig. 9.4.18

This figure clearly shows that the wave elevation near the port and that near the starboard is different. It is also found that there are local waves near bow of the hull (see the left side of all curves in this figure). This local wave contains the wave generated by the motion of the hull and the diffracted wave from the surface of the hull. This implies that the waves around the hull are affected by the motion of the hull. Therefore, the methods, in which the wave around the body is assumed not to be changed (for example, Ma & Patel, 2001), may introduce relatively large error in cases with steep waves or involving the floating body with large motion. Therefore it is necessary to use fully nonlinear numerical simulation, such as QALE-FEM method. The following section will discuss the efficiency of this method.

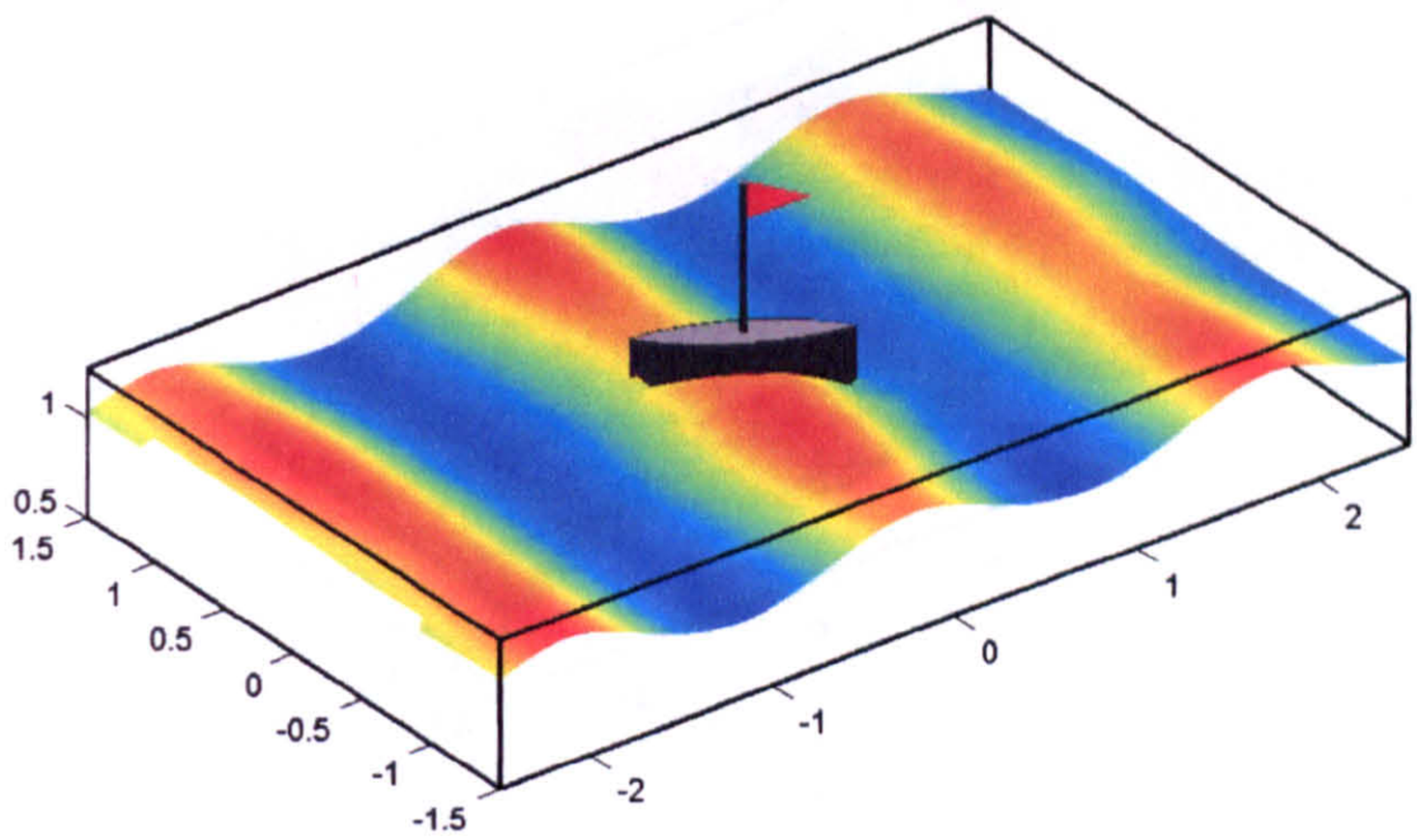

Fig. 9.4.14 (a) incident angle:30^0

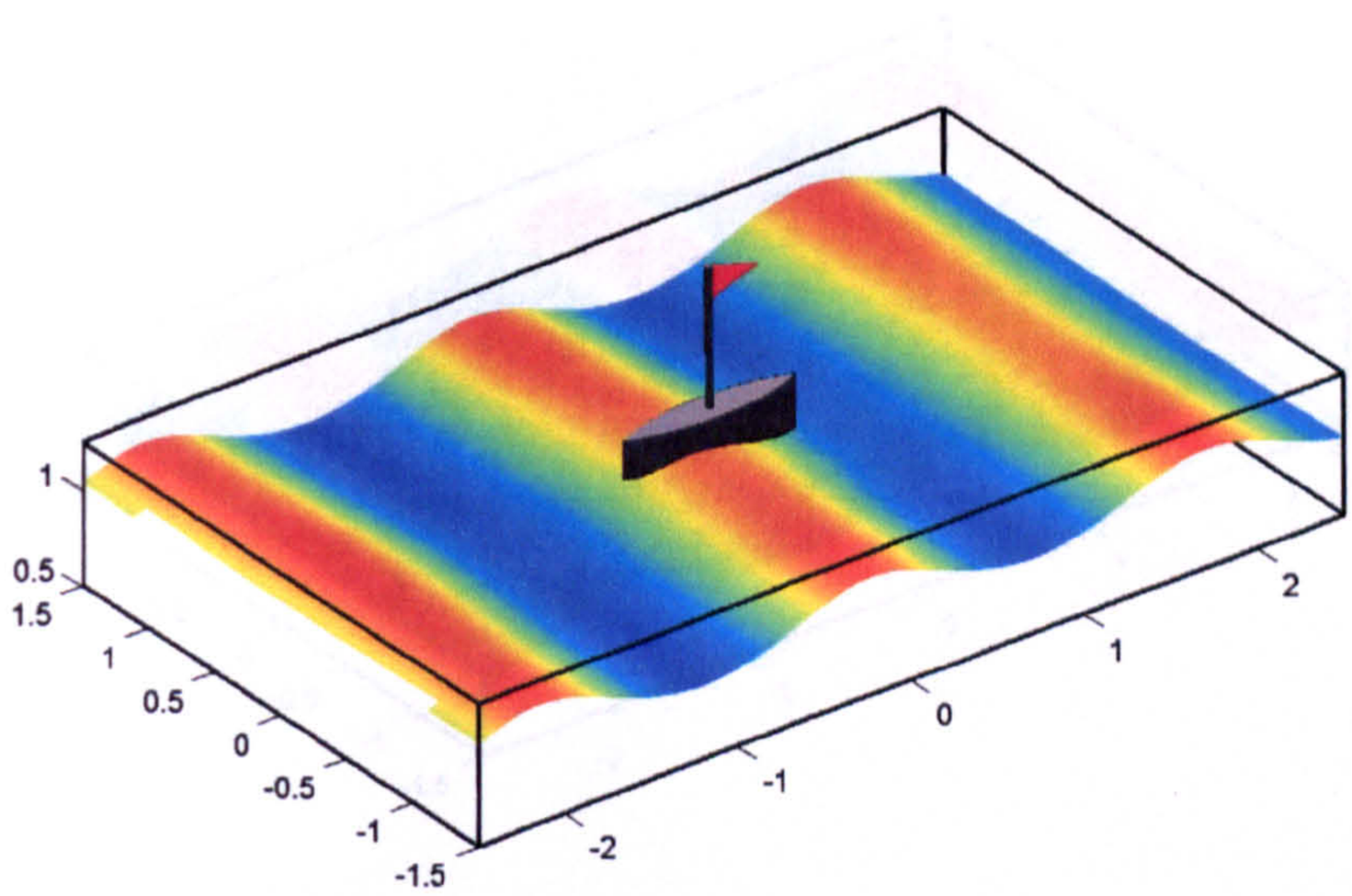

Fig. 9.4.14 (b) incident angle:0^0

Fig. 9.4.14 Snapshots of the free surface and the floating bodies in cases with different incident angles for $\tau \approx 81$ ($\omega = 1.7691$, a=0.025)

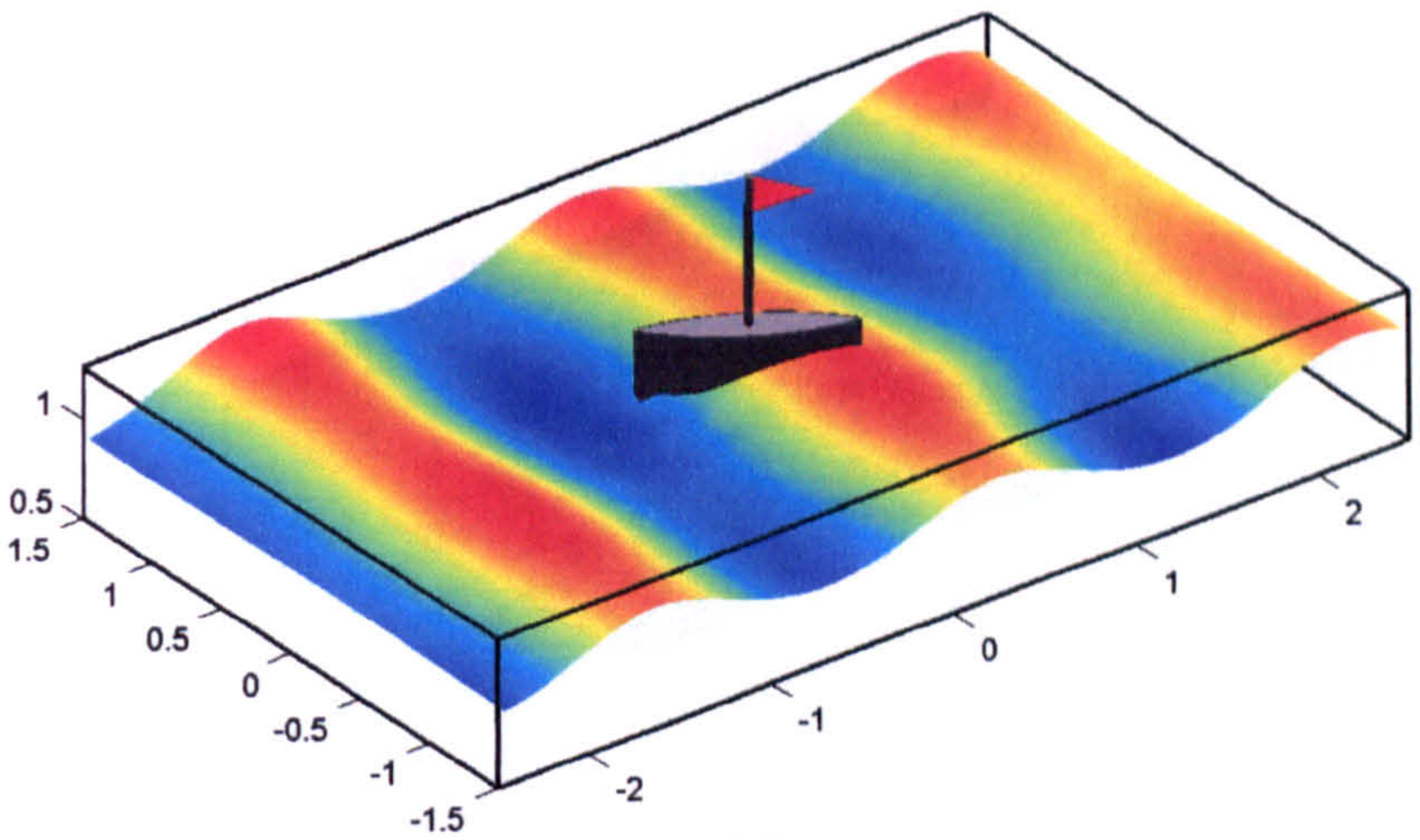

Fig. 9.4.15 (a) incident angle:30^0

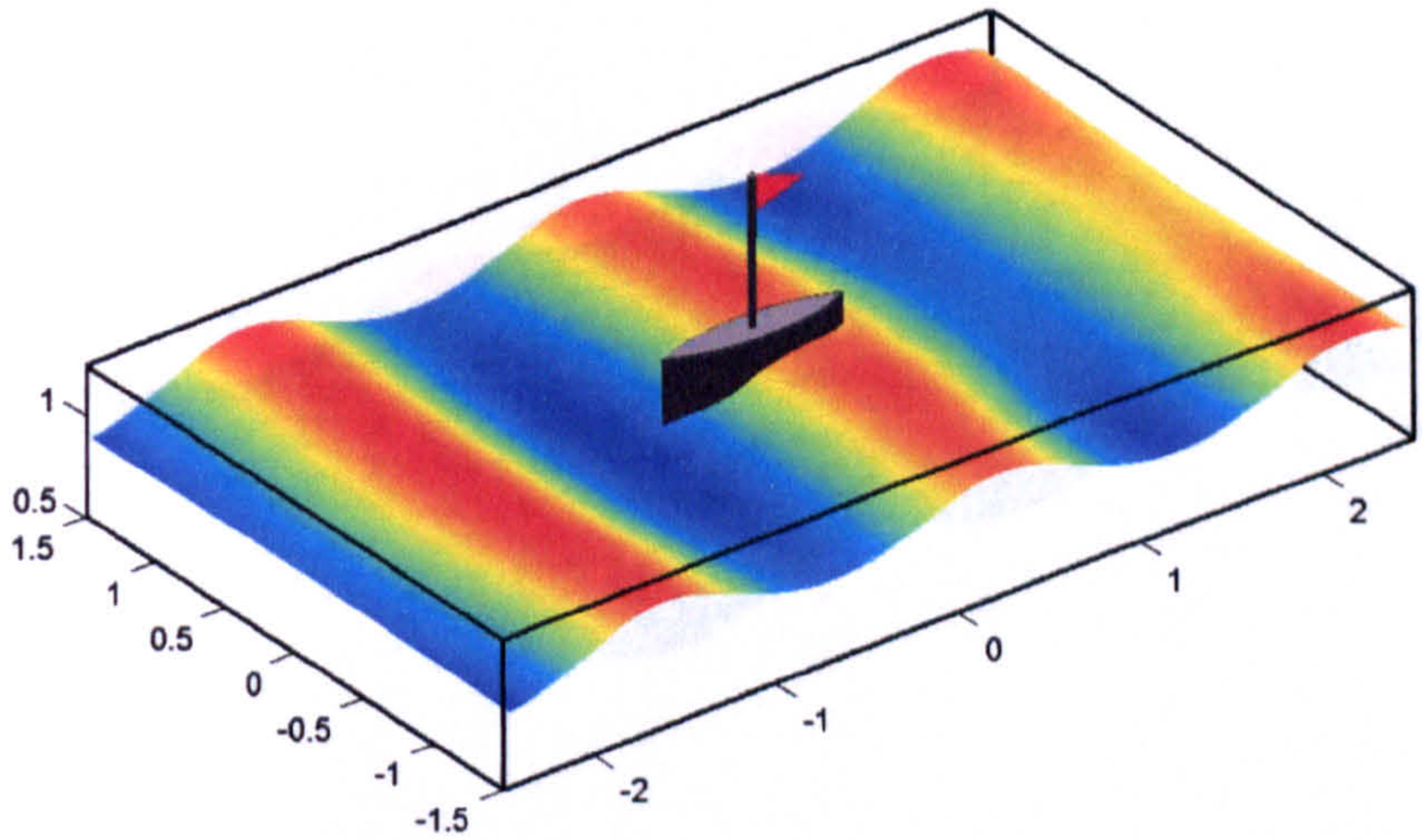

Fig. 9.4.15 (b) incident angle:0^0

Fig. 9.4.15 Snapshots of the free surface and the floating bodies

in cases with different incident angles for $\tau \approx 85$

($\omega = 1.7691$, α=0.025)

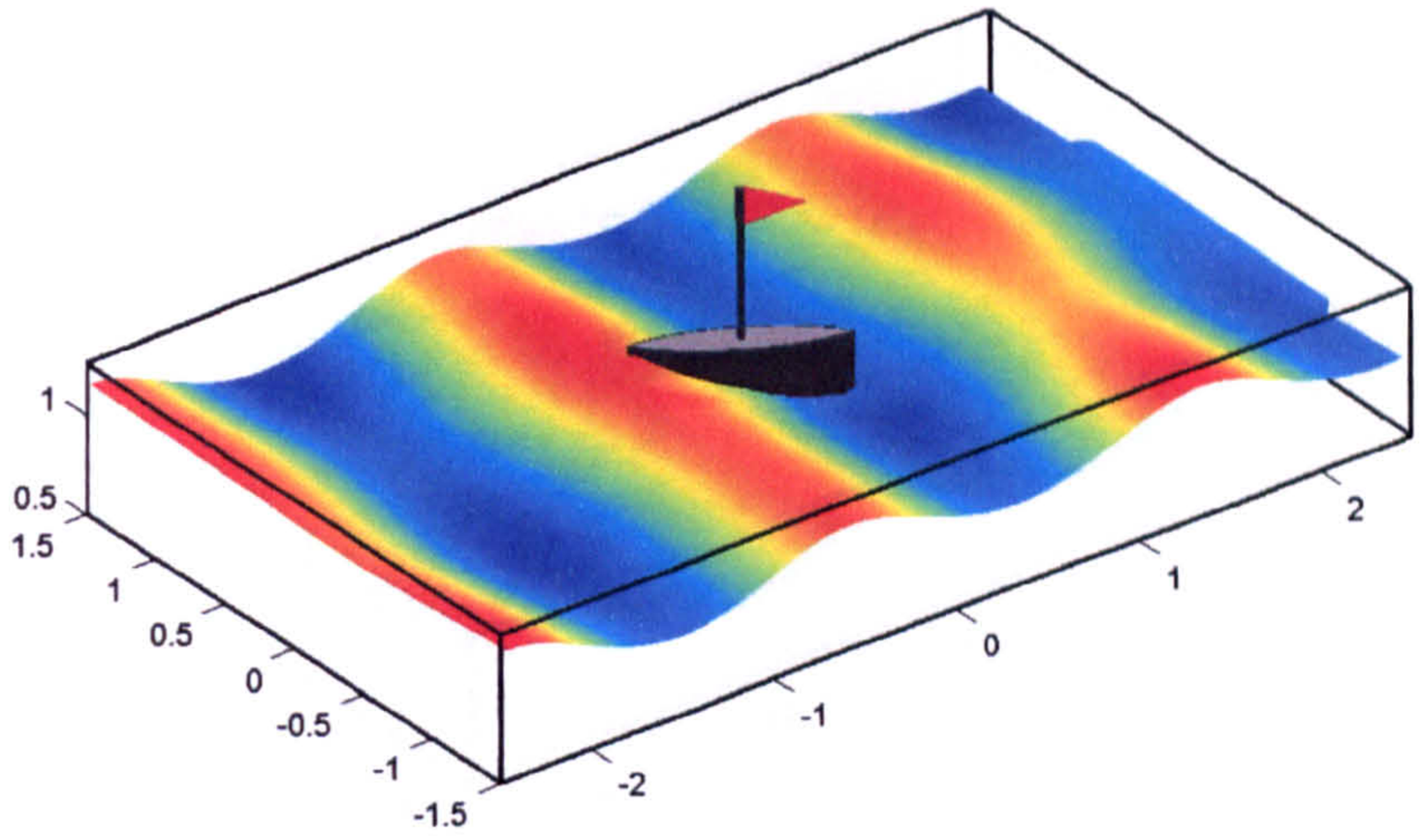

Fig. 9.4.16 (a) incident angle:30^0

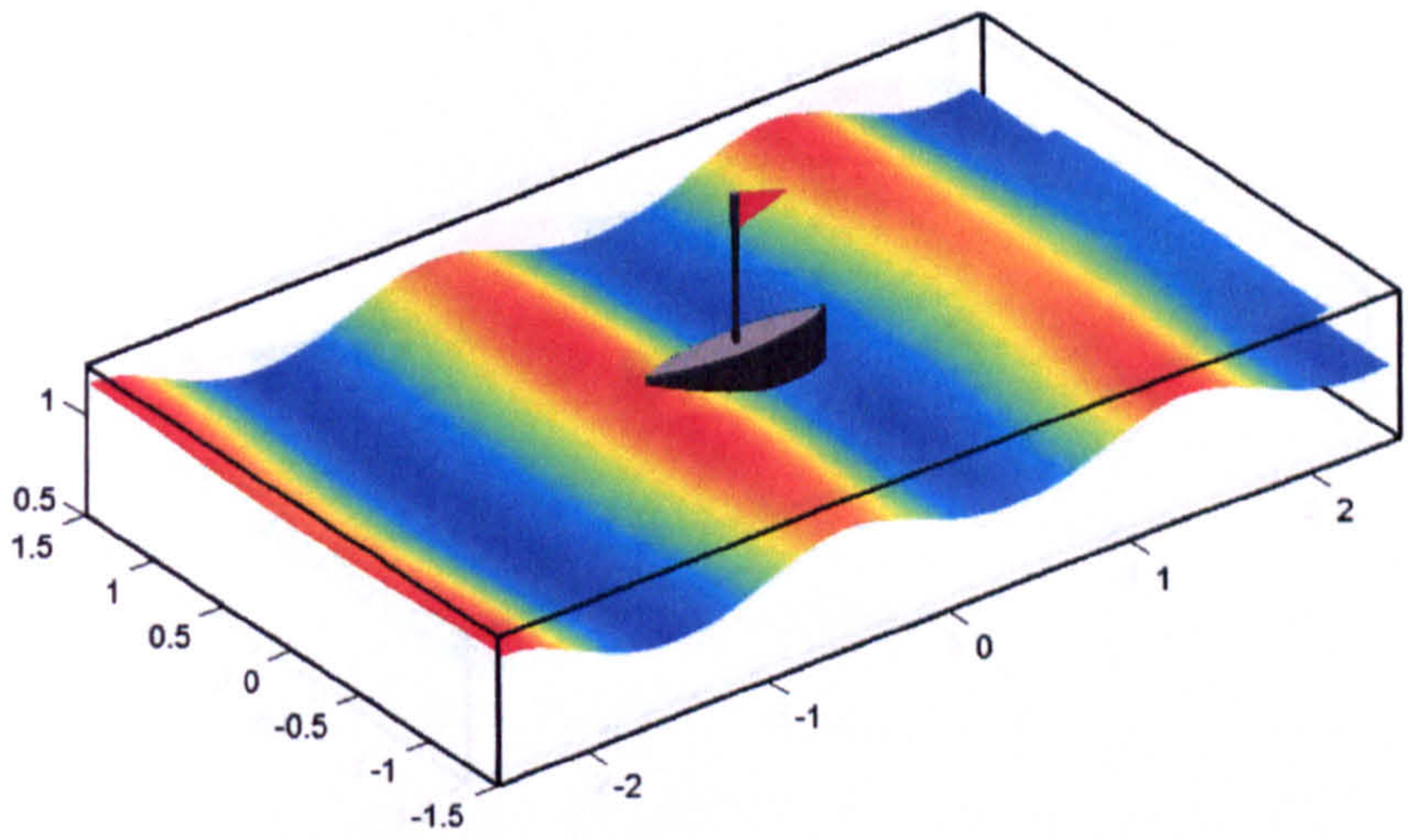

Fig. 9.4.16 (b) incident angle:0^0

Fig. 9.4.16 Snapshots of the free surface and the floating bodies in cases with different incident angles for $\tau \approx 91$ ($\omega = 1.7691$, α=0.025)

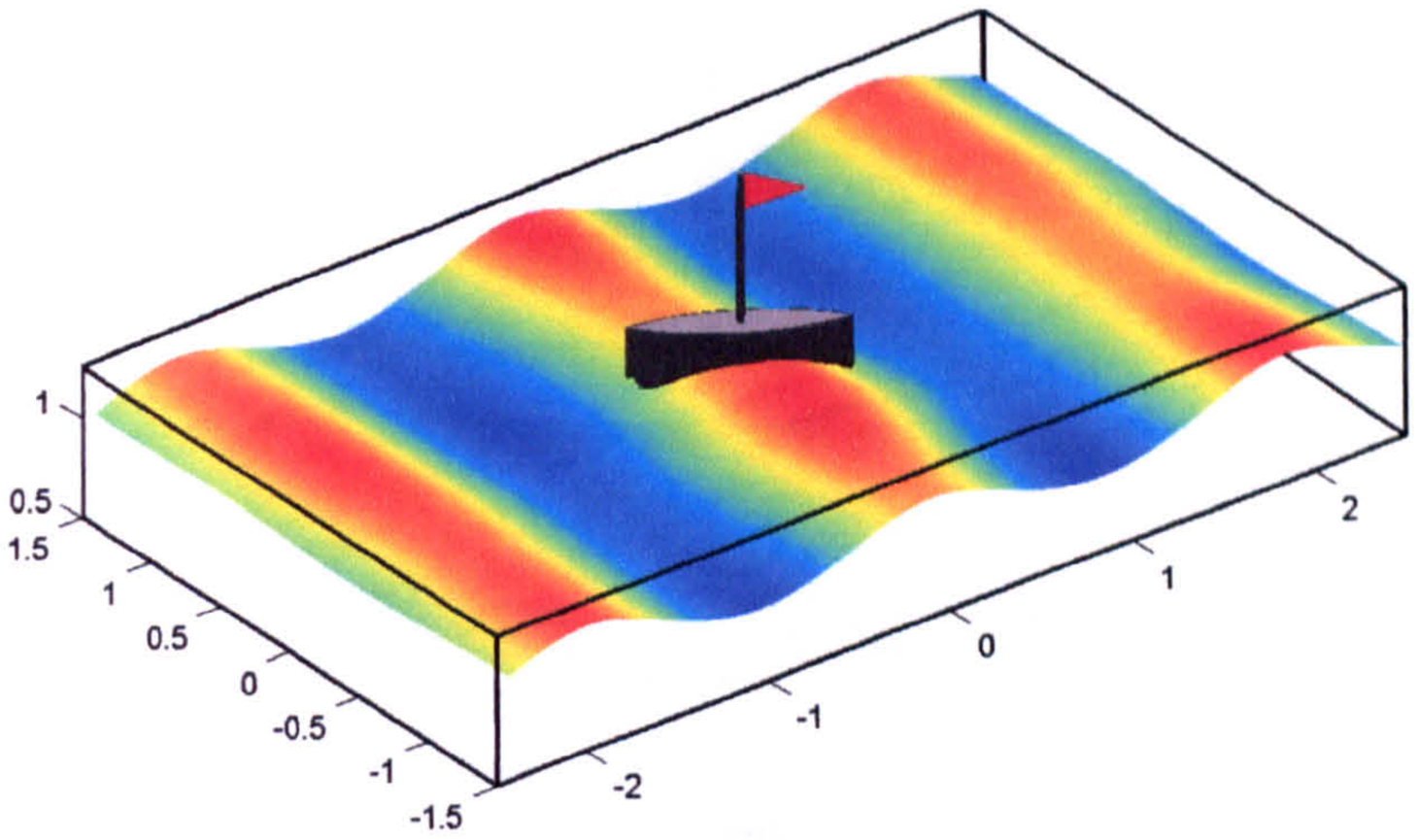

Fig. 9.4.17 (a) incident angle:30^0

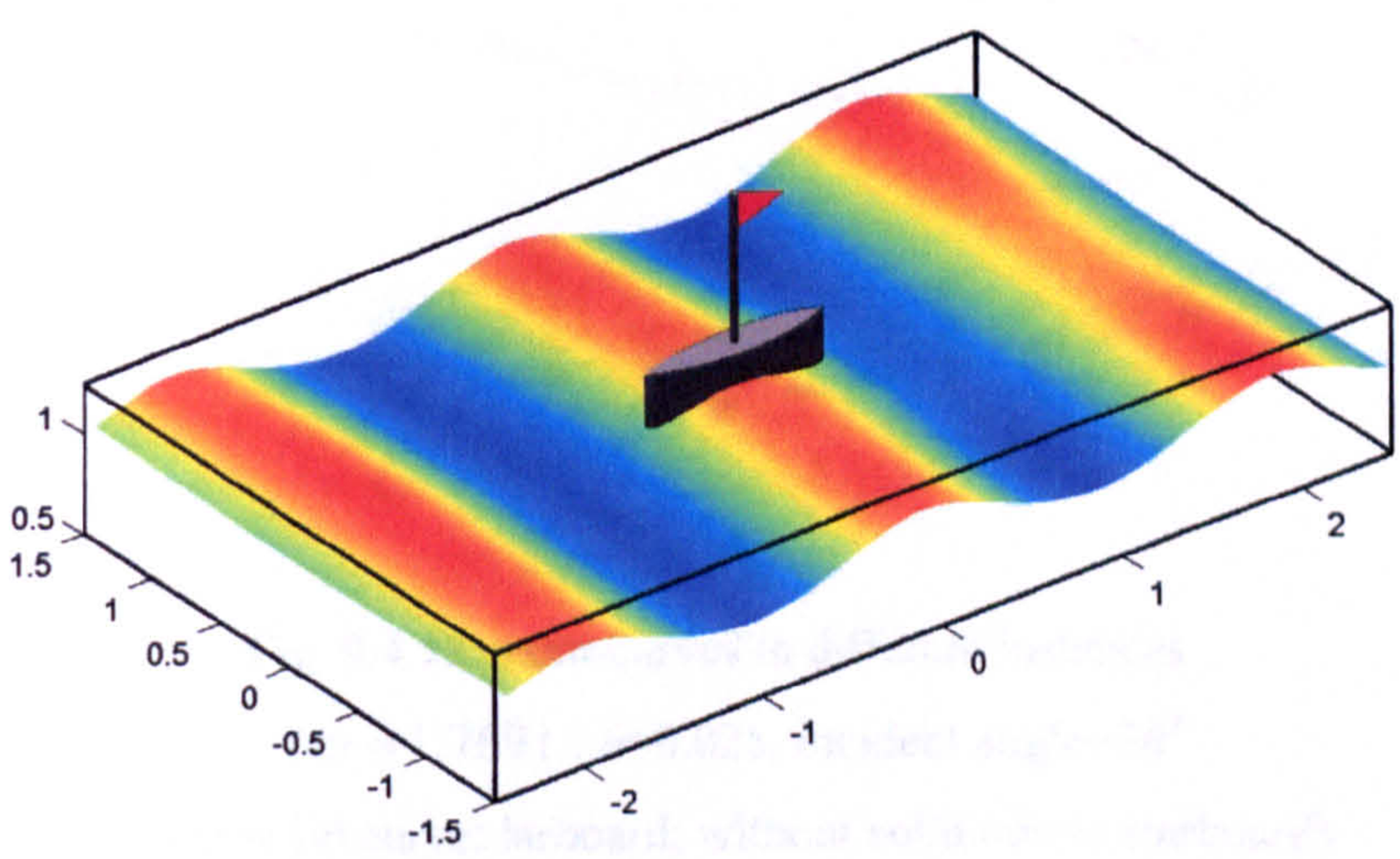

Fig. 9.4.17 (b) incident angle:0^0

Fig. 9.4.17 Snapshots of the free surface and the floating bodies in cases with different incident angles for $\tau \approx 95$ ($\omega = 1.7691$, α=0.025)

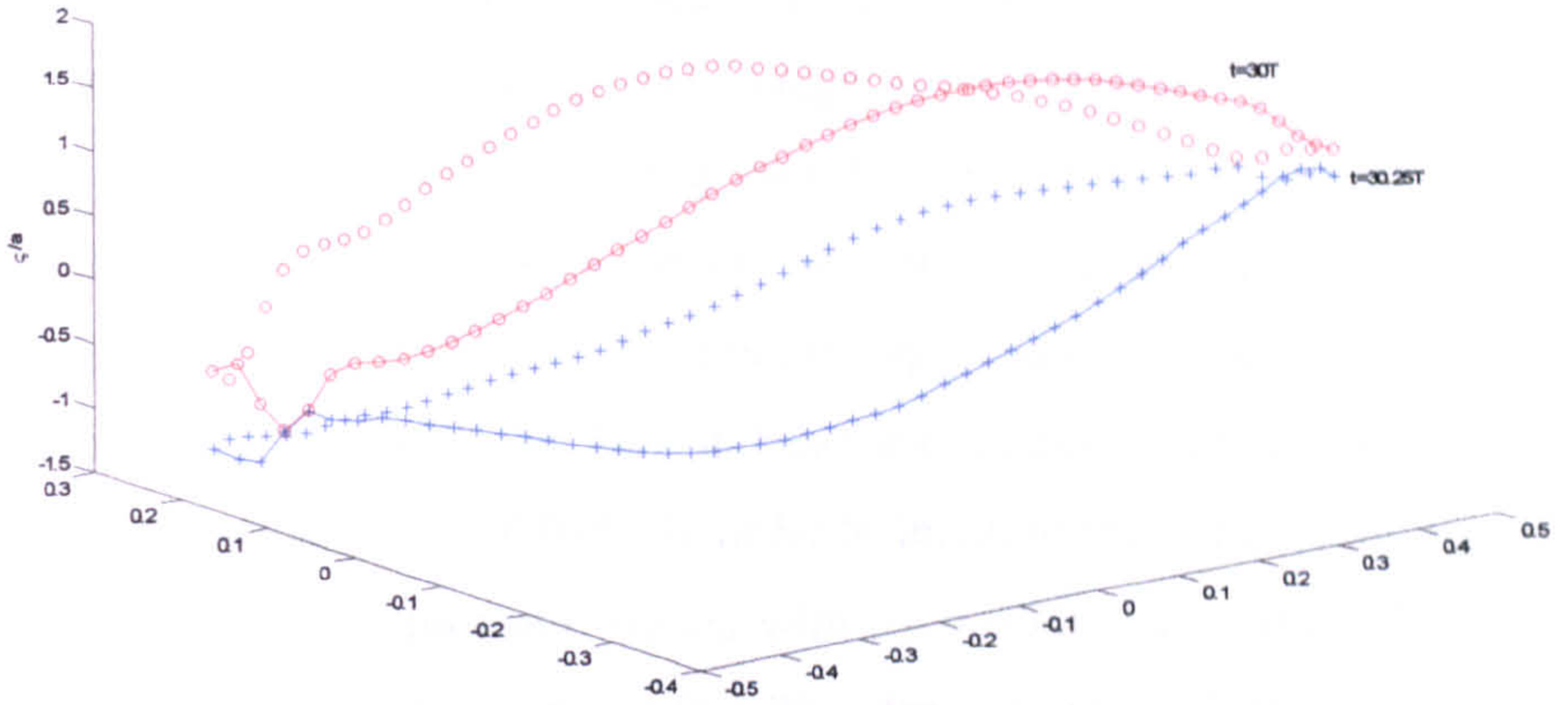

(a)

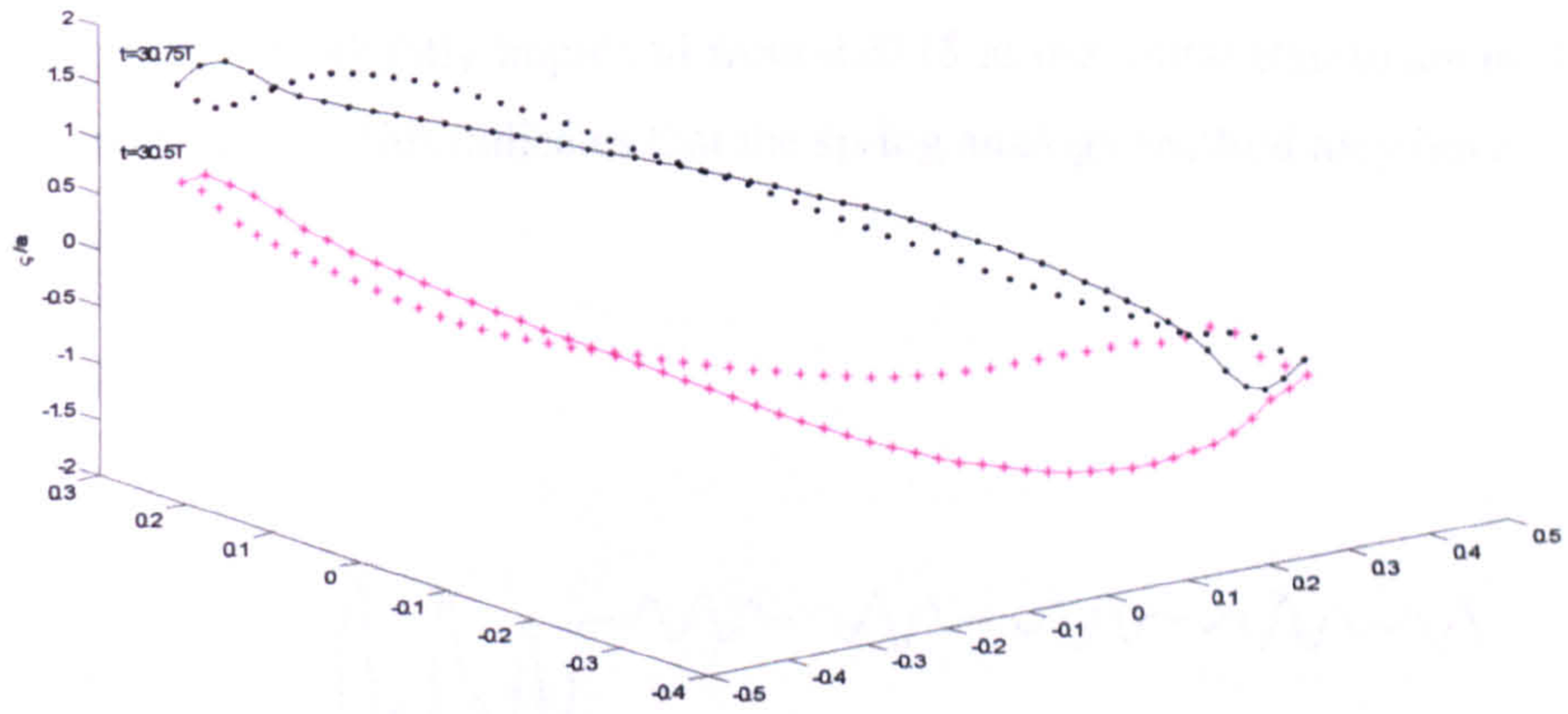

(b)

Fig. 9.4.18 water curves in different instances

($\omega = 1.7691$, a=0.025, incident angle=30^0

with solid curve: larboard; without solid curve: starboard)

9.5. The efficiency of the QALE-FEM in 3D cases

9.5.1. Mesh quality

As indicated in Chapter 8, the mesh quality in 2D cases retains high throughout simulation even in cases with large motions. The motion of the floating body in 3D cases has 6 degrees of freedom. The elements near the body are more likely to be distorted. It is necessary to investigate the quality of the mesh during the calculation. In a 3D case, the shape of the internal element is difficult to illustrate as Fig. 9.0.1. In addition, the quantitative analysis, in place of

the qualitative analysis, is more convincing. Therefore, the mesh quality coefficient defined by Eq. (4.2.7) is used to investigate quantitatively how the mesh quality changes with time during the calculation. The element quality estimated by Eq. (4.3.6) is also investigated to demonstrate the quality distribution in the mesh, i.e. percentage of the elements with specified quality (for example, the elements with quality ranging from 0.7 to 0.8) at a certain time step after long simulation. Two cases will be presented in this section to demonstrate the effectiveness of the spring analogy method in the QALE-FEM in producing good meshes at all time steps.

The first case involves a Wigley Hull in head sea conditions as shown in Fig. 9.4.6 . The moment of inertia is chosen as I_y=0.015. In order to increase the complexity, the motion of the Wigley Hull subject to a bichromatic waves with a_1=a_2=0.01, w_1=2.0,w_2=2.6 is investigated. The fluid domain is discretised into about 903,992 elements and 162,322 nodes. The quality of the mesh during the calculation is shown in Fig. 9.5.1 and Fig. 9.5.2.

Fig.9.5.1 shows the time history of the mesh quality during the long calculation. From this figure, it is found that the mesh quality is always around 0.65. This implies that the quality of the mesh is retained throughtout simulation. The interesting thing in this figure is that the element quality seems be slightly improved from 0.6518 at the initial step to about 0.6525 after variation in a short period. This indicates that the spring analogy method may have the ability to improve the mesh.

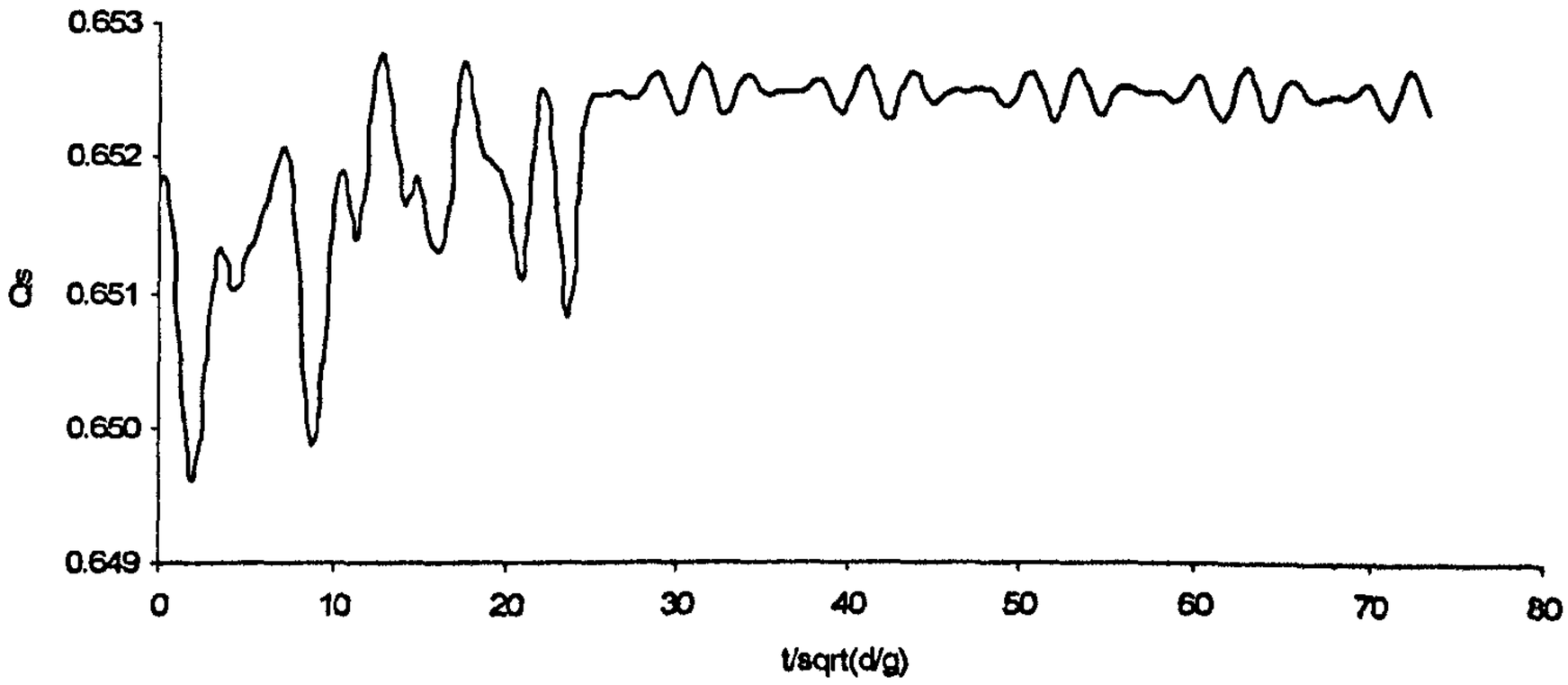

Fig.9.5.1 Mesh quality during the calculation in Case 1
(Bichromatic incident wave with a_1=a_2=0.01, w_1=2.0,w_2=2.6
Wigley Hull with L_b=1.0,B_b=0.2,D_r=0.15)

Fig. 9.5.2 shows the element quality distribution in two different instances. In this figure, the x-axis represents the range of the quality, e.g. 0.9-1.0 means the quality of the elements ranging from 0.9 to 1.0. The y-axis illustrates the percentage of the elements with specified range of

quality. It is observed that most of the elements in both the initial mesh and the mesh at $\tau \approx 73$ are with quality larger than 0.5 (about 80%). The distribution of quality does not change dramatically after the long-time simulation. More importantly, the near flat or very bad elements (quality less than 0.1) do not appear during the calculation.

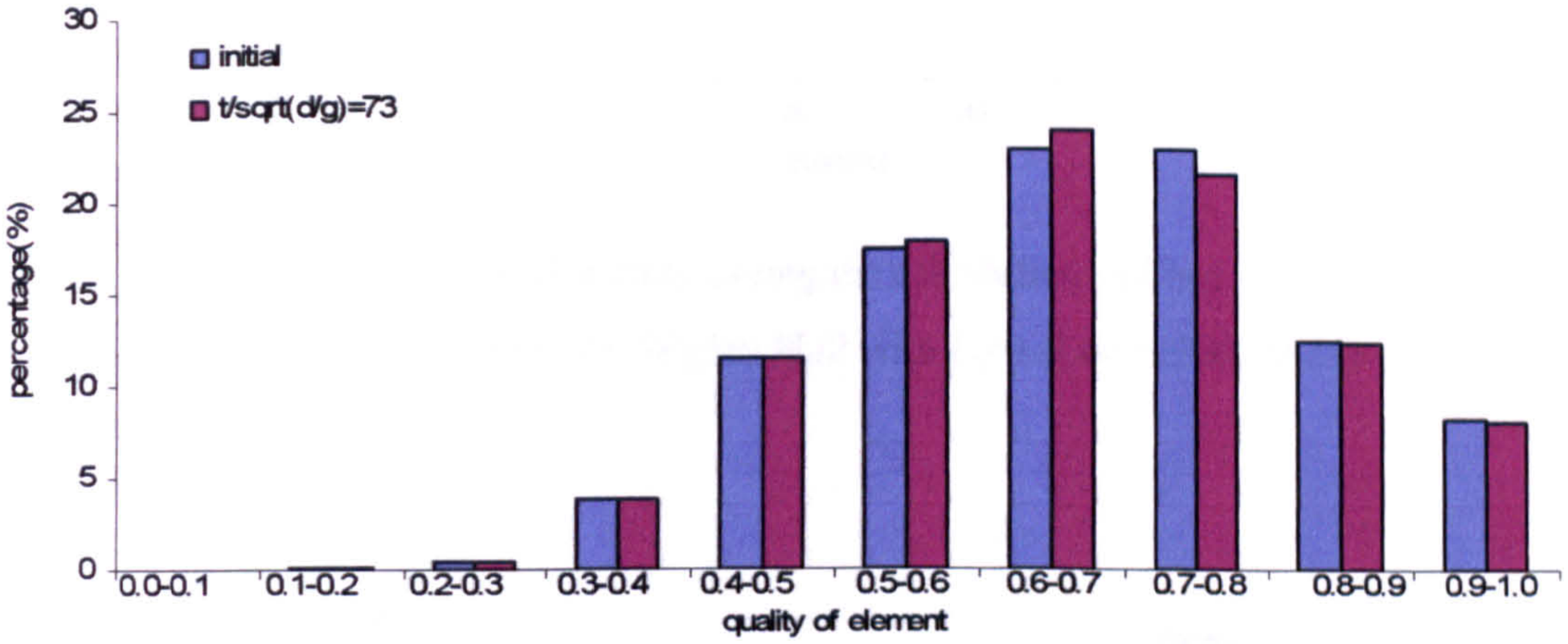

Fig.9.5.2 element quality coefficient distribution in different instance in Case 1

(Bichromatic incident wave with a_1=a_2=0.01, w_1=2.0,w_2=2.6

Wigley Hull with L_b=1.0,B_b=0.2,D_r=0.15)

Another case (Case 2) investigated here is the same as Fig.9.4.12 where a Wigley hull with incident angle of 30^0 is involved. The fluid domain in this case is discretised into about 660,747 elements and 117,678 nodes. The mesh quality coefficient and the element quality distribution in two different instances are plotted as Fig.9.5.3 and Fig.9.5.4. As seen in Fig.9.5.3, although the mesh quality was not improved, it was always larger than 0.73. This demonstrates that the quality of the mesh in this case is also retained during the calculation. From Fig. 9.5.4, it is also observed that most of the elements in both instances are with quality ranging from 0.6-0.9. There are no near flat elements or very bad (quality less than 0.1) elements. A similar conclusion is reached in this case.

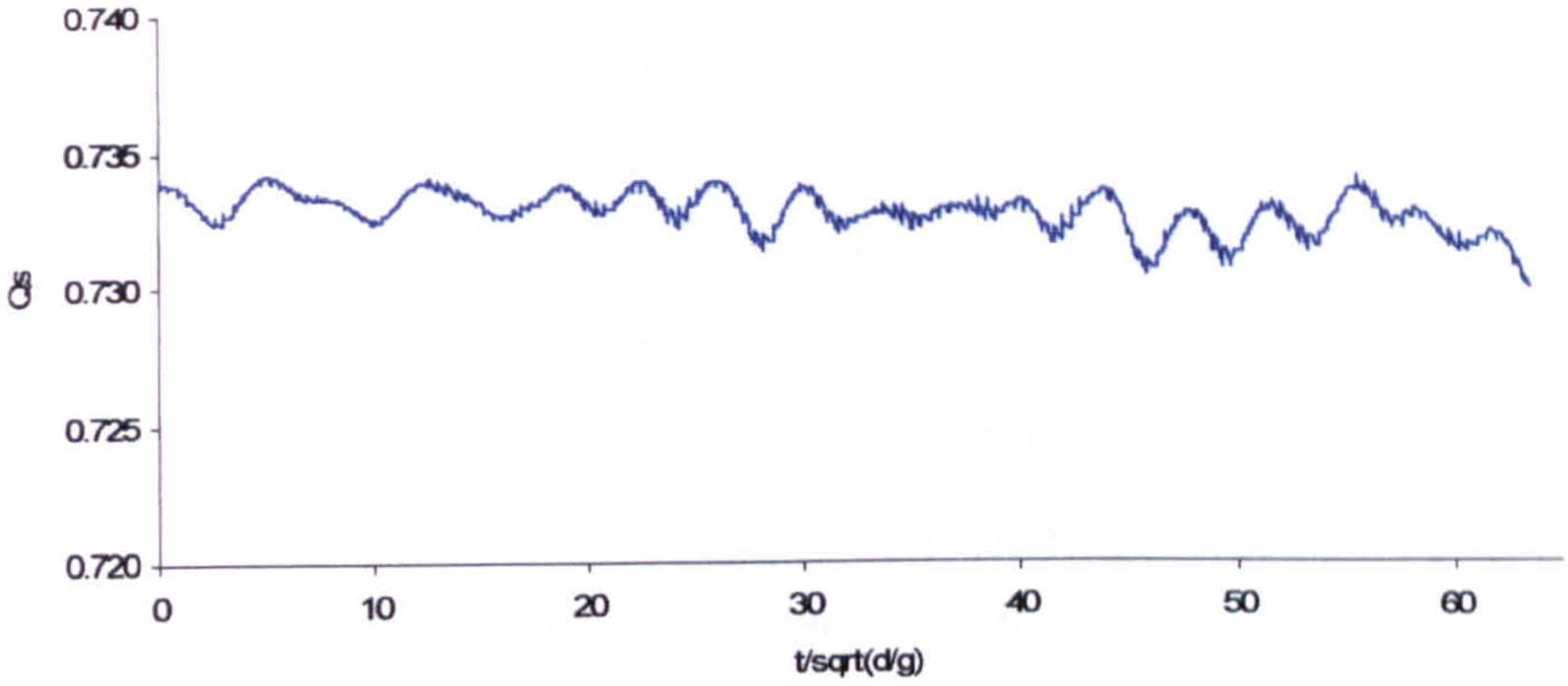

Fig.9.5.3 Mesh quality during the calculation in Case 2

($\omega = 1.7691$, a=0.025, Wigley Hull with L_b=1.0,B_b=0.2,D_r=0.15)

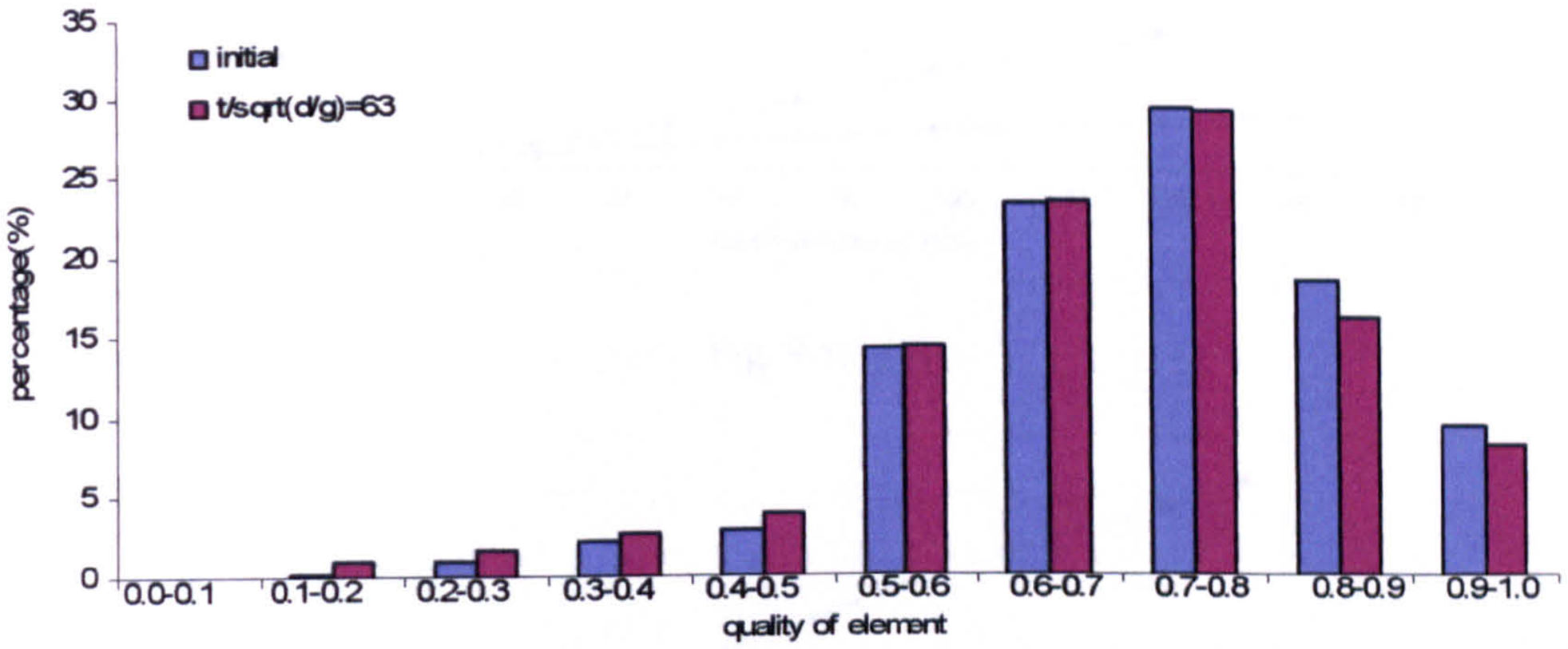

Fig.9.5.4 Element quality coefficient distribution in different instance in Case 2

($\omega = 1.7691$, a=0.025, Wigley Hull with L_b=1.0,B_b=0.2,D_r=0.15)

In these two cases, the shape of the floating body is relatively complicated and the incident waves are very steep as well. That QALE-FEM can deal with such a case implies it has high capability to deal with other complicated wave-structure interaction problems.

9.5.2. Efficiency of mesh moving process

In Section 7.5, the CPU time spent on the process for moving mesh in case without freely-floating bodies has been analysed. Once the freely floating bodies are involved, It is necessary to redistribute the nodes on the body surface and therefore more CPU time is required. In this section, the efficiency of mesh moving process is investigated using the cases with 3D freely floating bodies.

The CPU time used in the mesh moving process at every time step is also investigated by using the above case. This case is run on a PC (Pentium IV 2.53GHz processor, 1G RAM). In the initial mesh, there are 117,678 nodes in the fluid domain with 9,021 nodes on free surface, 2,221 nodes on the body surface. The CPU time spent on the mesh moving process is less than 2.5s, including around 1.0s for moving interior nodes and 0.5s for redistributing nodes on the body surface. The frequency for redistributing nodes on the free surface is once every 25 time steps. The CPU time spent is about 24.5s for each process of redistributing nodes on the free surface. Therefore, averaged 1.0s for every time step. However, generating such a mesh needs 53s using the in-house mesh generator. Compare to a conventional mesh regenerator, the present approach requires almost negligible CPU time.

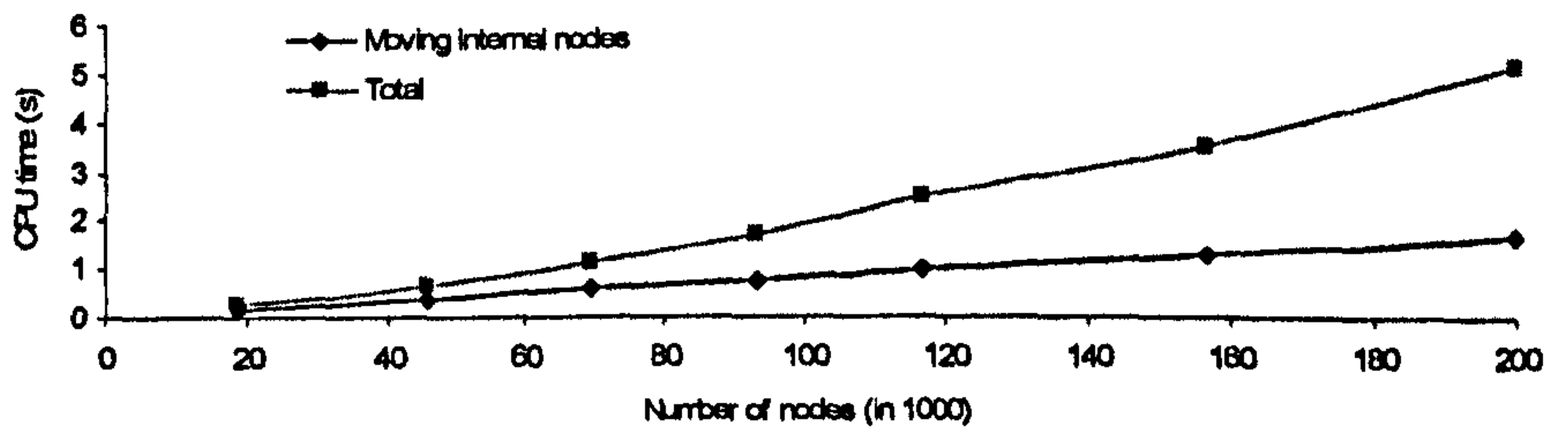

Fig. 9.5.5 (a)

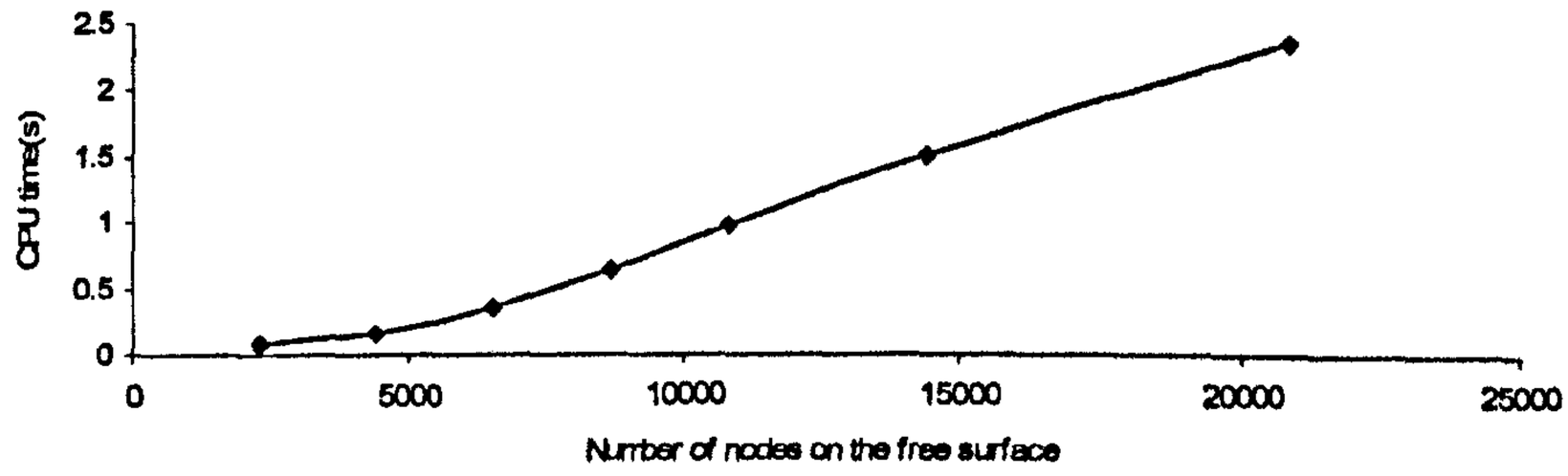

Fig. 9.5.5 (b)

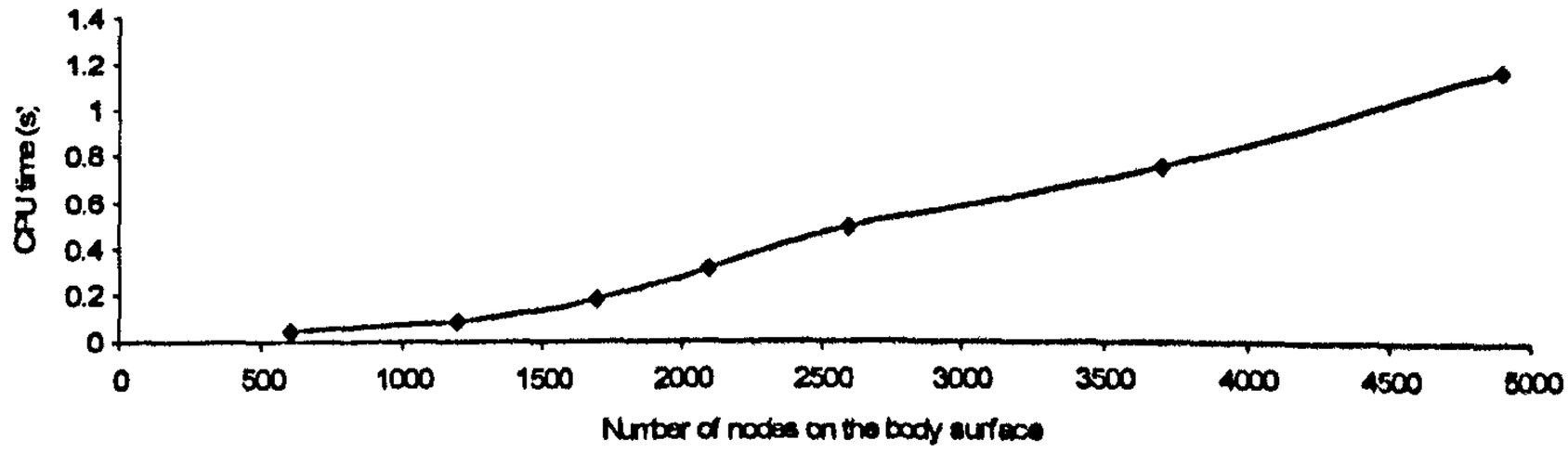

Fig. 9.5.5(c)

Fig. 9.5.5 CPU time spent on the mesh moving process in cases with different numbers of nodes

Further test is made to investigate the CPU time on mesh moving scheme in cases with different numbers of nodes. In this test, the incident wave is generated by a wavemaker with $\omega = 1.7691$, a=0.03. Wigley hulls with different parameters of shape are used. The time step is taken as $T/128$. The cases are run on the above PC and 3000 time steps are run. The averaged CPU times spent on every time step in different cases are shown in Fig. 9.5.5. Fig. 9.5.5(a) shows the CPU times for the whole mesh moving scheme and the process to move interior nodes. Fig. 9.5.5(b) and Fig. 9.5.5(c) show the CPU time spent on redistributing nodes on the free surface and those on the body surface, respectively. It is found from this figure that total CPU time for the mesh moving process is roughly in order of $O(N)$ where N is the numbers of nodes. Even when the N is close to 200,000, the CPU time for moving mesh is still about 5s for every time step. This is much less than the time for regenerating an unstructured mesh. For redistributing nodes on the body surface and the free surface, the CPU time also depends on the number of nodes (Fig.9.5.5b and Fig. 9.5.5c). It should be pointed out that the frequency of redistributing nodes on the free surface in this test is once every 20 time steps. If one uses smaller frequency, the averaged CPU time on redistributing nodes on the free surface will be shortened. One may also found that if the number of nodes on the body surface is the same as that on the free surface, the CPU time required is almost 3 times that for the free surface. This is because the 'Global method' and 'Local method 'are used to move the nodes on the free surface and body surface, respectively. The normal and tangential directions of every node need to be calculated in the 'Local method'. This process requires additional CPU time.

Based on this investigation, it can be concluded that the mesh moving scheme developed in this work is every efficient. Less than 5s CPU time is sufficient to deal with most of the cases on nonlinear wave-body interaction problems.

9.5.3. Computational efficiency

The computational efficiency is also investigated by using the above two cases. Two aspects are discussed. One is the efficiency of the ISITIMFB. The other one is the overall computational cost. In the first aspect, the present ISITIMFB is compared with the mode-decomposition method with the 4th-order Runge-Kutta method as the time integration scheme. In the latter one, the CPU time spent on every time step by the QALE-FEM method is compared with that by a fast BEM method.

As discussed in Section 2.6, the motion in the mode-decomposition method is decomposed into 7 modes in 3D cases to find the solution for the potential derivatives ($\partial\phi/\partial t$) by solving 7 different boundary value problems in addition to one for the velocity potential. Thus, a total of 8 different boundary value problems must be solved in each sub-step and therefore total 32 boundary value problems for calculating both velocity potential and its time derivative need to be solved in one time step forward in 4^{th}-order Runge-Kutta scheme. In Section 8.2, it is also

pointed out that the geometry of the fluid domain as well as the coefficient matrix needs to be updated to achieve a stable solution. To do this, massive CPU time is required. On the other hand, the number of the boundary value problems solved at every time step in the QALE-FEM method depends on the number of iterations in the ISITIMFB procedure. As an example, the number of iterations at different instants for the case in Fig. 9.5.12 is shown in Fig. 9.5.5 by using the control error of 0.5% in the procedure.

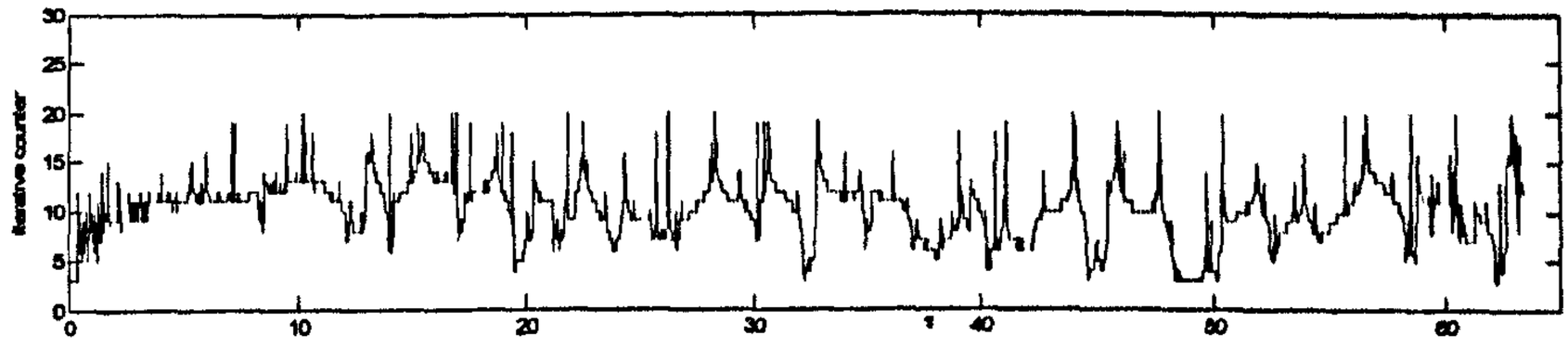

Fig. 9.5.6 Number of iterations in different instance in case shown in Fig. 9.4.12 (a_1=0.015, a_2=0.0075, w_1=1.45,w_2=1.74, incident angle=15^0)

It is observed that the maximum number of iterations in the calculation is 23 and the number of iterations in most time steps is around 10. The mean number of iterations in one step is 10.28 and so about 21 boundary value problems are solved without the necessity of updating the coefficient matrix. Therefore, the CPU time required by the ISITIMBF is less than that required by the mode-decomposition method together with 4-order Runge-Kutta method for time integrating. Of course, the iteration count in ISITIMFB is problem-dependent. The computational cost of the ISITIMFB may be more expensive in other cases. But, as long as the number of iterations in the ISIFIMFB procedure is less than 16, the ISITIMFB is more efficient. According to numerical experience in this work, if appropriate time step and control error are chosen, the number of iterations in the ISITIMFB procedure in most of the case can be less than 16. As indicated in Section 8.4, if the mode-decomposition method with the 4th-order Runge-Kutta scheme is used in the present QALE-FEM method, the calculation of velocities on the free surface with unstructured meshes must be performed five times in one time step forward, which likely requires considerable more CPU time. Consequently, the ISITIMFB used with the QALE-FEM is very efficient.

The overall computational efficiency of the QALE-FEM is subsequently compared with a fast BEM developed by Fochesato & Dias (2006).

As discussed in Chapter 2, only the grid on the boundaries is required for BEM method. The CPU time spent on every time step in the BEM depends on the number of boundary nodes. The most important contribution made by Fochesato & Dias (2006) is that they reduced the computing complexity from $O(N^2)$ required by the conventional BEM, to nearly $O(N)$, where N is the number of boundary nodes for their method. Fochesato & Dias (2006) applied

the fast BEM method to model a solitary wave shoaling over a seabed with complicated geometry by using a PC (2.2GHz processor, 1G RAM). In their case, the tank length is 19 and the width is 8. For the first stage before the wave overturns, a coarse grid with 1,422 boundary nodes is used. A finer grid with 6,022 nodes is used for the remained calculation. The CPU time spent on each time step is 320s for the finer mesh and 45s for the coarse mesh. For brevity, this case is referred as 'fast BEM case' in this sub-section.

When the QALE-FEM method is used, the whole computational domain needs to be discretised. The number of nodes is much more than the number of nodes on the boundaries. For example, in the case shown in Fig. 9.4.12, there are 117,678 nodes in the fluid domain with 21,285 nodes on the boundaries. This case is run on a PC (Pentium IV 2.53GHz processor, 1G RAM) which is similar to that used by Fochesato & Dias (2006). The mean CPU time spent on each time step is 33.25s over a simulation of 3000 time step. The length and the width of the tank used in this case are 10 and 4, respectively. This case is referred to as 'QALE-FEM case' in this sub-section.

To the author's knowledge, there have been no publications to date on the numerical simulation by fast BEM of interactions between water waves and a 3D free-response floating body. Here, the CPU time on the above examples are deduced for the purpose of analyzing the computational efficiency. Since the volume of the fluid domain in the 'fast BEM case' is almost 4 times that of the 'QALE-FEM case'. If the fast BEM by Fochesato & Dias (2006) is used for the 'QALE-FEM case', the number of boundary nodes required may be one-forth of that used in the 'fast BEM case'. That is $6,022/4 \approx 1,500$ boundary nodes for a finer grid and $1,422/4 \approx 350$ boundary nodes for a coarse grid. In the 'QALE-FEM case', the wave overturning does not occur. The coarse grid is therefore necessary for the fast BEM method. Since the CPU time spent on every time step by the fast BEM is proportional to the number of boundary nodes, therefore about 45/4=11.25s for every time step is required. However, this CPU time is only used to solve the BVP for the velocity potential because the 'fast BEM case' does not involve any free-response floating bodies. But in the 'QALE-FEM case' about 20 boundary value problems should be solved. This means the CPU time required by the fast BEM for the 'QALE-FEM case' should be almost $11.25 \times 20 = 225$s which is almost 7 times that (33.25) required by the QALE-FEM method. It should be noted that in the above analysis for the fast BEM method, the grid (350 nodes on the boundary) does not consider the fact that the nodes should be distributed tighter near the floating body than other area. Considering this, the number of the nodes used by the fast BEM method should be more than 350. So, the QALE-FEM method may be at least 7 times faster than the fast BEM in a 3D fully nonlinear water wave problem.

10. CONCLUSIONS AND RECOMMENDATIONS

In this work, the QALE-FEM based on FNPT model has been developed in order to simulate the three dimensional interaction between structures and steep waves using a time marching procedure. In this method, the boundary value problems for the velocity potential and its time derivatives are solved by using a FEM. The mesh is moved in order to conform to the variations of the free surface and the body surface by the spring analogy method specially developed for these problems. The method allows the efficient use of an unstructured mesh without the need to regenerate it at every time step, which is a necessary and very costly feature of the conventional FEM. In order to apply the above moving unstructured mesh, a technique for velocity calculation has been developed. It depends less on the structure of the mesh and can be applied to virtually any mesh. For the purpose of simulating the free response of the floating bodies to the nonlinear waves, an iterative procedure named ISITIMFB is developed. A computer code has also been developed during the course of the study by extending the one for the conventional FEM developed by Ma (1998) and has been applied to model the free response of both 2D and 3D moored floating bodies.

Numerical results obtained by the QALE-FEM method have been compared with analytical solutions, experimental data and the results from other methods in the public domain. The cases included the wave generated by a piston wavemaker, the reflection from sandbars on the sea bed, the interaction between the waves and 2D/3D floating bodies. Good agreement has been achieved. The flexibility of the numerical method has been demonstrated by different cases with different computational domains, such as with floating bodies or sandbars on the sea bed. It has also been illustrated by varying methods to generate waves, including the initial free surface elevation, the motion of a wave maker and the motion of floating bodies. The convergence and the efficiency of this model as well as the ISITIMFB procedure have been investigated by different cases and compared with different methods.

It can be concluded that the newly developed QALE-FEM method based on the FNPT models can use an unstructured mesh with any degree of complexity without the need of regenerating it at every time . It is 10 times faster than the conventional FEM method in case with unstructured mesh and at least 7 times faster than the fast BEM methods for the fully nonlinear waves and their interactions with free-response floating bodies. Its accuracy, flexibility and efficiency is shown to be satisfactory in different numerical examples. More specified contributions and conclusions in this work are summarised as follows.

10.1 Numerical technique

In order to achieve high computational efficiency, many numerical techniques are developed in this work. For the purpose of moving the computational mesh with high quality, a novel methodology is suggested and adopted. In this method, interior nodes and boundary nodes are considered separately; the nodes on the free surface and on rigid boundaries are considered separately; nodes on the free surface/body surface are split into two groups: those on waterlines and those not on waterlines (internal free-surface/ body-surface nodes); different methods are employed for moving different nodes. To move the interior nodes, a 3D spring analogy method is used. However, the spring stiffness in the QALE-FEM method is specified in a different way from that on applications without free surfaces, which depend on how far an element is away from the free surface and body surface. For the purpose of redistributing the nodes on the free surface without overturning waves, a spring analogy method based on the projected *x-y* plane is suggested. For the interior nodes on the body surface and those on the free surface with overturning waves, a spring analogy method based on a local normal-tangential coordinate system is developed. In order to redistribute the nodes on the waterlines, a method based on the principle for self-adaptive mesh is developed and used. The tests carried out in this work demonstrate that the moving mesh scheme works well with little CPU requirement even in cases with very large deformation of the boundary.

In order to conform to the moving unstructured mesh, a method to evaluate the fluid velocity is developed. In this method, the nodes are grouped into two: those on the free surface and those on the body surface. For nodes on the free surface, two points on its normal direction are added. The velocity potentials at those two points are approximated by using a moving least squares method. A mixed two-point and three-point FD scheme is adopted to find the normal component of the fluid velocity. Once the normal velocity component at this node is found, the corresponding tangential velocity components are evaluated by considering the free-surface nodes connected to it using a least squares method based on the concept of directional derivatives. Some special treatments are also suggested to deal with the nodes on the waterlines and those near the body surface and the shape crest. For the nodes on the body surface, the normal velocity component is given by the boundary condition. The tangential velocity components are estimated in the same way as for the free-surface nodes. This method erases the limitation of the mesh structure in the existing velocity calculation scheme used by the conventional FEM and therefore satisfies the requirement of the cases with unstructured meshes. The efficiency and the accuracy of this method have been demonstrated by several numerical tests. Furthermore, a patch recovery technique is extended to remove the saw-tooth problem and therefore improve the accuracy of the velocity calculation. This method is based on the local normal-tangential coordinate system to overcome the failure of the general patch recovery

method when recovering the velocity on the body surface and the free surface with overturning waves since the profile of those surfaces cannot be expressed as a single-valued function of (x,y).

In order to overcome the difficulty in calculating the acceleration of and the force on the free-response floating bodies, an iterative procedure named ISITIMFB is developed. In this procedure, the acceleration in the current step is considered when estimating the body velocity. This implicit treatment, instead of an explicit scheme, distinguishes the ISITIMFB method from others. A multi-step method scheme without the need of sub-step calculation is used for the time integration. The positions of the free surface and the floating body are not changed during the iteration of this procedure. Therefore the coefficient matrix for the FEM formulation does not need to be updated. In order to achieve high efficiency, a least-square-method based prediction scheme together with an optimized under-relaxation coefficient is proposed. The results of this procedure show that the new developed ISITIMFB can find the acceleration of and the force acting on the floating bodies with higher efficiency than other methods and is more suitable for the QALE-FEM method.

10.2. Application to the waves generated by a wavemaker and their interaction with sandbars

The newly developed QALE-FEM method is used to simulate the wave generated by a wave maker and its interaction with sand bars on the sea bed and has been validated by comparing its numerical predictions with published analytical solutions, experimental data and results from other methods. The validation cases included the monochromatic, bichromatic and random waves with or without sandbars. In all cases, the results given by the present method agree reasonably with published ones (the relatively errors are all smaller than 1%).

For cases with sand bars on the sea bed, the nonlinear effects on the reflection properties are also investigated. It is shown that the effects tend to reduce the reflection coefficients and make the wave profiles more complex.

Assessments are made on the efficiency of moving mesh and quality of elements obtained by moving the mesh in a long-period simulation and show that unstructured mesh quality is satisfactorily maintained and the QALE-FEM requires only a small fraction of CPU time that would be spent on cases using the conventional FEM.

10.3. Application to the interaction between the water waves and floating structures

The QALE-FEM method is then used to simulate the nonlinear interaction between the water waves and the floating bodies. A comparison is made between the numerical prediction of forces on bodies undergoing a forced motion and analytical solutions. The difference between those results is less than 0.5%. The convergence property associated with force calculation in terms of different mesh sizes and different time steps is also investigated. The results show that

the numerical results with a specified accuracy are achievable by using a sufficiently fine mesh and small time step.

A further validation of the QALE-FEM method on modelling the response of the 2D floating body is also made. The RAOs of a 2D barged-type floating body are calculated and compared with the linear solution, experimental data and numerical results from other methods. The RAOs obtained by using the present method are closer to the linear solution when the incident wave is small but closer to the experimental data in cases with steeper waves. Further numerical investigation on the viscous effect near the resonance area is also carried out. The results demonstrate that the QALE-FEM method can give acceptable results through adding an appropriate empirical damping. More cases on the transient response of the floating body and the effect from the sandbar on the seabed are run, the strong nonlinearities associated with these problems are revealed. The results also illustrate that the reflected waves from the sandbars make the floating body in front of it undergo a larger motion but decrease those inside of the bar patch or after the bar patch. In order to shorten the transient period so that one may get the necessary data for RAO as soon as possible, the use of wavemaker ramp functions and an artificial damping technique has been developed. The effectiveness of this technique is demonstrated to be favourable.

The QALE-FEM method is also employed to simulate the interaction between the waves and 3D floating bodies. The responses of a moored spar platform to either monochromic waves or bichromic waves are compared with the experimental data, which show good agreement. The convergence properties of the QALE-FEM method in 3D cases are also investigated in terms of different time steps, mesh sizes and different control error for the ISITIMFB procedure. The RAOs of surge, heave and pitch of a barge-type floating body in head sea condition (zero incident angles) are calculated and compared with the experimental data and the linear solution in publication. The results show the difference between the present results and the experimental data is negligible. After being validated using the above two problems, the response of the Wigley Hull to waves is investigated. For the vessel in a head sea condition, the effects from the wave amplitude and the mooring lines are discussed. The results show that as the wave amplitude increases, the ratio of the motion to the wave amplitude tends to be decreased. They also show that the stronger mooring lines reduce the response of the Wiley Hull when the incident wave frequency is far away from natural frequency. However, near the resonance area the response of the Wigley Hull becomes larger. Finally, the cases involving Wigley Hull with different incident angles are investigated. The results illustrate that the incident angles seem not to affect the surge and heave but make the other four components of the motion change dramatically.

10.4. Efficiency of the QALE-FEM method

Assessments are also made of the efficiency of moving mesh and the quality of elements obtained by the QALE-FEM in 3D cases. It has been found that the quality of the unstructured mesh is satisfactorily maintained (the mesh quality during the calcualtion is at most 0.1% lower than that of intial mesh) at all time steps even when complex interactions between waves and free-response floating bodies are involved and also that the QALE-FEM requires a little time for moving mesh. Furthermore, as one of the most important factors which affect the computational efficiency in cases with a freely floating body, the efficiency of the ISITIMFB procedure is studied. As long as the number of iterations in the ISITIMFB procedure is less than 16, which is true for most cases and if an appropriate time step and control error is chosen, this method will be faster than the mode-decomposition method with 4-order Runge-Kutta scheme for time integration. Finally the overall computational efficiency of the QALE-FEM method is compared with a fast BEM method recently developed by Fochesato & Dias (2006). The results show that the QALE-FEM method is at least 7 times faster than the fast BEM for a similar 3D case of nonlinear water waves and their interactions with structures.

10.5. Recommendations

With respect to future work on the development and extension of the numerical method, the following is recommended:

1) Although the numerical techniques developed in this thesis, such as the method to redistribute nodes on the free surface and the method to calculate velocity, are all based on the assumption that the overturning wave may exist in the simulation, the QALE-FEM has not been applied to simulate the overturning wave problems. It should be applicable to simulate these problems.

2) At a sharp corner, there are no unique tangential and normal lines. This results in two difficulties. The first one is concerned with the mesh moving process. The remedy for overcoming the difficulty in this work is to prescribe a node at the corner or to smooth the corner. The former approach may not work if there are not enough nodes near the corner or the nodes near the corner become too close to each other. The latter approach may result in errors caused by the loss of the volume of the body. A more robust method should be developed. The second one is due to the singularity problem with the velocity at the corner of the floating body. In this work, the velocities at those corners are approximated by using an interpolating method based on the nodes around them. This treatment is very simple. Although in the cases presented in this thesis, no evident error appears, further validation may be preferred.

3) The method for computing the velocities suggested in the Chapter 5 appears to be quite accurate and efficient, as demonstrated in various cases. However, this method may not be

applicable in cases where the wave profile near the floating bodies is very thin. Another specialised method should be developed to deal with this problem.

4) In cases with 3D floating bodies or sandbars on the sea bed, the reflected waves will be scattered again when they reach the wave maker. In addition, in cases with 3D floating bodies, the scattered wave from the body surface will be reflected by the *y=const* walls. These two reflections are not desirable. In order to ease the effect, a longer/wider tank is used in this work. The efficiency may be enhanced by applying radiation condition at these boundaries. The technique used at the end of the tank may be extended to treat other boundaries.

5) In all the cases with freely floating bodies, the body surface is regarded as rigid. An extension of this method may be made to simulate flexible floating bodies. The method to move the mesh may also be extended to the simulation of other problems, such as ship capsizes

REFERENCE

Anderson, W. K., 1997,Aerodynamic Design Optimization on Unstructured Grids with a Continuous Adjoint Formulation, AIAA Paper 97-0643, *35th AIAA Aerospace Sciences Meeting.*

Ataie-Ashtiani, B., Farhadi, L., 2006, A stable moving-particle semi-implicit method for free surface flows, *Fluid Dynamics Research* 38: 241-256

Atluri, S.N., Zhu, T.,1998. A new meshless local Petrov-Galerkin (MLPG) approach in computational mechanics, *Comput. Mech.*, 22:117-127.

Aymone , J.L.F., Bittencourt , E., Creus, G.J., 2001, Simulation of 3D metal-forming using an arbitrary Lagrangian-Eulerian finite element method, *J. Mater. Process. Tech.*, 110: 218-232.

Bai, K.J., Choo, S.M,Chung, S.K., Kim, D. Y., 2005, Numerical solutions for nonlinear free surface flows by finite element methods , *Appl. Math. Comput.*, 163: 941-959.

Batina, J. T., 1989, Unsteady Euler Airfoil Solutions Using Unstructured Dynamic Meshes, AIAA Paper 89-0115, *27th AIAA Aerospace Sciences Meeting.*

Beck, R.F., 1994, Time-domain computations for floating bodies, *Appl. Ocean Res.*, 16:267-282

Beck,R.F.,1999, Fully nonlinear water wave computations using a desingularized Euler-Lagrange time-domain approach, in: O.Mahrenholtz,M. Markiewicz (Eds), Nonlinear Water Wave Interaction, *Adv. Fluid Mech.*, WIT Press,1-58.

Beck, R.F., Cao, Y., Scorpio, S., Schultz, W.W., 1994, Nonlinear ship motion computations using the desingularised method, *Proc. 20th Symp. Naval Hydro.*, U.C., Santa Barbara, CA.

Behr M. , Abraham F., 2002 Free surface flow simulations in the presence of inclined walls, *Comput Methods Appl.Mech.Engrg.*191: 5467-5483.

Biausser,B., Grilli, S.T., Fraunié, P,2003, Numerical Simulations of Three-dimensional Wave Breaking by Coupling of a VOF Method anda Boundary Element Method. Proceedings of *13th International Offshore and Polar Engineering Conference*, Honolulu, Hawaii, USA.

Blom, F.J., 2000, Considerations on the spring analogy, *Int. J. Numer. Meth. Fluids* 32: 647-668.

Bottasso, C.L., Detomi, D., Serra, R., 2005, The ball-vertex method: a new simple spring analogy method for unstructured dynamic meshes, *Comp. Meth. Appl. Mech. and Engrg.* 194: 4244-4264.

Bratland, A.K., Korsmeyer, F.T. , Newman, J.N.,1997.Time domain calculation in finite water depth, *12th International Workshop on Water Waves and Floating Bodies*, Carry-le-Rouet, France.

Broderick, L.L. , Leonard, W., 1995, Nonlinear response of membranes to ocean waves using boundary and finite elements , *Ocean Eng.*, 22: 731-745 .

Burden, R. L., Fairs, J.D., 2004, Numerical analysis (8th edition), ISBN-10: 0534392008, Brooks-Cole Publishing.

Burg, C. O. E., A,2004, Robust Unstructured Grid Movement Strategy Using Three-Dimensional Torsional Springs, AIAA Paper 2004-2529, *34th AIAA Fluid Dynamics Conference and Exhibit*, Portland, Oregon.

Cai, X., Langtangen, H.P., Nielsen, B.F., Tveito, A. , 1998, A finite element method for fully nonlinear water waves, *J. Comp. Physics,* 143:544-568.

Cao Y., Beck R. F., Schultz W. W., 1994, Nonlinear Computation of Wave Loads and Motions of Floating bodies in Incident Waves. *9th international workshop on water waves and floating bodies*, Kuju, Oita, Japan, 33-37.

Cao, Y., Schultz, W.W. and Beck, R.F., 1991, Three-dimensional desingularised boundary integral method for potential problems, *Int. J. Num. Meth. Fluids*, 12 : 785-803.

Carpenter, EB, Leonard J.W. , Yim S.C.S., 1995, Experimental and numerical investigations of tethered spar and sphere buoys in irregular waves. *Ocean Engng.*, 22 (8): 765-784.

Cavendish, J.C., Field, D.A. , Frey, W.H.,1995, An approach to automatic three-dimensional mesh generation. *Int. J. Numer. Methods Engrg.* 21: 329-347.

Celebi, M.S., Kim, M.H., Beck, R.F., 1998, Fully nonlinear 3D numerical wave tank simulation, *J. Ship Res.* 42:33–45.

Chamberlain, P. G., Porter, D., 1995, The modified mild-slope equation, *J. Fluid Mech.*, 291 : 393–407.

Chen X.J., 2003, A free-surface correction method for simulating shallow water flows, *J. Comput. Phys.*, 189:557-578.

Cho,Y.S., Jeong, W.C. , Woo,S.B., 2004, Finite element method for strong reflection of water waves , *Ocean Eng*, 31:653-667.

Clauss G.F., Steinhagen U., 1999,Numerical simulation of nonlinear transient waves and its validation by laboratory data, *Proc.9th International Offshore and Polar Engineering Conference*, Brest, France, 368-375.

Contento, G., 2000, Numerical wave tank computations of nonlinear motions of two-dimensional arbitrarily shaped free floating bodies, *Ocean Eng*, 27 :531-556.

Dalen, E.F.G, 1993, Numerical and theoretical studies on water waves and floating bodies. PhD thesis, University of Twente, Enschede.

Davies, A.G., Heathershaw, A.D.,1984, Surface-wave propagation over sinusoidally varying topography, *J. Fluid Mech,* 144: 419-440.

Davies, C. B., Venkatapathy, E.,1999, SAGE: The Self-Adaptive Grid Code, Version 3, NASA/TM-1999-208792.

Debroux, F. Prakash M., Cleary, P.W.. 2001, Three-dimensional modelling of a Tsunami interacting with real topographical coastline using smoothed particle hydrodynamics. *14th Australasian Fluid Mechanics Conference*, Adelaide University, 10-14 : 311-314.

Degand, C, Farhat, C., 2002, A three-dimensional torsional spring analogy method for unstructured dynamic meshes, *Comput. Struct.*, 80: 305-316.

Devrard D., Marcer R., Grilli S.T., Fraunie P. , Rey V., 2005. Experimental Validation of a Coupled BEM-Navier-Stokes Model for Solitary Wave Shoaliing and Breaking. *Proc. 5th Intl. on Ocean Wave Measurement and Analysis* (WAVES 2005, Madrid, Spain, July 2005), IAHR Publication, paper 166, 10.

Donea, J., Fasoli-Stella, P., Giuliani, S. , 1976, Finite element solution of transient fluid-structure problems in Lagrangian coordinates, *Proc.International Meeting on Fast Reactor Safety and Related Physics*, Chicago, 3: 1427–1435.

Donea J., Giuliani S., Halleux JP.,1982, An arbitrary Lagrangian-Eulerian finite element method for transient dynamic fluid-structure interactions. *Comput. Meths. Appl.Mech.Engrg*, 33: 689-723.

Eatock Taylor, R.1996, Analysis of non-linear wave-body interaction using finite elements, in Waves and Nonlinear Processes in Hydrodynamics, edited by Grue,J., Gjevik, B. & Weber, J.E., Kluwer Academic, Dordrecht.

Eatock Taylor R., 2005, Wave-maker ramp functions in numerical tanks. *International Workshop on Water Waves and Floating Bodies*, Norway.

Eatock Taylor, R, Wang, B.T., Wu, G.X., 1994, On the transient analysis of the wavemaker, 9th *International Workshop on Water Waves and Floating Bodies*, Kuju, Oita, Japan.

Fabián Duarte, Raúl Gormaz, Srinivasan Natesan, 2004,Arbitrary Lagrangian–Eulerian method for Navier–Stokes equations with moving boundaries, *Comput. Meth. Appl. Mech. Eng.*, 193: 4819-4836.

Faltinsen, O.M., Newman, J.N.& Vinje, T., 1995, Nonlinear wave loads on a slender vertical cylinder , *J.Fluid Mech.*, 289:189-198.

Farhat, C., Degand, C., Koobus, B.m Lesoinne, M., 1998. Torsional springs for two-dimensional dynamic unstructured fluid meshes, *Comput. Methods Appl. Mech. Eng.* 163: 231-245.

Farhat, C., Degand, C., Koobus, B.m Lesoinne, M., 2002. A three-dimensional torsional spring analogy method for unstructured dynamic meshes, *Comput. Struct.*, 80:305-316.

Ferrant, P., 1994, Radiation and diffraction of nonlinear waves in three dimensions, *BOSS, MIT*, 507-524.

Ferrant, P., 1995, Nonlinear wave loads and runup upon a surface piercing cylinder, *10th International Workshop on Water Waves and Floating Bodies*, Oxford, UK

Ferrant, P., Touze, D.L., Pelletier, K., 2003, Nonlinear time domain models for irregular wave diffraction about offshore structures, *Int. J., Numer. Meth. Fluids*, 43:1257-1277.

Fochesato C. , Dias F., 2006, A fast method for nonlinear three-dimensional free-surface waves, *Proc. R. Soc.A*,462:2715-2735.

Fochesato, C., Dias, F., Grilli, S.T., 2003. Numerical Model Using the Fast Multipole Algorithm for Nonlinear Three-dimensional Free Surface Waves over Arbitrary Bottom. *Proc. 13th Offshore and Polar Engng. Conf.* (ISOPE03, Honolulu, USA, May).

Fochesato C., Dias F., Grilli S.T. 2005. Wave energy focusing in a three-dimensional numerical wave tank. *Proc. 15th Offshore and Polar Engng. Conf.* (ISOPE05, Seoul, South Korea), 3: 24-31.

Frey, P. J. , Borouchaki H., George P., 1998, 3D Delaunay mesh generation coupled with an advancing-front approach, *Comput. Meth. Appl. Mech. Eng.*, 157: 115-131.

Fuhrman, D.R., Bingham, H.B., 2004. Numerical solutions of fully non-linear and highly dispersive Boussinesq equations in two horizontal dimensions. *Int. J. Numer. Methods Fluids* 44, 231–255.

Fuhrman D. R., Bingham H. B., Madsen P. A., 2005, Nonlinear wave–structure interactions with a high-order Boussinesq model. *Coast. Eng.* 52 : 655–672.

Gadala, M. S., 2004, Recent trends in ALE formulation and its applications in solid mechanics, *Comput. Meth. Appl. Mech. Eng.*, 193: 4247-4275.

Gadala,M.S., Movahhedy, M.R., Wang, J., 2002, On the mesh motion for ALE modeling of metal forming processes *Finite Elem. Anal. Des.*, 38:435-459.

Gobbi M F, Kirby J T., 1999 Wave evolution over submerged sills: tests of a high-order Boussinesq model. *Coast Engrg*, 37: 57-96.

Greaves, DM, 2004, Simulation of interface and free surface flows in a viscous fluid using adaptive quadtree grids, *Int. J. Numer. Meth. Fluids*, 44: 1093-1117.

Grilli S.T., Fochesato C., Dias F., 2005. Wave Energy Focusing in a Three-dimensional Numerical Wavetank. *Proc. 5th Intl. on Ocean Wave Measurement and Analysis* (WAVES 2005, Madrid, Spain), IAHR Publication, 197-207.

Grilli, S.T., Guyenne, P. , Dias. F., 2000, Numerical computation of 3D overturning waves. Abstract in Proc. 15th *International Workshop on Water Waves and Floating Bodies* ,Dan Caesarea, Israel.

Grilli, S.T., Guyenne, P., Dias, F., 2001, A fully nonlinear model for three-dimensional overturning waves over arbitrary bottom, *Intl J. Numer. Meth. Fluids*, 35: 829-867.

Grilli, S.T. , Horrillo J. 1997, Fully Nonlinear Properties of Periodic Waves Shoaling over Slopes. *Proc. 25th Intl. Conf. on Coastal Engineering* (ICCE25), Orlando, USA, September 96), Vol 1, 717-730.

Grilli, S.T. , Skourup, J. 1998, Depth inversion for nonlinear waves shoaling over a barred-beach. In Proc. *26th Int. Conf. on Coast. Eng.* (ICCE26, Copenhagen, Denmark), 603-616.

Grilli, S.T., Skourup, J., Svendsen, I.A. 1989, An Efficient Boundary Element Method for Nonlinear Water Waves. *Eng. Anal. Bound. Elem.*, 6 (2):97-107.

Grilli, S.T., Subramanya, R. 1994, Quasi-singular Integrations in the Modelling of Nonlinear Water Waves. *Eng. Anal. Bound. Elem.*, 13 (2): 181-191.

Grilli, S.T. , Subramanya, R. 1996, Numerical Modeling of Wave Breaking Induced by Fixed or Moving Boundaries. *Comput. Mech.*, 17 (6): 374-391.

Grilli, S.T., Svendsen, I.A. 1990, Corner Problems and Global Accuracy in the Boundary Element Solution of Nonlinear Wave Flows. *Eng. Anal. Bound. Elem.*, 7 (4): 178-195.

Heathershaw, A.D., 1982, Seabed-wave resonance and sand bar growth. *Nature*, 296 : 343-345.

Heinze, C., 2003, Nonlinear hydrodynamic effects on fixed and oscillating structures in waves, PhD Thesis, Department of Engineering Science, Oxford University.

Heister, S.D., 1997, Boundary element methods for two-fluid free surface flows , *Eng. Anal. Bound. Elem.*, 19: 309-317.

Henning,B., Peter, W.,2000, Arbitrary Lagrangian Eulerian finite element analysis of free surface flow, *Comput. Methods Appl. Mech. Engrg.* 190 : 95-109.

Hieu, P.D.,Katsutoshi, T., Ca, V.T.,2004, Numerical simulation of breaking waves using a two-phase flow model, *Appl. Math. Modeling*,28:983-1005.

Hirt C., Nichols B.,1981, Volume of fluid (VOF) method for the dynamics of free surface boundaries, *J. Comput. Phys.*, 39 : 210–225.

Hu, P.X., Wu, G.X., Ma, Q.W.,2002, Numerical simulation of nonlinear wave radiation by a moving vertical cylinder. *Ocean Eng.*, 29:1733-1750.

Hu, Z.Z., Greaves D.M., Wu, G.X.,2002, Numerical simulation of fluid flows using an unstructured finite volume method with adaptive tri-tree grids. *Int. J.Numer.Meth. Fluids*, 39:403-440.

Huerta A., Liu W.K.,1988. Viscous flow with large free surface motion. *Comput. Meths. Appl.Mech.Engrg*, 69:277-324.

Kanoria,M., Mandal,B.N., 2002,Water wave scattering by a submerged circular-arc-shaped plate , *Fluid. Dynam. Res.*, 31:317-331.

Kashiwagi, M., 1996, Full-nonlinear simulations of hydrodynamic forces on a heaving two-dimensional body. *J. Soc. Nav. Archit. Jpn.* 180: 373–381.

Kashiwagi, M., Momoda, T., Inada, M., 1998, A time-domain nonlinear simulation method for wave-induced motions of a floating body. *J. Soc. Nav. Archit. Jpn.* 84:143–152.

Kashiwagi M., 2000, Nonlinear simulations of wave-induced motions of a floating body by means of the mixed Eulerian-Lagrangian method, *Mech. Engrs*,214: 841-855.

Kim M.H., Celebi M.S., Kim D.J.,1998, Fully nonlinear interactions of waves with a three-dimensional body in uniform currents. *Appl. Ocean Res.*,20: 309–321.

Kim M.H., Chen W. 1994, Slender-body approximation for slowly-varying wave loads in multi-directional waves. *Appl. Ocean Res.*,16:141-163.

Kjellgren P., Hyvarinen J.,1998, An arbitrary Lagrangian-Eulerian finite element method. *Comput. Mech.*,21: 81-90.

Koo, W., 2003, Fully nonlinear wave-body interactions by a 2D potential numerical wave tank. PhD Thesis, Texas A&M University.

Koo, W., Kim, M.,2004, Freely floating body simulation by a 2D fully nonlinear numerical wave tank. *Ocean Eng.*, 31: 2011-2046.

Koutandos, E. V., Karambas Th. V. , Koutitas C. G., 2004. Floating Breakwater Response to Waves Action Using a Boussinesq Model Coupled with a 2DV Elliptic Solver. *J. Wtrwy., Port, Coast., and Oc. Engrg.*, 130 (5): 243-255.

Kyoung, J.H., Hong, S.Y., Kim, J.W., Bai, K.J., 2005, Finite-element computation of wave impact load due to a violent sloshing, *Ocean Eng*, 32: 2020-2039.

Lalli,F.,1998, On the accuracy of the desingularized boundary integral method in free surface flow problems, *Int. J. Numer. Meth. Fluids*, 25:1163-1184.

Layton, A.T., Christara, C.C., Jackson,.K.R., 2006, Quadratic spline methods for the shallow water equations on the sphere: Galerkin. *Math. Comput. Simulat.*, 71:175-186.

Lee, J-F., Leonard, J.W. 1988. A finite element model of wave-structure interactions in the time domain. *Ocean Engrg* 14, 469-488.

Lewis, R.W., Zheng, Y., Gethin,.D.T., 1996, Three-dimensional unstructured mesh generation: Part 3. Volume meshes. *Comput. Meth. Appl. Mech. Eng.*, 134 (3-4): 285-310

Li, R., Tang T., Zhang P.,2002, A moving mesh finite element algorithm for singular problems in two and three space dimensions. *J. Comput. Phys.*,177:365-393.

Lin, W. M., Newman, J. N., Yue, D.K.P, 1984,D. K. Nonlinear forced motion of floating bodies. In Proc. *15th Symp. on Naval Hydrology*, Hamburg, Germany, 33–49.

Liu, Y, Yue, D. K. P., 1998, On generalized Bragg scattering of surface waves by bottom ripples, *J. Fluid Mech.*, 356: 297-326.

Lohner R, Yang C., 1996, Improved ALE mesh velocities for moving bodies. *Commun. Numer. Methods Eng.*, 12: 599–608.

Longuet-Higgins, M.S., Cokelet, E.D.,1976, The deformation of steep waves on water: I. a numerical method of computation, *Proc. R. Soc. Lond. A* 350 : 1–26.

Longuet-Higgins, M.S.,2001, Vertical jets from standing waves, *Proceedings of the Royal Society A: Mathematical, Physical and Engineering Sciences* . 457:495-510.

Ma, Q.W., 1998, Numerical simulation of nonlinear interaction between structures and steep waves, *PhD Thesis*, Department of Mechanical Engineering, University College London, UK.

Ma, Q. W. 2005, Meshless local Petrov-Galerkin method for two-dimensional nonlinear water wave problems, *J. Comput. Phys.*,205: 611-625 .

Ma Q. W., Patel M. H., 2001, On the nonlinear forces acting on a floating spar platform in ocean waves. *Appl. Ocean Res.*, 23: 29-40.

Ma, Q.W., Wu, G.X., Eatock Taylor, R., 2001a, Finite element simulation of fully non-linear interaction between vertical cylinders and steep waves. Part 1: Methodology and numerical procedure, *Int.J.Numer. Meth. Fluids*,36: 265-285.

Ma, Q.W., Wu, G.X., Eatock Taylor, R., 2001b, Finite element simulation of fully non-linear interaction between vertical cylinders and steep waves. Part 2: Numerical results and validation, *Int.J.Numer. Meth. Fluids*, 36: 287-308.

Ma, Q.W., Yan, S., 2006, Quasi ALE finite element method for nonlinear water waves. *J. Comput. Phys*, 212:52-72.

Madsen, P.A., Bingham, H.B., Liu, H., 2002. A new Boussinesq method for fully nonlinear waves from shallow to deep water. *J. Fluid Mech.* 462:1-30.

Madsen, P.A., Bingham, H.B., Schaffer, H.A., 2003. Boussinesq type formulations for fully nonlinear and extremely dispersive water waves: derivation and analysis. *Proc. R. Soc. Lond.*, A 459, 1075–1104.

Madsen, P A, Murray, R Sorensen, O R.,1991, New form of the Boussinesq equations with improved linear dispersion characterics. *Coast. Eng*,15 (4):371-388.

Madsen, P A, Murray, R Sorensen, O R.,1992. New form of the Boussinesq equations with improved linear dispersion characterics.part 2,A slowly varying bathymetry. *Coast. Eng*,18:183-204.

Maisano, G., Micheletti, S., Perotto, S. , Bottasso, C.L.,2006, On some new recovery-based a posteriori error estimators , *Comput. Meth. Appl. Mech. Eng.*, 195 : 4794-4815.

Malenica,S.,Molin.,B.,1995,Third-harmonic wave diffraction by a vertical cylinder, *J.Fluid Mech*, 302:209-229.

Markiewicz, M., Ben-Nasr, K., Mahrenholtz, O.,2003. Numerical simulation of nonlinear wave radiation in inviscid fluid with a free surface, *Int. J. Numer. Meth. Fluids*, 43:1279-1300.

Mayer S., Garapon, A., Sorensen L.,1997. Wave tank simulations using a fractional-step method in a cell-centred finite volume implementation. *12th international workshop on water waves and floating body*. Carry-le-Rouet, France.

Mei, C.C., 1985, Resonant reflection of surface water waves by periodic sandbars, *J. Fluid Mech.*, 152: 315-335.

Mei, C.C.,1989, The applied dynamics of Ocean Surface waves. *World Scientific.*

Monaghan, J.J. 1988, An introduction to SPH. *Comput. Phys. Commun.* 48:89-102

Monaghan, J.J. 1994, Simulating free surface flows with SPH, *J. Comp. Phys.*, 110:399-406.

Nakayama, T., Washizu, K., 1980. Nonlinear analysis of liquid motion in a container subjected to a forced pitching oscillation. *Int. J. Numer. Meth. Eng.*, 15: 1207–1220.

Navti S., Lewis R., Taylor C.,1998, Numerical simulation of viscous free surface flow, *Int. J. Numer. Methods Heat Fluid Flow*, 18: 445–464.

Nestegard, A.,1999, Status of Nonlinear hydrodynamic modelling, *Technical report, DNV*, Norway.

Newman, J.N.,1977. Marine Hydrodynamics. MIT press.

Nojiri N., Murayama K.,1975,A study on the drift force on two dimensional floating body in regular waves. *Trans. West-Japan Soc. Nav. Arch*, Vol.51.

Nwogu,O, 1993.Alternative form of Boussinesq equations for nearshore wave propagation. *J.Water.Port Coastal Ocean Eng.* ASCE, 119 (6):618-638.

Park, J.C., Kim, M.H., Miyta, H., 2001, Three dimensional numerical wave tank simulations on fully nonlinear wave-current-body interactions. J. *Mar. Sci. Tech.*, 6: 70-82.

Peregrine D H.,1967. Long waves on a beach. *J. Fluid Mech.*, 27: 815～827.

Porter, P., D.Porter, D., 2003, Scattered and free waves over periodic beds, *J. Fluid Mech.*, 483, 129–163.

Qiu, W., 2001, A panel-free method for time-domain analysis of floating bodies in waves, PhD thesis, Dalhousie University.

Rainey, RCT, 1989, New equation for calculating wave loads on offshore structures, *J. Fluid Mech*, 204: 295-324.

Rainey, R.C.T., 1997, Violent surface motion around vertical cylinders in large, steep waves- is it the result of the step change in relative acceleration?, *12th International Workshop on Water Waves and Floating Bodies*, Carry-le-Rouet.

Ran, Z., Kim M.H Zheng W., 1998, Coupled dynamic analysis of a moored spar in random waves and currents (time-domain vs. Frequency-domain analysis), OMAE98-0604.

Sannasiraj, S.A., Sundaravadivelu, R., 1995. The hydrodynamic behaviour of long floating structures in directional seas. *Appl. Ocean Res.* 17: 233–243.

Sannasiraj, S.A., Sundar, V., Sundarravadivelu, R., 1998. Mooring forces and motion responses of pontoon-type floating breakwaters. *Ocean Eng.* 25 (1): 27–48.

Sannasiraj, S.A., Sundaravadivelu, R., Sundar, V., 2000. Diffraction–radiation of multiple floating structures in directional waves. *Ocean Eng.* 28: 201–234.

Schoberg,T. Chaplin,J.R., 2003, Computation of Nonlinear Wave Reflections and Transmissions from Submerged Horizontal Cylinder. *Int. J. Offshore Polar Eng*, 13:29-37

Schønberg, T., Rainey, C.T.,2003, A hydrodynamic model of Green Water incidents, *Appl. Ocean Res.*, 24:299-307.

Sclavounos, P.D., Kim,Y.W., 1995, Third order diffraction of surface waves by a time-dimain ranking panel method, *10th International Workshop on Water Waves and Floating Bodies*, Oxford, UK.

Sen, D,1993, Numerical simulation of motions of two-dimensional floating bodies. *J. Ship Res.* 37, (4) :307-330.

Shashikala, A.P., Sundaravadivelu, R., Ganapathy, C., 1997, Dynamics of a moored barge under regular and random waves, *Ocean Engng*, 24 (5): 401-430.

Shao, S., Lo, E.Y.M., 2003, Incompressible SPH method for simulating Newtonian and non-Newtonian flows with a free surface. *Adv. Water Resour.* 26: 787-800

Skourup, J., Buchmann B., Bingham, H., 1997. A second order 3D BEM for wave-structure interaction. *12th International Workshop on Water Waves and Floating Bodies*, France.

Souli, M., Zolesio, J.P., 2001, Arbitrary Lagrangian–Eulerian and free surface methods in fluid mechanics, Comput. Methods *Appl. Mech. Engrg.*, 191: 451-466.

Souli M., Ouahsine A., Lewin L., 2000 AlE formulation for fluid-structure interaction problems. Comput. Methods *Appl. Mech.Eng*, 190: 659-675.

Spivak,B., Vanden-Broeck, J.M., Miloh,T.,2002, Free surface wave damping due to viscosity and surfactants. *Eur. J. Mech. B Fluid.*,21: 207-224

Sriram, V. , Sannasiraj S.A., Sundar, V.,2005, Simulation of 2-D nonlinear waves using finite element method with cubic spline approximation , *J. Fluid Struct.*,22:663-681

Tanaka, M. 1986, The stability of solitary waves. *Phys. Fluids*, 29 (3): 650–655.

Tanizawa, K.,1995, A nonlinear simulation method of 3-D body motions in waves (1st Report). *J. Soc. Nav. Arch. Japan*, 178:179-191.

Tanizawa K., Minami M.,1998, On the accuracy of NWT for radiation and diffraction problem. *The 6th Symposium on Nonlinear and Free-Surface Flow.*

Tanizawa K, Minami M., Naito S.,1999, Estimation of wave drift force by numerical wave tank. *Proc. 9th ISOPE Conf.* vol3, Brest.

Telste, J.G.,1985, Calculaion of fluid motion resulting from large-amplitude forced heave motion of a two dimensional cylinder in a free surface. *Proc. 4th Int. Conf. on Numerical Ship Hydrodynamics*, Washington, U.S.A., 81-93.

Teng B, Zhao M. , Bai W.,2001, Wave diffraction in a current over a local shoal. *Coast. Eng.*,42:163-172.

Tezduyar, T, Behr, M., Liou, J.A., 1992,A new strategy for finite element computations involving moving boundaries and interfaces- the deforming spatial domain/space-time procedure:1, the concept and the preliminary numerical tests. *Comput. Meth.Appl Meth.Eng*,94: 339-351.

Turnbull, M.S., Borthwick, A.G.L., Eatock Taylor, R., 2003, Wave–structure interaction using coupled structured–unstructured finite element meshes , *Appl. Ocean Res.*, 25: 63-77

Vinje, T. , Brevig, P., 1981,Nonlinear ship motion. In Proc. *3rd Int. Conf. on Numerical Ship Hydrodynamics*, Paris, France,. 257–268.

Walkley M. , Berzins M., 2002, A Finite Element Method for the Two-dimensional Extended Boussinesq Equations. *Int. J. Numer. Meth. Eng.*. 39 (10):865-885.

Wang C.Z. , Khoo, B.C.,2005, Finite element analysis of two-dimensional nonlinear sloshing problems in random excitations ,*Ocean Eng.*, 32: 107-133 .

Wang, C. Z., Wu, G.X., 2006. An unstructured-mesh-based finite element simulations with non-wall-sided bodies, *J. Fluid Struct.*, 22 (4):441-461.

Wang, P., Yao, Y., Tulin, M., 1995, An efficient numerical tank for nonlinear water waves, based on the multi-subdomain approach with BEM, *Int. J. Num. Meth. Fluids*, 20:1315-1336.

Wang, Q.X.,2005, Unstructured MEL modeling of nonlinear unsteady ship waves, *J. Comp. Phys.*,120:368-385.

Weggel, DC, Roesset JM., Davies RL, Steen, A, Frimm F., 1997, Neptune Project: Spar history and design considerations. OTC 8382, *Offshore Technology Conference*, Houston, TX, USA, 2: 237-251.

Wehausen,J.V., Laiton,E.V.,1960, Surface waves, Handbuck der physic IX.

Wei G, Kirby J T, Grilli S T., Ravishankar S. 1995, A fully nonlinear Boussinesq model for surface waves. Part 1 . Highly nonlinear unsteady waves. *J Fluid Mech*, 294: 71～92.

Westhuis, J.H., Andonowati , 1998, Applying the finite element method in numerically solving the two dimensional free-surface water wave equations, *13th International Workshop on Water Waves and Floating Bodies*, Alphen aan den Rijn, The Netherlands, 171-174.

William Gear C.1971, Numerical Initial Value Problems in Ordinary Differential Equations. Prentice-Hall , Inc. Englewood Cliffs, New Jersey.,102-115.

Wu, G.X., Eatock Taylor,R.,1994, Finite element analysis of two dimensional non-linear transient water waves, *Appl. Ocean Res.* 16:363–372.

Wu, G.X., Eatock Taylor, R.,1995, Time stepping solution of the two dimensional non-linear wave radiation problem, *Ocean Eng.* 22: 785–798.

Wu, G.X., Eatock Taylor, R.,1996, Transient motion of a floating body in steep water waves, *11th International Workshop on Water Waves and Floating Bodies*, Hamburg, Germany.

Wu, G.X., Eatock Taylor, R., 2003, The coupled finite element and boundary element analysis of nonlinear interactions between waves and bodies *Ocean Eng.* 30: 387–400.

Wu, G.X., Eatock Taylor, R , Greaves, D.M.,2004, The effect of viscosity on the transient free surface waves in a two-dimensional tank. *J. Eng. Math..*, 40:77-90.

Wu, G.X., Hu, Z.Z., 2004, Simulation of nonlinear interactions between waves and floating bodies through a finite-element-based numerical tank, *Proceedings A of the Royal Society*, 460, No. 2050, 3037-3058.

Xue, M. , Yue, D. K., 1995, Fully nonlinear three dimensional interaction between water waves and a surface-piercing body, *10th international workshop on water waves and floating bodies*, Oxford, UK

Xü, H., Yue, D.K.P.,1992, Numerical study of three dimensional overturning waves. *Proc. 7th International Workshop on Water Waves and Floating Bodies*, Val de Reuil, France.

Yan, S., Ma, Q.W., 2005, Application of QALE-FEM to the interaction between nonlinear water waves and periodic bars on the bottom, *20th International Workshop on Water Waves and Floating Bodies*, Norway:

Yan S., Ma Q.W., 2006, Numerical simulation of fully nonlinear interaction between steep waves and 2D floating bodies using the QALE-FEM method, *J. Comput. Phys.* doi:10.1016/j.jcp. 2006.06.046.

Yang S. , Lee, L., 1996, Aeroelastic analysis for flap of airfoil in transonic flow, *Comput. Struct.*, 61:421-430.

Yeung R.W. , Wu C.F., 1989, Nonlinear wave-body motion in a closed domain. *Comput Fluid*, 17 :351-370.

Yeung R.W., Vaidhanathan M.,1990. Nonlinear wave diffraction over submerged obstacles. *5th Workshop on Water Waves and Floating Bodies, Manchester*, UK.

Yue, W., Lin, C.L., Patel, V.C., 2003, Numerical simulation of unsteady multidimensional free surface motions by level set method, *Int. J. Numer. Meth. Fluids*, 42: 853-884.

Zeng, D., Ethier, C. R., 2005, A semi-torsional spring analogy model for updating unstructured meshes in 3D moving domains. *Finite Elem. Anal. Des.*, 41:1118-1139.

Zhang, D.H., Chwang, A, T., 1996, Numerical study of nonlinear shallow water waves produced by a submerged moving disturbance in viscous flow. *Phys. Fluid* 8:147-155.

Zhang, D.H., Chwang, A, T., 1999, On solitary waves forced by underwater moving objects. *J.Fluid Mech.*,389:119-135.

Zhang Q., Hisada T., 2001, Analysis of fluid-structure interaction problems with structural buckling and large domain changes by ALE finite element method. *Comput. Methods Appl.Mech.Engrg*,190:6341-6357.

Zhang S., Williams A. N., 1996. Time-domain simulation of the generation and propagation of second-order Stoles waves in a two-dimensional wave flume. Part 1: Monochromatic wavemaker motions. *J. Fluid and Structure*, 10:319-335.

Zheng, Y.H., Shen, Y.M., You,.Y.G., Wu, B.J, Jie, D.S., 2004,On the radiation and diffraction of water waves by a rectangular structure with a sidewall , *Ocean Engrg*, 31: 2087-2104 .

Zienkiewicz, O.C. Zhu, J.Z.,1987, A simple error estimator and adaptive procedure for practical engineering analysis, *Int. J. Numer. Methods Engrg.* 24: 337–357.

Zienkiewicz, O.C. Zhu, J.Z.1992,The superconvergent patch recovery (SPR) and adaptive finite element refinement, *Comput. Methods Appl. Mech. Engrg.* 101 :207–224.

APPENDIX A

Treatment of the rigid boundary condition for $\partial\phi/\partial t$ on the FEM formulation

In Section 3.5.2, the integrated rigid boundary condition for $\partial\phi/\partial t$ is written as

$$\iint_{\Delta S_n(e_k)} N_I f_n dS = B_{n1}^{e_k} + B_{n2}^{e_k} \tag{a1}$$

where

$$B_{n21}^{e_k} = -\oint_{sb} - N_i(U_{\tau_2}\phi_n - U_n\phi_{\tau_2})d\tau_1 + N_i(U_{\tau_1}\phi_n - U_n\phi_{\tau_1})d\tau_2 \tag{a2}$$

$$B_{n22}^{e_k} = -\iint_{\Delta S_n(e_k)}\left[\phi_{\tau_1}\frac{\partial(N_iU_n)}{\partial\tau_1} + \phi_{\tau_2}\frac{\partial(N_iU_n)}{\partial\tau_2} - \phi_n\frac{\partial(N_iU_{\tau_1})}{\partial\tau_1} - \phi_n\frac{\partial(N_iU_{\tau_2})}{\partial\tau_2}\right]dS \tag{a3}$$

in which $\phi_{\tau_1},\phi_{\tau_2}$ and ϕ_n represent $\frac{\partial\phi}{\partial\tau_1}$, $\frac{\partial\phi}{\partial\tau_2}$ and $\frac{\partial\phi}{\partial n}$, $U_n,U_{\tau_1},U_{\tau_2}$ are normal and tangential velocity components, respectively.

In a triangular element (i,*j*,*k*) on the boundary, the normal and tangential directions are constant. Therefore, the shape function in a local normal-tangential coordinate system $(\vec{\tau}_1,\vec{\tau}_2,\vec{n})$ can be written as

$$N_i = (a_i + b_i\tau_1 + c_i\tau_2)/2\Delta \tag{a4}$$

and

$$a_i = \tau_{1j}\tau_{2k} - \tau_{1k}\tau_{2j}; b_i = \tau_{2j} - \tau_{2k}; c_i = \tau_{1k} - \tau_{1j} \tag{a5}$$

in which Δ is the area. τ_1,τ_2,n are the coordinate values in the directions of $\vec{\tau}_1,\vec{\tau}_2,\vec{n}$, respectively.

1) Treatment of term $B_{n22}^{e_k}$

In order to treat $B_{n22}^{e_k}$, it is separated into several terms. Each term is expanded, as follows

$$\frac{\partial}{\partial\tau_1}(N_iU_n) = \frac{\partial N_i}{\partial\tau_1}U_n + \frac{\partial U_n}{\partial\tau_1}N_i = \frac{U_nb_i}{2\Delta} + \frac{a_i + b_i\tau_1 + c_i\tau_2}{2\Delta}\left(\vec{\Omega}\times\frac{\partial\vec{r}_b}{\partial\tau_1}\right)\cdot\vec{n} \tag{a6}$$

where $\vec{U} = \vec{U}_c + \vec{r}_b\times\vec{\Omega}$ is used; . it can be seen from this equation that $\frac{\partial\vec{r}_b}{\partial\tau_1}$ is required. The following is used to derive this term.

At an arbitrary curved surface $f(x,y,z)$, the position vector can be expressed as

$$\vec{r} = x\vec{e}_x + y\vec{e}_y + z\vec{e}_z \tag{a7}$$

where $\vec{e}_x,\vec{e}_y$ and $\vec{e}_z$ are the unit vectors in *x*-,*y*- and *z*-directions. The normal tangential coordinate $(\vec{\tau}_1,\vec{\tau}_2,\vec{n})$ can be expressed as

$$\tau_1 = \tau_1(x,y,z), \tau_2 = \tau_2(x,y,z), n = n(x,y,z) \tag{a8}$$

The position vector, therefore, is written as $\vec{r} = \vec{r}(\tau_1, \tau_2, n)$. Then the unit tangent vector in τ_1-direction is

$$\vec{e}_{\tau_1} = \frac{\dfrac{\partial \vec{r}}{\partial \tau_1}}{\left|\dfrac{\partial \vec{r}}{\partial \tau_1}\right|} = \frac{1}{h_1}\frac{\partial \vec{r}}{\partial \tau_1} \tag{a9}$$

therefore, $\dfrac{\partial \vec{r}}{\partial \tau_1} = h_1 \vec{e}_{\tau_1}$ and $h_1 = \left|\dfrac{\partial \vec{r}}{\partial \tau_1}\right|$. Similarly, it can be found that the unit vectors in the other two directions are giving by,

$$\frac{\partial \vec{r}}{\partial \tau_2} = h_2 \vec{e}_{\tau_{21}} \tag{a10}$$

and

$$\frac{\partial \vec{r}}{\partial n} = h_3 \vec{e}_n \tag{a11}$$

where $h_2 = \left|\dfrac{\partial \vec{r}}{\partial \tau_2}\right|$ and $h_3 = \left|\dfrac{\partial \vec{r}}{\partial n}\right|$. Since,

$$\frac{\partial \vec{r}}{\partial n} = \frac{\partial \vec{r}}{\partial \tau_1} \times \frac{\partial \vec{r}}{\partial \tau_2} = h_2 h_3 \vec{e}_n \tag{a12}$$

combining Eq. (a12) and (a11) , one can get

$$h_1 = h_2 h_3 \tag{a13}$$

Similarly, $h_2 = h_1 h_3$, $h_3 = h_1 h_2$ and so $h_1 = h_2 = h_3 = 1$. Therefore, one can get

$$\frac{\partial \vec{r}}{\partial \tau_1} = \vec{e}_1; \frac{\partial \vec{r}}{\partial \tau_2} = \vec{\tau}_2; \frac{\partial \vec{r}}{\partial n} = \vec{n} \tag{a14}$$

based on this, Eq. (a6) can be rewritten as

$$\frac{\partial}{\partial \tau_1}(N_i U_n) = \frac{U_n b_i}{2\Delta} + n_i \Omega \cdot (\vec{\tau}_1 \times \vec{n}) = \frac{U_n b_i}{2\Delta} - \vec{n}_i \cdot \vec{\Omega} \tag{a15}$$

Similarly $\dfrac{\partial}{\partial \tau_2}(N_i U_n)_{\tau_1}$, $\dfrac{\partial}{\partial \tau_1}(N_i U_{\tau_1})$ and $\dfrac{\partial}{\partial \tau_2}(N_i U_{\tau_2})$ are expanded. Therefore, the term $B^{e_k}_{n22}$ can be rewritten as

$$B_{n22}^{e_k} = -\frac{\Delta}{3}(-\frac{\phi_{\tau_1 i}\Omega_{\tau_2 i}}{2} - \frac{\phi_{\tau_1 j}\Omega_{\tau_2 j}}{4} - \frac{\phi_{\tau_1 j}\Omega_{\tau_2 j}}{4} + \frac{\phi_{\tau_2 i}\Omega_{\tau_1 i}}{2} + \frac{\phi_{\tau_2 j}\Omega_{\tau_1 j}}{4} + \frac{\phi_{\tau_2 k}\Omega_{\tau_1 k}}{4})$$

$$-\frac{b_i}{2\Delta}\iint_{\Delta S_n(e_k)}(U_n\phi_{\tau_1} - U_{\tau_1}\phi_n)ds + \frac{c_i}{2\Delta}\iint_{\Delta S_n(e_k)}(U_n\phi_{\tau_2} - U_{\tau_2}\phi_n)ds$$

$$= -\frac{b_i}{2\Delta}\frac{\Delta}{3}\left[(U_n\phi_{\tau_1} - U_{\tau_1}\phi_n)_i + (U_n\phi_{\tau_1} - U_{\tau_1}\phi_n)_j + (U_n\phi_{\tau_1} - U_{\tau_1}\phi_n)_k\right]$$

$$-\frac{c_i}{2\Delta}\frac{\Delta}{3}\left[(U_n\phi_{\tau_2} - U_{\tau_2}\phi_n)_i + (U_n\phi_{\tau_2} - U_{\tau_2}\phi_n)_j + (U_n\phi_{\tau_2} - U_{\tau_2}\phi_n)_k\right]$$

$$-\frac{\Delta}{3}(-\frac{\phi_{\tau_1 i}\Omega_{\tau_2 i}}{2} - \frac{\phi_{\tau_1 j}\Omega_{\tau_2 j}}{4} - \frac{\phi_{\tau_1 j}\Omega_{\tau_2 j}}{4} + \frac{\phi_{\tau_2 i}\Omega_{\tau_1 i}}{2} + \frac{\phi_{\tau_2 j}\Omega_{\tau_1 j}}{4} + \frac{\phi_{\tau_2 k}\Omega_{\tau_1 k}}{4}) \tag{a16}$$

(2) The treatment of $B_{n21}^{e_k}$

. Suppose the physical properties are linear on the element of a curve, then

$$N_i = \frac{\tau_1 - \tau_{1j}}{\tau_{1i} - \tau_{1j}} = \frac{\tau_2 - \tau_{2j}}{\tau_{2i} - \tau_{2j}} \tag{a17}$$

Let $\psi = -U_{\tau_2}\phi_n + U_n\phi_{\tau_2}$, $\vartheta = U_{\tau_1}\phi_n - U_n\phi_{\tau_1}$, then $B_{n21}^{e_k}$ can be rewritten as

$$B_{n21}^{e_k} = -\oint_{sb} N_i\psi d\tau_1 + N_i\vartheta d\tau_2 \tag{a18}$$

In an element on the waterline,

$$B_{n21}^{e_k} = \int_{1j}^{\tau_{1i}}\left(\frac{\tau_1 - \tau_{1j}}{\tau_{1i} - \tau_{ij}}\right)^2\psi_i d\tau_1 + \int_{1j}^{\tau_{1i}}\left(\frac{\tau_1 - \tau_{1j}}{\tau_{1i} - \tau_{ij}}\right)\left(\frac{\tau_1 - \tau_{1i}}{\tau_{1j} - \tau_{1i}}\right)\psi_j d\tau_1$$

$$+ \int_{2j}^{\tau_{2i}}\left(\frac{\tau_2 - \tau_{2j}}{\tau_{2i} - \tau_{2j}}\right)^2\vartheta_i d\tau_2 + \int_{2j}^{\tau_{2i}}\left(\frac{\tau_2 - \tau_{2j}}{\tau_{2i} - \tau_{2j}}\right)\left(\frac{\tau_2 - \tau_{2i}}{\tau_{2j} - \tau_{2i}}\right)\vartheta_j d\tau_2$$

$$= \frac{1}{3}\left|\tau_{1i} - \tau_{1j}\right|(\psi_i + \frac{1}{2}\psi_j) + \frac{1}{3}\left|\tau_{2i} - \tau_{2j}\right|(\vartheta_i + \frac{1}{2}\vartheta_j) \tag{a19}$$